

Smith

NASA CR-132896

HIGH DATA RATE OPTICAL TRANSCEIVER TERMINAL

E. S. Clarke, et al

McDonnell Douglas Astronautics Company - East

Box 516

St. Louis, Mo. 63166

May 1973

Final Report

Prepared for

GODDARD SPACE FLIGHT CENTER

Greenbelt, Maryland 20771

Reproduced by
**NATIONAL TECHNICAL
INFORMATION SERVICE**
US Department of Commerce
Springfield, VA. 22151

PRICES SUBJECT TO CHANGE

(NASA-CR-132896) HIGH DATA RATE OPTICAL
 TRANSCIVER TERMINAL Final Report, 30
 Jun. 1972 - 26 Jan. 1973
 (McDonnell-Douglas Astronautics Co.)
 CSCI 20E G3/16 27004
 Unclass N74-15149

JAN 1973
 RECEIVED
 NASA STI FAC II
 INPUT BR2

0111213191516171819202122232425262728

481

1. Report No.	2. Government Accession No.	3. Recipient's Catalog No.	
4. Title and Subtitle HIGH DATA RATE OPTICAL TRANSCEIVER TERMINAL		5. Report Date May 1973	6. Performing Organization Code
7. Author(s) E.S. Clarke, et. al	8. Performing Organization Report No.		
9. Performing Organization Name and Address McDonnell Douglas Astronautics Company—East Box 516 St. Louis, Mo. 63166		10. Work Unit No.	11. Contract or Grant No. NAS 5-23154
12. Sponsoring Agency Name and Address Goddard Space Flight Center Greenbelt, Maryland 20771 Attn: L.O. Caudill, Code 524.2		13. Type of Report and Period Covered Final Report	
14. Sponsoring Agency Code			
15. Supplementary Notes			
16. Abstract <p>The objectives of this study were: (1) to design a 400 Mbps optical transceiver terminal to operate from a high-altitude balloon-borne platform in order to permit the quantitative evaluation of a space-qualifiable optical communications system design, (2) to design an atmospheric propagation experiment to operate in conjunction with the terminal to measure the degrading effects of the atmosphere on the links, and (3) to design typical optical communications experiments for space-borne laboratories in the 1980-1990 time frame. As a result of the study, a transceiver package has been configured for demonstration flights during late 1974. The transceiver contains a 400 Mbps transmitter, a 400 Mbps receiver, and acquisition and tracking receivers. The transmitter is a Nd:YAG, 200 Mhz, mode-locked, CW, diode-pumped laser operating at 1.06 um requiring 50 mW for 6 dB margin. It will be designed to implement Pulse Quaternary Modulation (PQM). The 400 Mbps receiver utilizes a Dynamic Crossed-Field Photomultiplier (DCFP) detector. The acquisition receiver is a Quadrant Photomultiplier Tube (QPMT) and receives a 400 Mbps signal chopped at 0.1 Mhz. The tracking QPMT can operate on either a 400 Mbps uplink signal or on a simulated pulsed beacon having 200 nanosecond pulses occurring at 1.6 kHz. The opto-mechanical layout is configured to be carried on the elevation gimbal of the Balloon Atmospheric Propagation Experiment (BAPE) vehicle. The package weight is estimated at 162 pounds. It will require 296 watts of battery power. The experiment defined measures link performance parameters of bit error rate and outage and correlates these parameters with measured atmospheric parameters. The accuracy of the fine tracking system is measured as a function of system parameters of beacon power and servo loop bandwidth.</p> <p>Five manned laboratory optical communications experiments are described, three near space and two deep space. The near space experiments are: (1) mode locked Nd:YAG transceiver systems in 400 Mbps to 1 Gbps data rate regime, (2) simultaneous multi-access low data rate optical links with a single synchronous satellite, and (3) synchronous-to-ground link atmospheric propagation experiment. The deep space experiments are: (1) deep space laser communications receiving terminal experiment, and (2) a short pulse, Pulse Interval Modulation (PIM) deep space probe transmitter simulations experiment.</p>			
17. Key Words (Selected by Author(s))		18. Distribution Statement	
19. Security Classif. (of this report) UNCLASSIFIED	20. Security Classif. (of this page) UNCLASSIFIED	21. No. of Pages	22. Price*

*For sale by the Clearinghouse for Federal Scientific and Technical Information, Springfield, Virginia 22151.

PREFACE

This report was prepared by the McDonnell Douglas Astronautics Company-East, McDonnell Douglas Corporation, St. Louis, Missouri, under contract NAS5-23134, High Data Rate Optical Transceiver Terminal. This report covers the period from 30 June 1972 through 26 January 1973 and is the final report of this contract.

The work described herein was carried out by the Advanced Electronic Techniques Department at the McDonnell Astronautics Company-East, Box 516, St. Louis, Missouri 63166. In addition, the Electro-Optics Organization at the Western Division of GTE Sylvania, Mountain View, California, 94040 performed optical and mechanical analysis and design of the subject system as well as a portion of the atmospheric analysis.

The Project Engineer was E. S. Clarke. McDonnell Douglas contributors to the program were H. D. Brixey, J. P. Carter, L. H. Ebbesmeyer, J. A. Federhofer, R. B. Fluchel, J. E. Jackson, J. W. Kraemer, Dr. G. M. Lee, J. K. Lehman, H. B. McKee, N. F. Ruggieri, J. A. Smittkamp, T. D. Wormington, F. J. Vyzral. All of these contributors received technical direction from A. L. Furfine (Department Manager) and R. A. Stacy (Branch Manager), and M. Ross (Manager, Laser Communications) in the MDAC organization. J. A. Callahan and L. M. Williams coordinated artwork and test preparation.

A. R. Kraemer directed the activities at Sylvania. Contributors at Sylvania were: R. C. Jones, P. J. Titterton, and H. C. Ward. All of these contributors received technical direction from D. E. Caddes, Manager of Sylvania Electro-Optics Organization.

PRECEDING PAGE BLANK NOT FILMED

TABLE OF CONTENTS		<u>PAGE</u>
1.	INTRODUCTION	1
2.	BALLOON EXPERIMENT DEFINITION AND HARDWARE DESIGN	3
2.1	PROBLEM STATEMENT	3
2.2	REFERENCE SATELLITE SYSTEM DEFINITION	3
2.2.1	<u>Baseline Configuration</u>	4
2.2.1.1	Primary Characteristics	4
2.2.1.2	Method of Operation	11
2.2.1.3	Terminal Design	13
2.2.2	<u>Justification for Baseline Configuration</u>	15
2.3	BALLOON EXPERIMENT DEFINITION	22
2.3.1	<u>Experiment Objectives</u>	22
2.3.2	<u>Experiment Configuration</u>	23
2.3.3	<u>Communication Performance Evaluation</u>	31
2.3.3.1	Experiment configuration	32
2.3.3.2	Laser range equation	36
2.3.3.3	Signal processing losses	40
2.3.3.4	Bit error probability	40
2.3.3.5	Link margin	54
2.3.4	<u>Acquisition and Tracking Subsystem Evaluation</u>	56
2.3.5	<u>Atmospheric Propagation Experiments</u>	63
2.4	EXPERIMENT HARDWARE DESIGN	67
2.4.1	<u>Communications Hardware Description for Balloon Experiment</u>	67
2.4.1.1	PGBM receiver hardware description	68
2.4.1.2	RF telemetry	85
2.4.1.3	Relocking electronics	86
2.4.1.4	Error rate electronics	92
2.4.1.5	PQM detection electronics	95
2.4.2	<u>Acquisition and Tracking Subsystem Design</u>	97
2.4.2.1	Tracking error angle measurement	98
2.4.2.2	Control system design	117
2.4.3	<u>Atmospheric Propagation Experiment Hardware Design</u>	145
2.4.4	<u>Optomechanical Design</u>	161
2.4.4.1	Optical design	161
2.4.4.2	Mechanical design	173
2.4.4.3	Optics error analysis	178
2.4.4.4	BAPE interface requirements	216
2.5	CONCLUSIONS	218

TABLE OF CONTENTS (Continued)

	<u>PAGE</u>
3. TASK II - DEFINITION AND CONCEPTUAL DESIGN FOR 1980-1990 MANNED LABORATORY OPTICAL COMMUNICATIONS EXPERIMENTS	223
3.1 400 MBPS TO 1 GBPS TRANSCEIVER SYSTEMS	230
3.1.1 <u>Experiment Plan</u>	230
3.1.2 <u>Functional Description</u>	233
3.1.2.1 Transmitting terminal	236
3.1.2.2 Receiving terminal	237
3.1.3 <u>Operational Sequences</u>	237
3.1.4 <u>Operational Support Equipment</u>	238
3.1.5 <u>Data</u>	239
3.2 SIMULTANEOUS MULTIACCESS LINKS	239
3.2.1 <u>Experiment Plan</u>	239
3.2.2 <u>Functional Description</u>	241
3.2.3 <u>Operational Sequence</u>	253
3.2.4 <u>Support Equipment</u>	254
3.2.5 <u>Data Requirements</u>	255
3.3 SYNCHRONOUS TO GROUND COMMUNICATION LINK ATMOSPHERE PROPAGATION EXPERIMENT	255
3.3.1 <u>Experiment Plan</u>	255
3.3.1.1 Significance	255
3.4 DEEP SPACE RECEIVER	263
3.4.1 <u>Objectives</u>	264
3.4.2 <u>Functional Description</u>	270
3.4.3 <u>Operational Sequence</u>	270
3.4.4 <u>Support Equipment</u>	270
3.4.5 <u>Data Requirements</u>	272
3.5 DEEP SPACE PROBE TRANSMITTER	272
3.5.1 <u>Experiment Plan</u>	272
3.5.2 <u>Functional Description</u>	276
3.5.3 <u>Operational Sequence Experiments IV and V</u>	278
3.5.4 <u>Support Equipment</u>	279
3.5.5 <u>Data Requirements</u>	279
APPENDICES	
A IMPLEMENTATION TECHNIQUES	281
B REFERENCE SATELLITE SYSTEM DEFINITION	311

APPENDICES: (Continued)		PAGE
C	ACQUISITION AND TRACKING SIGNAL REQUIREMENTS	319
D	LINK MARGINS	331
E	ATMOSPHERIC PROPAGATION EFFECTS ANALYSIS	363
F	PROBABILITY DISTRIBUTION OF RECEIVED POWER IN THE PRESENCE OF ATMOSPHERICALLY INDUCED SCINTILLATION AND BEAM WANDER	395
G	ATMOSPHERIC PROPAGATION EFFECTS: BEAM SPREAD, BEAM WANDER, THE MODULATION TRANSFER FUNCTION, AND LATERAL COHERENCE LENGTH	399
H	ATMOSPHERIC PROPAGATION EFFECTS: SCINTILLATION AND LOG AMPLITUDE VARIANCE FOR THE POINT RECEIVER	419
I	COMPUTER PRINTOUT FOR OPTICAL TOLERANCE ANALYSIS	441
REFERENCES		453

ILLUSTRATIONS

<u>Figure</u>		<u>Page</u>
1	Possible Laser Communication Links	5
2	Package B Configuration	6
3	Package A Configuration	8
4	High Data Rate Transmitter for Satellite Optical Communications Systems	14
5	High Data Rate Receiver for Satellite Optical Communications System	16
6	Digital Baseband Format	18
7	PQM System	19
8	Comparison of PGBM and PQM Formats	20
9	Gondola Assembly	25
10	Balloon Borne Terminal Functional Schematic	26
11	Ground Station Optomechanical Configuration	29
12	Baseline Ground Station Data Handling System	32
13	Transceiver Terminal Communications Block Diagram (PQM Downlink)	33
14	Transceiver Terminal Communications Block Diagram (PGBM Downlink)	34
15	PGBM Bit Error Probability as a Function of Received Photoelectrons Per Bit	42
16	Graph of Probability of Error versus Mean Number of Signal Photoelectrons/Bit with $C_{\ell}(0)$ as a Parameter for $N_E = 30$ and $n_{pG} = 0$	45
17	Extra Power Required to achieve $P_e = 10^{-6}$ as a Function of $C_{\ell}(0)$, the Log Amplitude Variance	46
18	Extra Power Required for PGBM System to Obtain $P_e = 10^{-6}$ in the Presence of Scintillation and Wander	49
19	PGBM Bit Error Probability when $C_{\ell}(0)$ is Log Normal	51
20	Average Probability of Error Ignoring Outage Periods	53
21	Extra Power Required Due to Scintillation and Wander as a Function of Cutoff Probability	54
22	Percentage of the Time Link is Operational as a Function of P_e	55
23	Ground-To-Balloon, Data-PGBM	57
24	Balloon-To-Ground, Data-PQM	58
25	Balloon-To-Ground, Data-PGBM	59
26	Angle Noise Dependence on Signal Power	60
27	Effects of Bender Loop Bandwidth on Tracking Error	62

ILLUSTRATIONS (Continued)

<u>Figure</u>		<u>Page</u>
28	Effects of Bender Loop Bandwidth on Tracking Error Sensitivities to Detector Noise and Tachometer Noise	63
29	400 Mbps Optical Detector Block Diagram	69
30	Illustration of Dynamic Crossed Field Photomultiplier	71
31	RF Drive Chain Block Diagram	73
32	Sync Loop Electronics Functional Diagram	75
33	Non-Ideal Detector Model	78
34	Experimental Error Rate Curves for PGBM With and Without Optimum Threshold Control	80
35	Dynode AGC and Bias Compensation Functional Diagram	81
36	Threshold Detector Functional Diagram	83
37	Clock Synchronizer Functional Diagram	84
38	Reclocked Data Format	87
39	Bit Stuffing Electronics	88
40	Phase Relationship Between Input Data Clock and Isochronous Clock	89
41	Smoothing Buffer	91
42	Error Rate Electronics	93
43	PQM Transmitter	96
44	PQM - Receiver	97
45	Quadrant Photomultiplier Tube Tracker for Pulsed Input	101
46	QPMT Pulsed Tracker Timing Diagram	102
47	Integrator Circuit	103
48	High Data Rate Tracker Sensor Electronics	106
49	Power Spectrum of Wideband Detector Output for Random PGBM Data	107
50	Signal Power Loss at PMT Output versus Rise-time	109
51	Angle Processor Function and its Derivative	112
52	Analog Angle Processor Block Diagram	114
53	Digital Angle Processor Block Diagram	115
54	Gimbal Angle and Optical Detector Geometry Definition	121
55	Coarse Pointing Control Mode Functional Diagram	122
56	Acquisition Control Mode Functional Diagram	127
57	Acquisition Detector Angular Transfer Function	129
58	Acquisition from 0.9° Offset	130
59	Azimuth Acquisition System Performance	132
60	Azimuth System Time Response	133
61	Elevation Acquisition System Performance	134
62	Elevation System Time Response	135
63	Tracking Control System Functional Diagram	137

ILLUSTRATIONS (Continued)

<u>Figure</u>		<u>Page</u>
64	Bender Mirror Loop Gain and Phase Track Mode	138
65	Gimbal Loop Gain and Phase Track Mode	140
66	Tracking Error Performance for Two Gimbal Loop Stabilization Methods	142
67	Bender Deflection Requirement for Two Gimbal Loop Stabilization Methods	143
68	Tracking System Time Response to Sinusoidal Motion	144
69	Effects of Friction on Tracking Error and Bender Deflection	145
70	Effects of Bender Loop Bandwidth on Tracking Error and Bender Deflection	146
71	Effects of Bender Loop Bandwidth on Tracking Error Sensitivities to Detector Noise and Tachometer Noise	147
72	Measure Log-Amplitude Variance, $(\alpha_{\lambda}^2)_{\text{meas}}$ versus Dynamic Range, R, for Various True Values of Log-Amplitude Variance	149
73	Block Diagram of Balloon Atmospheric Detector Package Electronics	153
74	Link Simulator	156
75	Cumulative Probability Distribution of Received Optical Power Considering Scintillation and Beam Wander	157
76	Cumulative Probability Distribution of Received Optical Power Considering Scintillation and Beam Wander, 10,000 Samples	158
77	Cumulative Probability Distribution of Received Optical Power Considering Scintillation and Beam Wander, 2,000 Samples	159
78	Optical System Record	163
79	Lateral Interceptor Curves for Telephoto Attachment-on Axis	164
80	Optical System Record	165
81	Lateral Intercept Curves for 254 MM Objective on-Axis	166
82	Lateral Intercept Curves for 254 MM Objective - 4° Off-Axis	167
83	Lateral Intercept Curves for Telephoto Attach- ment + Objective - On Axis	168
84	Optical System Record	169
85	Lateral Intercept Curves for Objective + Relay- On-Axis (Monochromatic Design Focus)	170
86	Lateral Intercept Curves for Full System - On-Axis	171
87	Lateral Intercept Curves for Full System - 2 MRAD Off-Axis	172

ILLUSTRATIONS (Continued)

<u>Figure</u>		<u>Page</u>
88	Elevation Package Outline	175
89	Gondola Assembly	176
90	HDR Balloon Optics Optical Schematic	177
91	Electronics Bay - Elevation Package	179
92	Section B-B	180
93	Section C-C	181
94	Section D-D Cover Removed	182
95	Section E-E Cover Removed	183
96	Section F-F	184
97	Section G-G	185
98	Section H-H	186
99	Balloon Experiment General Arrangement	188
100	Telescope Thermal Model	190
101	Cylindrical Cover and Support Plate Thermal Program	191
102	Typical Flight Profile	193
103	Typical Component Response "Hot" Environment	194
104	Typical Component Response "Cold" Environment	195
105	Cover Thermal Response - Thermal Isolation at Connection Points	196
106	Support Plate Thermal Response - Thermal Isolation at Connection -I	197
107	Support Plate Thermal Response - Thermal Isolation at Connection -II	198
108	Typical Telescope Response "Hot" Environment	200
109	Typical Telescope Response "Cold" Environment	201
110	Finite Element Structural Model	204
111	Invar Has Low Coefficient of Thermal Expansion	206
112	High Data Rate Communication Links	224
113	Multi-Channel 10 Mbps Laser Links Simultaneous Operation	226
114	Synchronous Satellite Deep Space PIM Laser Communication Receiver Terminal	227
115	Manned Orbiting Vehicle Links and Effects to be Studied	229
116	High Data Rate Transmitting Terminal Block Diagram	234
117	High Data Rate Receiver Terminal Block Diagram	235
118	Front View of Synchronous Receiver and Beacon Unit	242
119	1/4 Earth Synchronous Receiver Unit	243
120	10 x 10 Detector Array	246
121	Synchronous Satellite Beacon Transmitter Schematic	252
122	Parameter Inter-Relationships for Atmospheric Effects Experiments	258
123	10 Meter Diameter Optical Collector	226

ILLUSTRATIONS (Continued)

<u>Figure</u>		<u>Page</u>
124	Segmented Collector Optical Quality	267
125	Segmented Collector Blur Patterns	269
126	Block Diagram - Deep Space Receiver	271
127	Use of Earth Shine as a Beacon	273
128	Laser Spot Diameter	275
129	Block Diagram - Deep Space Probe Transmitter	277
130	PIM Transmitter Cavity Dumping System	278
A-1	Laser Cavity Length	296
A-2	Multiple Demod Receiver 2-DCFP	300
A-3	PQM Block Diagram	301
A-4	Digital Baseband Format	302
C-1	Image Divider For Quadrant Photo Multiplier Tube Detector (OPMT)	325
C-2	Computing $f(y)$ For Uniform Spot	327
D-1	Sync-to-ground-Data-PQM	342
D-2	Sync-to-ground-Data-Acquisition	343
D-3	Sync-to-ground-Data-Tracking	344
D-4	Sync-to-ground-Beacon-Acquisition	345
D-5	Sync-to-ground-Beacon-Tracking	346
D-6	Las-to-sync-Data-PQM	347
D-7	Las-to-sync-Data-Acquisition	348
D-8	Las-to-sync-Data-Tracking	349
D-9	Las-to-sync-Beacon-Acquisition	350
D-10	Las-to-sync-Beacon-Tracking	351
D-11	Balloon-to-ground-Data-PQM	352
D-12	Balloon-to-ground-Data-PGBM	353
D-13	Balloon-to-ground-Data-Acquisition	354
D-14	Balloon-to-ground-Data-Tracking	355
D-15	Balloon-to-ground-Beacon-Acquisition	356
D-16	Balloon-to-ground-Beacon-Tracking	357
D-17	Ground-to-balloon-Data-PGBM	358
D-18	Ground-to-balloon-Data-Acquisition	359
D-19	Ground-to-balloon-Data-Tracking	360
E-1	Theoretical Turbulence Profiles vs Allitude	367
E-2	Typical Turbulence Profile Measured	368
E-3	$C_{\ell}(0)/C_{\ell}S(0)$ versus R with Feed Beam Radius, W_1 As a Parameter for the Balloon Defocused Uplink	372
E-4	The Balloon Defocused Downlink	373
E-5	Cumulative Probability of Log Amplitude Variance for Argon Wavelength	376
E-6	Log Amplitude Variance Aperture Averaging Reduction Factor Versus Receiver Diameters	378
E-7	Cumulative Probability Distribution of Received Wander	383

ILLUSTRATIONS (Continued)

<u>Figure</u>		<u>Page</u>
E-8	Reduction in Neon received Signal Versus Lateral Coherence Length, ρ_o , with Feed Beam Diameter (cm)	387
E-9	Angle of Arrival Standard Deviation Versus Optical Receiver Diameter	389
E-10	Frequency Spectrum For the Fluctuations of the Light Arrival Angle	390
E-11	Total Atmospheric Transmissibility Due to Rayleigh and MIE Scattering $\lambda = 0.53$ and 60° Zenith Angle	392
E-12	Total Atmospheric Transmissibility Due to Rayleigh and MIE Scattering $\lambda = 1.06$ and 60° Zenith Angle	393
H-1	Theoretical Turbulence Profiles Versus Altitude	420
H-2	$C_\ell(0)/C_s(0)$ Versus R with Feed Beam Radius, W_1 as a Parameter for the Balloon Defocused Uplink	432
H-3	$C_\ell(0)/C_s(0)$ Versus R with Feed Beam Radius, W_1 as a Parameter for Balloon Defocused Uplink	433
H-4	$C_\ell(0)/C_s(0)$ Versus R with Feed Beam Radius, W_1 as a Parameter for Balloon Defocused Uplink	434
H-5	$C_\ell(0)/C_s(0)$ Versus R with Feed Beam Radius, W_1 as a Parameter for Balloon Defocused Uplink	435
H-6	$C_\ell(0)/C_s(0)$ Versus R with Feed Beam Radius, W_1 as a Parameter for Balloon Focused Uplink	436
H-7	$C_\ell(0)/C_s(0)$ Versus R with Feed Beam Radius, W_1 as a Parameter for Balloon Defocused Uplink	437
H-8	$C_\ell(0)/C_s(0)$ Versus R with Feed Beam Radius, W_1 as a Parameter for Balloon Focused Downlink	438
H-9	$C_\ell(0)/C_s(0)$ Versus R with Feed Beam Radius, W_1 as a Parameter for Synchronous Satellite to Ground Defocused Uplink	439
H-10	$C_\ell(0)/C_s(0)$ Versus R with Feed Beam Radius, W_1 as a Parameter for Synchronous Satellite to Ground Defocused Uplink	439
I-1	Computer Analysis Results for Case A	442
I-2	Computer Analysis Results for Case B	447

TABLES

<u>TABLE</u>	<u>TITLE</u>	<u>PAGE</u>
1	Transmitter Characteristics	9
2	Receiver Characteristics	10
3	Reference Link Margin Summary	21
4	Reference System Configuration High Data Rate Receiver Terminal	22
5	Reference System Configuration High Data Rate Transmitter Terminal	23
6	Ground Station Optics Configuration Options	28
7	Ground Station Transceiver Characteristics	31
8	Ground Station Data Handling Equipment	35
9	Signal Processing Losses	40
10	Summary of Atmospheric Losses on Communication Link Performance	55
11	Summary of Atmospheric Parameter Values for Communication Link Performance Analysis	56
12	Atmospheric Propagation Experiments	65
13	Atmospheric Experiment Measurement Technique Summary	66
14	Balloon Transceiver Gimbal Configuration Trade Study	99
15	High Data Rate Tracker Alternatives	105
16	Comparison of Analog Digital Angle Processors	116
17	Summary of Link Margins	118
18	Summary Description of Beam Painting Control Systems	120
19	Gimbal Control Loop Devices and Requirements	124
20	Thermal Properties	192
21	Laser Communication System Components Power and Thermal Model Location	192
22	Node Temperatures	203
23	Balloon Experiment Calculated Component	208
24	Transformations For The Optical Component Displacements	209
25	Size, Weight and Power Estimates	217
26	Power Summary	218
27	Subcarrier Channel	219
28	Comparison of Proposed Balloon Experiment	221
29	Candidate Applications	225
30	Functional Parameters Subject to Change	231
31	Configuration Changes	232
32	Operational Support Equipment	238
33	Functional Receiver Parameters Subject to Change	240
34	Configuration Changes	240
35	Signal Power System Parameters	244
36	Time Spread of Fresnel Lens for Various F-Numbers	247

TABLES (Continued)

<u>TABLE</u>	<u>TITLE</u>	<u>PAGE</u>
37	Laser Acquisition and Tracking Sequence MLOS-S/S	249
38	Beacon Laser Requirements Analyses	251
39	O-S Link Synchronous Satellite Data Receiver and Beacon Transmitter for Low Orbit Users	254
40	Functional Parameters/Configurations Subject to Change	264
41	Advantages and Disadvantages of Three Photon Bucket Construction Techniques for Space Stations	268
42	Deep Space PIM Laser System Neptune - Earth Link	274
A-1	Variation of Power of Output Beam	283
A-2	Variation of Receiver Diameter	284
A-3	Variation of Transmitted Beamwidth	286
A-4	Variation of Optics Efficiency	288
A-5	Variation of Spectral Bandpass Filter	289
A-6	Variation of Quantum Efficiency	290
A-7	Variation of Power Split for Tracking	292
A-8	Variation of Field of View	293
A-9	Variation Detector Gate Width	294
A-10	Variation of Communication Data Rate	297
A-11	Variation of Modulation Format	298
A-12	Variation of Laser Type	304
A-13	Variation of Communication Detector Type	305
A-14	Variation of Acquisition Detector Type	306
A-15	Variation of Tracking Detector Type	307
A-16	Tracking Detector Characteristics	308
A-17	System Configuration or Parameter Variable	309
B-1	Angle Measurement Detector	312
B-2	High Data Rate Transmitter Acquisition and Tracking Detector	314
B-3	Initial Pointing Uncertainties	317
D-1	Link Analysis Program Input	332
D-2	Synchronous Satellite High Data Rate Transmitter	333
D-3	Ground Station (Satellite Link) High Data Rate Receiver	334
D-4	Low Altitude Satellite High Data Rate Transmitter	335
D-5	Synchronous Satellite High Data Rate Receiver	336
D-6	Balloon-borne Transceiver	337
D-7	Ground Station (Balloon Link)	338
D-8	Sync → Ground Link Parameter	339
D-9	Las → Sync Link Parameters	340
D-10	Balloon → Ground Li-k Parameters	341
E-1	Parameters for High Data Rate Optical Transceiver Balloon Experiment	384
E-2	Summary of Atmospheric Loss on Communication Link Performance	394
G-1	Computed Lateral Coherence Length	408
G-2	Point source Uplink	415
H-1	Computed Spherical Wave Log	422
H-2	Spherical Wave Log Amplitude	430

1. INTRODUCTION

This report documents the results of the "High Data Rate Optical Transceiver Terminal" study conducted by McDonnell Douglas Astronautics Company for the National Aeronautics and Space Administration, Goddard Space Flight Center, under contract number NAS5-23154. The work performed under this contract was divided into two primary tasks given in the study Statement of Work. The following brief descriptions of the work accomplished in these tasks indicate the scope of the study.

Task 1 - Balloon Experiment Definition and Hardware Design. An experiment was defined and hardware designed which permits the quantitative evaluation of a space-qualifiable optical communications system. The requirements for a satellite digital communication system using neodymium-doped yttrium-aluminum-garnet lasers at 4×10^8 bits per second (400 Mbps) were first defined. Link analyses were performed to determine a compatible and feasible set of parameters for links transmitting 400 Mbps data from a synchronous satellite to a ground station (SYNC-GND link) and from a low altitude satellite to a synchronous satellite (LAS-SYNC). The analyses defined required laser power, beamwidths, modulation format, receiver and transmitter aperture, pointing accuracy, and detectors for acquisition and tracking.

With these parameter values as guidelines, a transceiver was designed suitable for operation from the Balloon Atmospheric Propagation Experiment (BAPE) vehicle previously developed by NASA and utilized for measurement of atmospheric effects on laser light. The design effort included:

- (a) System Parameter Definition
- (b) Link Analysis
- (c) Detailed Optics Design
- (d) Electronics Definition
- (e) Control System Design
- (f) System Performance Analysis

An experiment was defined using the balloon-borne terminal in conjunction with a NASA owned mobile ground station having a 30 inch diffraction limited telescope. The experiment was designed to evaluate the performance of the communication link in the presence of atmospheric disturbance and beam pointing errors. It would also evaluate the performance of the fine pointing control system.

Task 2 - Definitions and Conceptual Hardware Designs for 1980-1990 Manned Laboratory Optical Communications Experiments. Five optical communications experiments were defined during performance of this task. They included three experiments in the near-space use of laser communications systems, and two experiments whose purpose would be to explore the feasibility of deep-space use of such systems. A plan for each experiment was developed, outlining its significance, the objectives of the experiment, the techniques required, and expected results. A functional description of the hardware required in each experiment is included along with the operational support requirements and the data requirements.

2. BALLOON EXPERIMENT DEFINITION AND HARDWARE DESIGN

2.1 PROBLEM STATEMENT. The best present predictions of earth resources surveillance requirements for the foreseeable future indicate that the need for higher and higher data rates transmitted over longer distances will continue into the 1980's. The wide bandwidths associated with optical communication systems make them suitable for these high data rates. The narrow beamwidths possible with laser light make lasers very efficient for transmission of data over great distances. Rapid advances in optical communication technology in the last few years make an operational high data rate laser communication system feasible within this decade. Consequently, optical communication is an obvious solution to the NASA's long-term satellite communications requirements.

Although excellent bit-error-rate performance and fine-tracking accuracy have been demonstrated by optical systems in the laboratory, neither has been satisfactorily verified for an earth/space link. The degradation of the performance of an optical link that includes the atmosphere has never been measured, nor has the current theory been proven adequate to predict this degradation.

This report describes the preliminary design of a balloon-borne experiment which will demonstrate high data rate optical communications and fine pointing through a vertical atmospheric path. Section 2.2 presents a baseline design of a satellite link to transmit data from synchronous orbit to a ground station. This design is used as a reference in configuring a balloon-borne experiment whose performance is representative of the reference system. Section 2.3 describes the experiment and explains how the desired data is obtained. Section 2.4 discusses the design details of the hardware used in the experiment.

2.2 REFERENCE SATELLITE SYSTEM DEFINITION. As a first step in performing this study, we defined the characteristics of an optical communication system between satellites using neodymium-doped yttrium-aluminum-garnet (Nd:YAG) lasers. These characteristics were then used as a model for the balloon experiment design. We have drawn substantially from our

previous work ¹ in defining our model, but we have imposed NASA's choices for the data rate (400 Mbps) and wavelength (1.06 μm) of the high-data-rate link. This section describes the model thus generated and presents justification for the parameter values chosen.

2.2.1 Baseline Configuration. The reference satellite laser communication system defined requires a unit at each end of each link. These units are the high data rate transmitter unit, Package A, which also contains a low data rate receiver for cooperative acquisition, tracking, and command data reception, and the beacon (low data rate) transmitter unit, Package B, which contains a high data rate receiver for communication and detectors for cooperative acquisition and tracking. Each package must track the other during communication.

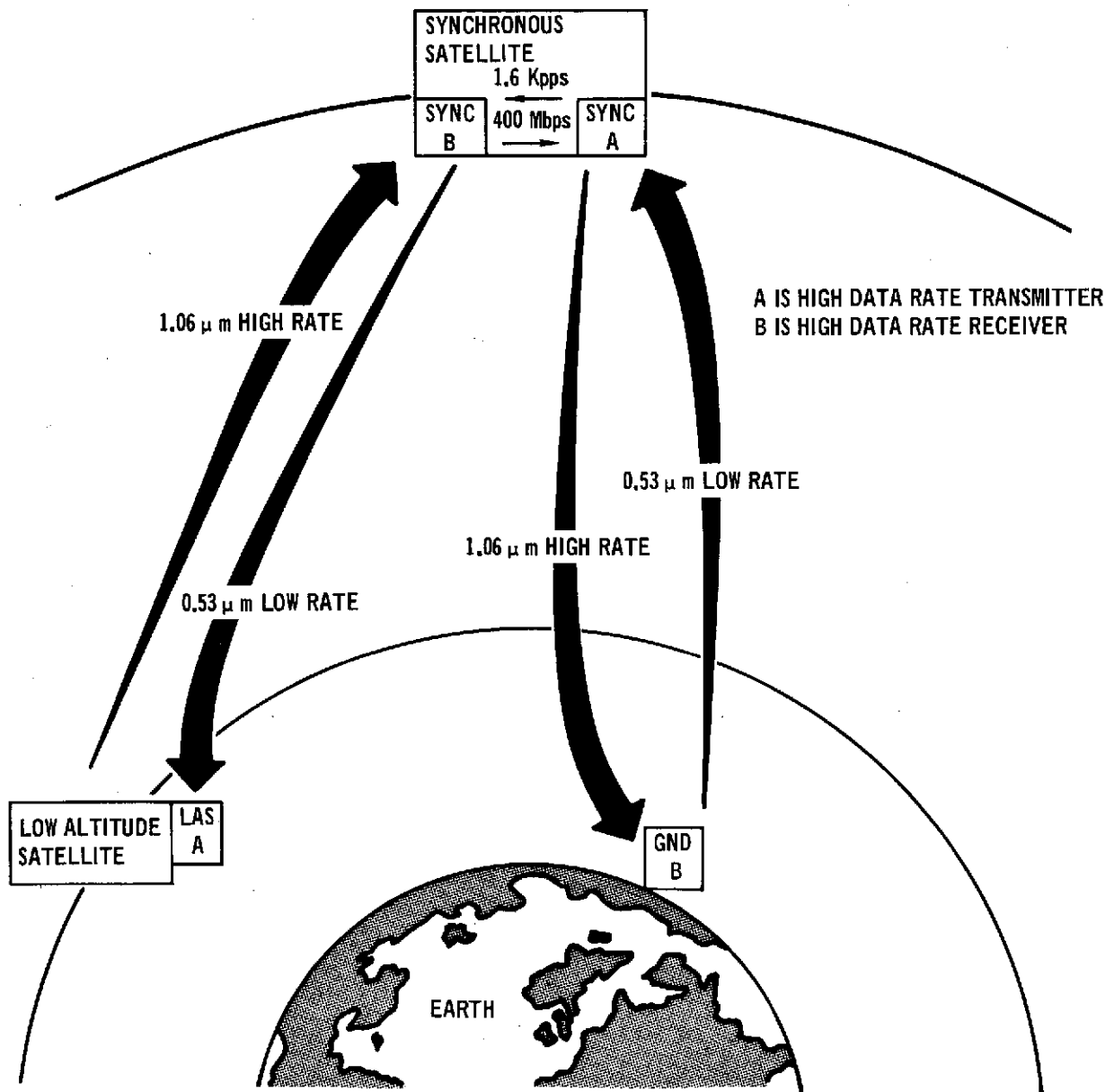
The basic geometry for the synchronous-satellite-to-ground link (SYNC-GND) and the low-altitude-satellite-to-synchronous-satellite link (LAS-SYNC) are shown in Figure 1.

2.2.1.1 Primary characteristics. The low altitude satellite Package A configuration consists of an electrooptics assembly and a 1 foot diameter Cassegrain telescope which serves to focus the high data rate laser beam transmitted to the synchronous satellite and collect energy from the low data rate beam coming from Package B in the synchronous satellite.

The electrooptics assembly houses a 200 Mpps mode-locked Nd:YAG laser with associated modulators to produce a 400 Mbps output of 200 mW at 1.06 μm . This assembly also contains the acquisition/tracking/command receiver which uses a 25% quantum efficiency quadrant photomultiplier for the acquisition detector and a similar unit for tracking and command reception.

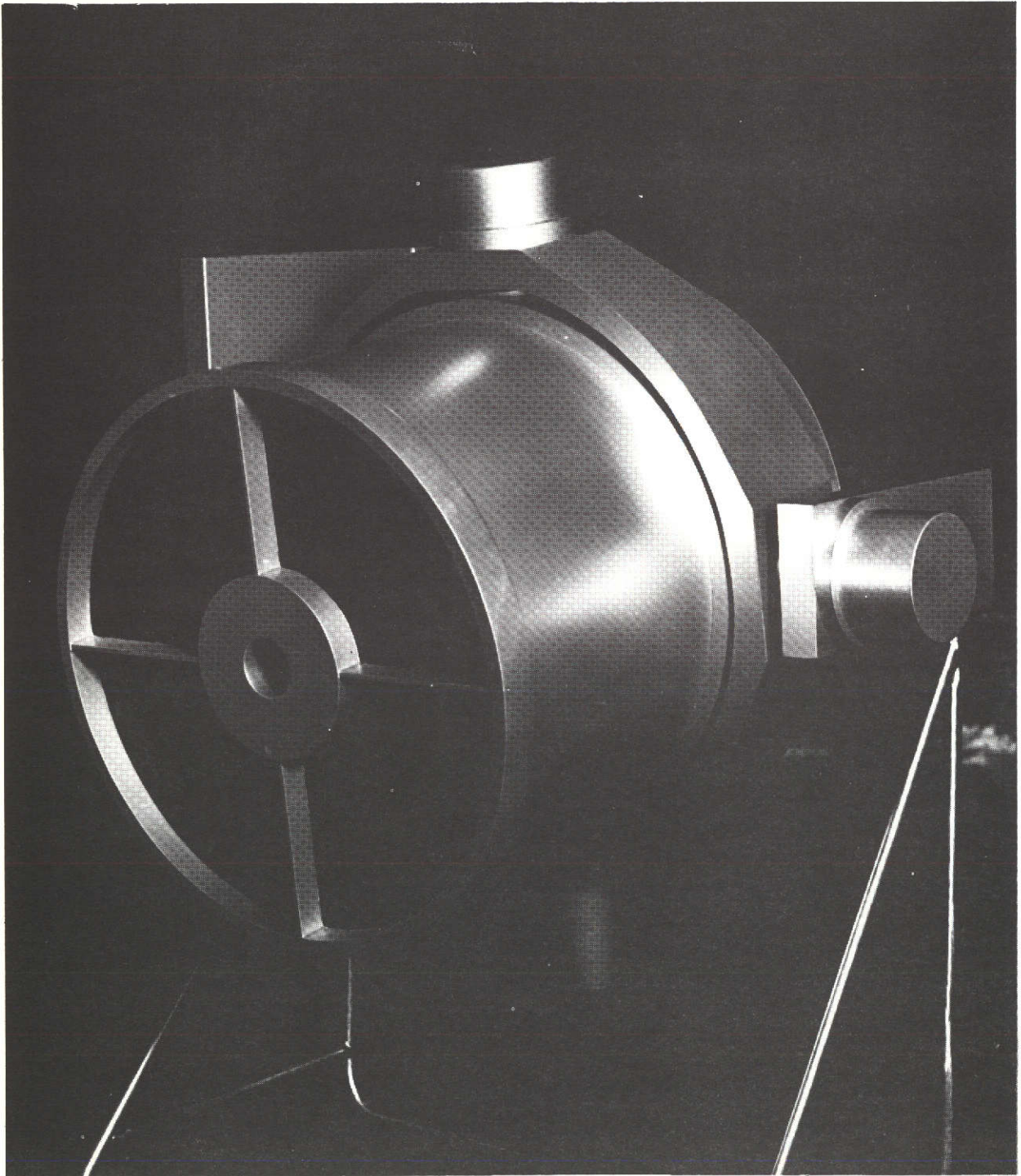
A synchronous satellite Package B configuration at the other end of this link is depicted in Figure 2 . It consists of an electrooptical assembly and double gimballed 24-inch dia-

FIGURE 1 POSSIBLE LASER COMMUNICATION LINKS
Sync-Ground and LAS Sync



meter Cassegrain telescope with $\pm 10^\circ$ gimbal freedom in both axes. The telescope is pointed directly at the Package A located at the low altitude satellite and serves as a collector of energy from the high data rate laser beam coming from the low altitude satellite. The telescope is not used for transmission of the low data rate laser beam to satellite, but rather energy from

FIGURE 2 HIGH DATA RATE RECEIVER FOR SYNCHRONOUS SATELLITE



the beacon laser is directed out through a hole in the center of the Cassegrain secondary mirror on the telescope axis.

The electrooptics assembly houses a 1.6 kpps frequency doubled Nd:YAG laser with associated modulators to produce an output of

25 mW at 0.53 μm . This assembly also contains the acquisition and tracking receivers which used quadrant photomultiplier tubes, and the communications receiver which has dynamic crossed field photomultiplier tubes for detection of the high rate data.

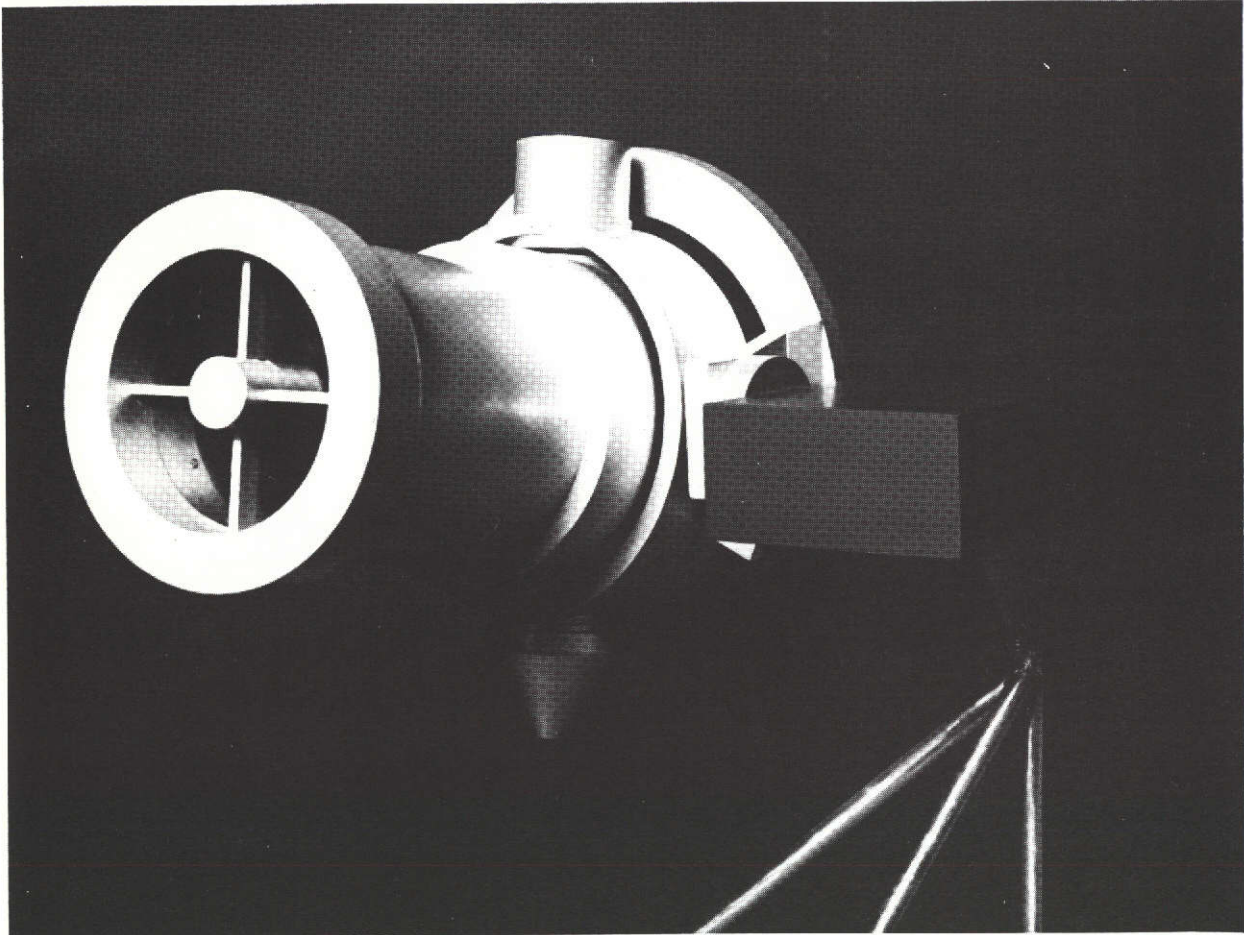
Demodulated high rate data from this package is sent by wire to Package A in the synchronous satellite (see Figure 1) for relay to the ground. Demodulated low rate data from Package A in the synchronous satellite is received by wire by Package B for relay to the low altitude satellite Package A.

A synchronous satellite Package A configuration is depicted in Figure 3 . It consists of an electrooptical assembly and a double gimballed 7.5-inch diameter Cassegrain telescope with $\pm 10^\circ$ gimbal freedom in each axis. This telescope serves to focus the high rate laser beam transmitted to the ground and collect energy from the low rate laser beam from Package B on the ground. The telescope is pointed directly at the ground-based Package B. Electrooptical components are identical to the low altitude satellite Package A.

The ground station Package B configuration consists of the electrooptics assembly similar to that of the other Package B configuration, but is mounted to, and optically coupled to an existing 60-inch diameter astronomical telescope owned by NASA. This telescope serves to collect energy from the high rate laser beam coming from the synchronous satellite. The low data rate laser beam from this package is boresighted with the telescope but does not use the telescope optics to focus the beam. The electrooptics components are identical to the synchronous satellite Package B except that the laser power is increased to 200 mW.

The above package configurations implement two links which enable cooperative acquisition and tracking, transmission of command data from ground Package B to the synchronous satellite

FIGURE 3 HIGH DATA RATE TRANSMITTER FOR SYNCHRONOUS SATELLITE



and to the low altitude satellite Package A, and transmission of 400 Mbps communication data from the low altitude satellite Package A to the synchronous satellite and to the ground Package B.

The primary electrooptical characteristics of the transmitters in the packages are summarized in Table 1 .

The primary electrooptical characteristics of the receivers in the packages are summarized in Table 2 .

These characteristics represent projected state-of-the-art for the 1975-1980 time frame.

The baseline high data rate modulation format in all cases is Pulse Quaternary Modulation (PQM). The PQM modulator controls

TABLE 1
TRANSMITTER CHARACTERISTICS

STATION	PULSE WIDTH	LASER WAVE LENGTH	MODULA-TION*	DATA RATE	LASER OUTPUT POWER	LASER TYPE	PUMP TYPE	BEAM SIZE
Package A Low Altitude Satellite	250 ps	1.06 μm	PQM	400 Mbps	200 mW	Nd:YAG	diode	5.1 μrad
Package A Sync Satellite	250 ps	1.06 μm	PQM	400 Mbps	200 mW	Nd:YAG	diode	8.1 μrad
Package B Sync Satellite	200 ns	0.53 μm	PIM	1.6 Kpps	25 mW	Nd:YAG	diode	300 μrad
Package B Ground	200 ns	0.53 μm	PIM	1.6 Kpps	200 mW	Nd:YAG	lamp	600 μrad

*Pulse Quaternary Modulation (PQM)

Pulse Interval Modulation (PIM)

TABLE 2

RECEIVER CHARACTERISTICS

STATION	WAVE LENGTH	DATA RATE	MODULA- TION	ACQUISITION MODE		TRACKING		COMMUCATION	
				FIELD OF-VIEW	DETECTOR* TYPE	FIELD OF-VIEW	DETECTOR* TYPE	FIELD OF-VIEW	DETECTOR* TYPE
Package A Ground Low Altitude Satellite	0.53 μ m	1.6 Kpps	PIM	4 mrad	QPMT	400 μ rad	QPMT	200 μ rad	QPMT
Package A Sync Satellite	0.53 μ m	1.6 Kpps	PIM	4 mrad	QPMT	400 μ rad	QPMT	200 μ rad	QPMT
Package B Sync Satellite	1.06 μ m	400 Mbps	PQM	4 mrad	QPMT	400 μ rad	QPMT	300 μ rad	DCFP
Package B Ground	1.06 μ m	400 Mbps	PQM	4 mrad	QPMT	400 μ rad	QPMT	300 μ rad	DCFP

*Dynamic Crossfield Photomultiplier Tube (DCFP)

Quadrant Photomultiplier Tube (QPMT)

independently which of two time slots and which of two polarization states each pulse exhibits, thereby imposing two bits of information upon each laser pulse. For the 400 Mbps data rate, therefore, the laser need operate at only 200 Mpps.

Pulse Interval Modulation (PIM) is the baseline modulation format for the command links. The average pulse rate is 1.6 Kpps and pulse width is 200 ns. At this low rate and large pulse width, it is relatively easy to modulate using the PIM format which simply adjusts the spacing between pulses by one of 64 possible intervals. This provides an M-ary modulation scheme with $M = 6$, i.e., there are six bits of information transmitted per pulse. This gives an equivalent binary data rate of $6 \times 1.6 = 9600$ bits per second.

- 2.2.1.2 Method of operation. The following basic method of acquisition/tracking and communication is common to both configuration variations of both packages.

Acquisition and Tracking Sequence - Acquisition is based on the assumption of an apriori pointing knowledge and accuracy of ± 0.1 degrees (3σ) at each package, i.e., the packages are pointed at each other with this uncertainty.

- (1) Package B initiates acquisition by scanning its low rate 0.53 μm laser beam over a 4 mrad x 4 mrad field using a beam width of 400 μrad .
- (2) Package A is "looking" throughout a 4 mrad x 4 mrad field for Package B. When Package B's beam illuminates Package A, Package A begins coarse tracking a low pulse rate signal (10-40 pps).
- (3) Package A now transmits a high rate 1.06 μm beam to Package B. At this point Package A's beam is spoiled to 100 μrad to allow for the fact that Package A is only coarse tracking Package B.
- (4) Package B's tracking receiver is boresighted with its

transmitter so that it now "sees" and tracks Package A. Upon tracking, Package B terminates scanning and points its beam directly at Package A, increasing the received pulse rate at Package A to 1.6 kpps.

- (5) This increased pulse rate allows Package A to fine track on Package B. When in the fine track mode, Package A's high rate transmitter beam is pointed ahead by the lead angle required for transit time. This beam is then narrowed to 8.1 μ rad, increasing the received signal at Package B by 22 dB.
- (6) At this point 99% of the received signal in Package B is diverted to the communication receiver, and Package B sends Package A a message over the low rate beam, commanding Package A to commence high rate data dump.

Communication - After the systems are angle tracking each other, the baseline systems provide the following margins above the signal level required to achieve a 10^{-6} bit error rate:

- (1) LAS-SYNC, 4.4 dB, and
- (2) SYNC-GND, 9.2 dB.

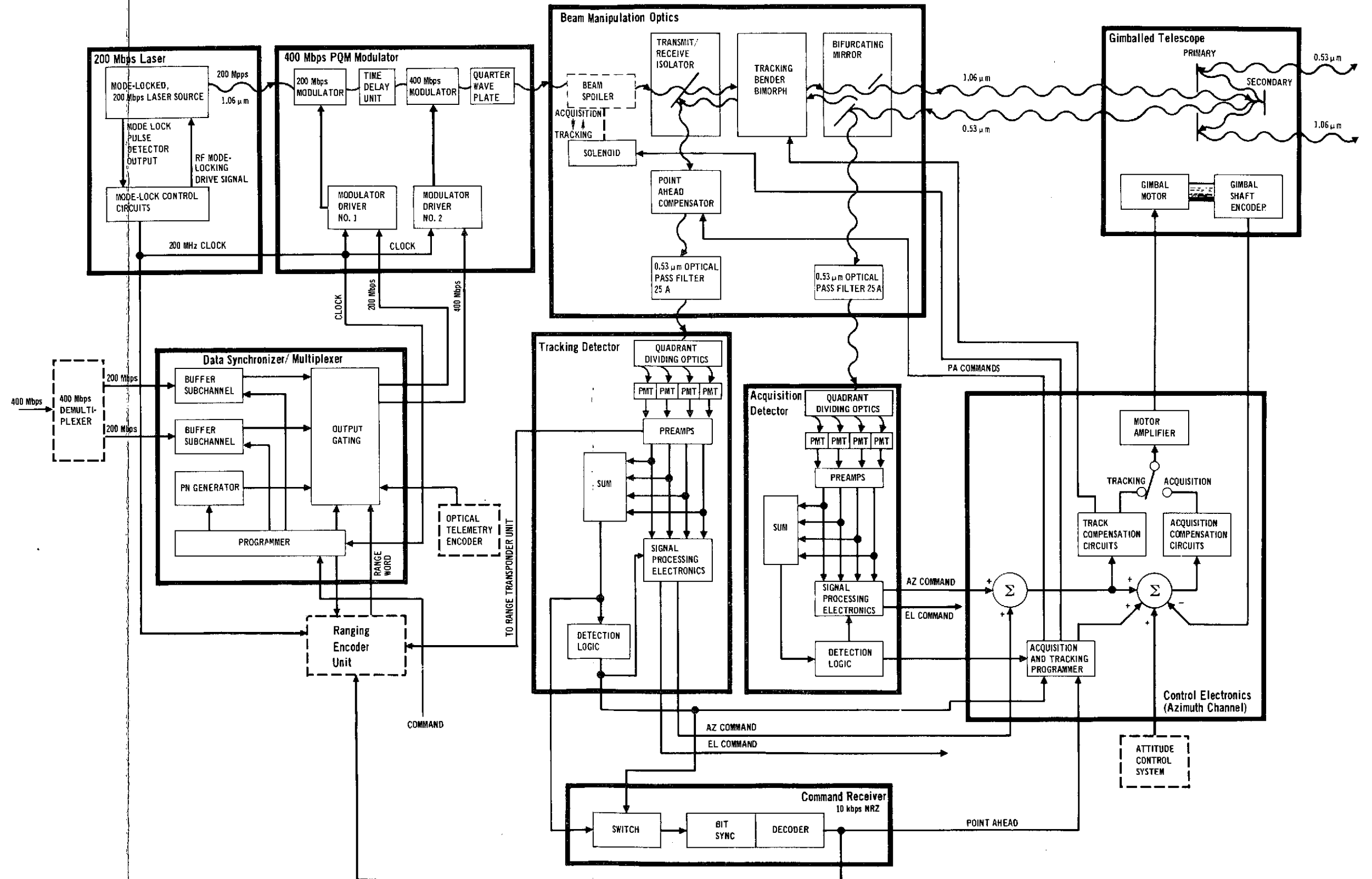
One of the requirements of the synchronous communications relay system is to receive data from several users, combine the data into a single high rate digital baseband, and retransmit it. In the synchronous satellite Package A baseline, multiplexing of several low rate (250 Mbps, 50 Mbps, etc.) user bit streams into one \sim 400 Mbps data stream is accomplished by an asynchronous multiplexing technique. In principle, a small portion of the low rate streams are stored in a small temporary storage, or buffer, as they are received. The storage is read-out at a rate slightly higher than the sum of the incoming rates. On an average, this depletes the buffer. When the buffer runs low, "dummy" or "stuff" bits are added to the outgoing high rate stream with proper identification so they can be later discarded. This "stuffing" process allows the buffer to fill up again and

the natural depletion process recurs. This technique, chosen for the baseline, accommodates slight average rate changes between the input and output of the multiplexer and is therefore used to adjust the rate of the received high rate data in the synchronous satellite to match the natural mode-lock rate of the high rate laser in the synchronous satellite, obviating laser cavity tuning in the satellite.

- 2.2.1.3 Terminal design. Figure 4 shows a block diagram of the high data rate transmitter. The 200 mega-pulse-per-second (Mpps) laser output is modulated in the PQM format.

The Beam Manipulation Optics steer the transmitted and received beams to their respective targets within the field of view permitted by the positions of the azimuth and elevation gimbals. The Bifurcating Mirror is tilted at 45° with respect to the optical axis and has an elliptical hole centered on the optical axis. The hole is oriented to appear circular when viewed along the optical axis. When the terminal is initially attempting to acquire the beacon signal, the misalignment between the axis and the line of sight to the receiver is sufficiently large that the incoming beacon beam falls on the surface of the bifurcating mirror and is diverted to the acquisition detector. When closer alignment is achieved, the beacon beam falls through the hole and illuminates the tracking detector, automatically switching the mode of operation. In the tracking mode, the tracking bender bimorphs perform two-axis fine steering of both the incoming and outgoing beams. A bender bimorph is a piezoelectric crystal with a mirrored surface which tilts in response to a voltage applied to the crystal. The transmit/receive isolator is a dichroic element which permits $1.06 \mu\text{m}$ light to pass straight through while deflecting $0.53 \mu\text{m}$ light 90° . The acquisition and tracking detectors are Quadrant Photo Multiplier Tubes (QPMT). Each detector assembly consists of image-dividing optics and an array of four standard photomultiplier tubes. The incoming light is focused to a circular spot which is

FIGURE 4 HIGH DATA RATE TRANSMITTER FOR SATELLITE OPTICAL COMMUNICATIONS SYSTEM



FOLDOUT FRAME

FOLDOUT FRAME

2

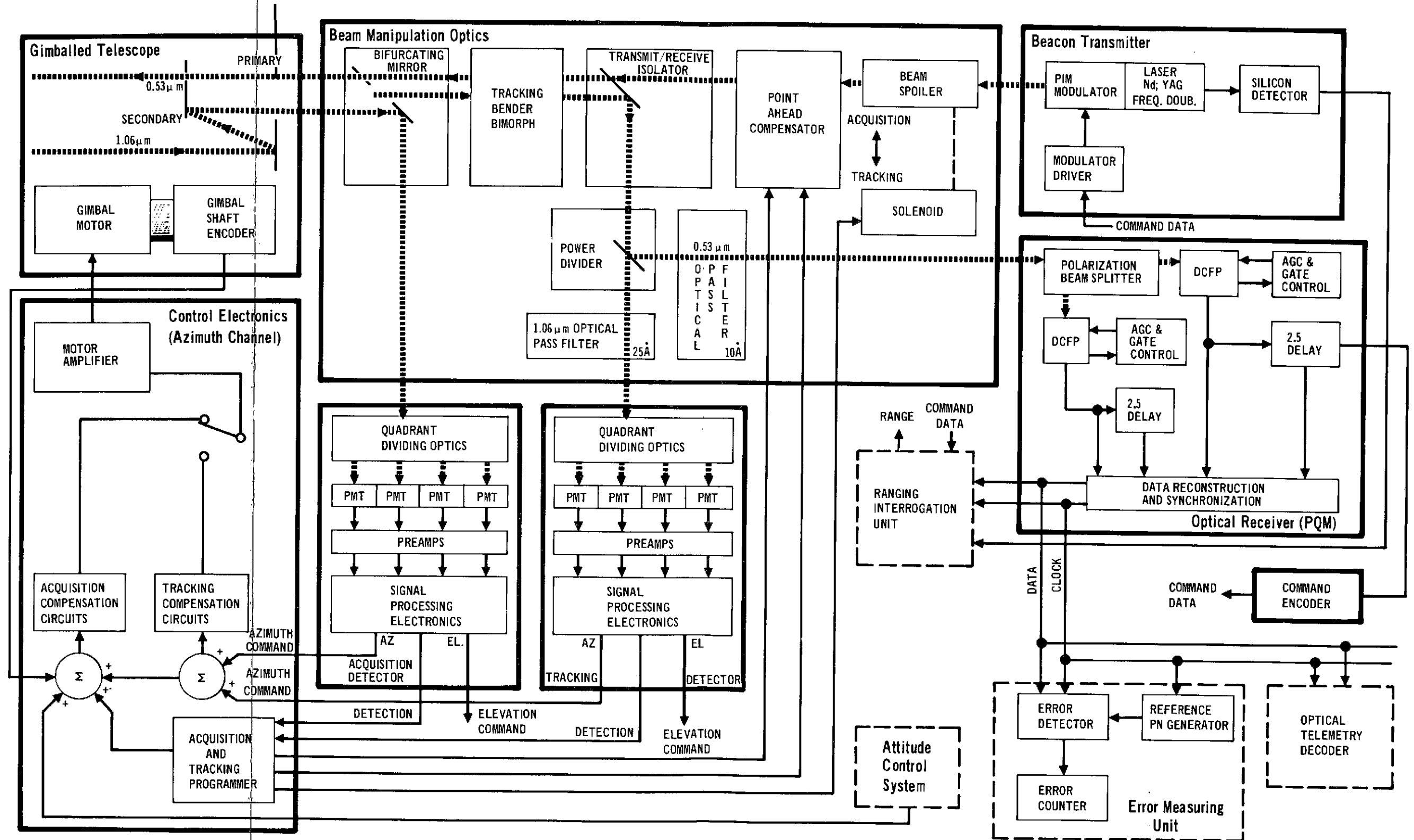
divided to form a beam to each tube. The difference between angle of arrival of the incoming beam and the angle of departure of the outgoing beam, as determined by the gimbal positions and bender bimorph deflections, determines the position of the focused spot on the image divider, which, in turn, determines the relative intensities of the radiation incident on the four PMT's. The PMT outputs are then processed to generate gimbal and bender bimorph commands for bringing the transmit and receive beams into alignment. The point ahead compensator introduces a bias in the angle of arrival in order to cause a misalignment in the incoming and outgoing beams which corrects for the pointing error due to the relative velocity of the transmitter and receiver in conjunction with finite photon transit time between transmitter and receiver.

Figure 5 shows the functional schematic of a high-data-rate receiver. Note in the schematic the similarity with the transmitter as far as acquisition and tracking are concerned. The beacon laser is modulated in a Pulse Interval Modulation (PIM) format for transmission of approximately 10 kbps of data for ranging, closed-loop boresight alignment or any other purpose desired. The PIM receiver at the other terminal measures the elapsed time between beacon pulses and generates a six-bit (typically) number corresponding to the interpulse period. The PQM receiver consists of a polarization beam splitter and two DCFP's. The beam splitter separates the pulses according to polarization. The synchronization and detection logic following each DCFP determines the time slot of each pulse and reconstructs the original 400 Mbps bit stream.

2.2.2 Justification for Baseline Configuration - This section presents brief analyses showing how the parameter values for the reference satellite system were selected.

Modulation Format Selection - The choices of modulation formats are rather limited due to the high data rate. Subcarrier formats (i.e., a digitally phase modulated RF subcarrier which is

FIGURE 5 HIGH DATA RATE RECEIVER FOR SATELLITE OPTICAL COMMUNICATIONS SYSTEM



FOLDOUT FRAME

FOLDOUT FRAME

2

used to modulate the polarization of a CW laser) were eliminated from consideration due to their relative inefficiency and complexity. The following four baseband modulation formats were considered for use with a mode-locked laser:

- (1) Pulse Gated Binary Modulation (PGBM) is a low duty cycle PCM with a binary "1" represented by a pulse and binary "0" represented by the absence of a pulse.
- (2) Pulse Delay Binary Modulation (PDBM) is a two-state low duty cycle PPM with a delayed pulse representing a binary "1" and an undelayed pulse representing a binary "0".
- (3) Pulse Polarization Binary Modulation (PPBM) is a low duty cycle format which uses a right-circularly polarized pulse to represent a binary "1" and a left-circularly polarized pulse to represent a binary "0".
- (4) Pulse Quaternary Modulation (PQM) is a low duty cycle format which uses one pulse to represent two bits of information. The pulse is in one of four states which are formed from the combination of two pulse position states and two pulse polarization states.

Figure 6 and Figure 7 show basic functional block diagrams for the various modulation formats.

We selected PQM for the reference satellite system because, while it presents no serious implementation difficulties at 400 Mbps, it is the most efficient format of the four candidates considered. Figure 8 compares the four formats with respect to error rate versus signal level. Note that for a given number of photoelectrons per bit, PQM produces the lowest error rate. The modulator extinction ratio (N_E) assumed was 30.

PQM was developed by MDAC on internal funds prior to this contract and is, therefore, considered proprietary. A patent application is in process.

FIGURE 6 DIGITAL BASEBAND FORMAT

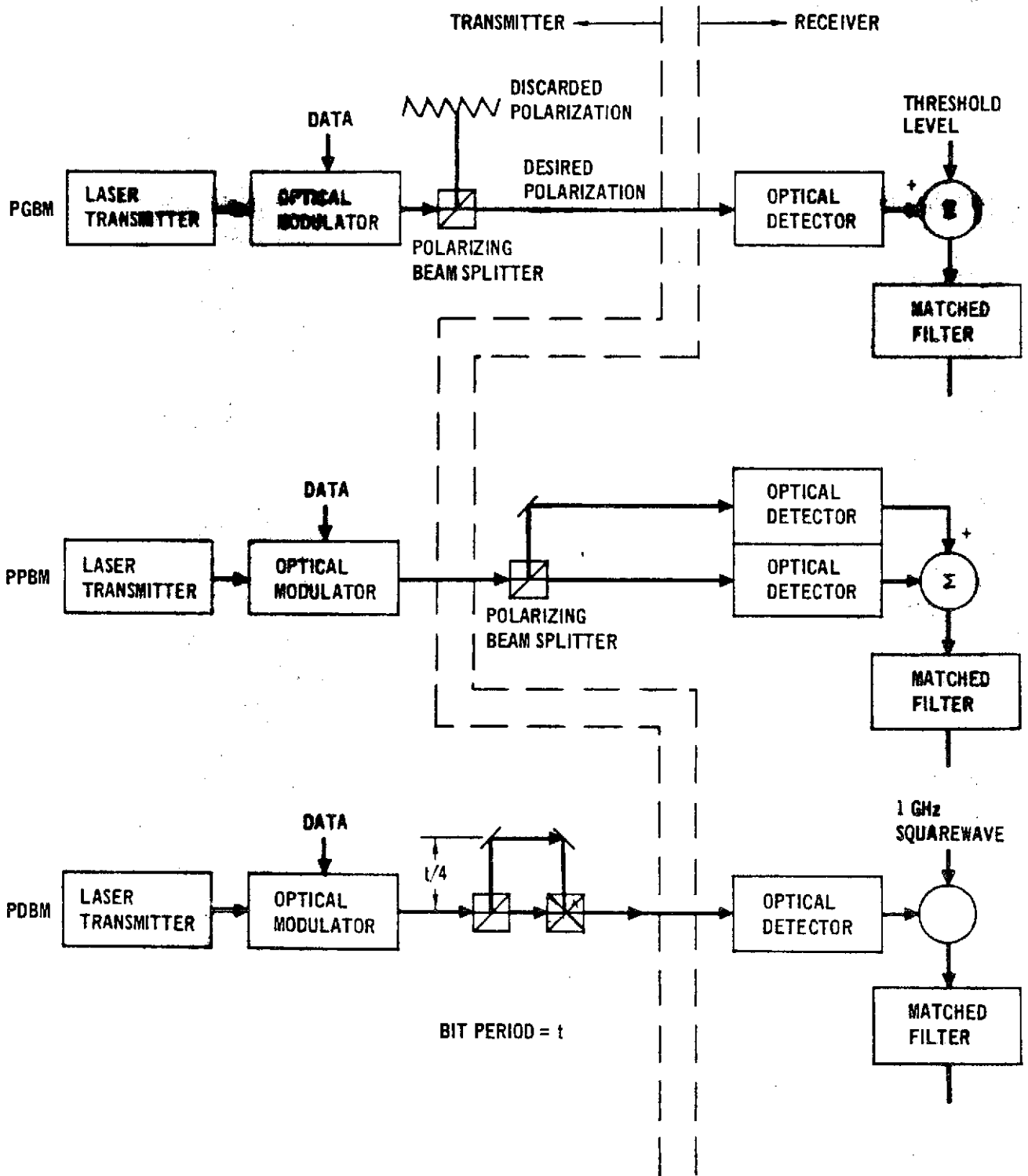
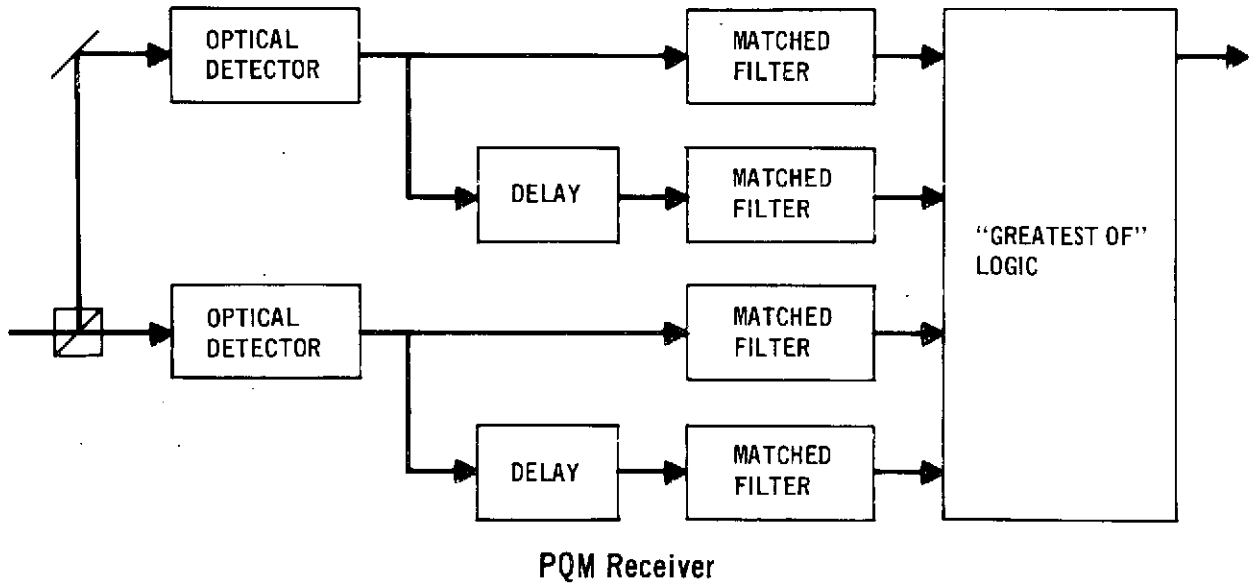
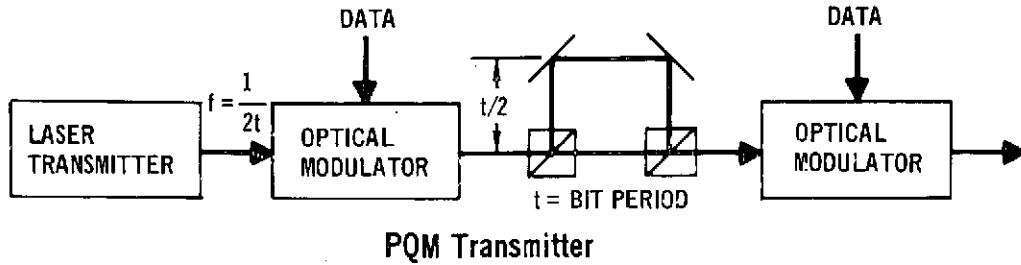
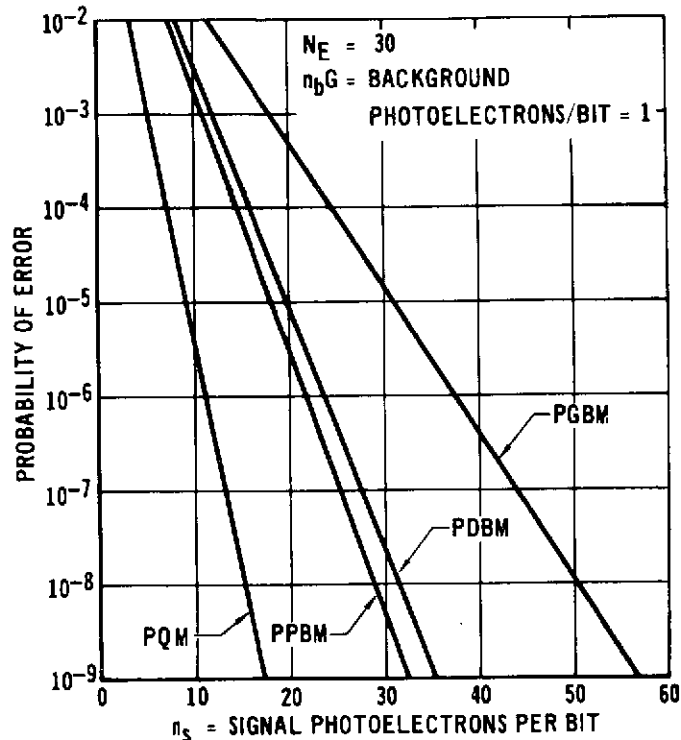


FIGURE 7 PQM SYSTEM



Beacon Laser Selection - A Q-switched beacon laser was chosen because it can perform both acquisition and tracking functions efficiently. The acquisition process is primarily peak power limited while tracking angle noise is primarily average power dependent. The continuously pumped Q-switched laser loses peak power if the interpulse period is too short because the population inversion has not built up sufficiently. The efficiency of the laser suffers if the period is too long because pump power is wasted if it is applied after the inversion process saturates. The optimum pulse repetition

FIGURE 8 COMPARISON OF DIGITAL BASEBAND MODULATION FORMATS



frequency lies in the region from 1 to 5 kpps, depending on the decay time constant of the rod. Our selected design point is 1.6 kpps with a pulse width of 200 nanoseconds. This pulse rate provides a sufficient information rate to the bender bimorph tracking loop to support a 200-Hertz bandwidth.

Acquisition and Tracking Detector - The Quadrant Photo-Multiplier Tube (QPMT) was chosen over the Deflectable Photo-Multiplier Tube (DPMT) and Silicon Quadrant Detector (SQD) for both the acquisition detector and the tracking detector because the OPMT minimizes the average beacon laser power required. A supporting analysis is presented in Appendix B.

Acquisition Field of View - A 4 milli-radian acquisition field of view (diameter) was selected based on a 2 kilometer (3 σ) satellite ephemeris error (indicative of NASA's satellite

tracking capability). A supporting analysis is also presented in Appendix B.

Other Parameters - The results of a link analysis program developed during a previous study ¹ dictated the optics sizes based on projected values of quantum efficiencies and transmission losses. This analysis is discussed in Appendix C for acquisition and tracking and in Section 2.3.3 for communications. Table 3 is a summary of the margins of the various links. Note that the LAS-to-SYNC communications link margin is only 4.4 dB in spite of a 5 μ rad beamwidth. In order to permit 6 dB margin, either the beamwidth must drop to 4.15 μ rad by increasing the transmit aperture to 14.4 inches, or the quantum efficiency achieved must approach 1.45% instead of the 1% projected state-of-the-art for a photocathode at 1.06 μ m. The link analysis computer printouts for the reference links is contained in Appendix D.

TABLE 3
REFERENCE LINK MARGIN SUMMARY

<u>Link</u>	<u>Margin (dB)</u>
Sync-to-Ground, Data-PQM	9.2
Sync-to-Ground, Data-Acquisition	8.8
Sync-to-Ground, Data-Tracking	16.5
Sync-to-Ground, Beacon-Acquisition	6.1
Sync-to-Ground, Beacon-Tracking	11.0
LAS-to-Sync, Data-PQM	4.4*
LAS-to-Sync, Data-Acquisition	7.0
LAS-to-Sync, Data-Tracking	11.1
LAS-to-Sync, Beacon-Acquisition	10.0
LAS-to-Sync, Beacon-Tracking	7.6

* Requires 20% larger transmit aperture or 45% higher quantum efficiency at 1.06 μ m to achieve 6 dB margin.

Tables 4 and 5 summarize the design choices and rationales.

TABLE 4
REFERENCE SYSTEM CONFIGURATION
HIGH DATA RATE TRANSMITTER TERMINAL

PARAMETER	VALUE	RATIONALE
<u>TRANSMITTER</u>		
LASER	MODE-LOCKED Nd:YAG DIODE-PUMPED	DIODE PUMP DEVELOPMENT PROGRAMS UNDERWAY.
WAVELENGTH	1.06 μ M	SPECIFIED BY NASA.
POWER	200 mW	TI HAS ACHIEVED 80 mW; CLAIMS 200 mW WITHIN DEVELOPMENT CAPABILITY.
MODULATION FORMAT	PULSE QUATERNARY MODULATION	MINIMIZES PRIMARY OPTICS DIAMETER.
BEAMWIDTHS: COMM. (DIAMETER)	8.1 μ RAD FOR SYNC-GND 5.1 μ RAD FOR LAS-SYNC	SUFFICIENT LINK MARGINS.
ACQ	100 μ RAD FOR SYNC-GND 60 μ RAD FOR LAS-SYNC	
<u>ACQ. & TRACK RECEIVER</u>		
RECEIVER DIAMETER	7.5 INCHES FOR SYNC-GND 12 INCHES FOR LAS-SYNC	REQUIRED FOR 6 dB ACQ. LINK MARGIN. DICTATED BY HDR BEAMWIDTH ASSUMING DIFFRACTION-LIMITED OPTICS.
ACQUISITION DETECTOR	QPMT WITH III-V P.C. AT 25% QUANTUM EFFICIENCY	REQUIRES LESS BEACON POWER THAN SQD OR DPMT FOR 95% P_d AT 0.5 FAR.
TRACKING DETECTOR	QPMT WITH III-V P.C. AT 25% QUANTUM EFFICIENCY	
ACQUISITION FOV (DIA)	2 mRAD SYNC-GND AND LAS-SYNC	DICTATED BY INITIAL POINTING UNCERTAINTIES.
TRACKING FOV (DIA)	400 μ RAD	NOT CRITICAL; AFFECTS ACQ. TIME.
LINEAR PORTION (DIA)	30 μ RAD	DICTATED BY EXPECTED TRACKING ERROR.
<u>SERVO SYSTEM</u>		
ENCODER RESOLUTION	15 BITS	SUFFICIENT FOR INITIAL POINTING ERROR.
GIMBAL CONFIGURATION	LAS: GIMBALED FLAT MIRROR SYNC: GIMBALED OPTICS	WIDE LOOK ANGLE. NARROW LOOK ANGLE, LOWER SPACE, WEIGHT, AND POWER.

2.3 BALLOON EXPERIMENT DEFINITION. Using the previously described system design as a model, we designed an experiment to prove the feasibility of the reference satellite system within the constraints imposed by the balloon-borne BAPE vehicle.

2.3.1 Experiment Objectives. The primary objective of the experiment is to provide quantitative data on the performance of a system which resembles the reference system as closely as possible with regard to communication performance and fine

TABLE 5
**REFERENCE SYSTEM CONFIGURATION
HIGH DATA RATE RECEIVER TERMINAL**

PARAMETER	VALUE	RATIONALE
BEACON TRANSMITTER LASER	SYNC-GND: LAMP PUMPED Nd:YAG FREQUENCY DOUBLED Q-SWITCHED LAS-SYNC: SAME BUT DIODE- PUMPED	PRIME POWER UNLIMITED. LIFETIME NO PROBLEM. LONG LIFETIME REQUIRED. PRIME POWER LIMITED
WAVELENGTH	0.53 μ M	SPECIFIED BY NASA
POWER	SYNC-GND: 200 mW LAS-SYNC: 25 mW	LAMP PUMPED. DIODE PUMPED.
BEACON BEAMWIDTH (DIAMETER)	SYNC-GND: 400 μ RAD LAS-SYNC: 300 μ RAD	PERMITS ADEQUATE LINK MARGIN
FREQUENCY	1600 Hz	8 SAMPLES/CYCLE FOR 200 Hz CONTROL BANDWIDTH
PULSEWIDTH	200 NS	TYPICAL FOR WEAKLY-PUMPED LASERS
RECEIVERS		
APERTURE	SYNC-GND: 5 FT DIA PRIMARY LAS-SYNC: 2 FT DIA PRIMARY	SIZE AND WEIGHT NO PROBLEM. SIZE AND WEIGHT LIMITED.
COMM. DETECTOR	III-V SEMICONDUCTOR P.C. AT 1% Q.E.	PROJECTED STATE-OF-THE-ART
A&T DETECTORS	QPMT, III-V SEMICONDUCTOR P.C. AT 1% Q.E.	MORE SENSITIVE THAN SQD DPMT NOT AVAILABLE AT 1.06 μ M

tracking capability. Therefore the experiment must be capable of exercising and measuring the significant relationships between system parameters and the performance parameters of bit error rate and tracking error.

2.3.2 Experiment Configuration. The basic configuration of the experiment consists of an airborne transceiver and a ground based transceiver integrated into existing NASA owned equipment. The flight vehicle is a balloon-borne gondola developed under NASA's Balloon Atmospheric Propagation Experiment (BAPE). The ground station receiver uses a portable 30-inch gimballed cassegrain telescope.

In order to make the simulation of the SYNC-GND reference satellite system authentic, we made as many of the experimental parameter values identical to the reference system values as

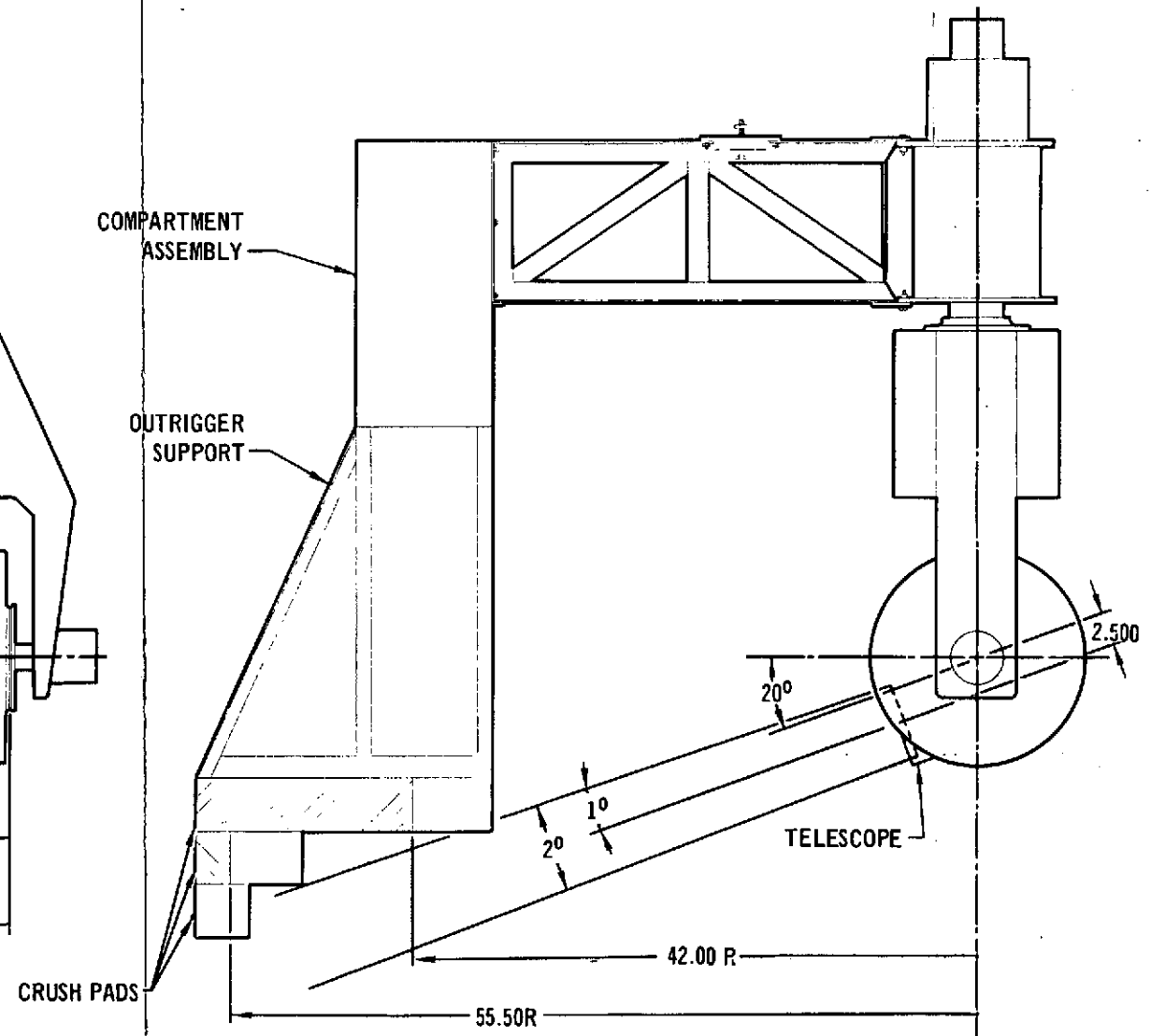
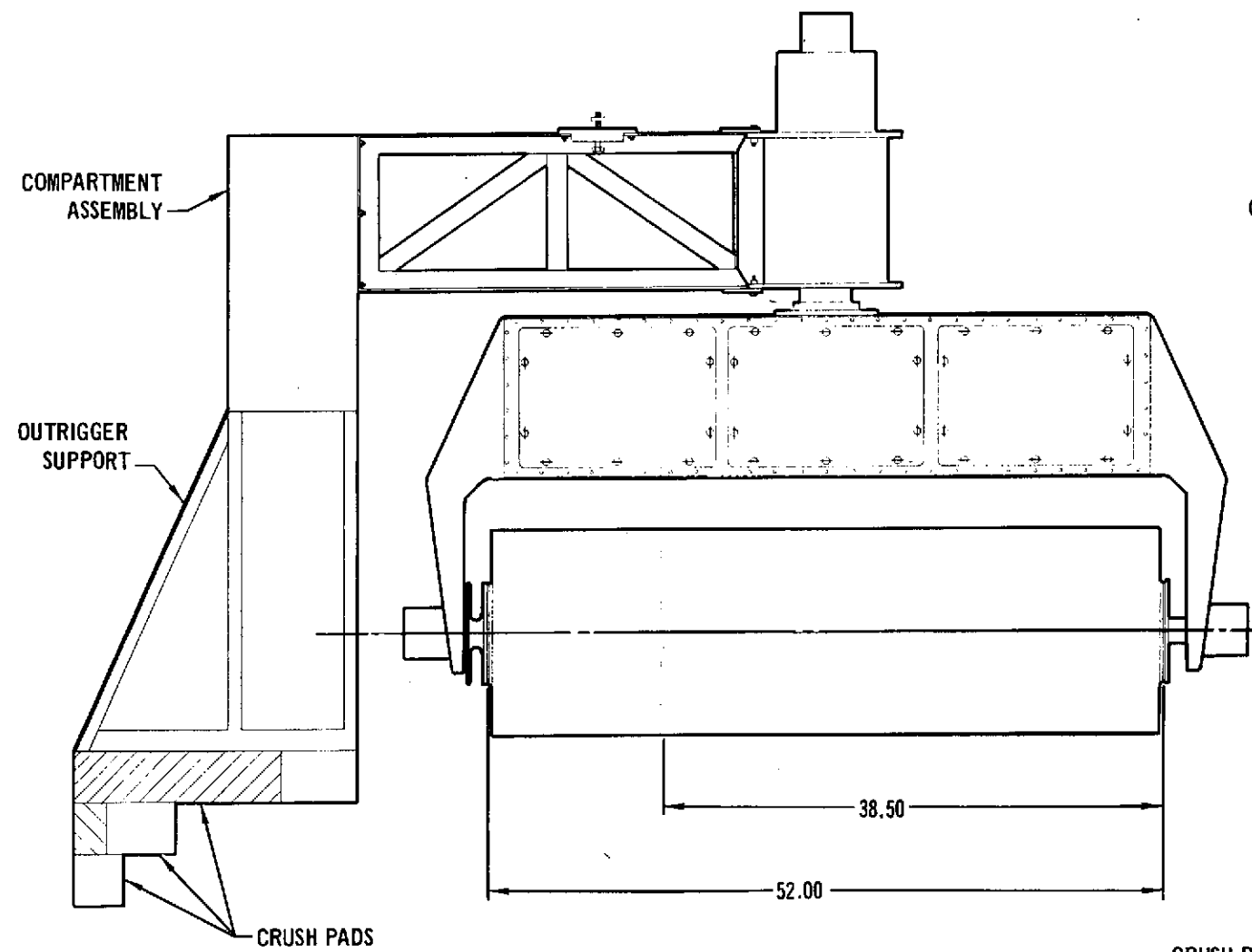
possible. Accordingly, we chose 400 Mbps for the downlink data rate, PQM for the primary downlink modulation format, and 1.06 μm for downlink wavelength.

The uplink data rate could have been chosen as low as a few kilobits and still satisfy the basic system simulation goal. However, it was decided that it was also desirable to simulate a high data rate repeater satellite and to demonstrate a high data rate atmospheric uplink capability. Thus, the uplink data rate was also chosen to be 400 Mbps so that uplink data could be cross-strapped and sent back by the downlink. This arrangement demonstrates a high data rate uplink and a repeater satellite capability. To simulate the Q-switched beacon laser, the PGBM modulator permits 200 nanosecond bursts of 400 Mpps pulses at the desired beacon pulse rate of 1600 pps.

BAPE Gondola - Figure 9 shows the terminal package envelope and the orientation of the package and telescope in relation to the BAPE gondola. Note that when the telescope axis is offset 2.5 inches from the elevation axis of the gimbal set, a maximum look angle of 69° from the azimuth axis is possible without obscuration of the receiver. For a vertical azimuth axis, this capability permits 28 kilometers of slant range for each 10 kilometers of balloon altitude above the ground station.

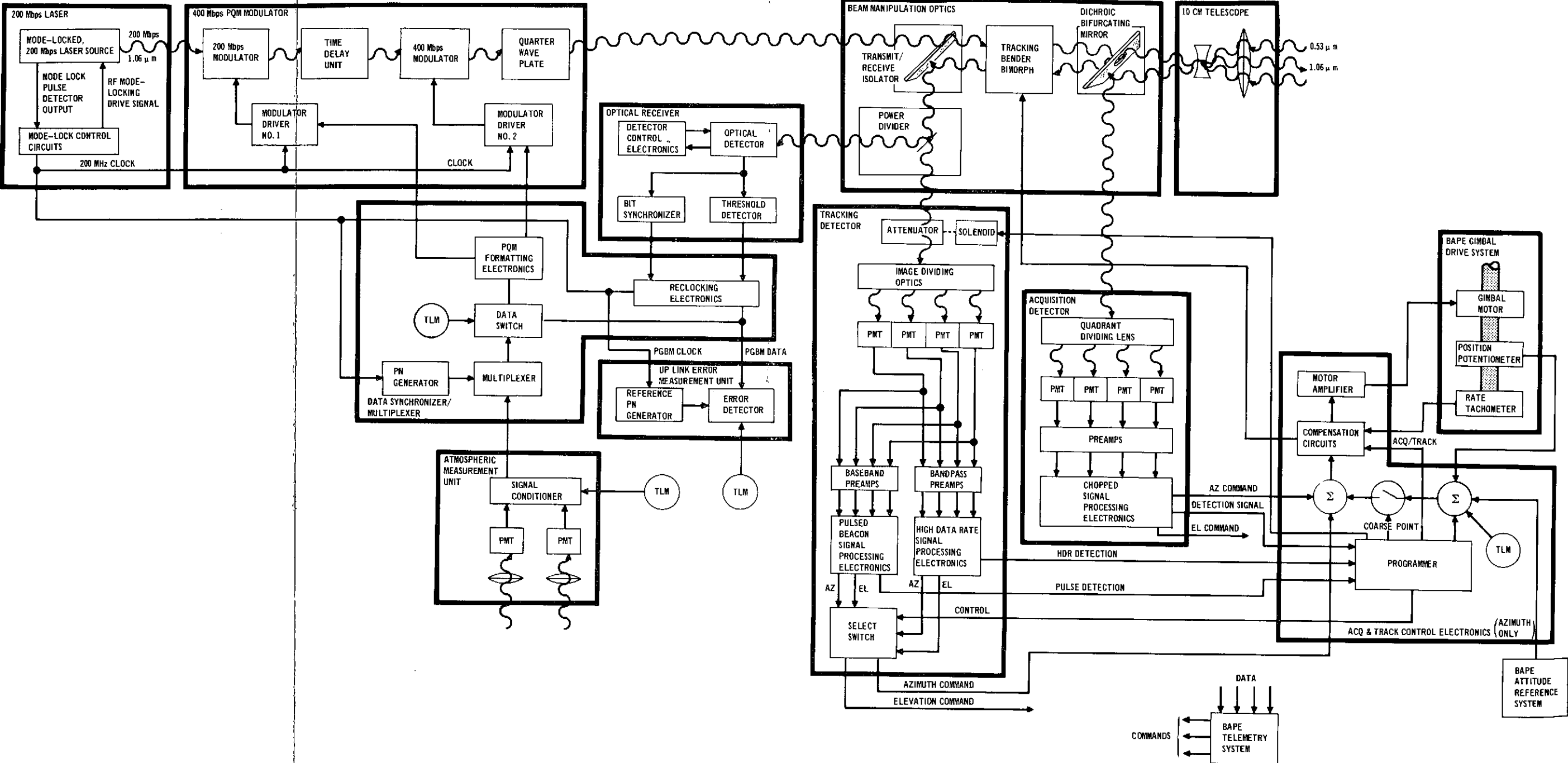
Airborne Transceiver - Figure 10 is a functional schematic of the balloon-borne transceiver terminal. Note the similarity with the schematic for the satellite system (Figure 4). The operation is very similar, so only the differences will be described here. Since the balloon-borne system is a receiver as well as a transmitter of 400 Mbps data, it takes on some of the features shown in both Figure 4 and Figure 5. For example, it contains both the mode-locked laser and the high data receiver we have selected, a Dynamic Crossed Field

FIGURE 9 GONDOLA ASSEMBLY



ALL DIMENSIONS IN INCHES

FIGURE 10 BALLOON BORNE TERMINAL FUNCTIONAL SCHEMATIC



FOLDOUT FRAME

FOLDOUT FRAME

2

Photomultiplier (DCFP). The balloon-borne terminal has the capability of operating the uplink and downlink independently or in a cross-strapped mode in which data received is impressed on the transmitted laser beam. In the latter mode, a reclocking circuit synchronizes the received data with the on-board laser transmitter. The acquisition system operates on a signal composed of 400 Mbps mode-locked laser pulses occurring in bursts of 5-microsecond duration repeated at a 100 kHz rate. To the acquisition detector array, this signal appears as a CW signal modulated at 0.1 MHz with 50% duty cycle. This arrangement permits ease of discriminating the signal from a slowly varying background radiation. The tracking detector is a QPMT, the same type as that of the satellite system. Two signal processing electronics sets are required, one compatible with the 400 Mbps data stream transmitted from the ground when uplink communications is in process, and another compatible with the Q-switched beacon laser signal transmitted from the ground when satellite tracking characteristics are being simulated and evaluated. On-board circuits sense the type of signal received and perform the necessary switching. The detector signals are processed by the compensation circuits and drive the BAPE gimbal set. The gimbal set will be upgraded to permit sufficiently accurate pointing to limit the bimorph bender deflection to achievable values under expected dynamic conditions. The amplitude measurement detectors are present to perform atmospheric propagation measurements. The resulting measurement data is transmitted on the high data rate downlink. A bit-error-measurement electronics package is contained at the terminal for the purpose of evaluating the uplink bit integrity. The measurement data is transmitted via telemetry to the ground station.

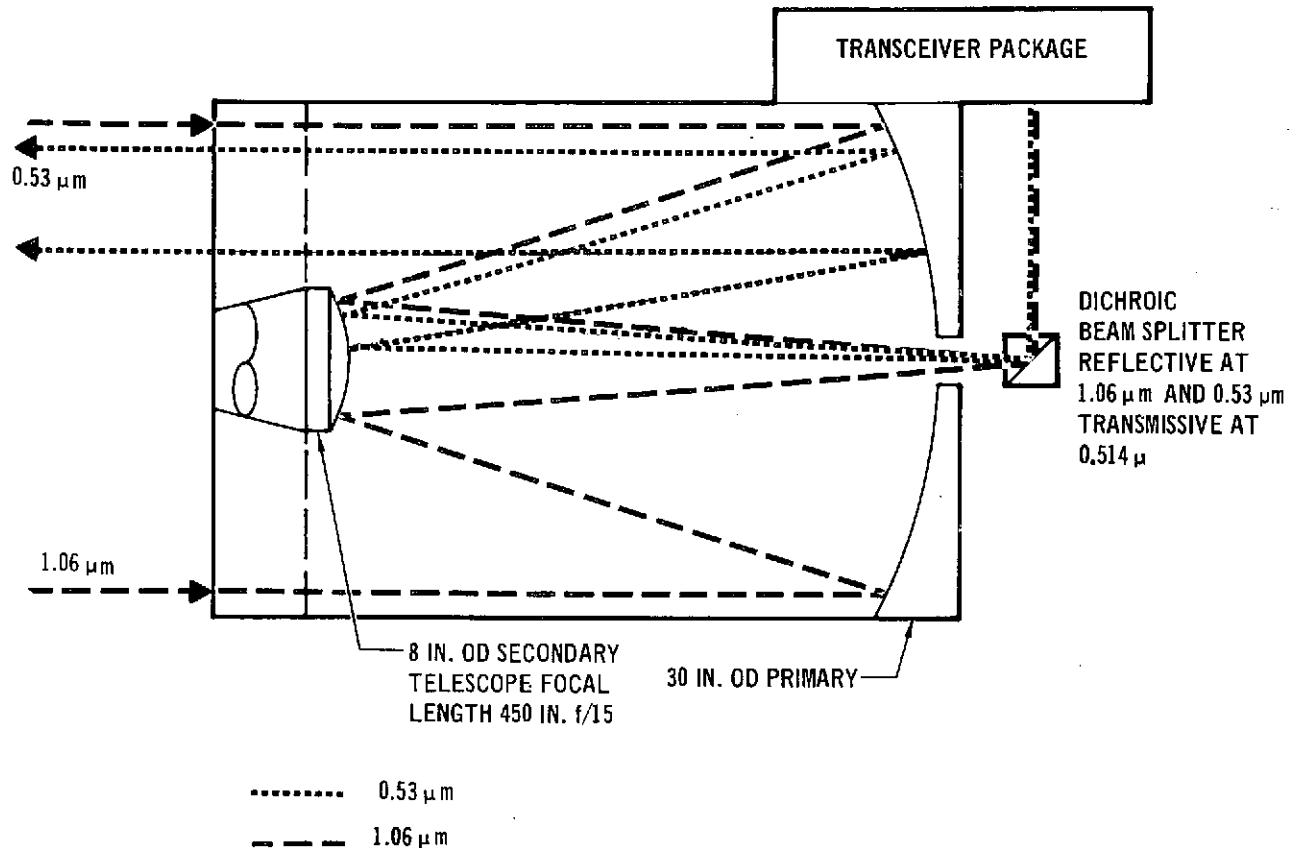
Ground Station - On the basis of a trade study of possible ground station configurations (Table 6), we chose the ground station optics configuration illustrated in Figure 11 and described as:

TABLE 6

GROUND STATION OPTICS CONFIGURATION OPTIONS

- | | |
|--|---|
| <p>A Received 1.06 μm Beam Optical Path</p> <p>A1. Beam collected with 30" diameter telescope and directed to transceiver package mounted on telescope tube via a dichroic beam splitter positioned near the focus behind cassegrain telescope mirror (see Figure 11).</p> <p>A2. Beam collected with 30" diameter telescope and directed to transceiver package located in BAPE Instrument Van along gimbal axis via Coude mirror, gimbal axis mirror, etc.</p> <p>A3. Beam collected with 4" refractive optics of transceiver package mounted on telescope tube.</p> | <p>B Transmit 0.53 μm Beam Optical Path</p> <p>B1. Beam fed from transceiver package mounted on telescope tube through 30" cassegrain telescope mirror via a dichroic beam splitter (see Figure 11).</p> <p>B2. Beam fed from transceiver package located in BAPE Instrument Van via relay mirrors, along gimbal axis to dichroic coated Coude mirror and 30" cassegrain telescope mirror.</p> <p>B3. Beam fed from transceiver package located in BAPE Instrument Van on telescope by relay mirror to ceostat for transmission uplink.</p> <p>B4. Beam fed directly from transceiver optics of transceiver package which is mounted on the telescope tube.</p> |
|--|---|

FIGURE 11 GROUND STATION OPTOMECHANICAL CONFIGURATION



- (1) the ground station transceiver package is mounted on the exterior of the telescope,
- (2) the downlink 1.06 μm beam is collected with a 30" aperture cassegrain telescope mounted on the NIKE-AJAX mount. The collected energy is directed through the hole in the main 30" mirror and separated from the 0.48 μm (or other wavelengths desired) with a dichroic beam splitter. The 1.06 μm beam is then directed to the transceiver detection optics chain in the transceiver package, and
- (3) the uplink 0.53 μm beam is directed by the appropriate optics including a dichroic beam splitter through the focus of the 30" diameter aperture cassegrain telescope. The main 30" mirror is illuminated by a beam 1.75 centimeters in diameter in a region which avoids obscuration. The

advantages of utilizing this configuration are:

- (a) it minimizes vibration effects on optical paths of received and transmitted beam due to shorter path length than if the arrangement A2 and B2 (Table 6) are used,
- (b) it eliminates the complexity of acquisition and tracking Electronics required to interpret the angle tracking detector outputs properly for A2,
- (c) nearly the same transceiver package configuration could be used as on the balloon except for the primary optics selection, arrangements and packaging,
- (d) it will reduce the effect of scintillation on both links,
- (e) it appears to be the configuration that requires the fewest additional optical components and other equipment minimizing costs,
- (f) it maintains the capability to perform a variety of uplink atmospheric experiments if they are desired.

The disadvantages of this configuration are:

- (a) it will require more elaborate transceiver packaging to maintain the thermal environment and isolate this heat source from the telescope tube,
- (b) this configuration may be somewhat inconvenient for adjustment of the transceiver package optical component alignment, etc., before and during the balloon flights, in comparison to the configuration where the transceiver components would be mounted in BAPE instrumentation van.

Transceiver - The ground station transceiver has the characteristics listed in Table 7 . The operation is similar to that of the satellite system and the balloon-borne transceiver. The optical system and the servo system must interface with the NIKE-AJAX mount which steer the 30 inch cassegrain collector. The bender bimorphs are recommended for this package to achieve errors as low as 5 μ rad in the face of mount vibrations and atmospheric phenomena.

TABLE 7

GROUND STATION TRANSCEIVER CHARACTERISTICS

TRANSMITTER

Laser: Mode-locked frequency-doubled Nd:YAG 400 Mpps
 Wavelength: 0.53 μm
 Output power: 100 mW
 Modulation Format: PGBM
 Beamwidth: Acquisition - 1.5 mrad
 Tracking - 100 μrad

ACQUISITION AND TRACKING RECEIVER

Receiver diameter: 30 inches
 Acquisition Detector: QPMT
 Tracking Detector: QPMT

SERVO SYSTEM

Bimorphic beam benders
 Nike-Ajax Tracking mount gimbal drive

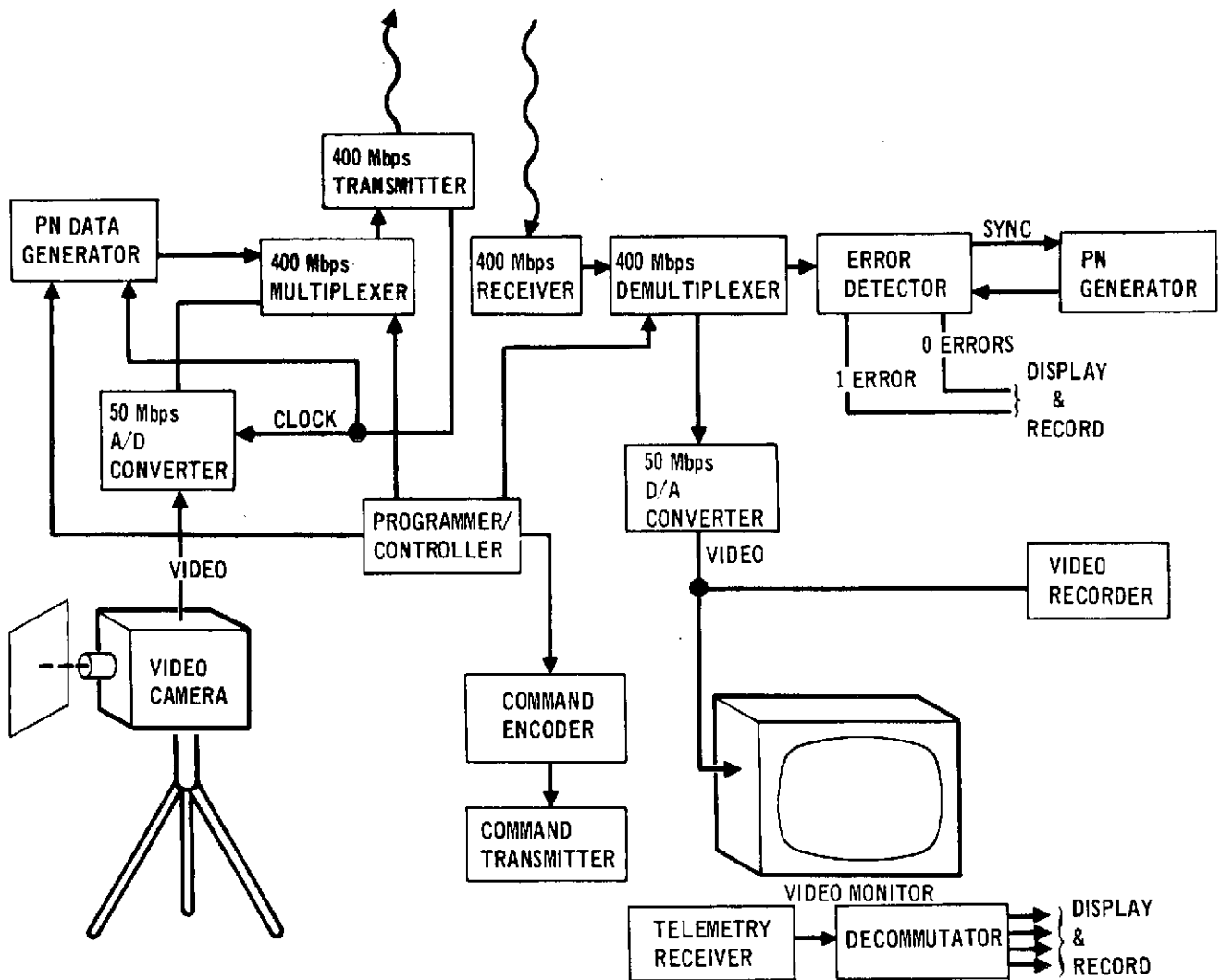
COMMUNICATIONS RECEIVER

Detector: DCFP
 Modulation Formats: PQM, PGBM

Data Handling System - Figure 12 is a block diagram of the data handling system concept. The equipment required to implement this system is summarized in Table 8.

- 2.3.3 Communication Performance Evaluation. In this section we analytically relate link performance (i.e., probability of error) to various system and atmospheric parameters. We define the manner in which these parameters will be experimentally measured and how these measurements will be correlated to test the theoretical results. The hardware necessary to implement the experiment is discussed in Section 2.4.

FIGURE 12 BASELINE GROUND STATION DATA HANDLING SYSTEM



2.3.3.1 Experiment configuration. Figure 13 and Figure 14 show block diagrams of the present baseline transceiver configuration with both PQM and PGBM downlink. The uplink PGBM laser will be modulated at the ground to simulate a low pulse rate beacon signal for modeling the sync satellite reference system. For this case, the high data rate flows only in one direction (i.e., on the downlink). The beacon link is used for acquisition and reciprocity tracking as well as for the transmission of low data rate "house-keeping" data required by the satellite. In

**FIGURE 13 TRANSCEIVER TERMINAL COMMUNICATIONS BLOCK DIAGRAM
(PQM Downlink)**

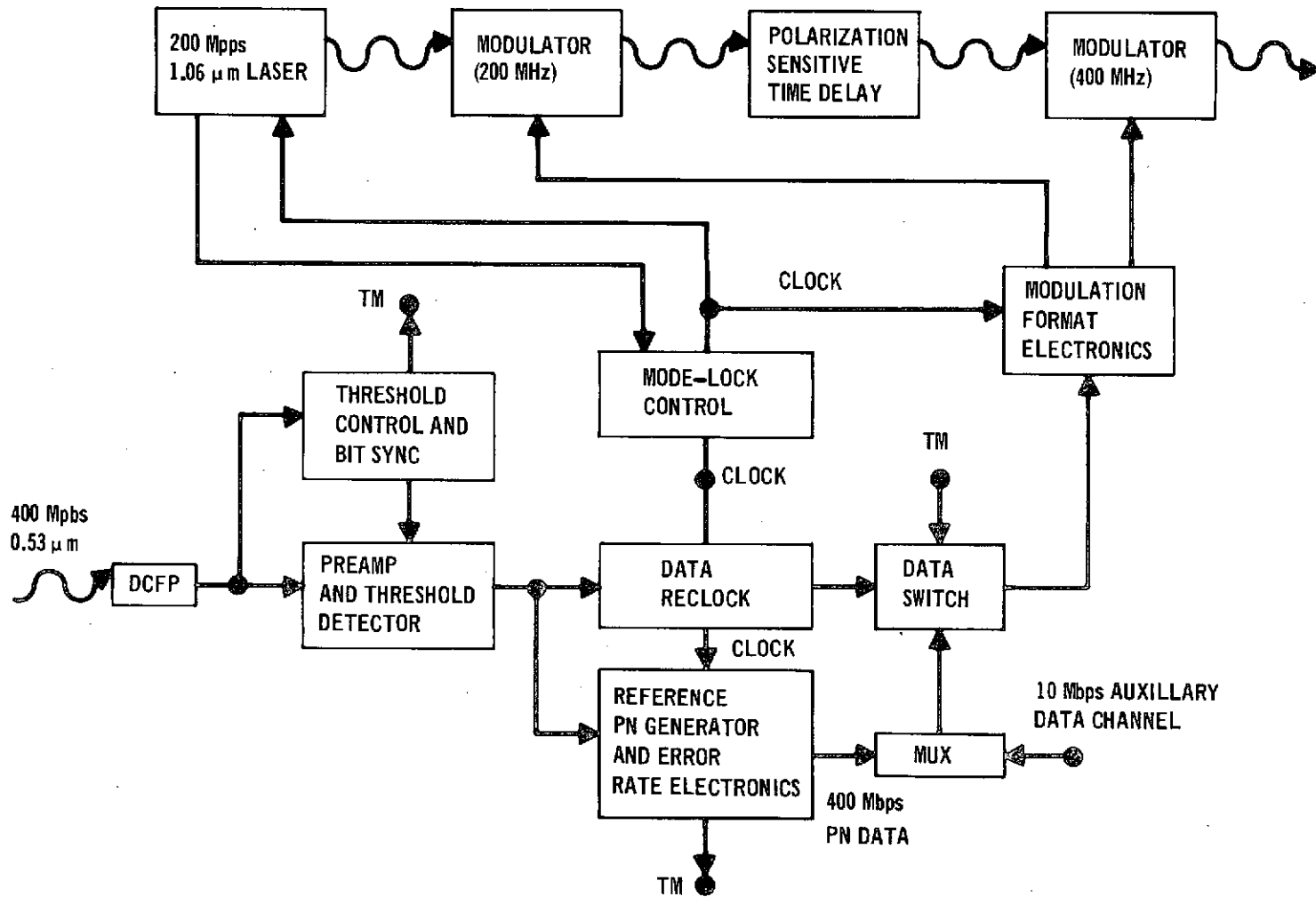
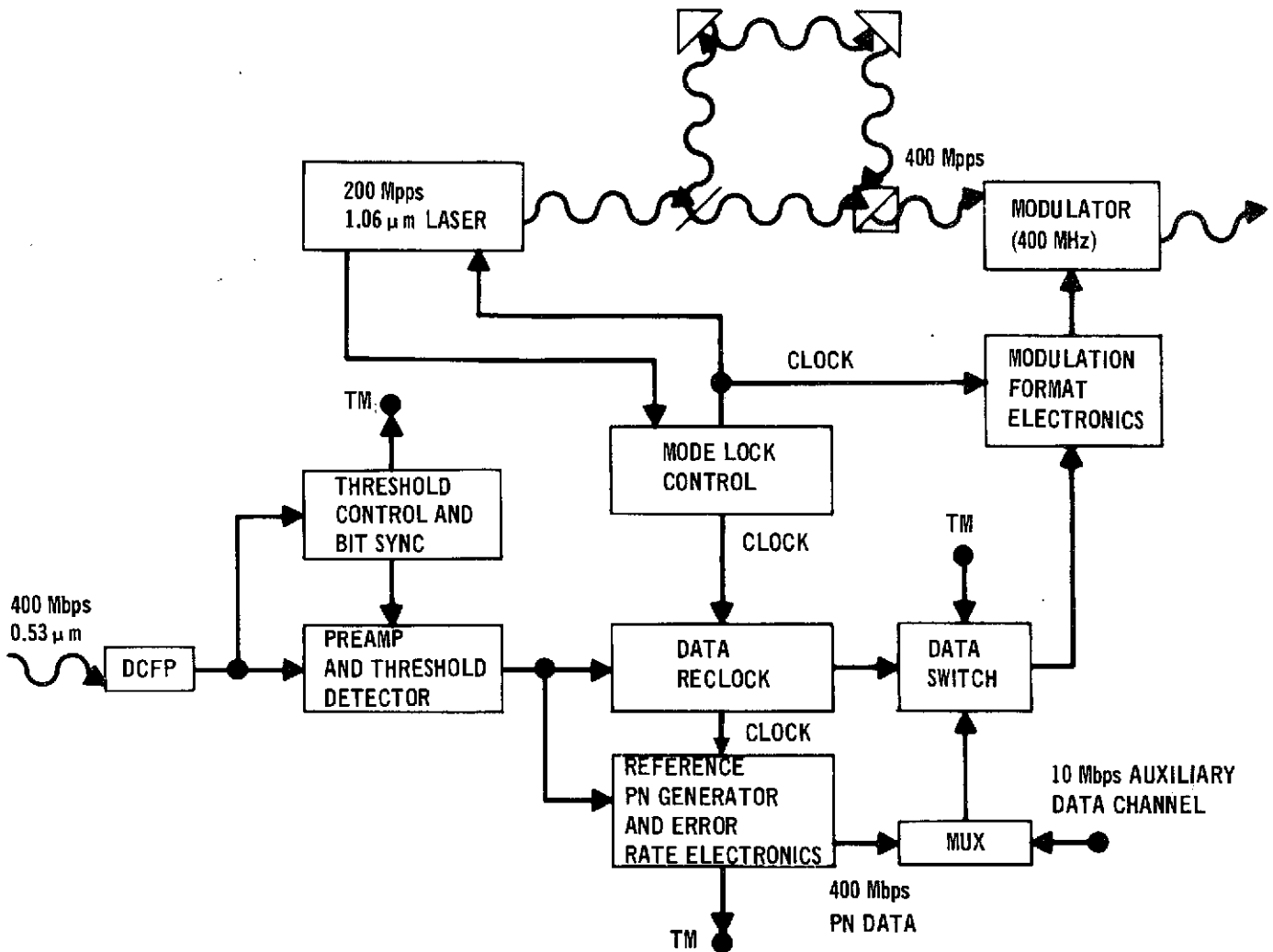


FIGURE 14 TRANSCEIVER TERMINAL COMMUNICATIONS BLOCK DIAGRAM
(PGBM Downlink)



this mode, 400 Mbps PN data generated at the transceiver is used to modulate the PGBM or PQM downlink. Error rate measurements (i.e., ones and zeroes error rates) are made at the ground to determine downlink data quality. These measurements are then correlated with downlink scintillation, wander, tracking error, transceiver laser output power variation, atmospheric turbulence and background measurements. All these measurements will be recorded so that various statistical correlation techniques can be used for data interpretation.

TABLE 8
GROUND STATION DATA HANDLING EQUIPMENT

<u>ITEM</u>	<u>PURPOSE</u>
525-Line Video Camera	Video experiment
50 Mbps A/D Converter	
50 Mbps D/A Converter	
525-Line Video Monitor	
400 Mbps Multiplexer	
Analog Recorders	Record telemetered signals, ground equipment signals, transmitted and received video.
Digital Recorders	
Atmospheric Measurements Assembly	Measures downlink scintillation and lateral coherence length.

The balloon transceiver will also be used to simulate a high data rate repeater satellite. For this case, the received 0.53 μm signal is modulated by a 400 Mbps PGBM data stream. The repeater satellite configuration accepts the 400 Mbps (PGBM) data stream, demodulates the data, and then remodulates the data on 1.06 μm mode-locked laser and transmits to the ground. The downlink modulation format can be either PQM or PGBM. The baseline downlink format is PQM. Figure 13 shows a free running 1.06 μm laser with a reclocking circuit. The reclocking circuit accepts the PGBM digital data stream and stuffs and reclocks the data so that it is properly time synchronized for use by the PQM modulators.

An alternate approach locks the mode-locked 1.06 μm laser directly to the upcoming data stream. This simplifies the electronics (i.e., no reclocking) but puts considerably more strain on the 1.06 μm laser stability since now the laser must be

detuned to follow upcoming data frequency variations. Thus, to enhance laser stability this approach was discarded. Another problem with the discarded approach is that it is really only simulating a single user repeater whereas the reclocking approach can be combined with a digital multiplexer to accept any number of users.

For the repeater simulation, the uplink data is a combination of digitally encoded TV video and PN data. This configuration allows TV to be transmitted up and back down while error rate data is being simultaneously measured on the uplink alone and on the combined up and down link. The error rate data will also be subjectively compared with TV video quality to verify that the same relationships between error rate and picture quality that exist in RF systems also hold in optical systems.

Combined up and down link error rate measurements must be correlated with scintillation, tracking error, received power variation and background measurements made at both the transceiver and at the ground. Ones and zeroes errors are counted separately for PCBM to aid in the detection of nonoptimum threshold control.

The next section determines the analytical relationships between error rate and the previously discussed atmospheric and link parameters.

2.3.3.2 Laser range equation. To determine the performance capability of a communication system, the first step is to determine received power using the fundamental laser range equation. The range equation expresses the received power in terms of the following system parameters.

P_T = average transmitted power (watts)
 λ = optical wavelength (microns)
 R = range (meters)
 G_T = transmit antenna gain

G_R = receiver antenna gain
 N_T = transmitter efficiency
 N_R = receiver efficiency
 N_{SP} = signal processing efficiency

The average received power P_S is given by

$$P_S = P_T N_T N_R N_{SP} G_T G_R \left(\frac{\lambda}{4\pi R}\right)^2 \quad (1)$$

The received energy per pulse E_S is given by

$$E_S = \frac{P_S}{PRF} \quad (2)$$

where PRF is the pulse repetition frequency. Thus the average number of received photoelectrons/pulse is given by

$$n_S = \frac{E_S \eta}{hf} \quad (3)$$

where h is Plancks constant, f is the laser frequency and η is photo-detector quantum efficiency.

Given the received number of signal photoelectrons per bit and a statistical model for the signal and noise, the amount of excess signal power or margin (over that required for some given probability of error) can be calculated.

There are two different types of losses listed and added together in the link margins. One type of loss directly reduces received signal power (for instance space loss, transmitter efficiency, etc.). The second type acts to change the statistics of the received signal in such a manner that the probability of error is degraded and thus extra signal power must be added to achieve the desired probability of error. Examples of this type of loss are atmospheric loss due to scintillation and receiver signal processing losses.

The noise sources which may be significant in our case are signal generated shot noise, background, dark current, and receiver generated thermal noise. The signal generated noise,

background noise, and dark current all have Poisson distributed amplitudes whereas the thermal noise has a continuous gaussian amplitude distribution.

The dominant source of noise in the communication mode is due to background. The received background power P_B is given by

$$P_B = B_I B_F A_R N_R \quad (4)$$

where

B_I = received irradiance due to background $\left(\frac{\text{watt}}{\text{m}^2 \cdot \text{A}}\right)$

B_F = optical filter bandwidth (A)

A_R = effective receiver antenna area (m^2)

The average number of received background photoelectrons/second n_b is given by

$$n_b = \frac{P_B n}{hf} \quad (5)$$

Dark current is normally specified in amps at the detector output. Thus, if i_d is dark current, the average number of dark current generated photoelectrons/second n_d is given by

$$n_d = \frac{i_d}{GQ_E} \quad (6)$$

where G = photo detector gain

Q_E = charge of an electron

The thermal noise power is also reflected to the photocathode to simplify calculation of error rate. The thermal noise generated by the input electronics is specified at the photodetector output as N_o (amps^2/Hz). Thus the equivalent mean square thermal noise power expressed in units of (photoelectrons)² at the photocathode, σ^2 , is given by

$$\sigma^2 = \frac{N_o B}{G^2 Q_E^2} \quad (7)$$

where B = detection bandwidth $\sim \left(\frac{1}{2 (\text{pulse width})}\right)$

Transmitter Efficiency, $N_T - N_T$ is equal to the product of the optical losses in the electro-optical modulator (~ 0.72) and the losses in the optics chain (~ 0.95).

Receiver Efficiency, $N_R - N_R$ is equal to the product of four factors which represent receiver optics losses (~ 0.90), receiver optical filter losses (~ 0.80) and power split-off for tracking (~ 0.99).

Transmit Antenna Gain, $G_T - G_T$ is given by

$$G_T = \frac{32}{\alpha_T^2} \left[e^{-\left(\frac{d_s}{R_o}\right)^2} - e^{-\left(\frac{d_p}{R_o}\right)^2} \right] \quad (8)$$

where α_T = transmission beam width (diameter in radians)

d_p = primary antenna diameter (m)

d_s = secondary antenna diameter (m)

R_o = feedbeam diameter (m)

The expression for G_T assumes a centrally obscured cassegrain telescope. The antenna illumination beam has a Gaussian amplitude taper, and nominally flat phase distribution. For these conditions, G_T can be computed using the Fraunhofer approximation in the Fresnel-Kuchoff integral. This expression is equally valid for a non-obscured antenna by setting $d_s = 0$.

Receiver Antenna Gain, $G_R - G_R$ is given by

$$G_R = \left(\frac{\pi d_R}{\lambda} \right)^2 \quad (9)$$

where d_R is the receiver antenna diameter (m).

since the receiver obscuration losses are accounted for in N_R .

Pointing error can be taken into account by introducing the loss factor

$$e^{-2 \left(\frac{2.5A}{\alpha_T} \right)^2}, \quad (10)$$

where A is the rms pointing error in microradians.

2.3.3.3 Signal processing losses. Table 9 is a summary of the losses due to non-ideal signal processing for PGBM. The loss due to a non-ideal counter comes from the fact that the receiver does not use an integrate-and-dump filter. A passive filter is used instead due to the lack of time to dump an integrator. Thus there is loss due to intersymbol interference and non-ideal integration (i.e. non-ideal counting). The amount of the loss depends on data rate and the passive filter bandwidth and flatness. Also the threshold detector does not have perfect amplitude or timing resolution. In particular the inability of the threshold detector to precisely measure pulse amplitude contributes approximately 0.3 dB loss. Deviations of the DCFP output statistics from the Poisson model results in another 0.5 dB loss. Laser power variation also contribute to non-ideal performance. All these effects are discussed in detail in reference 2.

TABLE 9

SIGNAL PROCESSING LOSSES

<u>Degradation Source</u>	<u>Power Loss</u>
Non-ideal counter	1.0 dB
Finite threshold amplitude resolution	0.3 dB
Detector excess noise factor	0.5 dB
Laser power variations	0.2 dB
Total	2.0 dB

Losses for PQM have not been experimentally verified but are arbitrarily assumed to be the same as for PGBM. Signal processing losses are often combined with the receiver efficiency factor to determine the total receiver losses.

2.3.3.4 Bit error probability. Section 2.3.3.2 determined an expression for the mean received number of photoelectrons/pulse (n_s). This section will define the probability of bit error for PGBM

and PQM as a function of n_s and the atmospheric effects model and parameters.

The probability of error for PGBM can be written as

$$P_e | n_s = \frac{1}{2} \left(\sum_{k=0}^{n_t-1} \frac{m_1^k}{k!} e^{-m_1} + \sum_{k=n_t}^{\infty} \frac{m_0^k}{k!} e^{-m_0} \right) \quad (11)$$

where

$$m_0 = \frac{1}{N_F+1} n_s + n_b G \quad (12)$$

$$m_1 = \frac{N_E}{N_E+1} n_s + n_b G \quad (13)$$

n_s = signal photoelectrons/bit

$n_b G$ = background photoelectrons/bit

N_E = modulator extinction ratio

$$n_t = \frac{(m_1 - m_0) + \ln \left[\frac{P(0)}{P(1)} \right]}{\ln \left(\frac{m_1}{m_0} \right)} \quad (14)$$

where

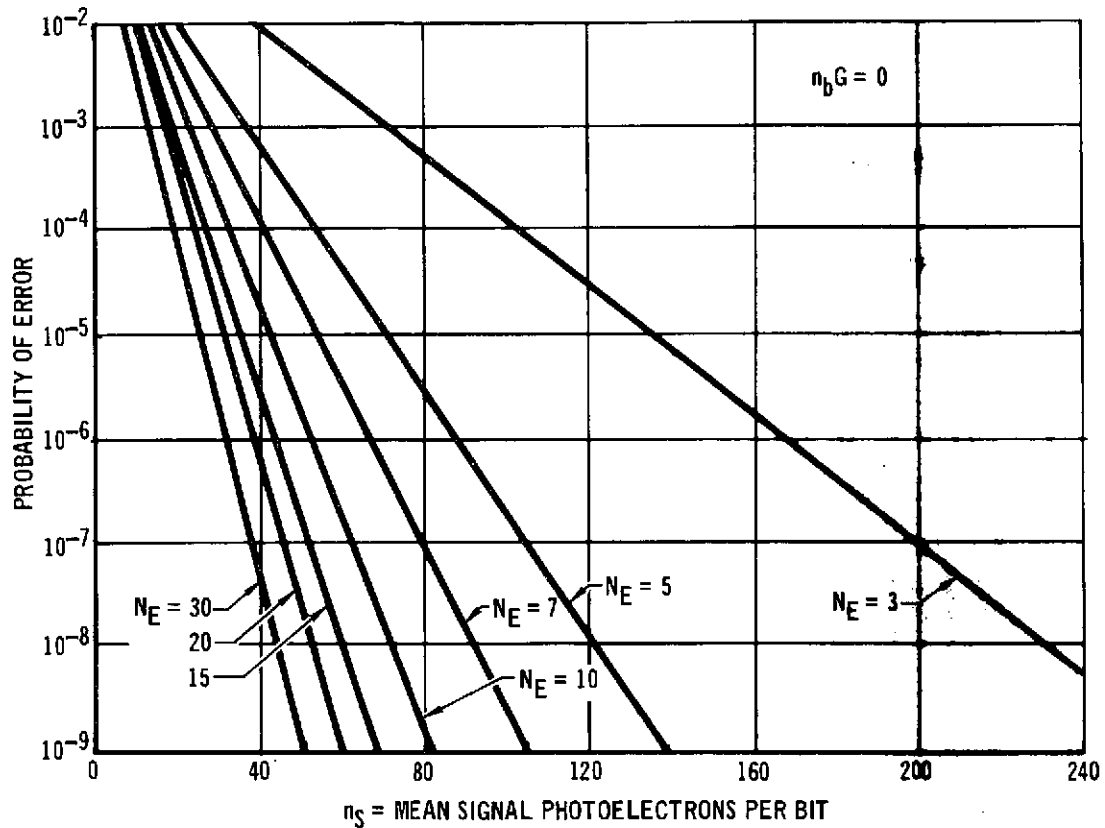
$P(1)$ = a priori probability of a one

$P(0)$ = a priori probability of a zero

Figure 15 is a plot of P_e as a function of n_s for typical values of N_E .

Equation [11] assumes an ideal photoelectron counter. The justification for this model comes from assuming that when an electron is emitted from the photocathode due to the arrival of a light photon, it goes through an essentially noiseless, very high gain multiplication process. Thus, for each photoelectron there is a large current pulse (of essentially constant amplitude

FIGURE 15 PGBM BIT ERROR PROBABILITY AS A FUNCTION OF RECEIVED PHOTOELECTRONS PER BIT



and shape) at the photomultiplier output. The amplitude of this pulse is much greater (on the order of 60 times or more) than the equivalent rms thermal noise level at the input to the first preamplifier. After amplification, the photomultiplier output is assumed to pass into an integrate-and-dump filter which is synchronized to the expected pulse arrival time. Since each photoelectron causes an identical output pulse into the integrator, the output of the integrator takes on only discrete values depending completely on the total number of pulses which arrived during the integrate time. Since the integrator output is dumped and reset to zero after each bit period, there is ideally no intersymbol interference. Finally, the output of the integrator is compared with an ideal threshold for PGBM to

determine the presence or absence of an optical information pulse.

Equation [11] assumes no atmosphere, or equivalently that n_s is a constant (i.e., time independent). Unfortunately the atmosphere causes the actual received power to vary as a function of time. Variations in received power are caused by various atmospheric effects such as scintillation, beam wander, beam spread and attenuation due to scattering. Beam spread and atmospheric scattering are usually assumed to only reduce the average received power and not to cause variations in received power. The effect of the atmosphere is calculated by assuming that the index of refraction is a random function of time and space. A considerable amount of literature on experimental and analytical results is available concerning the mean square variation in received power and to a lesser extent the probability density of the instantaneous received power. The instantaneous received power, considering only scintillation, can be thought of as proportional to the time varying gain X of the atmosphere. Thus, if we assume that the atmospheric gain consists of a set of N slabs of random gain,

$$X = \prod_{i=1}^N A_i \quad (15)$$

$$\therefore \log X = \sum_{i=1}^N \log A_i \quad (16)$$

For N large, $\log X$ can be shown to be approximately gaussian by use of the central limit theorem, or in other words, X can be shown to be log-normal. The variance of $(1/2) \log (X/E(X))$, the so-called log amplitude variance, $C_{\ell}(0)$, must now be known to compute the probability of error for transmitting through the atmosphere. P_e for PGBM in the atmosphere is given by

$$P_e|C_\ell(0) = \int_0^{\infty} P_e|n_s f(n_s) dn_s \quad (17)$$

where

$P_e|n_s$ is given in Equation (11)

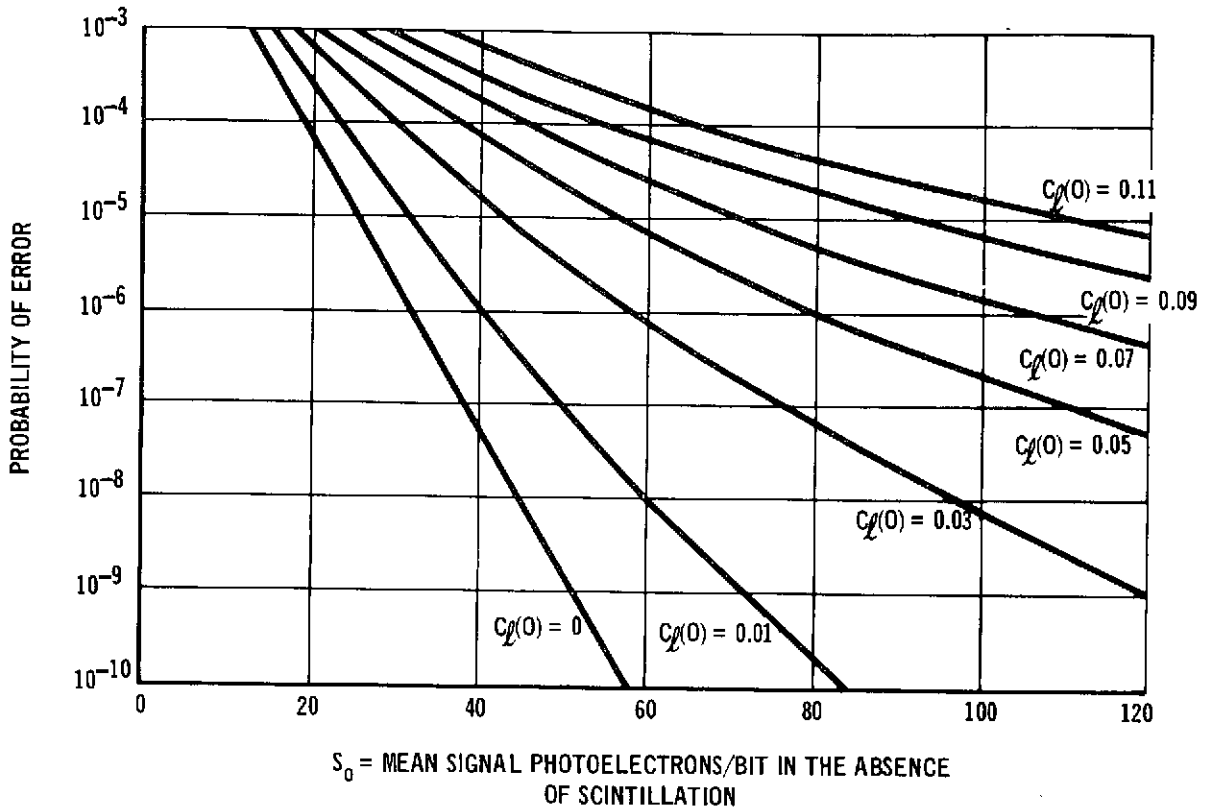
$$f(n_s) = \frac{1}{2n_s \sqrt{2\pi C_\ell(0)}} e^{-\left\{ \frac{\frac{1}{2} \ln \left(\frac{n_s}{S_0} \right) + C_\ell(0)}{2 C_\ell(0)} \right\}^2}, n_s > 0 \quad (18)$$

$$S_0 = E(n_s) \quad (19)$$

Figure 16 is a plot of P_e versus S_0 for various values of $C_\ell(0)$. Figure 17 shows the extra power required to achieve a 10^{-6} bit error probability as a function of $C_\ell(0)$. Note that, here and in the following, S_0 is the mean number of received photoelectrons per bit which would be received in the absence of atmospheric disturbances. Equation 17 assumes ideal threshold control. Unfortunately, there is still another level of difficulty because the log normal variance is itself a function of time. There are two general approaches to characterizing $C_\ell(0)$.

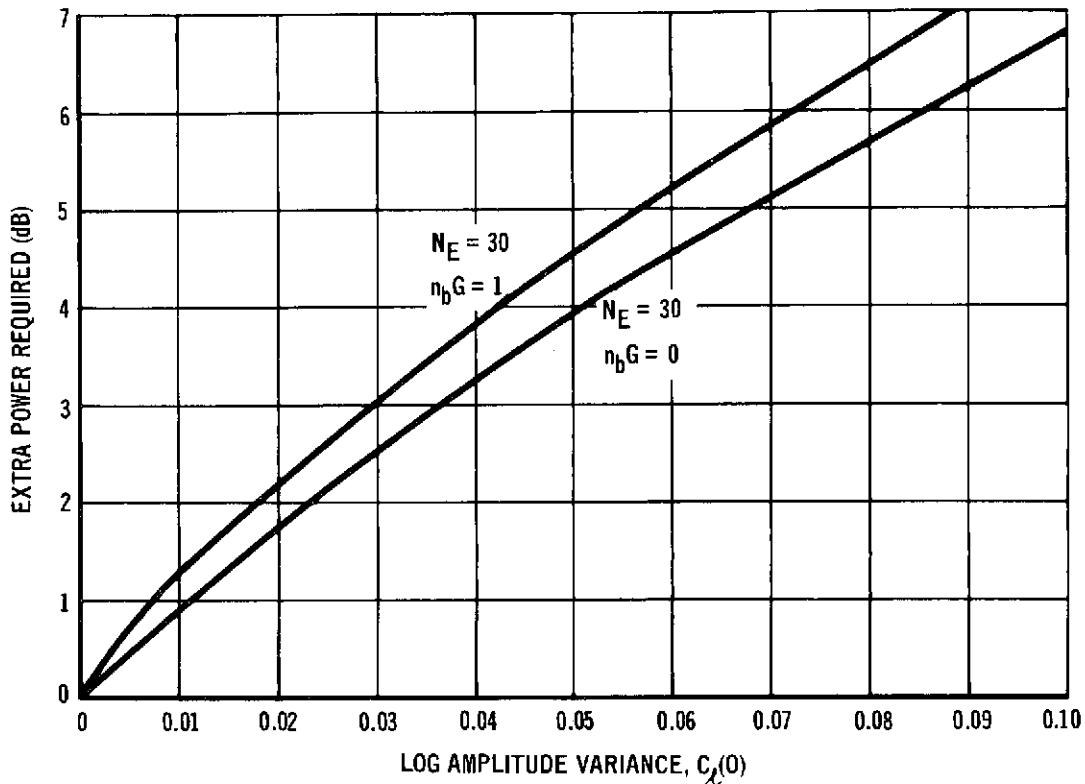
The first approach is a legacy of the atmospheric scientists that did the pioneering work in this area (see Appendix E). They were interested in developing and validating a general mathematical model for the effect of the atmosphere on light but were not primarily concerned with predicting communication link performance. Their mathematical model predicted the average value of $C_\ell(0)$ for a fixed turbulence profile. Thus, the experiments they performed tried to determine an instantaneous turbulence profile by experimentally measuring temperature variations versus altitude. They then compared the prediction

FIGURE 16 GRAPH OF PROBABILITY OF ERROR VERSUS MEAN NUMBER OF SIGNAL PHOTOELECTRONS/BIT WITH $C_{\lambda}(0)$ AS A PARAMETER FOR $N_E = 30$ AND $n_B G = 0$



of the instantaneous value of $C_{\lambda}(0)$ from the experimentally measured turbulence profile to the instantaneous value of $C_{\lambda}(0)$ measured experimentally from the output of a photodetector. Since these comparisons were performed at different times and different places, they also obtained some information on the expected range of values of $C_{\lambda}(0)$ from these comparisons. They were able to heuristically obtain analytical forms for typical average turbulence profiles which, of course, correspond to some average value of $C_{\lambda}(0)$. Communication system designers then used these average values of $C_{\lambda}(0)$ in Equation 17 to compute probability of error (which implicitly assumes that $C_{\lambda}(0)$ is a constant). This leads to a very optimistic estimate of P_e since worst case situations (i.e., where $C_{\lambda}(0)$ is much greater than its mean value) tend to dominate error rate calculations

FIGURE 17 EXTRA POWER REQUIRED TO ACHIEVE $P_e = 10^{-6}$ AS
A FUNCTION OF $C_{\lambda}(0)$, THE LOG AMPLITUDE VARIANCE



even when the worst case situations are themselves of rather low probability of occurrence.

The second approach to the problem of characterizing $C_{\lambda}(0)$ is to try to measure the complete distribution of $C_{\lambda}(0)$ rather than just its mean value. Or, rather than trying to characterize the distribution of received power as log normal with a random $C_{\lambda}(0)$, one would attempt to directly define the overall distribution of received power by averaging over periods much longer than the correlation time of $C_{\lambda}(0)$. One of the problems in these characterizations come about from the fact that there are several time frames or correlation intervals involved. Looking at the signal from the optical detector over a single pulse period, the received optical power is constant and the output of the photomultiplier is a Poisson random variable. If, instead, we look at the incident optical power or equivalently the optical detec-

tor output averaged over many pulses (i.e., average for milliseconds) we see a process that is usually characterized as log normal. If we observed the received power over periods of time long enough for significant changes in the atmosphere to occur we would observe changes in the estimated parameters of the log normal distribution. These changes can be regarded as a deterministic nonstationarity if a mathematical relationship between $C_{\ell}(0)$ and meteorological conditions can be found, or they can also be assumed random and a statistical distribution experimentally defined for them. These remarks indicate that experimental measurements of error rates will be very sensitive to the measurement periods used. The communications link operates for periods longer than any of the correlation times and thus its average error rate comes from averaging over all the various time frames. However, short term error rate statistics will depend on the individual atmospheric processes involved.

Combined Atmospheric Degradation - The previous remarks discussed the statistics of received power variations due to scintillation alone. In this section we develop a model for the combined atmospheric effects.

Attenuation due to scattering and beam spread both act primarily to reduce the magnitude of received power but do not cause variations in power. Appendix E gives equations for the reduction in power due to beam spread and attenuation.

Wander causes the apparent beam center to move. Thus, for a Gaussian beam intensity pattern with beam radius R (i.e., power is down by $\frac{1}{e^2}$ at R radians), the received power at a point detector for a distance between the center of the beam and the detector of η radians is reduced by

$$e^{-2\eta^2/R^2}.$$

A non-zero η is caused by both angle tracking error and atmo-

spherically induced wander. We assume that the components of the tracking error and wander along two orthogonal axes are Gaussian. That is, $\eta^2 = X^2 + Y^2$ where X and Y are zero mean Gaussian random variables with variance $\frac{\alpha R^2}{2}$. Typical values for α are given in Appendix E. If we also assume that variations due to wander and scintillation are independent, and scintillation is log-normal, we note that the instantaneous received power S can be written as

$$S = S_0 e^{(\alpha' - 2C_\ell(0))} e^{-2\eta^2/R^2} \quad (20)$$

where α' is a Gaussian random variable with zero mean and variance $4 C_\ell(0)$. S_0 is the received power in the absence of scintillation. η^2 is chi-squared with two degrees of freedom since $\eta^2 = X^2 + Y^2$ where X and Y are gaussian. The $2C_\ell(0)$ in the exponent is only a normalization factor. Appendix F determines an expression for the distribution of S which is given below

$$g(S) = \frac{S^{\frac{1}{2\alpha} - 1}}{4\alpha(S')^{1/2\alpha}} e^{(C_\ell(0)/\alpha)} \left(1 - G\left(\frac{\ln(S/S')}{2\sqrt{C_\ell(0)}} + \sqrt{\frac{2 C_\ell(0)}{\alpha}}\right) \right) \quad (21)$$

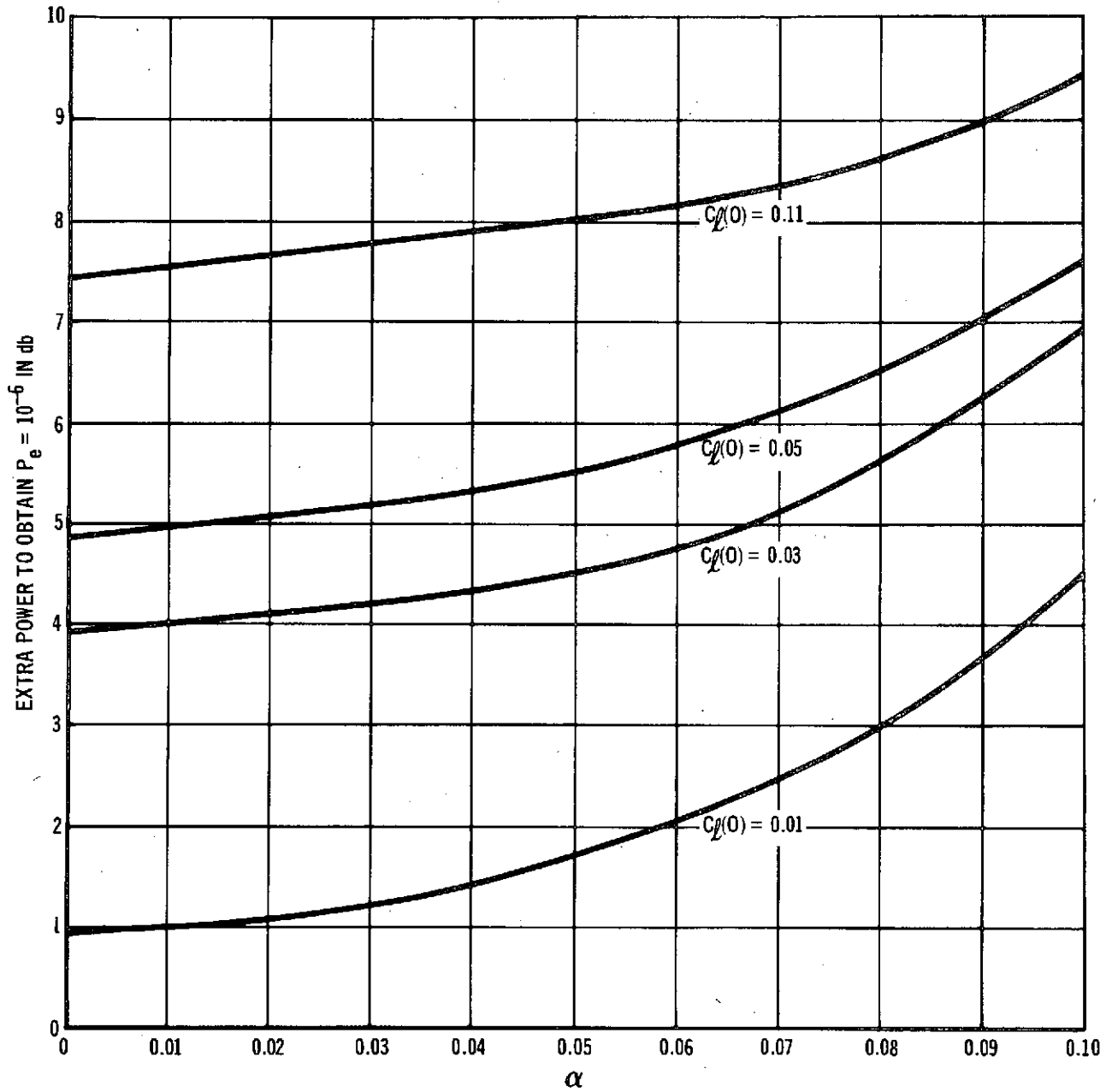
where

$$G(X) = \frac{1}{\sqrt{2\pi}} \int_{-\infty}^X e^{-t^2/2} dt, \text{ and} \quad (22)$$

$$S' = S_0 e^{-2 C_\ell(0)} \quad (23)$$

This expression can now be used with Equation 17 by noting that n_s is proportional to S to obtain the probability of error P_e as a function of $C_\ell(0)$ and the wander (and tracking error) parameter α . Figure 18 shows the extra power required to obtain $P_e = 10^{-6}$ over the case of no atmosphere ($C_\ell(0) = \alpha = 0$) as a function of $C_\ell(0)$ and α .

FIGURE 18 EXTRA POWER REQUIRED FOR PGBM SYSTEM TO OBTAIN $P_e = 10^{-6}$ IN THE PRESENCE OF SCINTILLATION AND WANDER



We now find the probability of error for the case where $C_\ell(0)$ is a random variable. The BAPE I data taken by NASA ³ as well as other experimental results ⁴ indicated that $C_\ell(0)$ is also approximately log normal (at least in the central lobe of the distribution if not on the tails). These results indicated that for a point detector, the mean value of $C_\ell(0)$ was 0.19 and the variance of $C_\ell(0)$ was 4.3×10^{-3} . Assuming $C_\ell(0)$ is itself log-normal, P_e is then given by

$$P_e = \int_0^{\infty} P_{e|C_\ell(0)} h(C_\ell(0)) dC_\ell(0) \quad (24)$$

where: $P_{e|C_\ell(0)}$ is given in Equation [17] and

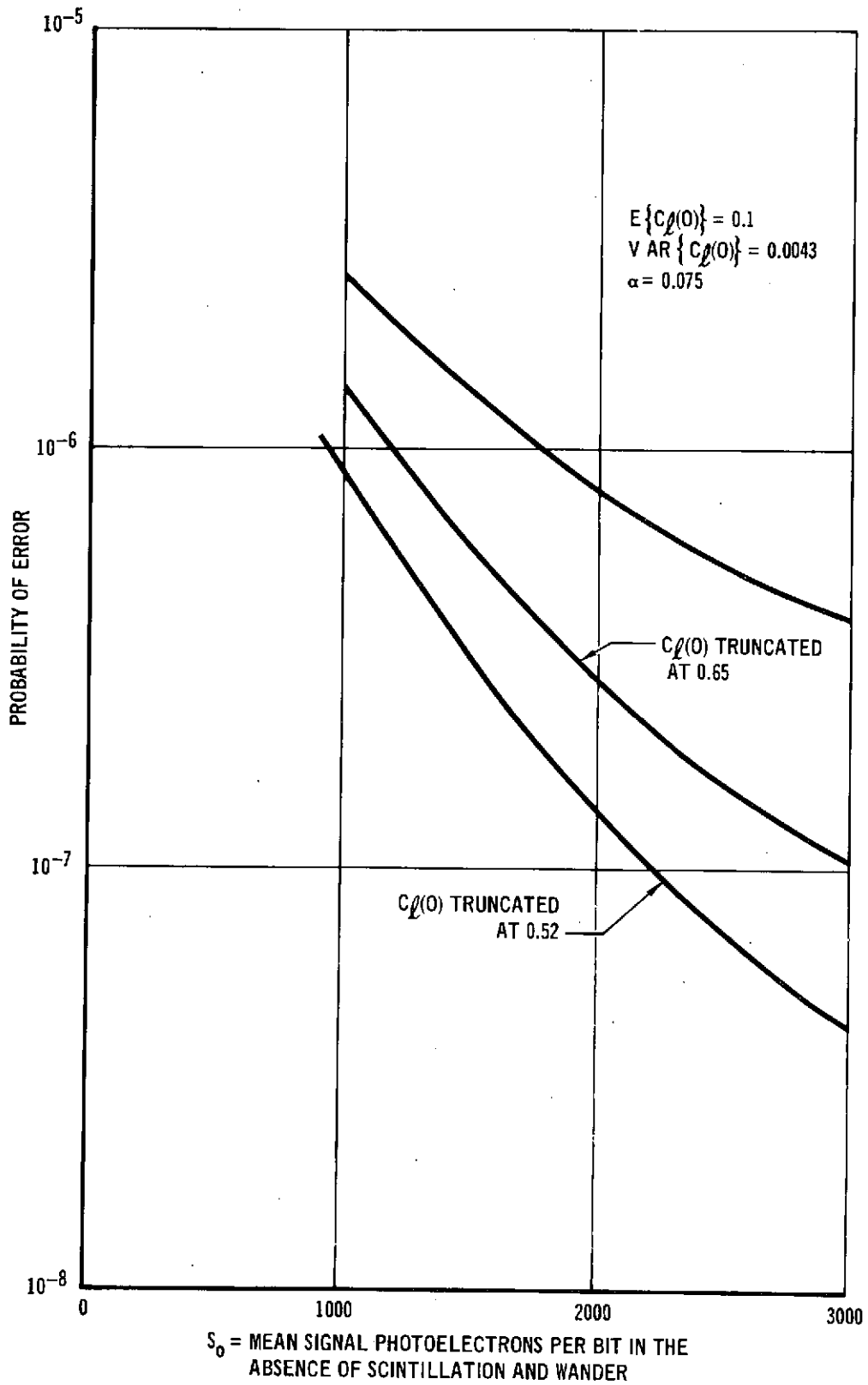
$$h(C_\ell(0)) = \frac{e^{-\left\{ \left(\ln \frac{C_\ell(0)}{M_c} + \frac{1}{2} \ln \left(\left(\frac{V_c}{M_c} \right)^2 + 1 \right) \right)^2 / 2 \ln \left(\left(\frac{V_c}{M_c} \right)^2 + 1 \right) \right\}}}{C_\ell(0) \sqrt{2\pi \ln \left(\left(\frac{V_c}{M_c} \right)^2 + 1 \right)}} \quad (25)$$

$C_\ell(0) > 0$

where $M_c = 0.1$ is the mean of $C_\ell(0)$ and $V_c = 4.3 \times 10^{-3}$ is log-normal variance of $C_\ell(0)$. Experimental measurements of high turbulence horizontal paths 5-9 have also shown a saturation of $C_\ell(0)$ at approximately 0.55. The combination of these two results indicate that a truncated log-normal distribution for $C_\ell(0)$ might also be appropriate. Figure 19 shows P_e for both a truncated and nontruncated log-normal distribution for $C_\ell(0)$.

The point of this whole discussion becomes evident by comparing Figures 15 and 19. The difference in the estimate of the required received power for a point detector to obtain $P_e = 10^{-6}$ ranges over 17 dB as we go from the most optimistic estimate (Equation 11, no fading) to the most pessimistic estimate (Equation 24, $C_\ell(0)$ log-normal with $M_c = 0.1$ and

FIGURE 19 PGBM BIT ERROR PROBABILITY WHEN $C_1(0)$ IS LOG NORMAL



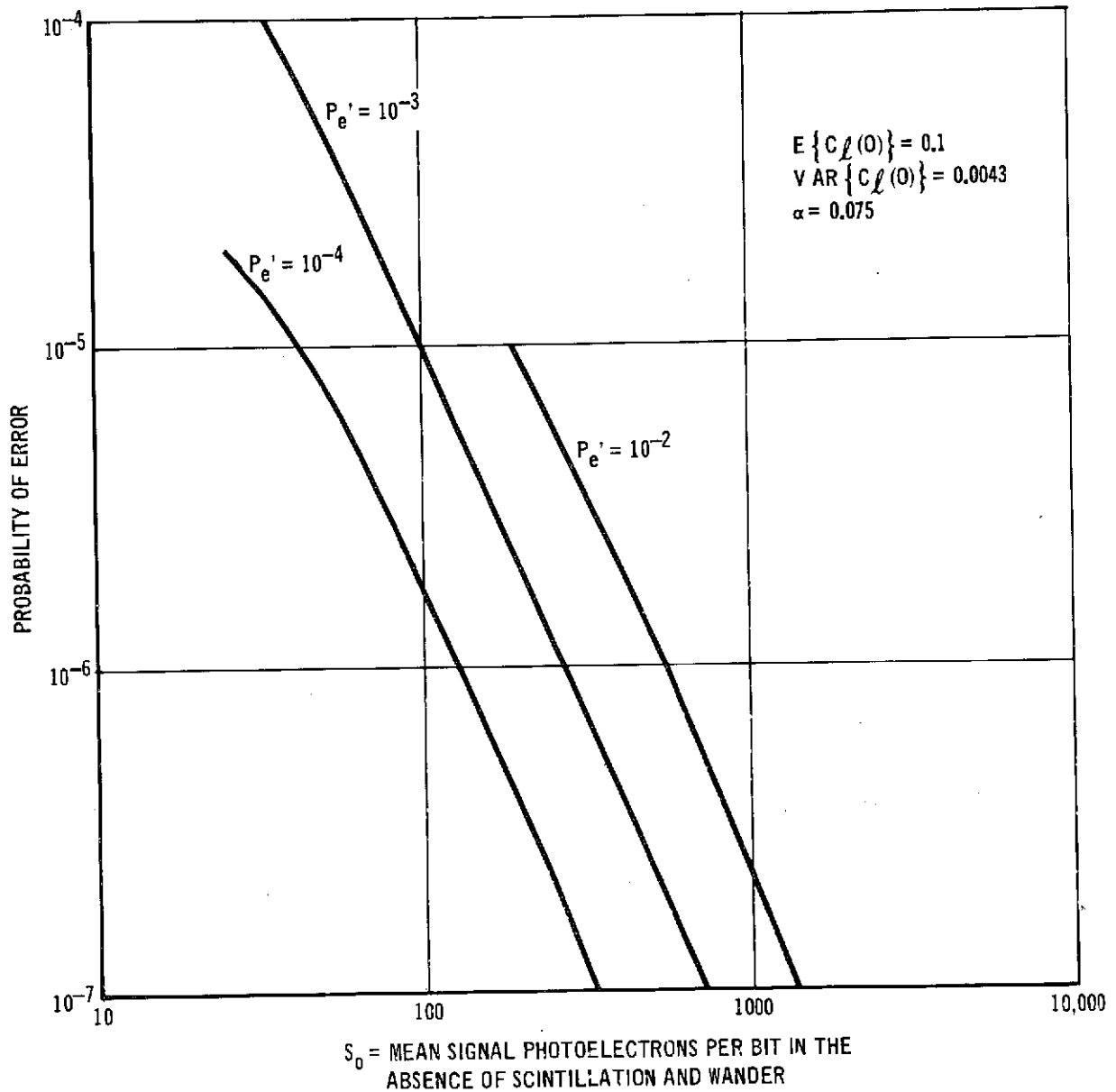
$V_c = 4.3 \times 10^{-3}$). For a downlink, aperture averaging at the ground can certainly reduce the required power significantly making the resolution of this question for the downlink less important than for an uplink where no aperture averaging is expected. We propose in this experiment to determine the statistics of the received power to the accuracy necessary to define the laser power required to obtain $P_e = 10^{-6}$ at 400×10^6 bps.

Outage - The previous discussion assumed that the link must operate 100% of the time and showed various predictions of the average probability of error. Another approach is to recognize that there may be short periods during which the link is inoperative and design the receiver to shut down whenever the average received power drops below some preset value (which corresponds to some given probability of error, P_e'). We then define link performance by calculating the average probability of error when the link is operating and the average % of the time the link operates.

Figure 20 shows P_e (the average probability of error ignoring outage periods) as a function of S_o and P_e' . Figure 20 assumes that $C_\ell(0)$ is log-normal. Figure 21 shows the extra power required to obtain $P_e = 10^{-6}$ over the case of no atmosphere for various values of P_e' . Figure 22 shows the % of time the link operates as a function of P_e' for $P_e = 10^{-6}$. Note that even for the worst case atmospheric model that the link will still operate 98% of the time with $P_e = 10^{-6}$ ($P_e' = 10^{-4}$) and less than 6 dB of extra power.

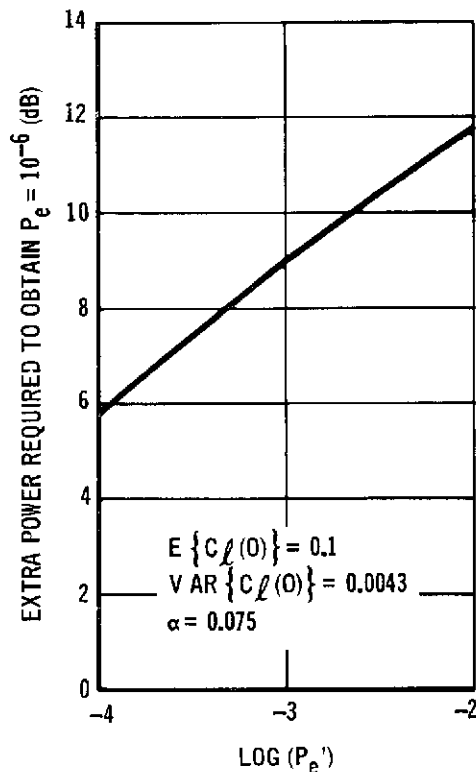
In summary, we note (1) the extra power required to obtain $P_e = 10^{-6}$ with a point detector (i.e. no aperture averaging) is uncertain. (2) A $P_e = 10^{-6}$ may be impossible at this time with a point detector (see Figure 19). (3) aperture averaging makes the effect of the atmosphere on the downlink insignificant.

FIGURE 20 AVERAGE PROBABILITY OF ERROR IGNORING OUTAGE PERIODS



Since we use a reciprocity tracker, we require both an up and down link to achieve high data rate flow in either direction. The extra-power required to achieve a downlink beacon link may be more than the state of the art in Q-switch laser permits (again see Figure 19).⁴ Even though $P_e = 10^{-6}$ may not be achievable with a point detector, this appears to result from

FIGURE 21 EXTRA POWER REQUIRED DUE TO SCINTILLATION AND WANDER
AS A FUNCTION OF CUTOFF PROBABILITY



the relatively infrequent occurrence of very deep fades. If these deep fades are short enough in duration that the angle tracking system does not lose lock, this will probably not cause a serious effect on system usefulness. Note that the truth of these conjectures can only be determined by a carefully designed experimental program such as one outlined here.

2.3.3.5 Link margin. Section 2.3.3.3 defines expressions for P_e as a function of various atmospheric parameters. Values of these atmospheric parameters for the balloon experiment are discussed in Appendix E. Table 10 shows the total predicted losses due to the atmosphere assuming a constant $C_l(0)$. The values of α and $C_l(0)$ assumed are shown in Table 11. Finally Figures 23 thru Figure 25 present the total link margins for both the up and down balloon links. Note that even for the worst case (PGBM

FIGURE 22 PERCENTAGE OF THE TIME LINK IS OPERATIONAL AS A FUNCTION OF P_e'

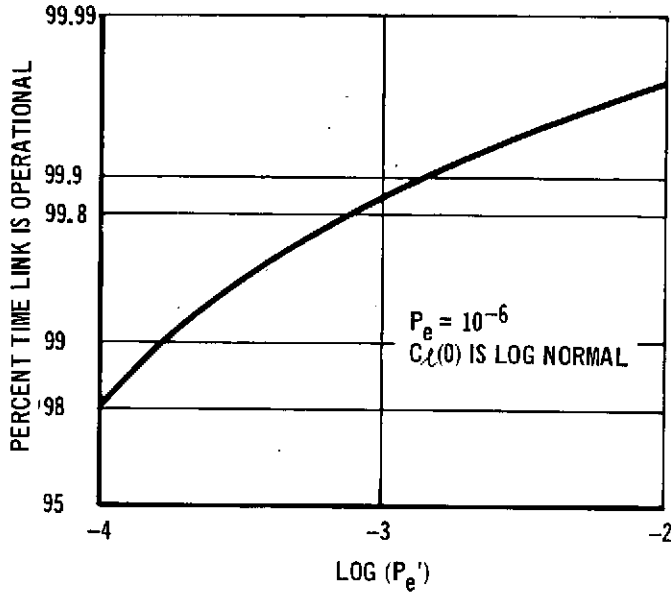


TABLE 10

SUMMARY OF ATMOSPHERIC LOSSES ON COMMUNICATION LINK PERFORMANCE

Balloon Link

	Scintillation and Beam Wander Losses	Beam Spread Losses	Atmospheric Attenuation Losses	Total Estimated Power Losses
Uplink	-7.1 dB	-1.7 dB	-1.41 dB	-10.2 dB
Downlink	-0.01 dB	-0.65 dB	-0.5 dB	-1.16 dB

Reference Satellite Link

	Scintillation and Beam Wander Losses	Beam Spread Losses	Atmospheric Attenuation Losses	Total Estimated Power Losses
Uplink	-8.8 dB	-1.0 dB	-1.41 dB	-11.21 dB
Downlink	-0.0 dB	-0.0 dB	-0.5 dB	-0.5 dB

TABLE 11

**SUMMARY OF ATMOSPHERIC PARAMETER
VALUES FOR COMMUNICATION
LINK PERFORMANCE ANALYSIS**

Balloon Link

	$C_{\lambda}(0)$	α
UPLINK	0.1	0.02
DOWNLINK	0.005	0.001

Reference Satellite Link

	$C_{\lambda}(0)$	α
UPLINK	0.1	0.09
DOWNLINK	0.001	0.001

downlink), the 50 mW 1.06 μm transceiver laser provides a comfortable margin. Thus, we expect to have enough power to obtain $P_e = 10^{-6}$ on all links.

- 2.3.4 Acquisition and Tracking Subsystem Evaluation. The objective of this task is to obtain quantitative data on the tracking system performance in such a manner as to permit extrapolation to the satellite system. To accomplish this objective, our experiment will investigate (1) the effect of transmitter power on angle noise for both the pulsed and high-data-rate trackers, (2) the effect of bender loop bandwidth on tracking error, and (3) the effect of beacon pulse rate on angle noise. The beacon waveform is simulated by appropriately modulating the 400 Mpps mode-locked laser at the ground station.

Figure 26 shows the first dependency given above: angle noise as a function of beacon laser average power. The level at high powers is dependent largely upon dynamical inputs to the BAPE vehicle such as local turbulence and wind gusts. The value of 1 μrad shown is for very quiet conditions in the vicinity of the

FIGURE 23

LINK CHANNEL WAVELENGTH	GND TO BALLOON DATA=PGBH .53 MICRON				73/01/12
S1	LASER POWER	DB	-10.00	1.00	WATTS
S2	TRANSMITTER LOSSES	DB	-7.79	.834	EFF
S3	TRANSMIT. ANTENNA GAIN	DB	95.05	1.000E+04	RADIANS
S4	POINTING LOSSES	DB	-1.56		
S5	SPACE LOSS	DB	-244.56	7.212E+14	M
S6	ATMOSPHERIC LOSS	DB	-10.22	.095	TRANS
S7	RECEIVE ANTENNA GAIN	DB	115.46	1.00	M DTA
S8	RECEIVER LOSSES	DB	-3.88	.409	
S9	RECEIVED POWER	DB	-60.71	8.509E-07	WATTS
S10	BIT PERIOD	DB	-86.02	2.500E-09	SEC
S11	RECEIVED ENERGY/BIT	DBJ	-146.72	2.127E-15	JOULES
S12	ENERGY/PHOTON	DBJ	-184.26	3.748E-19	JOULES/PHOTON
S13	RECEIVED PHOTONS/BIT	DB	37.54	5676.202	
S14	QUANTUM EFFICIENCY	DB	-10.00	1.00	
S15	RECEIVED PHOTOELECTRONS/BIT	DB	27.54	567.620	
S16	REQUIRED PHOTOELECTRONS/BIT	DB	16.00	39.844	
S17	MARGIN	DB	11.54	14.246	
B1	BACKGROUND RADIANCE	DBM	-19.11	.612	W/M2-STERRADIANS-A
B2	RECEIVER FOV	DB	-71.51	3.000E-04	RAD
B3	BACKGROUND IRRADIANCE	DBA	0.00	0.	W/M2-A
B4	OPTICAL FILTER BANDWIDTH	DBA	20.00	100.000	A
B5	RECEIVER ANTENNA AREA	DBM	-21.05		
B6	RECEIVER GATE WIDTH	DB-SEC	-89.03	1.250E-09	SEC
B7	RECEIVER LOSSES	DB	-1.00		
B8	RECEIVED ENERGY/BIT	DBJ	-162.58		
B9	ENERGY/PHOTON	DBJ	-184.26		
B10	RECEIVED PHOTONS/BIT	DB	1.68	1.473	
B11	QUANTUM EFFICIENCY	DB	-10.00		
B12	RECEIVED PHOTOELECTRONS/BIT	DB	-8.32	.147	

FIGURE 24

LINK		BALLOON TO GROUND			
CHANNEL		DATA-PQM			
WAVELENGTH		1.06 MICRON		73/01/12.	
S1	LASER POWER	DB	-13.81	0.50	WATTS
S2	TRANSMITTER LOSSES	DB	-1.94	.640	EFF
S3	TRANSMIT ANTENNA GAIN	DB	81.07	5.00E-04	RADIANS
S4	POINTING LOSSES	DB	-1.00		
S5	SPACE LOSS	DB	-238.64	7.212E+34	M
S6	ATMOSPHERIC LOSS	DB	-1.16	.765	TRANS
S7	RECEIVE ANTENNA GAIN	DB	127.05	.760	M DIA
S8	RECEIVER LOSSES	DB	-3.95	.403	
S9	RECEIVED POWER	DB	-50.58	8.748E-15	WATTS
S10	BIT PERIOD	DB	-86.02	2.500E-09	SEC
S11	RECEIVED ENERGY/BIT	DBJ	-136.66	2.187E-14	JOULES
S12	ENERGY/PHOTON	DBJ	-187.27	1.874E-19	JOULES/PHOTON
S13	RECEIVED PHOTONS/BIT	DB	50.67	116714.381	
S14	QUANTUM EFFICIENCY	DB	-30.00	.001	
S15	RECEIVED PHOTOELECTRONS/BIT	DB	20.67	116.714	
S16	REQUIRED PHOTOELECTRONS/BIT	DB	10.59	11.719	
S17	MARGIN	DB	9.98	9.960	
B1	BACKGROUND RADIANCE	DBM	-35.73	.0.0	W/M2-STERRADIANS-A
B2	RECEIVER FOV	DB	-71.51	3.000E-04	RAD
B3	BACKGROUND IRRADIANCE	DBA	0.00	0.	W/M2-A
B4	OPTICAL FILTER BANDWIDTH	DBA	20.00	100.000	A
B5	RECEIVER ANTENNA AREA	DBM	-3.43		
B6	RECEIVER GATE WIDTH	DB-SEC	-85.02	2.500E-09	SEC
B7	RECEIVER LOSSES	DB	-1.95		
B8	RECEIVED ENERGY/BIT	DBJ	-178.64		
B9	ENERGY/PHOTON	DBJ	-187.27		
B10	RECEIVED PHOTONS/BIT	DB	8.63	7.295	
B11	QUANTUM EFFICIENCY	DB	-30.00		
B12	RECEIVED PHOTOELECTRONS/BIT	DB	-21.37	.007	

58

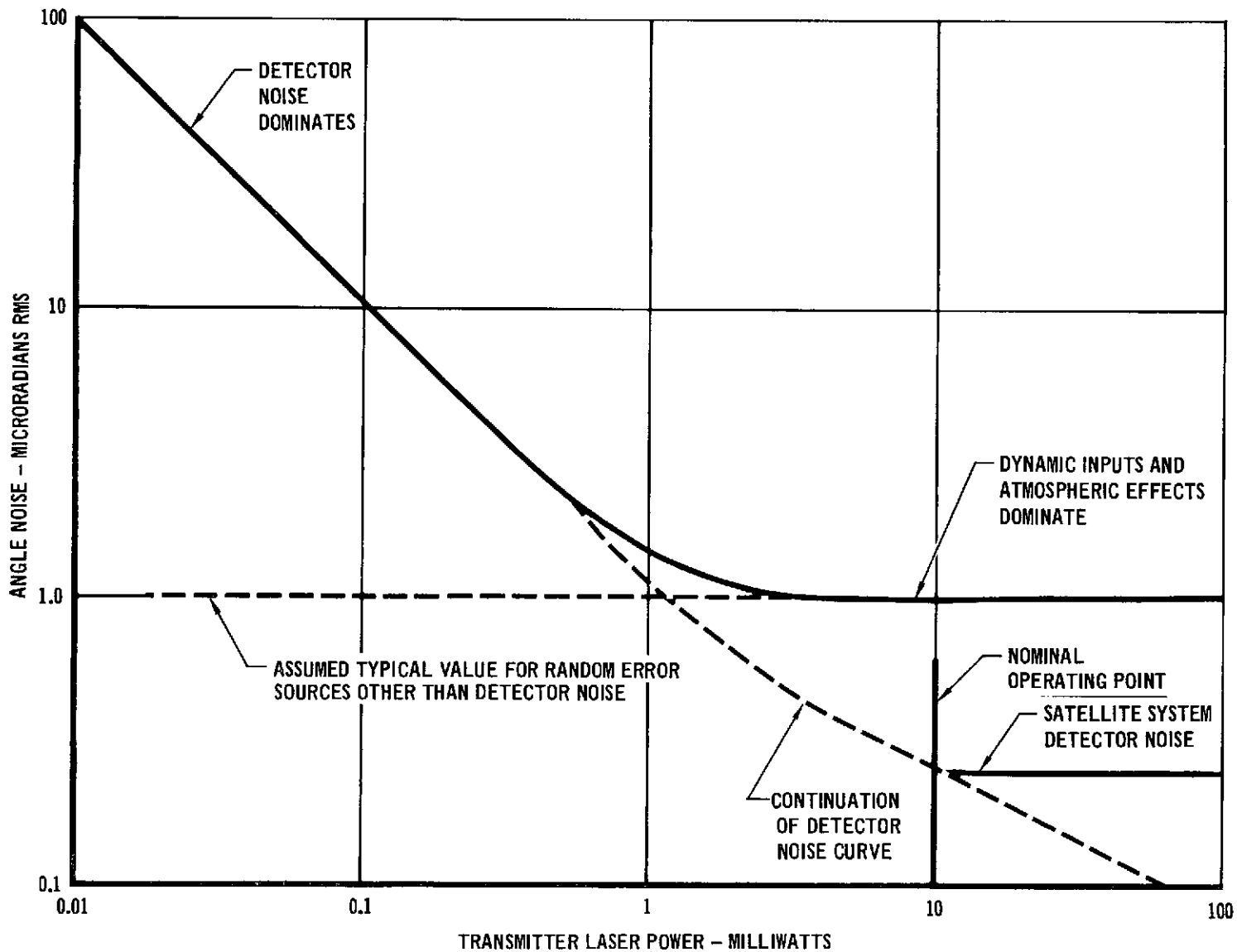
FIGURE 25

LINK CHANNEL	BALLOON TO GROUND DATA-PGBM	WAVELENGTH 1.06 MICRON				73/01/12.
S1	LASER POWER	DB	-13.01	.050	WATTS	
S2	TRANSMITTER LOSSES	DB	-1.16	.765	EFF	
S3	TRANSMIT ANTENNA GAIN	DB	81.07	5.000E-14	RADIANS	
S4	POINTING LOSSES	DB	-0.01			
S5	SPACE LOSS	DB	-238.64	7.212E+14	M	
S6	ATMOSPHERIC LOSS	DB	-1.16	.765	TRANS	
S7	RECEIVE ANTENNA GAIN	DB	127.05	.760	M DIA	
S8	RECEIVER LOSSES	DB	-3.95	.403		
S9	RECEIVED POWER	DB	-49.81	1.046E-5	WATTS	
S10	BIT PERIOD	DB	-86.02	2.510E-09	SEC	
S11	RECEIVED ENERGY/BIT	DBJ	-135.83	2.615E-14	JOULES	
S12	ENERGY/PHOTON	DBJ	-187.27	1.874E-19	JOULES/PHOTON	
S13	RECEIVED PHOTONS/BIT	DB	51.45	139531.960		
S14	QUANTUM EFFICIENCY	DB	-30.00	.001		
S15	RECEIVED PHOTOELECTRONS/BIT	DB	21.45	139.532		
S16	REQUIRED PHOTOELECTRONS/BIT	DB	15.89	38.794		
S17	MARGIN	DB	5.56	3.597		
B1	BACKGROUND RADIANCE	DBM	+35.73	.000	M/M2-STERRADIANS-A	
B2	RECEIVER FOV	DB	+71.51	3.000E-14	RAD	
B3	BACKGROUND IRRADIANCE	DBA	0.00	0	M/M2-A	
B4	OPTICAL FILTER BANDWIDTH	DBA	20.00	100.000	A	
B5	RECEIVER ANTENNA AREA	DBM	-3.43			
B6	RECEIVER GATE WIDTH	DB-SEC	-89.03	1.250E-03	SEC	
B7	RECEIVER LOSSES	DB	-1.95			
B8	RECEIVED ENERGY/BIT	DBJ	-181.65			
B9	ENERGY/PHOTON	DBJ	-187.27			
B10	RECEIVED PHOTONS/BIT	DB	5.62	3.648		
B11	QUANTUM EFFICIENCY	DB	-33.01			
B12	RECEIVED PHOTOELECTRONS/BIT	DB	-24.38	.004		

59

COMMERCIAL RESEARCH CORPORATION BALLOON BUSINESS SYSTEM INC 21

FIGURE 26 ANGLE NOISE DEPENDENCE ON SIGNAL POWER



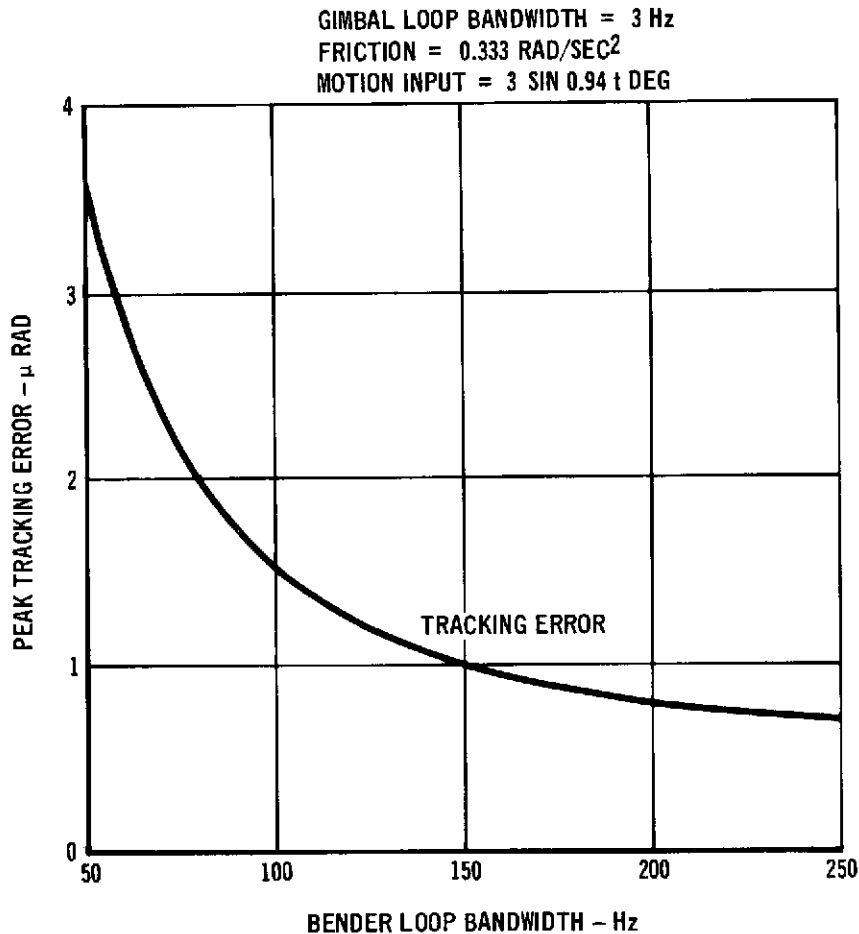
balloon. Our experiment will be instrumented to reproduce this curve experimentally.

The effect of bender bandwidth on tracking error is shown in Figures 27 and 28 (discussed in detail in Section 2.4.3). Figure 27 shows that the peak tracking error in response to sinusoidal pendulum motion decreases with bender bandwidth. Although the satellite disturbances are not like those the balloon will experience, nevertheless, if the experiment produces results similar to those predicted using our model for the tracking system, then extrapolating to the satellite case using this model will have been proven valid. The response of the tracking system to random noise sources in the detector and the tachometer are shown in Figure 28. The bender compensation circuits in the transceiver control electronics are designed to be switched through 5 discrete steps of bender bandwidth under uplink telemetry command control from 50 Hz to 250 Hz.

The effect beacon pulse rate on angle noise should be negligible if average power is held constant. We can verify this by starting a test with a 1600 pps pulse rate and 100 μ W of laser power (see Figure 26). As the pulse rate is decreased by changing the modulation on the ground based laser, the laser peak output power is increased by varying an attenuator holding average transmitted power constant. This process is continued until the data rate is so low that integration of random errors between pulses produces high tracking errors, causing the tracking system performance to degrade. This experiment will provide a measure of the data rates required to support a bender loop bandwidth sufficiently wide to track out expected satellite dynamical inputs.

Tracking error is the angle between the airborne transceiver tracking receiver optical axis and the line of sight between the ground station and airborne transceiver. Tracking error is measured at the output of the tracking detector in the transceiver. Pointing error is the angle between the transmitter beam axis and the line of sight. Differences between pointing error and track-

FIGURE 27 EFFECTS OF BENDER LOOP BANDWIDTH ON TRACKING ERROR



ing error arise from (1) optical misalignment in the transceiver, (2) noise in the tracking error measurement, and (3) the point ahead angle required to allow for finite photon transit time in the presence of relative tangential velocity between transmitter and receiver. Ideally, these differences are small or can be compensated by introducing controlled biases or by averaging, thereby requiring measurement of only one, tracking error, for systems evaluation. We chose to implement a pointing error measurement at the ground station to permit verification that the aforementioned differences are in fact negligible in the experiment setup. Pointing error is measured by an array of detectors at the ground station. The signal amplitudes at the detector outputs, in con-

FIGURE 28 EFFECTS OF BENDER LOOP BANDWIDTH ON TRACKING ERROR SENSITIVITIES TO DETECTOR NOISE AND TACHOMETER NOISE

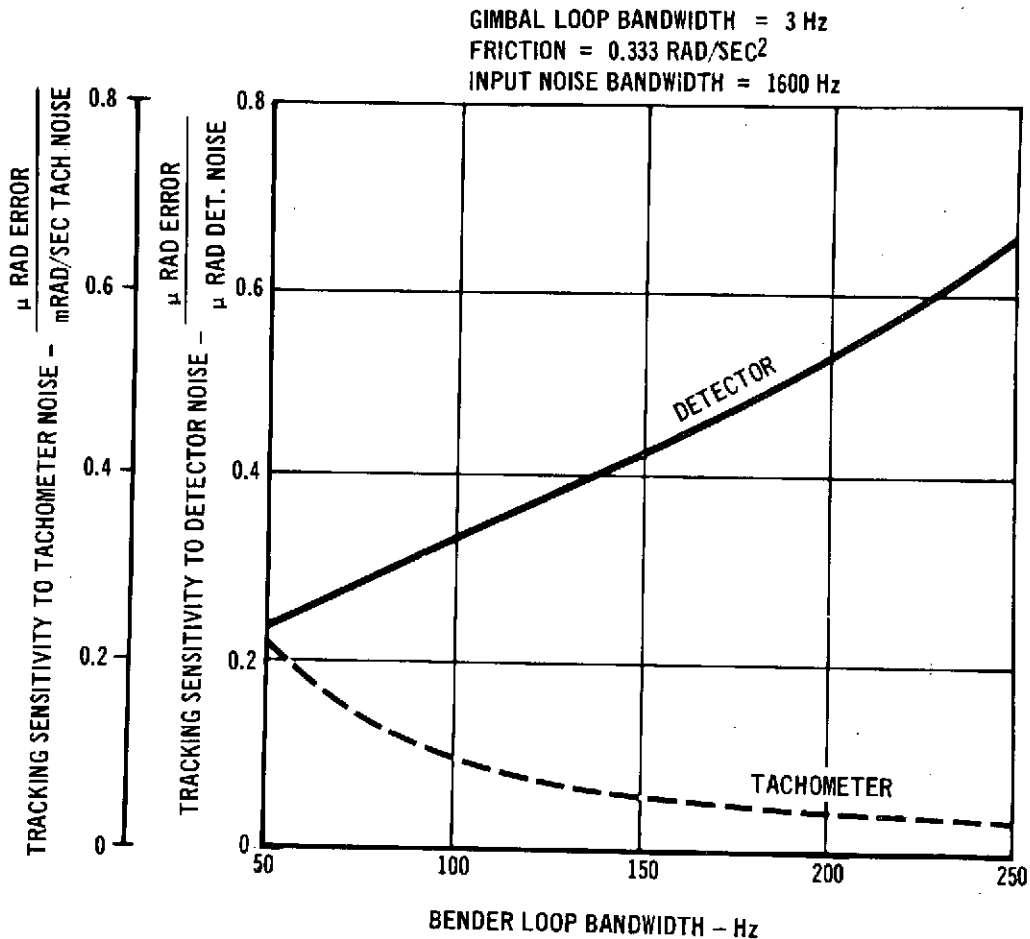


FIGURE 20

junction with a prior assumption as to the power distribution in the received beam permit estimation of beamwidth and pointing error. Unfortunately, atmospheric scintillation corrupts the estimation in periods of high turbulence.

Due to the lack of similarity between the acquisition subsystems of the reference satellite system and experiment system, we do not plan an acquisition performance experiment.

2.3.5 Atmospheric Propagation Experiments. Previously, we have defined the satellite reference system to be simulated and the communication and tracking experiments to be performed using the BAPE as well as the laser power required to obtain $P_e = 10^{-6}$ on each link. This

section defines the atmospheric measurements to be performed and how they will be experimentally related to link performance.

Communication performance degradation by the atmosphere is usually understood in terms of the phenomena listed in part I of Table 12. The atmospheric propagation experiments outlined herein will investigate the phenomena and measure the parameters listed in Table 12. Measurement of these statistical variables will provide the data required to verify the theoretical relationships discussed in Appendix E between link performance, turbulence, and meteorological variables. See Sections 2.3.3.4 and 3.3 for discussion of these relationships.

The approach taken in our experiment design emphasizes experimental measurements of the link performance parameters (mainly error rate) which will be supported by the coincident, direct measurements of atmospheric and received beam variables. Hence the confidence in predictions of link degradation through the vertical atmospheric channel will be improved. Selection and implementation of techniques to measure received beam properties will be discussed next. The details of turbulence and meteorological measurement techniques have been thoroughly documented in the literature, references 10 through 20, and will not be described here.

Experimental Technique Selection Rationale - A set of candidate measurement techniques listed in Table 13 were identified to measure the received beam variables. The experimental techniques to be used were selected subject to the following constraints:

1. Measurement schemes should permit accumulation of accurate statistical data independent of a priori statistical assumptions about the distribution of the process of interest.
2. These techniques should be capable of operation coincident with the high data rate transceiver link.
3. They should be capable of measuring parameters of interest for the severest turbulence expected.

TABLE 12

ATMOSPHERIC PROPAGATION EXPERIMENTS

- I Phenomena to be Investigated
 - 1. Scintillation
 - 2. Beam wander
 - 3. Beam spread
 - 4. Reduction in mean received signal
 - 5. Aperture averaging and spatial correlation of scintillation
 - 6. Angle of arrival fluctuations
 - 7. Vertical turbulence profile
 - 8. Meteorological conditions
 - 9. Wavefront degradations
 - 10. Link error rate and outage
- II Received Beam Parameter Measurements
 - 1. Fluctuations of received optical power
 - 2. Spatial correlation of received optical power
 - 3. Reduction of received optical power fluctuations by aperture averaging
 - 4. Spectra of some time varying quantities
 - 5. Angle of arrival fluctuations
 - 6. Mean value of received signal versus atmospheric parameters and turbulence conditions
 - 7. Wavefront degradation
- III Turbulence and Meteorological Measurements
 - 1. Vertical profile of microthermal fluctuations, i.e., C_T^2 (h)
 - 2. Vertical profile of temperature and pressure
 - 3. Vertical profile of wind velocity
 - 4. Humidity profile
 - 5. Atmospheric transmissibility
- IV Link Parameter Measurements
 - 1. Long and short term variation of bit error rate
 - 2. Link outage rate variations and frequency of occurrence.

TABLE 13

ATMOSPHERIC EXPERIMENT MEASUREMENT TECHNIQUE SUMMARY

EXPERIMENT TECHNIQUE	DATA RECEIVER CONFIGURATION	PURPOSE	IMPLEMENTATION PROBLEMS
BALLOON PACKAGE (UPLINK)			
I. SINGLE DETECTOR	0.53 μm DETECTOR PACKAGE MOUNTED ON GIMBALED ELEVATION AXIS. OUTPUT TELEMETERED TO GROUND.	a) MEASURE MEAN AND FLUCTUATIONS OF RECEIVED OPTICAL POWER.	a) REDUCED DYNAMIC MEASUREMENT RANGE DUE TO DAYLIGHT BACKGROUND. b) NO CAPABILITY TO TEST VARIABLE BEAM PROPERTIES.
II. DUAL DETECTOR	0.53 μm AND 0.514 μm DETECTOR PACKAGE MOUNTED ON GIMBALED ELEVATION AXIS. OUTPUT TELEMETERED TO GROUND	a) MEASURE MEAN AND FLUCTUATIONS OF RECEIVED OPTICAL POWER. b) ALLOWS DAYLIGHT MEASUREMENT OF RECEIVED POWER FLUCTUATION DURING THE DAYLIGHT BALLOON FLIGHTS WITH ATMOSPHERIC PROBE BEAM. c) REDUNDANCY IN MEASUREMENT CAPABILITY. d) MAKES USE OF VARIABLE BEAM PROPERTIES OF AN ADDITIONAL UPLINK BEAM TO TEST SCINTILLATION AND BEAM SPREAD CHANGE WITH TRANSMIT BEAM CHARACTERISTICS.	a) POINTING THE ATMOSPHERIC PROBE BEAM IS LIMITED TO 25 μ RAD RMS BECAUSE OF TELESCOPE POINTING LIMITATIONS.
III. DETECTOR ARRAY	40 TO 60 DETECTOR ARRAY TO DETECT 0.53 μm (OR 0.514 μm) LASER BEAM	a) MEASUREMENT OF THE SPATIAL PROFILE OF THE UPLINK BEAM. b) MEASUREMENT OF SCINTILLATION, BEAM WANDER BEAM SPREAD, CORRELATION LENGTH, ETC. c) MAKE USE OF VARIABLE BEAM PROPERTIES OF AN ADDITIONAL UPLINK BEAM TO TEST SCINTILLATION AND BEAM SPREAD.	a) INSUFFICIENT TELEMETRY CAPACITY. b) REQUIRES REDESIGN OF BAPE PHYSICAL STRUCTURE. c) INSUFFICIENT POWER CAPABILITY.
GROUND STATION (DOWNLINK)			
I. APERTURE AVERAGING DETECTOR	ONE ADDITIONAL 1.06 μ ATMOSPHERICS DETECTOR PACKAGE MOUNTED AT BACK OF CASSEGRAIN TELESCOPE PLUS VARIABLE SIZE IRIS.	a) MEASURE MEAN AND FLUCTUATIONS OF RECEIVED OPTICAL POWER. b) MEASURE APERTURE AVERAGING EFFECTS.	a) REDUCED DYNAMIC MEASUREMENT RANGE DUE TO DAYLIGHT OPTICAL BACKGROUND
II. SPATIAL CORRELATION DETECTORS	ONE 1.06 μ DETECTOR MOUNTED BEHIND CASSEGRAIN PLUS ADDITIONAL TWO 1.06 μ POINT DETECTORS. (ONE AT FIXED LOCATION AND ONE LOCATED AT A VARIABLE DISTANCE FROM THE OTHER PLUS VARIABLE SIZE TELESCOPE APERTURE.	a) MEASURE MEAN AND FLUCTUATION OF RECEIVED OPTICAL POWER WITH A POINT DEFECTOR b) MEASURE SPATIAL CORRELATION LENGTH	a) REDUCED DYNAMIC MEASUREMENT RANGE DUE TO DAYLIGHT OPTICAL BACKGROUND.
III. STELLAR IMAGE MONITOR	TELESCOPE WITH OPTICALLY CHOPPED REFERENCE AND COLLECTED STELLAR LIGHT DETECTED INDEPENDENTLY OF ONE ANOTHER.	a) MEASURE STELLAR, SCINTILLATION AND ANGLE OF ARRIVAL FLUCTUATIONS b) MEASURE TIME AVERAGE MODULATION TRANSFER FUNCTION OF THE ATMOSPHERE.	a) NOT CAPABLE OF MAKING DAYLIGHT STELLAR MEASUREMENTS.

4. Measured data should be as accurate as practically possible.
5. These experimental techniques should permit an adaptive experiment capability for different link operational conditions.
6. The acquired data should permit link performance, received beam, and atmospheric variables to be related to one another.

The variables selected for measurement were restricted to those whose values are critical to link design.

Hence, we decided to measure the following beam properties at the balloon package.

1. Statistical fluctuations in received optical power
 2. Mean received optical power
- and at the ground station
1. Statistical fluctuations in received optical power
 2. Mean received optical power
 3. Spatial correlation function of the received optical power
 4. Reduction of received optical power fluctuations due to aperture averaging.
 5. Wavefront degradation (including the image motion, time averaged atmospheric modulation transfer function (MTF), and ρ_0 lateral coherence length).

2.4 EXPERIMENT HARDWARE DESIGN. This section describes the design details of the transceiver hardware. Section 2.4.1 describes the communications hardware; Section 2.4.2 describes the acquisition and tracking hardware design; 2.4.3 describes the atmospheric propagation experiments hardware; and 2.4.4 discusses the optical and mechanical hardware.

2.4.1 Communications Hardware Description for Balloon Experiment. This section discusses the electronic hardware required for the balloon experiment. The PGBM receiver is described first and then the RF telemetry requirements are discussed. Next considered is the reclocking electronics which is followed by a discussion of the error rate electronics. Finally, a brief discussion of PQM electronics is presented.

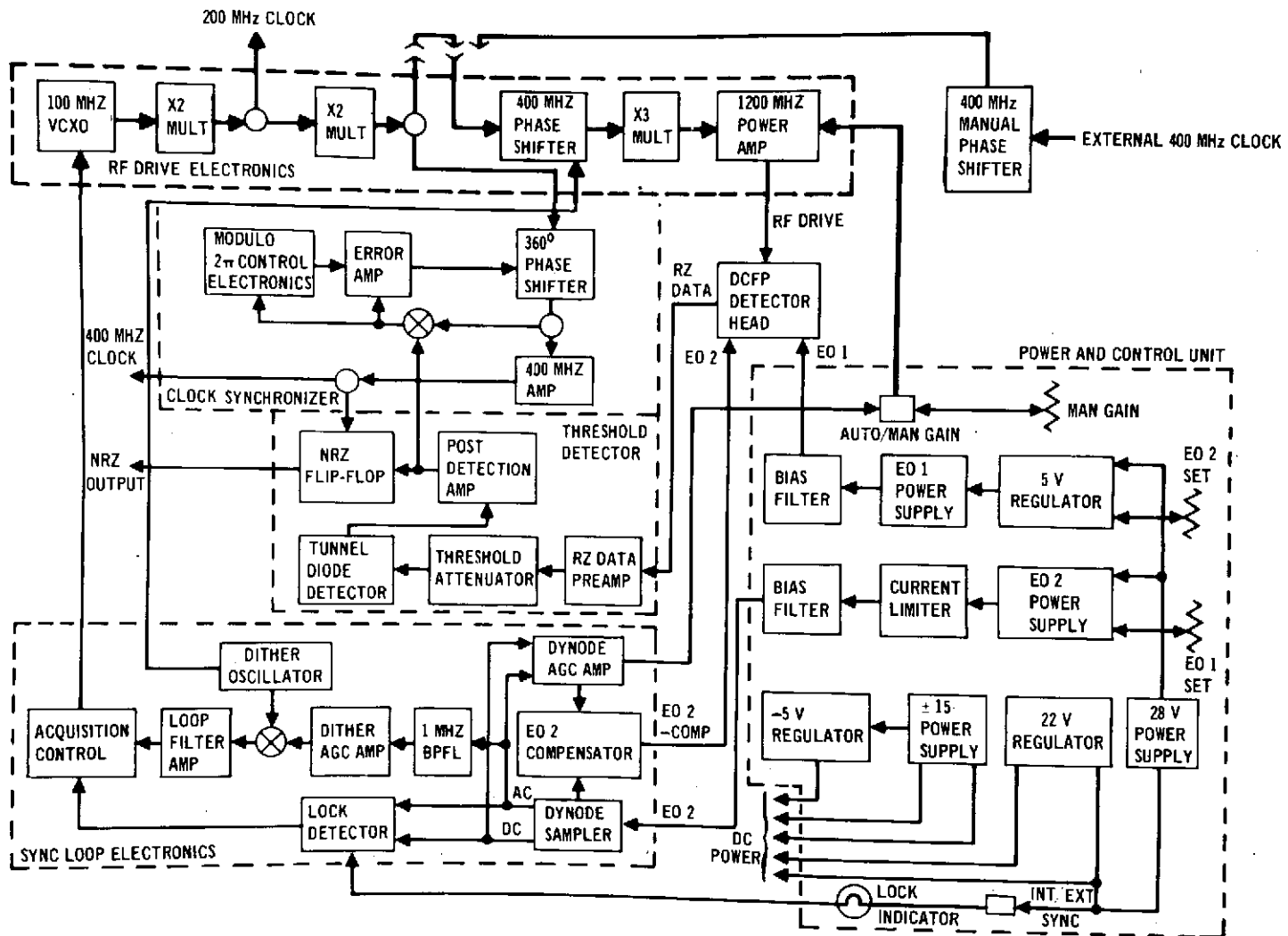
2.4.1.1 PGBM receiver hardware description. A functional block diagram of the 400 Mbps PGBM Receiver is shown in Figure 29. It is comprised of a power supply and control unit, a stack of electronic modules, and a detector head containing the DCFP, the adjustable magnetic field assembly, and protective circuitry which prevents the application of RF drive power in the absence of dc dynode bias voltages. The electronic modules perform the tasks of RF drive power generation, acquisition and synchronization, automatic gain control, threshold detection, and regeneration of received data in NRZ format.

Optical Detector - A DCFP was chosen as the 0.53 μm optical detector in the transceiver for the following reasons. (1) It has already been integrated into a working laboratory PGBM system. (2) It has sufficient gain, bandwidth and noise figure for this application. (3) It has an already developed and tested AGC capability which will be required due to the wide range of input signal levels expected from atmospheric scintillation and range changes. (4) If background turns out to be greater than expected, its gating capability will provide significant power savings.

The function of the DCFP detector is to convert the pulsed laser signal into an electrical pulse train with sufficient amplitude to drive the post detection electronics.

The DCFP is a high speed photomultiplier which is driven by a radio frequency (RF) electric field, dc biasing fields, and a crossed static magnetic field. It offers the advantages of high gain, relatively large photocathode area, and internal subnanosecond gating. Receiver gating is useful in rejecting a portion of the extraneous background radiation by temporal discrimination. The gating recurs at a specific position in

FIGURE 29 400 Mbps OPTICAL DETECTOR BLOCK DIAGRAM

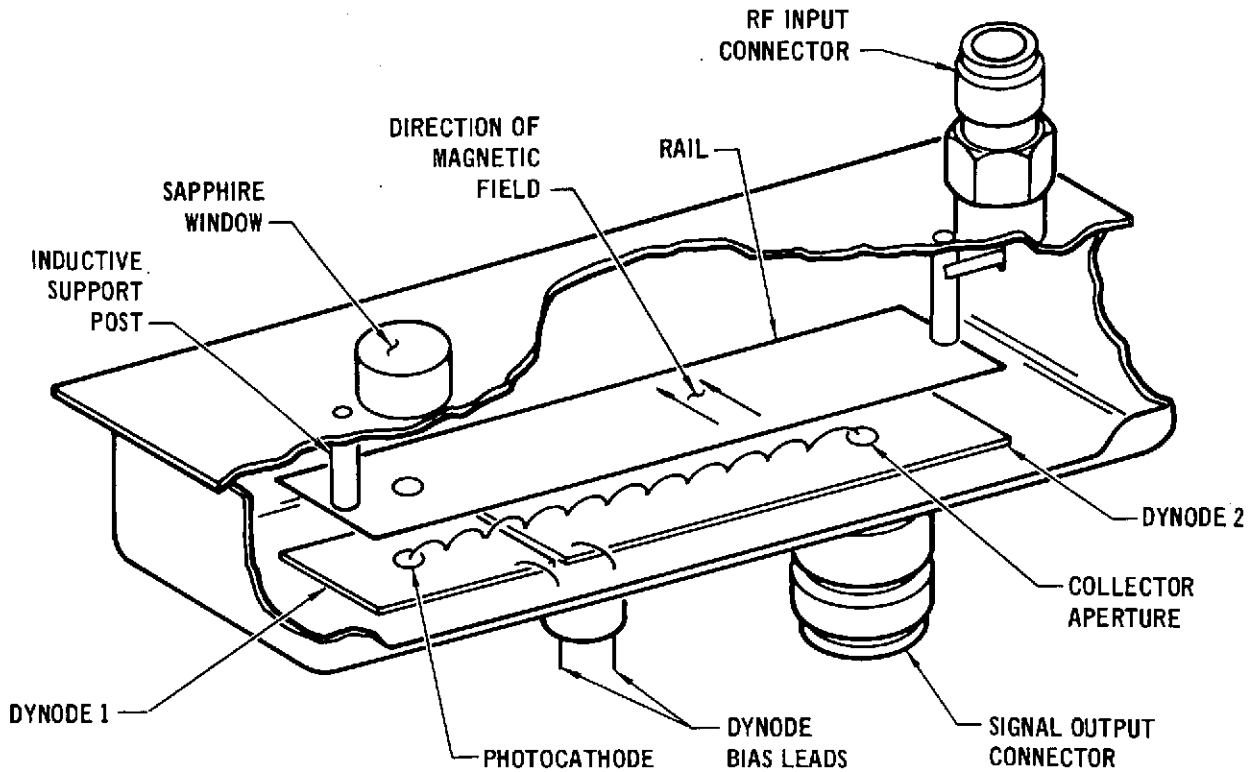


each cycle of the RF drive frequency, so that the DCFP is particularly useful for receiving regularly recurring optical pulses from a mode-locked laser transmitter.

Detection of pulsed optical inputs is achieved in the DCFP by sampling the photoelectrons generated at the photocathode at the frequency of the RF driving field. These electron bunches are then multiplied in successive steps by means of secondary emission. The electron bunches are focused in position and phase, such that large current gains are achieved without pulse to pulse overlap. The DCFP is illustrated in Figure 30.

The DCFP consists of two parallel metal strip electrodes between which is applied an RF driving electric field and a dc biasing electric field. A static magnetic field is applied normal to the electric field, and normal to the length of the strips, so that an electron in motion between the strips moves along the direction of the strips. The lower strip has a photocathode near one end, a collecting hole near the other, and is treated to be a good secondary emitting surface. Photoelectrons generated at the photocathode are accelerated towards the top strip, or rail, during the positive half cycle of the RF drive, and the magnetic field will cause them to curve in a cycloidal path towards the collector end of the assembly. On the opposite half cycle, the electrons are returned to the lower strip with sufficient energy so that each electron will generate several secondary electrons. The secondary electron multiplication process is repeated until reaching the collecting hole near the end of the lower strip. After passing through the collecting hole, the multiplied secondary electrons strike the collector, or anode.

FIGURE 30 ILLUSTRATION OF DYNAMIC CROSSED FIELD PHOTOMULTIPLIER



Only photoelectrons which are generated during the proper phase of the RF drive cycle are "sampled" and amplified by the phase-focusing secondary multiplication sequence, hence the gating effect of the DCFP. Photoelectrons generated at other phases of the RF cycle are collected by the upper electrode which is biased strongly positive, or follow a suboptimal trajectory in which they receive insufficient kinetic energy to generate secondary electrons when reaching the lower electrode. Changing the input pulse arrival time or shape does not result in an equivalent change in output pulse shape or arrival time. The output pulse occurs synchronously with the RF drive to the DCFP. Since there is no phase change in the DCFP output for a phase change of the optical input, a dithered gate tracking loop is required to keep the DCFP gate aligned with the input pulse.

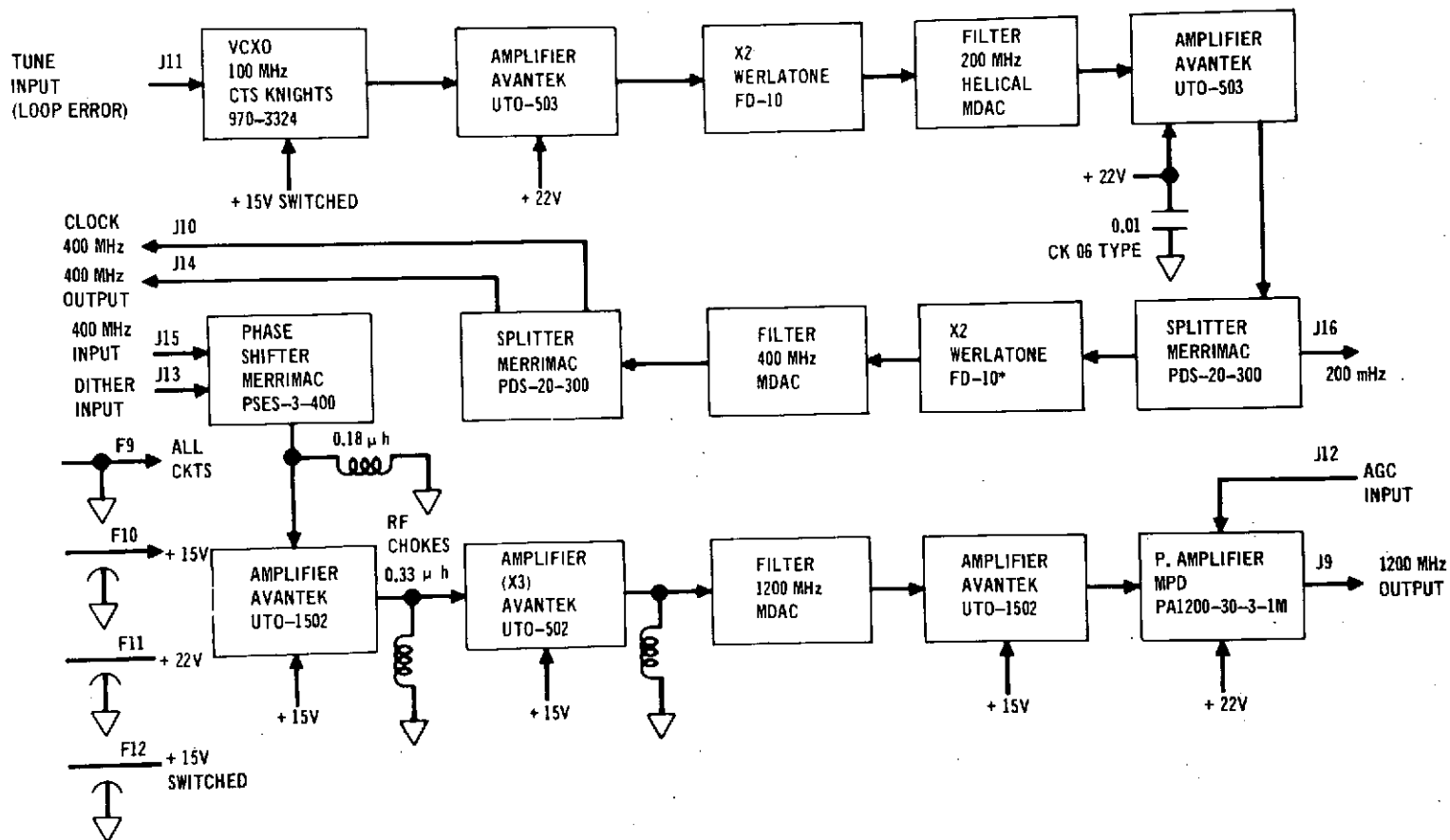
The gain of the DCFP is proportional to RF drive power level. Only a slight compensation of DC bias is required as the RF drive power level is varied. This feature allows manual and automatic control of DCFP gain.

RF Drive Chain - The purpose of the RF drive chain is to provide the 400 MHz source, with appropriate amplitude, frequency, and phase characteristics, for the DCFP tube. The output signal is modulated by control signals from other portions of the receiver in order to control the current gain of the DCFP and to implement acquisition and synchronization to the input optical pulse train.

The required 400 MHz drive source must be a very stable low noise RF signal. A block diagram of the RF drive chain is presented in Figure 31. The tuning range is ± 240 kHz at 400 MHz. The oscillator tuning range is dc to 20 kHz. The phase of the 400 MHz signal is dithered 0.1 radian peak-to-peak in order to implement the dithered gate phase discriminator. DCFP gain is controlled by varying the RF drive power from 0.5 to 1.8 watts.

The fundamental frequency source is a Voltage Controlled Crystal Oscillator (VCXO). Its 100 MHz output is amplified, frequency doubled, and filtered. A portion is sampled by a power divider to provide an external 200 MHz signal in addition to the required internal signal. The 200 MHz signal is then frequency doubled, filtered, and split to provide two 400 MHz outputs. One 400 MHz output is then fed to the clock synchronizer while the other is fed back into the RF chain with an external jumper. An external 400 MHz source is used in place of this internally generated 400 MHz signal in the external synch mode. The 400 MHz signal is then "phase dithered", and amplified to produce the high level 400 MHz signal. The final amplifier has a gain control input to electronically set the power output level. The 400 MHz output drives the DCFP and supplies the energy for the secondary multiplication process.

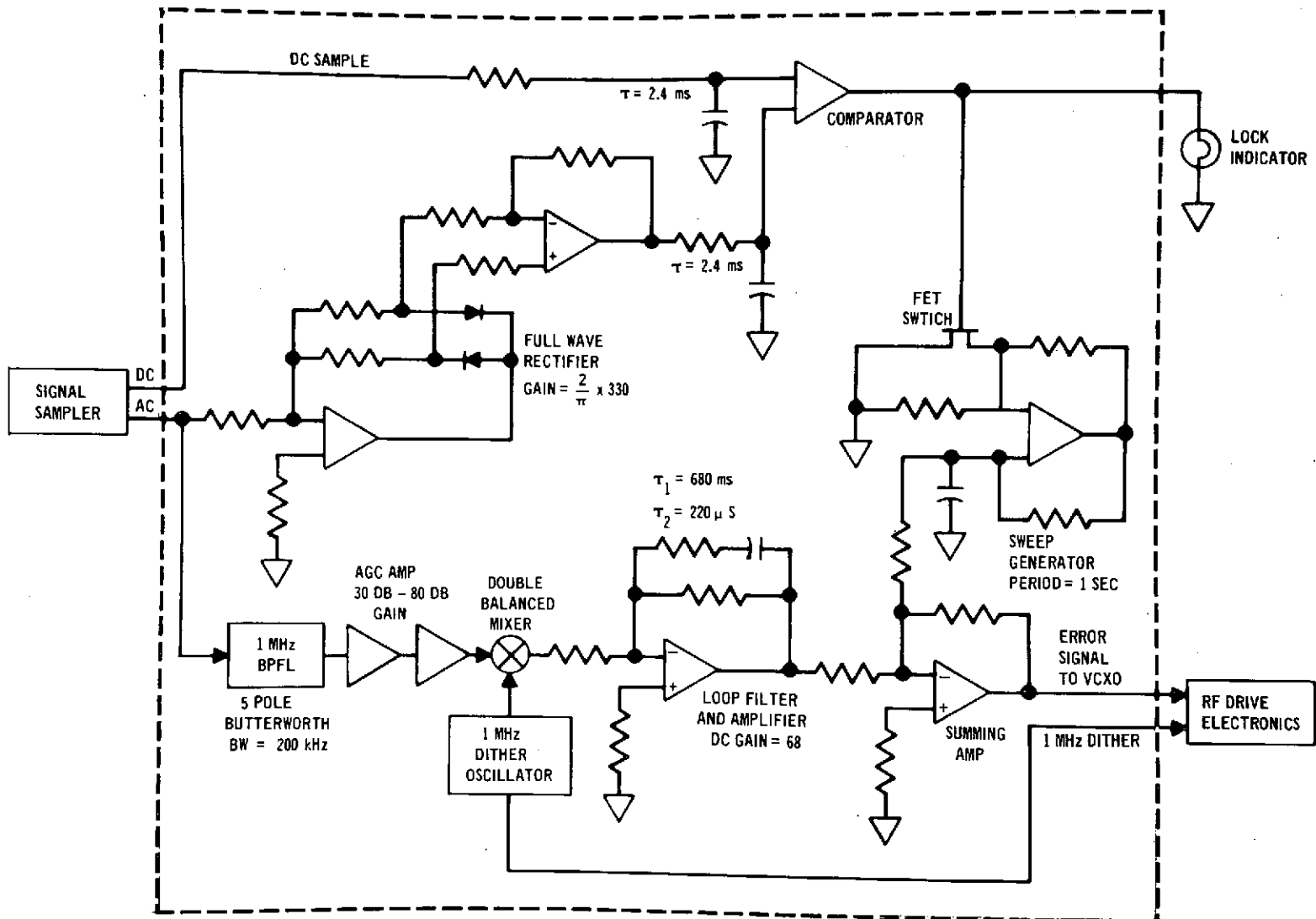
FIGURE 31 RF DRIVE CHAIN BLOCK DIAGRAM



Synchronization Loop Electronics - Synchronization of the DCFP gate with the incoming optical pulse train is achieved by the synchronization loop electronics. A functional diagram of the synchronization circuitry is shown in Figure 32. A 1.0 MHz crystal oscillator is the dither signal source. The dither signal phase modulates the DCFP RF drive signal and causes the gate to alternately advance and retard with respect to the optical pulse train. This process produces a 1 MHz component at the DCFP output which is in phase or out of phase with the dither signal depending on whether the gate precedes or follows the optical pulse. This dither frequency signal component is sampled at the second dynode. The phase and amplitude of the recovered dither signal depend upon the relative timing error between the gate and pulse positions. The recovered dither frequency signal is then filtered to eliminate harmonics and beat frequency signals. The amplified signal component is dependent upon the magnitude of the RF carrier phase deviation, the average second dynode current, the gating characteristics of the DCFP, and the width of the input optical signal pulse. Typically, for 0.1 radians peak-to-peak deviation and 0.3ma dynode current, this signal level is 0.3 mV. The AGC amplifier output level to the mixer remains constant at approximately 500 mV and thus normalizes the loop gain for all operating conditions.

The double balanced mixer is used as a phase detector which produces an error voltage proportional to the phase difference between the recovered dither component and a reference signal from the dither oscillator. The loop filter is a conventional lead-lag network producing a natural loop frequency of $\omega_n = 6.28 \times 10^3$ rad/sec and a damping factor of 0.7. The summing amplifier adds the error signal and a triangular sweep voltage which is enabled when the receiver is not synchronized. This composite error signal controls the phase and frequency of the 100 MHz VCXO in the RF drive electronics which in turn controls the phase and frequency of the DCFP RF drive signal.

FIGURE 32 SYNC LOOP ELECTRONICS FUNCTIONAL DIAGRAM



The lock detector determines whether the loop is locked, controls the operation of the acquisition sweep generator, and also provides a signal to light the remote lock indicator. When the loop is not locked, a beat note is present at the dynode at the difference frequency between the optical pulse train and the RF drive frequency. A fullwave rectifier with an overall gain of about 200 produces a sufficiently large signal at the comparator to switch it when a beat note is detected. When the loop locks, the beat note disappears and the comparator switches to the locked state after a suitable holding time determined by the input RC network.

Automatic Threshold Control - Automatic threshold control is required with PGBM since range changes and atmospheric scintillation cause wide variations in input signal amplitude. There are two general approaches to threshold control. One approach estimates the probability of a "one" and "zero" error directly from a known code word inserted in the data. This technique works well for relatively high data rate links with high error probabilities. For that case many bit errors are seen in a time short compared with the time constant of the input signal amplitude so that the "one" and "zero" error probabilities can be accurately estimated. At 4×10^8 bits/sec and a nominal error rate of 10^{-6} , we see approximately 0.4 errors per millisecond. Thus, since the ATC must be capable of responding to input signal level changes in approximately one millisecond, this approach alone would not be practical for this case even if all the data could be used for estimating error probabilities.

The second approach is to estimate the mean received signal level with a binary one and with a binary zero. These estimates are then used in either an exact or approximate evaluation of the expression for the optimum threshold given known signal statistics. The main difficulty with this approach is obtaining accurate estimates of the mean one and mean zero signal levels.

To derive an expression for the optimum threshold level the received signal from the optical detector is assumed to consist of N impulses where N is a Poisson random variable with mean rate per bit

$$m_1 = n_s \frac{N_E}{N_E + 1} + n_b G \quad (26)$$

when a binary one is transmitted and mean rate per bit

$$m_0 = n_s \frac{1}{1 + N_E} + n_b G \quad (27)$$

when a binary zero is transmitted. N_E is the modulator extinction ratio and G is the DCFP gate period (in seconds). Then the optimum threshold, in the sense of minimizing the probability of bit error, is given by

$$n_t = \frac{(m_1 - m_0) + \ln \left(\frac{P(0)}{P(1)} \right)}{\ln \left(\frac{m_1}{m_0} \right)} \quad (28)$$

$P(1)$ and $P(0)$ are respectively the a priori probabilities of receiving a binary one and a binary zero. This expression assumes a perfect counter (i.e. an integrate and dump filter), but it has been shown that the same general relationship (except for a known constant factor) holds when the perfect counter is replaced by a real passive filter as shown in Figure 33. Reference 21 gives the optimum threshold as a function of signal level for both a perfect counter and a first order RC transfer function. Note that they appear to differ by only a fixed constant. A second effect not considered in Equation [28] is that the wideband amplifiers which precede the threshold detector are in general not dc coupled. The lack of a fixed dc level causes the threshold to vary with $P(1)$ and $P(0)$ in an undesirable manner. However dc restoration is easily accomplished by feeding back the dc level of the output of the threshold detector.

FIGURE 33 NON-IDEAL DETECTOR MODEL



*FILTER REPRESENTS TRANSFER FUNCTION OF THE PREAMPLIFIER AND AMPLIFIER CHAIN

For both the balloon-to-ground and ground-to-balloon links, the background per bit is insignificant. For this case, the expression for n_t can be simplified somewhat. That is for

$$n_b G \gg \frac{n_s}{N_E + 1}, m_0 \approx \frac{n_s}{N_E + 1} \quad (29)$$

$\ln \frac{P(0)}{P(1)}$ in general will be insignificant with respect to $(m_1 - m_0)$ (since the data will be formatted such that $0.3 \leq P(0) \leq 0.7$). Thus

$$n_t \approx \frac{(N_E - 1)n_s}{\ln(N_E)(N_E + 1)}, \quad (30)$$

or the threshold is linearly related to the average ones level, for a fixed modulator extinction ratio. Note also that the average current is

$$K (m_1 P(1) + m_0 P(0)) \approx K \frac{P(1) N_E + P(0)}{N_E + 1} n_s \quad (31)$$

where K is a constant which depends on pulse shape and duty cycle. Thus if P(1) and P(0) are relatively constant, holding the average current fixed makes the optimum threshold a constant. The average current can be held essentially constant by using a standard current controller AGC in the output signal path. The DCFP also has an internal AGC capability which tends to keep a constant average output current. This solution to the ATC problem has been tested experimentally in other laser communication MDAC Gigabit PGBM contracts.

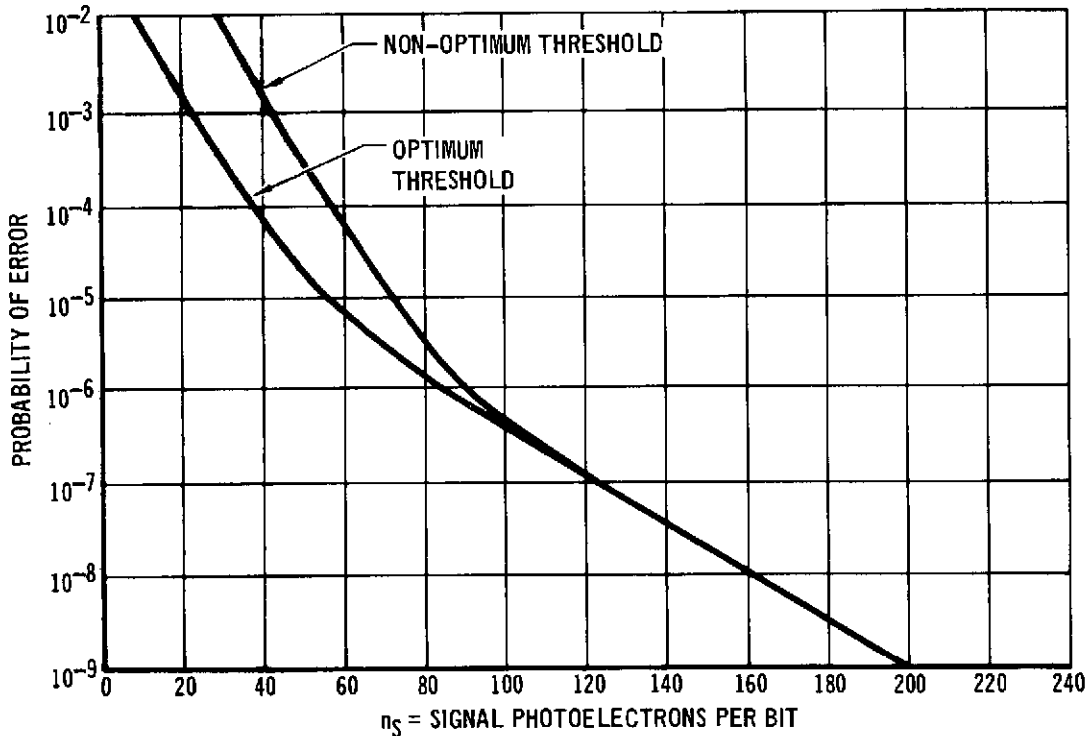
Figure 34 shows the probability of error for various input signal levels with the threshold set to optimize error rate performance only at $P_e = 10^{-6}$. Figure 34, which was derived from experimental data, indicates that the AGC does not work perfectly since there is more degradation from theoretical performance at low signal levels than at high signal levels. We have calculated that for typical atmospheric conditions ($C_x(0) = 0.1$) approximately 2.3 dB more power is required due to the non-ideal ATC characteristics shown in Figure 34. Note, however, that the AGC is necessary for efficient system operation, and considerably more loss would occur due to saturation if the AGC were not used. We have not included this 2.3 dB loss in the PGBM link margin because it is expected that more careful attention in the AGC design would eliminate this loss.

Automatic Gain Control - The function of the dynode automatic gain control (AGC) and bias compensation circuitry is to provide a constant output pulse amplitude to the threshold decision circuits.

The secondary multiplication current gain of the DCFP is proportional to the applied RF drive power. Thus the DCFP is well suited to automatic gain control. Performance does not deteriorate over a wide range of applied RF drive power. However, a slight change in step size, with changes in RF electric field, requires a small tracking correction in dc bias in order that the last step passes through the center of the dynode aperture to reach the anode.

The AGC bias compensation circuitry is shown functionally in Figure 35. The average dynode current is sensed by a resistor in series with the second dynode bias return line. The sensed dc voltage is amplified in two cascaded operational amplifiers. The second of these provides a frequency rolloff with a time constant of 1 ms. The amplified voltage is then

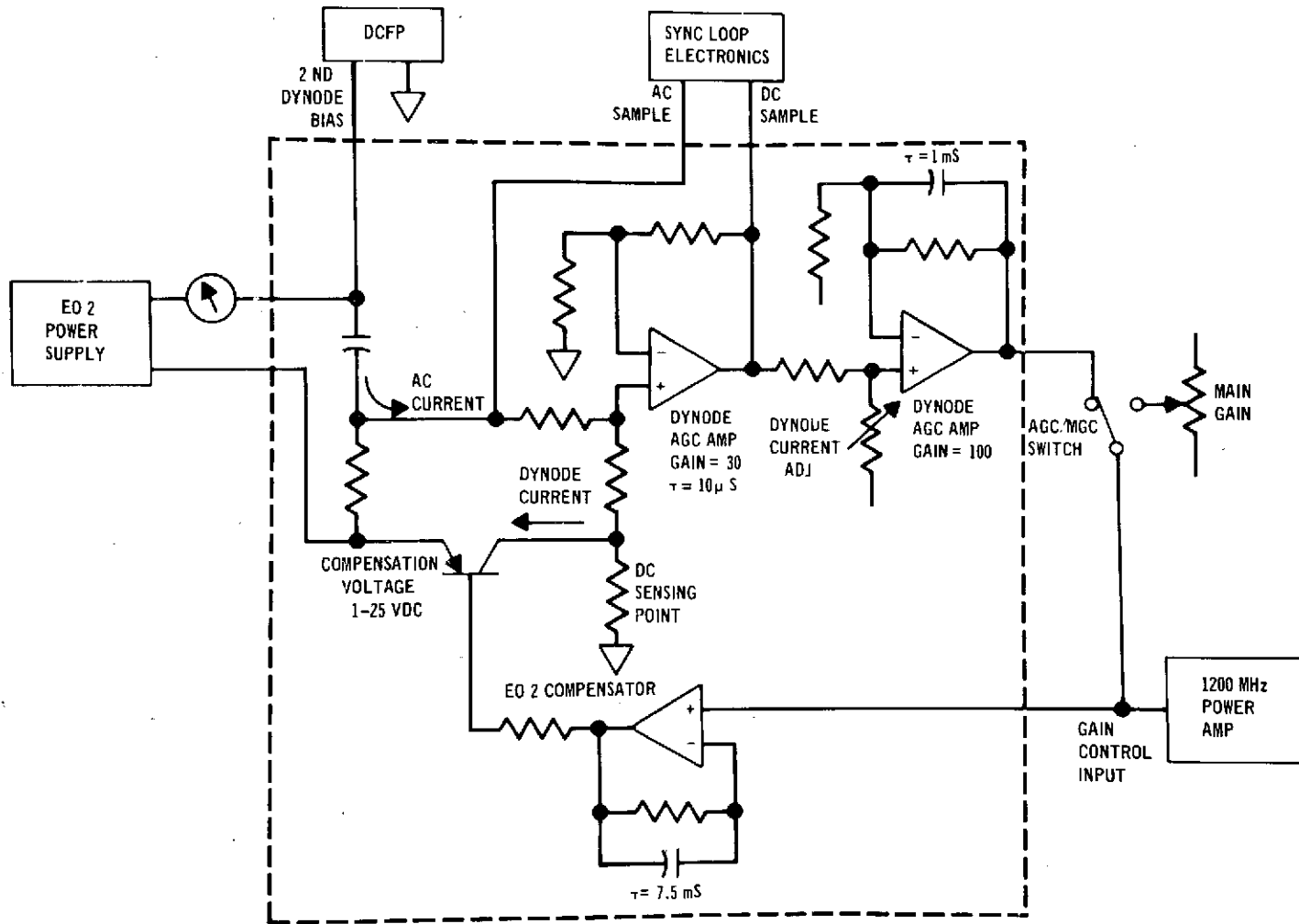
FIGURE 34 EXPERIMENTAL ERROR RATE CURVES FOR PGBM WITH AND WITHOUT OPTIMUM THRESHOLD CONTROL



used to control the output power of the 1200 MHz power amplifier, which in turn controls the DCFP gain and the DCFP second dynode current, closing the loop.

The AGC control voltage to the power amplifier is related to the RF field and is also used to control the bias compensator. The bias compensator consists of a variable gain operational amplifier and a series pass transistor in the return side of the second dynode bias supply. The series pass transistor acts as a voltage source subtracting from the bias supply some value from 1 to 25 volts. The ac component of the dynode signal is capacitively coupled from the high side of the bias supply to the synchronization loop electronics. A portion is also used in the AGC loop to extend its bandwidth and improve the phase margin.

FIGURE 35 DYNODE AGC AND BIAS COMPENSATION FUNCTIONAL DIAGRAM



Handwritten signature or mark.

Threshold Detector - The threshold detector provides wideband amplification of the DCFP output pulse train, binary decision of the serial data on the basis of pulse amplitude, and conversion from return-to-zero (RZ) to a non-return-to-zero (NRZ) format. A functional diagram of the threshold detector is shown in Figure 36 .

The data preamplifier has an overall gain of 100 from dc to 600 MHz. This wideband operation is achieved by combining two cascaded ac coupled hybrid amplifiers with an operational dc amplifier having suitable input and output matching networks. The effective gain to the narrow DCFP output pulse is a factor of 2 to 3 less, due to the spectral components above 600 MHz.

The threshold decision is made by a tunnel diode monostable flip-flop which is biased into the unstable state when a "one" level signal is present. The threshold attenuator controls the amplitude of the RZ data pulse train to the tunnel diode. The amplitude is set so that "ones" trigger the tunnel diode, but "zeros" do not.

The post detection amplifier is similar to the preamplifier with a gain of 10. The output of this amplifier is at MECL levels of -800 mV and -1600 mV. The RZ to NRZ conversion is accomplished by a D-type flip-flop. The flip-flop is clocked at a 400 MHz rate to recover the data in NRZ format. An emitter coupled pair and two emitter followers provide complimentary outputs.

Clock Synchronizer - The 400 MHz clock synchronizer shown functionally in Figure 37 maintains the clock signal and the data signal in a fixed phase relationship. A narrow range of relative phase shift between the clock and data signals is required for proper operation of the RZ to NRZ conversion flip-flop. As the DCFP gain changes, the phase shift through the amplifier changes, leading to some clock/data uncertainty.

FIGURE 36 THRESHOLD DETECTOR FUNCTIONAL DIAGRAM

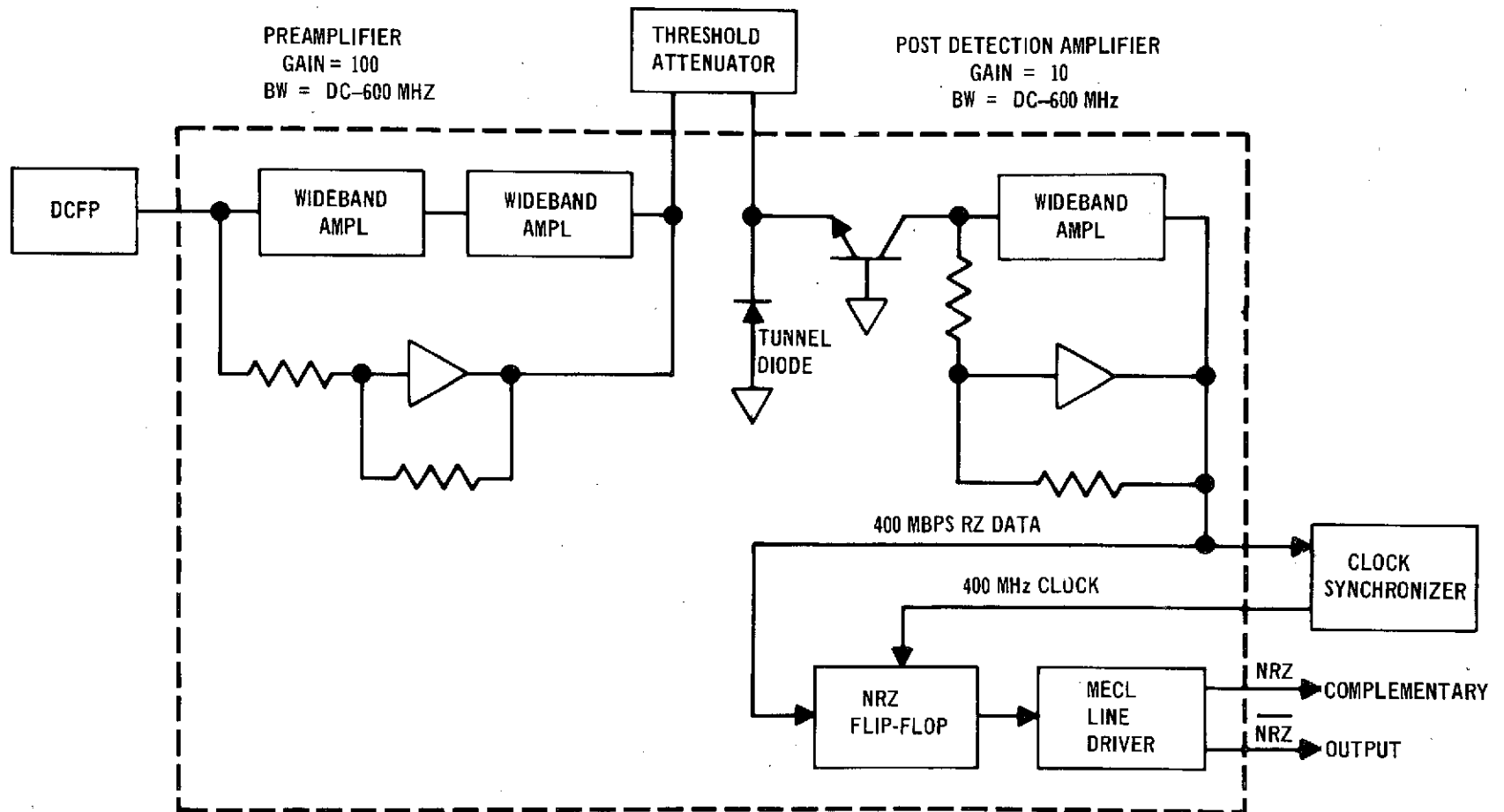
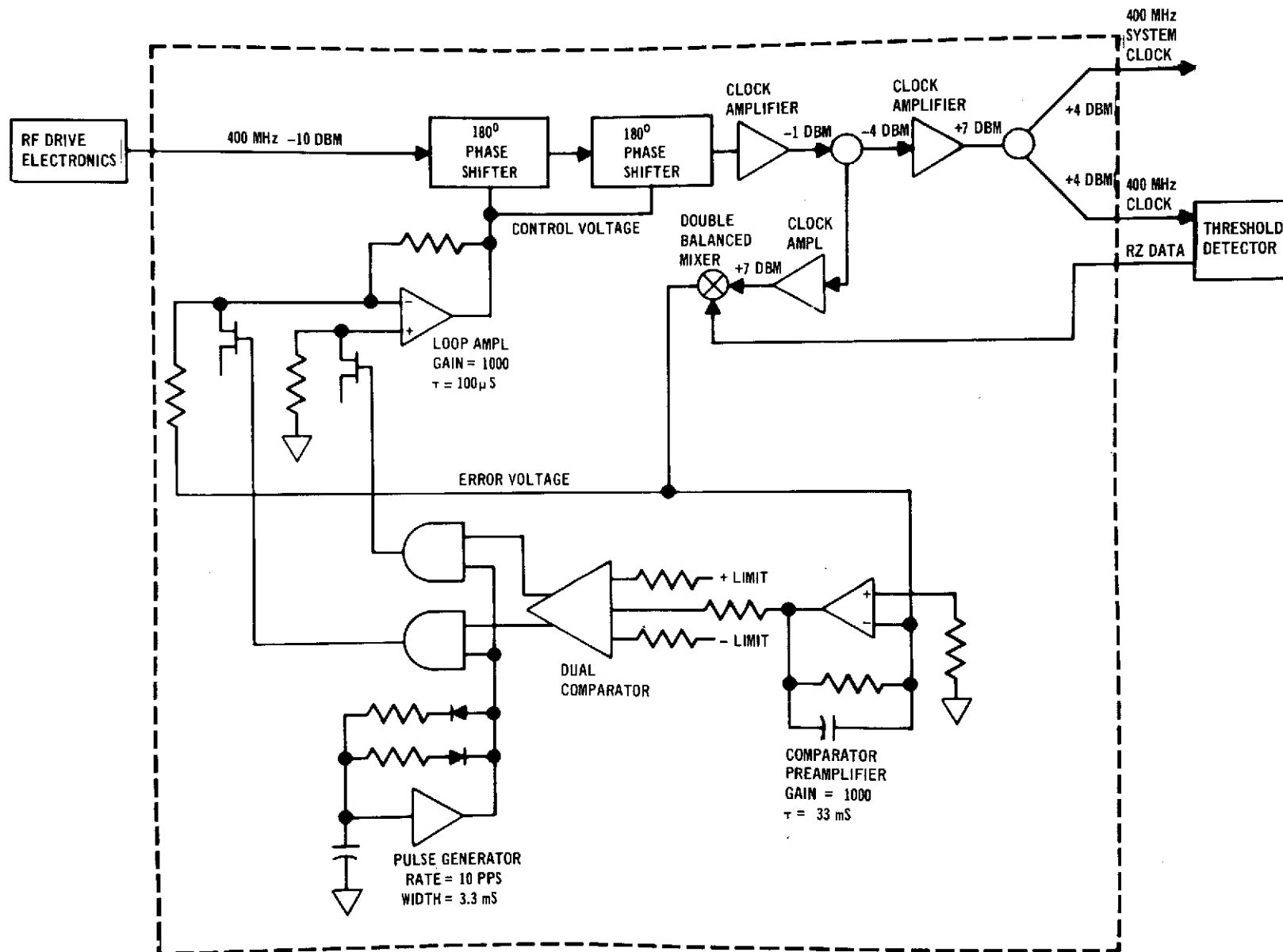


FIGURE 37 CLOCK SYNCHRONIZER FUNCTIONAL DIAGRAM



A second order phase control loop is used to minimize these phase variations. A sample of the RZ data from the threshold detector is taken as a reference and the 400 MHz clock signal from the RF drive electronics is phase shifted to minimize the relative phase error. Two electronic phase shifters are cascaded to give a total control range in excess of 360° . The clock amplifiers and hybrid power splitters provide gain and signal distribution for the synchronized clock signal and a high level drive to the double balanced mixer which acts as the phase error detector in the control loop. The resulting error voltage from the mixer is amplified to produce an approximate closed loop gain of 60.

The remainder of the clock synchronizer electronics is required to make the phase control loop operate modulo 2π . When the phase shifter reaches a phase extreme, the loop saturates and further correction is not possible. The presence of a saturated control loop is detected by the comparator, which gates a pulse from the pulse generator into the loop amplifier. This pulse, when steered to the correct input, forces the loop amplifier to the opposite saturation state thus subtracting 360° from the accumulated phase. After the pulse is removed, the loop corrects toward the linear region of operation since the polarity of the error voltage remains unchanged.

2.4.1.2 RF telemetry. - Various diagnostic transceiver variables are monitored at the ground by RF telemetry. The main variables used for communication system analysis are listed below.

- (1) "Ones" Error count/millisecond
- (2) "Zeroes" Error count/millisecond
- (3) DCFP video output (1.0 kHz bandwidth)
- (4) PN synchronization indicator
- (5) 1.06 μm laser output power (1.0 kHz bandwidth)
- (6) Background (0.53 μm) detector output power.

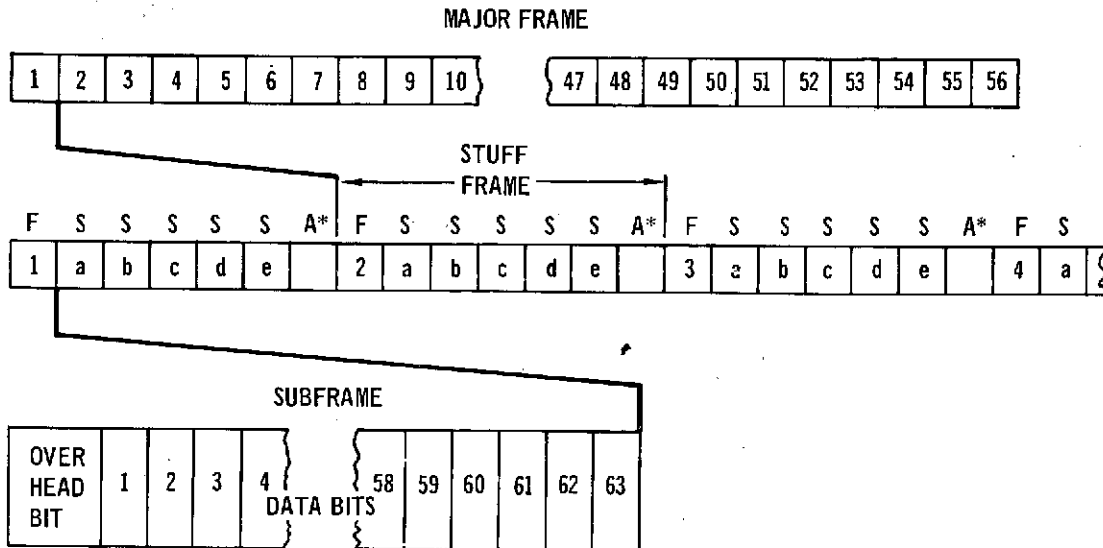
The digital data used on the downlink POM or PGBM link is either the ~~cross~~-strapped PGBM uplink data or 400×10^6 bits/sec PN data generated at the transceiver. This choice is made by RF telemetry from the ground.

2.4.1.3 Reclocking electronics. - Before the downlink modulation process can take place, the upcoming detected PGBM data stream must be time synchronized to the 1.06 μ m mode-locked transceiver laser output. The 1.06 μ m laser thus acts as the master clock. The asynchronous PGBM data rate is chosen so that it is at a slightly lower frequency than the master clock. The data synchronizers "sample" the lower data rate asynchronous PGBM input data and inserts extra bits as required to synchronize the data streams. The data asynchronizer in the ground receiver performs the opposite function in that it removes the extra bits which were inserted by the data synchronizer and also smoothes the output data rate.

The extra bits are either overhead bits or redundant data bits. The "overhead" bits contain two types of information; 1) frame synchronization and 2) stuff code information, and are inserted into the data stream every 64 bits. They allow the data asynchronizer to identify and remove the redundant data bits.

The synchronizer output bit structure is illustrated in Figure 38. A stuff frame consists of 7 subframes of 64 bits each. The first bit of each subframe is either a frame sync bit position, a stuff code bit position or an auxiliary bit. Every seventh subframe contains an auxiliary bit in the slot normally assigned to an overhead bit. The redundant or stuff bits occur in the middle of the subframe which contains the auxiliary data bit. Each stuff frame contains 5 bits of stuff code information, and may contain one stuff bit. The frame synchronization code is a 7 bit PN code and the stuff code is either a 5 bit PN code or its complement.

FIGURE 38 RECLOCKED DATA FORMAT



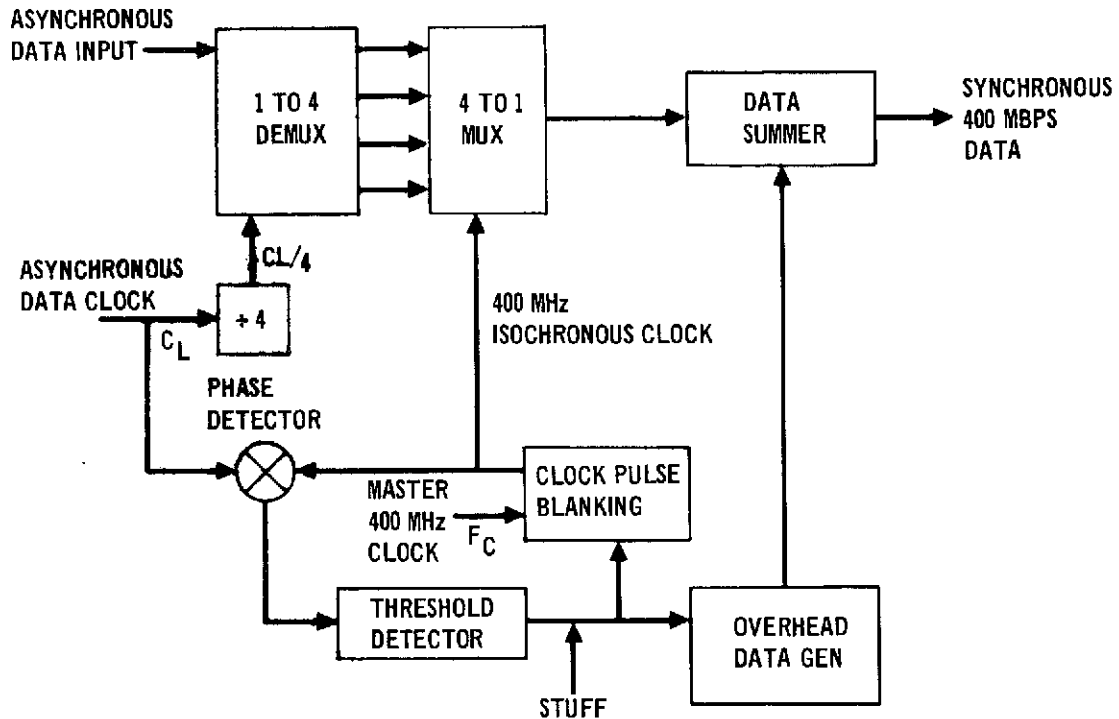
*REDUNANT OR STUFF BITS MAY OCCUR IN CENTER OF THE LAST SUBFRAME OF ANY STUFF FRAME

F - REFERS TO A SUBFRAME WHICH BEGINS WITH A FRAME SYNC BIT
 S - REFERS TO A SUBFRAME WHICH BEGINS WITH A STUFF WORD BIT

The input to the data synchronizer is demultiplexed into four data streams by the input clock, as shown in Figure 39 . The readout of the 4 to 1 multiplexer is controlled by the isochronous 400 MHz clock. The isochronous clock is a 400 MHz clock with every 64th pulse blanked. These gaps or blanks correspond to the time slots where the "overhead data" has been inserted into the synchronous 400 Mb/s data stream. An additional clock pulse is removed whenever a stuff is performed.

The isochronous clock phase is compared to the input data clock phase as shown in Figure 40 . The time interval, Δt , is the length of a subframe. If the isochronous clock phase begins to lag the input data clock phase, the threshold detector indicates a need to insert an additional data bit into the output data stream instead of a "redundant data" bit. The

FIGURE 39 BIT STUFFING ELECTRONICS



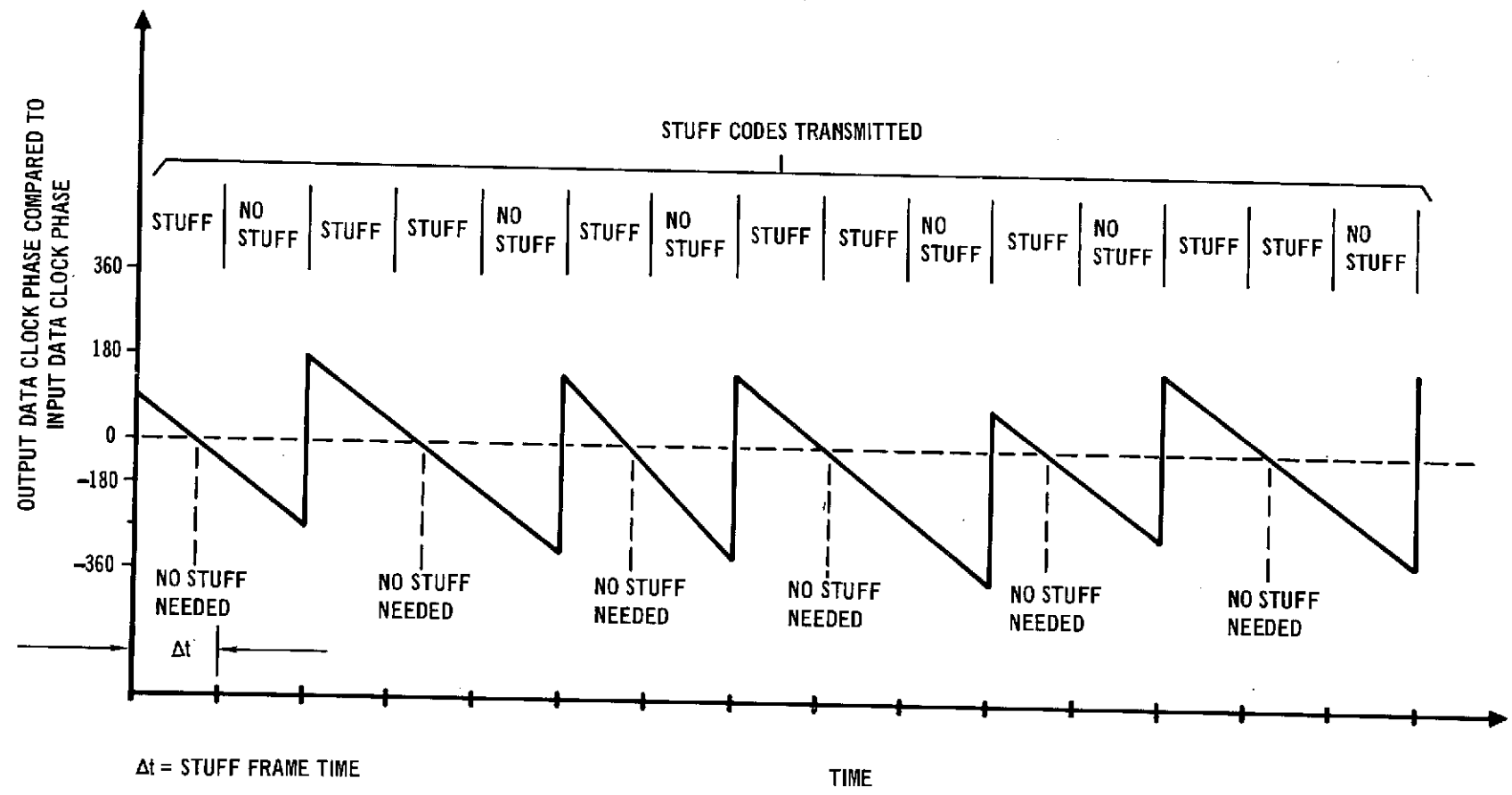
"no stuff" code is then transmitted, and an additional data pulse is inserted into the output data stream during the next stuff bit slot. This additional data bit produces a 360 degree phase shift between the input clock and the isochronous clock and keeps the average frequency of the isochronous clock exactly that of the input asynchronous clock.

The data asynchronizer accepts a 400 megabit data stream and its associated clock from a bit synchronizer. The "redundant data" bits and "overhead data" bits are removed from the 400 Mb/s data stream which results in a channel of discontinuous 400 Mb/s data that is then converted to a continuous rate bit stream.

After frame synchronization is established, the 400 MHz clock is used to generate an isochronous clock by blanking out every 64th pulse in the 400 MHz clock. The missing pulse in the isochronous clock is then time coincident with the frame sync bits and stuff code bits. Once frame synchronization has occurred, the transmitted stuff code is checked to

FIGURE 40 PHASE RELATIONSHIP BETWEEN INPUT DATA CLOCK AND ISOCHRONOUS CLOCK

68



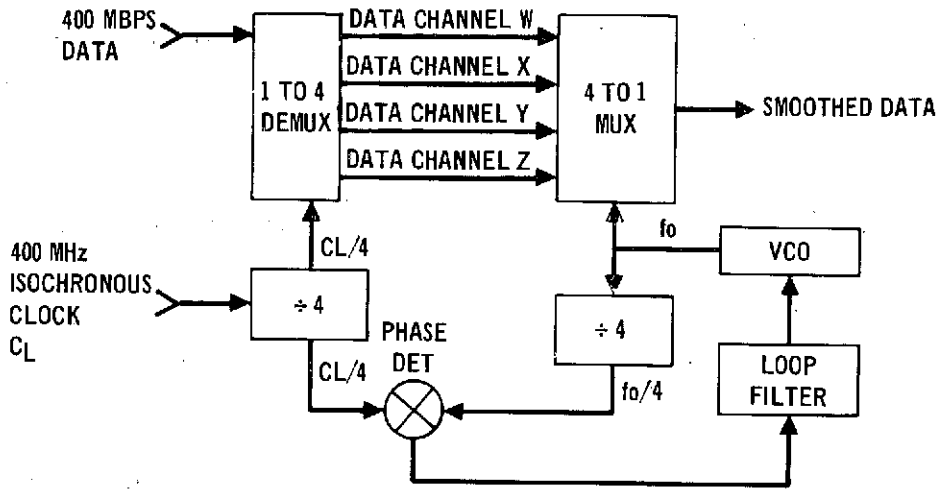
see whether or not the middle bit in the subframe containing the auxiliary data is a true data bit or a "redundant data" bit. If the stuff code indicates "a stuff", then an extra clock pulse is blanked in the 400 MHz isochronous (asynchronizer) clock. The auxiliary bits are synchronously demultiplexed out of the 400 Mb/s data stream and presented to the front panel along with the frame sync clock.

The removal of the "redundant data" bits and "overhead data" bits is referred to as "destuffing" and is performed by the smoothing buffer illustrated in Figure 41. The synchronous 400 Mb/s data is synchronously demultiplexed into four channels. The phase detector is driven by the isochronous clock divided by four and output data clock, f_o , divided by four. The isochronous clock has a 90 degree phase step every time a clock pulse is skipped. The output of the phase detector is presented to the loop filter which smooths the signal and provides a control voltage for the VCO.

The data in the 4 to 1 demultiplexer is then clocked out by the f_o clock, and the output data is then presented to the front panel at a continuous data rate which is the average frequency of the isochronous clock.

Once the data asynchronizer has established "LOCK", the received 7 bit PN code is compared bit-by-bit, in the lock detector, with a model of the known transmitted pattern. Outputs from an exclusive - OR gate, in the lock detector, indicates bit errors in the received PN code. These error pulses are counted over a stuff frame time interval in the lock detector to determine if the data asynchronizer is out of "LOCK". The error pulses are also presented to the front panel as a means of measuring bit error rate (P_e).

FIGURE 41 SMOOTHING BUFFER



Performance Requirements

Data Synchronizer

The data Synchronizer maximum and minimum data rates are calculated below using the following definitions:

1. K = Number of bits/stuff frame = 448
2. N = Number of data bits + stuff bits/stuff frame = 441
3. $K - N$ = Number of overhead bits/stuff frame = 7
4. F_c = Master clock rate = 400 MHz

$$F_{dmax} = \frac{N}{K} \times F_c = \frac{441}{448} (4 \times 10^8) \quad (32)$$

$$F_{dmax} = 393.750 \text{ MHz} \quad (33)$$

In order to eliminate timing problems, assume two stuff frames per stuff bit.

$$F_{dmin} = \frac{881}{896} \times 4 \times 10^8 \quad (34)$$

$$F_{dmin} = 393.303 \text{ MHz} \quad (35)$$

Therefore, the nominal data clock rate is 393.526 MHz \pm 223 PPM. The data synchronizer efficiency is 393.526 MHz \div 400 MHz = 98.38 percent.

- 2.4.1.4 Error rate electronics. - The Error Rate Electronics remotely acquire the 400 Mbps pseudorandom noise (PN) code, and perform error rate measurements on the received code.

A Reference PN Generator within the Error Rate Electronics is automatically synchronized to the incoming data stream, and a PN lock indicator is actuated when the received and reference PN codes are phase aligned. The two PN codes are compared serially to obtain the error count.

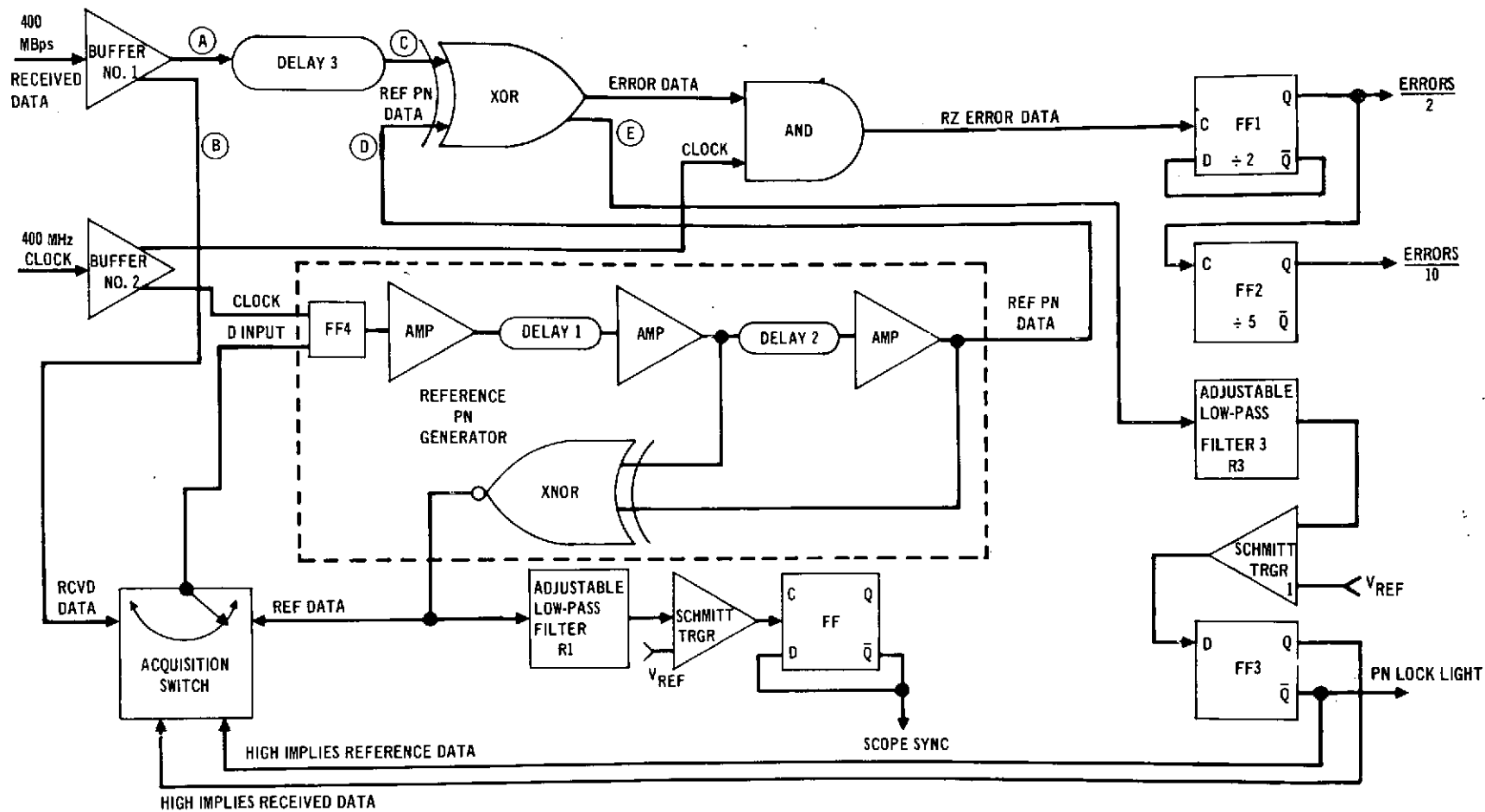
The supply voltage is -5.2 volts DC and the power supply used should be capable of supplying at least two amperes. Power dissipation is approximately 10 watts total.

Input and output signals are specified below:

- Inputs: 1. Received PN data stream:
400 Mbps, NRZ, pseudorandom noise code. MECL level, dc coupled. Error rates can be measured on codes of 6, 7, 9, 10, 11, and 15 stages. The rise and fall times of the received pulses should be approximately 1.5 nanoseconds (10% to 90%).
2. Clock:
400 MHz sinusoidal waveform, 1 volt peak-to-peak, \pm 5 volts.
Maximum dc offset, synchronized to incoming data.

Figure 42 is a block diagram of the error rate electronics. The 400 Mbps pseudo-random noise pulse train is first amplified by Buffer Amplifier number 1. One of the outputs is routed through a coaxial delay line (D3) which can be changed to correspond to

FIGURE 42 ERROR RATE ELECTRONICS FUNCTIONAL DIAGRAM



the various PN code lengths which are available. This system has been designed to operate with code lengths of 6, 7, 9, 10, 11, and 15 stages. The PN code, after having been delayed, is used as one input to the exclusive OR (XOR) gate. The other input to the XOR gate is the reference PN code which is generated by the reference PN generator within the error rate electronics system. The reference PN generator delay cables (D1 & D2) is selected to generate a reference PN code which is the same stage length as the code being received.

The two PN codes are compared in the XOR gate, and if the two codes are alike in every bit, there is a constant low level out of the XOR. One of the outputs of the XOR is an input to the AND gate, where a logical AND is performed with a 400 MHz clock signal which is synchronized with the PN codes. The AND gate output is routed to a flip-flop where the AND output frequency is divided by two.

The XOR gate output is high each time the PN code inputs disagree. The AND gate output is high each time the PN codes disagree "AND" the clock is low. The Errors/2 output is high once for each two input pulses to FF1 and the Errors/10 output is high once for each ten input pulses to FF1, or five input pulses to FF2.

The second output of Buffer Amplifier 1 is used as one of the inputs to the acquisition switch. The second input to the acquisition switch is the reference PN code. The output of the acquisition switch is either the received PN code, or the reference PN code, depending on the position of the switch. If the received and reference PN codes agree, i.e. the XOR gate output is low, the acquisition switch will be in the reference PN code position. If the reference PN generator loses synchronization with the received PN code, the output of the XOR gate will increase. This condition will be detected by lowpass filter number 1, and Schmitt trigger number 1. The

output of the Schmitt trigger will increase, and cause the \bar{Q} output of FF3 to increase. This condition will cause the acquisition switch to change to the received PN code position.

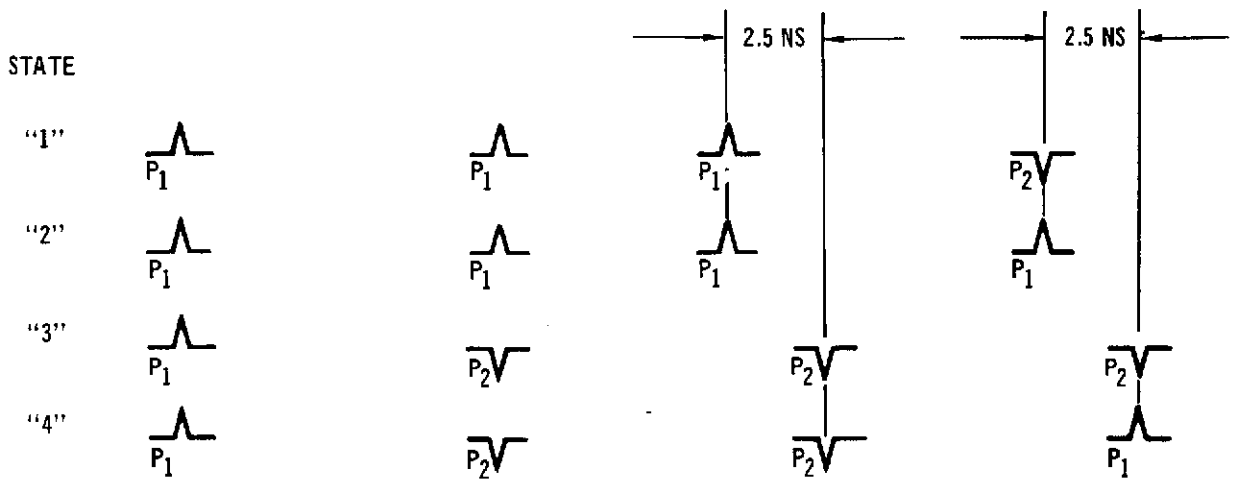
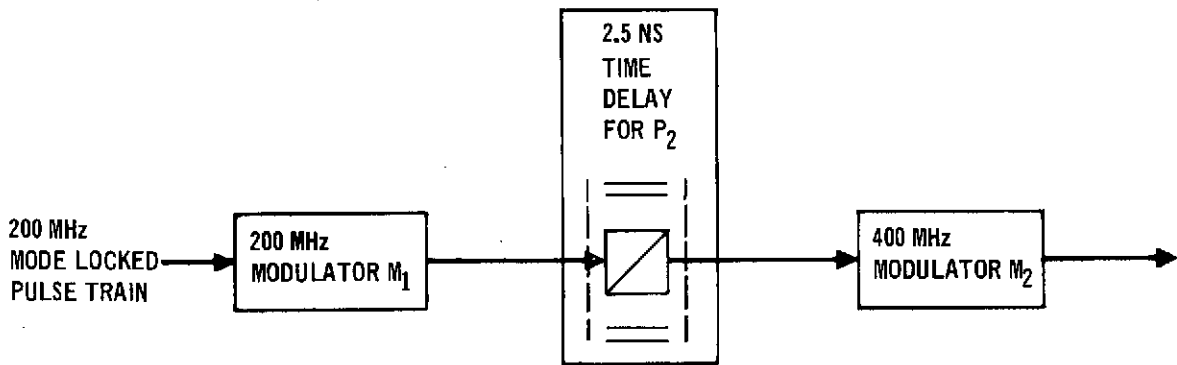
With the acquisition switch in the received PN code position, the received PN code is the output of the switch, and the input to the reference PN generator will then acquire the received PN code, and will again become synchronized to the received code. Shortly after synchronization has been obtained, the XOR gate output will decrease, the Schmitt trigger output and Q output of FF3 will decrease, \bar{Q} of FF3 will increase, and the acquisition switch will switch to the reference PN code position once again.

Low-pass filter number 1 can be adjusted, in most instances, to distinguish between a large number of errors in the received PN code and loss of synchronization; however, if the received signal is either a constant high, or constant low, the XOR output will appear similar to loss of synchronization. This is of no particular consequence however, since the reference PN generator will not re-establish synchronization until a satisfactory PN code is received.

- 2.4.1.5 PQM detection electronics. M-ary modulation formats in short pulse direct detection laser communications have long been recognized for their high information efficiency.

In PQM, a pulse is sent in one of four possible states made up from two polarization and two time position states. Figure 43 shows the block diagram for the PQM transmitter. Assume the power into the modulator is initially in polarization 1 (P_1). The first modulator determines whether or not the pulse is delayed. If the pulse is switched to P_2 it will be delayed; otherwise, it will be passed undelayed. The second modulator determines the polarization of the output pulse.

FIGURE 43 PQM TRANSMITTER



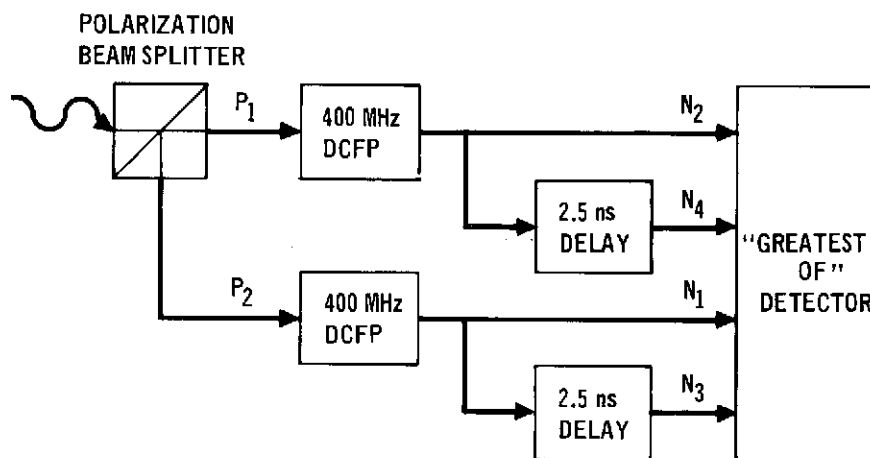
M₁ DECIDES DELAY OR NO DELAY
M₂ DECIDES WHICH POLARIZATION

MODULATOR STATE		OUTPUT STATE
M ₁	M ₂	
-	+	1 P ₂ NO DELAY
-	-	2 P ₁ NO DELAY
+	-	3 P ₂ DELAY
+	+	4 P ₁ DELAY

+ IMPLIES MODULATOR CHANGES THE POLARIZATION
- IMPLIES MODULATOR DOES NOT CHANGE THE POLARIZATION

Figure 44 shows the PQM receiver block diagram assuming uniform spacing between time slots (i.e., 400 Mbps implies time slots separated by 2.5 ns). The incoming optical signal is split into its component polarizations. The DCFP outputs are sampled at each time slot. The four possible outputs are compared and a "greatest of" detector determines which of the possible states was sent.

FIGURE 44 PQM - RECEIVER



2.4.2 Acquisition and Tracking Subsystem Design. The acquisition and tracking subsystem for the balloon transceiver consists of acquisition and tracking detector optics, the detectors themselves and their angle measurement signal processors, the gimbal set including bearings and drive motors for coarse pointing, two single-axis bimorph benders for fine pointing, and compensation circuits which drive the gimbals and benders. This section describes the design and performance of the acquisition and tracking subsystem.

We have designed the subsystem to resemble the reference satellite system as closely as is consistent with minimum impact on the BAPE hardware and with low cost for the flight experiment. With these objectives in mind, we selected the Quadrant Photo-Multiplier Tube (QPMT) for both acquisition and tracking detectors. As we showed

in Section 2.2, this configuration is best for the satellite system as well. We also included bender bimorphs for fine pointing as in the satellite case. As a result, the tracking system functionally duplicates the reference satellite configuration. We elected to use the BAPE gimbal set and the BAPE attitude reference system in order to avoid the costs of: (1) precision satellite gimbals and bearings, (2) a new precision attitude reference system for the BAPE, and (3) possible extensive rework of the BAPE platform to meet the mechanical constraints imposed by incorporation of an auxiliary gimbal set. The present BAPE gimbals must be outfitted with ABEC 7 grade bearings to permit accurate pointing. Table 14 summarizes the alternative gimbal configurations considered, along with the advantages and disadvantages of each. As a result of this choice, our system will not give acquisition characteristics representative of those of the satellite system in terms of gimbal and bender motions during the acquisition process, time to acquire, and probability of acquisition. Therefore, we have not attempted to duplicate other aspects of the acquisition process, such as the pulsed beacon, where such duplication would involve additional cost to the present experiment. However, the fine tracking performance is not strongly dependent upon the gimbal characteristics, but rather upon the detector and bender bimorph behavior. Since we have included in the balloon transceiver the same detectors and benders as specified for the satellite system, the fine tracking performance of the balloon transceiver will be very similar to that of the reference satellite system.

- 2.4.2.1 Tracking error angle measurement. As discussed in Appendix B. the use of a Q-switched beacon laser is a primary reason for choosing the QPMT for both the acquisition and the tracking detectors for the reference satellite high data rate transmitter. In the current experiment, a high-data-rate signal is received at each end of the link. The $0.53 \mu\text{m}$ signal received at the balloon terminal could, therefore, be processed by a DPMT.

TABLE 14

BALLOON TRANSCEIVER GIMBAL CONFIGURATION TRADE STUDY

SYSTEM	ADVANTAGES	DISADVANTAGES
1) BAPE GIMBALS WITH ACQUISITION AND TRACKING GIMBALS	<ul style="list-style-type: none"> • REALISTIC TEST OF SATELLITE ACQUISITION AND TRACKING SYSTEM • BAPE GIMBALS COULD POSSIBLY BE USED FOR TEST-MOTION INPUTS. 	<ul style="list-style-type: none"> • WOULD ADD APPRECIABLE COST (\$100K) • DYNAMIC ENVIRONMENT PROVIDES MORE STRINGENT REQUIREMENT FOR ACQUISITION AND TRACKING SYSTEM.
2) BAPE GIMBALS AUGMENTED WITH BIMORPHIC MIRRORS	<ul style="list-style-type: none"> • LOW COST • UTILIZES EXISTING (PROVEN) SYSTEM TO LARGE EXTENT • SIMPLE MECHANICAL DESIGN • PROVIDES LARGE LOOK ANGLE 	<ul style="list-style-type: none"> • ACQUISITION CHARACTERISTICS UNLIKE SATELLITE • SLIGHTLY DEGRADED TRACKING • REQUIRES REFURBISHMENT OF BAPE GIMBALS AND BEARING FOR SATISFACTORY PERFORMANCE • ACQUISITION AND TRACKING SYSTEM MUST INTERFACE WITH BAPE CONTROL SYSTEM • BAPE CONTROL SYSTEM MUST BE MODIFIED. • EXHIBITS CONTROL DIFFICULTIES NEAR -90 DEGREE ELEVATION.
3) ACQUISITION AND TRACKING GIMBALS ALONE	<ul style="list-style-type: none"> • REALISTIC TEST OF SATELLITE ACQUISITION AND TRACKING SYSTEM • EXPERIMENT IS INDEPENDENT OF GIMBAL CONTROL PECULIARITIES (ERRATIC MOTIONS DUE TO FRICTION, BAD BEARINGS, VIBRATION, ETC.) 	<ul style="list-style-type: none"> • WOULD ADD APPRECIABLE COST (\$75K) • SEVERE MODIFICATION TO PRESENT BAPE HARDWARE • OBTAINABLE LOOK ANGLE IS SEVERELY LIMITED. • USE OF BAPE FOR OTHER EXPERIMENTS MORE DIFFICULT.
4) BAPE GIMBALS AND ADDITIONAL GIMBAL AUGMENTED WITH BIMORPHIC MIRRORS	<ul style="list-style-type: none"> • ELIMINATES -90 DEGREE CONTROL DIFFICULTY • ELIMINATES AZIMUTH GIMBAL FROM CLOSED LOOP TRACKING TASK. 	<ul style="list-style-type: none"> • WOULD ADD COST (\$50K) • ACQUISITION AND TRACKING SYSTEM MUST INTERFACE WITH BAPE CONTROL SYSTEM • BAPE CONTROL SYSTEM MUST BE MODIFIED.

Nevertheless, the QPMT was chosen in order to add validity to the experiment for predicting how the satellite link will perform when deployed.

As a consequence of choosing the QPMT for the balloon-borne terminal, the problem arises of designing an angle tracker which will operate both with a pulsed received signal, which simulates the output of a Q-switched beacon laser, and with the high-data-rate output of the ground station mode-locked laser transmitter, upon which the airborne transceiver must track during data transmission on the uplink.

Pulsed Tracker - Figure 45 is a block diagram of the QPMT signal processing circuitry for a pulsed input signal. The incoming light is focussed on a pyramidal mirror which divides the beam into four separate beams. The fraction of the incoming light power contained in each of the four beams is dependent on the position of the center of the beam with respect to the point of the pyramid. When the receiver is aligned perfectly with the received beam, the power divides equally.

A timing diagram is shown in Figure 46 . A pulse of current (typically 200 nanoseconds) is generated by each photomultiplier tube in the QPMT array in response to the light pulse illuminating the tube. These four current pulses are converted to voltage pulses by the current-mode preamps which are ac coupled to the PMT's. The preamp outputs are detected by the threshold detector, which then triggers the timing and control logic. The pulses are delayed momentarily (100 nanoseconds) in the fixed delay lines to permit the integrators to dump their previous values and to switch from the HOLD mode to the TRACK mode. The INTEGRATE mode is initiated just prior to the leading edge of the delayed pulse, and the HOLD mode is reentered just after the trailing edge of the delayed pulse. The integrator then holds the computed area of the pulse. The integrator circuit is shown in Figure 47. It has excellent signal-to-noise performance when detecting a pulse. The impulse response of an integrate-and-dump circuit is a square pulse occurring at $t = 0$ with a duration T . Thus the circuit is a matched filter for a square pulse of width T occurring at time $t = 0$. The implementation, however, requires prior knowledge of the pulse time of occurrence, necessitating the time delays and threshold detector. The circuit shown in Figure 47 integrates when the feedback switch is open and dumps when the feedback switch is closed. The HOLD command opens the input to the integrator. The operational amplifier is required to be a high speed device similar to integrated circuits that presently are available commercially.

FIGURE 45 QUADRANT PHOTOMULTIPLIER TUBE TRACKER FOR PULSED INPUT

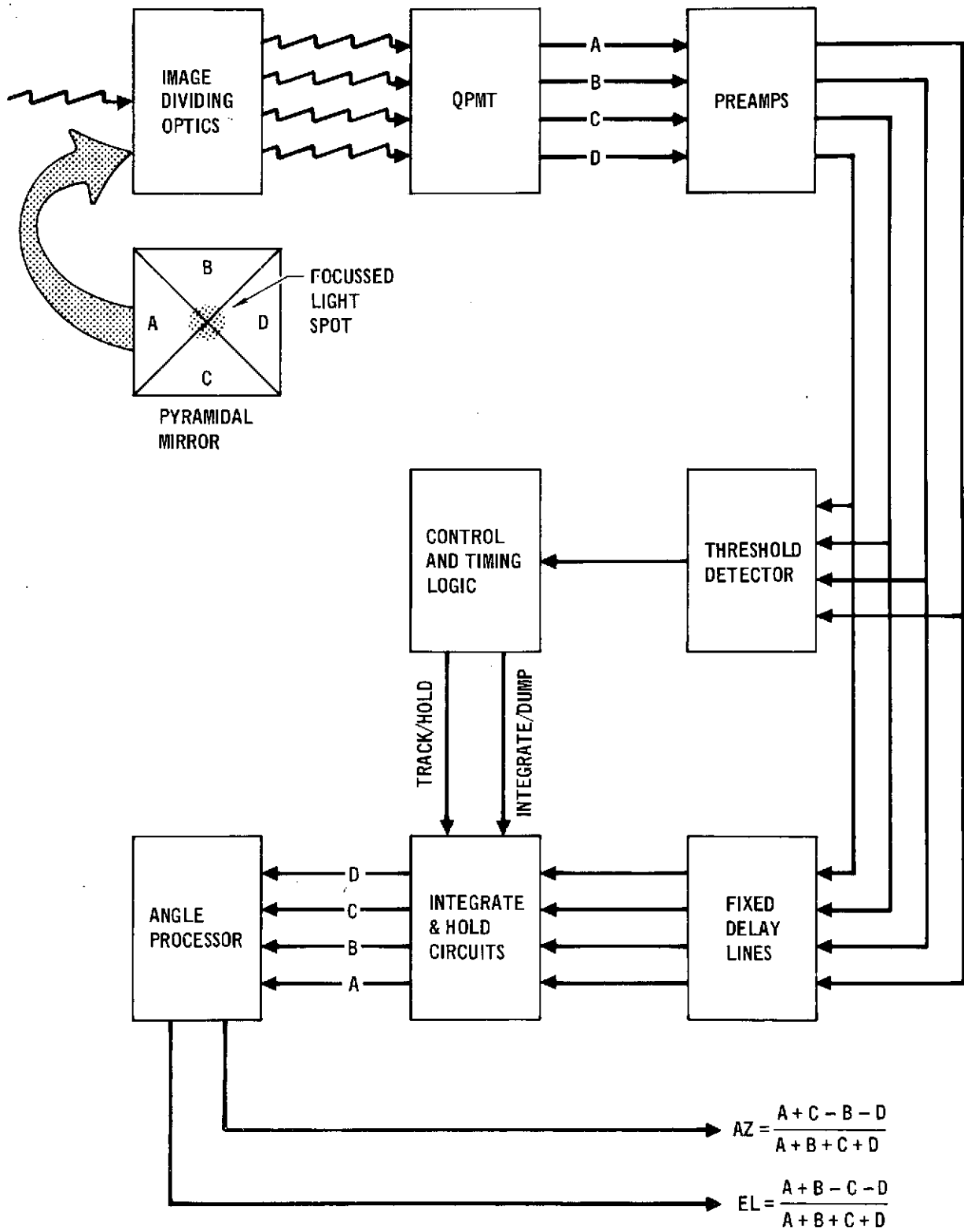
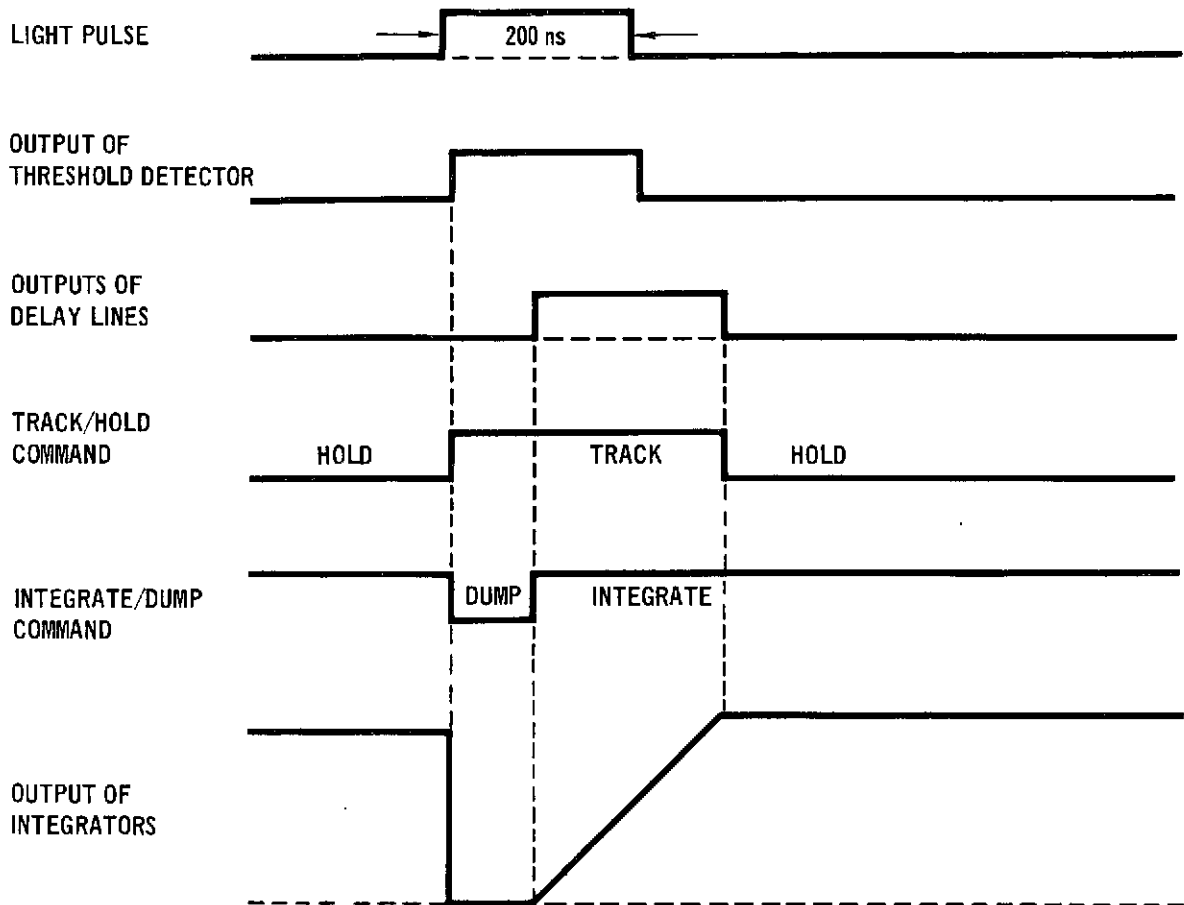


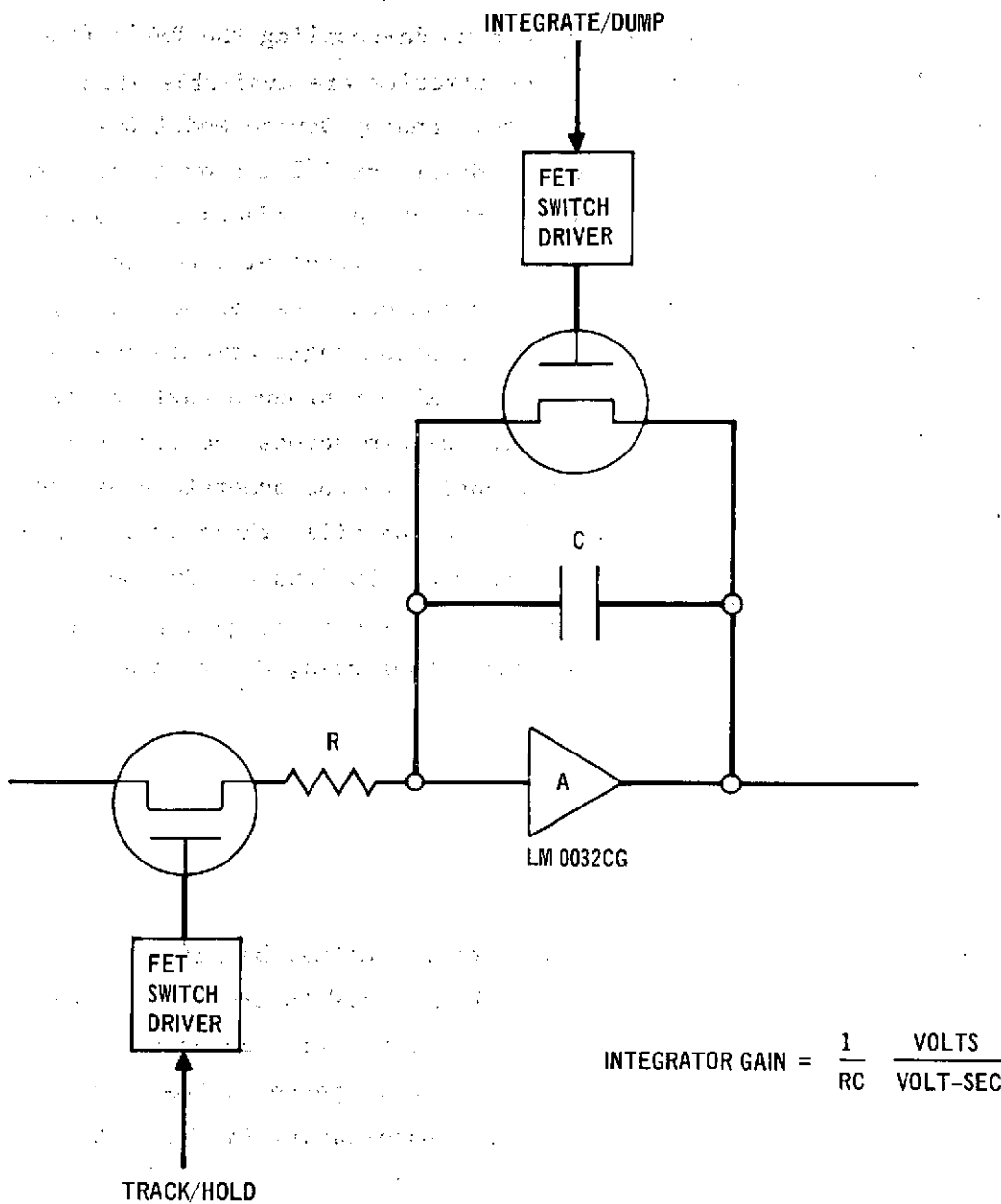
FIGURE 46 QPMT PULSED TRACKER TIMING DIAGRAM



The angle processor is discussed below, but first, we discuss the tracker front-end required when the received signal is a high-data-rate pulse train.

High-Data-Rate Tracker - The high-data-rate tracker is less straightforward than the pulsed tracker due to the fact that the desired signal spectrum is concentrated at or near dc, precluding ac coupling. The ramifications of dc coupling the PMT's to the angle processor are: (1) the electronics must be designed for very low dc drifts in order to avoid boresight shifts in the angle measurement, (2) the dc currents due to background illumination and tube dark current represent a bias on each of the four channels, whereas with ac coupling, only the tube shot noise due to the background and dark currents is processed.

FIGURE 47 INTEGRATOR CIRCUIT



During acquisition, the signal can be chopped at the transmitter because transmission of data has not been initiated. The acquisition detector output currents are then ac coupled to signal conditioning electronics consisting of current-to-voltage preamps, rectifier and low-pass filters. The resulting four dc voltages are processed by the angle processor to produce voltages proportional to azimuth and elevation angular errors.

Table 15 lists four possible candidate approaches to the design of the tracker used in the fine tracking mode, wherein reception of data is required. With regard to dc-coupling the PMT's (the first candidate), high-stability circuits are available which can provide the accuracy required. Analog Device Model 604 instrumentation amplifier has dc drifts of 1/2 microvolt or less per degree Centigrade. However, the channel offsets due to the background illumination of a particular flight will not be known prior to flight to permit adjustment. As can be seen by the formula for the azimuth and elevation angle computation in Figure 45, the background biases will not produce angle biases if the background illumination is uniform across the receiver aperture. The background contribution to the numerators of the formulae will be equal for each term and will, therefore, cancel with subtraction. However, these contributions add in the denominators, thereby reducing the angle tracker gain in volts per unit angle. The ratio of the actual gain, G_A , to the desired gain, G_D , is given by:

$$\frac{G_A}{G_D} = \frac{1}{1 + \frac{\Delta P_B}{P_S}} \quad (1)$$

where ΔP_B is the difference between the actual background power and the background power for which the offsets are nulled, and P_S is the signal power received at the tracking detector. In order to limit the gain uncertainty to 10 percent, the signal power must be at least 10 times the uncertainty in the background power.

The addition of a chopper (the second candidate in Table 15) avoids the dc stability requirement, but adds the complexity of a chopper without relieving the offset problem. Since the background and signal are both chopped, the amplitude of the ac signal at each tube output is proportional to the sum of the signal and background, thereby producing a channel offset due to background.

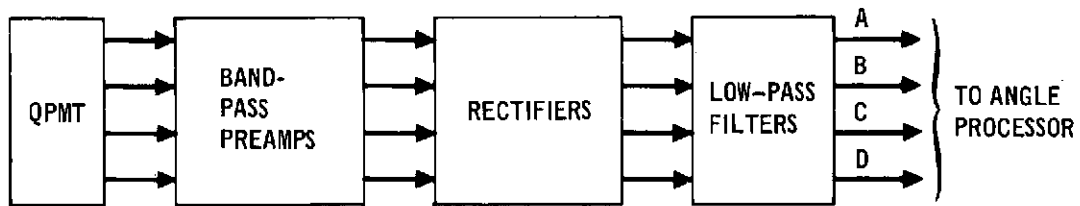
TABLE 15

HIGH DATA RATE TRACKER CANDIDATES

<u>Approach</u>	<u>Advantages</u>	<u>Disadvantages</u>
DC couple the PMT's	<ul style="list-style-type: none"> o No chopper or wide-band PMT required 	<ul style="list-style-type: none"> o Requires dc stability in electronics o Flicker noise present o Background and dark current are channel offsets
Chop light ahead dividing optics	<ul style="list-style-type: none"> o AC - coupling permitted 	<ul style="list-style-type: none"> o Electromechanical or Electrooptical chopper required at transceiver o Background and dark current are channel offsets
Detect the 400 MHz	<ul style="list-style-type: none"> o AC coupling permitted o Background and dark current offsets eliminated 	<ul style="list-style-type: none"> o Wideband PMT required

Detecting the 400 MHz component of the signal (the third candidate in Table 15) relieves both of the undesirable conditions which exist with a straightforward approach using standard components. A block diagram is shown in Figure 48. The PMT's in the QPMT array must have sufficient bandwidth to pass the fundamental harmonic of the received data pulse train. The bandpass filter isolates the desired portion of the signal spectrum, and the rectifiers and low pass filters form a detector of the amplitude of the harmonic. This approach permits ac coupling without chopping the background, thereby eliminating the dc components of background and dark current from the computation of angle. Figure 49 shows the power spectrum of a random PGBM signal received by detector of

FIGURE 48 HIGH-DATA-RATE TRACKER SENSOR ELECTRONICS



unlimited bandwidth. The mathematical expression for the spectrum is given by:

$$S(f) = Q^2 \left\{ \frac{1}{f_D} \left(\frac{N_E - 1}{N_E + 1} \right)^2 \text{sinc}^2 f_D T + \sum_{n=-\infty}^{\infty} \text{sinc}^2 (n f_D T) \delta (f - n f_D) \right\} \quad (2)$$

where

$$Q = \frac{\beta P_p f_D T}{2} \left(1 + \frac{1}{N_E} \right) = \beta P_{av} \quad (3)$$

β = tube sensitivity in amps per watt (40)

P_p = peak power received

f_D = pulse repetition frequency, (400 MHz)

T = pulse width (300 nanoseconds)

N_E = modulator extinction ratio (30)

P_{av} = average power received

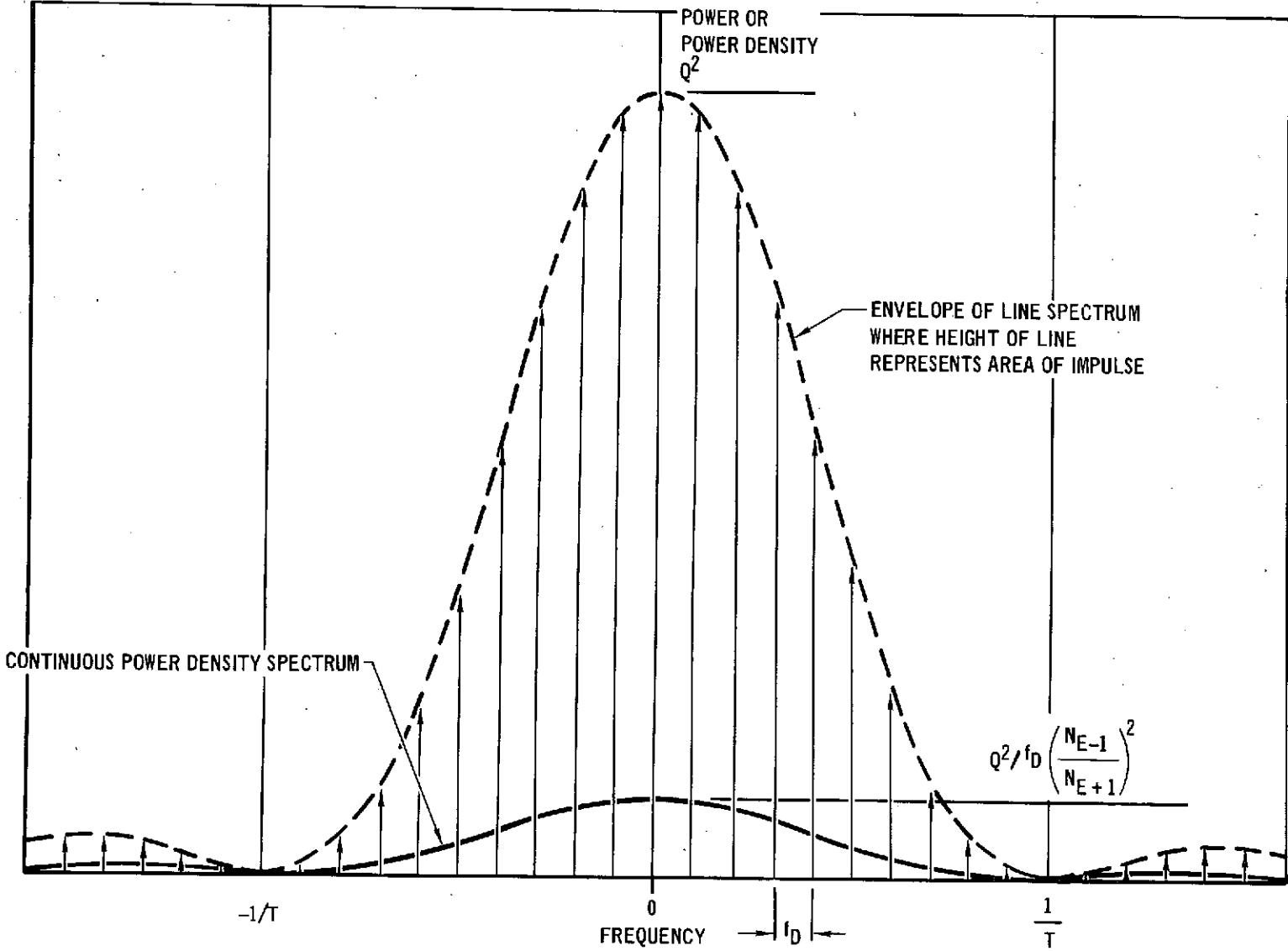
$\text{sinc } x = \frac{\sin \pi x}{\pi x}$

$\delta(x)$ = unit impulse at $x = 0$

This result assumes square light pulse and equal probability of pulse or no pulse at each pulse repetition interval. At the output of a narrow band filter of bandwidth B_o centered at f_D , the signal power is given by:

$$P = \int_{f_D - \frac{B_o}{2}}^{f_D + \frac{B_o}{2}} 2 S(f) df \quad (4)$$

FIGURE 49 POWER SPECTRUM OF WIDEBAND DETECTOR OUTPUT
FOR RANDOM PGBM DATA



$$\approx 2Q^2 \text{sinc}^2 f_D T \left(1 + \frac{B_o}{f_D} \left(\frac{N_E - 1}{N_E + 1} \right)^2 \right)$$

for a $B_o/f_D = 0.01$, the second term in parentheses can be ignored. The resulting amplitude is given by:

$$\sqrt{P} \approx \sqrt{2} Q |\text{Sinc } f_D T| \quad (5)$$

Photomultiplier speed of response is typically given in nanoseconds of risetime. Risetime is defined as the time during which the output current is between 10 percent and 90 percent of its final value when responding to a step input. For a single pole filter, whose transfer function is:

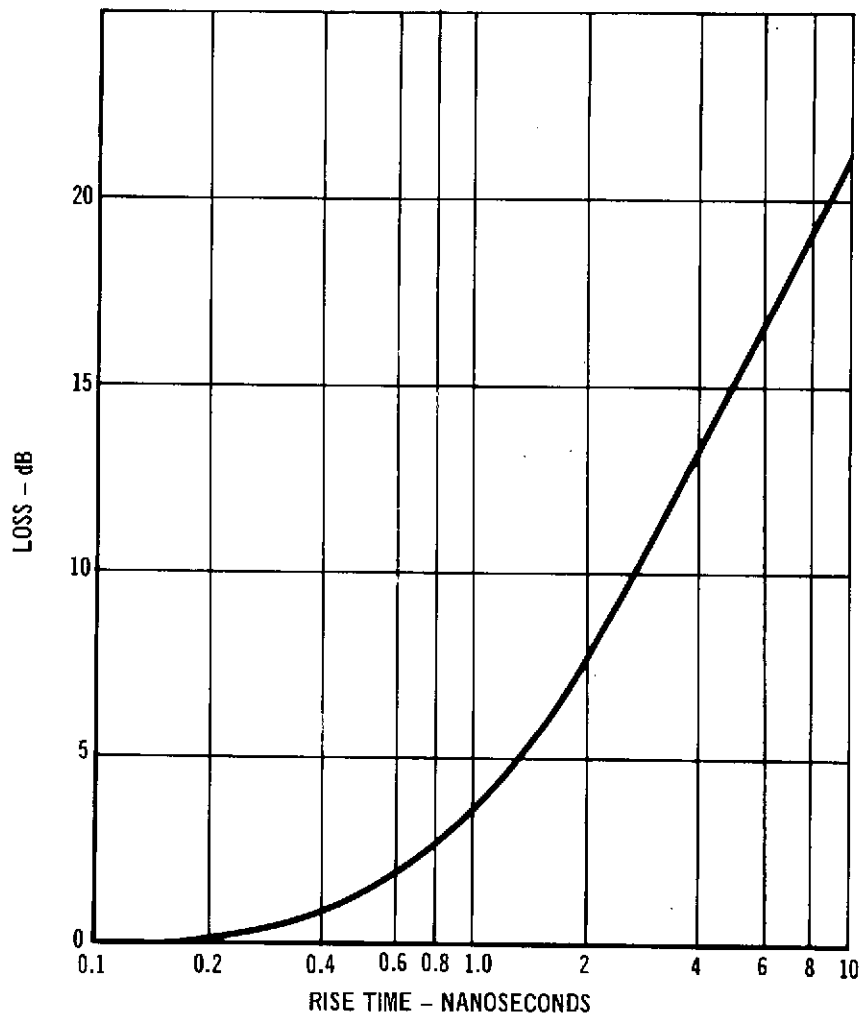
$$H(s) = \frac{1}{1 + s/2\pi f_c}, \quad (6)$$

the corner frequency, f_c , is related to the risetime, t_r , by

$$f_c = \frac{\ln 9}{2\pi t_R} = \frac{0.350}{t_R} \quad (7)$$

Assuming that this model describes the frequency response of the PMT, Figure 50 shows the power loss at 400 MHz at the PMT output as a function of the rise time. RCA has several PMT's in the region below 2 nanoseconds where the loss is acceptable. We have tentatively selected the RCA 4460, with its temperature-stable S-11 photocathode and ruggedized construction. However, the RCA C31024 tube may be required. It achieves additional speed by having 5 high-gain gallium phosphide dynodes, rather than 10 medium-gain beryllium oxide dynodes. The final choice must be made on the basis of empirical tests of the frequency response of the tubes. If the 4460 is acceptable, it is recommended because of its lower cost and rugged construction. Both the first and the third alternatives in Table 15 are viable approaches to the high-data-rate tracker. We have tentatively selected the latter concept for our baseline design. The final choice will be based on laboratory evaluations of the stability of the dc coupled circuits and the frequency response of candidate PMT's.

FIGURE 50 SIGNAL POWER LOSS AT PMT OUTPUT VERSUS RISE TIME



To summarize the angle measurement hardware at the balloon-borne terminal, there are two angle trackers: an acquisition-mode tracker and a fine-tracking-mode tracker. The acquisition-mode tracker is a QPMT consisting of a quadrant dividing field lens providing 4 beams to illuminate 4 PMT's. The signal from the ground station is chopped at 100 kHz during the acquisition process. The resulting ac outputs of the four PMT's are rectified and filtered to produce 4 dc voltages proportional to the quadrant irradiances. These voltages are processed by the angle processor discussed below.

The large acquisition field of view and sunlit-earth background radiance result in significant background current in the tube. The total tube current is limited to 10 percent of its saturation value by limiting the gain of the tube to a factor of 2000. The gain is established by setting the supply voltage to the tube cathode and dynode chain.

When the angular error is within ± 2 milliradians, the incoming beam falls through the hole in the bifurcating mirror to illuminate a QPMT for tracking. A pyramidal mirror divides the beam into 4 parts in order to illuminate 4 PMT's. The 400 MHz components of the PMT outputs are extracted via bandpass filters, rectified, and filtered to produce 4 dc voltages proportional to the irradiances of the 4 faces of the pyramidal mirror. Since the 100 MHz modulation is still present on the incoming beacon, there is a 100 MHz ripple on the bandpass filter output. The low pass filters have a bandwidth of 5 kHz, attenuating the ripple by 26 dB. This ripple will not be noticeable to the tracking loop.

When the angular error at the balloon terminal is less than $1/2$ milliradian, the ground station receives the mode-locked laser signal from the balloon. The ground station narrows its beam from 1.5 milliradians to 100 microradians (diameter), points back along the incoming beam, terminates the chopping action on its transmitted signal, and initiates data transmission.

When testing the characteristics of pulsed-beacon tracking, the ground transmitter is modulated to form bursts of pulses. Logic circuits in the balloon sense that the incoming waveform has changed to the pulsed format and connect the pulsed tracker electronics to the angle processor. At the same time, a 20 dB optical attenuator is pulled out of the beam by a solenoid actuator in order to provide sufficient signal power to the detector to track in the pulsed beacon mode. The removal of

the attenuator is accomplished one millisecond or less after the signal changes to the pulsed mode. The time constant of the gimbal control loop is at least 50 times the actuation time. Therefore, the incoming beam is assured of remaining with the hole in the bifurcation mirror when the transition to pulsed mode is complete, precluding the necessity for reacquisition. The inner control loop (bimorph beam bender loop) reacts much faster than the gimbal loop, permitting a small error to develop while the transition is in process. This error is quickly nulled out after the transition is complete.

Angle Processor - The angle processor computes the azimuth and elevation error angles from the dc voltages at the output of each of the four channels. As shown in Figure 45, the formulae for small angle deviations about boresight are:

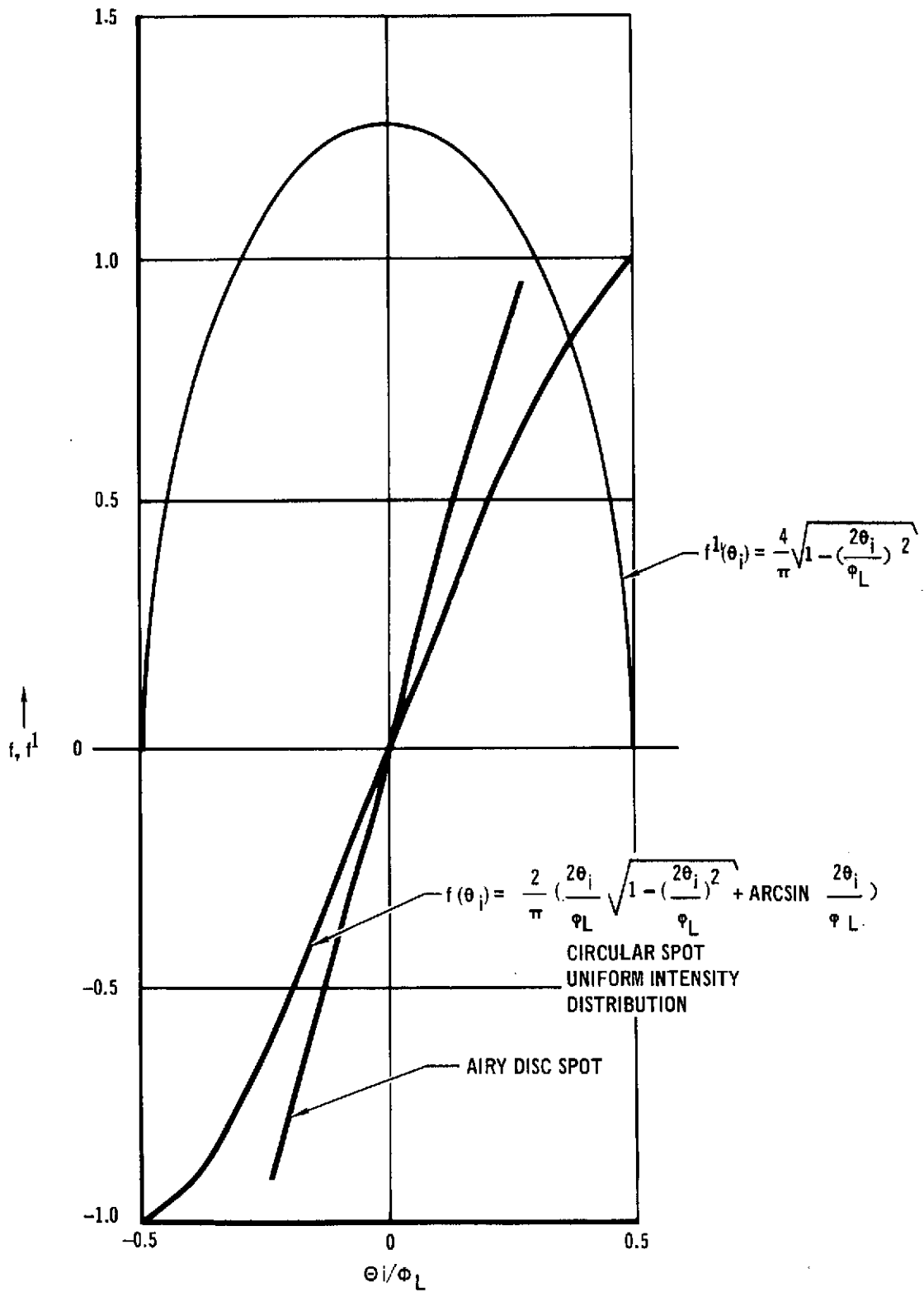
$$\begin{aligned} V_A &= \frac{A+C-B-D}{A+B+C+D} \\ V_E &= \frac{A+B-C-D}{A+B+C+D} \end{aligned} \tag{8}$$

where A, B, C, and D are the voltages from the upper left, upper right, lower left, and lower right quadrants of the QPMT, respectively, and V_A and V_E are voltages proportional to the azimuth and elevation error angles, respectively. For a circular focussed spot of uniform intensity and whose diameter subtends an angle ϕ_L at the effective center of the optical system, the relationship between output voltage and input angle is given by:

$$\begin{aligned} V_A &= \frac{2}{\pi} \left(\frac{2\theta_A}{\phi_L} \sqrt{1 - \left(\frac{2\theta_A}{\phi_L} \right)^2} + \arcsin \frac{2\theta_A}{\phi_L} \right) \\ V_E &= \frac{2}{\pi} \left(\frac{2\theta_E}{\phi_L} \sqrt{1 - \left(\frac{2\theta_E}{\phi_L} \right)^2} + \arcsin \frac{2\theta_E}{\phi_L} \right) \end{aligned} \tag{9}$$

This function and its derivative are plotted in Figure 51. Note that the linearity is quite good over the central region of diameter $\phi_L/2$ where the derivative remains relatively constant.

FIGURE 51 ANGLE PROCESSOR FUNCTION AND ITS DERIVATIVE



Since the control system which uses the tracker angle information is a null-seeking system, the primary requirement of the tracker is very low null offset (0.1 μ rad). The third curve in Figure 51 is the tracker characteristic when a diffraction-limited (Airy disc) pattern illuminates the pyramidal mirrors. For this case, ϕ_L represents the diameter of the first dark ring. Because the spot has a higher energy density near the center than a uniform spot of the same diameter, the detector gain (volts per unit angle) is higher for the diffraction-limited case. The actual case for the present design will be between these two limits.

We chose an analog implementation of the angle processor. The block diagram for such a system is shown in Figure 52. The sample-and-hold circuits are required for the pulsed beacon signal. Their function is to extend the time the signal is held from the capability of the integrator to the 625 microseconds required by a 1600 pulse-per-second repetition rate. These circuits are bypassed by the high-data-rate tracker front end. The amplifiers and dividers represent functionally the adding, subtracting, and dividing required to compute the desired quantities. These devices must have low dc drift characteristics to avoid boresight shifts with time and temperature. Assuming a 10 volt output corresponds to the 50-microradian radius of the linear region, a 20-millivolt offset corresponds to a 0.1-microradian offset. This performance is readily achievable. The bandwidth of these devices need be no more than 10 kHz to support the 200-Hertz bender bandwidth.

A digital approach is illustrated functionally in Figure 53. The integrators hold the four signals resulting from a beacon pulse long enough for the Analog-to-Digital Converters to convert the voltages to binary numbers. The resulting numbers are then sequentially added to the Accumulator by the Arithmetic Logic Unit (ALU) and the result stored in the Sum Signal Register. The ALU then sequentially adds and subtracts the four binary

FIGURE 52 ANALOG ANGLE PROCESSOR BLOCK DIAGRAM

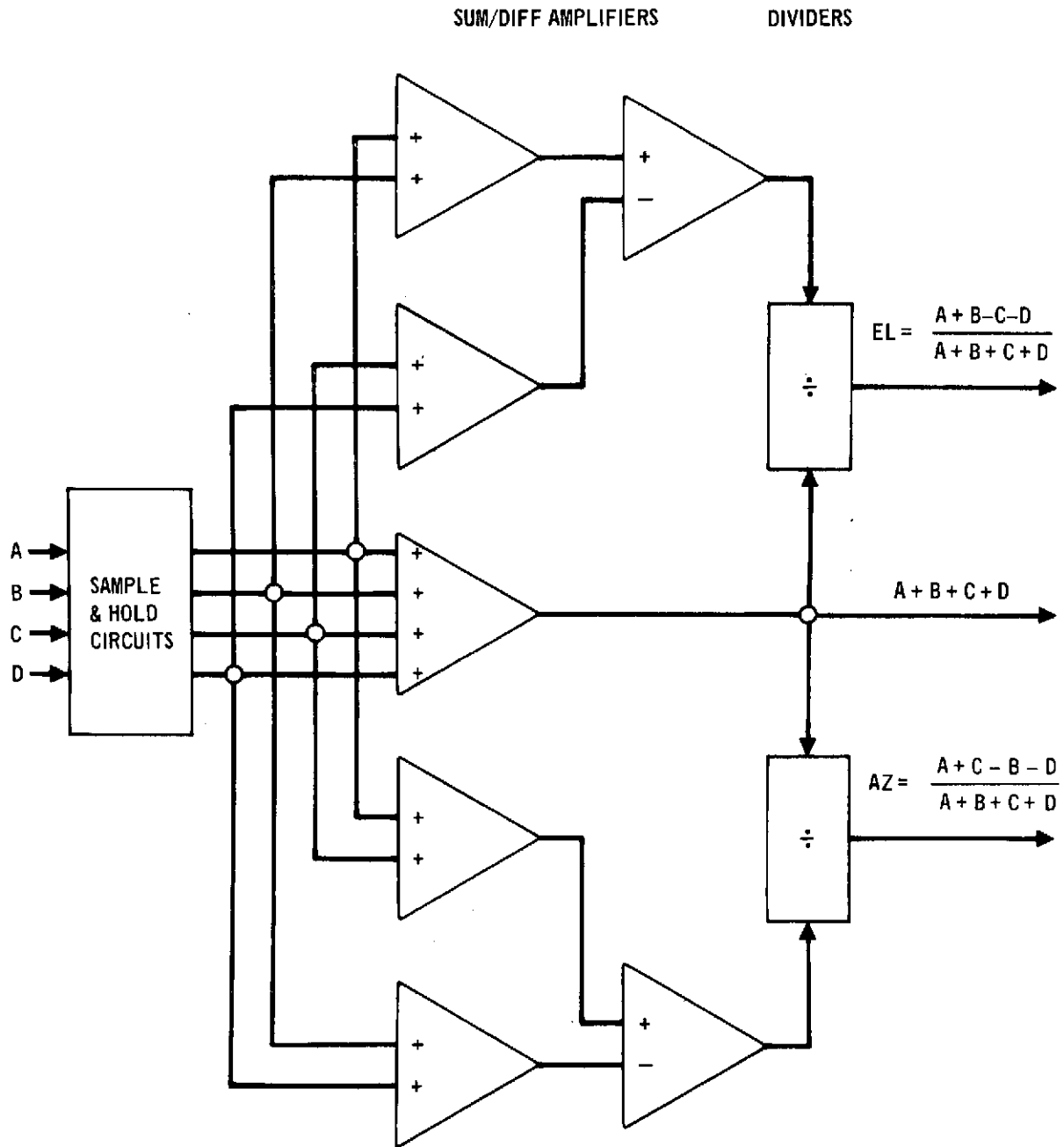
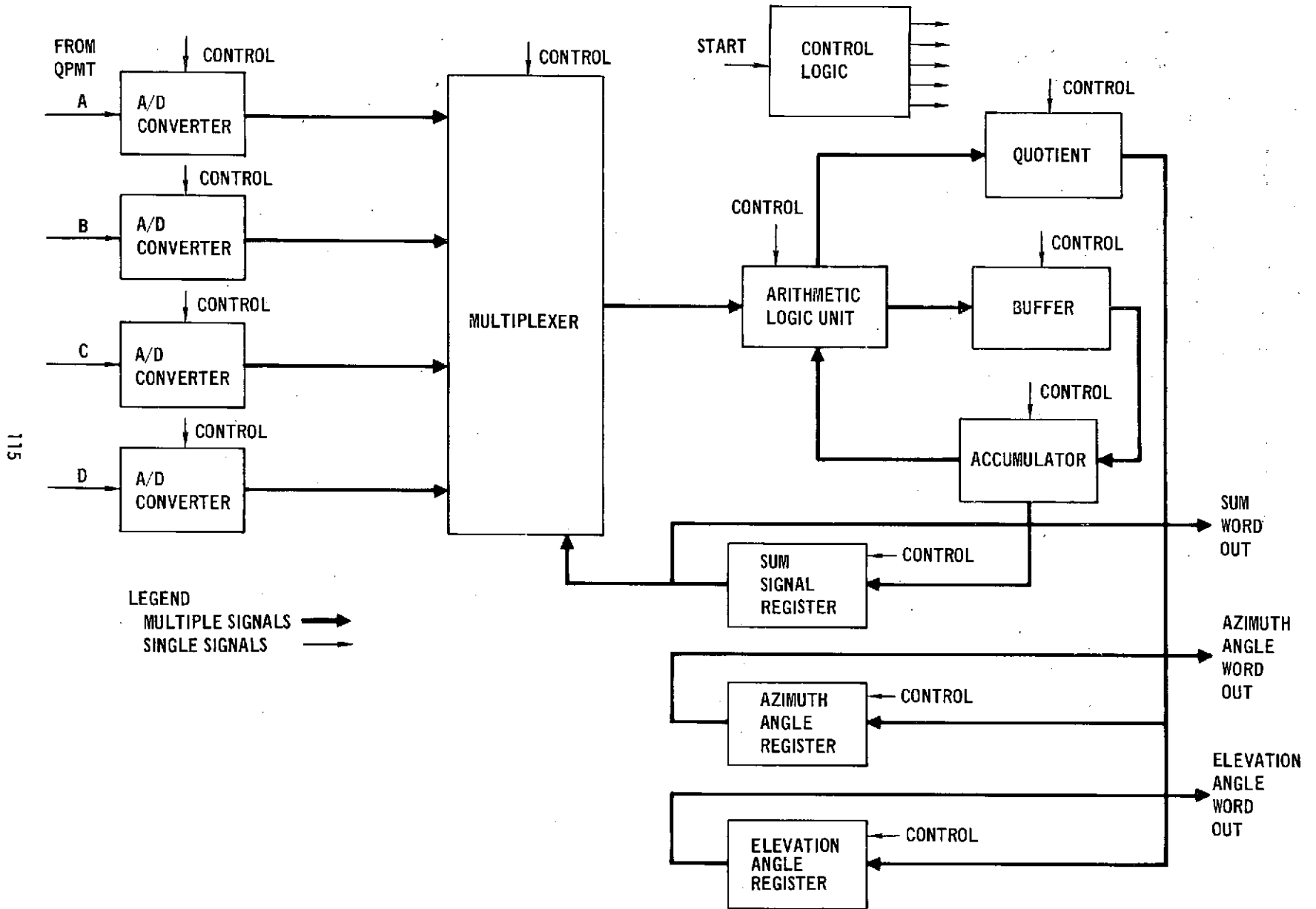


FIGURE 53 DIGITAL ANGLE PROCESSOR BLOCK DIAGRAM



115

numbers to form A+B-C-D in the accumulator. Then the ALU, with the aid of the Quotient module, computes the quotient of the accumulator and the Sum Signal Register and stores the result in the Elevation Angle Register. The azimuth angle is computed in a similar manner. The control logic is signalled by a threshold crossing to initiate the compute cycle. It then controls the functioning of the various modules during the computational routine. Table 16 indicates the advantages and disadvantages of both the digital and analog approaches. MDAC is constructing a digital angle processor at present for a similar program in which the angle information is required in digital form thereby making the digital approach attractive. Digital angles are not required for the present system, so the savings associated with the analog approach can be realized.

TABLE 16

COMPARISON OF ANALOG DIGITAL ANGLE PROCESSORS

<u>Approach</u>	<u>Advantages</u>	<u>Disadvantages</u>
Analog	<ul style="list-style-type: none"> o Simple, straightforward o Less space, weight, and power than the digital approach 	<ul style="list-style-type: none"> o Requires components with low dc drift
Digital	<ul style="list-style-type: none"> o Excellent long-term stability o Already developed under another MDAC laser communications program 	<ul style="list-style-type: none"> o Complex o More space, weight, and power than the analog approach

Angle Noise Performance - The angle noise produced by the angle trackers discussed above can be predicted by means of the analysis shown in Appendix D. The resulting function is:

$$\sigma_{\theta} = \frac{\pi\phi_L}{4\sqrt{S/N}} (1 + f^2(\theta))^{1/2} \quad (10)$$

where

σ_{θ} = rms angle noise

ϕ_L = diameter of the linear region of the tracker

S/N = electronic power signal-to-noise ratio in the
bandwidth of the tracker

$f(\theta)$ = noiseless tracker characteristic previously given
in Equation (9)

Acquisition and Tracking Link Margins - The acquisition and tracking link margins for the experiment system is based on the equations in Appendix D. The required power is computed to limit the false alarm rate to 0.5 false alarms per second, achieve a probability of detection of at least 95 percent, and limit the angle noise to a value that depends on the tracking accuracy required for the link. Table 17 is a summary of the link margins of the various balloon experiment links. The convention used in naming the link analyses is as follows: the direction of high data-rate transmission can be inferred from the name of the link (e.g., Balloon to Ground). The words "Beacon" or "Data" indicate to whether the low rate beacon signal or the high rate data signal is being analyzed. In addition, the mode (acquisition or tracking) is indicated. Appendix D contains a complete tabulation of the input data and tabular output of the link analyses for the satellite and balloon experiment links.

2.4.2.2 Control system design. Beam pointing control systems in the transceiver are designed to have a close similarity with an operational satellite control configuration, and yet have a minimal cost impact in terms of required hardware changes in the BAPE gondola. The system features three control modes and automatic control logic electronics which select the appropriate control mode for a particular situation. The three control modes are: Coarse pointing, Acquisition, and Tracking. The coarse pointing mode controls the telescope gimbal angles and points the boresight relative to the gondola. The primary

TABLE 17

SUMMARY OF LINK MARGINS

<u>Link</u>	<u>Margin (dB)</u>
Balloon to Ground	
Data-Acquisition	24.6
Data-Tracking	17.9
Beacon-Tracking	8.4
Ground to Balloon	
Data-Acquisition	6.4
Data-Tracking	15.0

requirement in this mode is a tracking accuracy which assures that the ground transmitting site is located in the ± 1 degree optical field of view of the transceiver acquisition detector. When the beacon laser signal is detected on the acquisition detector, the acquisition control mode is actuated. In this mode, the telescope gimbals also provide the control required to reduce the pointing error to a value less than 2 mrad based on angle errors measured by the acquisition detector. When the pointing error is controlled to a value less than 2 mrad, the incoming beacon beam passes through the bifurcating mirror in the collecting optics and enters the tracking optics. The tracking optics consist of tracking bimorph bender mirrors and the tracking optical angle detector. When the tracking detector receives an input signal, the track control mode is automatically selected by the control logic. In the track mode, the bimorph bender mirrors are driven by the fine angle detector outputs in a wideband control loop which can provide beam pointing angle corrections for deflections less than 2 mrad. A gimbal control loop is also included in the track mode to "unload" bender deflections by removing the large-amplitude, low-frequency error signals. High-frequency, low-amplitude dynamical inputs are tracked by the bender mirror loop exclusively since the bandwidth of the gimbal loop is much lower than that of the bender.

A summary description of the three control modes is listed in Table 18. The normal sequence of operations which sets up the precise mutual tracking for laser communication begins with the coarse pointing mode. Large angle realignments of the telescope and initial pointing at the ground transceiver site are performed in this mode. Commanded gimbal angle values are relayed to the gondola via telemetry from ground control. A magnetic compass mounted on the azimuth gimbal and a potentiometer mounted on the elevation gimbal are the position angle sensors in the Coarse Pointing Mode. A low-frequency dither in the commanded gimbal angles can be added to the ground-command telemetry angle commands, if necessary, to ensure that the ground site falls in the acquisition detector field of view. Detection of the ground site beacon by the acquisition detector automatically initiates the acquisition control mode. The acquisition detector and angle processor electronics provide the pointing angle error measurement for the acquisition mode. Similarly, detection of the optical signal by the tracking detector activates the track mode; the narrow-range tracking detector and processing electronics are the angle error measuring device for the track mode.

Coarse Pointing Mode - Coarse pointing control is exercised in the North-Vertical coordinate system illustrated in Figure 54. Commanded values of azimuth angle (ψ) measured from north, and elevation angle (θ), measured from horizontal, are telemetered to the gondola from ground control. The coarse pointing control loops are illustrated functionally in Figure 55. These loops are Type 1 servomechanisms and include both angular rate and position sensors for feedback. A potentiometer mounted directly to the elevation gimbal shaft is the elevation axis position angle sensor; a magnetic compass is the azimuth position angle sensor. Both control loops employ conventional brush-type dc motors to generate control torques. Loop gains in the control system are:

$$K_p = 2 \pi f_c$$

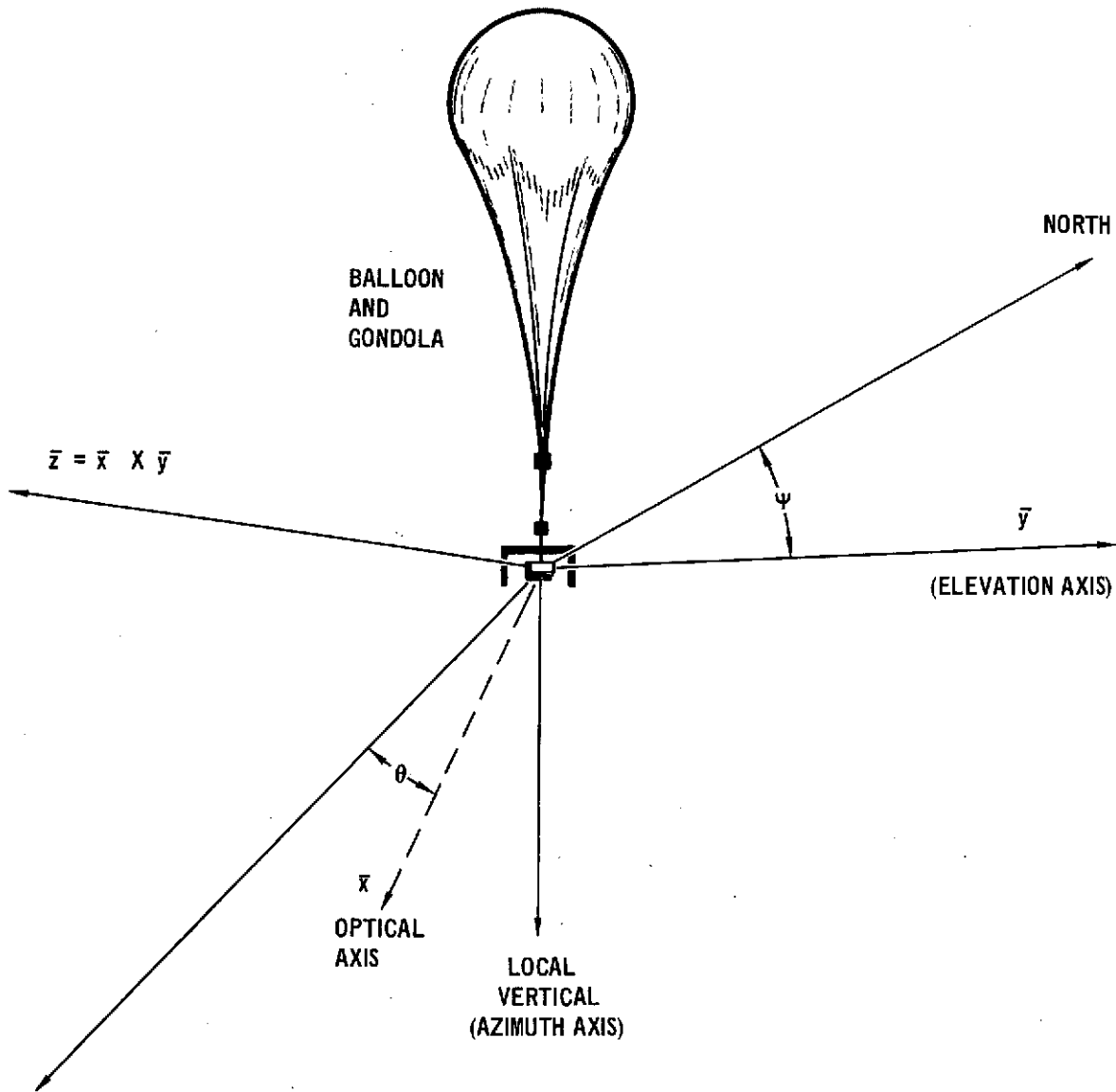
$$K_r = 3 \pi f_c$$

TABLE 18

SUMMARY DESCRIPTION OF BEAM POINTING CONTROL SYSTEMS

1) Coarse Pointing	<u>Azimuth</u> : Compass, Tachometer, Motor, Telemetry Receiver <u>Elevation</u> : Potentiometer, Tachometer, Motor, Telemetry Receiver	Absolute Sensor Error < 1.5 deg Sensor Incremental Resolution < 0.15 deg System Incremental Control Error < 0.25 deg Gimbal Control Bandwidth \geq 2.5 Hz Gimbal Static Frictional Acceleration \leq 0.25 rad/s ²
2) Acquisition	Acquisition Detector, Tachometer, Motor	Acquisition Time < 1 s Gimbal Control Bandwidth = 2 Hz Maximum Gondola Rate \leq 3 deg/s Frictional Accelerations = 0.167 and 0.333 rad/s ² Motor Torque Limit \geq 3.5 * Friction
3) Tracking	Tracking Detector Bimorph Bender Mirror Tachometer Motor	RMS Tracking Error < 0.5 μ rad Peak Tracking Error < 2.2 μ rad Bender Loop Bandwidth = 100 Hz Gimbal Loop Bandwidth = 3 Hz Detector Noise \leq 1 μ rad (rms) Tachometer Noise \leq 2 mrad/s (rms) 1600 Hz Bandwidth Maximum Gondola Rate \leq 3 deg/s Friction Acceleration \leq 0.333 rad/s ²

FIGURE 54 GIMBAL ANGLE AND OPTICAL DETECTOR GEOMETRY DEFINITION



GIMBAL AXES

- ELEVATION (θ, \bar{y})
- AZIMUTH ($\psi, \text{LOCAL VERTICAL}$)

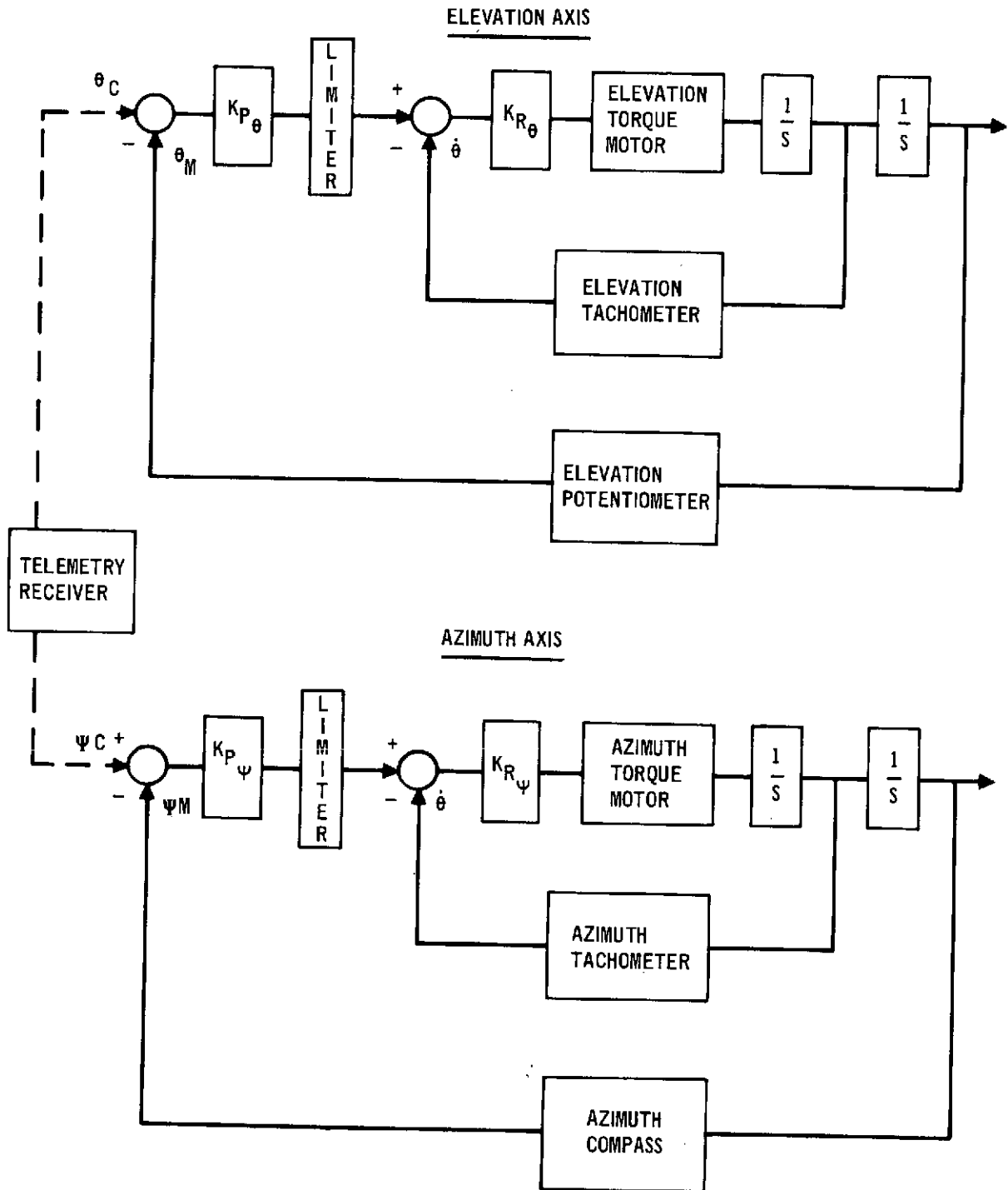
DETECTOR AXES

- ELEVATION (\bar{y})
- NORMAL (\bar{z})

BENDER MIRROR AXES

- ELEVATION (\bar{y})
- NORMAL (\bar{z})

FIGURE 55 COARSE POINTING CONTROL MODE FUNCTIONAL DIAGRAM



where f_c is the crossover frequency. These gain values produce a phase margin of 56 degrees which gives a combination of a well damped dynamic response and a large gain margin.

A summary description of the gimbal control loop components and their required characteristics are given in Table 19. The maximum error in the magnetic bearing angle measured by the azimuth compass is 0.75 degree relative to local magnetic north. In addition to this bias-type error, the resolution of the compass is approximately 0.1 degree. Alignment and scale factor errors of the elevation potentiometer are 0.5 degree and .36 degree, respectively; sensitivity of the potentiometer electronics is 2 mV and gives an angular resolution of 0.04 degree.

The key parameters affecting pointing accuracy in the coarse pointing mode are angle sensing accuracy and resolution, minimal friction, and the dynamical inputs. Dynamical inputs to the elevation axis coarse pointing are minimal since the control mode points the telescope relative to the gondola vertical axis. The azimuth axis control must point the gimbal relative to north and thus any balloon rotation about the local vertical axis must be removed by the control loop. Previous balloon flights have experienced a balloon steady spin (about vertical) of up to 2 deg/sec. Gimbal friction affects the pointing accuracy by causing a steady state offset error (statically) due to the limited acceleration constant of the Type 1 loop. Bias errors in the gimbal angle sensors obviously cause bias errors in pointing angle.

Coarse pointing errors relative to north (azimuth) and the gondola vertical (elevation) are summarized below.

ERROR ANALYSIS

Azimuth Axis

Bias Errors:

Compass Accuracy:	0.75 deg
Compass Alignment:	0.50 deg
RSS:	0.90 deg

TABLE 19

GIMBAL CONTROL LOOP DEVICES AND REQUIREMENTS

Device	Characteristics
<u>Elevation Axis</u>	
Torque Motor (Inland T2950)	$T_{MAX} = 1.2 \text{ ft/lb}; \tau_E = 2.1 \text{ ms}$ $V_{MAX} = 24.4 \text{ volts}; I_{MAX} = 3.25 \text{ amps}$
Tachometer (Inland TG2139)	$K_V = 1.2 \text{ volt/rad/s}$ $R_{load} = 100K \text{ ohms}; V_{Threshold} = 2 \text{ mV}$
Bearing Friction	$T_{Friction} \leq 0.25 \text{ ft/lb}$
Potentiometer	$0.5 \text{ deg alignment}; S = 55 \text{ mV/deg}$
Total Gimbal Inertia	$> 0.75 \text{ slug ft}^2$
<u>Azimuth Axis</u>	
Torque Motor (Inland T5730-A)	$T_{MAX} = 7.0 \text{ ft/lb}; \tau_E = 2.7 \text{ ms}$ $V_{MAX} = 19.8 \text{ volts}; I_{MAX} = 13.2 \text{ amps}$
Tachometer (Inland TG2139)	$K_V = 1.2 \text{ volt/rad/s}$ $R_{load} = 100K \text{ ohms}; V_{Threshold} = 2 \text{ mV}$
Slip Ring	$T_{Friction} \leq 2.0 \text{ ft/lb}$
Compass (Sperry #58726)	$\text{Accuracy} = 0.75 \text{ deg}$ $S = 13 \text{ mV/deg}$
Total Gimbal Inertia	$> 12.0 \text{ slug ft}^2$

Control Errors:

Compass Resolution:	0.15 deg
Friction Offset*	0.026 deg
Balloon Spin Offset (2 deg/sec):	0.013 deg
SUM:	0.19 deg

Elevation Axis

Bias Errors:

Potentiometer Scale:	0.50 deg
Gondola Alignment:	0.50 deg
RSS:	0.71 deg

Control Error

Friction Offset*:	0.05 deg
Potentiometer Resolution:	0.04 deg
SUM:	0.09 deg

* for 2.5 Hz control bandwidth

The worst case bias errors due to sensor bias and sensor alignment are 0.90 and 0.71 degree for azimuth and elevation. Control errors relative to the null indicated by the sensors are 0.19 degree and 0.09 degree for gimbal control bandwidths of 2.5 Hz (Bode crossover frequency).

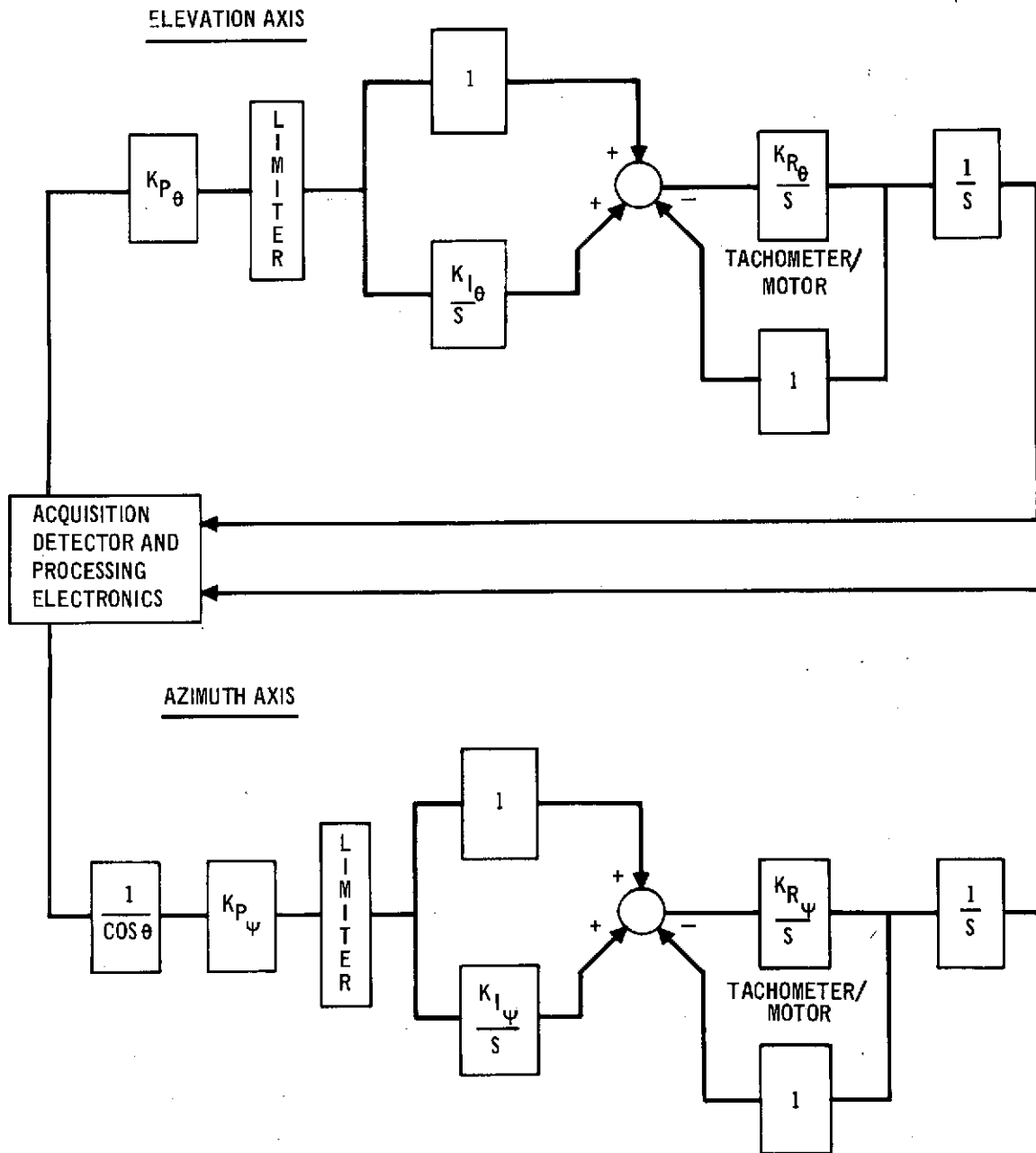
The time spent in the coarse pointing phase of the acquisition sequence is nominally governed by the time required by the gimbals to slew to the commanded orientation at the maximum slew rate of 10 deg/sec. For the case when the balloon is rotationally still, the probability that the beacon laser will illuminate the acquisition detector is high since the (3σ) azimuth pointing error is 1.09 degrees and the elevation error is .80 degree. Assuming the errors are independent, the probability that the RSS error is less than the 1 degree radial field of view of the acquisition detector is approximately 0.9828. If there are no acquisition detections, ground control can initiate a scan pattern in the gondola gimbal pointing to search for the boresight to the ground site. When the balloon is not still but

is rotating as a free pendulum at its natural frequency of 0.15 Hz, the elevation pointing error relative to local vertical will be the sum of the potentiometer bias error and the pendulum motion. In this case, the scan procedure should maintain an elevation pointing command for at least half the pendulum period or 3.4 seconds to assure that the transceiver detector field of view has the possibility of rotating past the ground site. A scan pattern with 5 sub-fields, each held for 3.4 seconds, results in a 17 seconds time period for acquisition detection and virtual certainty of detection.

Acquisition Control Mode - The acquisition control mode is activated when the optical signal detection criterion indicates the acquisition detector is receiving the beacon signal. Operation in the Acquisition Mode continues until the gimbal controls rotate the transceiver telescope boresight to within 2 mrad of the incoming beacon beam and the optical signal enters the tracking optics. Typically, a time period of 1 second or less is required for this control function. Pointing accuracy performance of the acquisition mode is dominated by the gimbal control bandwidth, gimbal friction, and gondola motion during acquisition.

A functional diagram of the acquisition control mode is illustrated in Figure 56. Gimbal position error feedback comes from the acquisition detector angle processing electronics. The same motor-tachometer loop used in the coarse pointing mode is incorporated in the acquisition mode. Unlike the coarse pointing mode, this mode utilizes a Type 2 control loop to increase the low frequency gain. The Type 2 loop develops an infinite velocity constant which permits the azimuth gimbal loop to control to very small errors while the balloon is spinning at a fixed rate, even with gimbal friction included. A multiplier which forms the product of the azimuth detector yaw output and the inverse of the cosine of elevation angle is included at the azimuth loop input. This operation is required

FIGURE 56 ACQUISITION CONTROL MODE FUNCTIONAL DIAGRAM



because the azimuth detector axis is normal to the line of sight and not coincident with the azimuth control axis for elevation angles other than zero. Figure 54 illustrates the detector and gimbal geometry.

Values of the position, rate, and integrator gains in the control loop (K_P , K_R , K_I) are selected to give a phase margin of 53 degrees. The gain margin is conservative such that the phase margin is 47 degrees for a 6 dB gain change. Equations for the gain values are:

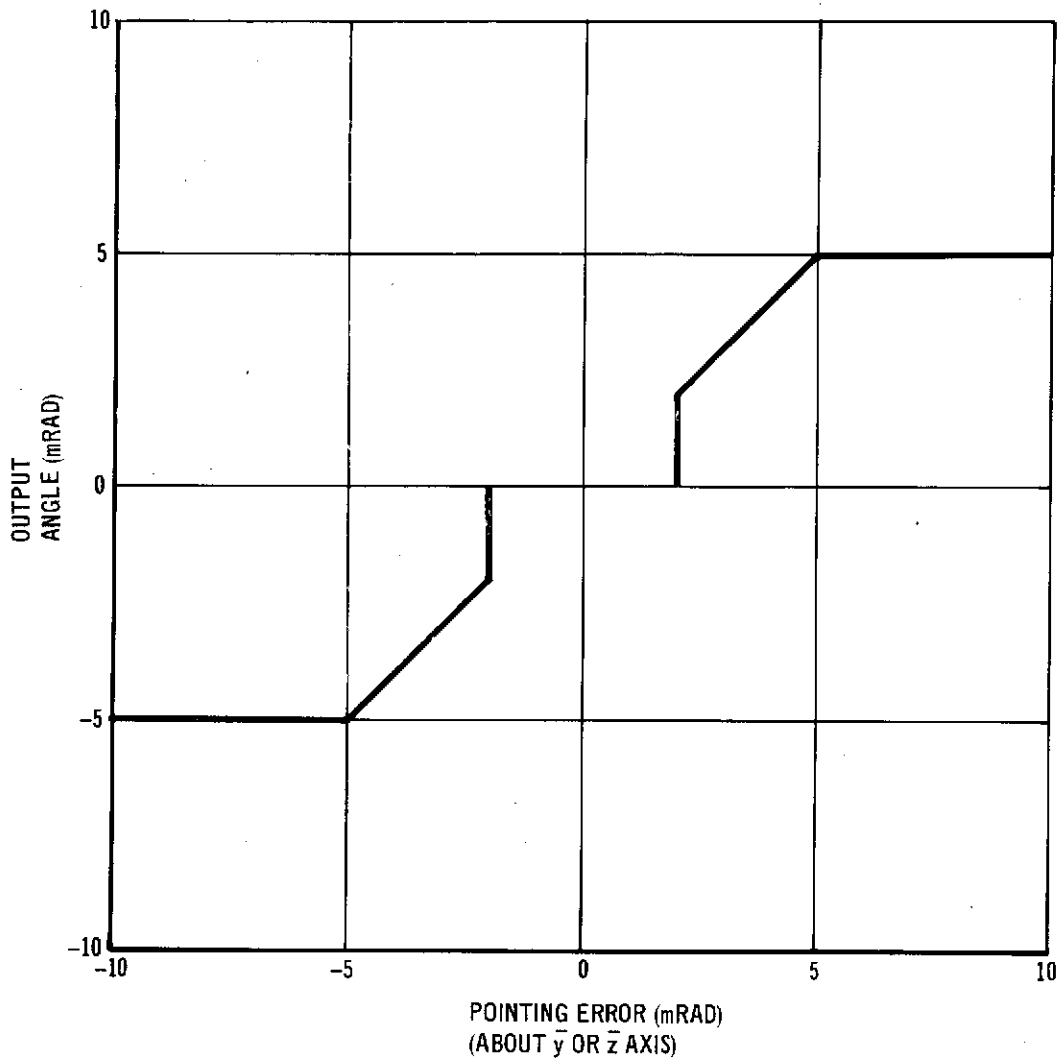
$$\begin{aligned}K_P &= \omega_C \\K_R &= 3\omega_C \\K_I &= \frac{\omega_C}{3}\end{aligned}$$

where $\omega_C = 2\pi f_c$ and f_c is the loop crossover frequency.

The acquisition detector processing electronics produce outputs in elevation and azimuth when the RSS pointing error is between 2 mrad and 17.4 mrad. A saturated output angle of 5 mrad is generated when the error angle about a particular axis exceeds 5 mrad; the output is proportional to the input when the error is between 2 mrad and 5 mrad. Figure 57 illustrates the detector transfer function for a single axis.

We have chosen to analyze the pointing accuracy of the acquisition control by simulating the system on an analog computer. More convenient, linear analyses are not applicable to this situation because of the gimbal friction and detector saturation nonlinearities. In the analysis, the effects of control bandwidth and gondola dynamics on control error are investigated parametrically. The dynamic inputs to the analysis consist of pendulum motion of the gondola with peak to peak displacements up to 10 degrees and spinning motion of the balloon about the vertical axis with a rate up to 5 deg/s.

FIGURE 57 ACQUISITION DETECTOR ANGULAR TRANSFER FUNCTION

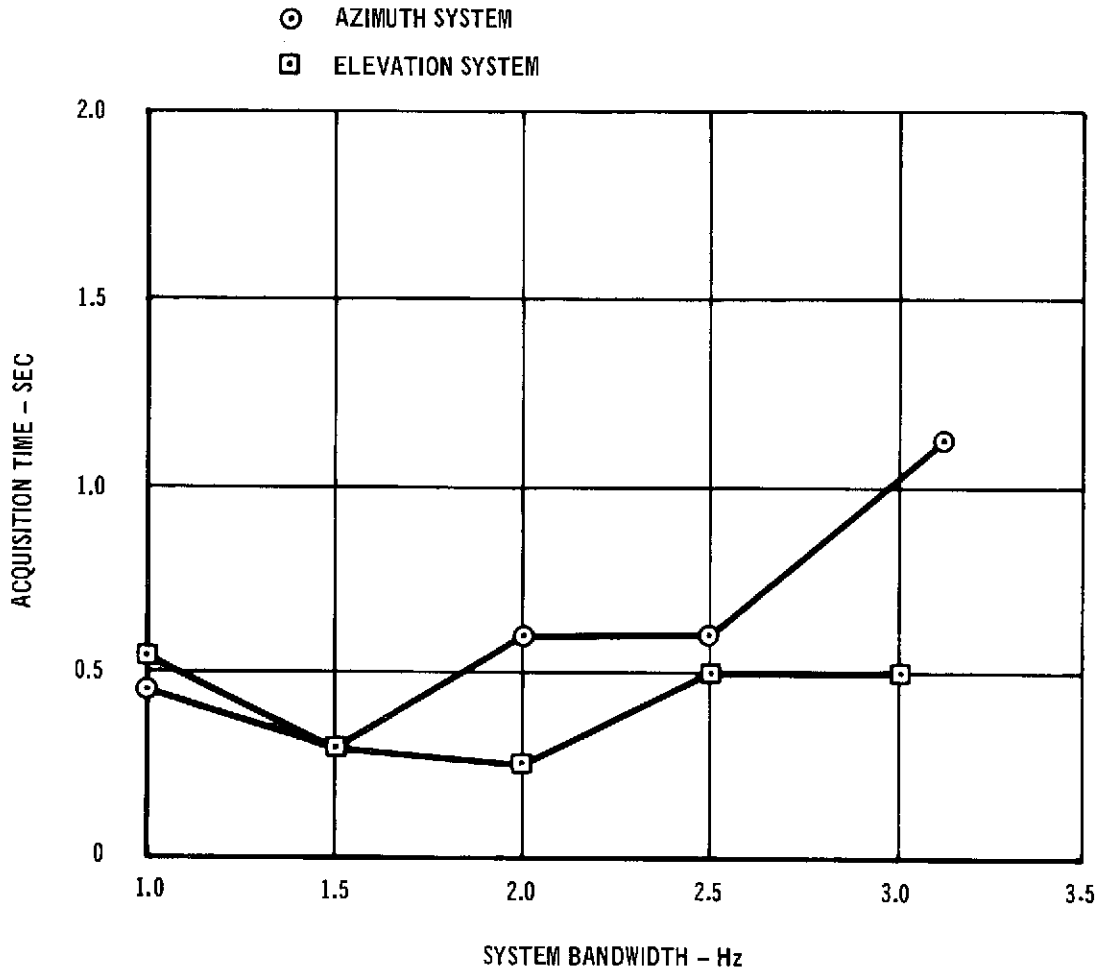


NOTE: THE BEACON SIGNAL PASSES THROUGH THE BIFURCATING MIRROR AND INTO THE TRACKING OPTICS FOR RSS POINTING ERRORS LESS THAN 2 mRAD.

Acquisition time is defined in this analysis as the time from the first switching into acquisition mode to final switching into the track mode. A simulated tracking system, with a 100 Hz bender loop bandwidth, a 3 Hz gimbal loop bandwidth, and mode switching logic are used in conjunction with the acquisition system simulation.

Figure 58 shows acquisition time as a function of system bandwidth for the azimuth and elevation systems. The input is a

FIGURE 58 ACQUISITION FROM 0.9° OFFSET



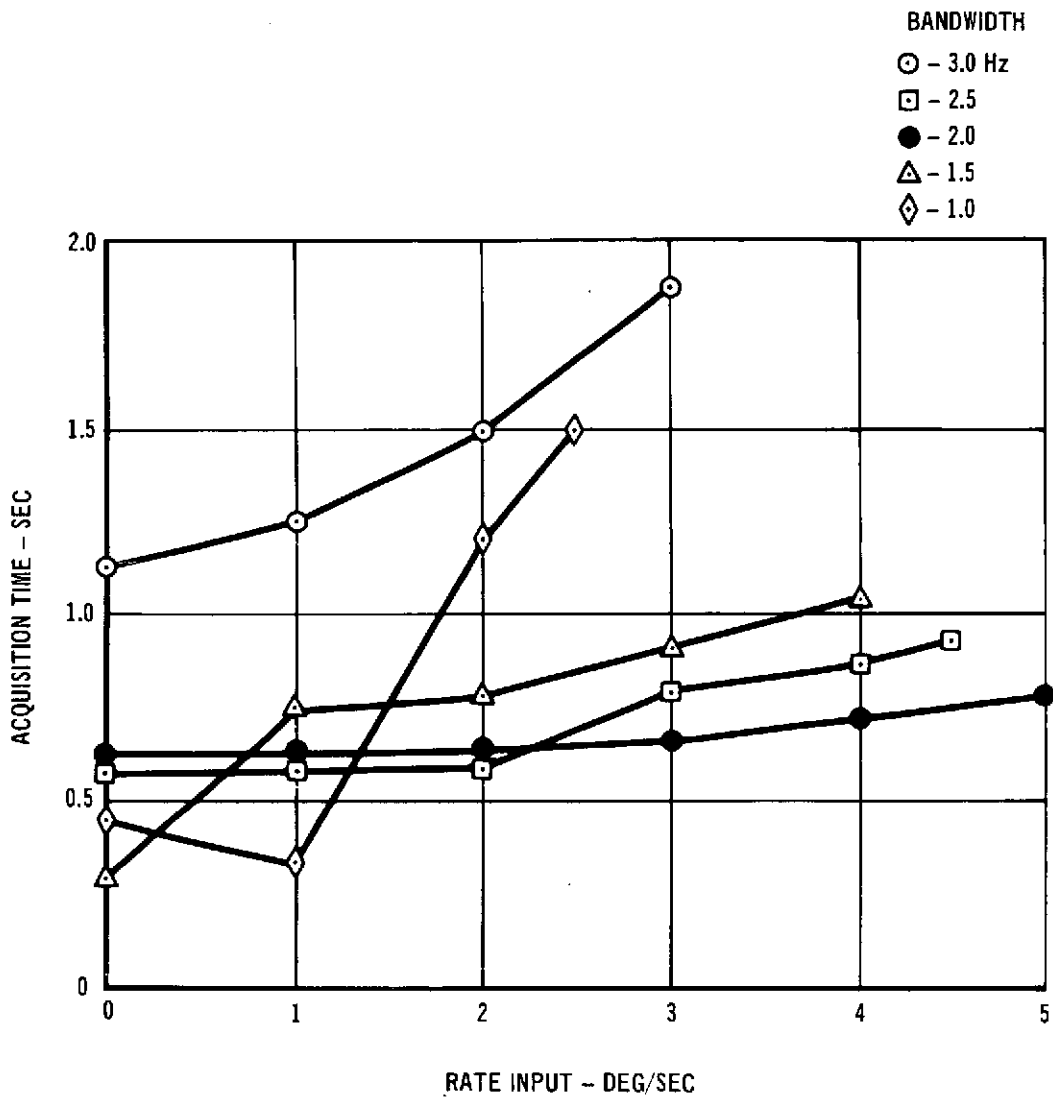
static offset of 0.9 degree. Acquisition time decreases with increasing bandwidth so long as the transition to tracking can be accomplished without overshooting the tracking detector. After the bandwidth is increased sufficiently to cause one overshoot, acquisition time is independent of bandwidth until torque limiting decreases the effective damping of the system sufficiently to result in additional crossings of the tracking detector. In this simulation the acceleration commands are limited to 0.58 rad/s^2 in azimuth and 1.0 rad/s^2 in elevation. Effects of acceleration limiting are quite noticeable in the acquisition time required for the azimuth system with a 3 Hz bandwidth.

A more detailed analysis of the azimuth system was performed with rate inputs corresponding to balloon spinning. Results of this analysis are shown in Figure 59. These data indicate that a 2 Hz bandwidth is optimum since it gives acquisition time almost independent of rate input up to 5 deg/s. No higher rates were evaluated since this gives adequate margin over the maximum expected rate of 2 deg/s. The other curves are terminated at the highest rate input with which the systems will acquire.

With the chosen 2 Hz bandwidth and a 3 deg/s input to the azimuth system, a typical acquisition to tracking time response is illustrated in Figure 60. In this example the tracking system cannot reverse the gimbal direction quickly enough during the first transition and the gimbal overshoots the tracking detector by 8 mrad. The system switches back to acquisition mode and the acquisition system returns the gimbal. After the second transition into track, the tracking system retains control. The gimbal system would have to be quite sluggish to acquire without one overshoot in response to a rate input because of saturation in the acquisition detector. Initial acceleration is in the wrong direction and the command to accelerate in the correct direction does not occur until the beam crosses boresight.

The primary dynamical input to the elevation system is expected to be pendulum motion of the balloon and gondola. This effect is evaluated with a sinusoidal input centered about boresight and starting at peak displacement. Figure 61 shows results of this evaluation. This data indicates that bandwidths from 2 Hz to 3 Hz are acceptable for acquiring in the presence of sinusoidal motion with amplitudes up to 5 degrees. From the acceptable bandwidths, 2 Hz has been chosen for this system since acquisition time is only 25 percent longer with motion present and is only half as long with no motion input.

FIGURE 59 AZIMUTH ACQUISITION SYSTEM PERFORMANCE



A typical acquisition to tracking time history is shown in Figure 62 for the elevation system in response to a 3 degree amplitude sinusoidal input. The tracking system retains control after the second transition.

The gimbal control loop used in acquisition is similar to that used in tracking except for the error signal source and loop bandwidth. This similarity minimizes switching transients and permits short delays in mode switching without causing loop stability problems since the stabilizing rate feedback from the

FIGURE 60 AZIMUTH SYSTEM TIME RESPONSE

(Bandwidth = 2 Hz; Rate Input = 3 Deg/Sec)

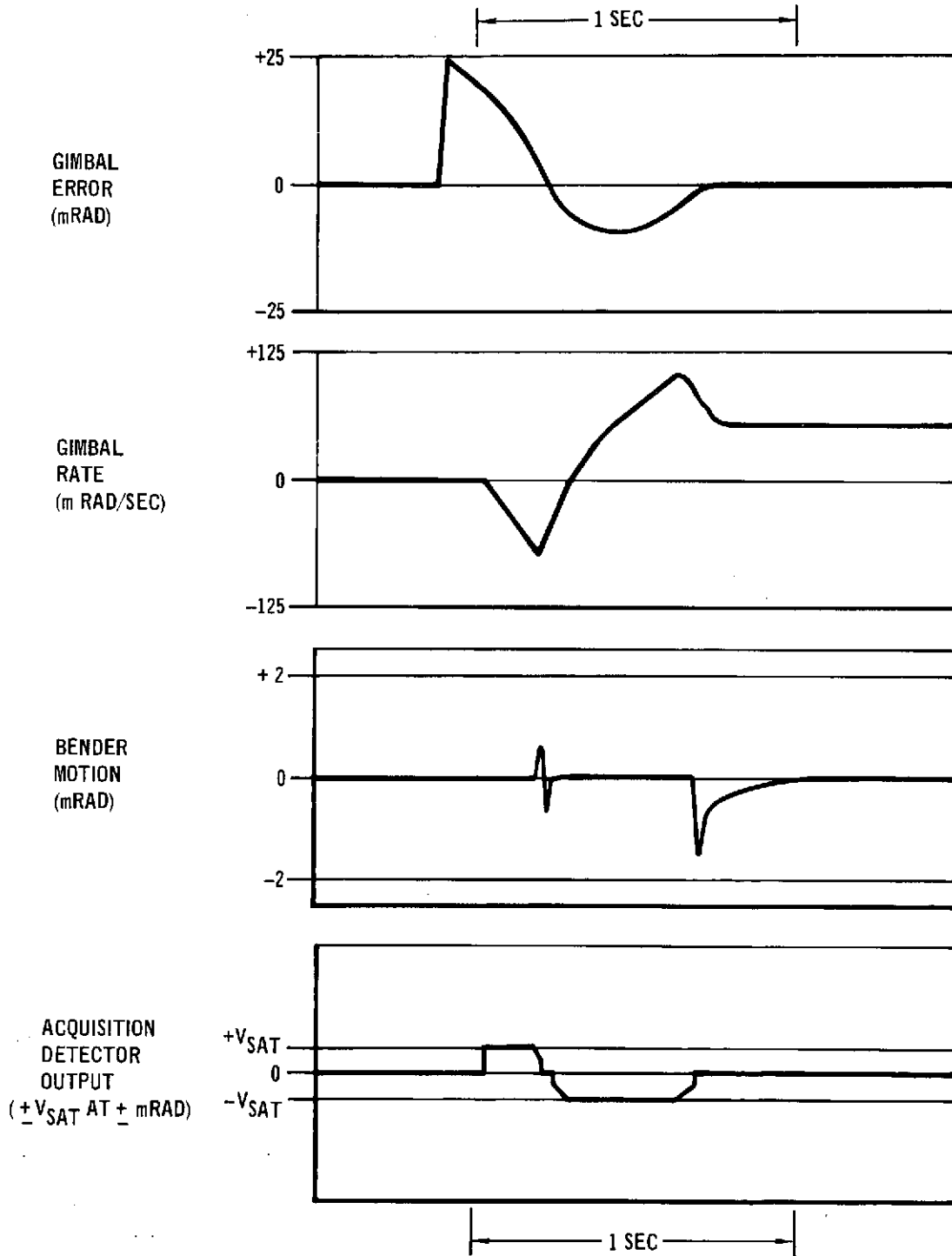
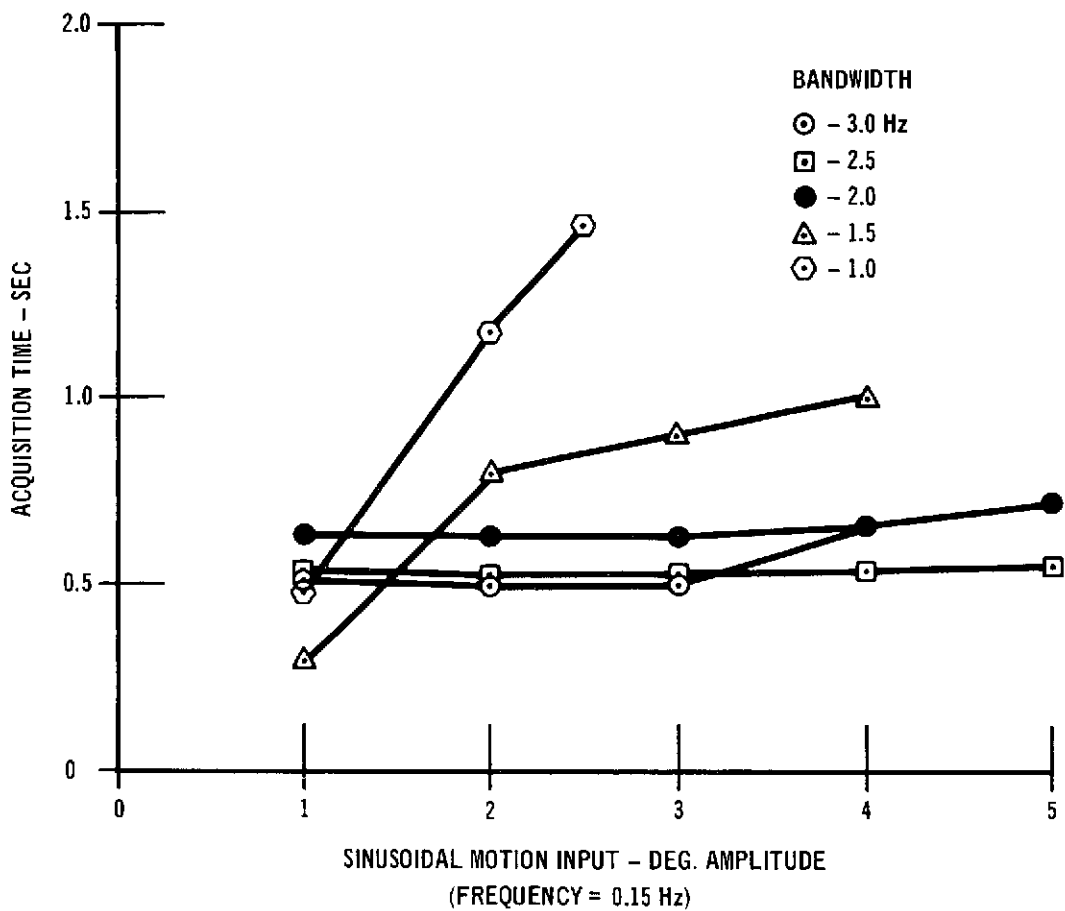


FIGURE 61 ELEVATION ACQUISITION SYSTEM PERFORMANCE

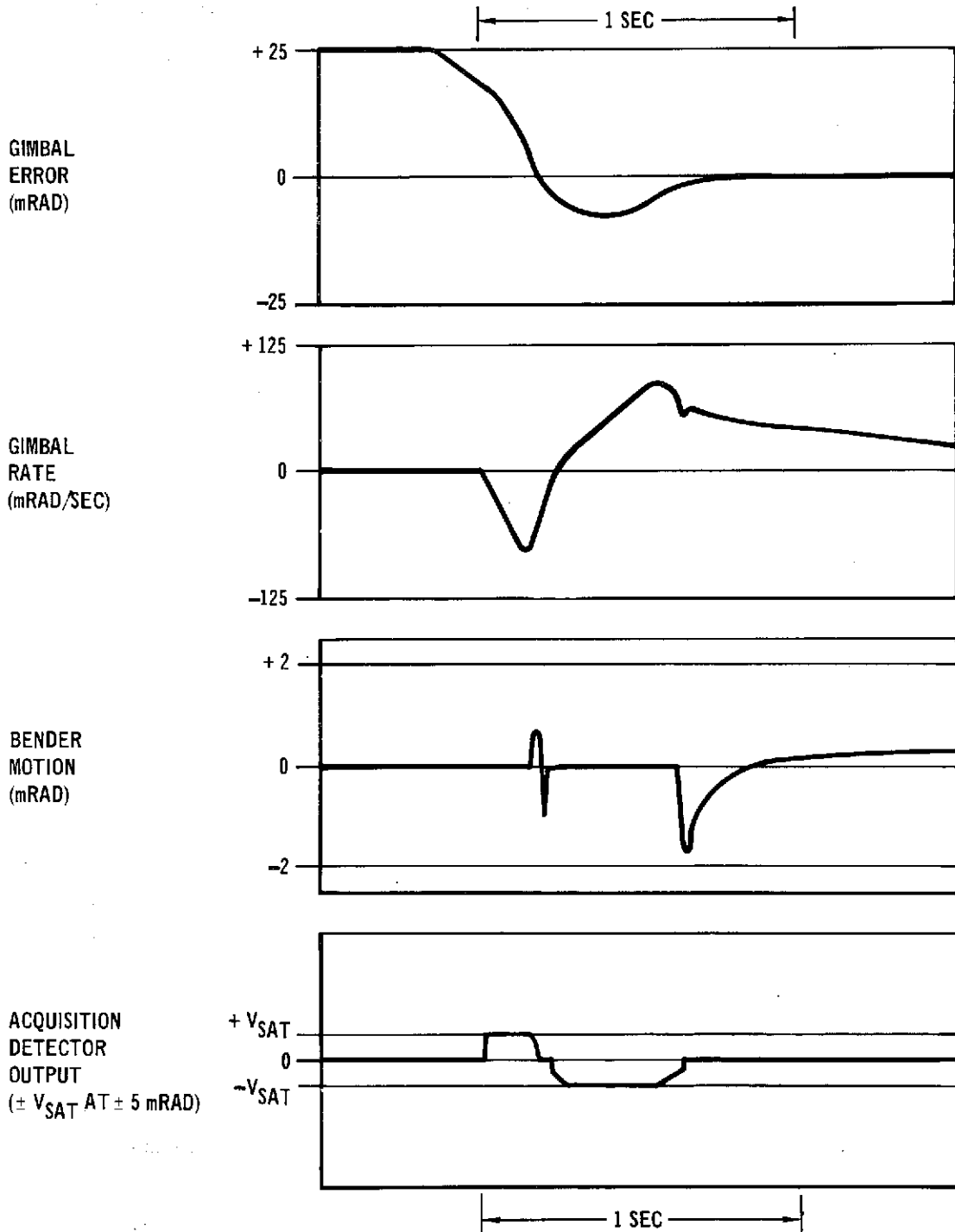


tachometer has its gain changed but is never switched out. In this simulation, the mode switching had no built-in time delays; however, a dwell time requirement could be included in the mode switching logic to eliminate the first switching transition, which causes a high frequency bender transient but otherwise has little effect on acquisition.

Tracking Mode - The function of the tracking mode is to maintain the precise pointing of the transceiver optical boresight or transmitted beam relative to the beacon beam received from the ground site. Peak pointing errors less than 2.5 μ rad are provided by the tracking control system, which utilizes a quadrant PMT detector and processing electronics to measure pointing errors about each axis in the range of ± 50 μ rad. A dual-loop

FIGURE 62 ELEVATION SYSTEM TIME RESPONSE

(Bandwidth = 2 Hz; Input = $3 \cos 0.94 t$ DEG)



control system for each axis is driven by the detector output signal. A wide-band loop which features bimorph bender mirrors as the pointing device provides the high precision. The bender mirrors can be deflected through an angle of ± 0.3 degree by their piezoelectric crystals and are located in the optical train so that the far field beam deflection capability is ± 2 mrad. The drive signal to the bender mirror is used as the control loop position error signal for the gimbal control, and the tachometer signal is used to stabilize the gimbal loop.

The tracking control system uses a dual-loop control system with bender mirrors for controlling high frequency, low amplitude disturbances and a gimbal loop to provide large amplitude but low frequency control. A functional block diagram of the system is given in Figure 63. The bender control is Type 1 and includes a lag-lead function to increase the low frequency open-loop gain. Values of the gain and break frequencies are defined by the equations:

$$K = 7 \omega_{CB}$$

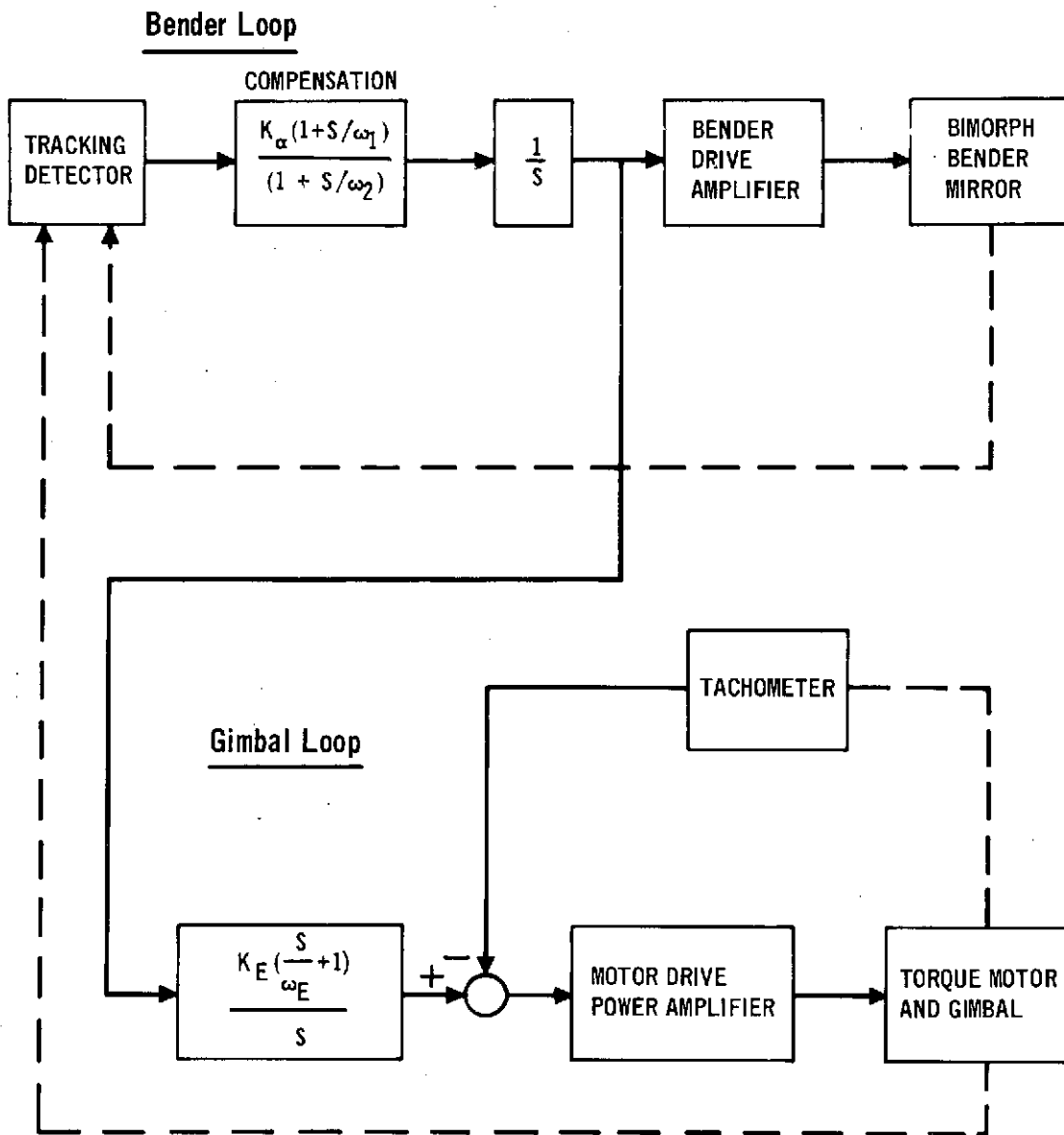
$$1 = \frac{\omega_{CB}}{3}$$

$$2 = \frac{\omega_{CB}}{21}$$

where ω_{CB} is the frequency (radians per second) at which the bender open loop gain drops below 0 dB. This loop configuration produces the gain and phase angle profiles as functions of frequency which are shown in Figure 64. Data in the figure applies for a 100 Hz ω_{CB} , a bender mirror first resonance at 1300 Hz, and a bender and driver system equivalent damping ratio of $\zeta = 0.2$. The gain margin is very generous (13 dB) as indicated in the figure. The phase margin is 72 degrees which indicates well-damped system roots. Furthermore, for control bandwidths up to 300 Hz, the phase margin is at least 40 degrees.

The gimbal control loop is also illustrated in Figure 63. This loop is Type 2 and is driven by a signal from the bender loop

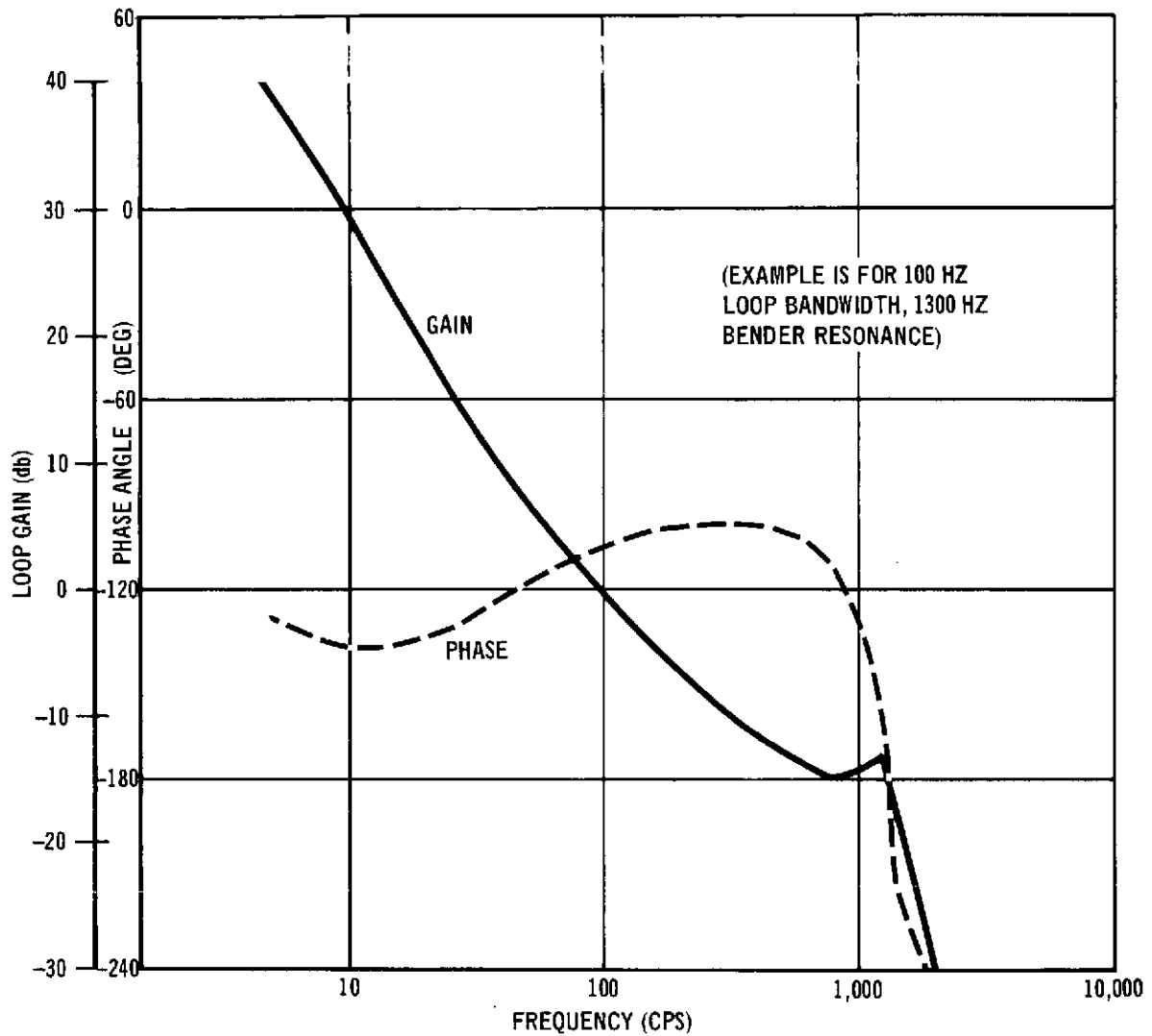
FIGURE 63 TRACKING CONTROL SYSTEM FUNCTIONAL DIAGRAM



compensation. This signal is passed through a lag-lead compensation to increase the low frequency open loop gain. The loop is stabilized with a rate feedback signal from the tachometer. The open loop transfer function for the gimbal loop is:

$$G(s) = \frac{K_E \left(\frac{s}{\omega_E} + 1 \right)}{s^2 \left[\frac{s}{\omega_R} \left(\frac{s}{\omega_M} + 1 \right) + 1 \right]}$$

FIGURE 64 BENDER MIRROR LOOP GAIN AND PHASE
TRACK MODE



where ω_E and ω_R are compensation and rate loop break frequencies and $\tau_M = \frac{1}{\omega_M}$ effective time constant of the power amplifier and motor. Values of the gains and break frequencies are determined from the equations:

$$K_E = \frac{\omega_{CG}^2}{3}$$

$$\omega_E = \frac{\omega_{CG}}{3}$$

$$\omega_R = 3\omega_{CG}$$

$$\omega_M \geq 10\omega_{CG}$$

where ω_{CG} is the gimbal loop crossover frequency (in rad/s). This gain schedule produces a phase margin of 53 degrees, or in a linear system sense the gimbal loop is underdamped and gives an overshoot of 20 percent to a step input. Since gimbal friction adds damping, the actual overshoot of the gimbal loop is less than 20 percent and the nonlinear system with friction has more damping. Figure 65 shows plots of the open loop gain and phase functions versus normalized frequency. The break frequencies are selected to give high gain at low frequency and to provide adequate stability margins. The loop maintains at least 47 degrees phase margin for gain variations up to 6 dB; ω_M is assumed to be equal to $20 \omega_{CG}$.

The key design variables to be selected to optimally configure the tracking system are (1) the gimbal and bender loop control bandwidths, (2) the tracking detector linear output range, and (3) the diameter of the bifurcating mirror (in terms of far field angle). The dynamic inputs to the control process which come with the experiment are the driving functions which must be handled by the system design. Factors which we have considered in the system design are summarized briefly in the following table:

Gondola Motion: $a \sin 0.94t$ deg, $1 \leq A \leq 5$. (0.15 Hertz)

Friction: $0.1 \leq \text{Friction} \leq 0.5$ rad/s² (Coulomb)

Noise Effects: Detector and Tachometer

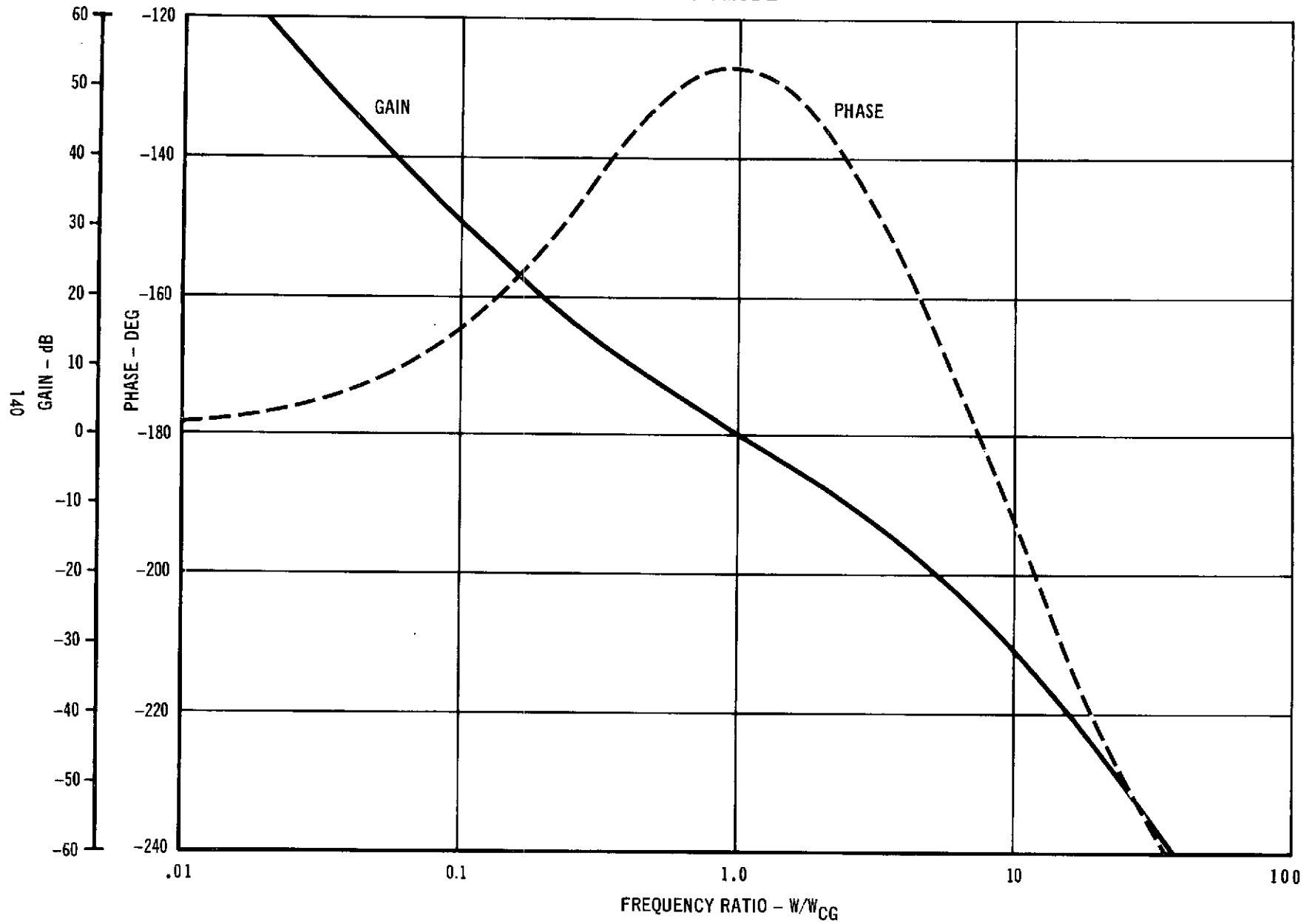
Detector Linear Range (Radius): 50 μ rad

Bifurcating Mirror Radius: 2 mrad

The tracking system was evaluated parametrically using an analog simulation.

In the tracking system, two different signals are available for stabilizing the gimbal loop. These are bender command rate and

FIGURE 65 GIMBAL LOOP GAIN AND PHASE
TRACK MODE

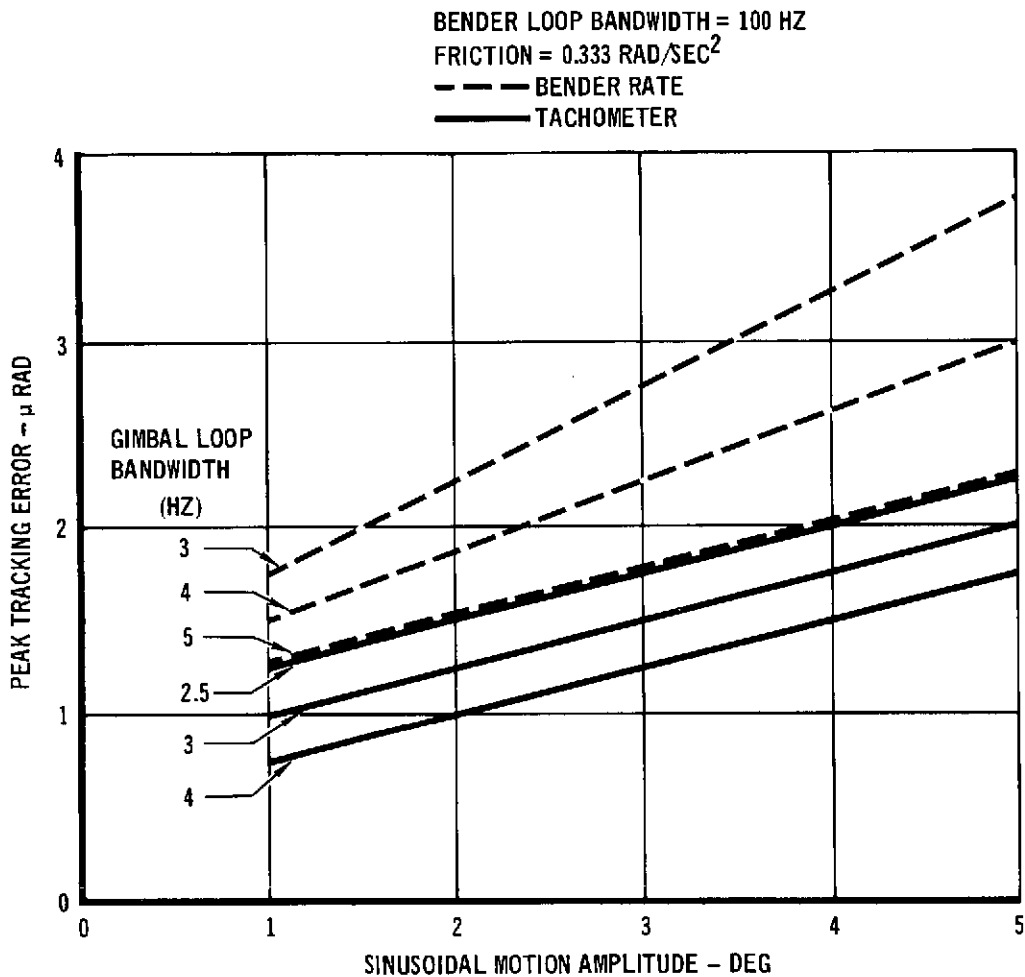


gimbal tachometer signals. An analog simulation analysis was used to obtain a performance comparison between the two methods. Since a transient tracking error occurs each time the gimbal breaks out of friction, sinusoidal motion was used as the input to the tracking system. Quantities evaluated were peak tracking error and peak bender deflection. Figure 66 shows tracking error performance for these two methods of gimbal loop stabilization. This data shows that for equivalent bandwidths the tachometer method provides a lower peak tracking error. Figure 67 shows the peak bender deflection requirements as a percentage of maximum bender deflection capability. This data indicates that for adequate tracking margin the bender rate method would require a 4 Hz bandwidth and the tachometer method would require a 3 Hz bandwidth. At these bandwidths the tracking data shows that the bender rate method produces a 50 percent higher peak tracking error. These data comparisons indicate that the tachometer method is the better choice. Figure 68 shows a typical time history of the tracking systems response to a 3 degree amplitude sinusoidal input. These time histories show that the system tracks very accurately except during the transient that occurs when the gimbal breaks friction.

Tracking analysis data presented so far has included the elevation axis nominal friction level. Figure 69 shows effects of friction variation on peak tracking error and peak bender deflection. This data indicates that both tracking error and peak bender deflection decrease with reduced friction acceleration; therefore, the azimuth tracking system will produce lower transient tracking errors than the elevation system for equivalent motion inputs.

Figure 70 shows effects of bender loop bandwidth on tracking error and bender deflection. Increased bender loop bandwidth represents increased speed of response to sharp inputs, and the result is a smaller tracking error. Bender deflection is essentially independent of bender loop bandwidth, since peak bender

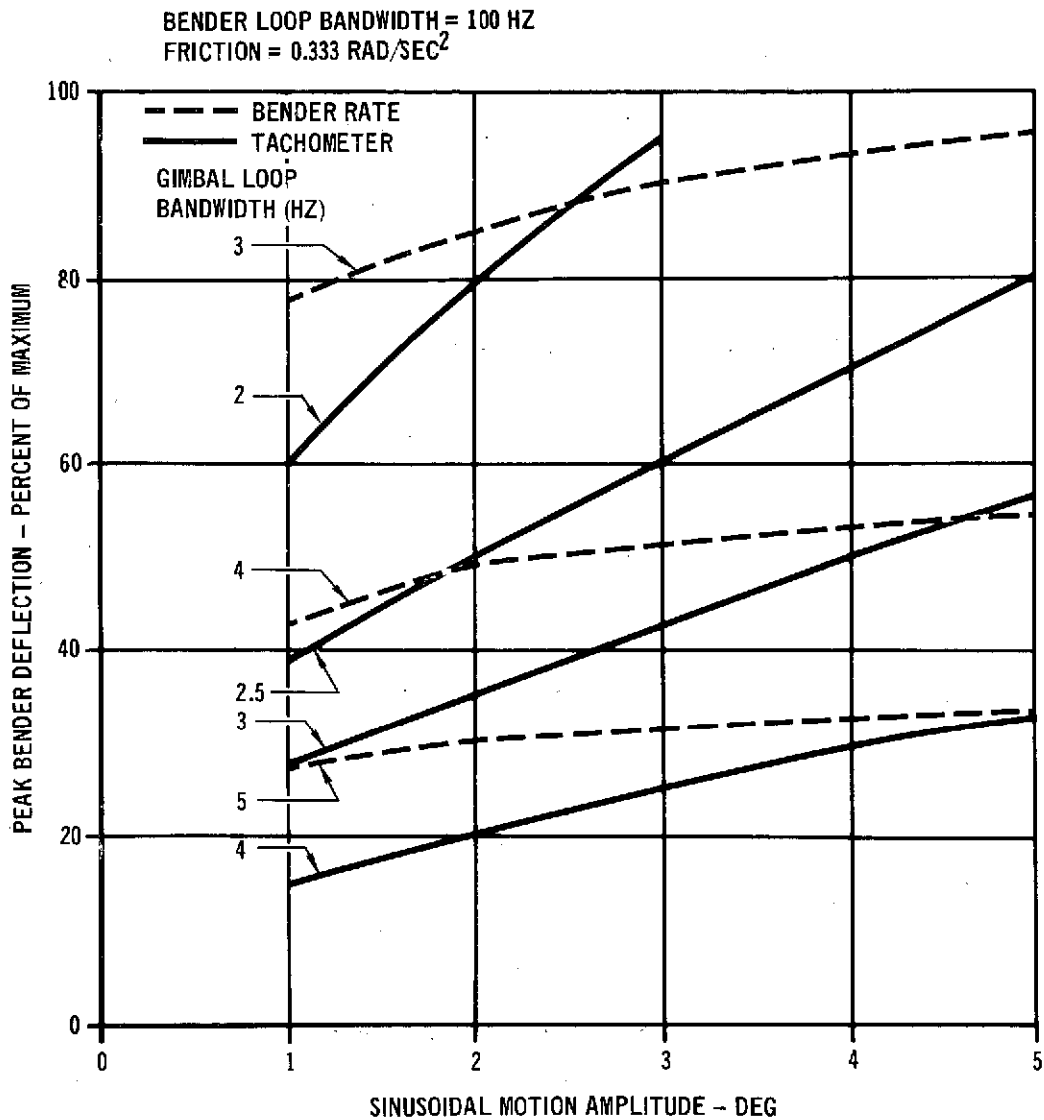
FIGURE 66 TRACKING ERROR PERFORMANCE FOR TWO
GIMBAL LOOP STABILIZATION METHODS



deflection is primarily dependent upon the gimbal loop speed of response.

Figure 71 shows the effects of bender loop bandwidth on tracking error sensitivities to detector noise and tachometer noise. The detector noise curve deviates from a straight line at the high frequency end, which indicates a slight decrease in loop damping as the bandwidth is increased. The noise level was kept well within the linear range of the detector. The tachometer curve will shift up or down approximately linearly with gimbal loop

FIGURE 67 BENDER DEFLECTION REQUIREMENT FOR TWO
GIMBAL LOOP STABILIZATION METHODS



bandwidth. The curve shown is for a 3 Hz gimbal loop bandwidth and was evaluated with a small rate input to maximize tachometer noise effects on gimbal motions. To obtain total noise effects on tracking error requires determination of noise level for each source. If we assume detector noise equivalent to 1 μ rad rms and tachometer noise equivalent to 2 mrad/sec rms and then RSS their effects for a 100 Hz bender loop bandwidth, the resultant tracking error is .39 μ rad rms.

FIGURE 68 TRACKING SYSTEM TIME RESPONSE TO SINUSOIDAL MOTION

Bender Loop Bandwidth = 100 Hz; Friction = 0.333 Rad/Sec²
Gimbal Loop Bandwidth = 3 Hz; Input = 3 SIN 0.94 t Deg

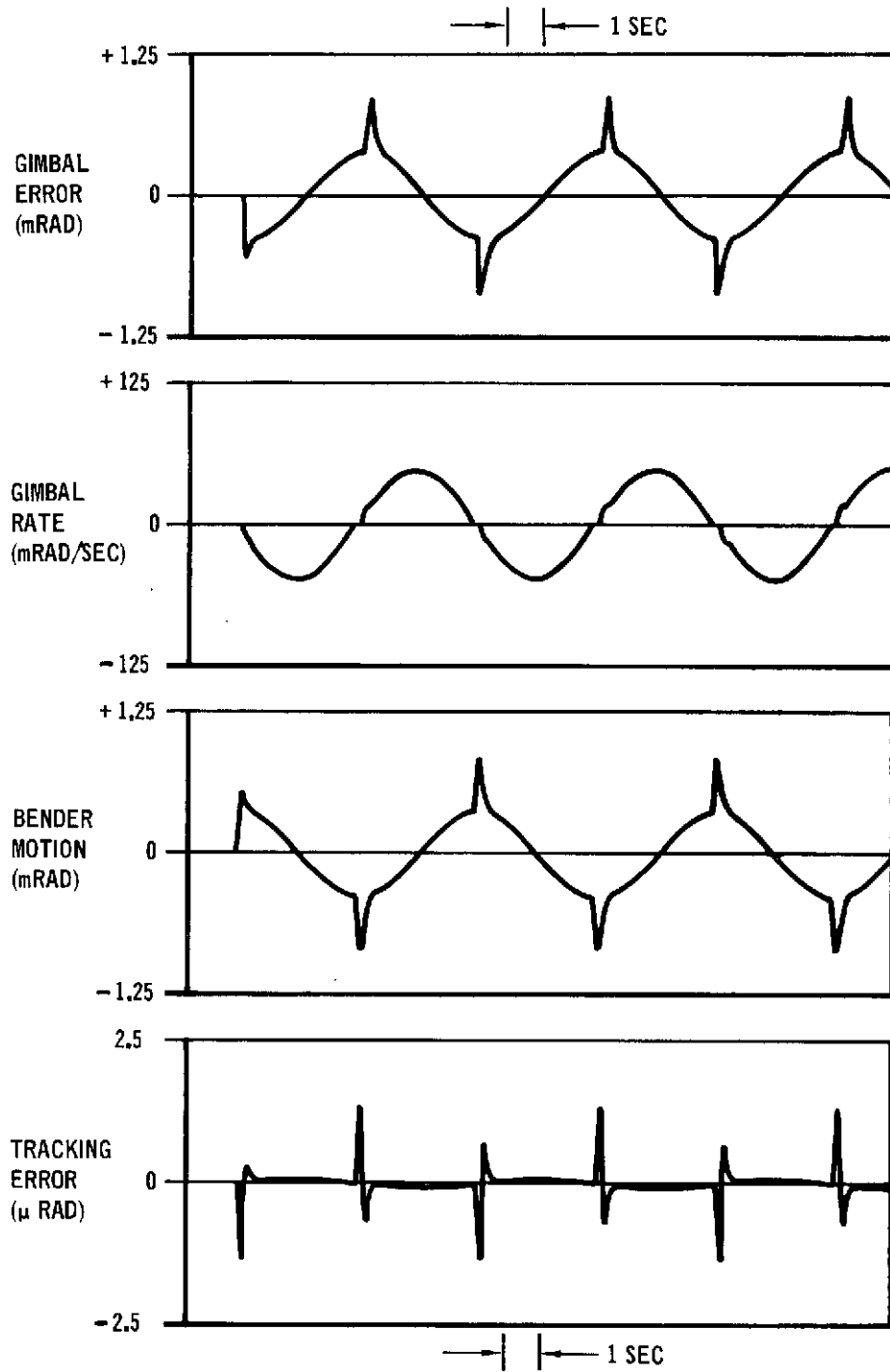
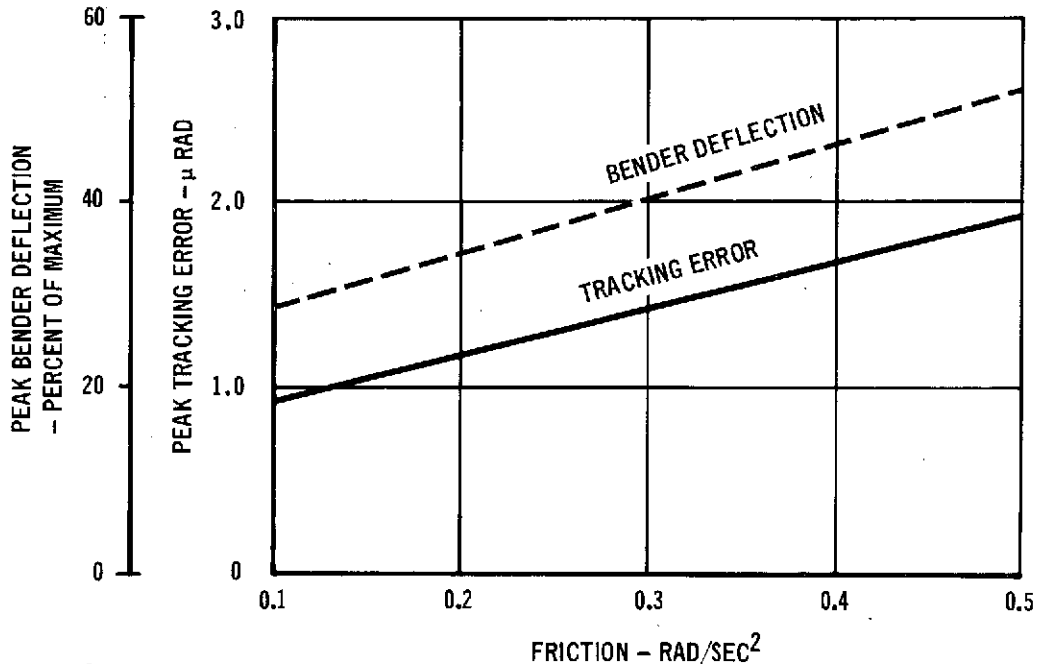


FIGURE 69 EFFECTS OF FRICTION ON TRACKING ERROR AND BENDER DEFLECTION

Bender Loop Bandwidth = 100 Hz; Gimbal Loop Bandwidth = 3 Hz
 Motion Input = $3 \text{ SIN } 0.94 t \text{ Deg}$

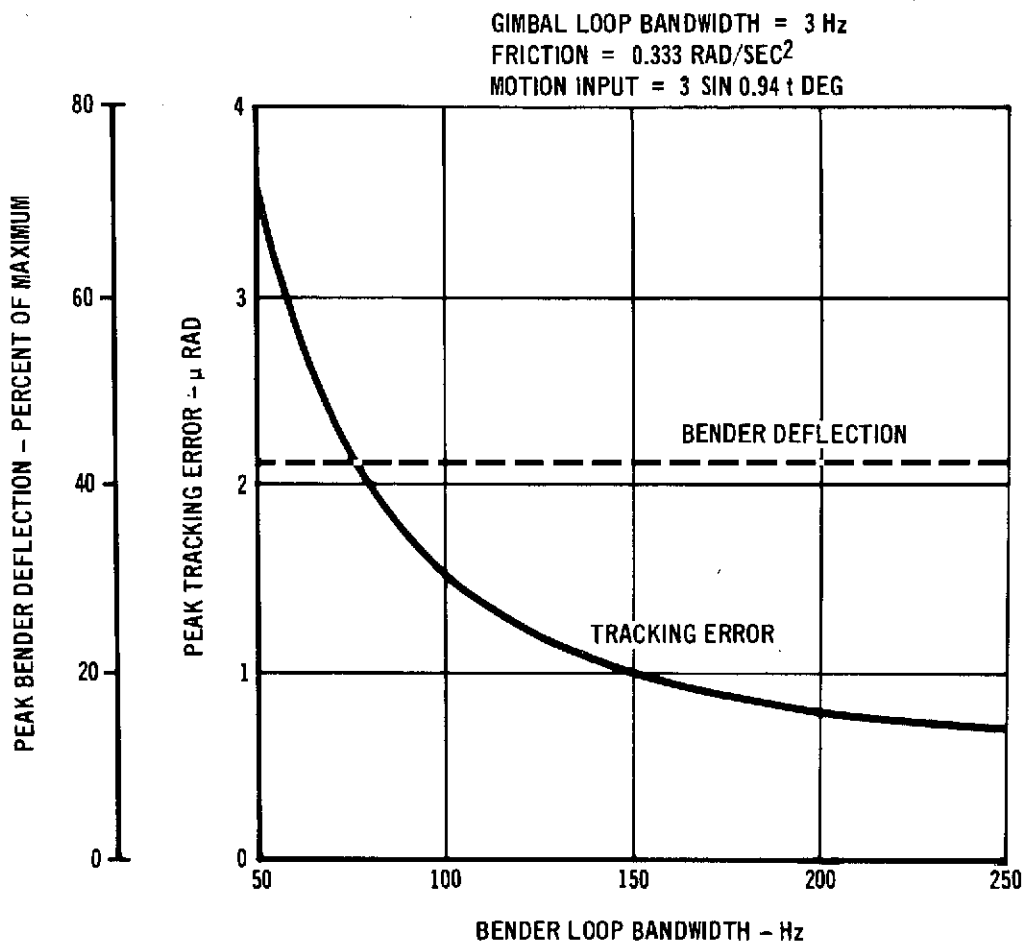


2.4.3 Atmospheric Propagation Experiment Hardware Design. To perform the measurements suggested in Section 2.3.5 above, we have investigated a detector array technique (among others). With this approach, the spatial distribution of received optical power is sampled with an array of detectors at the balloon.

The detector array measurement technique was abandoned because of insufficient RF telemetry capacity and battery power, increased elevation axis package weight, and the necessity of balloon package redesign. The single detector technique was also abandoned because of dynamic range limitations of the detector output caused by the expected daylight background.

Hence, we propose to use the following measurement techniques at the ground station and on the balloon package to measure received

FIGURE 70 EFFECTS OF BENDER LOOP BANDWIDTH ON TRACKING ERROR AND BENDER DEFLECTION



beam variables. At the ground station, an

- I Aperture Averaging Detector
- II Spatial Correlation Detector, and
- III Stellar Image Monitor

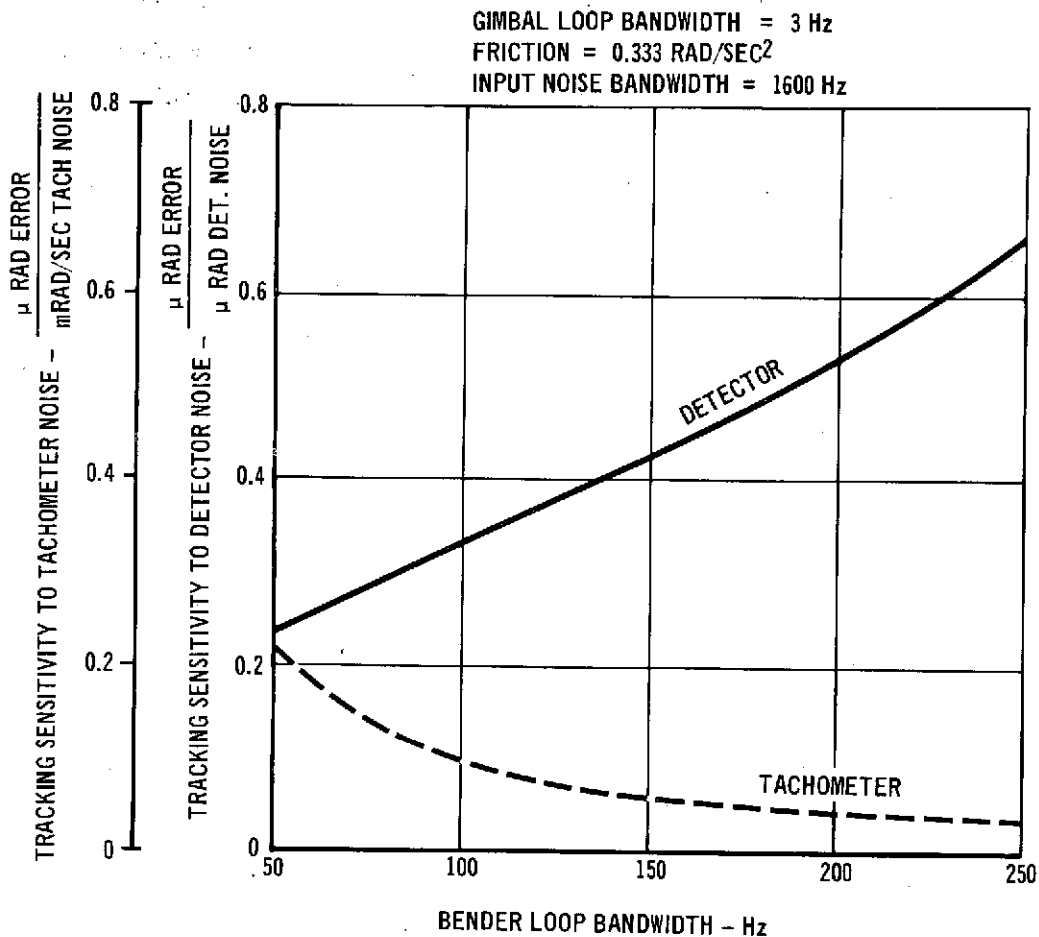
and at the balloon a

- IV Dual Detector

measurement technique.

Optical Detector Signal Processing - Several researchers have noted large amplitude variations in received intensity caused by turbulence. The problems involved in implementing accurate statistical measurements of the receiver optical power fluctuations.

FIGURE 71 EFFECTS OF BENDER LOOP BANDWIDTH ON TRACKING ERROR SENSITIVITIES TO DETECTOR NOISE AND TACHOMETER NOISE



are:

1. Detector dynamic range limitations.
2. Post-detection signal processing accuracy and dynamic range limitations.

We investigated the signal processing techniques available to discover how to make the best use of the optical detector's dynamic range.

Detector saturation will limit or clip the output signal for high amplitude fluctuations. Assuming for purposes of analysis that the instantaneous received optical power is log normally distributed, Mevers et al⁸ have shown the effect of optical detector

dynamic range limitations on the measured log amplitude variance, $C_\ell(0)$. These results are shown in Figure 72. There we observe a dynamic range, R , of ~ 60 dB is required to directly measure a log amplitude variance $C_\ell(0) \lesssim 0.5$ and $R \sim 75$ dB is required for a $C_\ell(0) \sim 0.7$. The dynamic range in this case is defined as the intensity excursions about the mean received optical power.

Mevers, Keister, and Freid point out that measurement of the accessible portion of the probability distribution, $p(S)$, is the correct approach to use when dynamic range limitations effect the measurement of $C_\ell(0)$. However, we have adopted the philosophy of not making a priori assumptions about the statistical distribution of the variable of interest.

We consider the dynamic range available at a photomultiplier tube output to make an estimate of how large a log amplitude variance could be measured. The absolute dynamic range, R_{abs} , at the output of a photomultiplier tube (PMT) is given by

$$R_{abs} = i_{max}/i_{min}$$

where i_{max} and i_{min} , respectively, denote the maximum (saturation) and the minimum output current. The minimum output current i_{min} corresponds to the output of the PMT when illuminated only by background light. In addition, if the PMT output is connected to a current amplifier, the minimum current at the input to the amplifier is

$$i_{min} = i_{BG} + i_{DK} + i_{AMP}$$

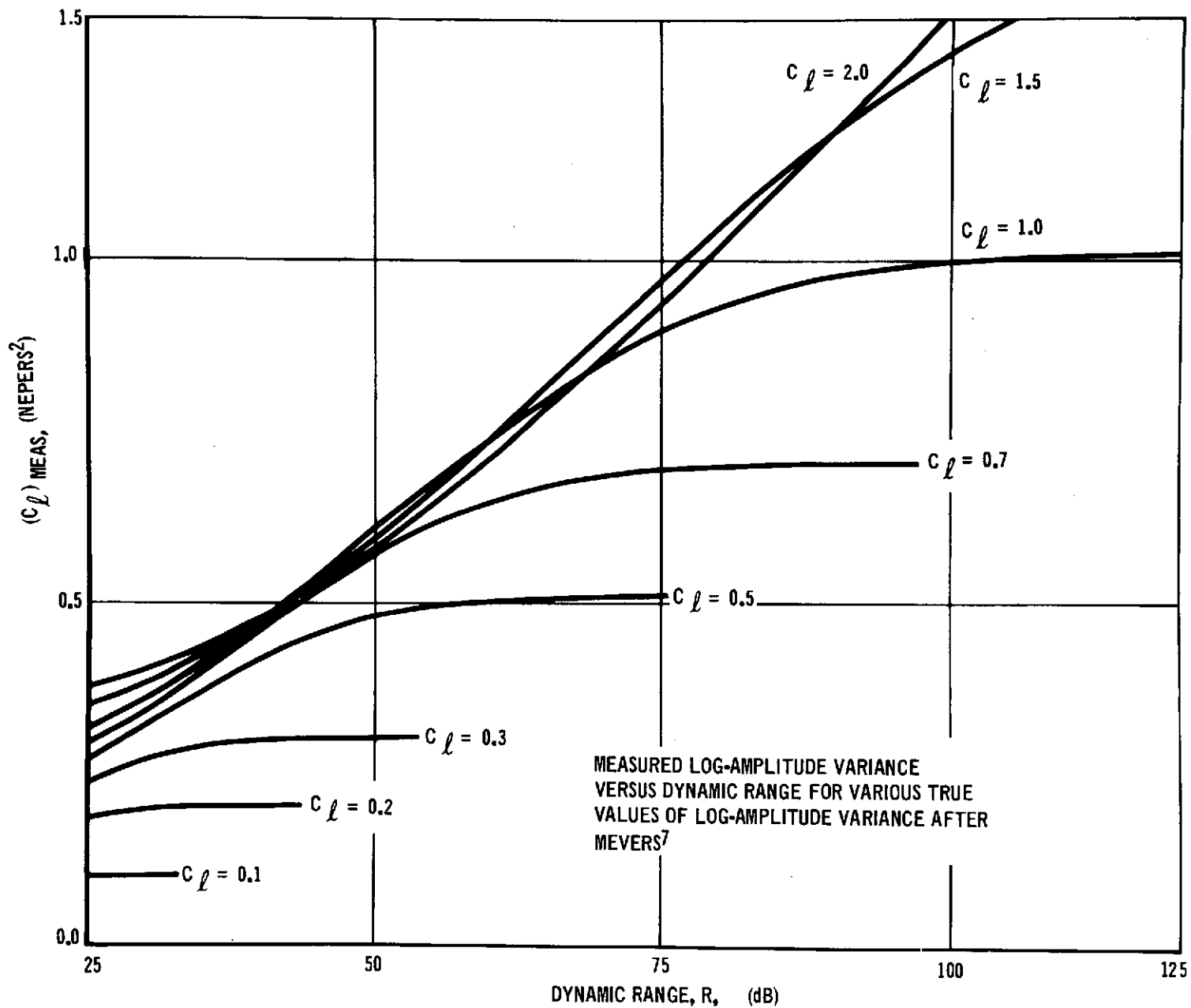
for i_{BG} = the average current output due to background light

i_{DK} = the PMT dark current

i_{AMP} = input bias current of the current amplifier

To make the best use of the available dynamic range, we would also like to adjust the mean received signal power to a level corresponding to half the dynamic range measured in decibels.

FIGURE 72 MEASURED LOG-AMPLITUDE VARIANCE VERSUS DYNAMIC RANGE FOR VARIOUS TRUE VALUES OF LOG-AMPLITUDE VARIANCE AFTER MEVERS⁷



Hence, one can easily show that to make optimum use of the PMT's dynamic range capability, the average signal current should be adjusted to

$$i_s \approx (i_{\max}/i_{\min})^{1/2},$$

where $i_s = \alpha S_o$ is the PMT current output due to the laser light alone, S_o is the mean received optical power, and α is the PMT anode radiant sensitivity (amp/watt) at the wavelength of interest. This relationship results from the definition used to evaluate the results shown in Figure 72. It also implies that optical attenuation via neutral density filters is required to set the received mean power (and, hence, the average signal current) to the optimum value.

We have performed a preliminary analysis of the dynamic range attainable by using a selected PMT and current amplifier. A RCA 8644 PMT with an S-20 photocathode and maximum average current of 0.5 ma. was chosen for this analysis. It was found that the absolute dynamic range at the balloon-borne PMT output (or current amplifier output) is $R_{\text{abs}} \text{ (dB)} \approx 53.6 \text{ dB}$ where the detector optical system had the following specifications

Operating wavelength = 0.53 μm
 Daylight background irradiance = $1.7 \times 10^{-2} \text{ watts/m}^2/\text{\AA}/\text{sr}$
 Optical filter bandwidth = 30 \AA
 Neutral density filter attenuation = $7 \cdot 10^{-4}$
 Field of view = 5 mrad
 Effective collection aperture diameter = 1 in.

For night time experiments, the PMT dark current and current amplifier are the limiting factors. The background radiance is negligible. In this case, $R_{\text{abs}} \text{ (dB)} \approx 74 \text{ dB}$ should be attainable. We see from Figure 72 that a dynamic range of $\approx 75 \text{ dB}$ is required to measure log amplitude fluctuations with a variance, $C_{\lambda}(0) \approx 0.7$.

This dynamic range is available for night time experiments.

For daylight experiments, we have determined, $R_{abs} \text{ (dB)} \approx 73.4 \text{ dB}$ can be obtained for a second detector which observes a second uplink laser beam (the atmospheric probe beam). An Ion Argon laser capable of a 2 watt output at $0.514 \text{ } \mu\text{m}$ is available for this purpose. Hence, for daylight measurements, the contribution of the background radiance can be decreased with increased optical attenuation by a factor of 10 or 20 because of the increased laser power available. The variance of fluctuations in received optical power is therefore directly measurable over the required dynamic range during daylight experiments with use of a $0.514 \text{ } \mu\text{m}$ detector package on the balloon and the 1 - 2 watt atmospheric probe beam. A full angle beam width of $100 \text{ } \mu\text{rad}$ is required for these daylight measurements with the atmospheric probe beam. Use of this probe beam reduces the uplink communication link margin to 5 dB. This should not degrade the experiment.

Further analysis shows that for optimum use of the detector's available dynamic range, the optical attenuation of the atmospheric detector package should be adjusted so that the mean PMT anode signal current is $i_s \approx 1 \mu \text{ amp}$.

The post detection signal processing options include directing the current amplifier output either

- (1) directly to the S-band telemetry VCO,
- (2) to a logarithmic amplifier then to the VCO, or
- (3) A/D converted and telemetered to ground via the S-band telemetry link.

Further analysis and hardware evaluation will be necessary before a final choice is made between these options. However, our preliminary choice is to log process the output of the current amplifier and telemeter the signal to ground via the S-band link.

Functional Description of Experimental Hardware - Two atmospheric detector packages, used to measure the fluctuations and mean received optical power, are located in the balloon transceiver package. Each package contains the electronic components illustrated in Figure 73. One measures the turbulence induced optical power fluctuations due to the 0.53 μm uplink beam and the other fluctuations of the 0.514 μm atmospheric probe beam. Each environmentally controlled detector package has a 30 Å optical bandwidth, a 5 mrad field of view, and a 1-inch effective collection aperture diameter. The light collection aperture is to be kept free of frost with evacuated windows and the PMT and associated electronics shown in Figure 73 is housed in a pressurized container filled with dry nitrogen gas.

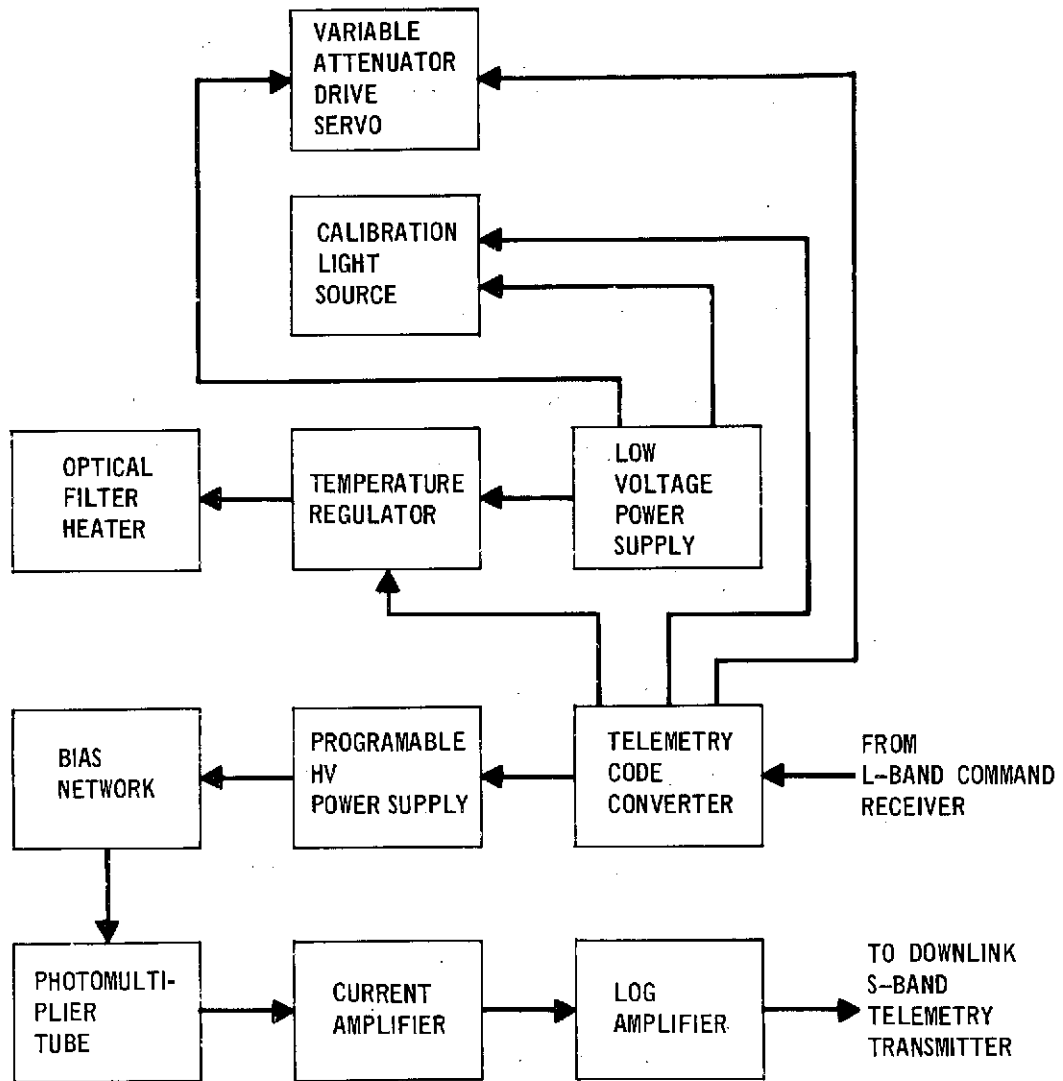
The output of the PMT will be input to a transresistance amplifier whose output is input to a log amplifier for transmission downlink via the S-band telemetry link.

A comparable signal processing system is utilized to handle the optical detector outputs at the ground station.

The ground station also includes the aperture averaging and spatial correlation experiment and Stellar Image Monitor. The Stellar Image Monitor has been described in detail by Mevers et al⁸ and Bufton¹² and is not discussed further here.

The aperture averaging experiment is implemented by positioning a 1.06 μm optical detector package in the optical path behind the telescope primary. A servo driven adjustable iris positioned before this detector is adjusted to limit the effective collection aperture size observed. A variable optical attenuator is also required to adjust the mean power level incident on the detector as the iris size is changed. The iris is the aperture stop for this detector.

FIGURE 73 BLOCK DIAGRAM OF BALLOON ATMOSPHERIC DETECTOR PACKAGE ELECTRONICS



The apparatus for the spatial correlation experiment consists of two 1.06 μm optical detector packages mounted outside of the primary collector telescope tube. One of these detectors is movable and the spatial separation between these detectors is adjusted through calibrated lengths. As the spatial separation between these two point detectors is varied, their output will be recorded on magnetic tape and also correlated with one another to obtain the spatial correlation length of the received power fluctuations.

During the experiment, the state of the atmosphere is measured with weather balloons and balloon borne thermosondes. Several negative bouyancy balloons (or parachutes) with attached thermosondes are carried aloft with the main balloon package. They are released during the communication experiments with a telemetry command to measure the turbulence profile on descent. One thermosonde is also supported on a 300 foot cable attached to the balloon package to monitor the turbulence on ascent and descent.

Several weather balloons are also flown during each experiment to measure gross weather conditions.

The qualitative dependence of received optical power fluctuations and mean received power on atmospheric probe beam transmit characteristics is also measured. A variable zoom lens arrangement is utilized to increase the atmospheric probe beam feed beam diameter while maintaining a constant angular beam width. Additional optics also permit the atmospheric probe beam to be collimated or focused. Variation of the atmospheric probe beam transmit characteristics allows a test of reduction in scintillation and increase in beam spread as a function of beam characteristics at the transmitter. A direct comparison of received power fluctuations will be made with the 0.53 μm detector output, which observes the fixed beam width uplink communications beam.

The theoretical speculation about these effects warrant at least a qualitative investigation. See Appendices E and H.

Data Handling Techniques - During the balloon experiment, the analog signals from the five atmospheric detectors are monitored with real time display and analysis instrumentation and simultaneously recorded on magnetic tape. The selected output from any one detector are monitored on either an oscilloscope and a calibrated long time average voltmeter and/or

analyzed with a real time correlator/probability density analyzer. Real time spectral analysis is also performed on any desired signal and recorded photographically. The analog signals recorded on the five magnetic tape data channels are periodically commutated with a reference voltage to calibrate each channel. The data sets recorded on magnetic tape is identified with a voice channel on the analog recorded. The data stored on magnetic tape is processed between each flight and also saved for later digital computer analysis.

Data Analysis - The frequency spectra of all time varying signals are measured real time. A statistical analysis of all the data recorded on magnetic tape is performed. This includes a probability density and correlation analysis. The analog data recorded on magnetic tape is A/D converted for this analysis.

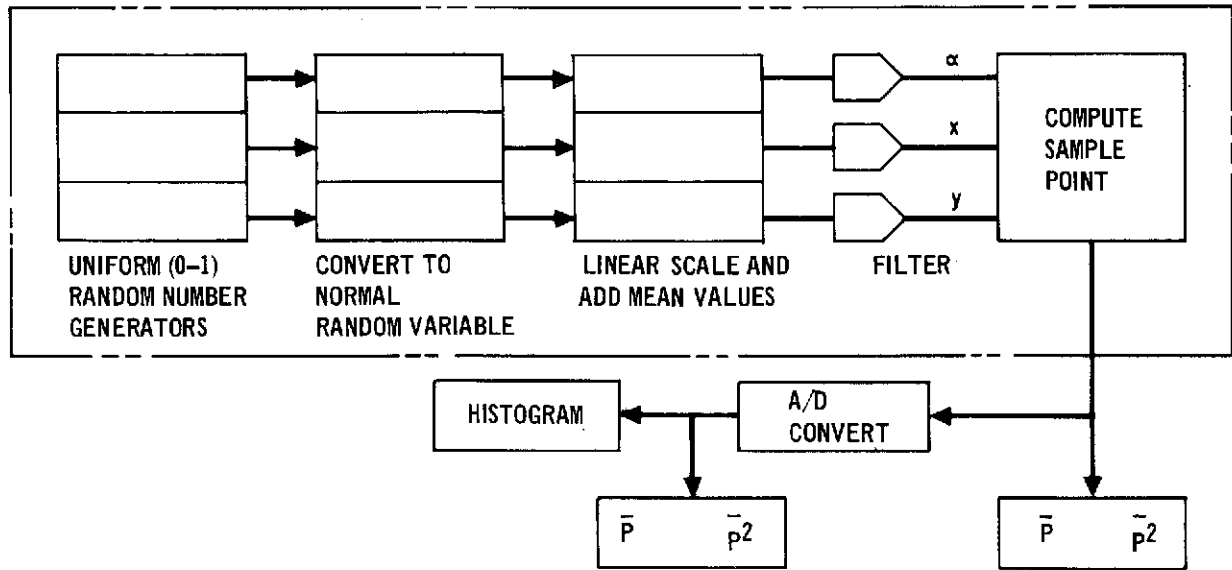
In addition to a probability density analysis, the moments of the digitized data are computed and analyzed.

In order to test the data analysis, we have simulated the random signal output expected from the atmospheric detectors. The fluctuations in received optical power were assumed to be well approximated by the probability density of instantaneous received optical power, $p(S)$, discussed in Section 2.3.3 and Appendix F .

A digital computer program was developed to perform the operations illustrated in Figure 74 . Typical results of the simulation are illustrated in Figures 75, 76 and 77.

A suitable algorithm will be developed to curve fit the assumed theoretical distribution to the measured probability densities and estimate the confidence of the measurements.

FIGURE 74 LINK SIMULATOR



$$p = \ln(P) = \ln(P_0) + \alpha + 2(x^2 + y^2)/R^2$$

WHERE α , x & y ARE NORMAL RANDOM VARIABLES
AND P_0 REPRESENTS MEAN RECEIVED
OPTICAL POWER

Functional Description of Data Acquisition - After the balloon reaches float altitude and before acquisition, the atmospheric detectors are activated to measure background light level. Data recording will also begin. A calibrate command is then transmitted to the balloon to check atmospheric detector, preamp, and A/D converter gain. This command is transmitted periodically during the course of the experiment.

The balloon borne atmospheric effects detector package will continue to operate until acquisition. Then an uplink command is transmitted to adjust the variable attenuation filters for optimum average atmospheric detector output. Then one of the negative buoyancy thermosonde balloons to measure the vertical profile of turbulence is released via an uplink telemetry command. The other three thermosonde balloons are released at time intervals equal to 1/4 of the expected total balloon flight time.

FIGURE 75 CUMULATIVE PROBABILITY DISTRIBUTION OF RECEIVED OPTICAL POWER CONSIDERING SCINTILLATION AND BEAM WANDER

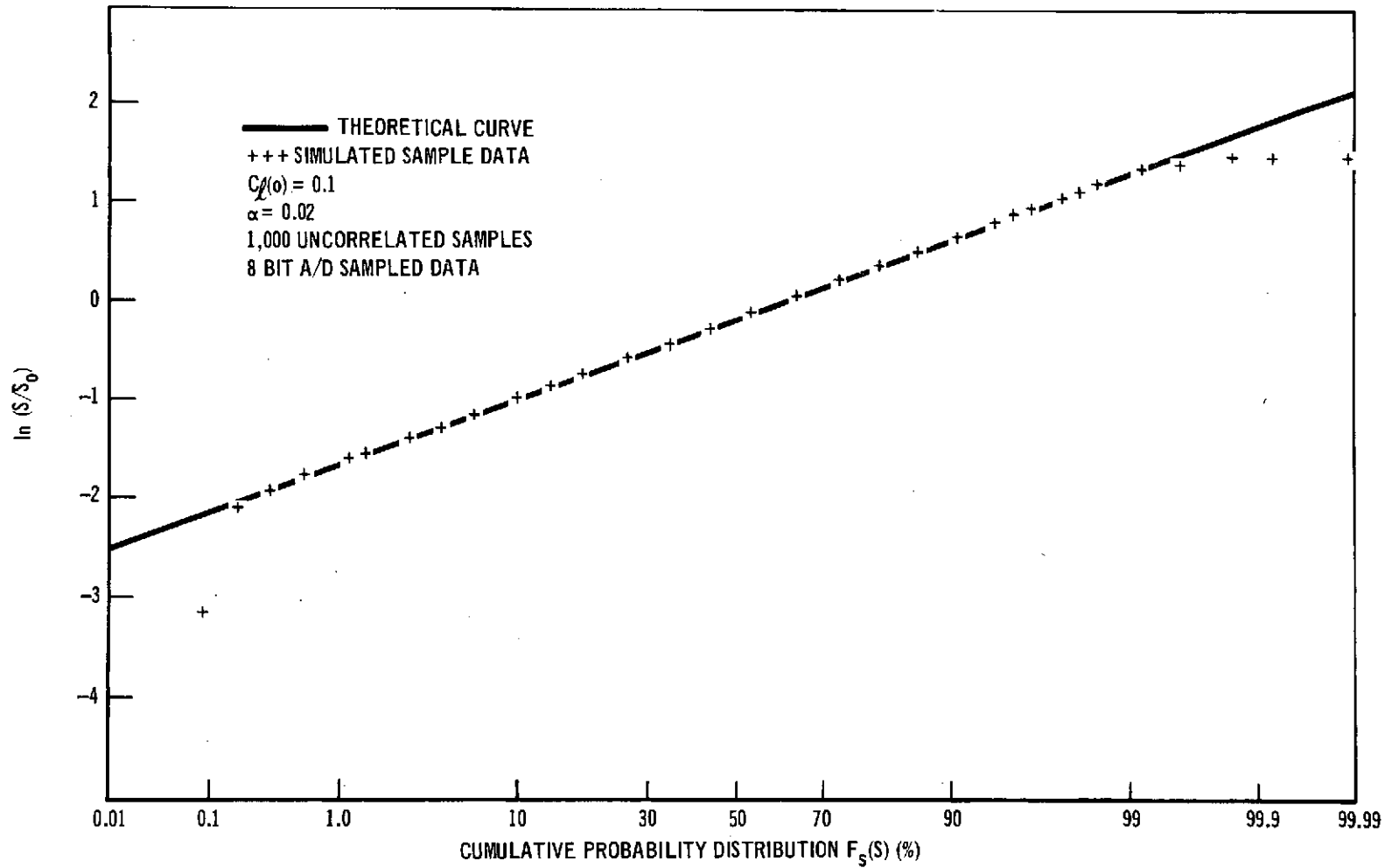


FIGURE 76 CUMULATIVE PROBABILITY DISTRIBUTION OF RECEIVED OPTICAL POWER CONSIDERING SCINTILLATION AND BEAM WANDER

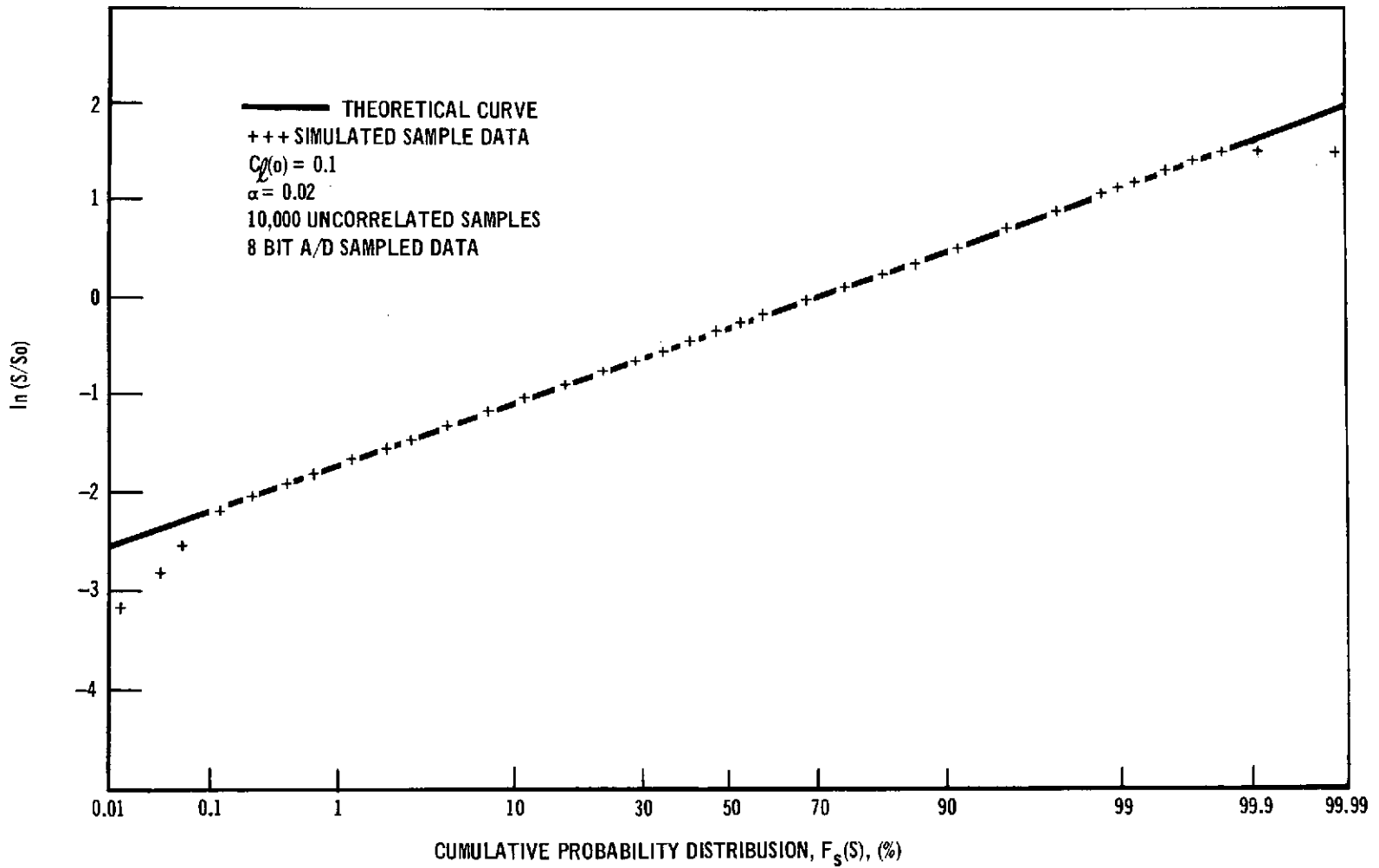
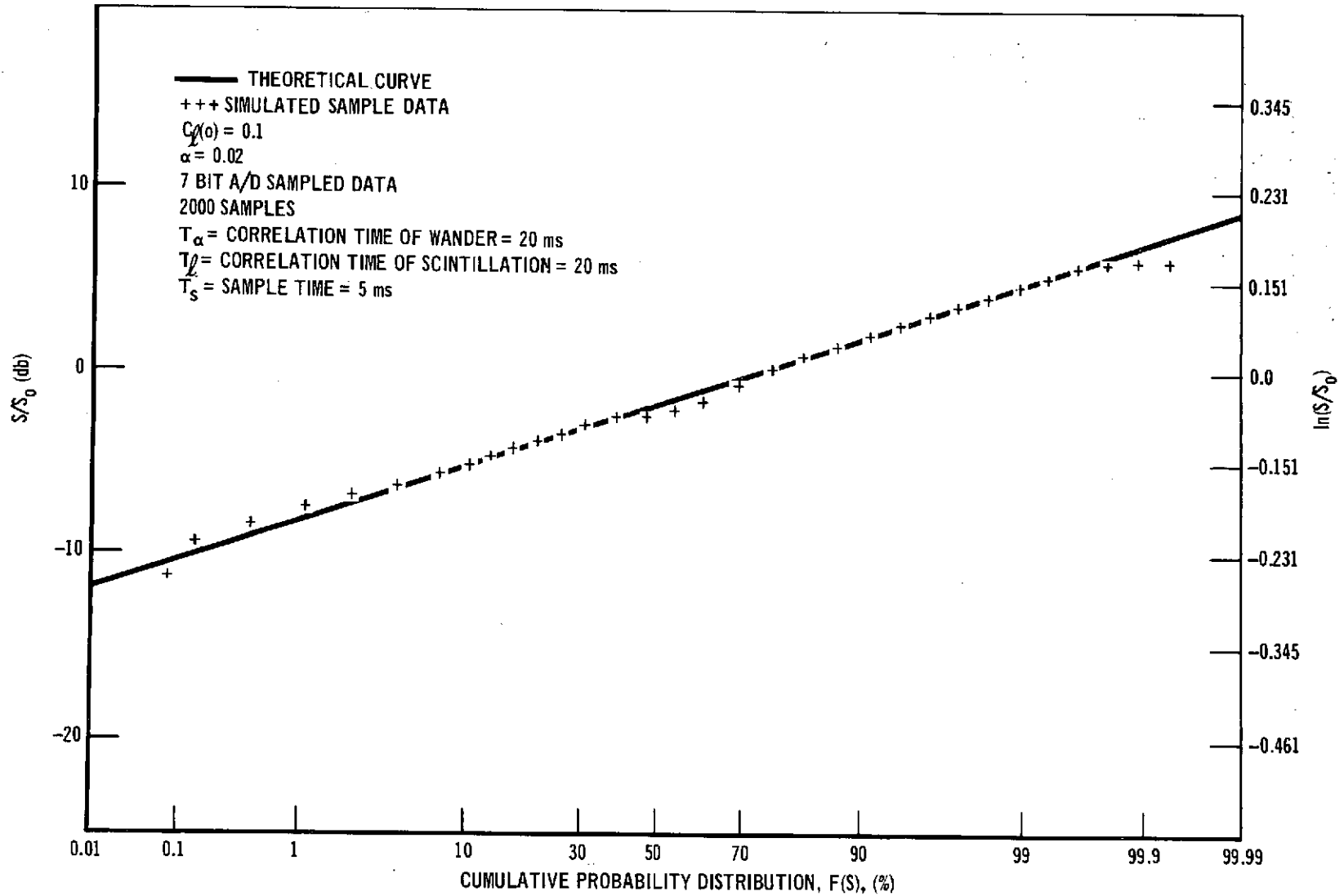


FIGURE 77 CUMULATIVE PROBABILITY DISTRIBUTION OF RECEIVED OPTICAL POWER CONSIDERING SCINTILLATION AND BEAM WANDER



The ground station atmospheric experiment optical detectors is activated. A star near the balloon flight path is next acquired with the Stellar Image Monitor and wavefront degradation measurements begin. Both the aperture averaging detector and spatial correlation detector are also exercised.

After a limited amount of data is acquired, a real time check analysis of the data is performed.

If the data appears to be satisfactory, the beam diameter of the atmospheric probe beam is readjusted with the zoom lens optics. The diameter is changed again after another check of the real time data.

Baseline of the Atmospheric Experiments - All the atmospheric experiments outlined in this section can be performed for any night balloon flight. However the test of the variation of uplink probe beam transmit characteristics on received beam properties is only a secondary experiment. It will be executed only after data from the primary experiments is acquired and checked. Therefore the secondary experiment may be performed halfway through the first night flight or on the second night flight. At least two night flights are required to exercise the night time atmospheric experiments.

Because daytime turbulence effects are known to be more pronounced, it is proposed that at least two daytime balloon flights be flown. During the day, the atmospheric probe beam is required to obtain sufficient dynamic measurement range for sensing large received power fluctuations. Hence, only on the second daylight flight will the atmospheric probe beam transmitter characteristics be varied.

2.4.4 Optomechanical Design. This section describes the optical system design, the mechanical layout, and the optics error analysis.

2.4.4.1 Optical design. The transceiver optical system described herein has been configured in such a manner as to minimize susceptibility to thermal and structural perturbational effects upon the optical performance.

The basic design problem was aggravated by the need to optimize and correct the all-refractive optical system at two widely separated wavelengths. Without an absolute correction of primary lateral chromatic aberration, a built-in reciprocity tracking bias would exist, expressed as a percentage of the tracking bender offset. (Since the transmitter requires a rather wide beam divergence, the degree of correction is not as severe a requirement as if the output beam were diffraction limited.)

A normal lens design effort applied to photo/visual imaging systems aims at eliminating primary chromatic aberration between $0.65 \mu\text{m}$ (Hydrogen C) and $0.4861 \mu\text{m}$ (Hydrogen F) with monochromatic correction established at $0.5876 \mu\text{m}$ (the Helium d line). In addition, a concerted effort is made to minimize the focal difference between the F/C image and the d image, described as secondary chromatic aberration.

In this program, primary chromatic aberration correction is mandated between $0.53 \mu\text{m}$ and $1.06 \mu\text{m}$, a range three times as broad as in the standard photo/visual approach. Hence, an approach to try to correct secondary chromatic aberration would require glasses with exotic partial dispersions (expensive) and an inordinately large number of elements for the task required. Since the aberrational condition at wavelengths other than 0.53 and $1.06 \mu\text{m}$ is irrelevant in the balloon package, the design approach was to try to correct primary chromatic aberration absolutely at these two wavelengths and completely ignore any secondary

spectrum. (As the system description will reveal, some residual spherochromatism remains in the design, but the blur circles are within the bounds established by the system performance requirements.) Also, since a quality image is only required within 2 mrad of the optical axis, correction at the acquisition field angles was weighted down in the design efforts.

In order to minimize the number of large optical elements and reduce the system sensitivity to perturbational thermal effects, the receiver optics are split into two separate major subsections: a 4x afocal telephoto attachment containing the large refractive elements, and what should properly be labeled the tracking optics.

The lens record for the telephoto attachment is presented in Figure 78 . It consists of a three element $P_+(PN)_f/4$ positive group, and a two element $(PN)_{negative}$ group housed in an invar barrel for thermal perturbational stability. The attachment's positive group forms the largest, fastest, and hence, the most sensitive assembly of optical elements in the entire balloon package. By housing them in a separate, very stable environment, the viability of the entire system is enhanced.

The lateral intercept curves for the telephoto attachment are presented in Figure 79 . (The lateral intercept curve is an evaluation plot of geometric ray error as a function of aperture.)

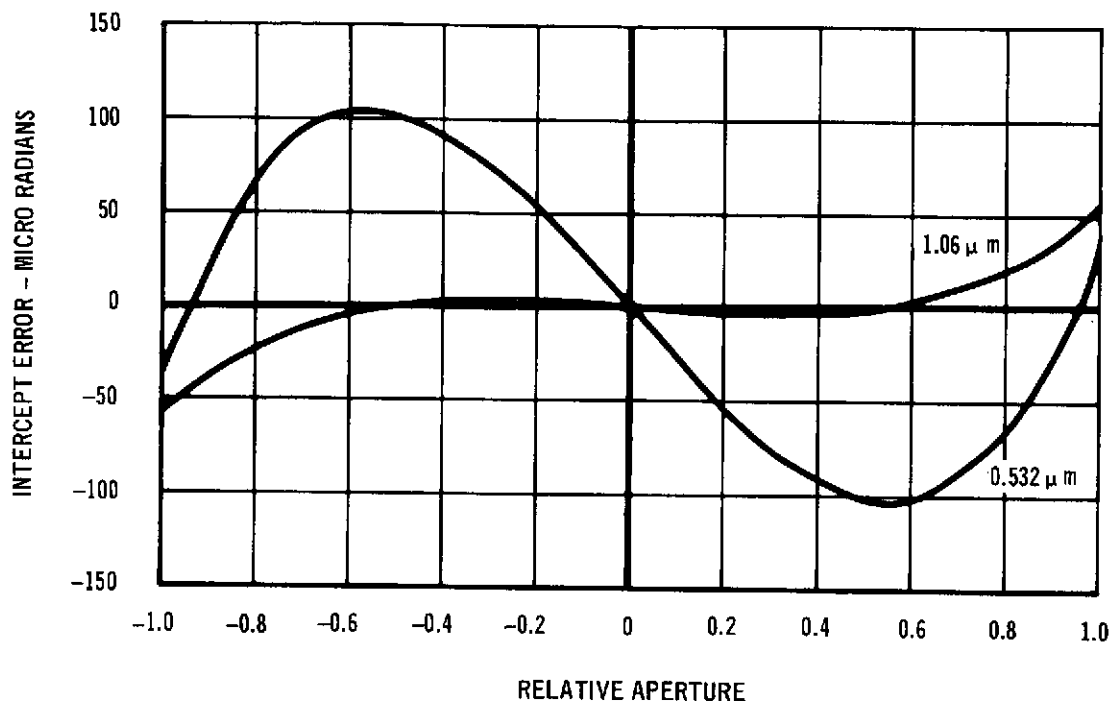
The limiting aperture for the optical system is formed by the objective lens following the fold prism. This causes the diameter of the positive group elements in the telephoto attachment to grow considerably beyond the 100 mm entrance pupil diameter, but allows the remainder of the optical elements to stay within the one inch clear aperture range.

FIGURE 78 OPTICAL SYSTEM RECORD

TITLE: Telephoto Attachment		JOB NO.: 697		DATE: 17 October 1972					
UNITS - ALL DIMENSIONS IN: Millimeters		INSTRUMENT: High Data Rate Balloon System							
		EFL =		APER STOP SURF NO. 11					
		BFL =		EXT PUPIL DIA = 100.0					
		FFL =		EXT PUPIL DIA = 25.0					
		f/NO.		EXT PUPIL LOC = -1905.5					
		SEMI FIELD ANGLE: 1°		EXT PUPIL LOC = 0					
		SPEC RANGE: 1.064 μm & 0.532 μm		MAGNIFICATION: 4					
		OVERALL LENGTH: 367.1		DESIGNED BY:					
SURF NO.	RADIUS		THICKNESS		CLEAR AP	OUTSIDE DIA	EDGE THICK.	GLASS	
	TEST PLATE	CALCULATED ± TOL	CENTER ± TOL					CODE	MELT NO. OR ± TOL
1		CX 345.983	18.4070	147.				LaKN-9	
2		CC 4104.107	.6422	145.				Air	
3	POS. GROUP	CX 195.373	23.0484	141.				SF-15	
4		CX/CC 411.654	4.8008	139.				LaKN-9	
5		CC 222.604	254.500	129.				Air	
6		CC 140.453	11.5151	29.				SF-15	
7	NEG. GROUP	CX/CC 35.107	4.7577	28.				LaKN-9	
8		CC 170.708	10.	27.				Air	
9	PRISM	PLANO	30.	26.				BK-7	
10		PLANO	10.	26.					
11	AP. STOP			25.					
12									
13									
14									
15									
16									
17									
18									
19									
20									
λ ₁ .532 μm λ ₂ 1.064 μm		NOTES: OPTIMIZED TO CORRECT PRIMARY CHROMATIC ABERRATION AT 1.06 μm & 0.532 μm							
SIEDEL COEFFICIENTS: (Grey)									
SPH = -.00031									
COMA = -.0023									
AST = -.1177									
DIST = -10.454 (SCALED 0.27%)									
PETZ = -.222									
LCHR = -.099									
TCHR = 4.113									

FIGURE 79

LATERAL INTERCEPT CURVES FOR TELEPHOTO ATTACHMENT: ON AXIS



The objective itself is an $f/10$, 254 mm, effective focal length, four element PNPP air-spaced achromat correcting primary longitudinal chromatic aberration at the two laser wavelengths. The lens record is presented in Figure 80, and the lateral intercept curves for on-axis, and 4° off-axis are presented in Figures 81 and 82 drawn at the place of best focus for the design wavelength.

Figure 83 is a lateral intercept plot of the on-axis performance of the combined telephoto attachment/objective assemblies. The spherochromatism noted is a near perfect transfer of the residuals of the telephoto attachment by the objective assembly (inverted due to the transformation from angular to linear error measurement). At the focus of the objective lens, a bifurcating mirror splits off the acquisition field (2 mrad to one degree off-axis) and passes it through a 100 Å bandwidth interference filter to a quadrant lens assembly which images the

FIGURE 80 OPTICAL SYSTEM RECORD


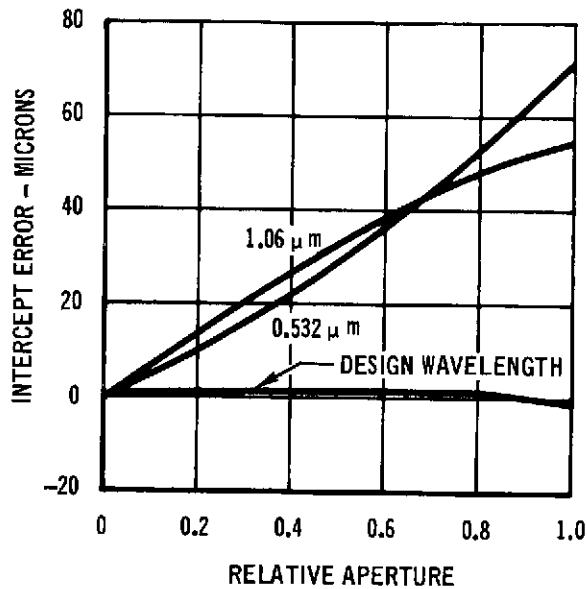
TITLE: Objective Lens		JOB NO.: 697		DATE: 17 October 1972				
UNITS--ALL DIMENSIONS IN: Millimeters		INSTRUMENT: High Data Rate Balloon System						
		EFL = 254 mm		APER STOP SURF NO. 1				
		BFL = 205.5 mm		ENT PUPIL DIA = 25.0				
		FFL =		EXT PUPIL DIA = 25.8				
		f/NO.: 10		ENT. PUPIL LOC = 0				
		SEMI FIELD ANGLE: 4°		EXT PUPIL LOC = -57.4				
		SPEC RANGE: 532 μm & 1.064 μm		MAGNIFICATION:				
OVERALL LENGTH: 53.882		DESIGNED BY:						
SURF. NO.	RADIUS		THICKNESS	CLEAR AP	OUTSIDE DIA	EDGE THICK.	GLASS	
	TEST PLATE	CALCULATED ± TOL	CENTER ± TOL				CODE	MELT NO. OR ± TOL
1		CX 36.569	6.6968	25.			BK-7	
2		CC 157.507	15.8845	24.			Air	
3		CC 209.514	3.7004	20.			SF-5	
4		CC 35.991	16.2925	19.			Air	
5		CX 555.455	2.7334	23.			SF-5	
6		CX 229.596	.5470	24.			Air	
7		CX 71.496	8.0277	24.			SK-4	
8		CC 319.878		24.				
9								
10								
11								
12								
13								
14								
15								
16								
17								
18								
19								
20								
λ ₁ 0.532 μm λ ₂ 1.064 μm			NOTES: OPTIMIZED TO CORRECT PRIMARY CHROMATIC ABERRATION AT 1.06 μm & 0.532 μm					
SEIDEL COEFFICIENTS: (Grey)								
SPH = -.0503								
COMA = -.0537								
AST = -.0109								
DIST = .2110 (Scaled: 0.09%)								
PETZ = .0951								
LCHR = .6556								
TCHR = .2083								

FIGURE 81 LATERAL INTERCEPT CURVES FROM 254 MM OBJECTIVE – ON AXIS



entrance pupil onto four photomultiplier tubes. The acquisition blur radius at the quadrant dividing lens is 5 mrad, referenced to object space.

The energy that passes through the bifurcating mirror is relayed to the communications detector and fine tracking assembly by a four element PNNP airspaced achromat at a magnification ratio of 1:1. The lens record for this relay group is presented in Figure 84. This lens was designed as an integral part of the objective assembly, in order to preserve precise pupil and ray angle characteristics of the full system. Figure 85 is the on axis plot of the aberrational residuals of the combined objective/relay assemblies.

The relay is situated such that its principal planes are equally spaced from the azimuth/elevation tracking benders, and such that the bender gain (physical bender motion to object space beam deflection) has a value of 3.5. This provides the required

FIGURE 82 LATERAL INTERCEPT CURVES FOR
254 MM OBJECTIVE - 4° OFF AXIS

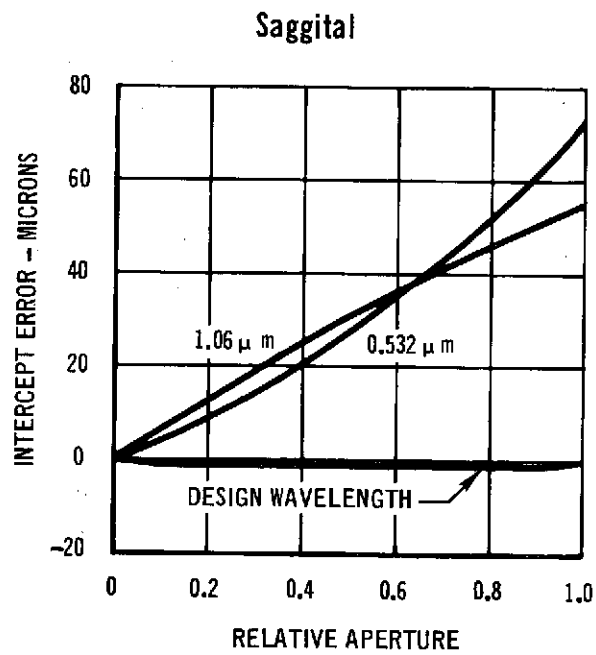
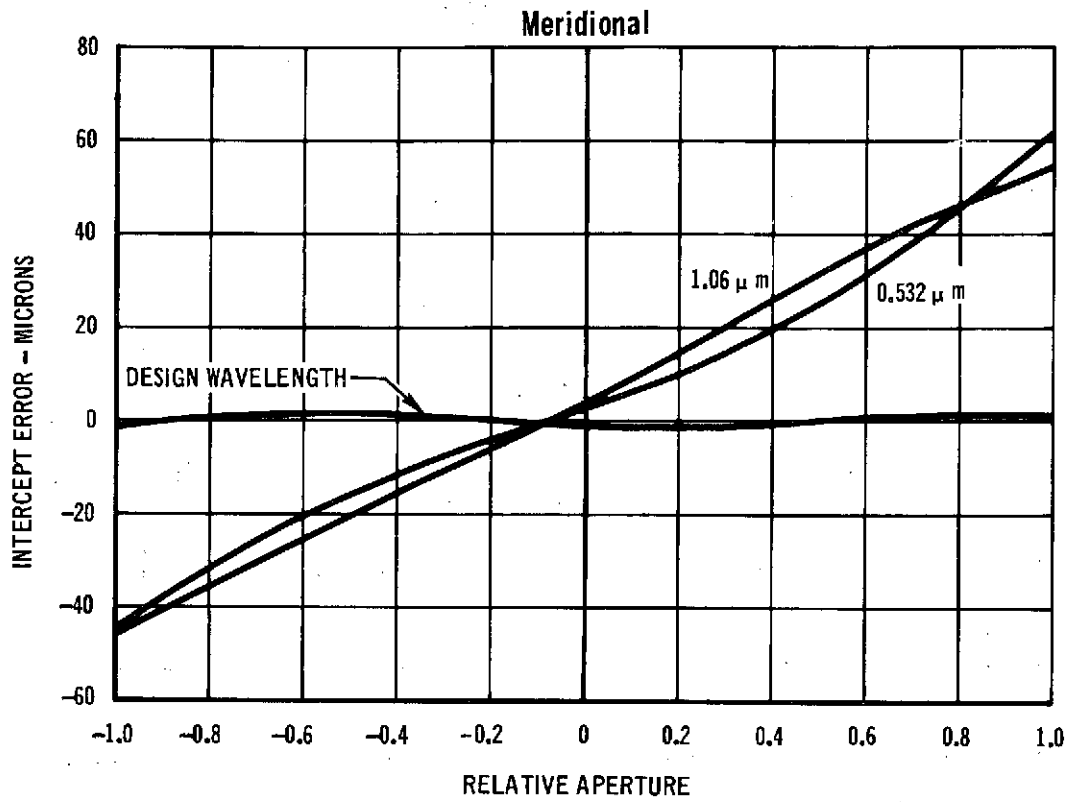
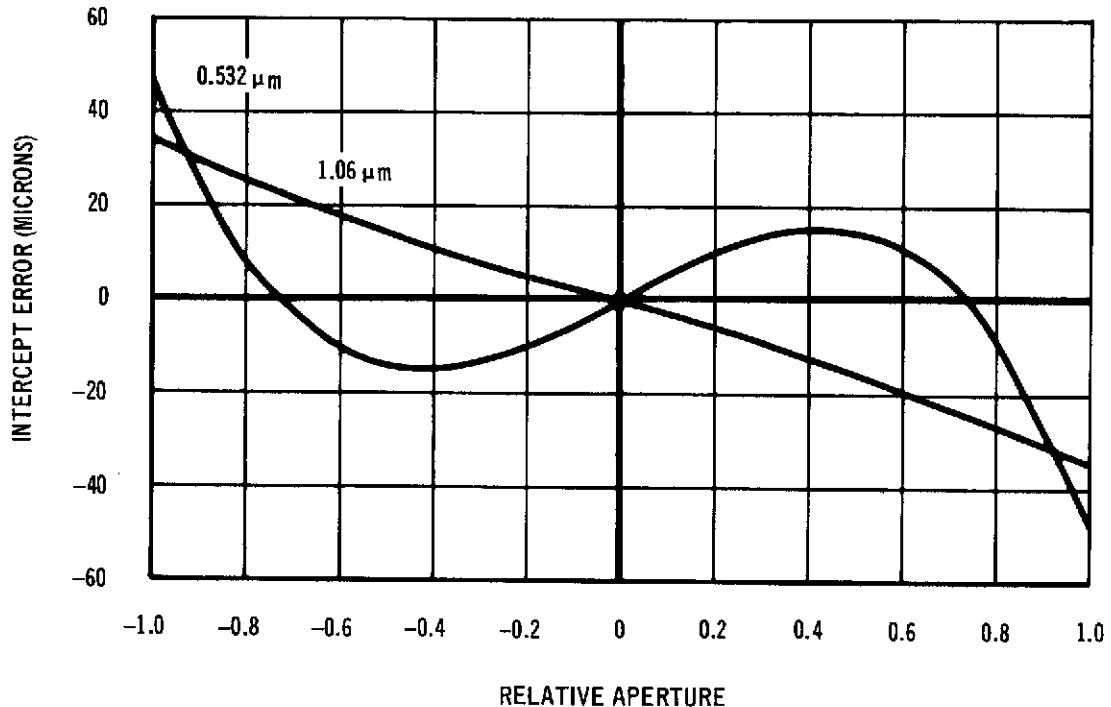


FIGURE 83 LATERAL INTERCEPT CURVES FOR
TELEPHOTO ATTACHMENT +
OBJECTIVE - ON AXIS



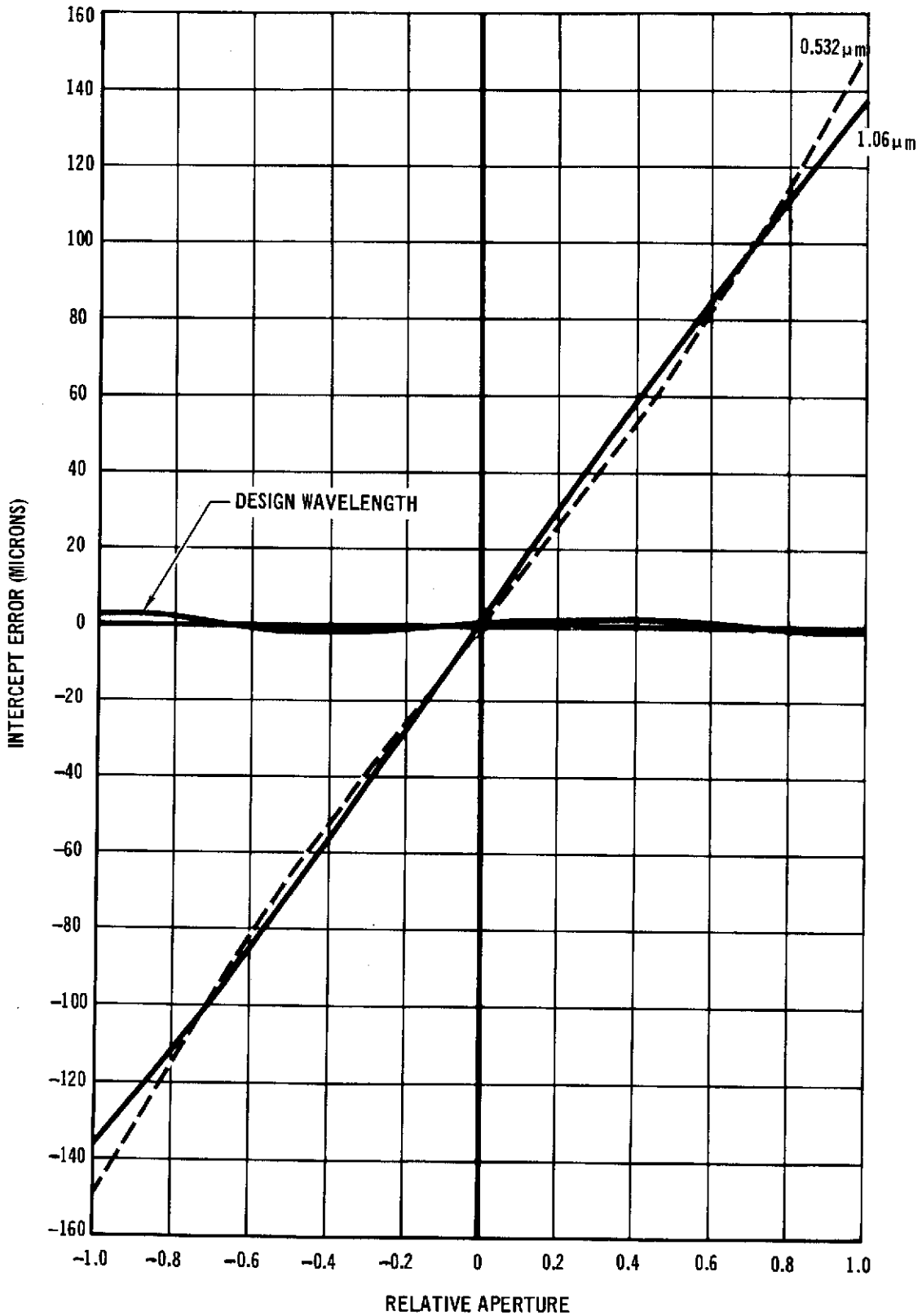
± 2 mrad fine tracking field without substantial vignetting by the standard 0.707-inch x 0.707-inch projected profile of the bender bimorph design.

Following the final tracking bender, and before reaching the communications detector/fine tracking assembly beamsplitter, the received .532 μm beam is intercepted by a dichroic mirror which introduces the reciprocally-pointed 1.064 μm beam into the reciprocity tracking optics. This dichroic, properly considered a parallel plate at 45°, introduces a modicum of astigmatism into the received beam, but by proper compensatory focusing of the following optics, no major system performance degradation results.

FIGURE 84 OPTICAL SYSTEM RECORD

TITLE: Relay		JOB NO.: 697		DATE: 17 October 1972				
UNITS--ALL DIMENSIONS IN: Millimeters		INSTRUMENT: High Data Rate Balloon System						
		EFL = 109.663		APER STOP SURF NO.:				
		BFL = 85.796 AT No. Lens Only		EXT PUPIL DIA = 25.8"				
		FFL = 200 AT 1:1		EXT PUPIL DIA = 7.82				
		f/NO. 5		EXT PUPIL LOC = -431.3 FROM 1				
		SEMI FIELD ANGLE + 2 MM		EXT PUPIL LOC = -118 FROM 8				
		SPEC RANGE: 1.064 μm & 0.532 μm		MAGNIFICATION: 1:1				
OVERALL LENGTH:		DESIGNED BY:						
SURF. NO.	RADIUS		THICKNESS	CLEAR AP	OUTSIDE DIA	EDGE THICK.	GLASS	
	TEST PLATE	CALCULATED \pm TOL	CENTER \pm TOL				CODE	MELT NO. OR \pm TOL
1		CX 68.906	6.3726	27.			SK-16	
2		CX 34.337	.5020	27.			Air	
3		CC 33.470	2.3166	27.			BaF-4	
4		CC 344.087	20.4650	26.			Air	
5		CC 132.770	6.5751	24.			Baf-4	
6		CC 27.873	2.1073	24.			Air	
7		CX 31.721	6.1416	26.			SK-16	
8		CX 77.679	95.5852	26.			Air	
9	BEAMSPLITTER, DICHOIC, & FILTER	PLANO	25.000 \dagger				BK-7	
10		PLANO	82.7576				Air	
11								
12								
13								
14								
15								
16								
17								
18								
19								
20								
λ_1 λ_2		NOTES: *PUPILS BASED UPON CHARACTERISTICS OF ACCOMPANYING OBJECTIVE LENS. OPTIMIZED WITH OBJECTIVE TO CORRECT PRIMARY CHROMATIC ABERRATION AT 1.06 μm & 0.532 μm						
SEIDEL COEFFICIENTS								
SPH =								
COMA =								
AST =								
DIST =								
PETZ =								
LCHR =								
TCHR =								

FIGURE 85 LATERAL INTERCEPT CURVES FOR OBJECTIVE +
RELAY: ON AXIS (MONOCHROMATIC DESIGN FOCUS)



After transmission through the dichroic, the received beacon is split into two components by a beamsplitter. One component is imaged directly onto the communications detector, and the other guided into the fine tracking detector amplification optics.

The beam transmitted to the fine tracking channel is relayed to the fine tracking dividing optics by a 4x achromatic microscope objective, yielding a total effective tracking system focal length of 4064 mm. Figures 86 and 87 present lateral intercept curves of the full system up to the microscope objective focal plane for on-axis and 2 mrad off-axis, respectively. As an off-the-shelf commercially produced microscope objective is planned for inclusion in this system, no computer ray trace can be conducted completely to the fine tracking image. However, since the numerical aperture of the objective being considered is considerably greater than the f/10 bundle, we are presenting to it, very little risk of image degradation is involved.

**FIGURE 86 LATERAL INTERCEPT CURVES
FOR FULL SYSTEM - ON AXIS**

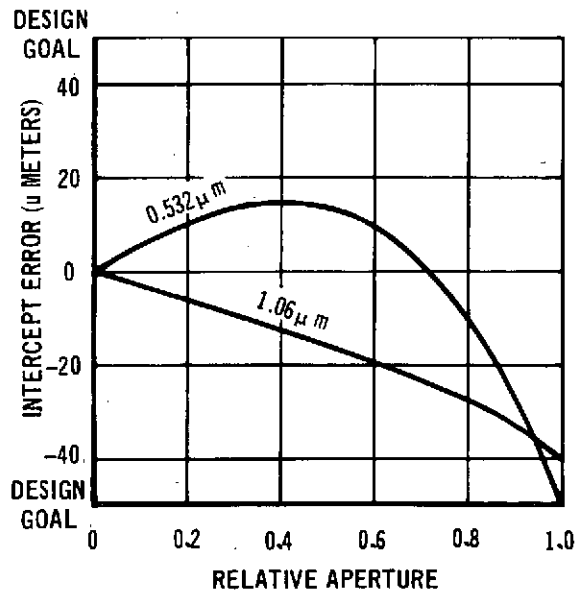
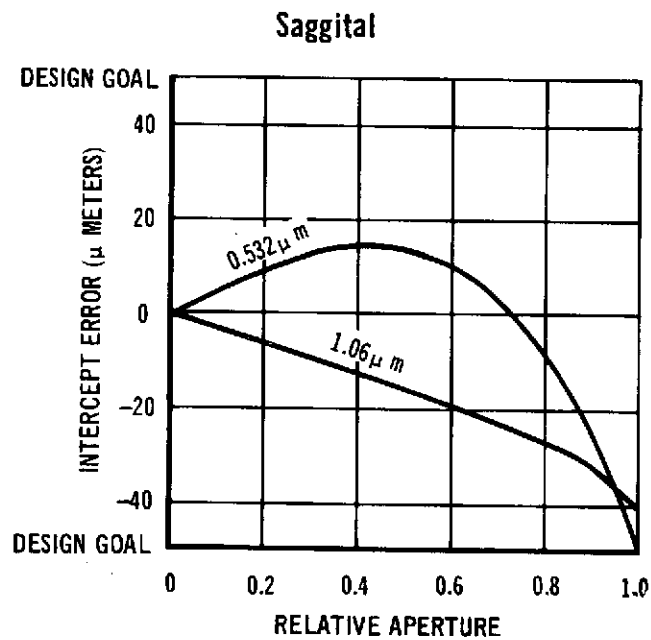
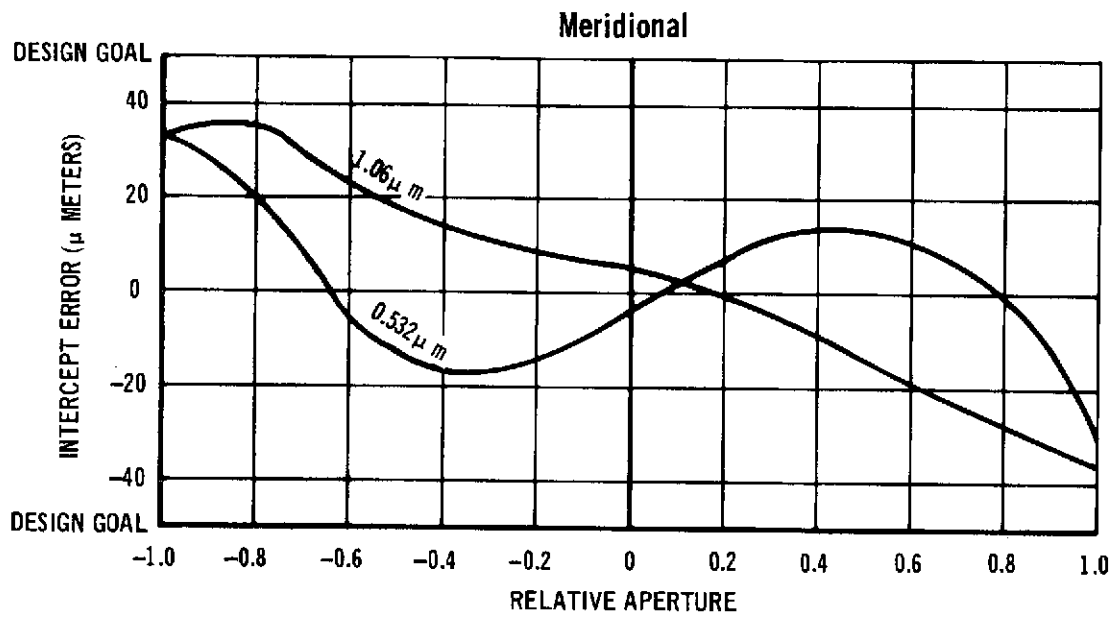


FIGURE 87 LATERAL INTERCEPT CURVES FOR
FULL SYSTEM - 2 mRAD OFF AXIS



The bundle relayed by the microscope objective is imaged with a 50 microradian (object space reference) blur radius onto the apex of a reflective tetrahedron which splits the fine tracking image into four segments. Each segment is reflected through an entrance pupil imaging lens onto the face of one of four matched PMT's. The image presented to the PMT is a pupil image, thus negating beam walking tendencies and the deleterious effects of local nonuniformities in the PMT photocathodes.

Let us now turn our attention to the laser transmitter portion of the package. The 1.06 μm beam, having passed through the modulator is circularly polarized by a quarter wave plate, to reduce reception problems in the ground based receiver. The beam is then focused by a commercially available focus lens assembly and transmitted to the dichroic to exit the system through a reciprocal path to the received beam.

The transmitted beam will utilize the full system aperture, taking advantage of the remnants of spherochromatism plus a small amount of defocusing to achieve the required one-half milliradian output beam divergence. The defocusing will be an assembly adjustment rather than a design criterion, in order to optimally match the optics manufactured.

2.4.4.2 Mechanical design. The mechanical layout of the balloon-borne package was accomplished under the following guiding principles and constraints.

- (1) Mount the entire package on the elevation axis of the presently available gondola structure.
- (2) Provide a look-angle of 0 to 70° from the zenith for all locations of the line-of-sight with respect to the azimuth position of the gondola structure.
- (3) Provide a stable structure that can withstand the balloon environment.
- (4) Minimize the total weight and the moments of inertia about

the elevation and azimuth axes.

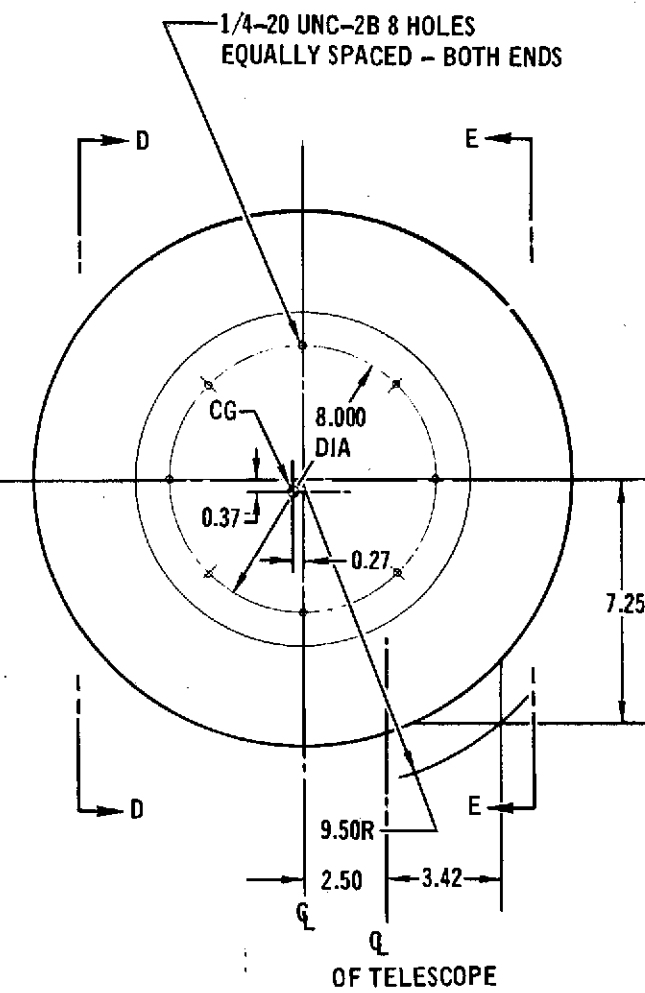
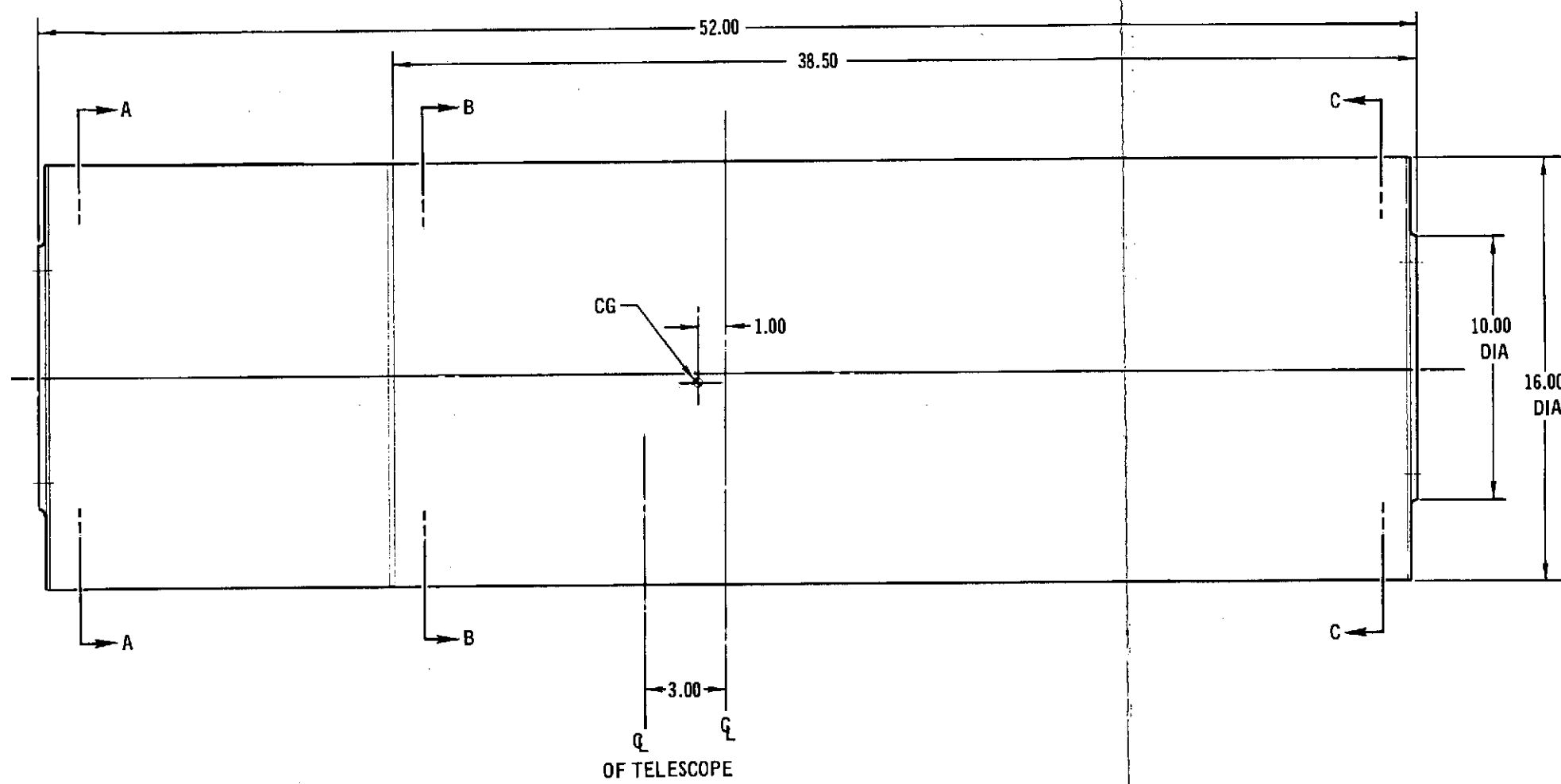
- (5) Provide easy access to all components to simplify the repair and cleaning process between flights.

The configuration as shown in Figure 88 contains all the balloon-borne elements nominally within a cylindrical package 16-inches in diameter and 52-inches long. This package will mount on the present gondola elevation axis. All of the optical elements are mounted in a 38.5-inch long portion of the cylinder leaving the remaining portion free for electronic assemblies. A small portion of the telephoto lens assembly extends beyond the 16-inch diameter because the optical axis of this assembly is offset from the center line of the cylinder. By allowing this offset, the elevation look angle can extend slightly past 70° from the zenith without the addition of a large flat folding mirror to clear the crush pads. (See Figure 89 ; the crush pad projection into the plane of the drawing is shown by the cross-hatched region.) Note that the gondola structure from which the crush pads extend has been lengthened by three-inches to accommodate the 16-inch cylinder. (The previous cylinder had a 10-inch diameter.) Since this part of the gondola is a simple angle-iron structure, this lengthening will be a task easily accomplished at a small cost.

The elimination of a large flat mirror not only reduces the configuration complexity, weight and moment of inertia, but also reduces the risk of damage during the balloon landing. To minimize any damage to the glass surfaces of the telephoto lens, the elevation axis can be commanded to rotate 90° prior to launch and descent such that the telephoto optical axis is perpendicular to the azimuth axis. Even in this position, the extension of the telephoto lens beyond the 16-inch cylinder will not interfere with the elevation yoke of the gondola structure.

An optical schematic showing the relationship of all the optical components is given in Figure 90 , and the details of the con-

FIGURE 88 ELEVATION PACKAGE OUTLINE

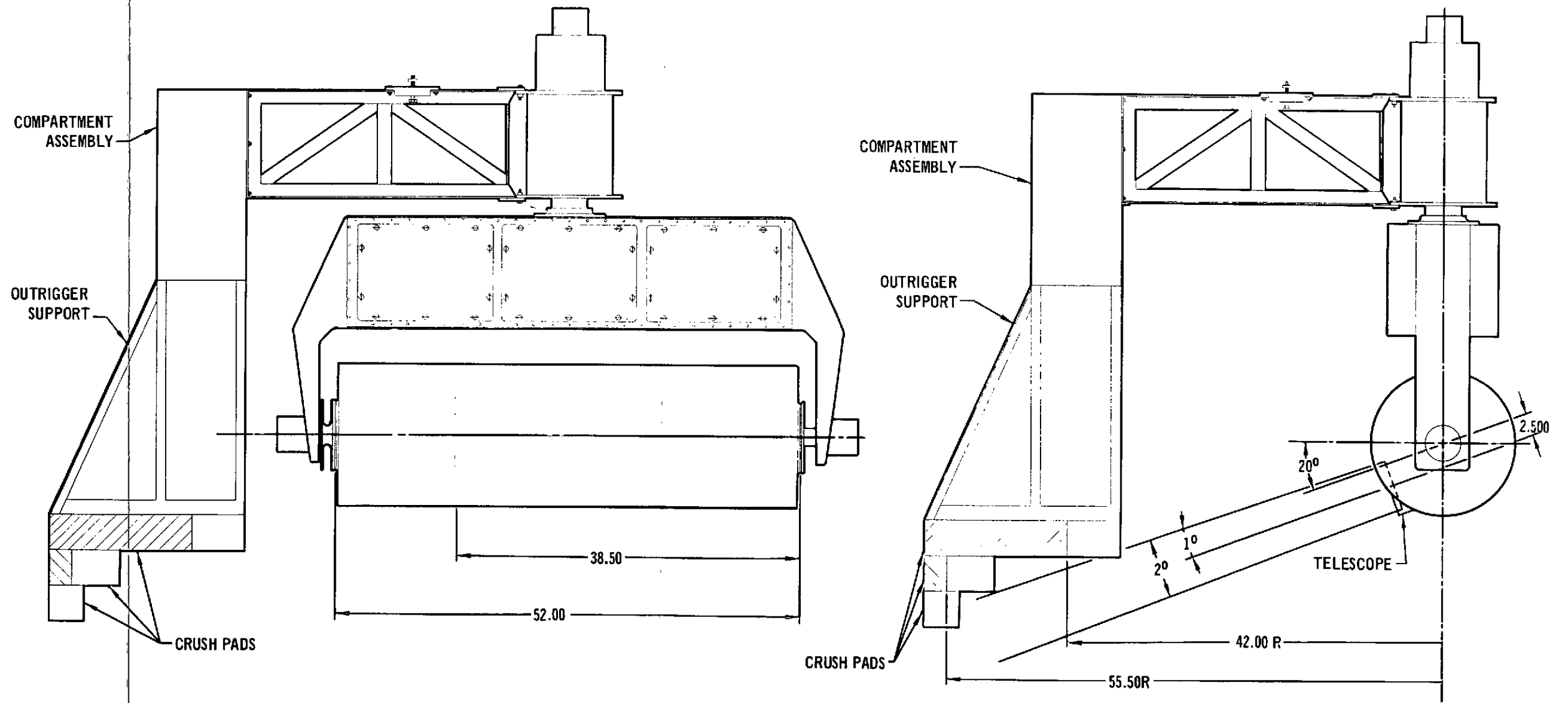


ALL DIMENSIONS IN INCHES

FOLDOUT FRAME

2

FIGURE 89 GONDOLA ASSEMBLY



ALL DIMENSIONS IN INCHES

FOLDOUT FRAME

↑

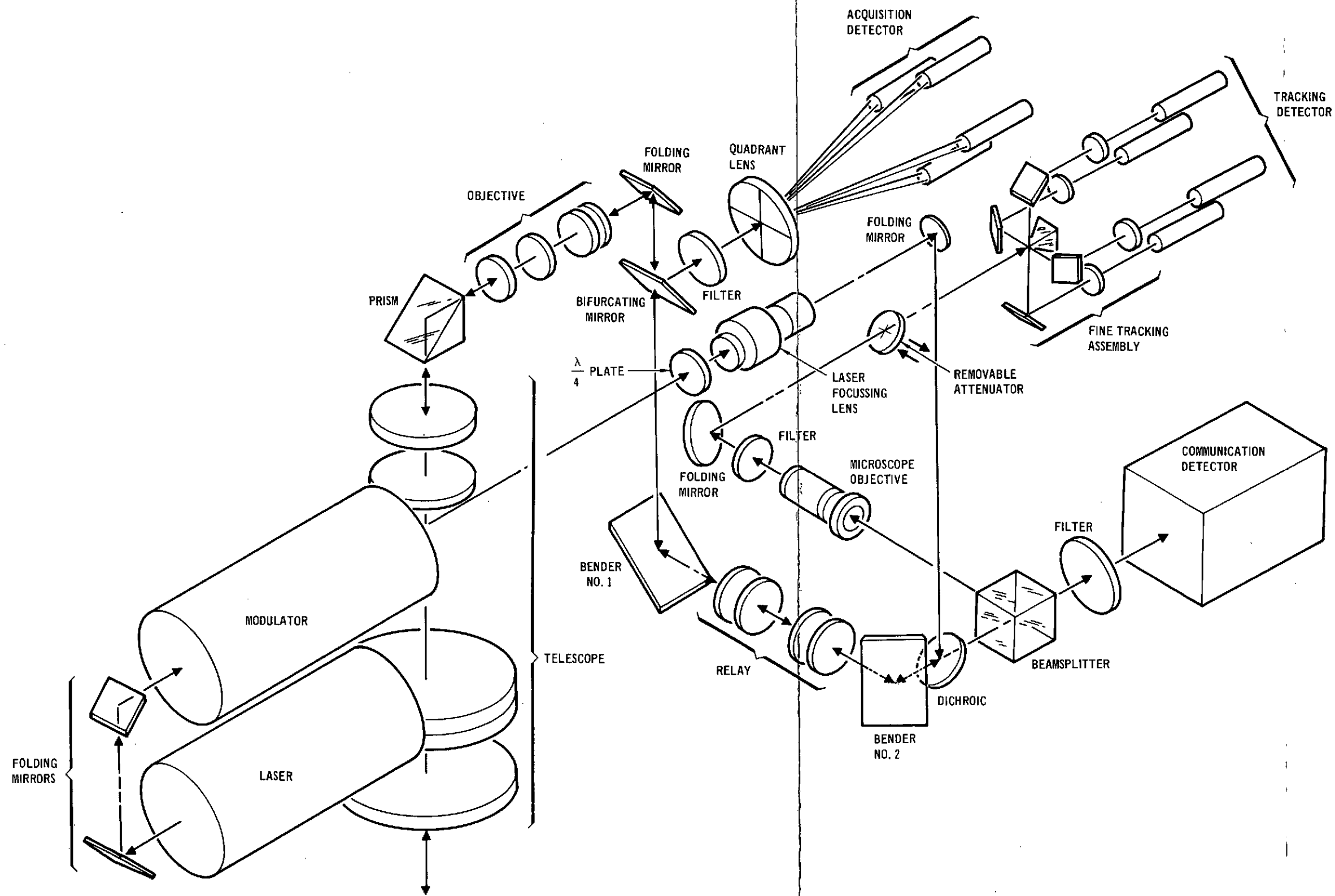
176

FOLDOUT FRAME

2

CB

FIGURE 90 HDR BALLOON OPTICS OPTICAL SCHEMATIC



FOLDOUT FRAME

FOLDOUT FRAME

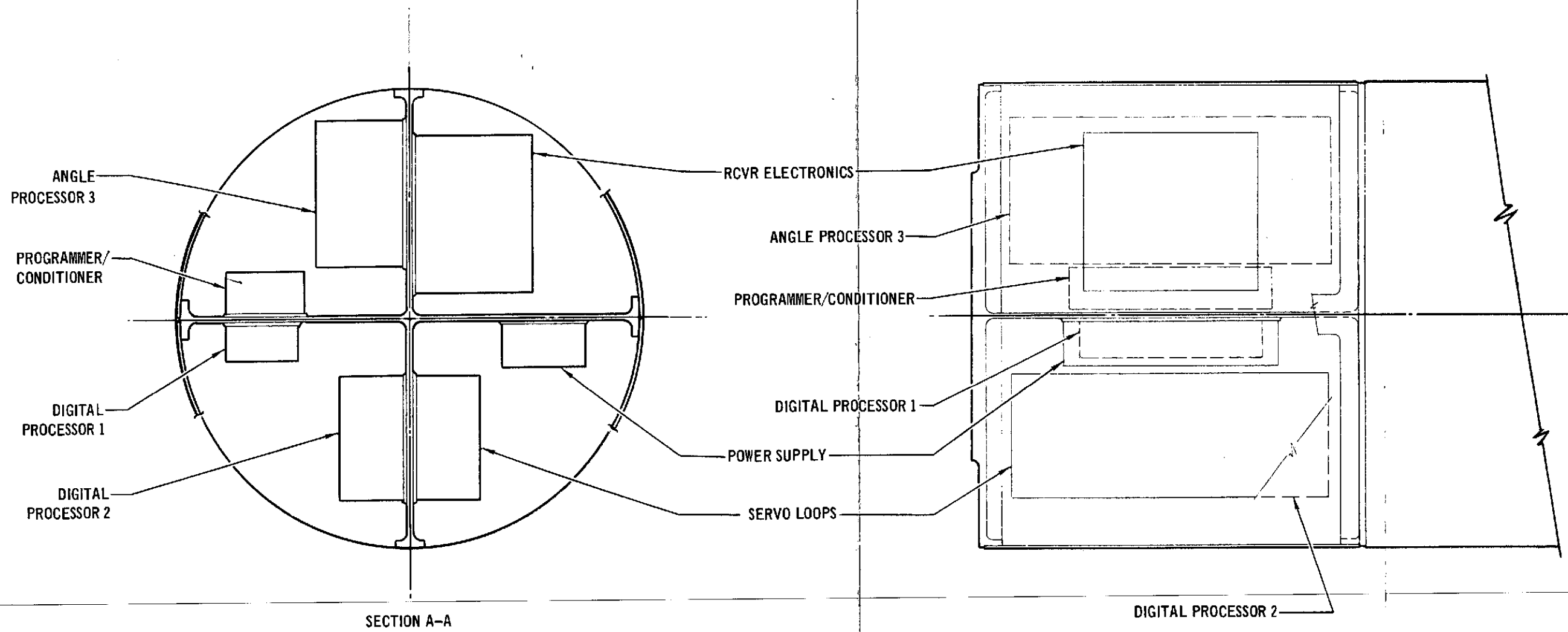
2

figuration are given in Figures 91 through 98 . The basic cruciform structure provides the necessary mechanical stability while allowing easy access to each optical component. The entire structure is made of aluminum except for the housing of the telephoto lens which is made of invar. The cylindrical cover is made in four pieces (two for the optical section and two for the electronic section), which allows quick and easy assembly procedures while also allowing quick access to any optical or electrical assembly.

The total weight of the balloon-borne package is 162 pounds. The center of gravity (see Figure 88) is located 0.27 and 0.37 inches from the elevation axis and 1.0 inch from the azimuth axis. This c.g. location is based on calculations which assumed the c.g.'s of the electronic boxes are located at their geometric centers. However, the calculations show that the nominal c.g. is presently close enough to the intersection of the elevation and azimuth axes to easily allow a balance to be accomplished. In addition, the cruciform structure with its ease of access will allow final balance adjustments to be quickly made. The calculated moments of inertia of the balloon-borne package are 0.85 ft/lb/sec² about the cylinder axis and 8.7 ft/lbs/sec² about any axis perpendicular to the cylinder axis through the center of the 52-inch long cylinder.

2.4.4.3 Optics error analysis. An analysis of the optical performance (image quality) and the transmit beam/receive beam collinearity for typical flight profiles was performed during this study. We performed a thermal analysis and a structural (deflection) analysis of the transceiver package. These two analyses provided us with six components of deflection (ΔX , ΔY , ΔZ , Θ_X , Θ_Y , Θ_Z) at critical points in the optical system. These differential displacements were processed by an optics tolerance analysis program designed to compute the final optical performance and the transmit beam/receive beam collinearity.

FIGURE 91 ELECTRONICS BAY - ELEVATION PACKAGE



FOLDOUT FRAME

FOLDOUT FRAME
2

FIGURE 92 SECTION B-B

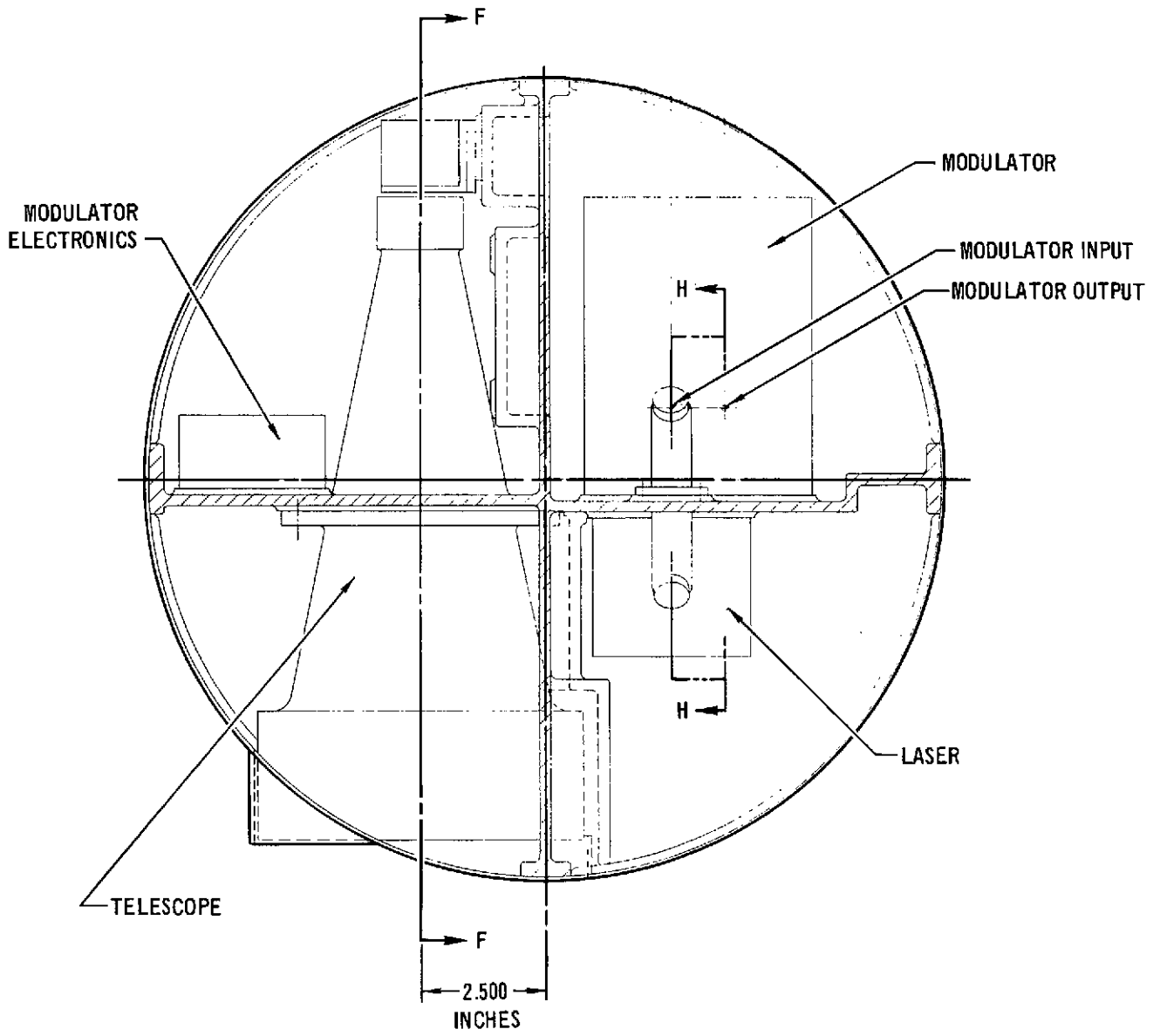
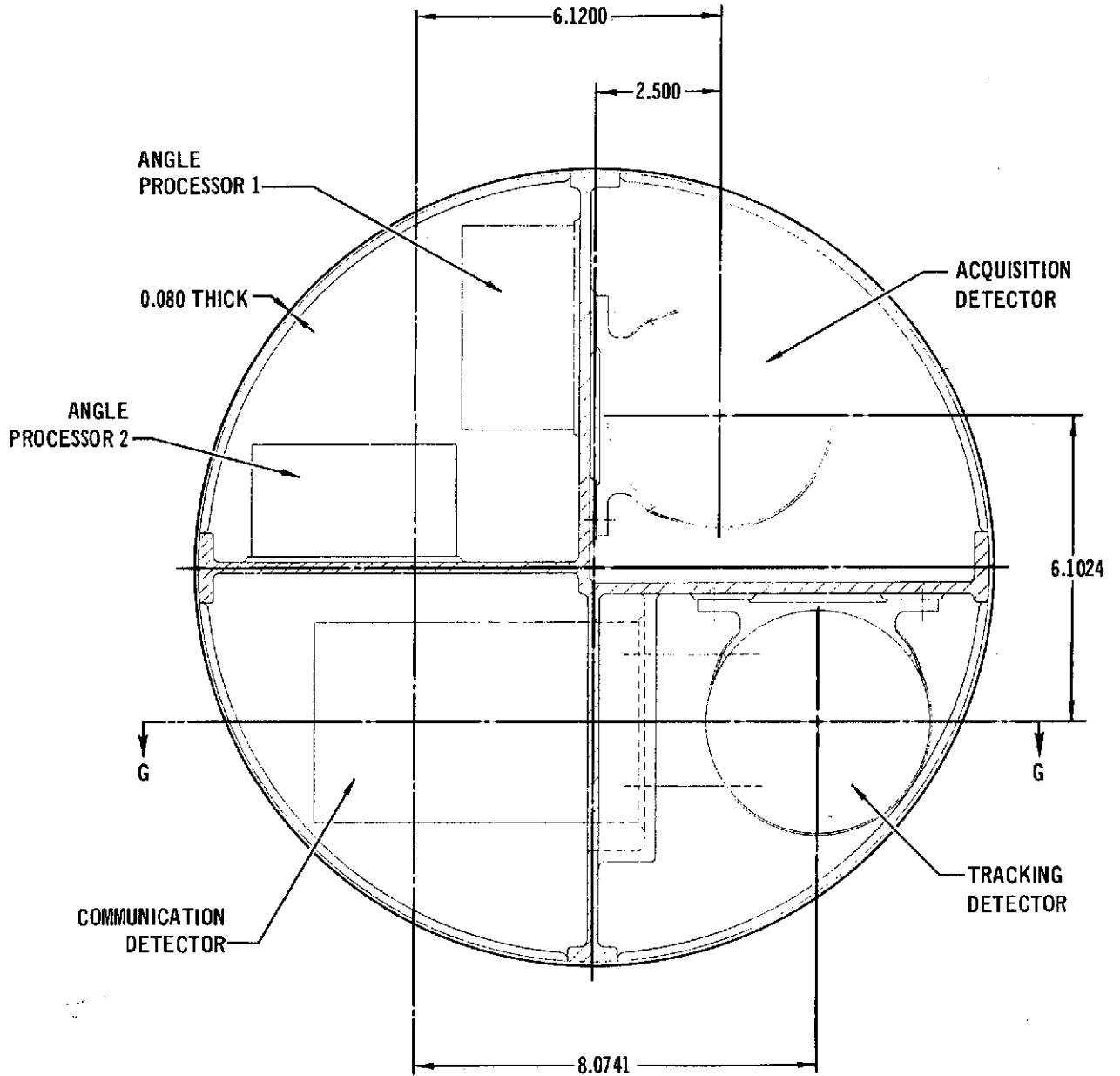
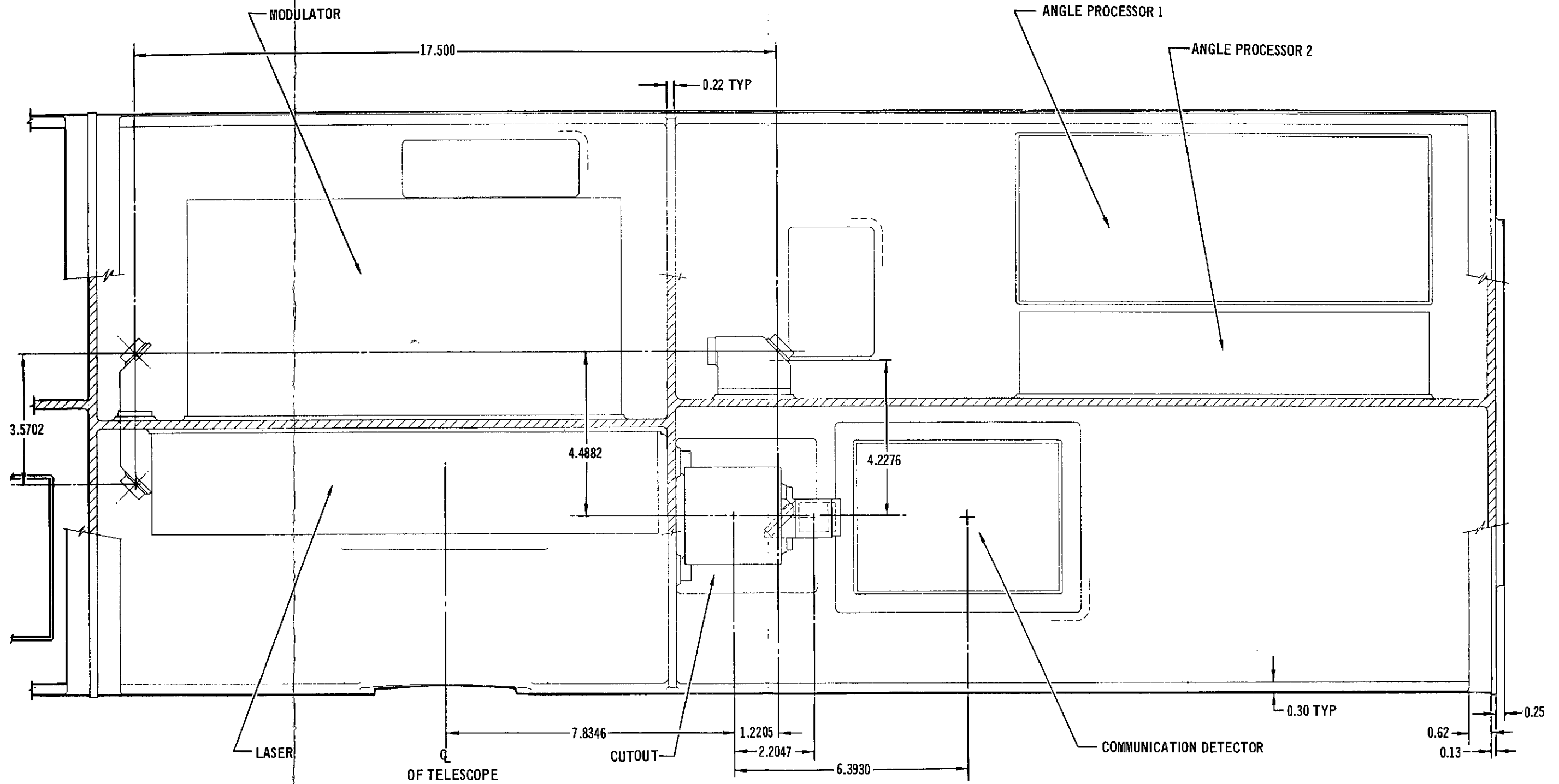


FIGURE 93 SECTION C-C



ALL DIMENSIONS IN INCHES

FIGURE 94 COVER REMOVED
SECTION D-D

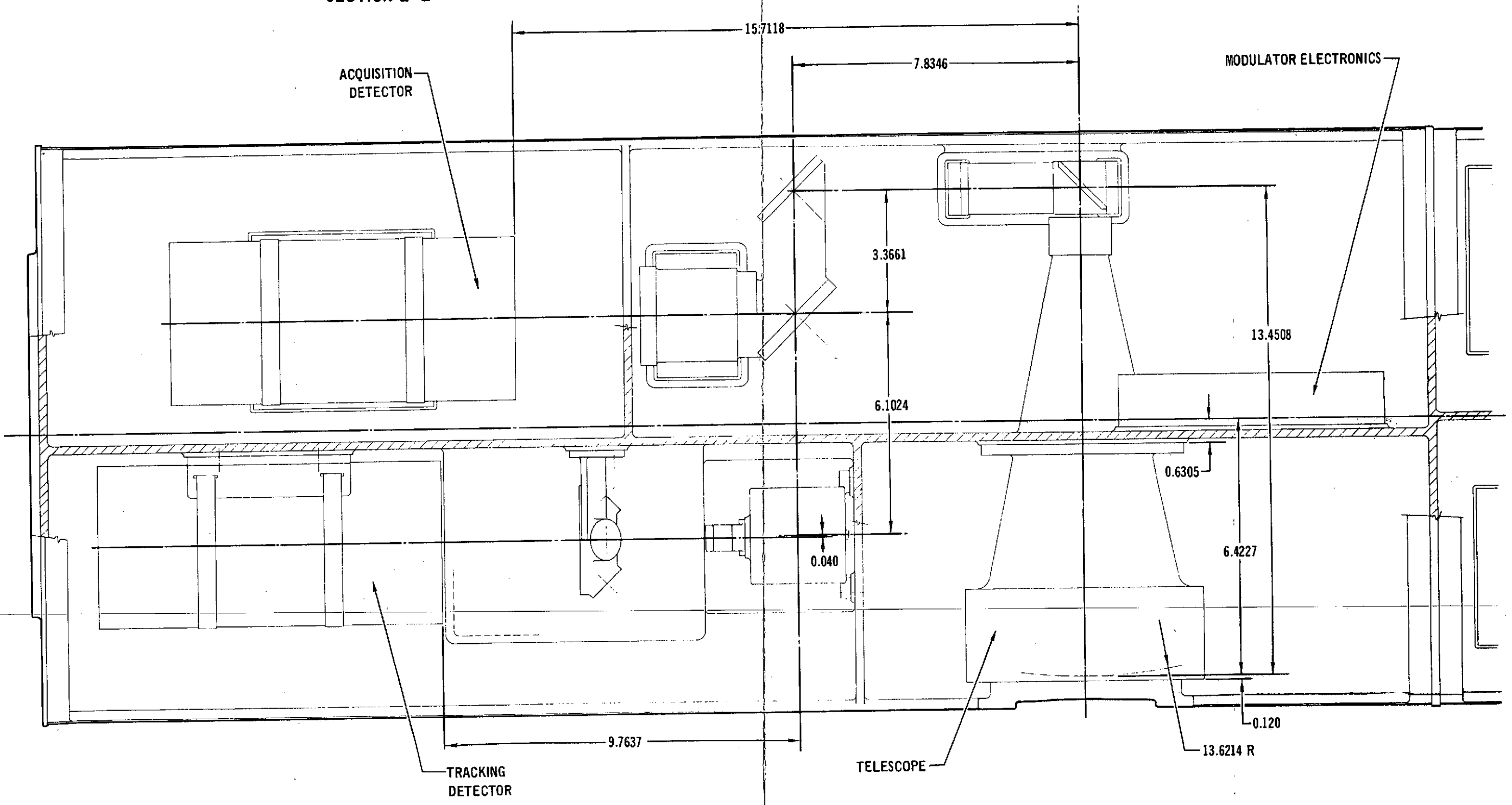


ALL DIMENSIONS IN INCHES

FOLDOUT FRAME
1

FOLDOUT FRAME
2

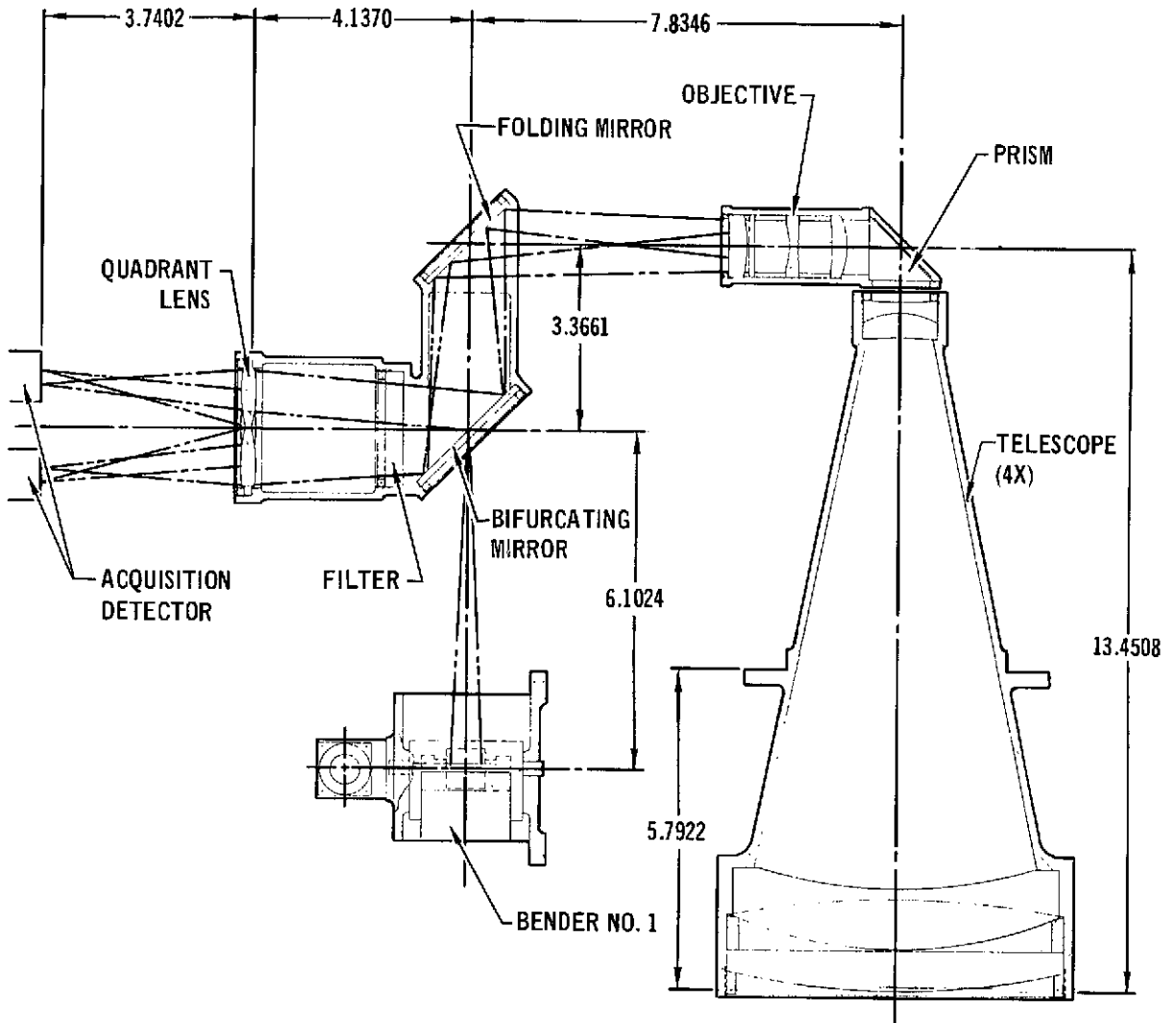
FIGURE 95 COVER REMOVED
SECTION E-E



ALL DIMENSIONS IN INCHES

2

FIGURE 96 SECTION F-F



ALL DIMENSIONS IN INCHES

FIGURE 97 SECTION G-G

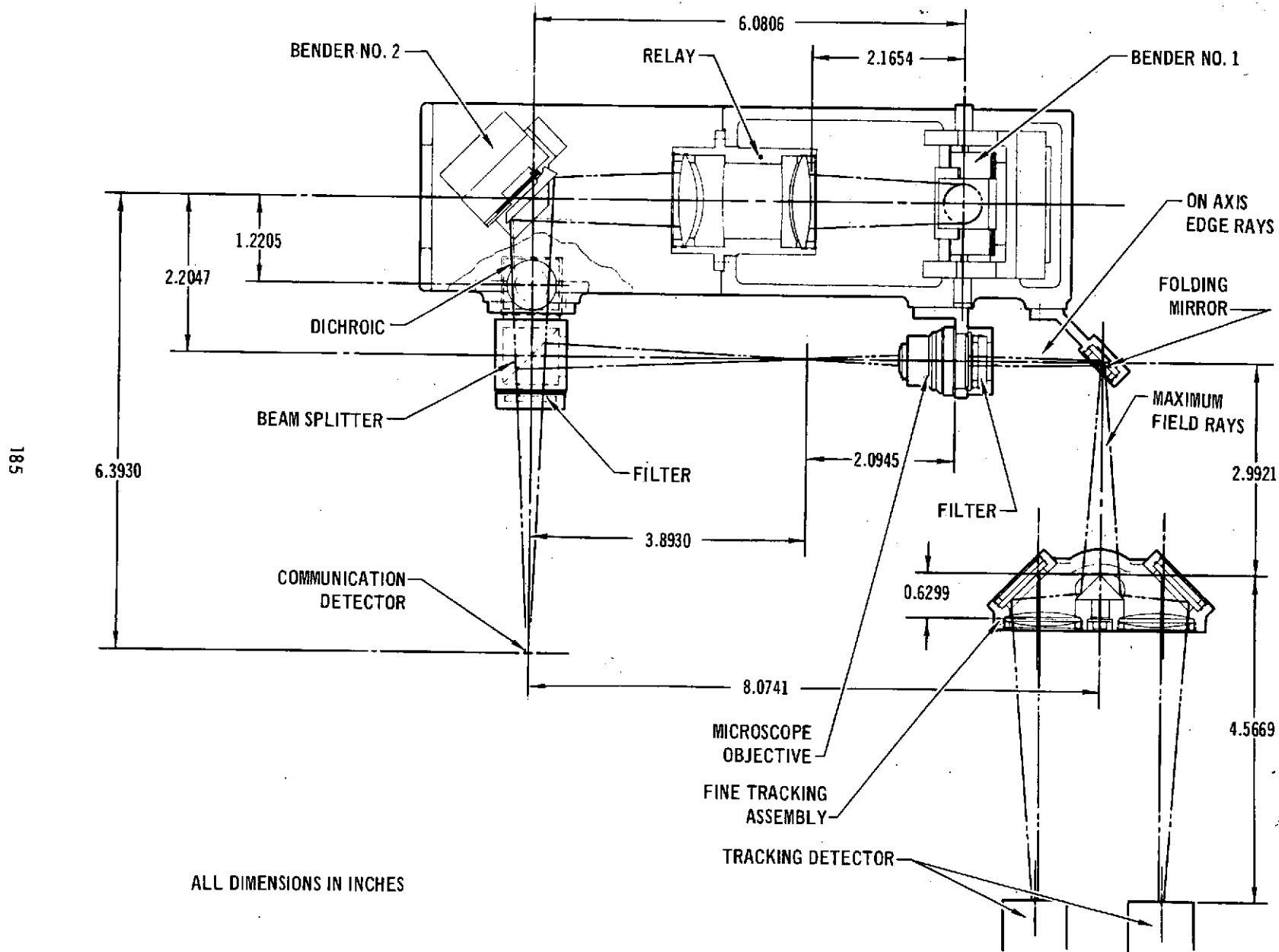
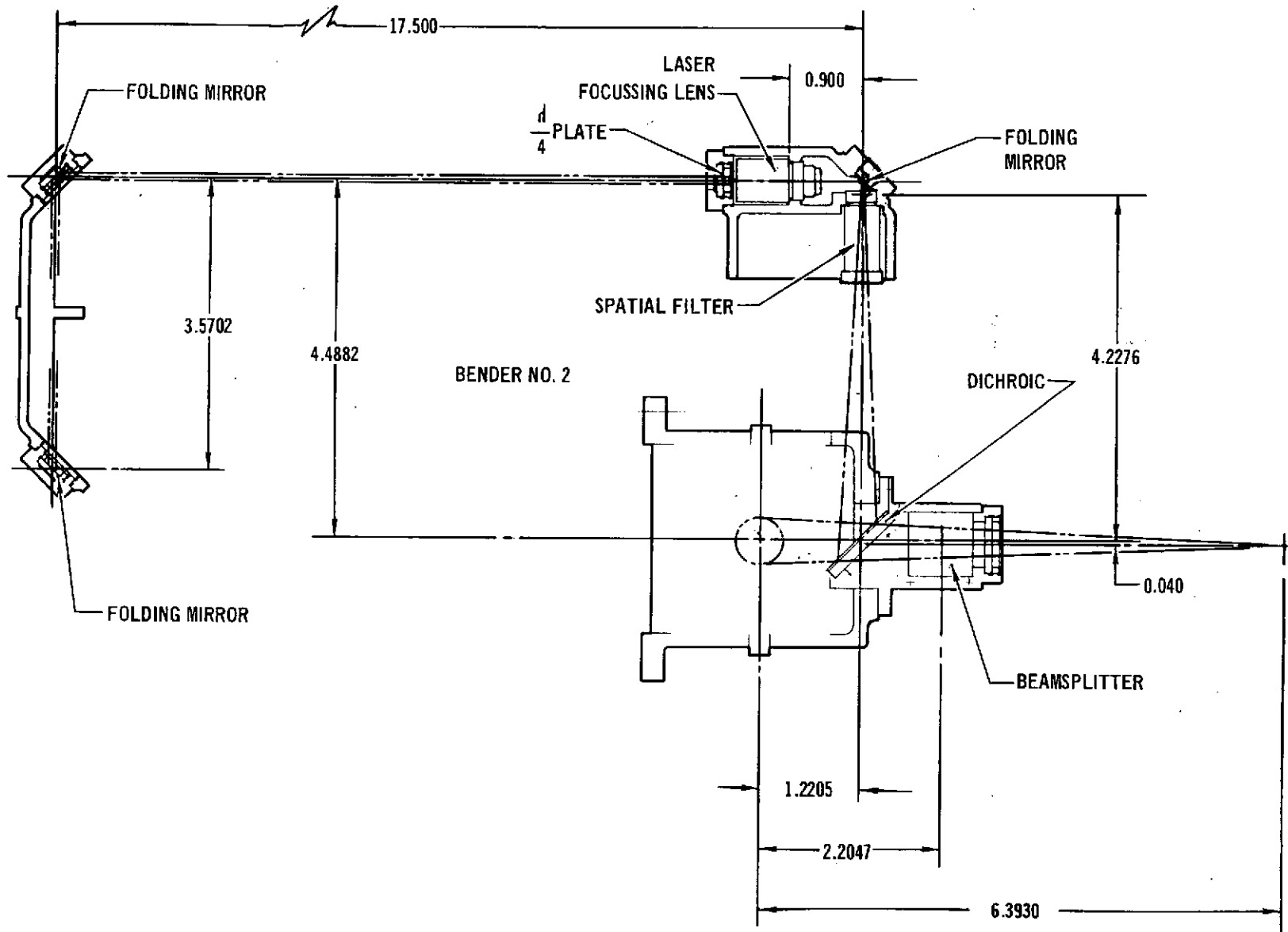


FIGURE 98 SECTION H-H



981

ALL DIMENSIONS IN INCHES

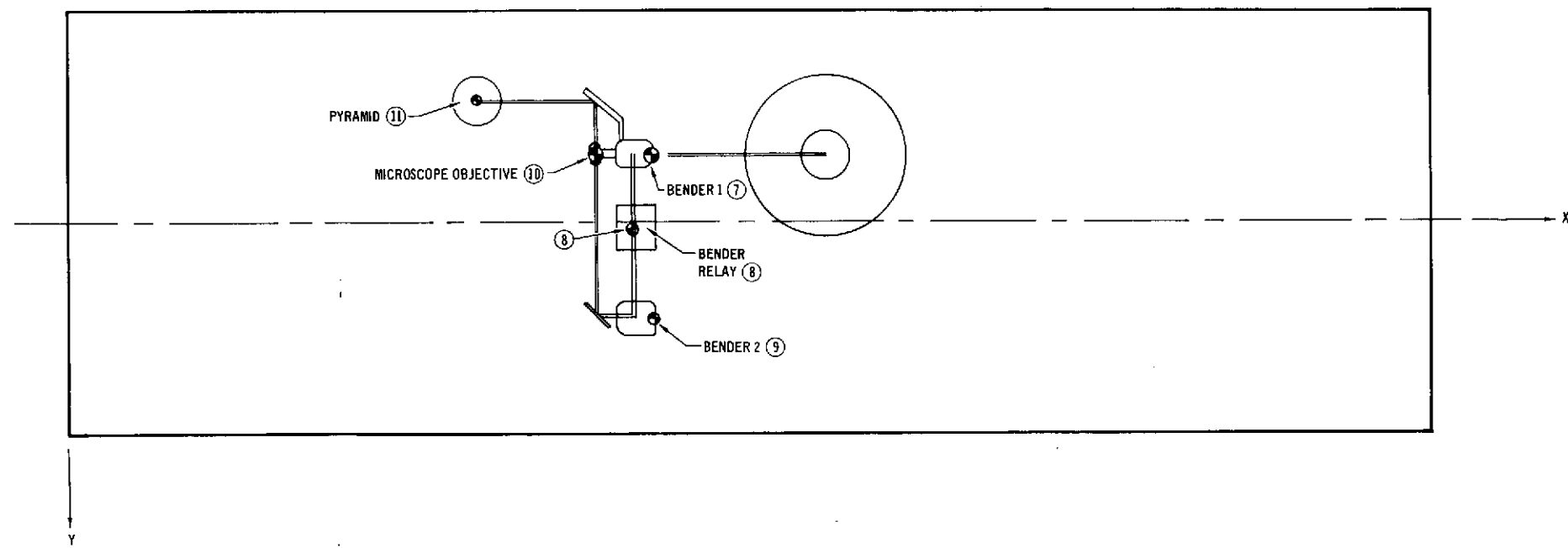
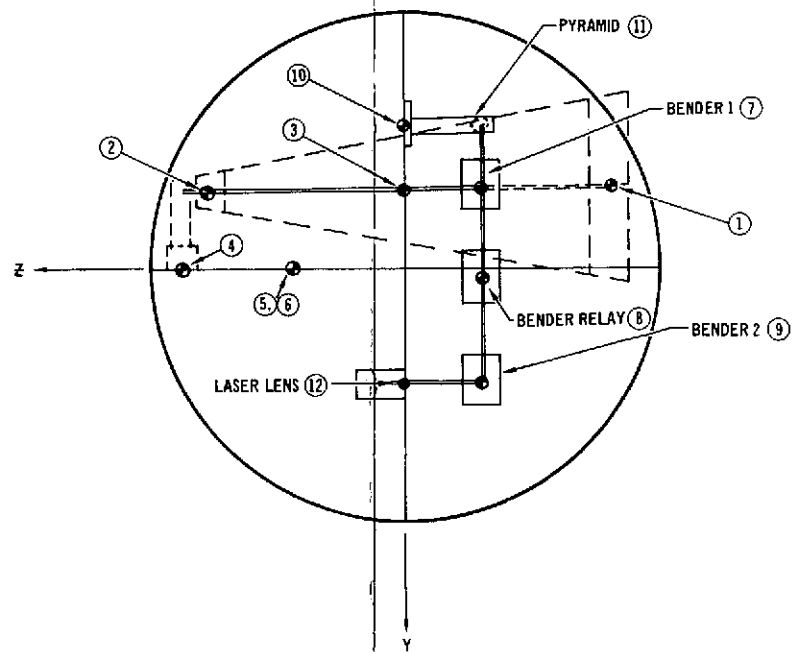
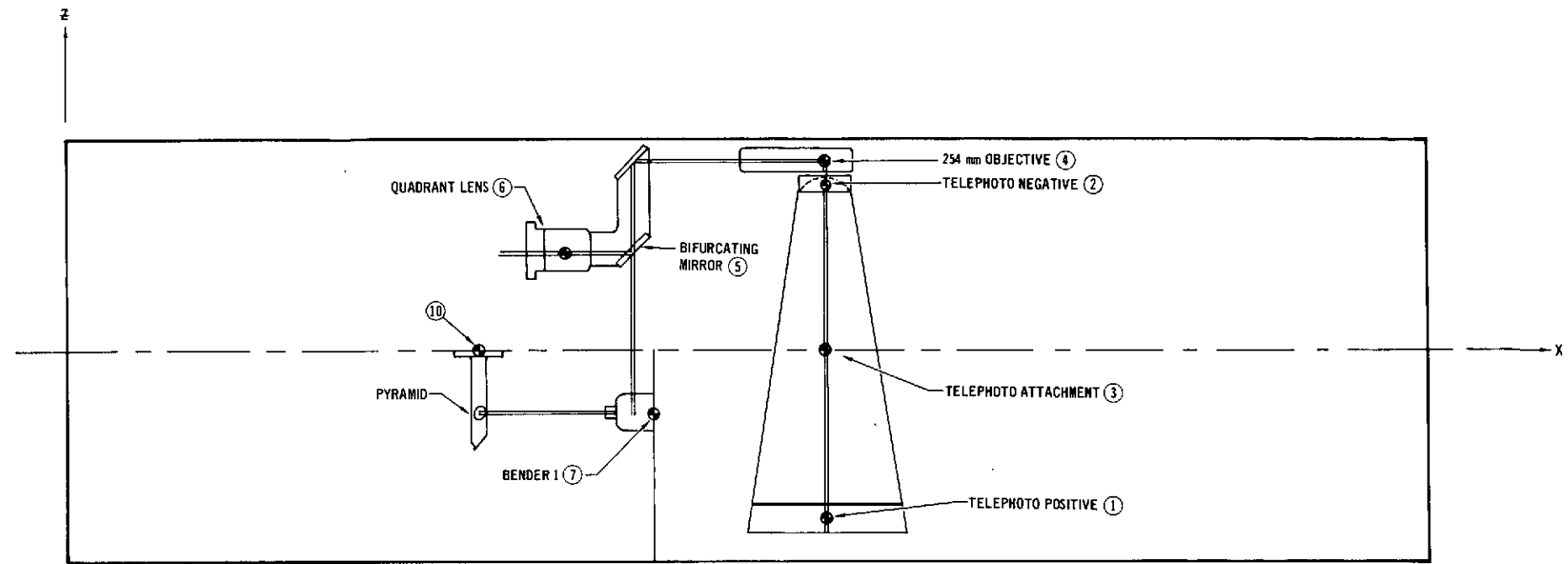
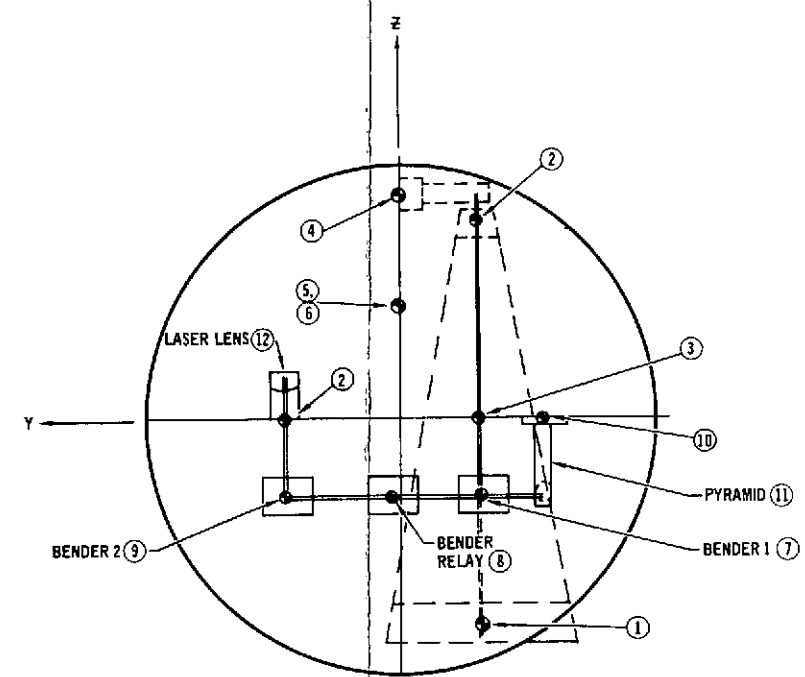
Summary results of the thermal analysis of the optical component support structure for the transceiver package are presented. A 130-node HEATRAN thermal model was developed to simulate the effects of conduction, radiation, thermal capacitance, heat sources, and component heat loads. Calculations were performed for simulated "hot" and "cold" nominal missions to provide bracketing worst cases. The entire package cools rapidly during ascent with most temperatures approaching the ambient temperature of -50°F . At two hours after launch when the laser system is activated, the maximum temperature differences occurring for the telescope barrel, individual lenses, and the mounting plates are 33, 1.6, and 7°F . At the end of the mission, the telescope barrel and lens ΔT s have been reduced to 3°F and 0.22°F . Because of the heating from the laser, the support plate ΔT increases to 38°F .

Insulation details have not been examined in this study. The use of a layer of insulation inside the cylindrical cover and isolation connections would retard the ascent cooling and raise the nominal equipment operating temperatures should that be desirable.

Deflections and rotations, due to thermal gradients, of critical components of the High Data Rate Optical Transceiver Terminal were determined. Locations of items within the terminal for which deflections were calculated are shown in Figure 99. The optical path is indicated by the solid dark line. It is important that items within the terminal do not deflect and rotate significantly relative to each other and alter the optical path. Deflections are due to thermal gradients caused by solar heating and internal heating from equipment items.

The results of the deflection analysis were integrated into a comprehensive optical system analysis program to determine the image degradation and transmit/receive collinearity error. The resulting optical performance data will aid in determining

FIGURE 99 BALLOON EXPERIMENT GENERAL ARRANGEMENT



FOLDOUT FRAME

1

FOLDOUT FRAME

2

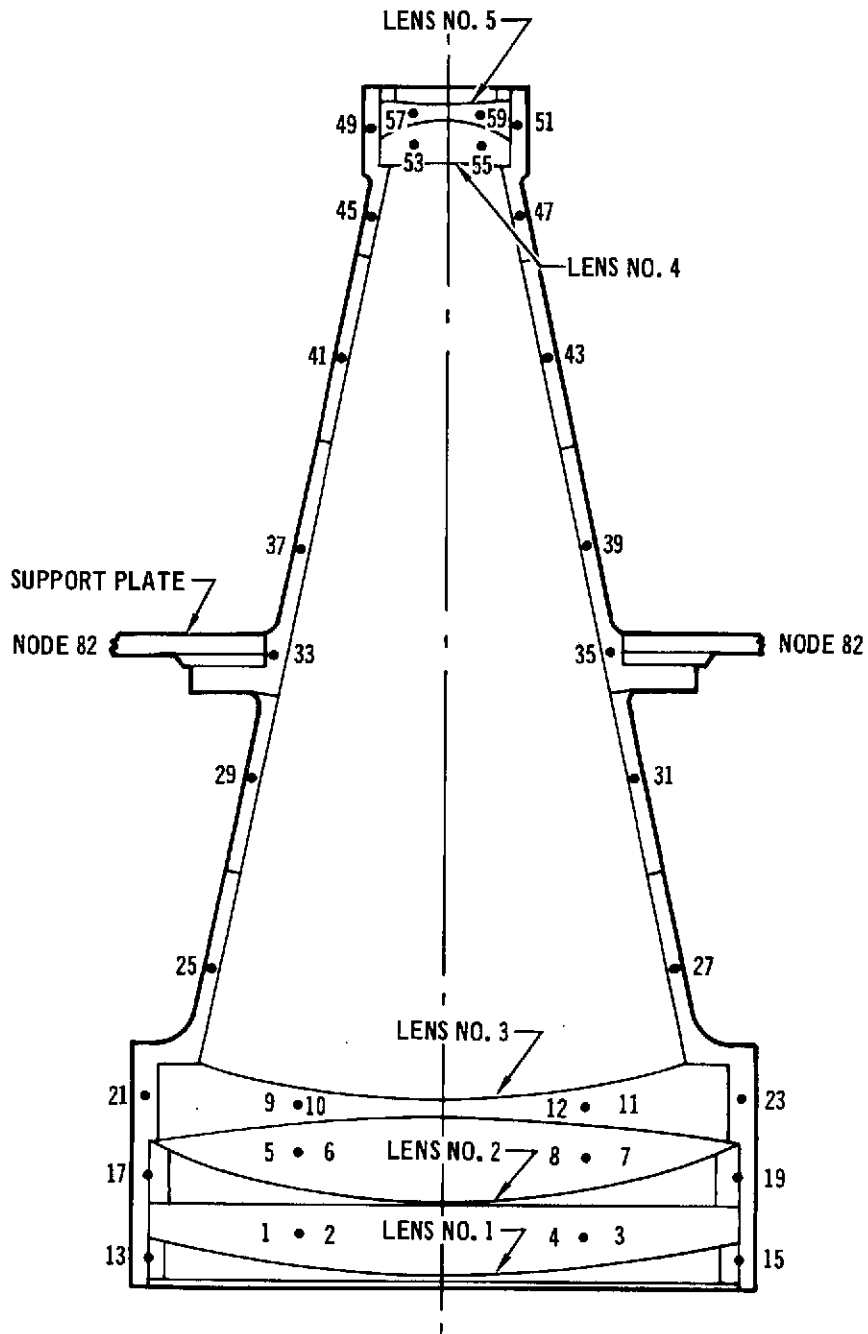
the final adjustment to optical element position during the fabrication process.

Transceiver Package Thermal Analysis - The thermal model has been constructed to model the HDR balloon package. The thermal model consists of 3 major segments which are combined to provide the model of the entire package. The first segment, the telescope, consisting of the barrel and 5 lenses, is composed of 60 thermal nodes as shown in Figure 100. Models of the second and third segments, the package cylindrical cover, and equipment mounting plates, are shown on Figure 101. Fourteen nodes are used to represent the cylindrical cover, 12 of which are divided around the surface with one on each end. The cross support structure is represented by 30 thermal nodes. Thermal properties of the component materials are shown in Table 20 . External surfaces subjected to solar and albedo radiation were assigned a solar absorptivity equal to the emissivity of 0.8 used for both internal and external surfaces. In addition to the radiative heat transfer, free convection (Grashof number dependent) heat transfer was computed for all externally exposed nodes.

Component power levels and the thermal nodes to which they were attached are shown in Table 21 .

For mission simulation the trajectory for the Balloon Atmospheric Propagation Experiment Flights of 1970 (BAPE I), Reference 3 reproduced in Figure 102 , was used. The major portion of the mission will be at about a 100,000 ft altitude. For all calculations, the laser communications package was turned on 2 hours after launch, a nominal ascent time, and remained on for the 8-hour calculation duration although this would probably exceed the available power. A simplified representation of the possible external environments was used to obtain bracketing cases. The cylindrical package in this analysis was oriented perpendicular to incident solar rays with the telescope facing the earth.

FIGURE 100 . TELESCOPE THERMAL MODEL



NOTES:

1. DIVIDED INTO 90° SECTORS
2. SKIN OF BARREL, 0.14 INCHES
3. CONICAL BARREL LENGTH, 9.6 INCHES

FIGURE 101 CYLINDRICAL COVER AND SUPPORT PLATE THERMAL PROGRAM

NOTES:

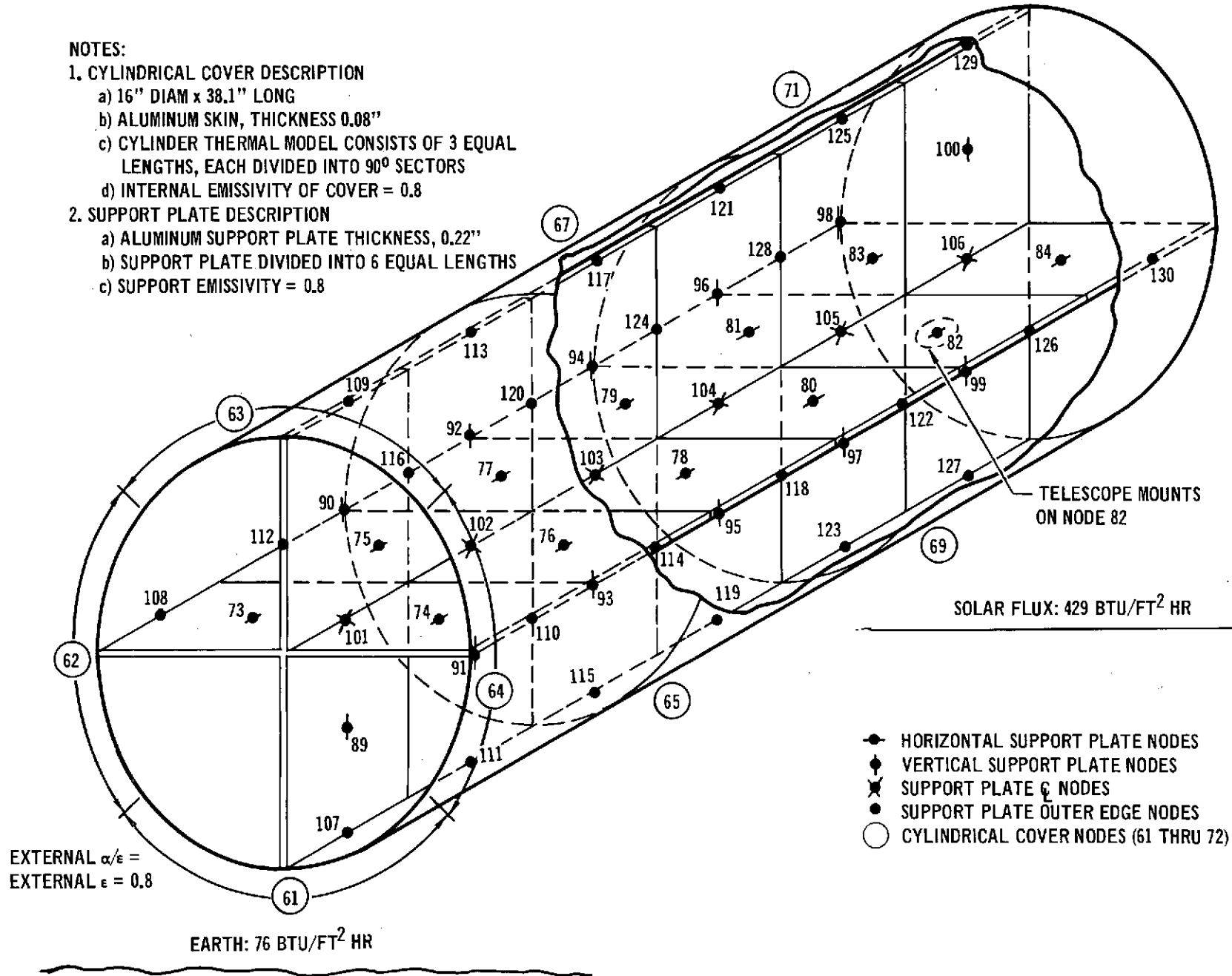
1. CYLINDRICAL COVER DESCRIPTION

- a) 16" DIAM x 38.1" LONG
- b) ALUMINUM SKIN, THICKNESS 0.08"
- c) CYLINDER THERMAL MODEL CONSISTS OF 3 EQUAL LENGTHS, EACH DIVIDED INTO 90° SECTORS
- d) INTERNAL EMISSIVITY OF COVER = 0.8

2. SUPPORT PLATE DESCRIPTION

- a) ALUMINUM SUPPORT PLATE THICKNESS, 0.22"
- b) SUPPORT PLATE DIVIDED INTO 6 EQUAL LENGTHS
- c) SUPPORT EMISSIVITY = 0.8

191



**TABLE 20
THERMAL PROPERTIES**

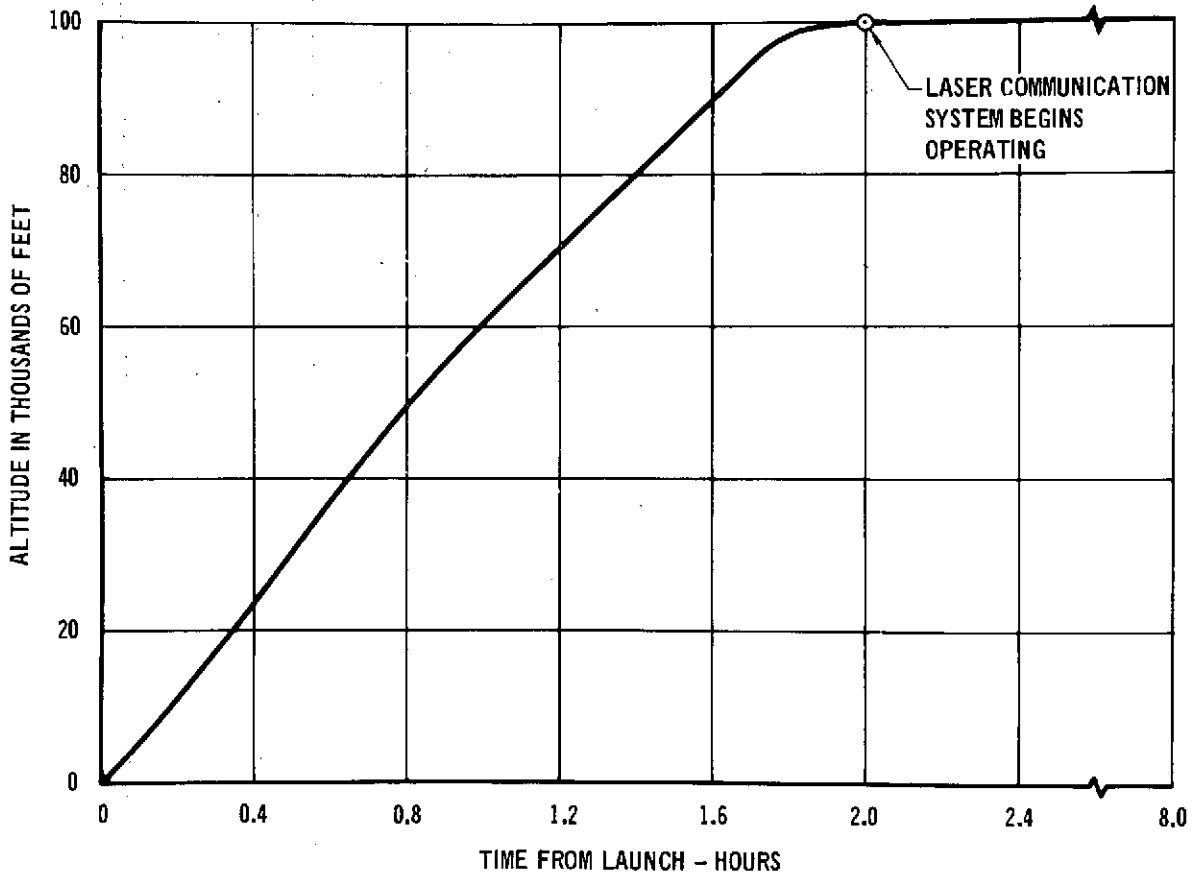
Material	Density (Lb/Ft ³)	Specific Heat (Btu/Lb-°F)	Conductivity (Btu/Hr-Ft-°F)	Thermal Model Item
Invar	503	.123	7.8	Telescope Barrel
Schott Glass (LAKN9)	221	.155	0.525	External Lenses (#1 and #5)
Schott Glass (SF15)	253	.155	0.525	Internal Lenses (#2, #3, #4)
Aluminum Alloy	169	.23	97.0	Cylindrical Cover and support plate

**TABLE 21
LASER COMMUNICATION SYSTEM COMPONENTS
POWER AND THERMAL MODEL LOCATION**

Component Package	Power (Watts)	Power Btu/Hr	Package Mounted on Node
Processing Filter #2	5	17	73 and 75
Tracking Detector	8	27	74 and 76
Laser and Modulator	50 44	337	81 and 83
Modulator Electronics	4	14	84
Processing Filter #1	5	17	90
Processing Filter #1 and Acquisition Detector	5 8	44	92
Communications Detector (One-Half)	11	37	95

The external thermal environment used for the package varies according to alternate times when the mission could be performed. The so-called "nominal" mission assumes a nighttime launch. At two hours after launch time, the laser communication system begins operating and the solar flux (429 Btu/ft²-hr) is "turned on." The second and third cases considered included a "hot"

FIGURE 102 TYPICAL FLIGHT PROFILE



case in which the sun was assumed "turned on" for the entire mission and a cold case in which no sun was assumed whatsoever.

Earth emitted radiation ($76 \text{ Btu/ft}^2\text{-hr}$) and earth reflected solar radiation ($145 \text{ Btu/ft}^2\text{-hr}$) also provided significant energy input to those sectors with a view of the earth. Some of the package surfaces were assumed to face zero temperature deep space an approximation neglecting shielding by the balloon itself.

Typical node temperature response histories are shown in Figures 103 through 107. Support plate and cover results to the hot and cold environment are shown in Figures 103, 104, and 105. Curves show that the temperature falls rapidly during the ascent period not

FIGURE 103 TYPICAL COMPONENT RESPONSE "HOT" ENVIRONMENT

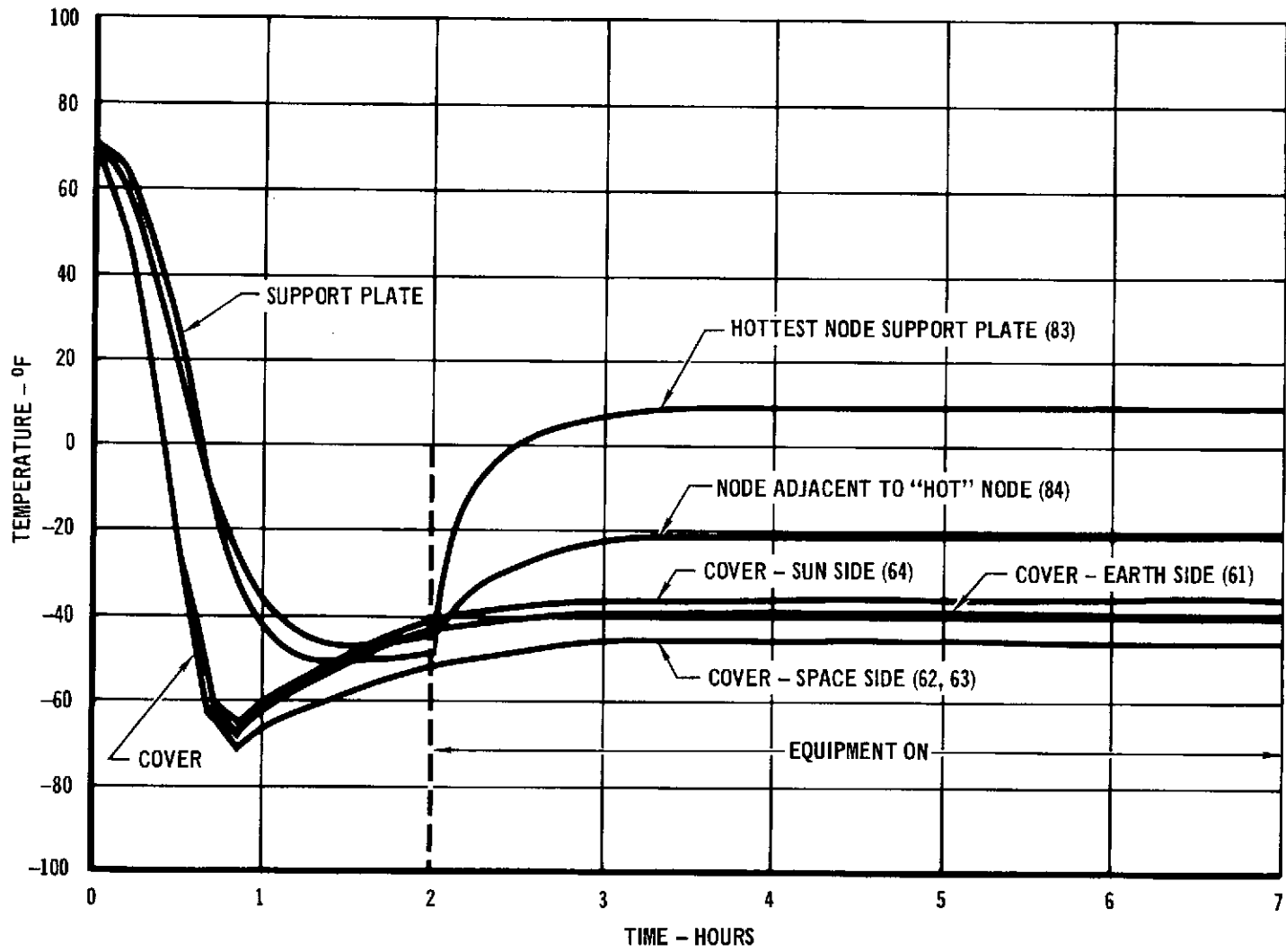


FIGURE 104 TYPICAL COMPONENT RESPONSE "COLD" ENVIRONMENT

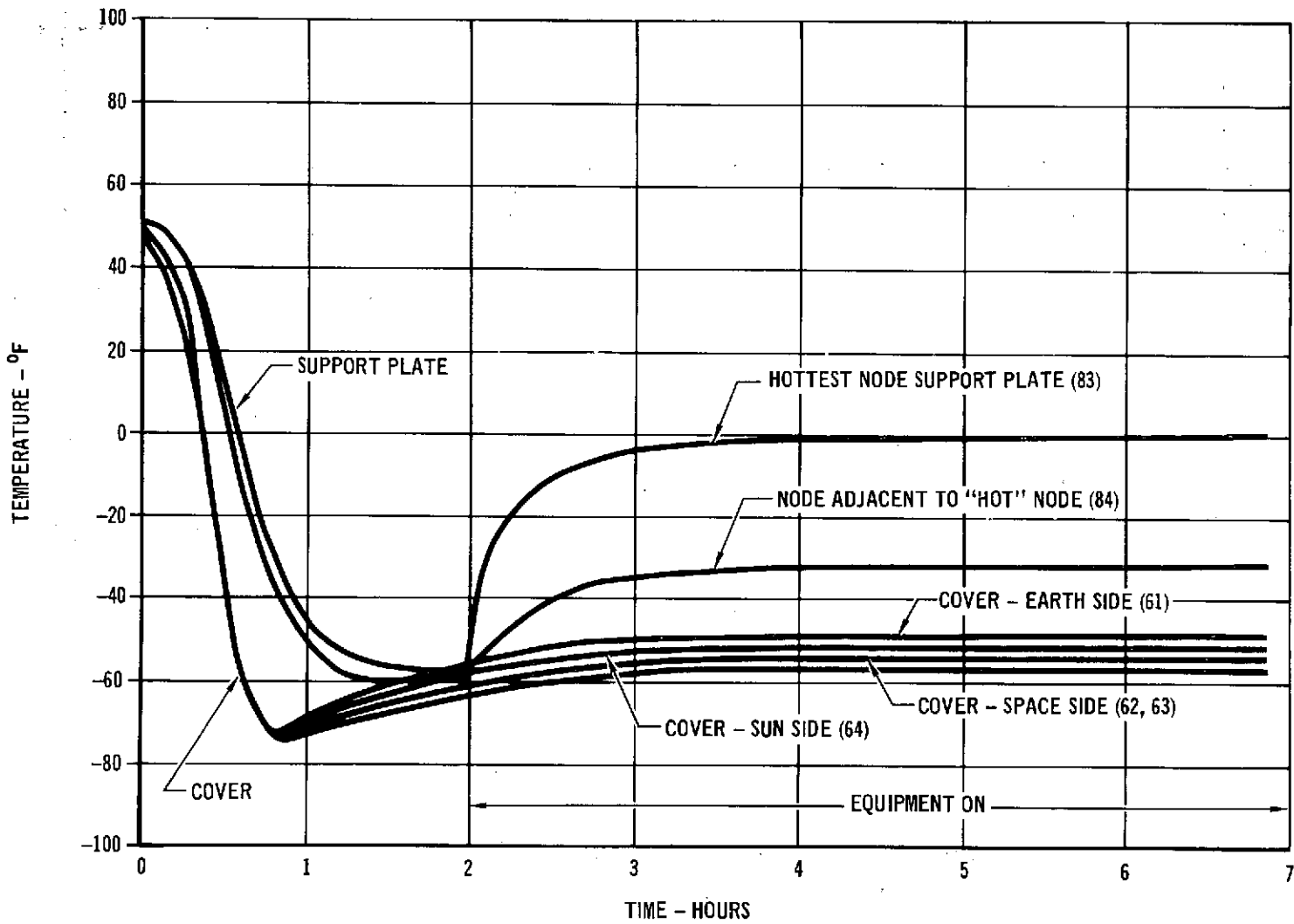


FIGURE 105 COVER THERMAL RESPONSE - THERMAL ISOLATION AT CONNECTION POINTS

- HOT ENVIRONMENT
- CONSTANT AMBIENT TEMPERATURE WITH ALTITUDE

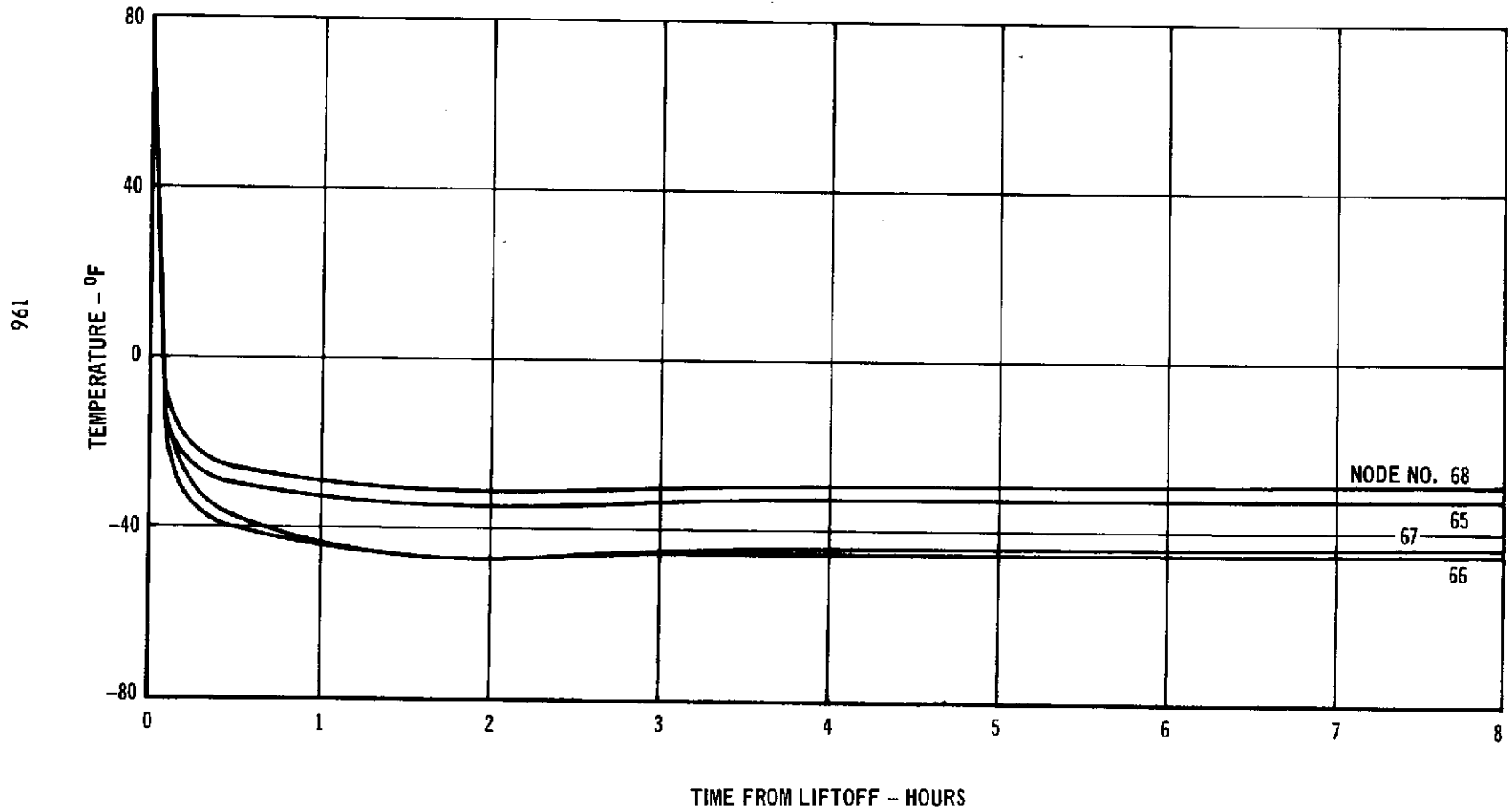


FIGURE 106 SUPPORT PLATE THERMAL RESPONSE -
THERMAL ISOLATION AT CONNECTION - I

- HOT ENVIRONMENT
- CONSTANT AMBIENT TEMPERATURE WITH ALTITUDE
- CONSTANT AXIAL LOCATION

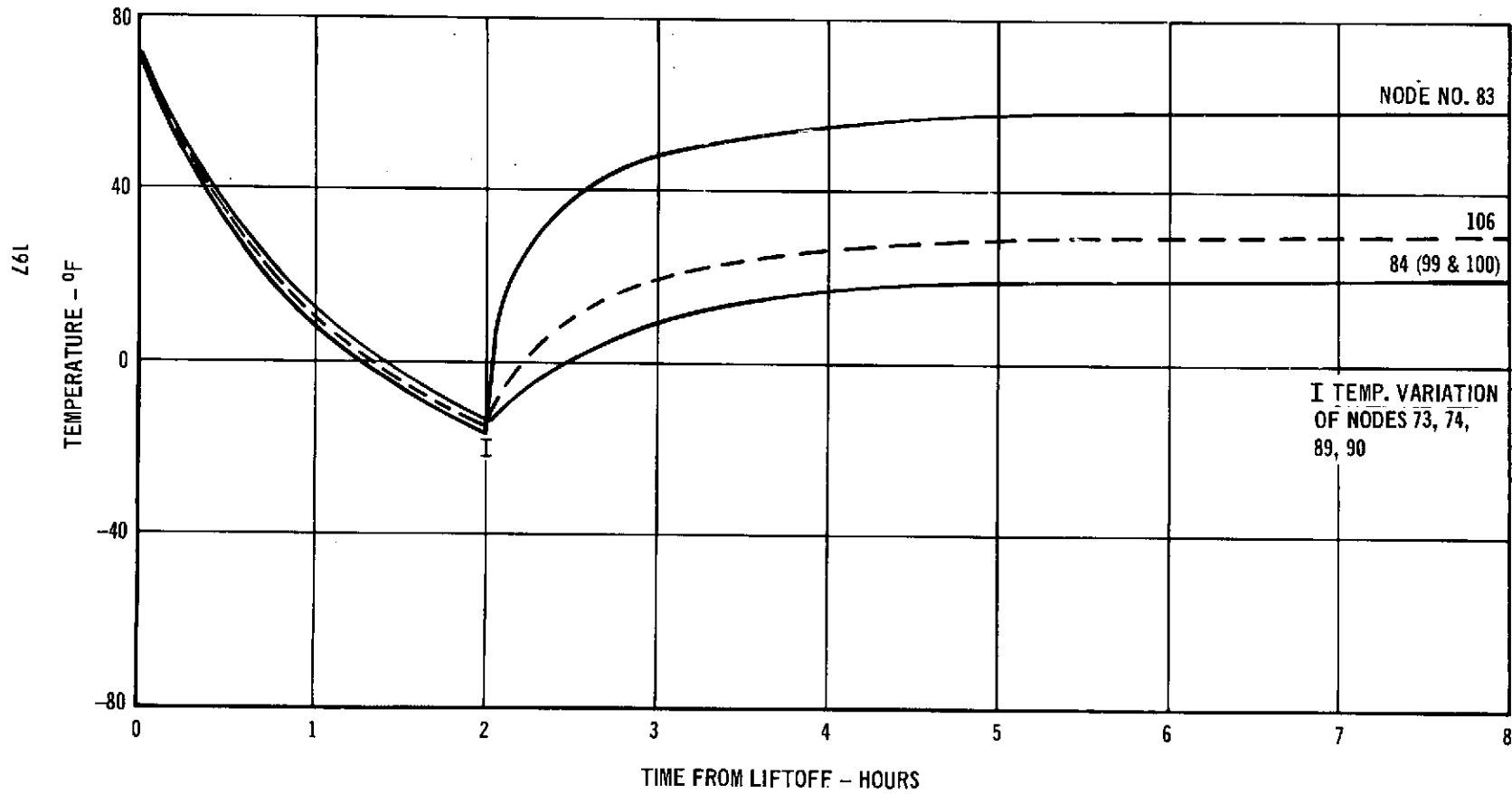
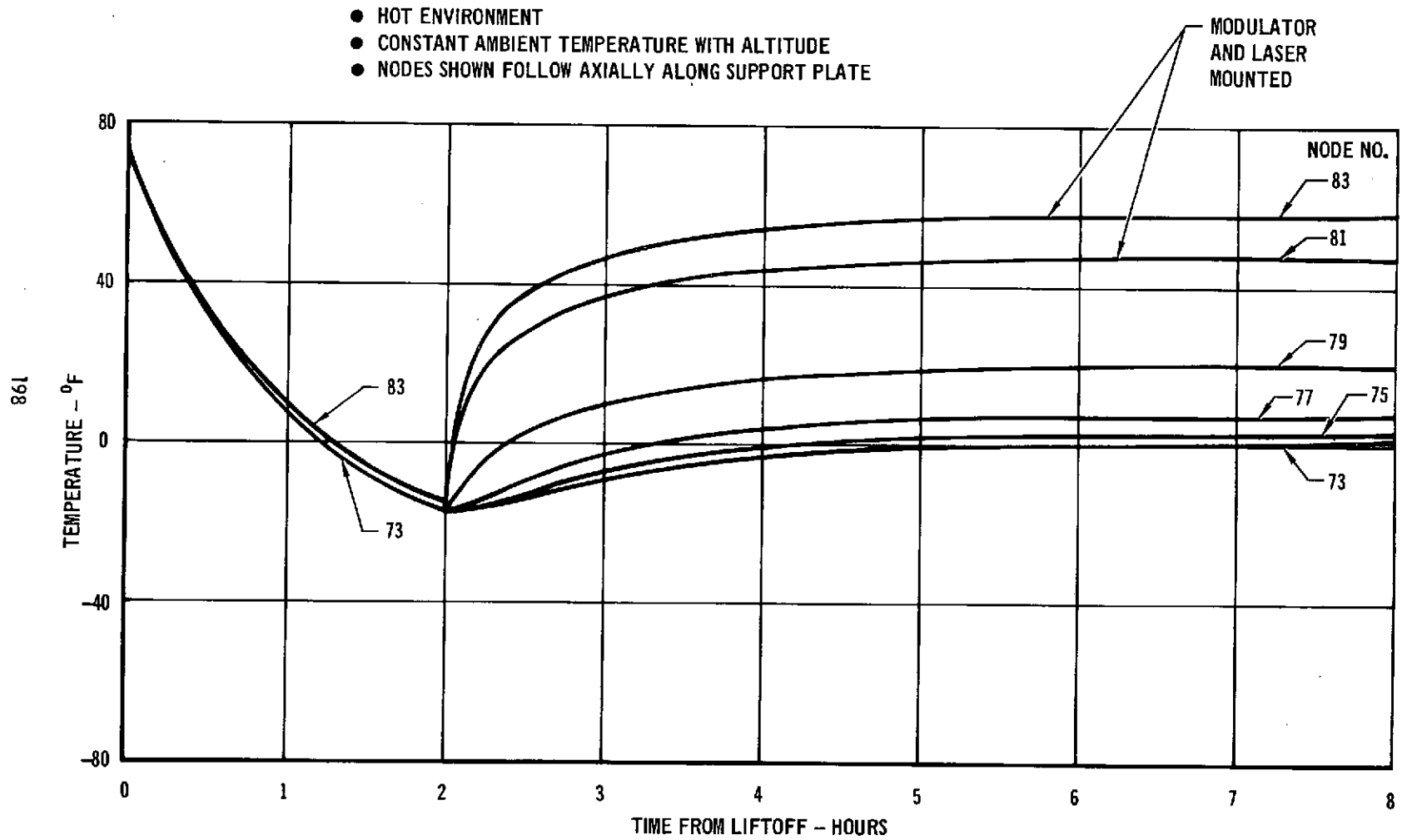


FIGURE 107 SUPPORT PLATE THERMAL RESPONSE -
THERMAL ISOLATION AT CONNECTION - II



only for the exposed cover, but also for the support plate which is thermally connected to the cover by conduction and radiation. The minimum in the cover temperature history at about 0.8 hour is a mirroring of the ambient temperature variation with altitude. This temperature falls below -70° , but rises back to -50° at 100,000 feet. At two hours when the equipment is activated, the temperature rises rapidly in about an hour and a half at the hottest node (No. 83 to which the laser is connected) to a steady state temperature. The gradient established between this node and the adjacent node, (No. 84), is then maintained throughout the mission. The hot case components operate at a nominal temperature about 10° hotter than those for the cold case without solar irradiation. In addition, the cover temperature possesses a somewhat greater temperature difference from side-to-side with the sun on. At two hours after launch, temperature differences as large as 7°F may exist between adjacent support plate nodes. This difference increases to 38°F at the laser during laser operation. The telescope and lens temperature histories are shown in Figures 108 and 109. Again, the temperatures fall during ascent, but instead of rising abruptly when the equipment is turned on, they stabilize in about an hour at a steady state condition. At two hours after launch, the calculated axial temperature variation on the telescope was a maximum of 33°F .

With a maximum circumferential variation of 5°F , individual lens' quadrants differ by less than 1.6°F . As laser operation continues, these gradients are reduced. Steady state axial telescope temperature variations are only 3°F and lens' quadrant variations are 0.22°F . The principal difference between the cold environmental case and the hot case, again, is a 10°F nominal increase in operating temperatures.

In addition to the cases just discussed, some preliminary calculations were made for missions in which the conductive connection between support plate and the cylindrical cover was not

FIGURE 108 TYPICAL TELESCOPE RESPONSE "HOT" ENVIRONMENT

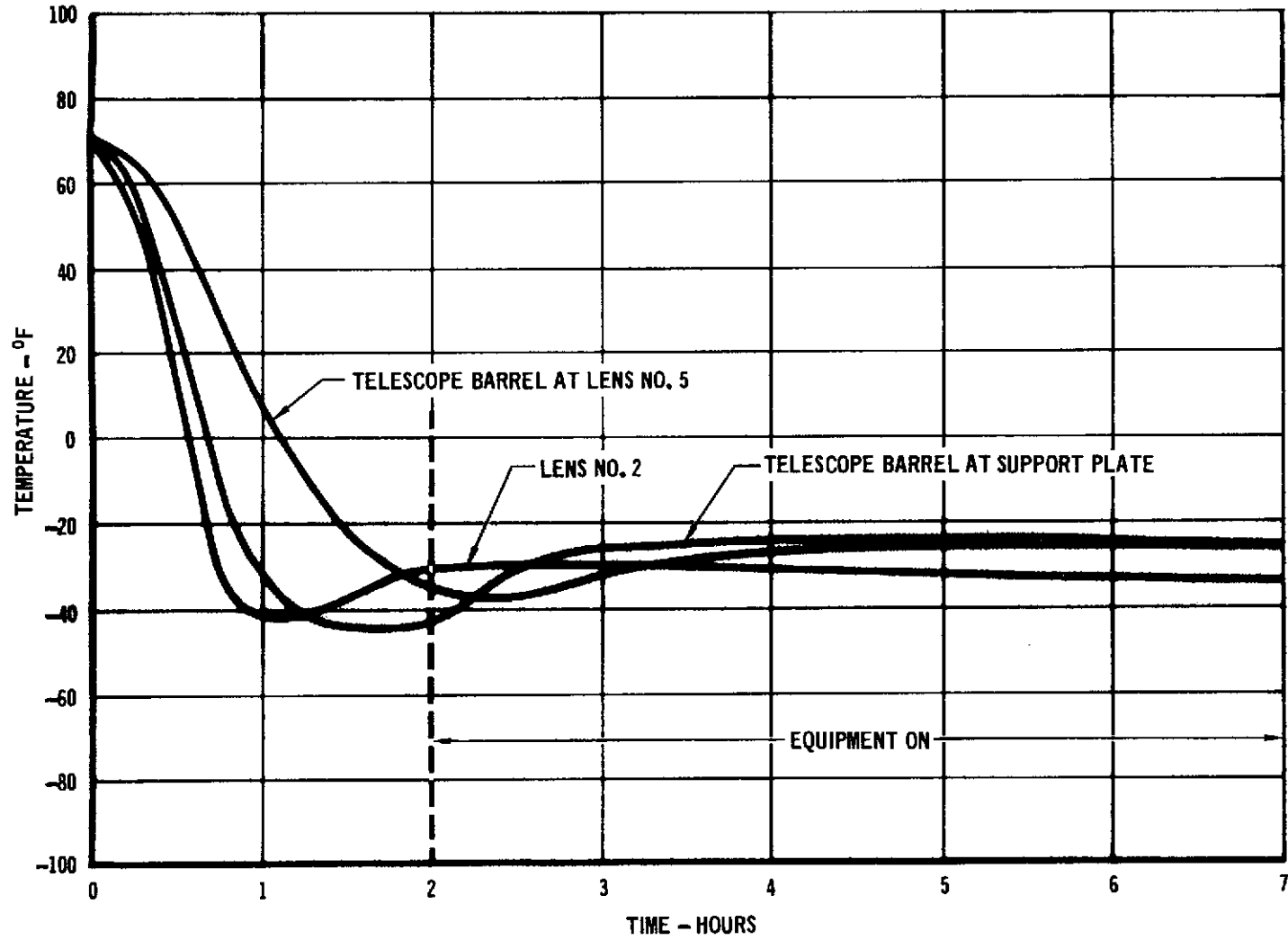
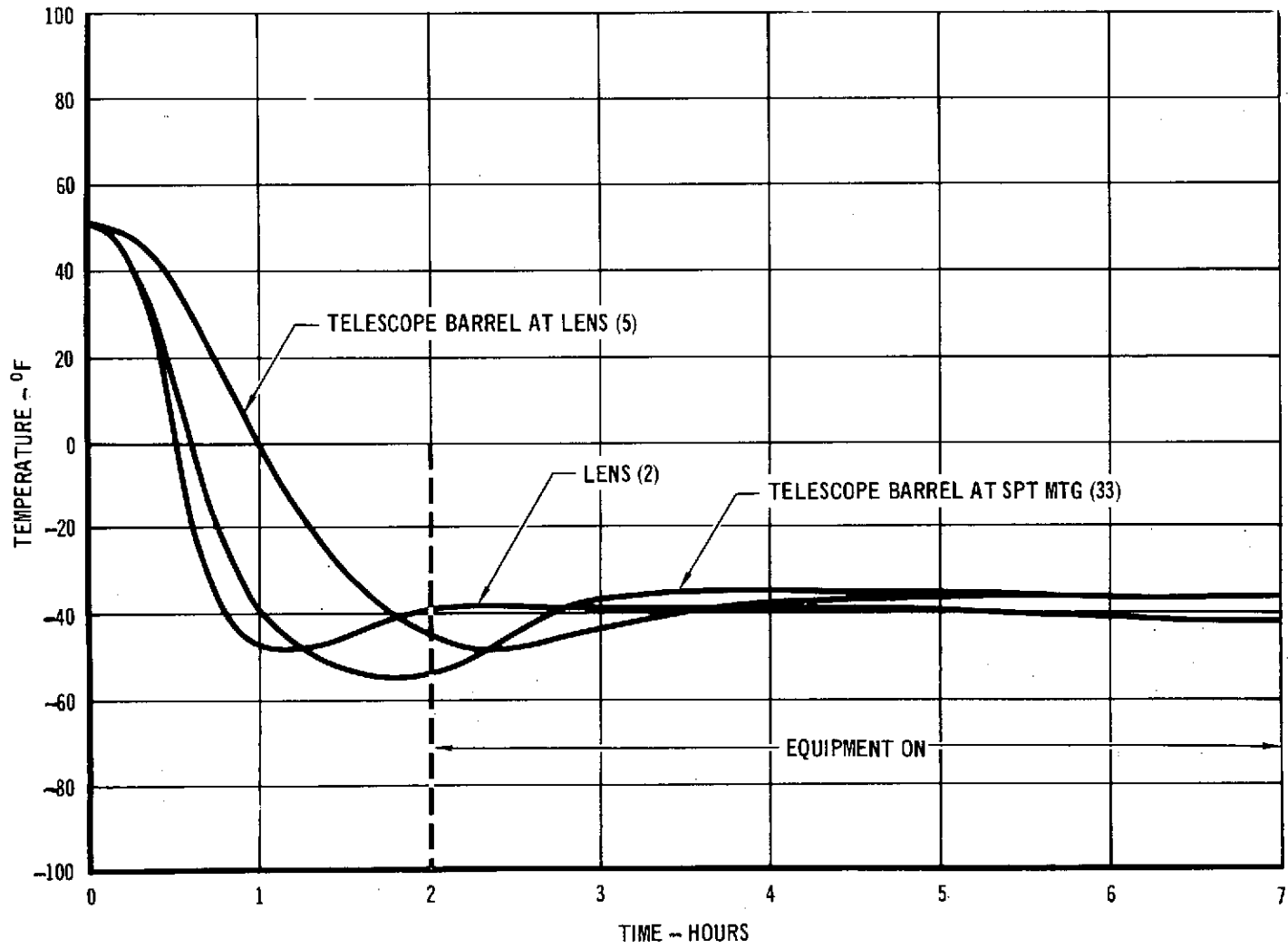


FIGURE 109 TYPICAL TELESCOPE RESPONSE "COLD" ENVIRONMENT



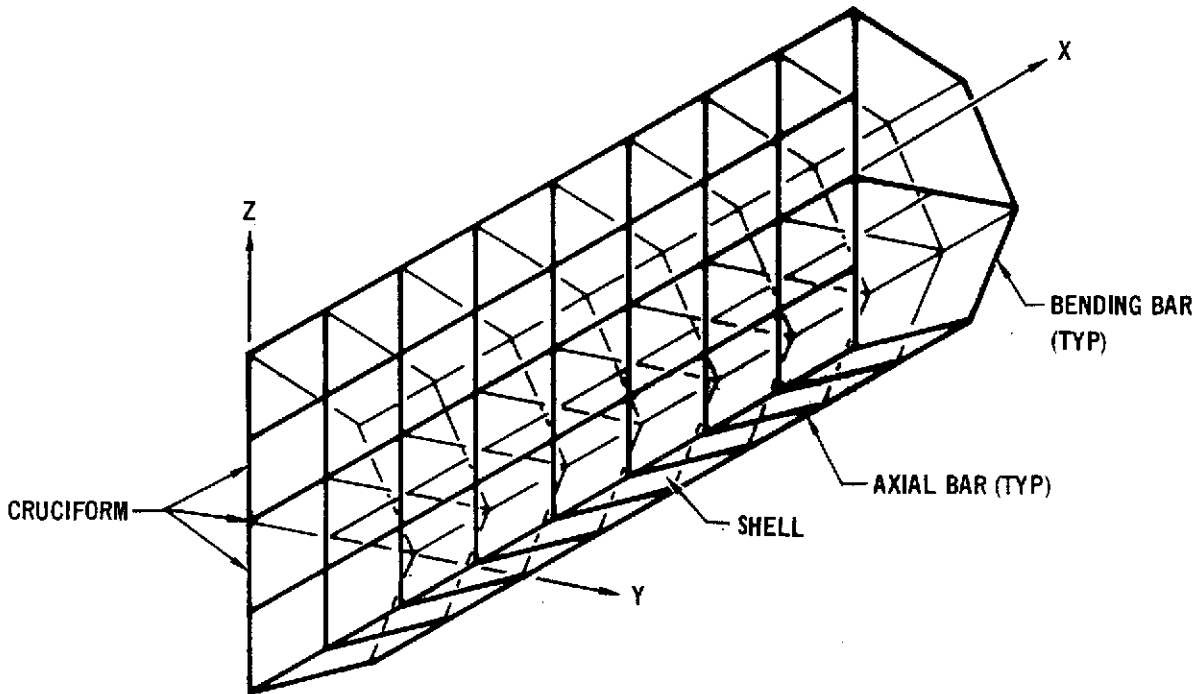
made. This model simulates the use of thermally isolating connectors between the support plate and the cylindrical cover although it does not represent the effect of placing insulation around the entire cover periphery. Figure 105 shows the temperature at one axial location around the cylindrical cover periphery for the hot case as a function of time. Node 68 is the portion of the cover facing the sun while node 66 is on the opposite side. Node 65 faces the earth. The maximum temperature gradient is 16°F between node 67 and node 68 and occurs two hours after launch. For these preliminary calculations no variation of ambient temperature with altitude was included. Thus, no temperature minimum was observed at 0.8 hours. For an all-night or "cold" mission, the temperatures are around 12° colder and the maximum ΔT across the cover is 14°F. However, the maximum temperature difference is between the upper and lower surfaces, nodes 67 and 65. This occurs because the earth-emitted heat flux is the only source of energy.

The temperature response for nodes of support structure are shown in Figures 106 and 107 for a hot case with the support isolated from the cover. It will be noted that for this case, the support structure is about 40° warmer than for the corresponding case shown in Figures 103 and 104, in which the cover was connected to the support structure.

For strain determination, the extreme cases at laser activation time and mission end five hours later were used. The node temperatures for these cases are shown in Table 22.

Deflection Analysis - A finite element model of the entire terminal package was constructed for computer analysis (Figure 110). The results of an IRAD study being conducted by MDAC-East indicate that conventional finite elements can be used to accurately predict rotations and deflections of the magnitude being considered. In the IRAD study, a laser detector measurement system capable of resolving rotations to one arc second

FIGURE 110 FINITE ELEMENT STRUCTURAL MODEL



was used to measure support platform and equipment box rotations. Predicted and measured rotations due to mechanical and thermal loads were compared and agreed within two arc seconds.

The Finite Element Modeling (FEM) computer program aided in modeling the structure. The FEM program allows the user to build a three-dimensional finite element model at a Computek interactive graphics terminal. The terminal is connected to an XDS Sigma 7 conversational direct access (time sharing) computer. The Computek terminal contains a cathode ray tube that displays the structural model as it is being built. The FEM program defines the geometry in a format compatible with finite element programs. The user has the option of using axial bar, bending bar, shear panel, triangular plate, and quadrilateral plate elements for his model.

Axial bars, bending bars, and shear panels were used to model the cruciform and shell structure for solution using the finite element program Computer Aided Structural Design (CASD). Since the structure is symmetric about a plane through the center of the shell, it was necessary to model only half the structure. Axial bar and bending bar members for half the structure are shown in Figure 110. Bending bars were used as circumferential members and axial bars run longitudinally. Shear panels were used to simulate cruciform and shell shear stiffness. For the total structure, 88 axial bars, 72 bending bars and 128 shear panels were used. The structure was assumed to be restrained for motion in three directions at one end ($X = Y = Z = 0$). This is consistent with the gimballed attachment to the gondola. The telescope was not included in the finite element model, however, rotations and deflections of telephoto positive and negative lenses relative to the telescope attachment were calculated manually.

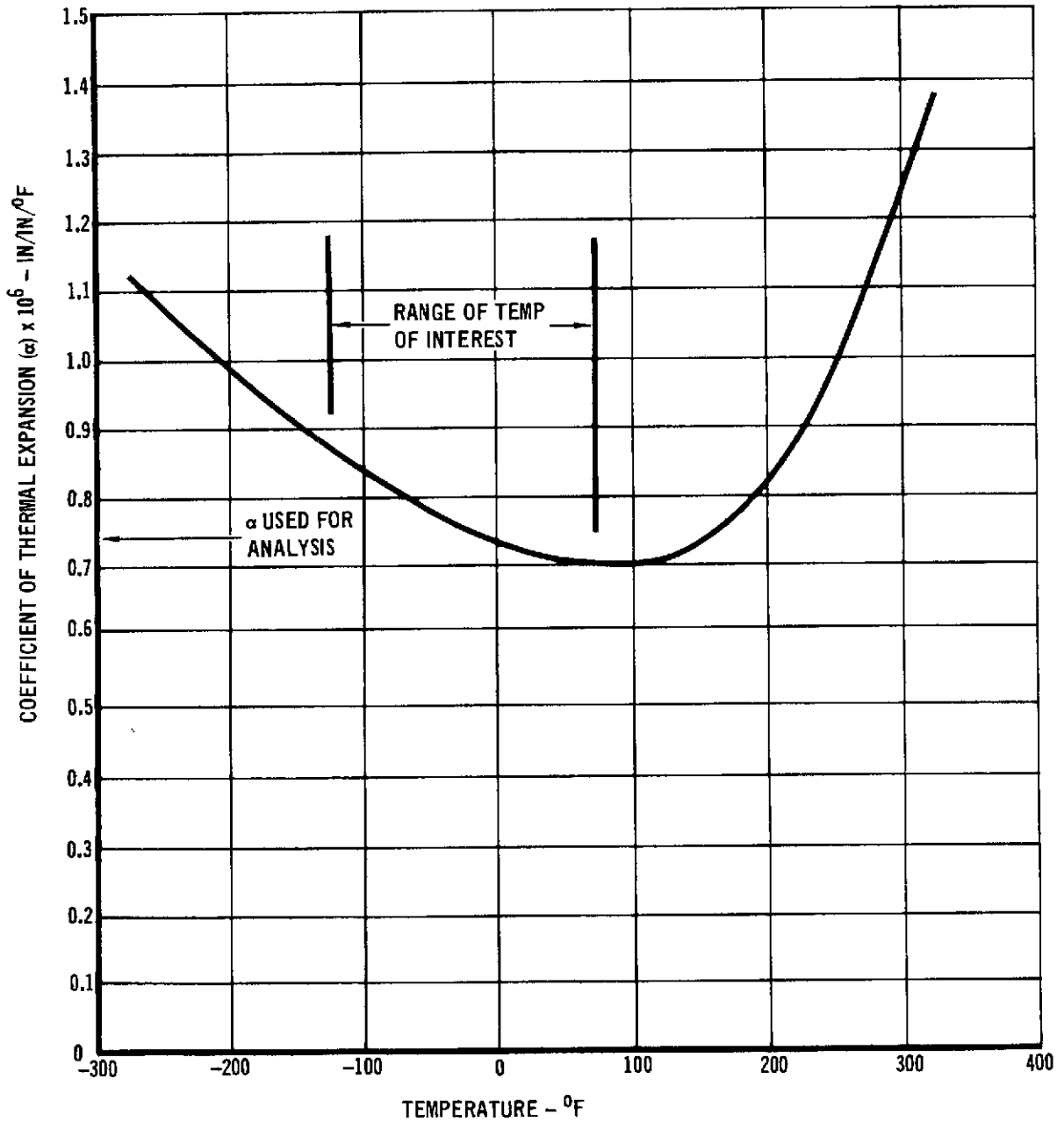
Two temperature conditions were analyzed. Both conditions are for daytime launch. Condition A is two hours after launch just prior to turning on electronics equipment. Condition B is seven hours after launch when structural temperatures resulting from equipment heating have stabilized.

Temperatures were applied to the structural model at node points. The computer program uses these applied temperatures to calculate bar expansions and contractions and resulting nodal deflections.

The cylindrical shell and cruciform are made of A356 cast aluminum. The coefficient of thermal expansion (α), reported in Reference 22, for this material is 11.9×10^{-6} in./in./°F. The telescope is made of invar which has a very low coefficient of thermal expansion near room temperature. The variation of α with temperature, taken from Reference 23, is shown in Figure

111. The coefficient of thermal expansion for invar was assumed to be 0.75×10^{-6} in./in./°F for the range of temperatures of interest.

FIGURE 111 INVAR HAS LOW COEFFICIENT OF THERMAL EXPANSION



Nodal deflections were obtained from the CASD computer program. Nodal deflections were used to calculate deflections and rotations of the following items:

- o Telephoto Attach
- o 254 mm Objective
- o Bifurcating Mirror
- o Quadrant Lens
- o Bender 1
- o Bender Relay
- o Bender 2
- o Microscope Objective
- o Pyramid
- o Laser Lens

Locations of all items are shown in Figure 99 . Deflections and rotations of equipment items were determined by interpolating between nodal deflections. Since the telescope was not modeled on the computer, Telephoto Positive and Telephoto Negative deflections and rotations were calculated manually and superimposed on Telephoto Attach motion. Resulting deflections and rotations of all components are summarized in Table 23 for the two thermal conditions analyzed.

Optical Tolerance Analysis - Using the data generated by the thermal/structural analysis described above, the resulting image degradation and transmit/receive collinearity were computed. The optical system was modeled in a straight-line fashion for computer analysis. The inversions and reversions of the meridional and sagittal fans due to the folds of the system were introduced into the analysis by means of the transformations shown in Table 24. The physical coordinates shown in the table, X, Y, and Z, are as defined in Figure 99. The computational coordinates, x, y, and z, relate to shifts along and across the unperturbed optical axis. Shifts in

TABLE 23

BALLOON EXPERIMENT CALCULATED COMPONENT DISPLACEMENTS

	COORDINATES			THERMAL CONDITION	DEFLECTIONS			ROTATIONS		
	X (IN.)	Y (IN.)	Z (IN.)		ΔX (IN.)	ΔY (IN.)	ΔZ (IN.)	ΘX (ARC SEC)	ΘY (ARC SEC)	ΘZ (ARC SEC)
1. TELEPHOTO POSITIVE	29.0	-2.5	5.0	A	-0.04112	-0.00176	-0.00074	+41.5	+6.4	+3.8
				B	-0.03595	-0.00421	-0.00045	+39.1	+6.0	+0.3
2. TELEPHOTO NEGATIVE	29.0	-2.5	-6.3	A	-0.04112	-0.00176	-0.00158	+41.2	+6.4	+3.8
				B	-0.03595	-0.00421	-0.00126	+39.1	+6.0	+0.3
3. TELEPHOTO ATTACH	29.0	-2.5	0	A	-0.04112	-0.00176	-0.00109	+41.2	+6.4	+3.8
				B	-0.03595	-0.00421	-0.00081	+39.1	+6.0	+0.3
4. 254 mm OBJECTIVE	29.0	0	8.0	A	-0.04145	+0.00172	-0.01180	-0.9	+3.2	+6.0
				B	-0.03627	-0.00102	-0.00916	+13.0	+15.2	+3.8
5. BIFURCATING MIRROR	19.1	0	3.7	A	-0.02783	-0.00171	-0.00622	-0.5	+1.3	-12.1
				B	-0.02483	-0.00089	-0.00493	-1.0	+5.4	+12.1
6. QUADRANT LENS	19.1	0	3.7	A	-0.02783	-0.00171	-0.00622	-0.5	+1.3	-12.1
				B	-0.02483	-0.00089	-0.00493	-1.0	+5.4	+12.1
7. BENDER 1	22.5	-2.5	-2.4	A	-0.02791	-0.00398	-0.00178	-3.6	+38.7	-3.8
				B	-0.02460	-0.00571	-0.00112	-45.0	+1.3	+14.3
8. BENDER RELAY	22.5	0	-2.4	A	-0.02775	+0.00170	-0.00067	-57.2	+1.3	-3.8
				B	-0.02482	-0.00091	-0.00025	-45.0	+1.3	-14.2
9. BENDER 2	22.5	+3.6	-2.4	A	-0.02760	-0.00744	+0.00164	-0.5	+38.7	-3.8
				B	-0.02520	-0.00381	+0.00150	+58.3	+38.7	-3.8
10. MICROSCOPIC OBJECTIVE	22.5	-2.5	-2.4	A	-0.02791	-0.00398	-0.00178	-3.6	+38.7	-3.8
				B	-0.02460	-0.00571	-0.00112	-45.0	+1.3	+14.3
11. PYRAMID	15.8	-2.5	0	A	-0.01883	-0.00437	-0.00185	+61.0	0.0	-11.9
				B	-0.01656	-0.00545	-0.00120	+48.0	+0.6	+14.0
12. LASER LENS	20.8	+3.6	0	A	-0.02760	-0.00744	-0.00184	-0.5	+38.7	-3.8
				B	-0.02520	-0.00381	-0.00138	+58.3	+38.7	-3.8

(1) A - 2 HR

B - 7 HR

EXPERIMENT PACKAGE ASSUMED SUPPORTED AT X = Y = Z = 0

the x direction perturb the focal point locations and affect magnification values. Shifts in the y direction are defined as meridional (azimuth) displacements, while shifts in the z direction are defined as sagittal (elevation) displacements.

TABLE 24
TRANSFORMATIONS FOR THE OPTICAL ANALYSIS

	<u>PHYSICAL COORDINATES</u>	<u>COMPUTER COORDINATES</u>
Telephoto Attachment	+Z	x
	+X	y
	+Y	z
254 mm Objective	-X	x
	-Z	y
	+Y	z
Folding Mirror to Bender #1	-Z	x
	-X	y
	+Y	z
Bender Relay	-Y	x
	-X	y
	-Z	z
Bender #2 to Beamsplitter and Communications Detector	-X	x
	+Y	y
	-Z	z
Dichroic to Laser Focusing Lens Folding Mirror	+Z	x
	+Y	y
	+X	z
Laser Focusing Lens	+X	x
	+Y	y
	+Z	z
Beamsplitter to Microscope Objective	-Y	x
	+X	y
	-Z	z
Fine Tracking Assembly	-X	x
	+Y	y
	-Z	z

The portion of the system which includes all of the components from the 4 x telephoto attachment to the focus at the communications detector (see Figure 90) was subjected to a computer ray-trace analysis. The program used in the analysis is called OTOL and was developed by D. S. Grey of D. S. Grey Associates. OTOL is available as part of the Control Data Corporation Computer Optics Package. It employs standard geometric ray tracing techniques to compute the sizes and locations of optical images throughout the system. Inputs to the program include the locations and curvatures of all optical surfaces and perturbations to element locations.

The computer analysis results indicate that the image quality is not affected significantly by the thermally-induced element displacements. The computer output is reproduced in Appendix I. The results show that the worst case difference in the path lengths of any two rays is on the order of 1/50 of a wavelength. Furthermore, the increase in the blur diameter is not significant based on the fact that the worst case ray intercepts the focal plane on the order of 10% further off axis than is shown in the analysis presented in Figures 86 and 87 on the unperturbed system.

The focal plane shift introduced by the perturbations causes a change in the effective focal length of the optical system, which in turn affects the angular sensitivity of the Fine Tracking Assembly. The focal point in front of the microscope objective is shifted toward the objective (+x). The total effect of the shift is the combination of the computer result, the beamsplitter shift (not included in the computer analysis), and the movement of the microscope objective toward the image point. This can be expressed

$$x_R = x_C + x_{BS} - x_{MO}$$

where x_R is the focal shift in the receiver channel, x_C is the computer result, shown on the last pages of Figures I-1 and I-2 of Appendix I, x_{BS} is the beamsplitter shift, and x_{MO} is the shift of the microscope objective in the opposite direction. Two components of motion of the beamsplitter in physical coordinates move the image point toward the microscope objective: motion in the +X direction and motion in the -Y direction. Because the fold is 90° (mirror at 45°), the resultant motion of the image is the sum of the two components, consequently,

$$x_R = x_C + X_{BS} - Y_{BS} + Y_{MO}$$

where the capital letters refer to physical coordinates (see Figure 99). Assuming the beamsplitter and bender #2 share the same motion due to their physical proximity:

$$x_R = x_C + X_{B2} - Y_{B2} + Y_{MO}$$

The values of x_C for Cases A and B are 2.727 mm and 1.994 mm, respectively. The corresponding values of x_R are 2.114 mm and 1.305 mm, respectively, using the shifts given in Table 23.

In order to determine the effect of this shift on the tracking performance, we determine its effect on the magnification of the microscope objective (nominally 4) and on the position of the image formed by the microscope objective. The objective itself has a 31.8 mm effective focal length (f). For 4-power magnification, the objective distance is $x_F = 39.8$ mm and the image distance is $x_B = 159$ mm. The new back focal length (x'_B) due to the thermal shift in the objective distance is given by the thin lens equations:

$$\frac{1}{f} = \frac{1}{x'_B} + \frac{1}{x_F - x_R}$$

$$x'_B = \frac{(x_F - x_R) f}{x_F - x_R - f}$$

The magnification is then

$$\frac{x'_B}{x_F - x_R} = \frac{f}{x_F - x_R - f}$$

For the Cases A and B, the magnification values are 5.4 and 4.8, respectively, as compared to the unperturbed value of 4.

The angular radius of a blurred image at a distance d from the focal point of a system with an aperture diameter D and an effective focal length F can be shown from trigonometry to be:

$$\tan \alpha = \frac{dD/2}{F(F - d)}$$

The contribution to d of the motions of elements behind the microscope objective can be neglected. The primary contribution comes from the change in the back focal length. Therefore,

$$d \approx x'_B - x_B$$

For Case B, α thus computed is 50 μ radians, indicating that this effect does not perturb the existing image angular size. However, for Case A, the image is enlarged to 78 μ radians. This increase causes a reduction in tracking loop gain, and, therefore, in bender loop bandwidth of a factor of 1.55. The

increased angle noise due to the larger linear field of view, although partially offset by the reduced bender bandwidth, will reduce the tracking link margin for Case A by 1 dB. Table 17 shows that this loss will not materially affect the performance of the tracking loop. The stability margin for the bender loop is adequate in the presence of the reduced gain, as can be seen if the gain curve in Figure 64 is dropped 2.6 dB.

Consequently, none of these effects are sufficiently deleterious to warrant thermal control for the balloon package.

Pointing error results from a misalignment of the transmit and receive beams. The closed-loop beam steering servo system locates the two beams such that the angle tracker output is nulled. The transmit beam pointing error then consists of the deviations from collinearity of the two beams plus any bias arising from mismatches in the angle tracker signal processing circuits. Mislocations of the optical elements which are shared by the transmit and receive beams do not give rise to transmit/receive beam misalignment. Deviation from collinearity is caused by differential displacements between the group of elements from the beamsplitter to the pyramidal mirror in the Fine Tracking Assembly and the group of elements from the dichroic back to the laser (Figure 90). The computer analysis locates the image formed by the common optical elements. This image appears at three positions in the optical system: at the communications detector, between the beamsplitter and the microscope objective, and, effectively, between the dichroic and the laser focussing lens. The optical gain at these points in the system is 1 microradian per micrometer; that is, an image shift of one micrometer at any of these three locations appears as a shift of one microradian in the far field of the system. For simplicity, therefore, the transmit/receive misalignment may be determined by (1) computing the apparent differential

shift between the position of the image at the laser focussing lens and that at the microscope objective due to shifts in the locations of the elements not common to both beams and (2) applying the gain factor quoted to obtain the angular misalignment. The effects of the rotations of the elements in question are negligible because both the magnitudes of the rotations and the moment arms through which they act are small.

The azimuth (meridional) component of the receive beam shift, y_R , consists of the computer generated value plus contributions due to the beamsplitter, microscope objective, and pyramid. In order to reflect pyramid motions to a point in front of the microscope objective, pyramid motions must be divided by the magnifications of the microscope objective, M_{MO} . Thus

$$y_R = y_C + y_{BS} + \frac{y_P}{M_{MO}}$$

The pyramid motion thus reduced is negligible. Also the beamsplitter is assumed to share the motion of bender 2 (See Figure 97). The meridional motion of the beam reflected off the beam splitter is the sum of the two components of beamsplitter motion in the plane of the incident and reflected beams. Therefore, in physical coordinates

$$\begin{aligned} y_R &= y_C + X_{BS} - Y_{BS} - X_{MO} \\ &= y_C + X_{B2} - Y_{B2} - X_{MO} \end{aligned}$$

where B2 refers to bender #2, BS to the beam splitter, and MO to the microscope objective. For the elevation (sagittal) displacement, the beamsplitter is not involved, since a displacement normal to the plane containing the incident and reflected rays does not affect the position of the reflected beam. Therefore,

$$z_R = z_C + z_{MO} = z_C + Z_{MO}$$

The elevation component of the transmit beam shift consists of the computer generated value plus contributions due to the dichroic (D), folding mirror (FM) in front of the laser focussing lens, the laser focussing lens (LFL), the laser/modulator assembly (LMA). Therefore,

$$z_T = z_C + z_D + z_{FM} + z_{LFL} + \frac{z_{LMA}}{M_{LFL}}$$

The LMA motion thus reduced by the magnification of the laser focussing lens is negligible. The FM is assumed to share the motion of the LFL (see Figure 98) and the D is assumed to share the motion of BS (see Figure 97). The elevation motion of the beams reflected off of the dichroic and the FM are the sums of the components in the plane of the incident and reflected rays.

Therefore,

$$\begin{aligned} z_T &= z_C + X_D + Z_D - (X_{FM} - Z_{FM}) + Z_{LFL} \\ &= z_C + X_{BZ} + Z_{BZ} - X_{LFL} \end{aligned}$$

For the azimuth case

$$\begin{aligned} y_T &= y_C + y_{LFL} + \frac{y_{LMA}}{M} \\ &= y_C - Y_{LFL} \end{aligned}$$

The net misalignments are, therefore,

$$y_{NET} = y_R - y_T = X_{B2} - Y_{B2} - X_{MO} + Y_{LFL}$$

$$z_{NET} = z_R - z_T = Z_{MO} + X_{B2} + Z_{B2} + X_{LFL}$$

Then the total pointing error is

$$\epsilon_T^2 = y_{NET}^2 + z_{NET}^2$$

For case A, $\epsilon_T = 8.6 \mu\text{rad}$, and for case B, $\epsilon_T = 17.3 \mu\text{rad}$. The signal power loss due to a pointing error of $17.3 \mu\text{rad}$ is negligible.

Based on this preliminary analysis of two typical cases when the system will be operating, it appears that no active thermal control system is necessary, permitting a savings in space, weight, and power in the experiment package. At the time the final design is performed, we recommend that this analysis be broadened to include more cases (mission profiles) and more precise thermal/structural models (more nodes).

2.4.4.4 BAPE interface requirements. Table 25 presents an estimate of the space, weight, and power requirements of the electronics and detector packages contained within the transceiver package. These estimates are reflected in the drawings in Section 2.4.4.2 and in the total package weight estimate of 162 pounds. Table 26 indicates that the present power aboard the BAPE is inadequate to serve the transceiver package and other equipment for a full 5 hours. Consequently, additional batteries will have to be added or the operation time reduced from the nominal 5 hours to 4 hours.

Telemetry Channel Assignments - We reviewed the FM/FM downlink telemetry subcarrier channel availability and assigned channels

TABLE 25
SIZE, WEIGHT, AND POWER ESTIMATE

	WIDTH	SIZE (mm) HEIGHT	LENGTH	VOLUME (cm ³)	WEIGHT (kg.)	POWER (watts)
1) Laser Transmitter	80	70	350		3.7	60
2) Modulator	115	150	300		3.2	44
3) PQM Formatting Electronics				492	.5	4
4) Communications Detector	102	165	140		3.7	*
5) Receiver Electronics	137	152	102	2140	2.5	15*
6) Data Synchronizer				1640	1.8	10
7) Uplink Error Measurement				330	1.4	10
8) Acquisition Detector	114-DIA		242		2.3	8
9) Acquisition Detector Signal Conditioner				1840	2.3	5
10) Tracking Detector	114-DIA		242		2.3	10
11) Tracking Detector Signal Conditioner				1840	2.3	5
12) Common Angle Processor				2840	3.2	10
13) Servo Loops				1640	2.3	20
14) Programmer/Controller				410	.5	1
15) Power Supply				500	1.4	70
16) Atmospheric Detector Assembly				1900	3	14
TOTAL PACKAGE POWER DISSIPATION						296

* #4 and #5 together consume 15 watts.

**TABLE 26
POWER SUMMARY**

Power Available on Present BAPE System (5-Hour Flight)

BATTERY	TYPE	NO.	WATTS
CD -	208	3	29
CA -	51	2	55
CA -	244	2	125
CA -	13	4	<u>112</u>
			321

Power Required

EQUIPMENT	WATTS
Experiment Package	296
Servo Motors	40
Telemetry System	<u>67</u>
	403

Therefore, additional batteries must be added to the BAPE outrigger structure or azimuth compartment structure.

to the data sources as in indicated in Table 27. A total of eighteen subcarrier channels will be required for the S-band downlink telemetry. This channel assignment requires at least one additional proportional bandwidth channel, #14. An additional subcarrier VCO and discriminator will be required to implement use of channel 14. The VCO will be added to the present BAPE telemetry package, and the discriminator will be added to the ground station S-band receiver.

2.5 CONCLUSIONS. The experiment described in this report will demonstrate the feasibility of high data rate optical communications through an atmospheric path. This experiment will demonstrate hands-off operation of a system wherein the communication hardware and the acquisition and tracking hardware function together. The

TABLE 27
SUBCARRIER CHANNEL DOWNLINK TELEMETRY ASSIGNMENTS
 (Total Subcarrier Multiplexed Subcarrier Bandwidth – 88 Hz to 136 kHz)

CHANNEL	NOMINAL INFORMATION BANDWIDTH (Hz)	CENTER FREQ. (Hz)	SUB CARRIER BANDWIDTH (Hz)	TYPE OF SUB CARRIER	FUNCTION
3B	800	32k	8k	4-kHz Const.	Low freq. DCFP output
14	330	22k	3.3k	P. B. W.*	Laser Power Monitor
5B	800	48k	8k	4-kHz Const.	Error Rate Data
7B	800	64k	8k	4-kHz Const.	Sum Output of Tracking Detector
13B	800	112k	8k	4-kHz Const.	0.53 μ m Atmospheric Detector Output
15B	800	128k	8k	4-kHz Const.	0.514 μ m Atmospheric Detector Output
9B	800	80k	8k	4-kHz Const.	x-axis Tracking Detector Output
17B	800	144k	8k	4-kHz Const.	y-axis Tracking Detector Output
4	14	960	144	P. B. W.*	Mode Indicator (Track, Acquisition, Non-track)
5	20	1300	196	P. B. W.*	Pressure Sensors (Commutated)
6	25	1700	256	P. B. W.*	Balloon Telemetry Receiver AGC
7	35	2.3k	346	P. B. W.*	Commutated Temperatures
8	45	3k	405	P. B. W.*	Azimuth Gimbal Position
9	59	3.9	586	P. B. W.*	Elevation Gimbal Position
10	81	5.4k	810	P. B. W.*	Azimuth Gimbal Rate
11	110	7.35k	1.102k	P. B. W.*	Elevation Gimbal Rate
12	160	10.5k	1.576k	P. B. W.*	x-axis Bender Position
13	220	14.5k	2.176k	P. B. W.*	y-axis Bender Position

*P. B. W. = Proportional Bandwidth

experiment will provide quantitative data on the degrading effects of atmospheric turbulence and random beam pointing errors on bit error rate. Due to the uncertainty in the theoretical models which predict these effects, only an experiment such as this can provide a high degree of confidence that the effects are tolerable. These two beneficial results of the experiment provide useful data for developing an Earth/space optical link.

Simulation fidelity is high in some areas, low in others. Table 28 presents a comparison of the SYNC-GND reference satellite system and the experiment system. The communication and fine tracking hardware are the same for both systems with the exception of closed loop boresight alignment (CLBA). CLBA is required in the satellite system to correct for optical alignment drifts which occur after long periods in space. The satellite system is more sensitive to misalignment due to its narrow beamwidth.

The primary areas where the systems differ are: (1) size and quality of the transmitter optics, (2) acquisition system hardware, and (3) beamwidth.

The satellite system requires a 7.5 inch diameter diffraction limited primary mirror. Diffraction limited performance must be closely maintained for long periods in the space environment in order that the fine tracking accuracy not degrade intolerably. By contrast, the experiment primary is 4 inches in diameter, non-diffraction limited. Therefore, the required optical performance for the satellite system is not demonstrated by this experiment.

The acquisition system hardware is entirely different for the two systems, as discussed in the report. The existing BAPE vehicle hardware has been used, where possible, to save the costs associated with encoders, precision attitude reference systems, and auxiliary gimbals. As a result, the acquisition performance of the satellite system cannot be evaluated in the experiment.

TABLE 28
COMPARISON OF PROPOSED BALLOON EXPERIMENT
AND SATELLITE CONFIGURATIONS

<u>System Component</u>	<u>Satellite</u>	<u>Experiment</u>	<u>Comments</u>
Communications Laser		Same	Experiment required high data rate uplink
Beacon Laser	Q-switched	Mode locked	
Data Rate		Same	
Modulation Format		Same	
Modulation		Same	
Electronics		Same	
Receiver detector		Same	
Transmitter Optics	7.5" dif- fraction limited cassegrain	4" refractive	BAPE constraint
Receiver Optics	60" Casse- grain	30" Cas- segrain	Experiment Constraint
Beamwidth	8 μ rad	500 μ rad	BAPE constraint
Fields of View: Com- munications, Acquisition and Fine tracking	4 mrad 10 μ rad	35 mrad 100 μ rad	BAPE constraint BAPE constraint
Acq. & Track Detectors		Same	
Bender Bimorphs		Same	
Acquisition signal waveform	pulsed	CW	Cost to experiment not warranted
Tracking signal waveform		Same	
Gimbals	BAPE	Precision	BAPE constraint
Gimbal Bearing	BAPE (upgraded)	Precision	BAPE constraint
Gimbal Readout	BAPE Pat. and Tack.	15 bit encoders	BAPE constraint not warranted with 500 μ rad beam
Closed-loop boresight alignment	Required	None	
Platform control accuracy	$\pm 1'$	± 2 mrad	BAPE constraint

Performance

Bit error probability		Same	
Acquisition time		Same	
Tracking Accuracy	≤ 1 μ rad rms	1 - 10 μ rad rms	Experiment performance for quiet conditions

Disturbances

Dynamical inputs	windgusts	small	
Scintillation		\sim less for satellite	Based upon current theory of atmospheric phenomina
Beam Wander	0.1 μ rad	\sim same	
Angle of Arrival Fluctuations	rms \sim same	3 μ rad rms	

The beamwidth of the transmit antenna affects the power distribution across the receiver aperture and the sensitivity of received power to pointing error. In order to scale these effects properly in the experiment, variable beamwidth capability is required in the balloon package. We feel that the variable-beamwidth feature compromises the reliability of the experiment. Therefore the fixed 500 μ rad beam configuration was chosen to provide a uniform illumination of the receiver. As the relationship between pointing error and received power is straightforward, we feel it is not necessary to simulate it in this experiment.

3. TASK II - DEFINITION AND CONCEPTUAL DESIGN FOR 1980-1990 MANNED LABORATORY OPTICAL COMMUNICATION EXPERIMENTS

The elements in the manned laboratory optical communications experiment are primarily those which require man-interactions, are of high value to NASA missions, cannot be accomplished on Earth, and are flexible enough to accomplish broad goals. In order to establish experiments that meet these criteria, we first examined the various possible operational links in the post-1980 time of interest, and the link data requirements.

The links of interest include:

LAS	↔	SYNC
SYNC	↔	SYNC
SYNC	↔	GROUND
SYNC	↔	AIRCRAFT
DEEP SPACE	↔	GROUND
DEEP SPACE	↔	SYNC SAT

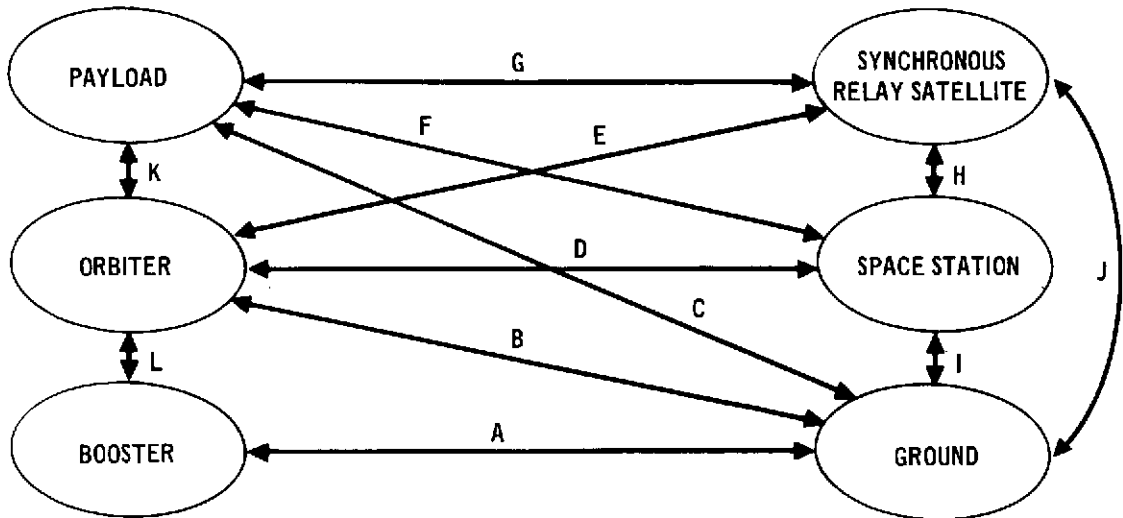
MANNED ORBITING VEHICLE LINKS

The manned orbiting vehicle links can take many forms with many variations as Figure 112 illustrates.

Some of these links vary in path length throughout the various phases of each mission. Certain links are only available on an intermittent scheduled basis. Some are subject to interruption or variation because of weather and plasma.

Of significant impact is the data rate requirements for each link. We examined the available information so that realistic data rates for each link were better established for the 1980-1990 time frame. Data rate estimation has been obtained by examining communication needs for various kinds of scientific instruments, as well as communication satellite needs and resources sensing requirements. Examples of the data requirements are given in Table 29.

**FIGURE 112 MANNED ORBITING VEHICLE LINKS
AND EFFECTS TO BE STUDIED**



LINK	RANGE VARIATION	WEATHER EFFECTS	PLASMA EFFECTS	SCHEDULED INTERMITTENT OPERATION
A	YES	YES	YES	YES
B	YES	YES	YES	YES
C	YES	YES	NO	YES
D	YES	NO	NO	YES
E	SLIGHT	NO	NO	YES
F	YES	NO	NO	YES
G	SLIGHT	NO	NO	YES
H	SLIGHT	NO	NO	YES
I	YES	YES	NO	YES
J	NO	YES	NO	NO
K	NO	NO	NO	NO
L	YES	NO	YES	NO

With respect to deep space probes, the data rate that a scientist would like to receive is much higher than that which is practical. 10^4 bps data rates for Neptune ranges appear to be a reasonable compromise between transmitter power requirements and engineering and scientific data requirements.

TABLE 29
CANDIDATE APPLICATIONS

APPLICATION	FUNCTIONAL DATA RATE (bps)	COMMAND DATA RATE (bps)	SOURCE ALTITUDE	SOURCE IN FOV	SOURCE STABILITY
SATELLITES					
Earth Observation	8 to 10 ⁹	10 ⁴	Sync	No	Excellent
			Low Orbit	Yes	Excellent
Comm Satellite Relay	10 ⁹	10 ⁴	Sync	No	Excellent
TDRS Relay	10 ⁹	10 ⁴	Sync	No	Excellent

Near Space Communication Experiment Candidates - The experiment candidates for near-space links include:

- I. Mode-locked Nd:YAG transceiver systems in the data rate regime 400 Mbps to 1 Gbps.
- II. Simultaneous multi-access low data rate optical links plus multi-access RF from low altitude satellites to a single asynchronous satellite for further transmission as on multiplexed data stream.
- III. Synchronous satellite to ground communications link atmospheric propagation experiments.

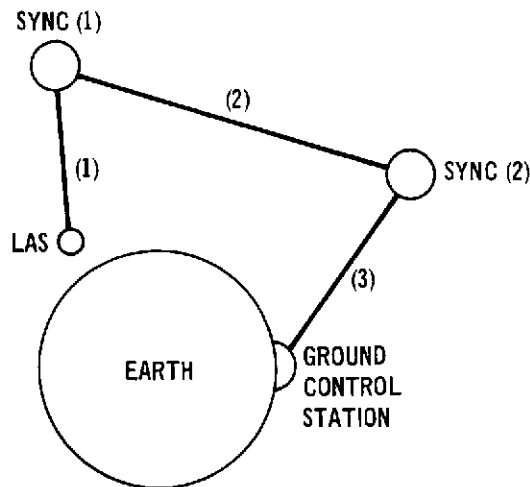
These three candidates exercise most of the potential problem areas for near space optical communications.

Deep Space Communication Experiment Candidates are:

- IV. Deep space laser communications receiving terminal evaluating a satellite relay of deep space optical data transmissions to ground.
- V. A short pulse, Pulse Interval Modulation (PIM), laser transmitting terminal in near space, simulating a deep space probe transmitter.

Experiment I consists of a synchronous orbit (SYNC) receiving terminal station (RT) and either a low altitude satellite (LAS) or synchronous orbit transmitting terminal station (TT) as illustrated by Figure 113.

FIGURE 113 HIGH DATA RATE COMMUNICATION LINKS



LINKS: (1) DATA INITIATION LINK
(2) RELAY LINK
(3) RELAY LINK

The following combinations are possible for this experiment:

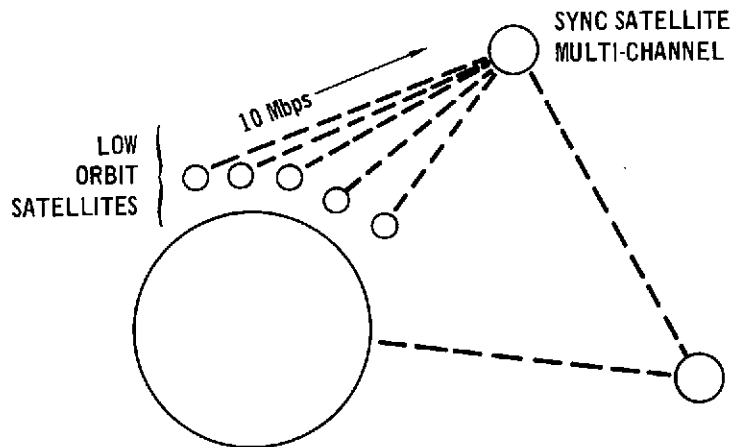
- (1) TT on MSL (manned space laboratory) - RT on MSL
- (2) TT on USL (unmanned satellite laboratory) - RT on MSL
- (3) TT on MSL - RT on USL

The first choice provides the maximum of experiment flexibility.

Numbers (2) and (3) can accomplish limited objectives. The system on the USL would be unadaptable to a great extent to the possible optimized configurations. The system on the MSL could be reconfigured to optimize it to its mating USL system. The communication link as a whole could not be optimized as easily with only one manned station.

Experiment II consists of a simultaneous multiple optical communications receiver (SMOCR) on a SYNC MSL. The transmitters required to exercise the SMOCR could be on LAS's and/or at ground sites. Short pulse low duty cycle optical communication techniques are used for the simultaneous communication links. Figure 114 illustrates the SMOCR link concept. A capability, such as that to be demonstrated by this experiment, would permit simultaneous low data rate interrogation of a number of LAS satellites from different portions of the Earth's circle. The data would be collected at the SYNC MSL and retransmitted to a central control terminal.

**FIGURE 114 MULTI-CHANNEL 10 Mbps LASER LINKS
SIMULTANEOUS OPERATION**

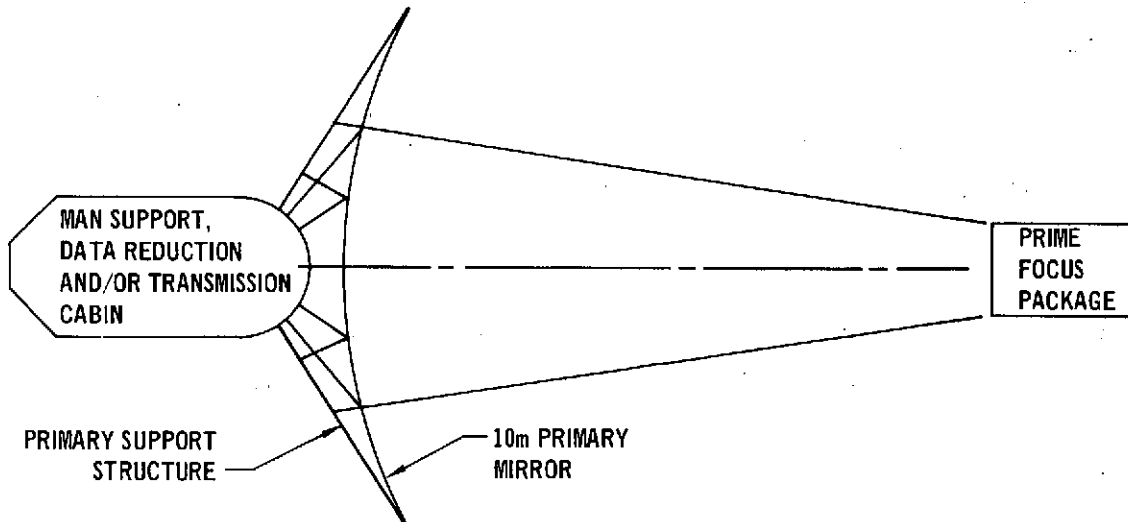


Experiment III is designed to evaluate atmospheric propagation effects on laser communications from a synchronous satellite to Earth. One of the manned stations described in experiment I would be used for the synchronous satellite terminal. The communications equipment would be essentially the same as that described in experiment I. Atmospheric parametric characterization and effects equipment would be the added requirement. The primary objectives of this experiment are to measure the effects of the atmosphere on communication performance and to investigate the effectiveness of various configuration changes in reducing adverse atmospheric effects.

Experiments IV and V evaluate deep space communication system. Experiment IV consists of a short pulse, Pulse Interval Modulation (PIM), laser receiving system evaluating the concept of an earth synchronous satellite receiver terminal. After the operational receiver receives the data, relay to ground by optical or RF means would be done. The deep space receiving terminal requires a large (10 meter diameter) nondiffraction limited collector. Figure 115 illustrates the concept. The source required to test the receiver could either be from another manned or unmanned synchronous spacecraft. A ground station may also perform as a system test source, although one would have to evaluate the differences in thermal loading on the large collector when it faces the Earth instead of deep space.

Experiment V consists of a short pulse, PIM, near space simulation of a deep space probe transmitter terminal. In future deep space missions to the outer planets, a higher data rate capability than that available by RF means today will be required. Experiment V is intended to demonstrate such a capability using laser communication techniques. It is envisioned that this experiment package will be aboard a synchronous manned space laboratory. The communication receiver could be at a ground site, an unmanned synchronous satellite, or the manned synchronous satellite described by Experiment IV. The mating of experiments IV and V is assumed in the experiment documentation which follows in this report.

FIGURE 115 SYNCHRONOUS SATELLITE DEEP SPACE PIM LASER COMMUNICATION RECEIVER TERMINAL



We have documented the conceptual design for each of the proposed experiments in the remainder of this report. The format of this documentation is:

Experiment Title

- (1) Experiment plan
 - a) Significance
 - b) Objectives
 - c) Techniques
- (2) Functional Description
 - a) Experiment subsystems
 - b) Modes of Operations
 - c) Required controls
- (3) Operational Sequence
- (4) Operational Support Equipment
- (5) Data Acquired

During this program, we studied five potential manned laboratory optical communication experiments and have included all of the study results in the report. However, we conclude that there are only two of the experiments which require man-interactions to fully realize the effectiveness of the experiment. These are Experiment-III Synchronous

manned laboratory to ground communications link atmospheric propagation experiments, and Experiment IV - Deep space laser communications receiving terminal evaluating a satellite relay of deep space optical data transmissions to ground. Experiment IV is by far the more attractive of these two, since it involves the fabrication and evaluation of a large optical receiving collector in space. This experiment would provide the NASA with a deep space high data optical communications receiving antenna, equivalent to the Goldstone RF antenna, for future planetary missions.

3.1 400 MBPS TO 1 GBPS TRANSCEIVER SYSTEMS. There will be a growing requirement for near space, mode-locked Nd:YAG transceiver systems in the data regime 400 Mbps to 1 Gbps. The manned space laboratory could conceivably be used:

- (1) To efficiently obtain engineering data on the communication system in an operational environment.
- (2) To investigate any problems arising from systems previously deployed.
- (3) To optimize new, advanced, and improved systems to be deployed after 1980.
- (4) To check out systems to be deployed in an operational network

Each of the uses requires a particular manned spacecraft capability. We have defined the experiment required to obtain engineering data.

3.1.1 Experiment Plan. In order to facilitate the acquisition of engineering data in an operational link environment, two test beds are required. One located at a manned transmitter station and one located at a manned receiver station. The respective acquisition, tracking, and communication subsystems will be located on the test beds. Input and output beams can be manipulated with gimballed telescopes aligned and hard mounted to the test beds. The transmitting system can be placed on board a manned LAS or a manned sync satellite. The receiver system

can be placed on board a manned sync satellite or ground based station. The objectives of this experiment are to exercise all of the configuration options, and measure and document the performance of the communications, acquisition, and tracking subsystems of each terminal package. The engineering data acquired is invaluable to evaluate performance of experimental and operational systems. The functional parameters that would be varied are listed in Table 30. In order to vary parameter values, system configuration changes would have to be made.

TABLE 30
FUNCTIONAL PARAMETERS SUBJECT TO CHANGE

- Data Rate
- Power Level
- Receiver Collector Diameter
- Modulator Extinction Ratio
- Transmitted Beamwidth
- Power Split for Tracking
- Field of View
- Modulation Format
- Pulse Width
- Open Loop Pointing Uncertainty
- Pointing Accuracy
- Optical Filter Bandwidth
- Operating Wavelength

Other system configuration changes would be made to evaluate alternate designs. Table 31 lists some of these possible configuration changes. Whenever a change in one part of the system is made, resultant changes throughout the system are generally required to enable the performance evaluation of an optimally configured link. For example, if the pulse width were increased for the communications transmit laser, a corresponding change in communications receiver bandwidth and possibly threshold detector operating input would be required. The

TABLE 31 CONFIGURATION CHANGES

- Acquisition Technique
 - Broad beam vs. scanning
- Filters
- Field stops
- Aperture stops
- Laser (beacon)
 - Lamp pumped
 - LED pumped
 - Sun pumped
- Beam splitters
- Communications Detector
 - DCFP (dynamic cross field photomultiplier)
 - SCFP (static cross field photomultiplier)
 - FPMT (fast photomultiplier tube)
 - APD (avalanche photodiode)
- Acquisition detector
 - QPMT (quadrant photomultiplier tube)
 - DPMT (deflectable photomultiplier tube)
 - QSPD (quadrant silicon photodiode)
 - SSSA (solid state detector array)
- Tracking Detecotr
 - QPMT
 - DPMT
 - QSPD
 - SSSA
 - PMT with scanning reticle
- Communication Laser Configuration
 - Mode-locking technique
 - Pumping technique
- Link
 - LAS → Sync (The arrow indicates the direction of the high data rate)
 - SYNC → SYNC
 - SYNC → GRD

TABLE 31 (Cont'd) CONFIGURATION CHANGES

- Modulator
 - Single pass binary path
 - Double pass binary path
- Point Ahead Configuration
 - Bender bimorph mirrors
 - Risely Prism
- Image Motion compensation
 - Single 2-axis bender bimorph mirror
 - Two, single axis bender bimorph mirrors
 - Two stage vernier control (i.e. two sets of benders in series)
- Focal positions

implementation techniques are discussed in Appendix A. The support equipment required to implement and measure the system parameters associated with a change are enumerated. The subsystem performance implications are enumerated and discussed.

The results of the experiment will be compared to a theoretical model of the system. For the acquisition subsystem, acquisition time, tracking accuracy, and break lock probability will be compared and analyzed. For the tracking subsystem, tracking accuracy and break lock probability will be compared. For the communications subsystem, the BER will be compared and any discrepancies analyzed.

- 3.1.2 Functional Description. The experiment equipment is located physically at two terminals. One terminal contains the high data rate transmitter and the associated acquisition and tracking subsystems (TT). The other terminal contains the high data rate receiver and the associated acquisition and tracking subsystems (RT). Both terminal stations should be man operated in order to provide maximum flexibility. Figure 116 and 117 are functional block diagrams of the two terminals,

FIGURE 116 HIGH DATA RATE TRANSMITTING TERMINAL BLOCK DIAGRAM

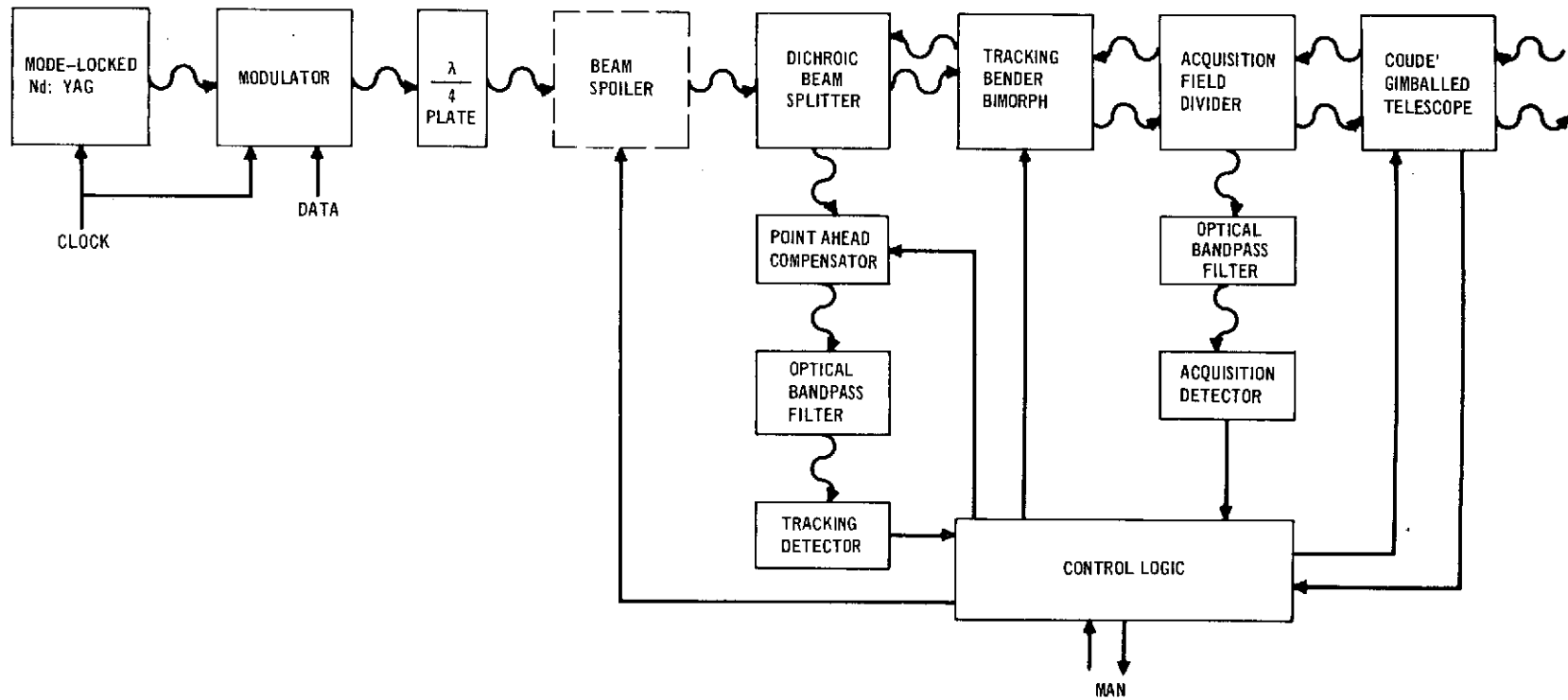
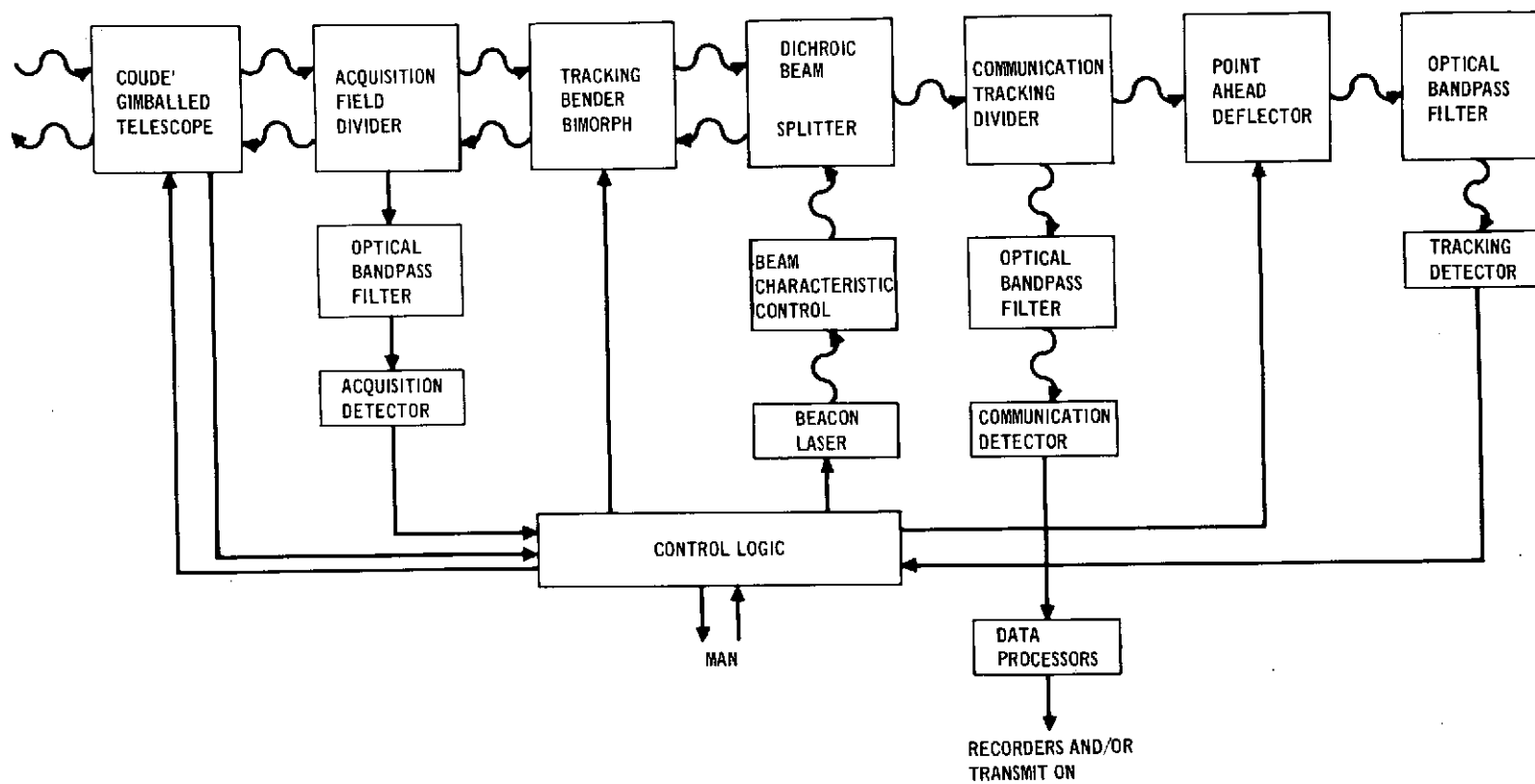


FIGURE 117 HIGH DATA RATE RECEIVER TERMINAL BLOCK DIAGRAM



TT and RT, respectively. All system components are mounted on a test bed to provide easy access by a man.

3.1.2.1 Transmitting terminal. Figure 116 is a generalized form of the block diagram of the TT. The receive and transmit wavelengths are either 1.06 μm and 0.53 μm . The particular modulator configuration is dependent upon the modulation format chosen. The mode-locked frequency is dependent upon the data rate required. The acquisition and tracking receiver configuration and processing electronics are a function of detector type and technique employed. With all of these components located on an accessible test bed, the operator can configure the system in any way that is compatible with the RT.

The telescope primary should be 12" diameter, diffraction limited to provide for a maximum of transmit beamwidth variation. In order to avoid obscuration of the transmit beam (which can pose serious far field beam degradations for a spoiled beam), an off-axis Gregorian design should be utilized. It should be highly reflective for both 1.06 μm and 0.53 μm . The telescope and/or scanning flat should be equipped with a field of view capability that is compatible with its terminal location requirements and the imposed constraints of the manned space laboratory.

The system parameter values of field of view, imposed obscuration, beamwidth, transmit and receive wavelengths, bandpass filter width, image spot size quality, etc. (all those responsible for system performance) are defined directly by the man in the loop configuring the TT to a defined test specification within the performance limitations. The particular techniques employed are described in

Appendix A. In order to assist the main interface, a boresighted operator telescope should be present, as should diagnostic instrumentation (enumerated in a later section).

3.1.2.2 Receiving terminal. Figure 117 is a generalized block diagram form of the RT. Provision will be made to have either a CW scanned beacon laser or a broad beam Q-switched beacon source for concept evaluation purposes. As for the TT, the RT has all of its components located on an accessible test bed, except for the telescope. Similarly to the TT, the man in the loop can configure the components in a way that is compatible with the TT, and within the performance limitations of the components. An operator's bore-sight telescope should be made available to the man, as should all required diagnostic equipment (see Section 3.1.4. The receiver system telescope should be at least 24" in diameter and of diffraction limited quality. Diffraction limited performance is not required operationally,^{24,25} but the effect of high optical quality should be experimentally investigated. The optical quality can easily be degraded to that required operationally.

3.1.3 Operational Sequences. The operational sequence for the experiment would be:

- (1) Configure the TT and RT systems according to a predetermined systems design specification.
- (2) Document (may require measurements) the TT and RT parametric characteristics.
- (3) Exercise the link and record the communication, acquisition, and tracking performances of both the TT and the RT.
- (4) Recycle sequence to (1) for new experiment design specification.

In exercising the link, the experiments may require different detailed sequences depending on the systems design specifications and the purpose of the particular part of the experiment. For example, the purpose of some specific test may be to determine acquisition time, given that the TT is open loop pointed initially within the fine tracking field of view. The sequence for this specific test would be to configure the TT and RT to the correct accuracy, switch to the automatic mode, and measure and record acquisition time.

3.1.4 Operational Support Equipment. In order to accomplish all of the postulated configuration changes and subsequent performance evaluations, a large amount of support equipment must be provided. Appendix A lists some of the support equipment required to exercise functional parameters and configuration changes. A summary list of some of the support equipment required is given in Table 32.

TABLE 32

THE OPERATIONAL SUPPORT EQUIPMENT INCLUDES:

- Optical Test Bench
- Real-time Oscilloscopes
- High Speed Optical Detectors
- Optical Scanning Interferometer
- Spectrum Analyzer
- Frequency Synthesizer
- Alignment Tools
- Alignment Detector and Lasers
- Low Power Test Lasers
- Calibrated Power Monitor
- Scope Cameras
- Chart Recorders
- TV Monitor
- Electronic Modules for the Required Changes
- Bit Error Rate Instrumentation
- Boresight Telescope

3.1.5 Data. The required data includes system parameters versus BER, acquisition time, and tracking and pointing accuracy.

3.2 SIMULTANEOUS MULTIACCESS LINKS. This experiment consists of simultaneous multiaccess low data rate optical plus multiaccess RF links from many low altitude satellites to a single synchronous satellite receiver for further transmission on a multiplexed data stream.

3.2.1 Experiment Plan. Future requirements indicate that there will be many low altitude satellites (LAS) such as the ERTS series and data relay type satellites requiring relatively low data rate interrogation. There are many proposed ways to transfer this data to a central receiving station on Earth. It appears to be very inefficient to have single dedicated receivers for each LAS. This experiment was designed to prove out an attractive alternative approach where a single receiver in synchronous orbit, receives data in either optical or RF format from many LAS's and transfers it on to another synchronous satellite or to the ground via a multiplexed high data rate stream utilizing a technique described by the first experiment (3.1). It is envisioned that a man would be available only at the multi-access receiver satellite. The LAS data transmission could be simulated at ground transmitting sites and any of LAS in existence at the time of the experiment.

The objective of this experiment is to demonstrate and document transmitter station. Since man is available at the receiver station, configuration and parameter changes could be made. In order to exercise the link, either LAS's or Earth stations simulating LAS's must be used. Except for the dynamics, an Earth station would appear like a LAS to the receiver; consequently, several Earth stations could address the satellite station utilizing several coding formats and data rates, with frequency shifts to simulate the Doppler effect of an actual LAS to synchronous link. Atmospheric effects may degrade an Earth station simulation of a LAS. Some of the functional

parameter changes that could be made at the multi-access receiver are listed in Table 33. Some of the receiver system configuration changes would have to be made to realize the functional parameter changes listed in Table 33. Other system configuration changes would be made to evaluate alternate designs. Table 34 lists some of the configuration changes. The techniques required to implement these changes are straightforward. The data processing and multiplexing into a single data stream are functions that could be demonstrated and optimized more practically in a ground experiment. But the system used will have to be exercised in the actual link. Consequently, performance evaluation techniques should be used to check out this particular operation.

TABLE 33
FUNCTIONAL RECEIVER PARAMETERS SUBJECT TO CHANGE

- o Received data rate
- o Beacon power level
- o Receiver diameter
- o Received power level
- o Sampling interval
- o Received pulse width
- o Beacon power
- o Beacon and received wavelengths
- o Field of view per detector

TABLE 34
CONFIGURATION CHANGES

- o Filters
- o Aperture Stops
- o Laser (beacon)
 - lamp pumped
 - LED pumped
 - Q switched broad beam
 - CW scanned
- o Detector types in detector array
- o Number of detectors in constant array size
(field of view per detector)

Because this receiver system is so radically different from those now being developed, all three subsystems (communications, acquisition, and tracking) and operational techniques would be subject to experimental scrutiny, justification, and optimization. The main emphasis of this experiment is on the multiple receiver system, although the other terminals are required to exercise the link. A few of the potential problem areas that require experimental investigation include:

- (1) Adequate beacon illumination of LAS users
- (2) Acquisition technique and system implementation
- (3) Adequate individual communication channel isolation.

3.2.2 Functional Description. There exists a communications requirement from multiple LAS's to a data collection ground based station. Because of the physical geometry of the low orbits, direct communication with the ground station is limited to a very small fraction. A geometrical schematic of the link is given in Figure 113. This relay link would consist of two or three synchronous satellite relay stations. In the worst case, the LAS, which would physically be on the opposite side of the Earth to the receiving station, would transmit to synchronous satellite #1. Synchronous satellite #1 would relay, or retransmit, to synchronous satellite #2 which in turn would complete the communication link by relaying the communication to the Earth ground control station. The data rate requirement from a single LAS could be very high, but normally it would be on the order of 10^7 bits per second or less. Pulse Interval Modulation (PIM) is an efficient format for this data rate regime.²⁶ The PIM transmitter will be described in experiment V. (Section 3.5.)

Several practical considerations accrue for the receiving system by using low duty cycle laser communications. The two most important are that 1) solid state lasers are capable of high peak powers and 2) the time - domain background discrimination

capability, inherent in low duty cycle systems, permits noncoherent detection, which, in turn, allows the use of much larger optical collectors since image forming quality in the optics is not necessary.

Synchronous Satellite Data Receiver System - The synchronous satellite data receiver must be capable of receiving PIM data over a wide field-of-view (20°) in the presence of a large background source (sunlit Earth). These requirements pose a significant system design problem.

Figures 118 and 119 illustrate a possible synchronous receiver system. It consists of four Fresnel lenses, each of which views a different quadrant of the Earth circle. The detectors consist of a 10×10 array of silicon photodiodes. The photodiodes are connected directly to preamplifiers and signal processing logic.

FIGURE 118 FRONT VIEW OF SYNCHRONOUS RECEIVER AND BEACON UNIT

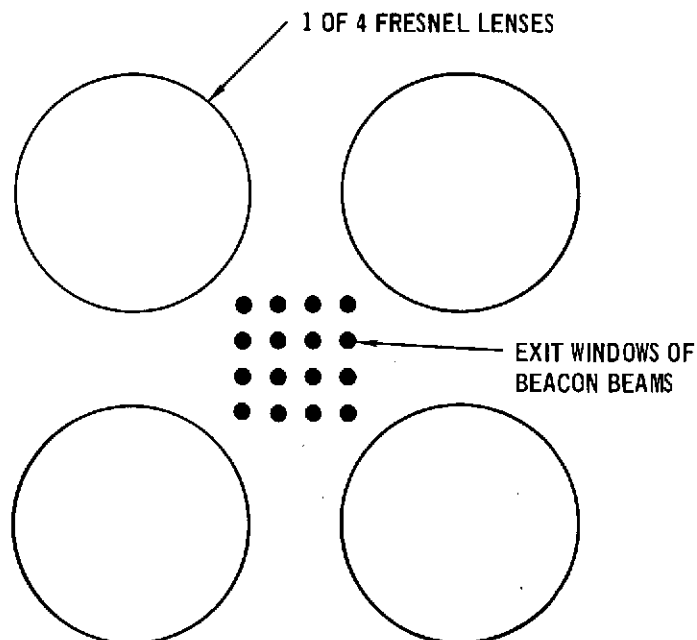


FIGURE 119 1/4 EARTH SYNCHRONOUS RECEIVER UNIT

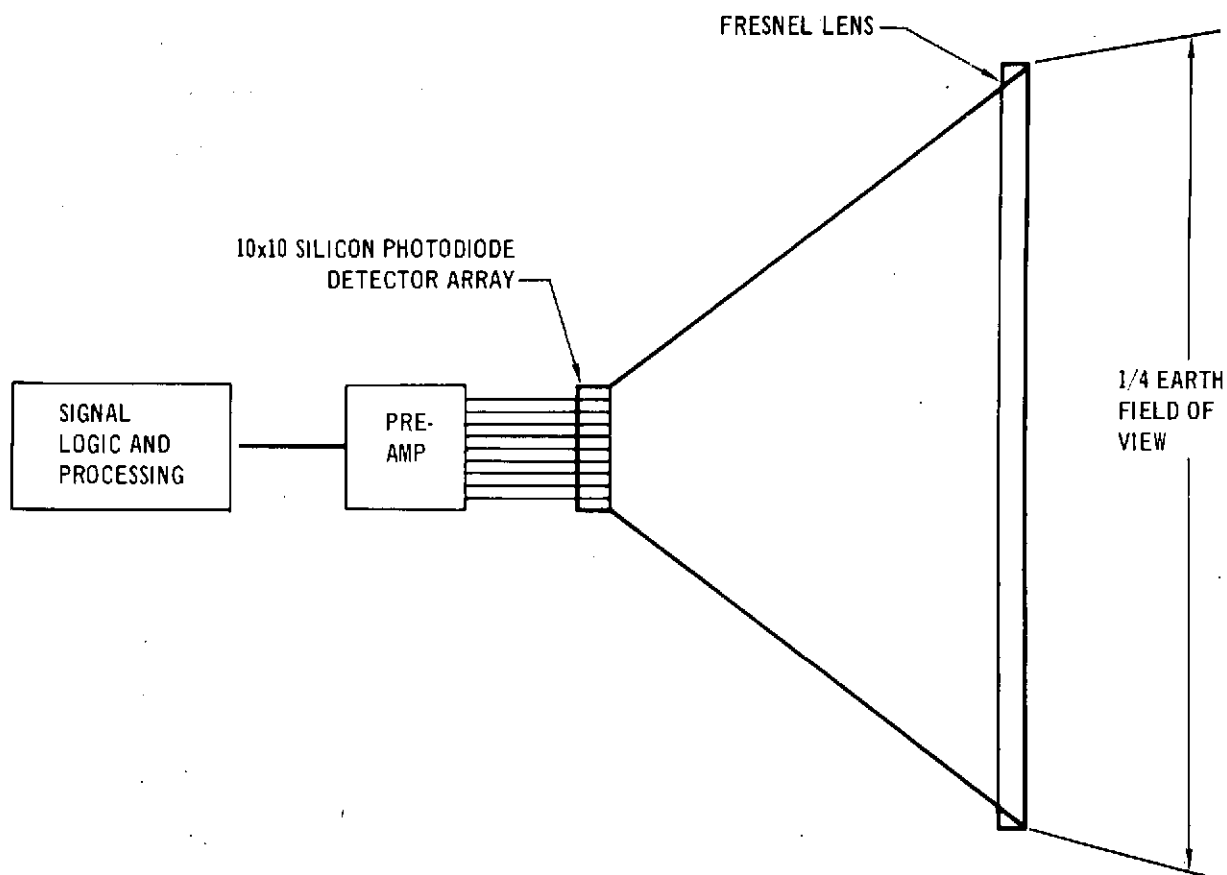


Table 35 gives a system parameter breakdown. Because of off-axis astigmatism of a single element primary, the detector array must be slightly larger than a perfect multiple element optical system would provide. Also the signal radiation from a single low orbit satellite will be blurred over a maximum of four detectors even at the edge of the field-of-view. The diode size should be equivalent to the astigmatic blur diameter for an optimum design, since if it were larger than a diode, it could irradiate more than four diodes and thus increase the resulting combined thermal noise of the reception. Figure 120 illustrates the 10 x 10 detector array and the signal from two low orbit users. With the use of photodetectors, the thermal noise limits the systems sensitivity even

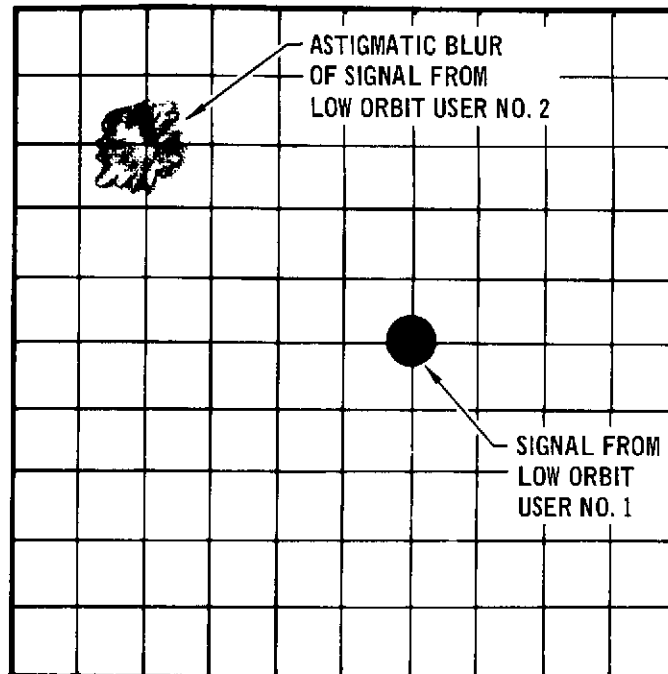
TABLE 35
SIGNAL POWER SYSTEM PARAMETERS

Parameter	Definition	Value
λ	Wavelength of the signal carrier	1.064 μm
ρ	Responsivity of silicon photodetector	0.3 A/W
e	Electronic charge	1.6×10^{-19} C
$h\nu$	Energy per photon	1.87×10^{-19} J
η	Quantum efficiency = $\frac{\rho h\nu}{e}$	35%
D_R	Diameter of Synchronous receiver	0.3 m
N_F	F-number of Fresnel receiver	0.8
τ_+	Transmission of filter	100%
Ω	Solid angle per each unit	0.0184 sr
P_A	Background Power = $\frac{H_{\lambda B} \pi D_R^2 \Delta\lambda \Omega \tau_o \tau_Y}{4}$	2.65×10^{-2} W
R	Range	4.5×10^7 m
X_t	Signal transmitted beamwidth	10×10^{-6} rad
C_1	Power Transmission factor = $\frac{D_R^2 \tau_f \tau_o}{R^2 \alpha_t^2}$	3.77×10^{-7}
P_{tav}	Average transmitted power	187 mW
PRR	Pulses per second	10^6 pps
τ	Pulse width	10^{-9} s
	Duty cycle	10^{-3}
P_T	Peak power transmitted per pulse	187 W
P_S	Laser power received = $P_T C_1$	7.05×10^{-5} W

TABLE 35 (Continued)
SIGNAL POWER SYSTEM PARAMETERS

Parameter	Definition	Value
N_F	F-number of Fresnel Receiver	0.8
$D_a \times D_a$	Detector array dimension for a $\pm 5^\circ$ $\delta.o.v.$	2.5" x 2.5"
B_{ast}	Astigmatic blur diameter at the edge of the field	0.36"
-	Assume that detectors are 0.25" x .25" or a 10 x 10 array and that most of the signal would fall on 4 detectors at any one time	
P'_E	Background power on 4 detectors = $\frac{P_B}{4}$	1.06×10^{-3}
G	Internal gain of detectors	1
T	Detector temperature	300 °K
B	Bandwidth	10^9 Hz
K	Foltzmann's constant	$1.38 \times 10^{-23} \frac{j}{^\circ K}$
F	Preamplifier noise factor	5
N_T	Thermal noise power per detector = 2 KFTB	4.13×10^{-11} W
N_T	$N_T' \times 4$ detectors	1.65×10^{-10} W
I_S	Signal current from 4 diodes = ρP_S	2.11×10^{-5} A
I_B	Background current from 4 diodes = $\rho P'_B$	3.18×10^{-4} A
$(I_S + I_B)$		3.39×10^{-4} A
P_{SH}	Shotnoise Power = $2 e B (I_S + I_B) R_L$	5.35×10^{-11} W
N	$P_{SH} + N_T$	2.18×10^{-10} W
S	$I_S^2 R_L$	2.18×10^{-8} W
$\frac{S}{N}$	Power signal to noise ratio	100 = 20 db

FIGURE 120 10 x 10 DETECTOR ARRAY



when no filter is used. A filter would be required to optimize the system if the detectors had sufficient internal gain to raise the shot noise due to background illumination, above the thermal noise component.

Optical Problems - A single element primary will yield off-axis astigmatic blur even for a parabolic mirror. This is normally corrected by using multiple elements. But multiple elements for a 1 or 2 foot aperture would add considerable weight. Optimally, the photodiode size will be equal to the astigmatic blur circle diameter. Thus, the blur image cannot irradiate more than 4 photodiode detectors. It may be possible to reduce the off-axis astigmatism appreciably without introducing a considerable weight penalty. If so, one of two system improvements are permitted:

- (1) Increased receiver diameter (and increased sensitivity)
- (2) Or larger field-of-view per primary for the same detector array and same S/N.

Fresnel lens primaries have been chosen since they are lightest but they do have their disadvantages. Their collection efficiency is about 85% due to the grooves blocking off a portion of the aperture at large incident field angles such as will be encountered for this system. Furthermore, the collection time spread for a Fresnel lens can be a consideration. For an F/0.5 system, $\Delta\tau$ (the time spread of the collected radiation at the focal plane) would be 0.227 ns for a 1 foot Fresnel lens. $\Delta\tau$ does not vary appreciably for angles of incidence less than 10° (the region of interest); it does vary appreciably with F-number though. Table 36 gives some values of $\Delta\tau$ for various F-numbers.

TABLE 36
TIME SPREAD OF FRESNEL LENS FOR VARIOUS F-NUMBERS

(10° Incident Angle)

<u>F-Number</u>	<u>Time Spread ($\Delta\tau$) (ns)</u>	
	<u>One Foot Diameter</u>	<u>Two Foot Diameter</u>
0.5	0.227	0.456
0.6	0.195	0.39
0.7	0.171	0.343
1.0	0.123	0.246
2.0	0.062	0.124

The resultant effect is that the pulse width is increased and the pulse shape somewhat distorted. Such effects could be experimentally investigated more efficiently in a laboratory environment.

Narrow bandpass filters are designed for narrow acceptance angles ($<2^\circ$). The peak of the transmittance shifts with incident angle. The minimum angles are experienced at the aperture. The angles at the focal plane are dependent primarily on the F-number of the

primary. A fast F-number is attractive to keep the size of the detector array to a minimum. Consequently, the angles of acceptance would be a minimum at the primary, and equal to the half angle of the field-of-view of the low orbits from the synchronous satellite, i.e., $\pm 10^\circ$ for a single primary or $\pm 5^\circ$ for the field-of-view for a system where each of four receiver units view a quarter Earth.

About 40 Å bandpass is applicable for a $\pm 10^\circ$ field-of-view, whereas a 10 Å bandpass is applicable for a $\pm 5^\circ$ field-of-view for a 4 segmented receiver.

Because these apertures are extremely large (for filters), the filters would probably be constructed of smaller ones segmented together to form one large area filter. If a single filter were made, it would be best to allow room in the bandpass for construction error.

Another effective filtering technique is to use detectors that are responsive in a narrow band around the carrier wavelength. These are sometimes called spectrally matched detectors.

For this application, and because internal gain is not available in the detector array, the thermal noise is much greater than the shot noise when a filter is employed. When no filter is used, the shot noise and thermal noise are comparable, but the signal-to-noise is increased since the signal is not attenuated by the filter and the signal-to-noise power ratio is a function of the signal squared. The filter considerations would become critically important if the internal gain of the detector (such as a PMT or equivalent photodiode) was such that the shot noise was larger than the thermal noise.

Acquisition and Tracking - Table 37 summarizes the proposed approach for acquisition and tracking. The synchronous satellite does not optically track the LAS. The data receiver is aligned to the center of the Earth via horizon or star sensors. The

TABLE 37

**LASER ACQUISITION AND TRACKING SEQUENCE
MULTIPLE LOW ORBIT SATELLITES – SYNCHRONOUS SATELLITE**

- (1) A low orbit satellite and the synchronous satellite are put into contact with the ground based mission control center via the low data RF command link.
- (2) The synchronous satellite beacon transmitter is open loop pointed to within $\pm 0.5^\circ$ of the low orbit satellite via command link computer data from ground.
- (3) The low orbit satellite is open loop pointed to within $\pm 2.5^\circ$ of the synchronous satellite via command link computer data from ground.
- (4) The laser beacon radiation from the synchronous satellite scans a 175×175 element raster of the $1^\circ \times 1^\circ$ field.
- (5) When the low orbit satellite is irradiated, the synchronous satellite receives RF command signals to narrow the scan to a 4×4 element raster around the low orbit satellite position and cooperatively maintains this raster scan around the low orbit satellite position.
- (6) The low orbit satellite automatically proceeds from coarse to fine alignment.
- (7) The low orbit satellite tracks the synchronous satellite beacon.
- (8) The low orbit satellite receives point ahead information via the low data RF command link.
- (9) The low orbit satellite laser beam is dithered about the informed point ahead angle until the synchronous satellite receives the maximum signal intensity.
- (10) Data dump is initiated from the low orbit satellite to the synchronous satellite.

synchronous satellite must provide a beacon for each LAS. This beacon laser is raster scanned about the open loop position. Once the LAS is irradiated, cooperative communication via the low data rate RF link keeps the beacon in a track raster scan mode centered about the LAS position.

After acquisition, the LAS tracks the beacon. Provided with open loop point ahead information, the transmitter dithers about the

point ahead direction until a maximum signal is received at the synchronous satellite receiver. This procedure is essentially a point ahead alignment calibration. From this point, data can be relayed. If the signal level falls below some minimum acceptable level at the synchronous satellite receiver, a point ahead alignment calibration can be redone.

Each low orbit user satellite requires that it be irradiated by a beacon laser from the synchronous satellite receiver station. In order to conserve power, it is best to provide a single output beacon beam for each low orbit satellite user rather than irradiate all users simultaneously with a single beam. Because the receiver optics aboard the synchronous satellite are of such low optical quality for the field of view required, the beacon laser requires its own transmit optics. Fortunately, the size of the the optics can be very small so as not to contribute appreciable weight.

Figure 121 is a schematic of a possible beacon laser system. The output wavelength would be 0.53 μm , since the 1.06 μm is most efficient for the data transmission which incorporates photodiode detectors. Table 38 defines the beacon laser requirements for efficient low orbit tracking. As defined, the beacon beamwidth is 115 μrad , which defines the beacon transmitter diameter (D_B) to be

$$D_B = 1.27 \frac{\lambda}{\alpha} = 1.27 \frac{0.532 \mu\text{m}}{115 \mu\text{rad}} = 5.87 \text{ mm}$$

The beacon average power is 10 mW per low orbit satellite user. Thus, many low orbit satellite users could be accommodated by a single beacon laser with presently available state of the art lasers. As is illustrated in Figure 121 an electrooptic modulator, polarizing beamsplitter, raster scan deflector unit, and course deflector unit is required for each user. The following is a discussion of how each of these components is used. The

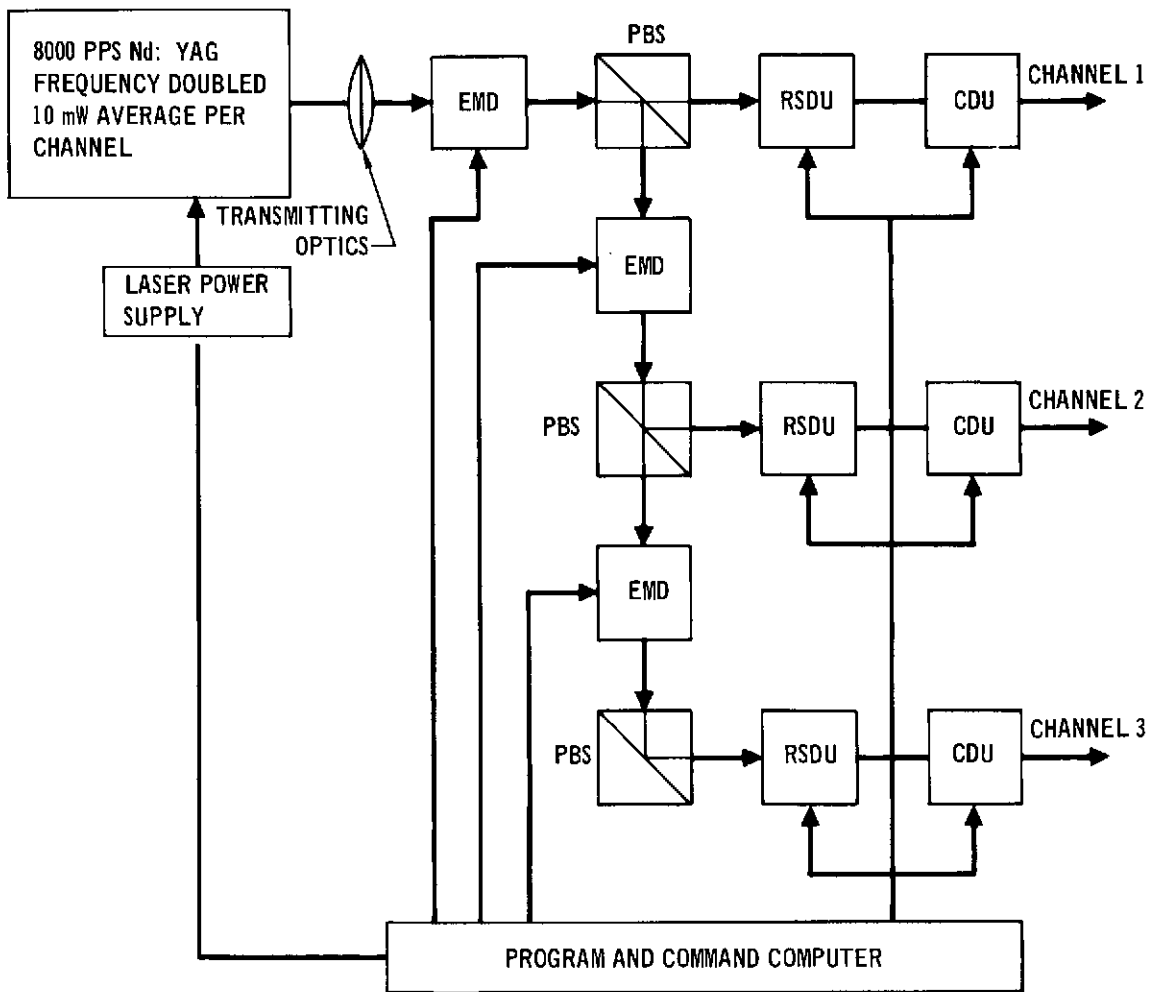
TABLE 38
BEACON LASER REQUIREMENTS ANALYSIS

Parameter	Definition	Value
λ_B	Beacon Wavelength	0.532 μm
$h\nu$	Energy per photon	$3.75 \times 10^{-19} \text{ J}$
R	Range	$4.5 \times 10^7 \text{ m}$
η	Quantum Efficiency of quadrant detector	0.20
T_L	Transmission of optics and filter	0.4
D_B	Diameter of beacon receiver	0.1 m
N_{bep}	Number of beacon photoelectrons that must be detected per received pulse	100 photoelectrons
α_{tb}	Beacon transmitted beamwidth	115 μrad
ϵ	Small raster scan resolution elements Overlap factor from resolution element to resolution element	4 x 4 1.15
Δ_s	Small raster scan field-of-view	400 μrad
URF	Updating repetition frequency required by the low orbit satellite for angle tracking	500 Hz
t_{ss}	Time to scan the small raster scan field $= \frac{1}{\text{URF}}$	2 ms
Δ	Acquisition raster scan field-of-view 1° x 1° Large raster scan resolution elements	17.5 mrad 175 x 175
t_s	Time to scan the large raster scan field-of-view = $(\frac{\Delta}{\Delta_{\text{ss}}})^2 t_{\text{ss}}$	4.13 s
BPRR	Beacon pulse repetition rate (one pulse per resolution element)	8000 pulses/s
P_{PBav}	Average power of beacon laser $P_{\text{PBav}} = \frac{N_{\text{bep}} h \nu R^2 (\Delta_s \epsilon)^2}{\eta T_L D_B^2 t_{\text{ss}}}$	10 mW

**TABLE 38 (Cont'd)
BEACON LASER REQUIREMENTS ANALYSIS**

Parameter	Definition	Value
t_{pW}	Beacon laser pulse width	~ 30 ns
N_{BE}	Background photoelectrons detected per pulse width by beacon receiver	$\ll 1$

**FIGURE 121
SYNCHRONOUS SATELLITE BEACON TRANSMITTER SCHEMATIC**



LEGEND:
 EMD = ELECTROOPTIC MODULATOR AND DRIVER
 PBS = POLARIZING BEAMSPLITTER
 RSDU = RASTER SCAN DEFLECTION UNIT
 CDU = COARSE DEFLECTION UNIT

electrooptic modulator is dc biased to rotate the polarization so that all but 10 mW will be reflected by the polarizing beamsplitter to the next electrooptic modulator. The 10 mW part that is transmitted by the polarizing beamsplitter passes through the raster scan deflector unit and the course deflector unit. A coarse deflector unit is required since the raster scan deflector unit is limited to about 300 open loop resolution elements of 100 μ rad each, or about 3 mrad, which is significantly below the $\pm 10^\circ$ beacon transmitter field required. The aperture requirement of the four devices is not a problem. The power requirement for the electrooptic modulator is very small since it need only work in a dc fashion. It may require some thermal control. Table 39 estimates the weight and power of the synchronous satellite receiver and beacon transmitter for 10 low orbit satellite users. The attractive features of such a receiver system are:

- (1) Extreme light weight of the Fresnel primaries.
- (2) Inherent simplicity of the system.
- (3) Utilization of the detector array to spacially isolate signals from different LAS users and discriminate background.
- (4) No large gimbal optics are required.

3.2.3 Operational Sequence. In order to exercise the experimental multiple receiver station, it must be constructed and either LAS transmitting sources or simulated LAS sources provided on the ground. Once in position, the RF channel must be checked. The operation of the acquisition and open loop tracking of the LAS according to the sequence previously described should be checked and its performance noted. Communication performance from one and then a multiple number of LAS users should be determined.

A primary part of the investigation are the acquisition and tracking techniques. Consequently, after the previous performance investigation, different acquisition and tracking techniques should be investigated to optimize the receiver system performance. Different scan patterns could be easily investigated. Various

TABLE 39

**O-S LINK SYNCHRONOUS SATELLITE DATA RECEIVER AND
BEACON TRANSMITTER FOR LOW ORBIT USERS (10 ASSUMED
FOR CALCULATION)
(10 Mbps/User, PIM, 10^6 pps)**

COMPONENTS	WEIGHT (LBS)	POWER (WATTS)
1. FOUR 1 FOOT DIAMETER FRESNEL LENS PRIMARIES AND STRUCTURAL SUPPORT	12.0	N/A
2. DETECTOR ARRAYS AT PRIME FOCUS AND PROCESSING ELECTRONICS	5.0	10.0
3. 8000 PPS BEACON LASER TRANSMITTER (10 USERS ($\lambda = 0.532 \mu m$, EFF = 0.02, $\alpha_t = 115 \mu RAD$ DOUBLING EFF = 0.5, $D_t = 4$ INCHES, $P_{BEAC} = 10 mW$)	10.0	10.0
4. 10 ELECTRO-OPTIC MODULATORS AND OVENS	5.0	5.0
5. 10 POLARIZING BEAMSPLITTERS	1.0	N/A
6. 10 RASTER SCAN DEFLECTOR UNITS	5.0	50.0
7. 10 COARSE DEFLECTOR UNITS	5.0	5.0
8. ALIGNMENT AND LASER ELECTRONICS RASTER SCAN DEFLECTOR ELECTRONICS LASER THERMAL CONTROL ELECTROOPTIC MODULATOR DRIVER ELECTRONICS COARSE DEFLECTOR ELECTRONICS	13.0	22.0
9. PACKAGING AND MOUNTING	10.0	N/A
TOTAL	66.0	102.0

coarse deflection units (CDU) could be evaluated, including a CDU employing flex pivot mounted scanning mirror and a CDU employing Risely prisms. All of these investigations will require some modification of the described beacon transmitting unit. A man in the loop will facilitate these modifications.

3.2.4 Support Equipment. The operational support equipment includes:

- Oscilloscopes and oscilloscope camera
- Alignment Tools
- Calibrated power monitor
- Chart recorders
- BER instrumentation
- Boresight telescope

Required replacement modules to investigate alternate techniques.

3.2.5 Data Requirements. The required data includes the receiver system parameters versus the performance parameters of BER, acquisition time, tracking and pointing accuracy.

3.3 SYNCHRONOUS TO GROUND COMMUNICATION LINK ATMOSPHERIC PROPAGATION EXPERIMENT.

3.3.1 Experiment Plan.

3.3.1.1 Significance. Several fundamental questions concerned with space-to-Earth and Earth-to-space laser communication links have yet to be answered. Of these, perhaps the most important questions deal with link performance degradations caused by the atmosphere. For example, the long and short term link performance capabilities in the open atmosphere as measured by error rates, link outages, and tracking error remain in some doubt. This uncertainty in duration and quality of link operation is primarily due to the nonstationary character of the atmosphere. Hence, at the present time there is a low level of confidence in theoretical performance estimates of the effect of atmospheric degradations on link performance.

There are two primary reasons for this lack of confidence. The foremost reason being the absence of empirical statistical data on link performance to compare with theoretical estimates. Consequently, from a systems view point, high priority should be assigned to measurement of parameters which directly describe link performance. An experiment designed to obtain data on statistical performance parameters such as bit error rate, link outages, tracking error, etc., for a link operating over near vertical paths in the open atmosphere would provide this vital information.

Obviously the best atmospheric channel characterization can be obtained by operating the laser communication link over the atmospheric path of interest. In this situation the manned synchronous satellite to ground laser communication link would provide an ideal opportunity to acquire the necessary performance data. Furthermore, the manned interaction capability of such a satellite will allow a more versatile experiment to be designed and implemented, and will thereby improve the confidence in the data obtained. Another reason for the use of the synchronous satellite for this purpose is the ability of a large orbital manned station to support much more laser link capability than could be afforded economically in an unmanned, long life relay satellite, thus permitting meaningful link evaluation with portable test equipment, which would be inadequate for an operational link.

The second reason for the low confidence in estimates of theoretical link performance degradation is the limitation of current theoretical models used to describe the effects of propagation in the open atmosphere. The atmosphere is noted for being statistically nonstationary and inhomogeneous. In this situation, only a nonstationary stochastic process exactly models the total effect on the received intensity of atmospheric propagation. However, the only situation for which a well developed statistical model exists is the case of homogeneous locally isotropic, stationary, turbulence. Here turbulence is defined as the fluctuations in atmospheric refractive index which are caused primarily by microthermal fluctuations. The present random models of turbulence only apply in the case of well-mixed random fluctuations.

The atmospheric refractive index is, in general, a random function of both space and time. For optical beam propagation, to first order approximation, only spatial variations are important and the time variations are suppressed. The spatial

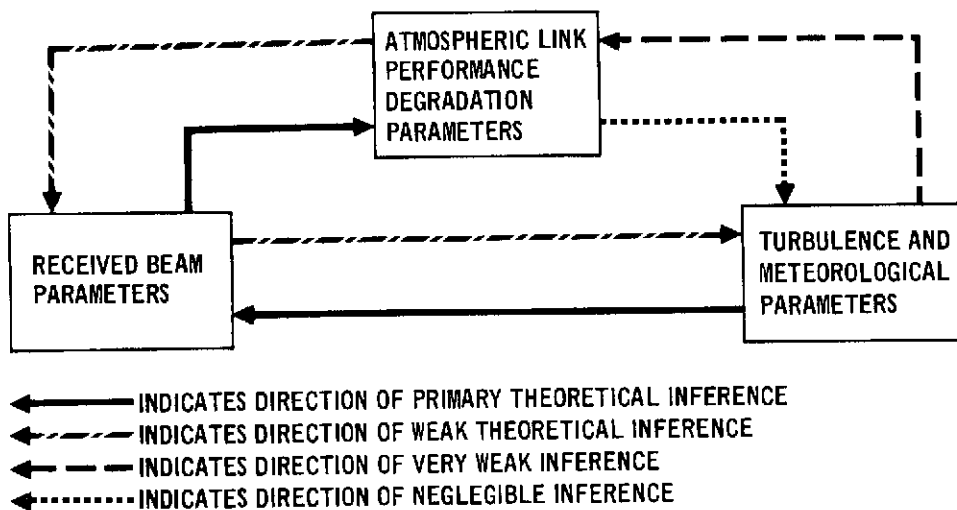
variations have been observed to cause multiplicative variations in the received beam intensity, and hence it is argued with use of the central limit theorem, that the logarithm of received power is normally distributed. In this case, the variance and covariance functions of the log of the amplitude (square root of intensity) are all that is required to specify the lognormal distribution of received signal.

These theoretical models are of limited utility however, because they approximate a highly nonstationary stochastic process, to the first order, with a stationary random process. The first order estimates of the statistics of received power which are attributable to fading, image motion, etc. do not adequately characterize the effect of long term variations in turbulence and meteorological conditions.

The assessment of laser communication link performance degradation caused by atmospheric effects is strongly dependent upon the combination of physical parameters measured. Received beam variable such as scintillation, beam wander, beam spread, and angle of arrival should also be measured in addition to meteorological, turbulence, and link performance parameters. Measurement of statistical beam parameters will provide the data required to verify the hypothesized theoretical relationship between link performance and turbulence and meteorological parameters. Figure 122 illustrates the inference paths between three subsets of both experimental and theoretical parameters representing the physical variables that characterize link performance over atmospheric paths.

Obviously experimental measurements of link performance parameters should be supported by coincident, direct, and indirect measurements of atmospheric variables. This data is required to verify the theoretical estimates of link performance degradation and test the hypothesized theoretic relationships between atmospheric, received beam, and performance parameters. For the

FIGURE 122 PARAMETER INTER-RELATIONSHIPS FOR ATMOSPHERICS EFFECT EXPERIMENTS



purposes of this experiment, however, it will not be sufficient to measure gross meteorological parameters such as wind velocity, pressure, humidity, and temperature gradients, and attempt to deduce turbulence properties and link performance degradation from them. The turbulence variables which are characterized by microthermal fluctuations must also be measured. In addition, observation of the statistical variations of the received beam variables will provide an indirect measure of atmospheric conditions.

In order to make high confidence experimental estimates of the long term statistical behavior of link performance degradation and the atmospheric channel, the laser communications link should be maintained at a given location for a sufficient time period. Here again the synchronous satellite, when compared to the alternatives of a high altitude balloon or airplane, would provide the optimum location for a transceiver and atmospheric experiment package. This is also based on the premise that the manned orbiting laboratory is at or near

synchronous altitude, so that tracking may be maintained for long time periods even in the absence of severe atmospheric turbulence.

Objectives - The objectives of this atmospheric propagation experiment are:

- (1) To obtain statistical estimates of laser communication link performance capabilities based on empirical link performance data alone.
- (2) To develop estimates of laser communication link performance degradation based on both short and long term meteorological and turbulence data.
- (3) To evaluate candidate ground station sites within the synchronous satellite line-of-sight.
- (4) To test the relationships between theoretical predictions and empirical measures of link performance degradations, received beam variables, and atmospheric conditions.

Each one of these objectives can be satisfied with the synchronous-satellite-to-ground laser communication link atmospheric propagation experiment.

Techniques - Several experiment techniques would be used to obtain the needed data.

A combination of a high data rate transceiver link (HDRTL) and atmospheric probe beams, in conjunction with appropriate probe beam optical receivers, would be configured to acquire the necessary physical measurements of link performance and received beam properties. Stellar scintillation and angle of arrival ground measurements would also be performed, coincident with other measurements, to test their correspondence with the beam wave scintillation and angle of arrival.

Vertical profile measurements of temperature, pressure, humidity, wind velocity, etc., and their fluctuations would be made with high altitude weather balloons. These balloons will

have controlled ascents and descents to and from above tropopause. The amount of cloud cover and gross atmospheric conditions would also be monitored by taking sequences of photographs of selected ground sites from the satellite.

Results - In addition to satisfying the above mentioned goals, these experiments will result in an engineering test of ground station sites before committing major construction expenditures. The ability to predict link performance degradations under a variety of turbulence conditions at both different times and locations will be established as will the limitations of the atmospheric channel. The same experimental setup will also serve to demonstrate a typical synchronous satellite repeater terminal.

Functional Description - Equipment for this experiment will be physically located at the two terminals of the communications link and several preselected sites will serve as alternative ground station terminals. Both terminals will contain a 400 Mbps to 1 Gbps mode locked Nd:YAG transceiver like the one described in section 3.1. These transceivers will permit establishment of a communication link whose performance degradation due to atmospheric perturbations will be measured. In addition, these transceivers will be capable of transmitting and receiving a variety of modulation formats so that the effect of the atmospheric channel versus modulation format may be observed.

The ground terminal will also have a Q-switched beacon laser to test and maintain link operation during periods of severe turbulence. This will permit evaluation of link performance and received beam properties for stronger turbulence conditions than could be tolerated with mode locked Nd:YAG uplink.

Each terminal will also contain an atmospheric experiment package consisting of an array of appropriate detectors and

an atmospheric probe laser. The probe beam laser for the ground station terminal will be a high power CW ion Argon laser and the one used at the satellite terminal will be a CW diode pumped Nd:YAG laser. Both probe beams will be fed through the appropriate optics so that the feed beam diameter and radius of curvature at the transmit aperture may be adjusted.

These probe beam lasers will be used to measure the atmospheric effects on the received beam variables. And after theoretical relationships between received beam variables and atmospheric conditions and link performance degradation are established and atmospheric conditions and link performance degradation is established and verified, the probe beams will be used to measure the state of turbulence conditions. The probe beams will be automatically fine pointed along the same line-of-sight as the communication beams and provisions will be included in the transceiver optics design to track and fine point the probe beams when the communication transmit lasers (or beacon) are not in operation. Thus reciprocity tracking will be established for either the communication or atmospheric probe beams alone.

The detector arrays will consist of between 25 and 40 optical detectors used to measure repetitive samples of the instantaneous received intensity profiles of the probe on communication beams thus allowing estimates of scintillation beam wander pointing error, beam spread, spatial correlation, etc. to be determined.

All system components except the detector arrays and the primary receiver optics will be mounted on a test bed to provide easy access by man. The manned interaction capability will also facilitate extra-vehicular construction of the satellite detector array, since it will be a size that will require it be prefabricated and launched in parts. The man in general will be available for aligning the system, monitoring its performance,

and reconfiguring it to optimize the communication system or to improve the data quality of the atmospheric effect on the communication link.

Operational Sequences - Once the high data rate transceivers are configured to a particular system design, the following general operational sequence will be pursued.

- (1) Configure the atmospheric detector package to system design specifications.
- (2) Document atmospheric probe beam and detector array characteristics.
- (3) Exercise atmospheric physical data acquisition instrumentation and record data as experiment proceeds.
- (4) Exercise the communication link and atmospheric probe beam and receivers.

Operational Support Equipment. In addition to the support equipment listed in Table 32 , instrumentation to record, store, and process the measured data will be required. This instrumentation will include a telemetry transmitter and receiver terminal capable of handling a 1 to 10 Mbps data rate on the downlink, analog and digital tape recorders for direct access data storage, a digital signal processor to perform real time statistical analysis, and a digital computer for general data evaluation and statistical analysis.

Experimental Data. The data gathered will include:

- (1) Bit error rate statistics
- (2) Link outage statistics
- (3) Tracking Error
- (4) Pointing Accuracy
- (5) Angle of arrival fluctuations
- (6) Scintillation
- (7) Beam wander
- (8) Beam spread

- (9) Spatial correlation of intensity fluctuations
- (10) Effect of aperture averaging
- (11) Mean received intensity
- (12) Atmospheric parameter fluctuations versus altitude
- (13) Atmospheric parameters versus altitude
- (14) Stellar scintillation, angle of arrival, and spatial correlation.
- (15) Photographic records of cloud cover.
- (16) Atmospheric attenuation

A statistical analysis will be performed on all the measured data and it will be compared with the best current estimates of theoretical statistical models which describe the variables of interest. If data is obtained that does not satisfy these theoretical models, new models will, of course, be evaluated.

3.4 DEEP SPACE RECEIVER. Experiment IV consists of a short pulse, Pulse Interval Modulation (PIM), laser receiving system evaluating the concept of an earth synchronous satellite receiver terminal for deep space reception for optical or RF relay to ground. Future deep space scientific spacecraft probing the outer planets will require as much communication bandwidth as can efficiently be made available. Short pulse low duty cycle laser communication systems will permit scientific data to be efficiently retrieved at rates exceeding 10^5 bps at Saturn and 10^4 bps at Neptune or Pluto. For data rates in the 1 Mbps and less range, PIM has shown to be the most efficient optical communications format for the visible and near IR wavelength region.²⁶ We can describe Pulse Interval Modulation (PIM) as follows. Consider an interval of time, T, containing M sub-intervals or slots. Each slot can represent a unique number. If we restrict our system to one and only one pulse occurring in time T (a so called M-ary system), then each pulse represents $\log_2 M$ bits.

Two receiver concepts exist:

- (1) Multiple Earth based receivers.

- (2) A synchronous satellite receiver with subsequent relay to the ground control station.

3.4.1 Objectives. The objectives of this experiment are to demonstrate and document the performance of the synchronous satellite deep space receiver. An actual deep space probe satellite will not be available for the experiment. But the deep space probe can be simulated by another synchronous satellite carrying the deep space probe transmitter (this simulated deep space transmitter is the subject of the next experiment).

Table 40 gives some of the parameters that could be changed to analyze the performance effect upon the system. Many of the techniques required to exercise those items in Table 39 are discussed in Appendix A.

TABLE 40
FUNCTIONAL PARAMETERS/CONFIGURATIONS SUBJECT TO CHANGE

- Detector type
- Acquisition technique
- Tracking technique
- Receiver Diameter
- Optical quality of primary
- Field of View
- Data rate
- Gate width
- Received Pulse width
- Received Power

Man-aided construction and performance evaluation of the primary receiver is very attractive since it eliminates the complexity of an automatic deployment system. By necessity this receiving primary must be very large - as large as possible. Manipulation of the optical quality of the primary can be facilitated by a

man in the loop. The goal during construction of the primary is for the best possible optical image quality. Degradation from this point is easily done using defocusing techniques.

Large diameter receiver optics are a fundamental requirement for efficient deep space communications. Fortunately, background is not a serious consideration and the collecting primary can have a large blur circle like a photon bucket. Several techniques exist for the construction of large photon bucket collectors; all of which would be facilitated by a man in the loop.

One technique is to build a large, light weight parabolic mirror on the ground; cut it into sections; transport it to its space station; and reconstruct the original parabolic collector with the aid of a suitable mounting platform. Another technique involves using a ring over which is laid a reflective coated foil and a clear foil. When gas is pumped between them, a parabolic surface is formed yielding the desired photon bucket. A third technique involves assembling many small spherical or parabolic mirrors on a large parabolic mounting structure with all of the individual mirrors focused at a common point.²⁷ A few of these types of photon buckets do exist for astronomical measurements. One such mirror shown in Figure 123 is at the Mt. Hopkins Observatory near Tucson, Arizona. It is a 10 meter collector with about 250 individually focused spherical mirrors. Figure 124 shows the theoretical blur circle capability of such photon bucket collectors. The aid of a man in the construction of this type of collector in space would be invaluable. Table 41 enumerates some of the advantages and disadvantages of these three possible photon bucket construction techniques. Mirror mounting techniques could also be facilitated by an astronaut. We have studied the mounting of spherical segment for collector arrays. We have shown that warping techniques can be used to advantage to decrease the off axis astigmatism of a spherical mirror placed in its off axis array position. Figure 125 shows the blur

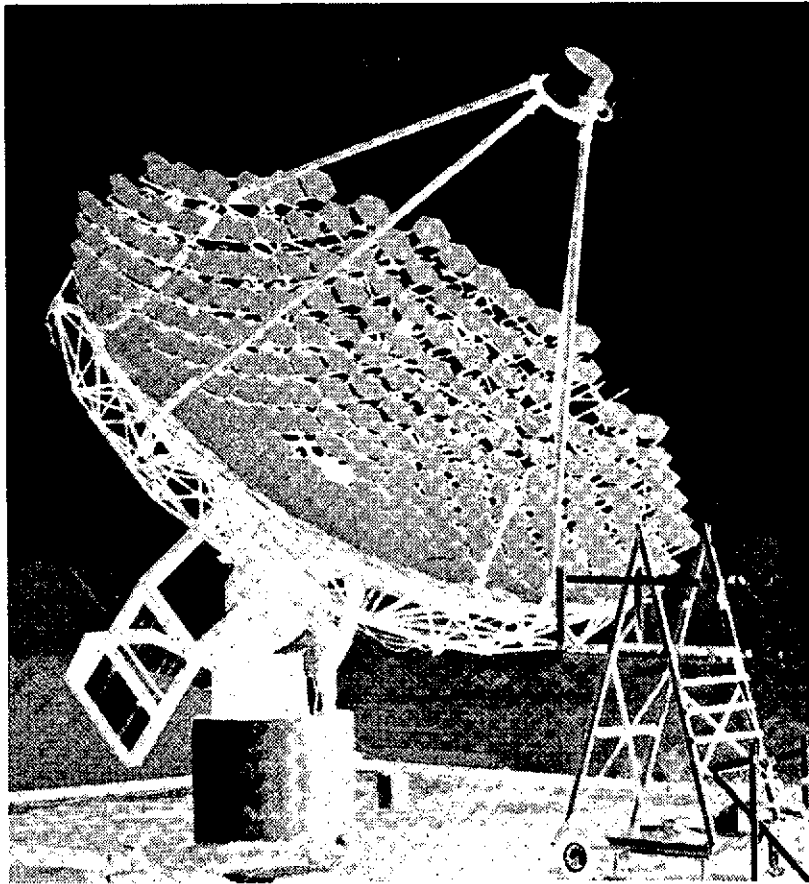


FIGURE 123 10 METER DIAMETER OPTICAL COLLECTOR

patterns of a spherical segment used in the Mt. Hopkin's 10 meter mirror. The top three photographs are at the tangential plane of minimum circle of confusion, and sagittal plane for the unwarped mirror. The bottom three photographs correspond to the same planes but with the mirror in a simple warping harness with a resultant decreased blur circle size. Mounting techniques similar to this could be proposed for an astronaut to master.

The results will be in the form of BER as a function of the other system parameters for the communications mode (e.g. receiver diameter, field of view, data rate, pulse width, gate width, optics quality, detector types, etc.). For the

FIGURE 124 SEGMENTED COLLECTOR OPTICAL QUALITY

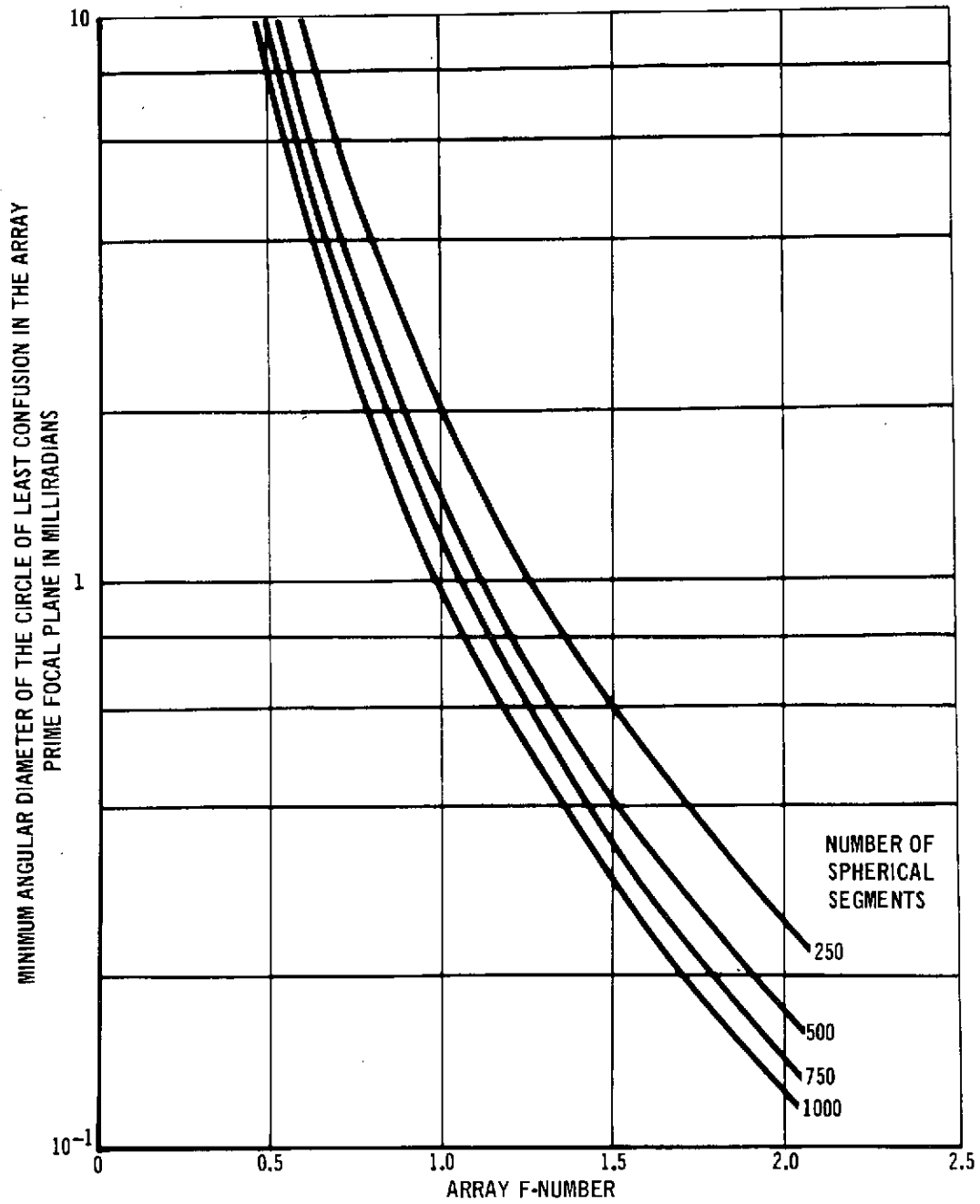
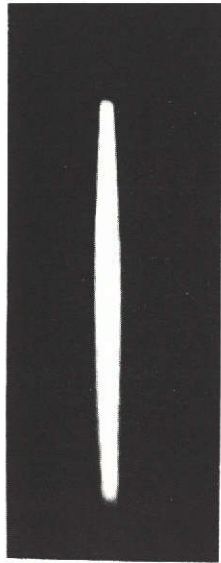


TABLE 41
ADVANTAGES AND DISADVANTAGES OF THREE PHOTON BUCKET
CONSTRUCTION TECHNIQUES FOR SPACE STATIONS

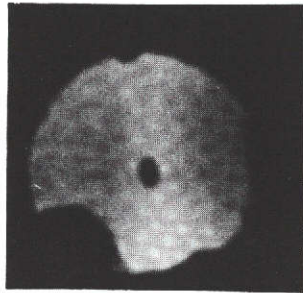
- (1) Technique: Segmented Parabolic Sections
Advantages: Highest possible blur circle accuracy obtainable
Disadvantages: High cost
 - Mounting structure thermal control required to maintain blur circle accuracy
- (2) Technique: Pressurized foil
Advantages: ◦ Low cost
 - Possibility of high accuracyDisadvantages: ◦ Subject to punctures and subsequent depressurization
 - Active pressurization control required to control focal length
- (3) Technique: Parabolic mirror mount with segmented spherical mirrors
Advantages: ◦ Moderate cost
 - Adequate blur circles obtainable
 - Replacement due to damage is inexpensive because all segments are identical.Disadvantage: ◦ Mounting structure thermal control required to maintain blur circle accuracy.

CL4

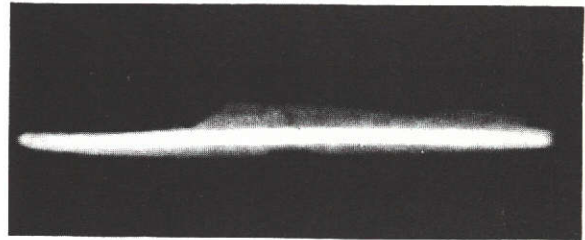
FIGURE 125 SEGMENTED COLLECTOR BLUR PATTERNS
UNWARPED MIRROR



TANGENTIAL

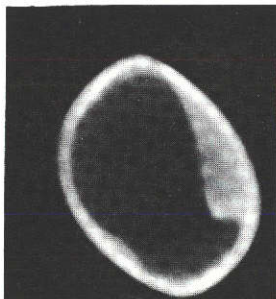


R/2

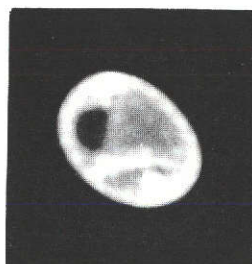


SAGITTAL

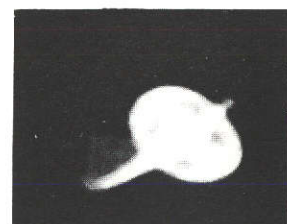
WARPED MIRROR



TANGENTIAL



R/2



SAGITTAL

acquisition and tracking modes, the results will be in the form of break lock probability and tracking accuracy vs received and transmitted power, beamwidths, acquisition techniques, transit time delay (simulated for the ranges of a deep space link), etc.

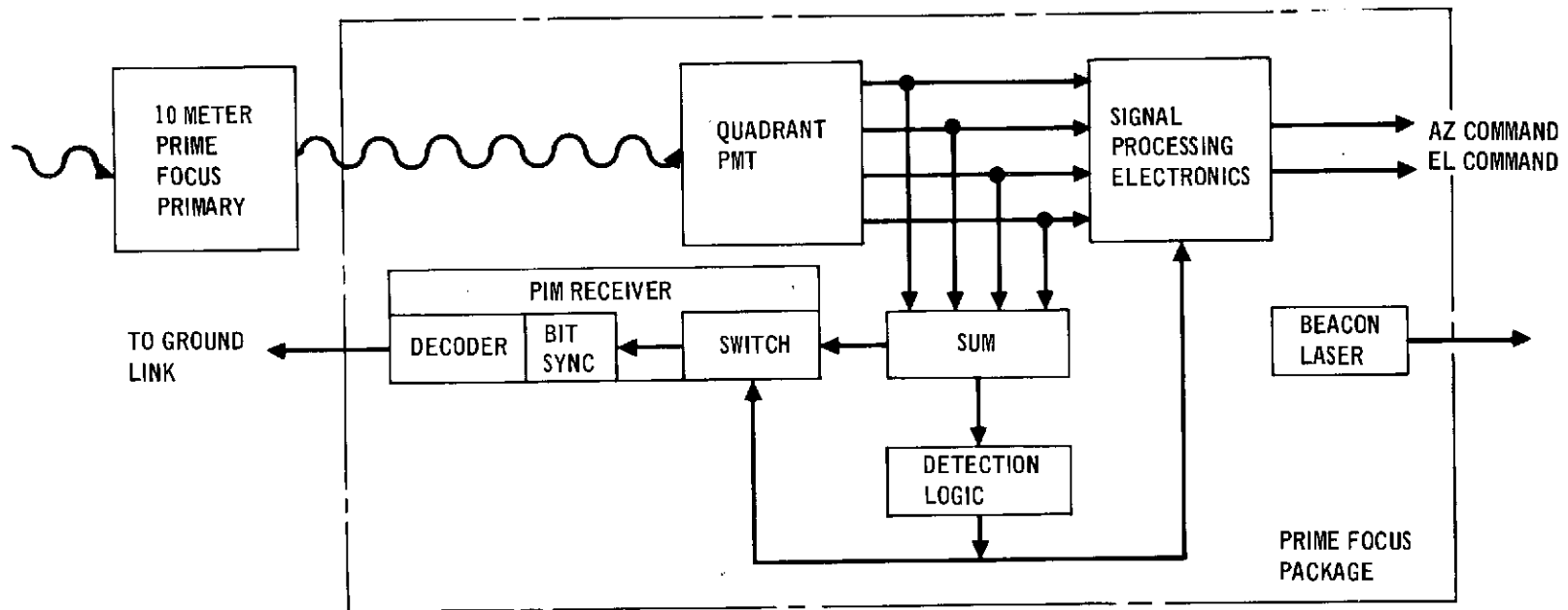
3.4.2 Functional Description. The deep space receiver will be located on a dedicated synchronous satellite. One conception is shown in Figure 115. The receiver system will consist of a large (10 meter diameter) primary mirror and a prime focus package containing the communication acquisition and tracking subsystems. Figure 126 is a conceptual block diagram of the deep space receiver system. The beacon laser in the prime focus package is required for the acquisition and tracking source of the simulated deep space probe transmitter to be discussed in the next experiment.

3.4.3 Operational Sequence. The operational sequence for both experiments IV and V will have to be coordinated. The operational sequence for both the receiver and transmitter is given in Section 3.5.

3.4.4 Support Equipment. The operational support equipment includes:

- Optical test bench
- Real time oscilloscopes
- Optical detectors
- Alignment Tools
- Alignment detector and laser
- Calibrated power monitor
- Scope camera
- Chart recorder
- TV monitor
- Modules (electronic and optic) for implementation of variations of the system functional parameters
- BER instrumentation

FIGURE 126 BLOCK DIAGRAM - DEEP SPACE RECEIVER



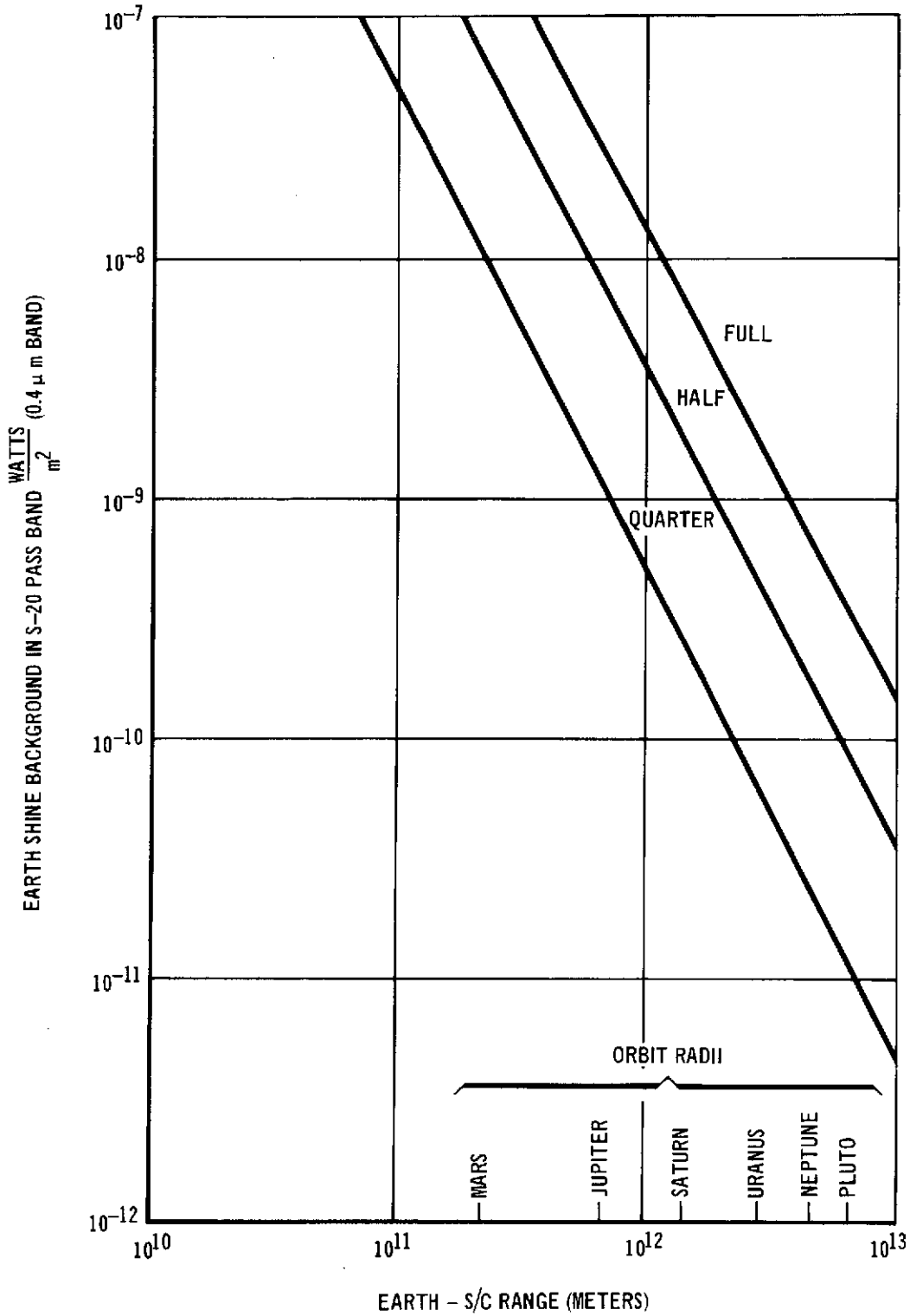
3.4.5 Data Requirements. The required data includes system parameters versus BER, acquisition time, tracking and pointing accuracy.

3.5 DEEP SPACE PROBE TRANSMITTER. Experiment V consists of a short pulse, Pulse Interval Modulation (PIM), near space simulated deep space probe transmitter terminal.

3.5.1 Experiment Plan. The significance of this experiment is to demonstrate and analyze the transmitter performance. The receiver, discussed in Section 3.4, or a suitable alternate is required for a complete communication link to be demonstrated and analyzed. As mentioned in Section 3.4, the acquisition and tracking technique utilized is subject to considerable experimentation. Open loop star tracking techniques are no better than 10 μ rad. So that a technique giving better accuracy is required. An earth beacon can be used, however, beacon power requirements are severe for deep space due to the effects of (1) beam spreading (2) restrictions of beamwidth due to the earth's atmosphere (beam wander) (3) earthshine background noise and 4) transmitter laser pointing requirements which affect tracking loop bandwidth. An alternate approach is to use the earthshine as a beacon source and offset from its energy centroid to the synchronous receiver. This approach requires (1) the earthshine source be large enough to track to a high enough precision (2) an onboard computer capable of updating the correct pointing from the energy centroid to the synchronous satellite deep space receiver. Analysis of outer planet missions show that one quarter earthshine from Neptune is satisfactory, and that this condition is readily achievable when the deep space probe nears Neptune. Figure 127 gives the signal available from earthshine for deep space ranges for full, half, and quarter earth.

At the rare times when earthshine is low and one needs to transmit, a beacon can be used at low power because now it is

FIGURE 127 USE OF EARTH SHINE AS BEACON



not competing with earth background. At 4×10^{12} m a 1 KW average power laser beacon is required (readily available today). A significant advantage of a night beacon is that the turbulence is much reduced allowing a narrower beacon transmitter beamwidth of 20 μ rad. A short pulse PIM system would require the characteristics given in Table 42 to obtain data rates ranging from 2 Mbps at Saturn to 10 Kbps at Neptune.

TABLE 42
DEEP SPACE PIM LASER SYSTEM NEPTUNE – EARTH LINK

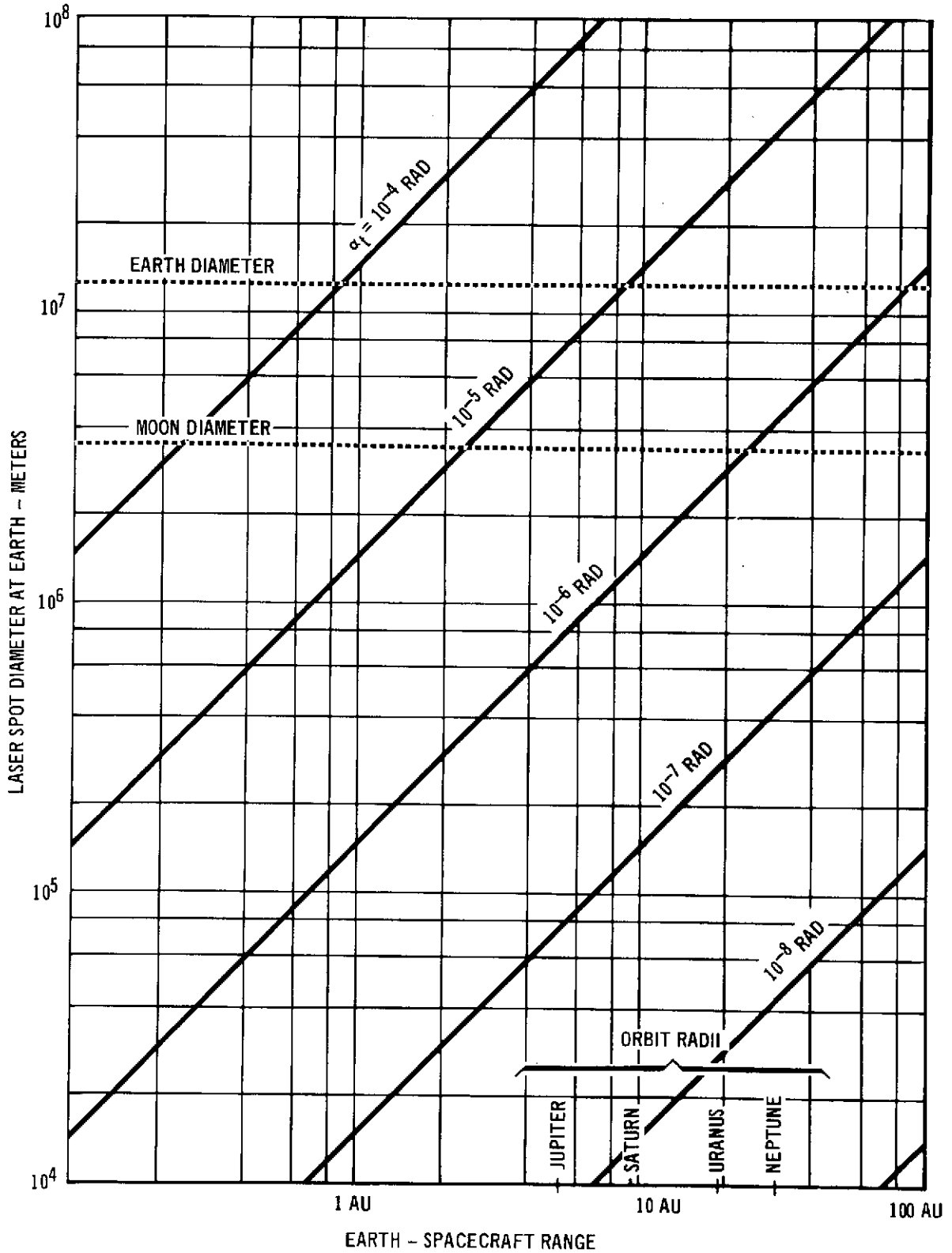
Data Rate	10^4 bps
Transmitter primary diameter	4 inches
Receiver primary diameter	10 meters
Laser pulse width	1 ns
Laser peak power	2 MW
REP rate	5 pps
Duty cycle	10^{-6}
Average signal power	1 W
Receiver spectral width	100 Å
Laser system efficiency *	10^{-3}
Battery input power	60 W

*This includes laser transmitter efficiency, optics losses in transmitter and receiver and quantum efficiency of photodetector. Figure 128 shows the spot diameter at the earth plane as a function of range and angular beamwidth.

The parameters that are subject to experimental investigation are:

- (1) Transmitter power
- (2) Transmitter beamwidth
- (3) Data rate
- (4) Received beacon power and source
- (5) Acquisition and tracking field of view

FIGURE 128 LASER BEAM SIZE VERSUS RANGE



Simulating an earthshine tracking source for a near earth test would be quite complex. A star or planet could be used only for the short time it was in a narrow angular region of the synchronous satellite deep space receiver. Another alternative would be to use a CW beacon source to simulate the earth shine source. This is an area requiring considerable investigation.

3.5.2 Functional Description. Figure 129 is the functional block diagram of the deep space probe transmitter. A deep space probe communication transmit system must be as light and power efficient as possible, but some liberties can be taken in exchange for experimental flexibility. This package will be similar in characteristics and function to that of a near space laser communications transmitter described in Section 3.1. The laser will be of a cavity dump type shown in Figure 130. The modulator is employed in the laser cavity to Q-switch the PIM pulse out of the laser in the correct coded time interval. Acquisition and tracking will be accomplished using an identical acquisition and tracking system. The acquisition source will be a beacon laser on the cooperative receiver that simulates a beacon from the earth or earthshine. The beacon laser will either be Q-switch pulsed or CW (simulating the earthshine source).

Operationally, data dumps from deep space to earth will be scheduled and/or preprogrammed from a previous data dump. A very low rf transmit-receive capability from ground to deep space probe will be available for command data. The initial step in acquisition is for the deep space probe transmitter to acquire either the earth (earth shine) or earth beacon using system technology similar to that available in star trackers today. There will be only one detector (quadrant PMT) for both acquisition and tracking with a variable field of view. The required field of view depends on the range. The object field must at least contain the earth. Acquisition time is not

FIGURE 129 FUNCTIONAL BLOCK DIAGRAM – DEEP SPACE PROBE TRANSMITTER

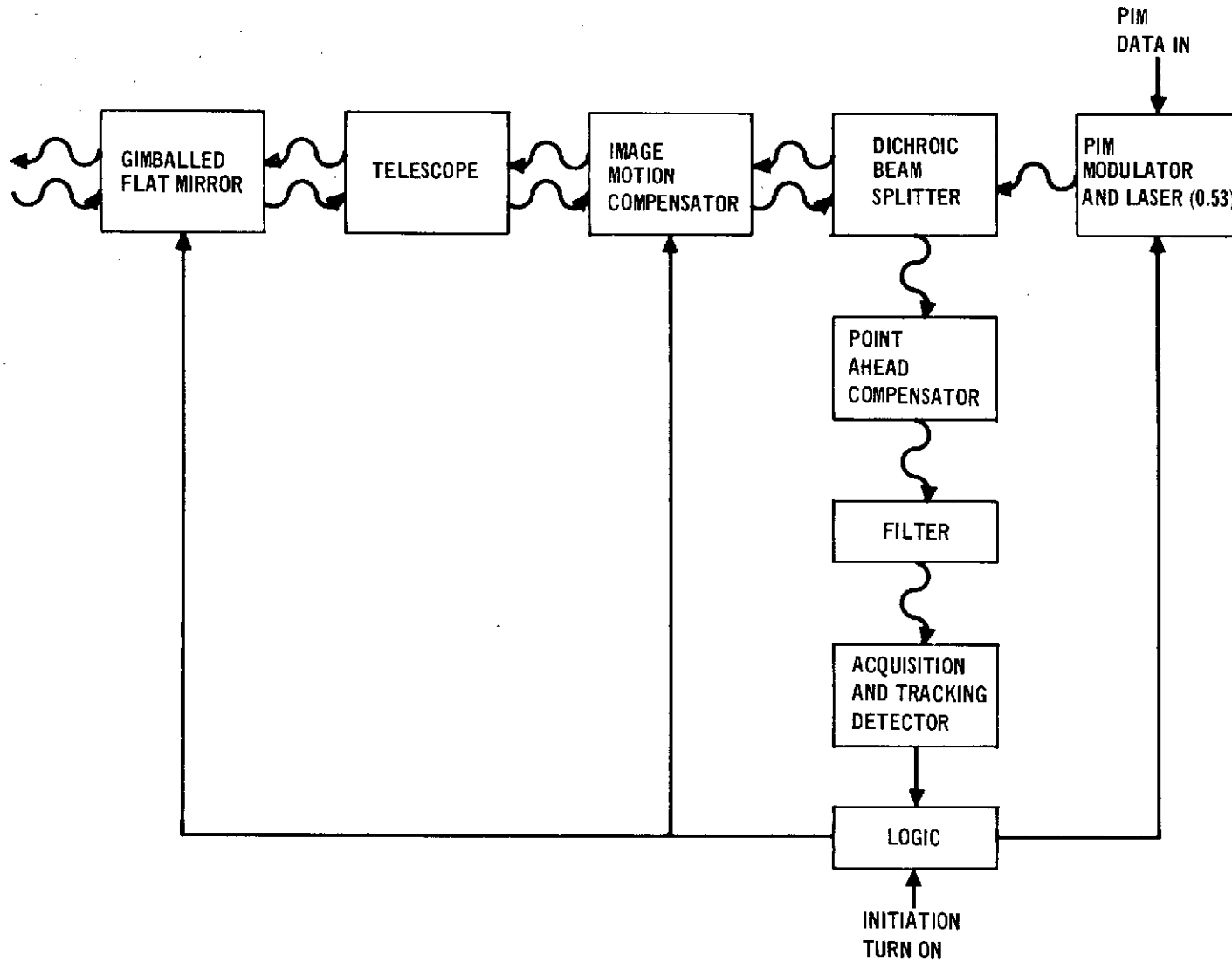
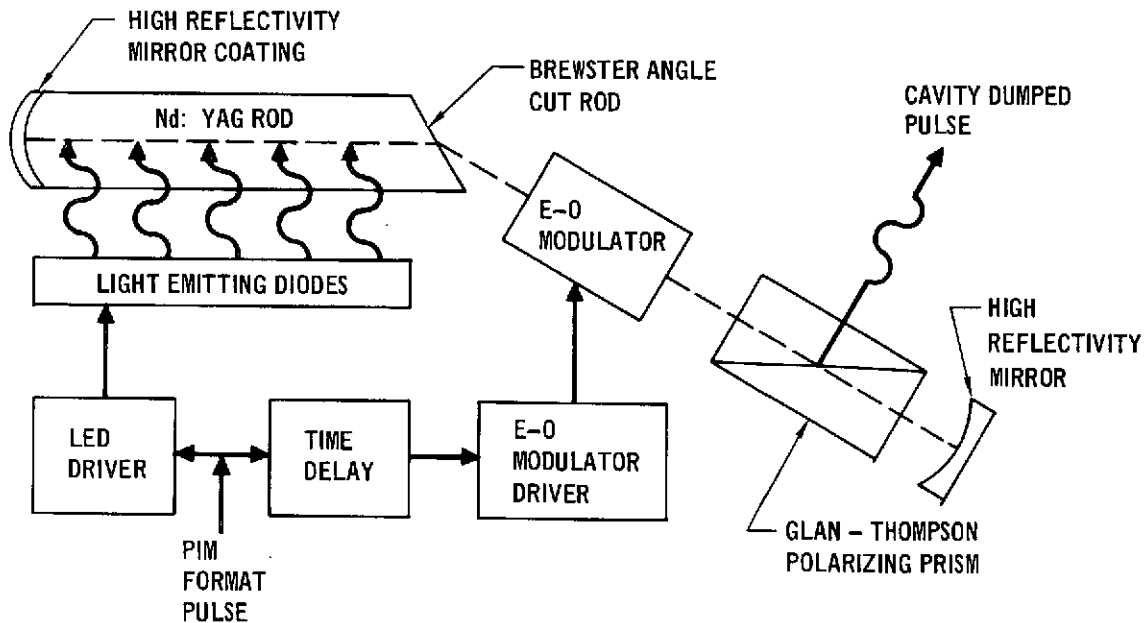


FIGURE 130 PIM TRANSMITTER CAVITY DUMPING SYSTEM



critical thus allowing time for searching the uncertainty field with a small field of view detector. Point ahead benders will be required for offset pointing from the received tracking line of sight to where the synchronous satellite will be when the transmit beam reaches it.

3.5.3 Operational Sequences Experiments IV and V. Both the deep space transmitter and receiver systems must be deployed in synchronous orbit. Man aided construction and alignment of the receiver primary is a major task. Once the systems have been configured to their respective design specifications, link testing can begin. The receiver and transmitter are open loop pointed at each other. The beacon is initialized and acquisition and tracking are exercised at the simulated deep space transmitter. Various beacon powers and a CW beacon (simulating earthshine) could then be used to investigate the efficiency of the acquisition and tracking performance. The PIM communication channel utilizing the 10m receiver could then be evaluated. Performance as a function of transmitter power and transmitter

beamwidth and the receiver parameters defined in Table 40 should then be investigated and the results documented.

3.5.4 Support Equipment. The operational support equipment for the simulated deep space transmitter include:

Oscilloscopes and oscilloscope camera

Alignment tools

Calibrated power monitor

Chart recorder

Modules (electronic and optic) for implementation of the system functional parameters.

3.5.5 Data Requirements. The data requirements for the simulated deep space transmitter system include the system parameters enumerated in Section 3.4 versus resulting link performance parameters of BER, acquisition time, and tracking and pointing accuracy.

APPENDIX A
IMPLEMENTATION TECHNIQUES

1.0 INTRODUCTION

In the experiment definitions of Section 3, particular system configurations were given. Configuration and/or system parameters can be changed by a man in the loop or by some automatic technique. This appendix consists of tables, one table for each system configuration or parameter variable. The table enumerates the implementation techniques; enumerates the required support equipment, and defines the subsystem performance implications of the communications, acquisition and tracking subsystems. The preferred technique is also indicated. Comments accompany each table.

The Tables are presented in the following order:

- 1) Power of output beam
- 2) Receiver diameter
- 3) Transmitted beamwidth
- 4) Optics efficiency
- 5) Spectral bandpass filter
- 6) Quantum efficiency
- 7) Power split for tracking
- 8) Field of view
- 9) Detector gatewidth
- 10) Communication data rate
- 11) Modulation format
- 12) Laser type
- 13) Communication detector type
- 14) Acquisition detector type
- 15) Tracking detector type
- 16) Acquisition technique

PRECEDING PAGE BLANK NOT FILMED

2.0 COMMENTS: POWER

A man could very easily affect this change by inserting a neutral density filter plate in a holding jig after the transmit collimating telescope. Unfortunately the beam diameter is quite large at this point, requiring an equally large neutral density filter diameter. The other alternative is placing a neutral density filter in the small beam before beam collimation. Unfortunately, the glass plate neutral density substrate also acts as a beam spoiling element if placed in such a position requiring focus adjustment to return the system to its original transmitted beamwidth. In the interest of reducing the man in the loop requirements to a minimum, the larger diameter neutral density filter should be chosen. The activity requirements of the man in the loop would be 1) place the neutral density filter in the holding jig; 2) measure output power. The neutral density filter will be calibrated but it is always wise to double check just to make sure nothing has changed.

The other technique of changing laser pump power eliminates the man in the loop requirement but at the expense of also changing the laser output statistics. A fundamental scientific principle is to maintain continuity in all parameters except the one under examination. Consequently, this technique is not preferred.

3.0 COMMENTS: RECEIVER DIAMETER

The receiver diameter can be decreased by reducing the aperture of the entrance pupil or image of a focused objective with the aid of an iris. Systems designed previously have not had an image of the objective that was accessible for implementation of an iris. A special system design and construction would be required to decrease the receiver diameter using any technique other than direct aperturing of the receiver entrance aperture. Special concern must be taken not to restrict the aperture to a point where it will affect the transmitted beam which must pass through the aperture. The received power is directly proportional to the square of the receiver diameter. If the optics system

* Preferred Techniques

TABLE A-1

SYSTEM CONFIGURATION OR PARAMETER VARIABLE: Power of Output Beams

IMPLEMENTATION TECHNIQUES	SUPPORT EQUIPMENT	SUBSYSTEM PERFORMANCE IMPLICATIONS		
		COMMUNICATIONS	ACQUISITION	TRACKING
* Direct attenuation at package output	Neutral density filter	higher BER	increase time	decrease accuracy
Reduce laser pump power	Power meter adapted with adequate collection system	higher BER + degrade laser output statistics > further increase BER	increase time	decrease accuracy

TABLE A-2

* Preferred Technique

SYSTEM CONFIGURATION OR PARAMETER VARIABLE: Receiver Diameter

IMPLEMENTATION TECHNIQUES	SUPPORT EQUIPMENT	SUBSYSTEM PERFORMANCE IMPLICATIONS		
		COMMUNICATIONS	ACQUISITION	TRACKING
* Iris at entrance pupil Iris at focused objective	Iris	decrease in power results in increased BER.	increased acquisition time due to decreased received power.	decreased accuracy due to decreased power and increased spot size.

131

where diffraction limited before aperturing, then the received signal spot sizes would increase with decreased receiver diameter according to the diffraction equation

$$s = F(2.44 \frac{\lambda}{D})$$

where

s is the image spot diameter.

F is the effective focal length for the imaged spot.

λ is the wavelength.

D is the diameter of the entrance pupil.

As s increases, the linear tracking range increases and the tracking sensitivity (accuracy) decreases.

4.0 COMMENTS: TRANSMITTED BEAMWIDTH

The received power, P_R , is related to beamwidth, α_T , by

$$P_R \propto \frac{1}{\alpha_T^2}$$

Consequently, the communication subsystem performance is degraded since the received power is decreased with increased beamwidth. Received acquisition time should remain a constant for a scanning beam (ie the average power per unit time per unit area remains a constant). Tracking performance for the tracker receiving the broadened beamwidth will be degraded according to its power dependence. But the required pointing for the broadened transmitter is decreased in proportion to the increased beamwidth.

For the high data rate transmitter the beamwidth is as narrow as the transmit telescope will permit. Therefore, only beam spoiling can be done without increasing aperture size. Beam spoiling can be done by using a zoom lens in the feed beam optics controlled manually or electronically or by using a beam spoiling element in the feed beam optics. The beam spoiler could also be introduced into the beam manually or with the aid of a solenoid operated mechanism. If beam spoiling plates were employed, it would required a different plate or plates in series to achieve different beamwidths. The technique of axially translating a

TABLE A-3

SYSTEM CONFIGURATION OR PARAMETER VARIABLE: Transmitted Beamwidth

IMPLEMENTATION TECHNIQUES	SUPPORT EQUIPMENT	SUBSYSTEM PERFORMANCE IMPLICATIONS		
		COMMUNICATIONS	ACQUISITION	TRACKING
Axial translation of a beam collimating lens - Manually * Electronically Beam spoiling element	Translation mechanism glass plate. Interferometer used to measure beamwidth	Increased BER with increased beamwidth	see comments	see comments

collimating lens gives a continuous control of the beamwidth. Also no additional losses are introduced in the system. An interferometer placed at the exit of the transmitting telescope could be used to measure the beamwidth.

5.0 COMMENTS: OPTICS EFFICIENCY

The same comments given for the power variable apply here.

6.0 COMMENTS: SPECTRAL BANDPASS FILTER

As with the gate width and field of view, the spectral bandpass filter controls the background level. There are four parameters that characterize the performance of a simple filter:

- 1) Acceptance angle
- 2) Bandpass
- 3) Transmission
- 4) Useable aperture.

Other performance characteristics of interest are the spectral blockage provided on the high and low side and the extinction ratio. Ideally one would like to choose a filter with a large acceptance angle, small bandpass, high transmission and a large useable aperture, but unfortunately, the performance parameters all compete and when stringent requirements are placed on one of them the others degrade correspondingly. Consequently, it may be of interest to exchange some high quality filters and obtain a direct correlation of their relative effect on the sub-system performances.

7.0 COMMENT: QUANTUM EFFICIENCY

Affecting a degraded quantum efficiency is easily accomplished by adding an optical lossy filter at the window of the detector. This technique is required to evaluate the performance degradation to the system as a whole when one of the involved detectors degrades.

TABLE A-4

SYSTEM CONFIGURATION OR PARAMETER VARIABLE: Optics Efficiency

IMPLEMENTATION TECHNIQUES	SUPPORT EQUIPMENT	SUBSYSTEM PERFORMANCE IMPLICATIONS		
		COMMUNICATIONS	ACQUISITION	TRACKING
Neutral density filter input	ND filter	same effect as power dependence	same effect as power dependence	same effect as power dependence

TABLE A-5

SYSTEM CONFIGURATION OR PARAMETER VARIABLE: Spectral Bandpass Filter

IMPLEMENTATION TECHNIQUES	SUPPORT EQUIPMENT	SUBSYSTEM PERFORMANCE IMPLICATIONS		
		COMMUNICATIONS	ACQUISITION	TRACKING
Manual exchange	None	BER increases with increased bandpass	acquisition time increases with increased bandpass	Increased bandpass results in increased background which degrades the signal to noise giving poorer tracking accuracy

TABLE A-6

SYSTEM CONFIGURATION OR PARAMETER VARIABLE: Quantum Efficiency

IMPLEMENTATION TECHNIQUES	SUPPORT EQUIPMENT	SUBSYSTEM PERFORMANCE IMPLICATIONS		
		COMMUNICATIONS	ACQUISITION	TRACKING
Can only degrade quantum efficiency - best technique and very easy to implement is to add optical loss filters at window of detector.	Loss filters	Degraded BER	Decrease S/N	Decrease S/N

8.0 COMMENTS: POWER SPLITTING RATIO - TRACKING/COMMUNICATIONS

For the systems that employ a tracking/communication beam splitter, only the relative powers affect the tracking and communication subsystem performances. A manual replacement of the splitter will vary the splitting ratio. Some systems use the same detector for tracking and communications and splitting is not a factor in such a system.

9.0 COMMENTS: FIELD OF VIEW

The only practical technique of varying the field of view is to use a variable iris at the field stop plane. This device could either be controlled electronically or manually. In the interest of keeping the system simple and reliable, the variable iris should be a manually operated type. The field of view can only be increased up to that accommodated by the detectors and the optics. The optical system should be designed for the largest field of view expected operational requirement.

Full field of view with full utilization of detector area may be a requirement. Zoom optics before the detector would thus be required. The variable iris is probably the preferred technique for the communication subsystem while zoom optics is probably the preferred technique for the tracking subsystem.

10.0 COMMENTS: GATE WIDTH

The gate width is the time interval the detector is turned on to accept the signal pulse. Unfortunately the gate width cannot be directly controlled on the gated tube now under development (DCFP). One technique to change the gate width is to change the 1st dynode bias but the offshoot effects mask off any gate width variable effects. Consequently, unless tubes are developed where the gate width can be controlled directly, the gate width variable will not be a parameter variable subject to experimental evaluation.

TABLE A-7

SYSTEM CONFIGURATION OR PARAMETER VARIABLE: Power Split for Tracking

IMPLEMENTATION TECHNIQUES	SUPPORT EQUIPMENT	SUBSYSTEM PERFORMANCE IMPLICATIONS		
		COMMUNICATIONS	ACQUISITION	TRACKING
Exchange of power splitter - Could be done either manually or by electronically controlled splitter wheel.	Adequate supply of power splitters with different splitting ratios	Strictly power dependence	None	Strictly power dependence

TABLE A-8

SYSTEM CONFIGURATION OR PARAMETER VARIABLE: Field of View

IMPLEMENTATION TECHNIQUES	SUPPORT EQUIPMENT	SUBSYSTEM PERFORMANCE IMPLICATIONS		
		COMMUNICATIONS	ACQUISITION	TRACKING
<p>Employment of variable iris at field stop</p> <p>- Could be controlled either electronically or manually.</p> <p>Zoom optics</p>	<p>variable iris</p> <p>Zoom optics</p>	<p>Background is increased with increased field</p> <p>_____</p> <p>If system is designed for a negligible background effect on BER, considerable changing in the field of view may be required to realize a change in BER</p>	<p>same</p> <p>_____</p>	<p>same</p> <p>_____</p>

TABLE A-9

SYSTEM CONFIGURATION OR PARAMETER VARIABLE: Detector Gate Width

IMPLEMENTATION TECHNIQUES	SUPPORT EQUIPMENT	SUBSYSTEM PERFORMANCE IMPLICATIONS		
		COMMUNICATIONS	ACQUISITION	TRACKING
-	None	Background discrimination	-	-

294

197

11.0 COMMENTS: COMMUNICATION DATA RATE

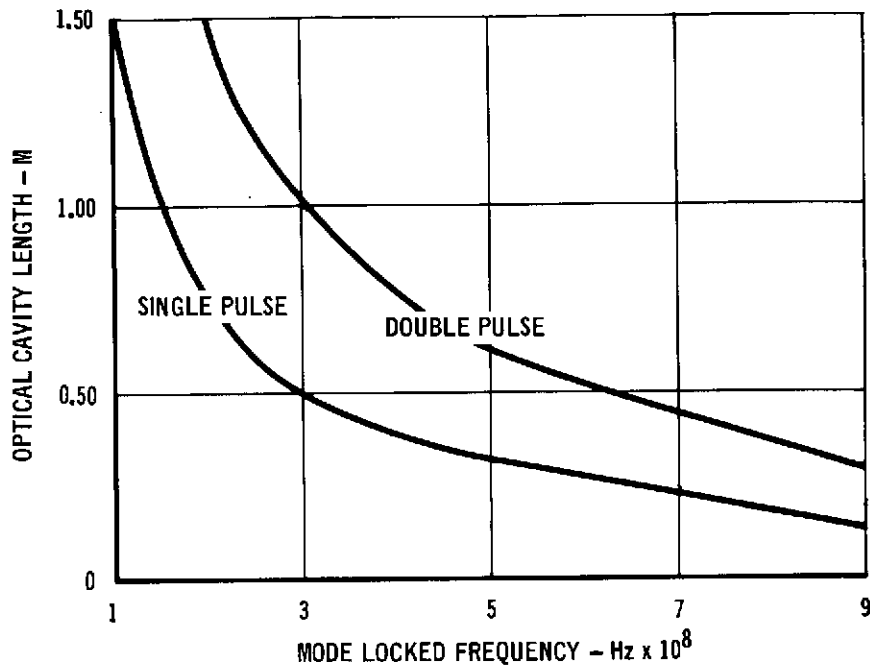
Reconfiguration of a system for a different data rate can be time consuming and require a considerable amount of support equipment. Technique #1 gives the system an essentially continuous choice of data rate. Techniques #2, #3, and #4 will give interger multiples and submultiples of the fundamental mode locked frequency and are much more easily implemented than technique #1. Technique #1 requires a complete realignment and system calibration. Figure A-1 is a plot of the required optical cavity length as a function of mode-locked frequency. For each cavity length there are optimum cavity end mirrors to achieve the maximum mode fill in the rod and thus the maximum efficiency. If a gating communications detector (such as the DCFP) is utilized at the receiving end, then the data rate can only be varied by interger multiples of the tubes designed frequency. All of the detection electronics should be tweaked for the receiving data rate. In this respect, it appears that techniques #2, 3, and 4 are most appropriate.

12.0 COMMENTS: MODULATION FORMAT

If an experimental communication link were available in the operational environment, one would like to exercise the various digital baseband formats:

- (1) PGBM (Pulse Gated Binary Modulation) is a two state low duty cycle PCM with a binary "1" represented by a pulse and binary "0" represented by the absence of a pulse.
- (2) PDBM (Pulse Delay Binary Modulation) is two state, low duty cycle PPM with a delayed pulse representing a binary "1" and an undelayed pulse representing a binary "0".
- (3) PPBM (Pulse Polarization Binary Modulation) is a two state, low duty cycle format which uses a right circularly polarized pulse to represent a binary "1" and a left circularly polarized pulse to represent a binary "0".
- (4) PQM (Pulse Quaternary Modulation) is a four state, low duty cycle format which uses the following M-ary pulse representations:

FIGURE A-1 LASER CAVITY LENGTH



- right circularly polarized, undelayed - "0"
- right circularly polarized, delayed - "1"
- left circularly polarized, undelayed - "2"
- left circularly polarized, delayed - "3"

Although larger dimensionality M-ary formats and coded digital baseband systems are attractive from an information efficiency viewpoint, implementation difficulties make them undesirable. Figure A-2 is a block diagram of the transmitter and receiver for PGBM, PPBM, and PDBM. Figure A-3 is a similar block diagram for PQM. The required receiver configurations for the four formats are very similar, PGBM and PDBM use a single detector while PQM and PPBM require two detectors. It is possible to design the receiver system to function on any of the formats without major reconfigurations or alignment difficulties. Figure A-2 (a) through (c) schematically portray the arrangement of a receiving system. This receiver arrangement is very attractive for a manned or unmanned experiment. This concept permits a demonstration of four different modulation formats and also provides a number of alternate modes to extend the useful life by providing redundancy for the PGBM and PDBM formats.

TABLE A-10

SYSTEM CONFIGURATION OR PARAMETER VARIABLE: Communication Data Rate

IMPLEMENTATION TECHNIQUES	SUPPORT EQUIPMENT	SUBSYSTEM PERFORMANCE IMPLICATIONS		
		COMMUNICATIONS	ACQUISITION	TRACKING
1. Change laser cavity length	(refers to #1)		None	None
2. Change from single to double pulsing of the mode locked laser.				
3. Employ pulse doubling techniques using modulators that have the capability..				
4. Divide the pulse rate by an integer amount by blanking with the modulator.				

297

981

TABLE A-11

SYSTEM CONFIGURATION OR PARAMETER VARIABLE: Modulation Format

IMPLEMENTATION TECHNIQUES	SUPPORT EQUIPMENT	SUBSYSTEM PERFORMANCE IMPLICATIONS		
		COMMUNICATIONS	ACQUISITION	TRACKING
<p>Reconfiguration of modulator subsystem and receiver subsystem to be compatible with the modulation format.</p> <p>* Adaptable PQM modulator and compatible receiver system.</p>	<p>Appropriate subsystem configuration alignment instrumentation.</p> <p>See comments</p>	Described by theoretical model.	None (Power dependence)	None (Power dependence)

On the transmitting end, the modulator must be changed to exercise the four modulation formats. But with the receiver system described above, all four formats can be exercised with the PQM modulator configuration. Referring to the transmitter in the PQM block diagram, Figure A-3 and the receiver diagram, Figure A-4 :

- (1) PGBM can be exercised by using modulator #2 (modulator #1 is passive) and the polarization separator at the receiver as the analyzer.
- (2) PPBM can be exercised by using modulator #2 (modulator #1 is passive).
- (3) PDBM can be exercised by using modulator #1 (modulator #2 is passive).
- (4) PQM can be exercised by activating both modulators.

This modulator and receiver configuration not only afford a maximum of flexibility but it also provides an identical link with nearly equal system losses for direct comparison of the modulation format efficiencies.

13.0 COMMENTS: LASER TYPE

The communication subsystem performance is highly dependent upon the degree of stability provided by the transmit laser. A man could be utilized by switching laser types; tweaking them up to their best performance; and measuring the resultant communication performance. The LED pumped, phase locked laser promises to be the most stable mode-locked laser. All four combinations (yielding four different communication lasers) should be tried in the operational environment provided.

Similarly, the beacon laser type will affect the pulse width and pulse repetition rate which affect the acquisition and tracking subsystem performance. The narrower the pulse width and the higher the repetition rate the better the performance will be. The basic laser cavity end mirrors, pump, and rod could be utilized to configure the different lasers by adding and subtracting intra cavity components as required.

FIGURE A-2 MULTIPLE DEMOD RECEIVER 2-DCFP

Figure 2a PGBM by DCFP-1

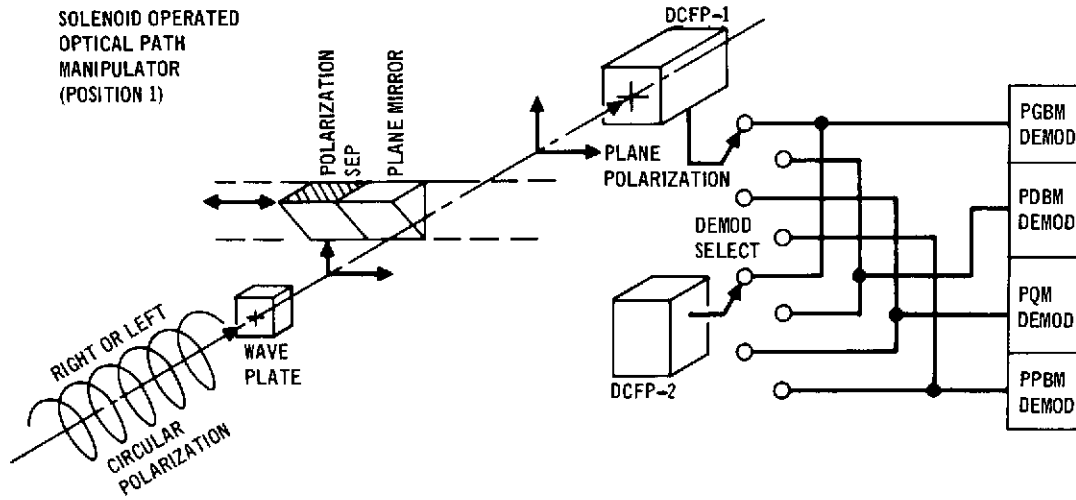


Figure 2b PGBM by DCFP-2

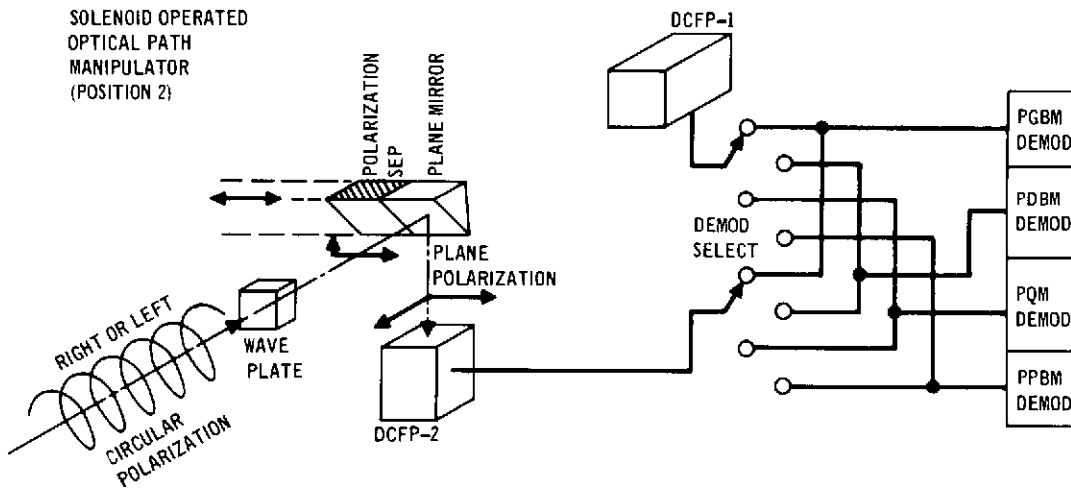


Figure 2c PQM by Both DCFP -1 and -2

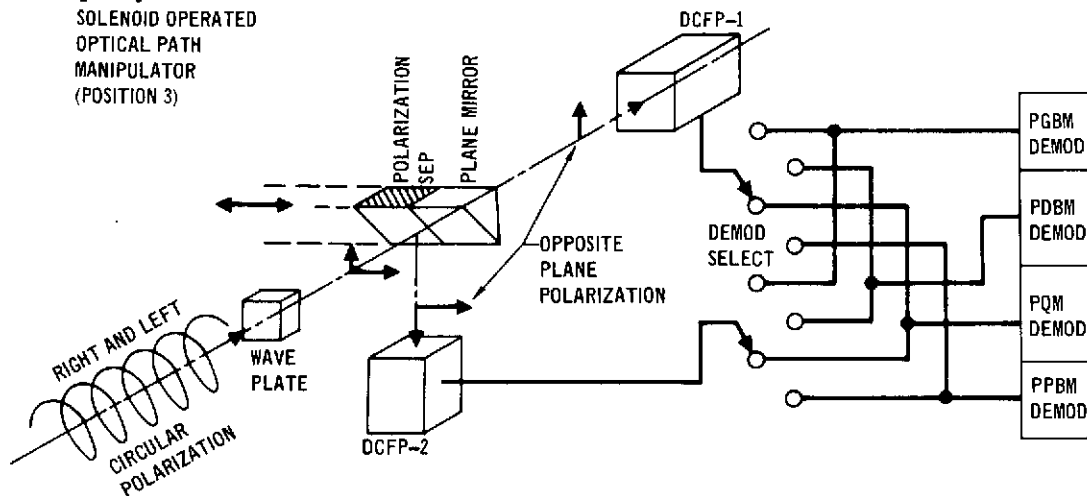


FIGURE A-3 PQM BLOCK DIAGRAM

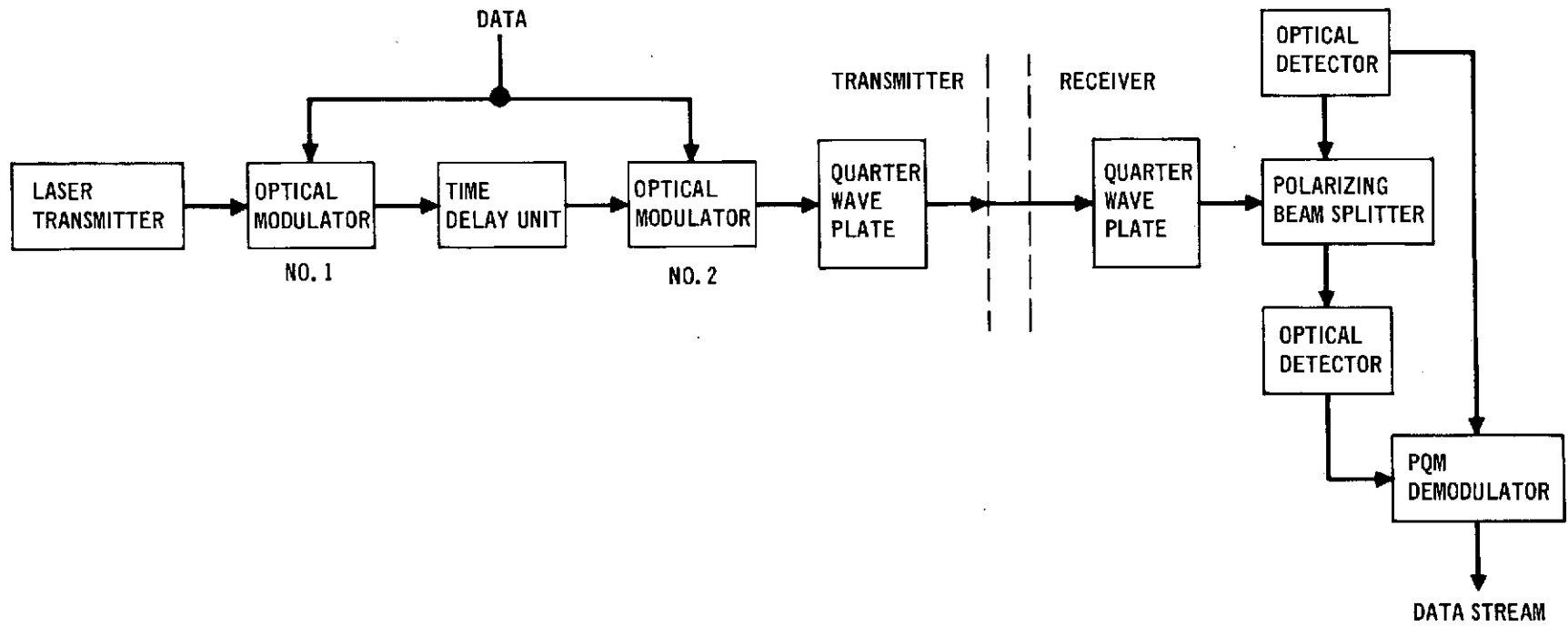
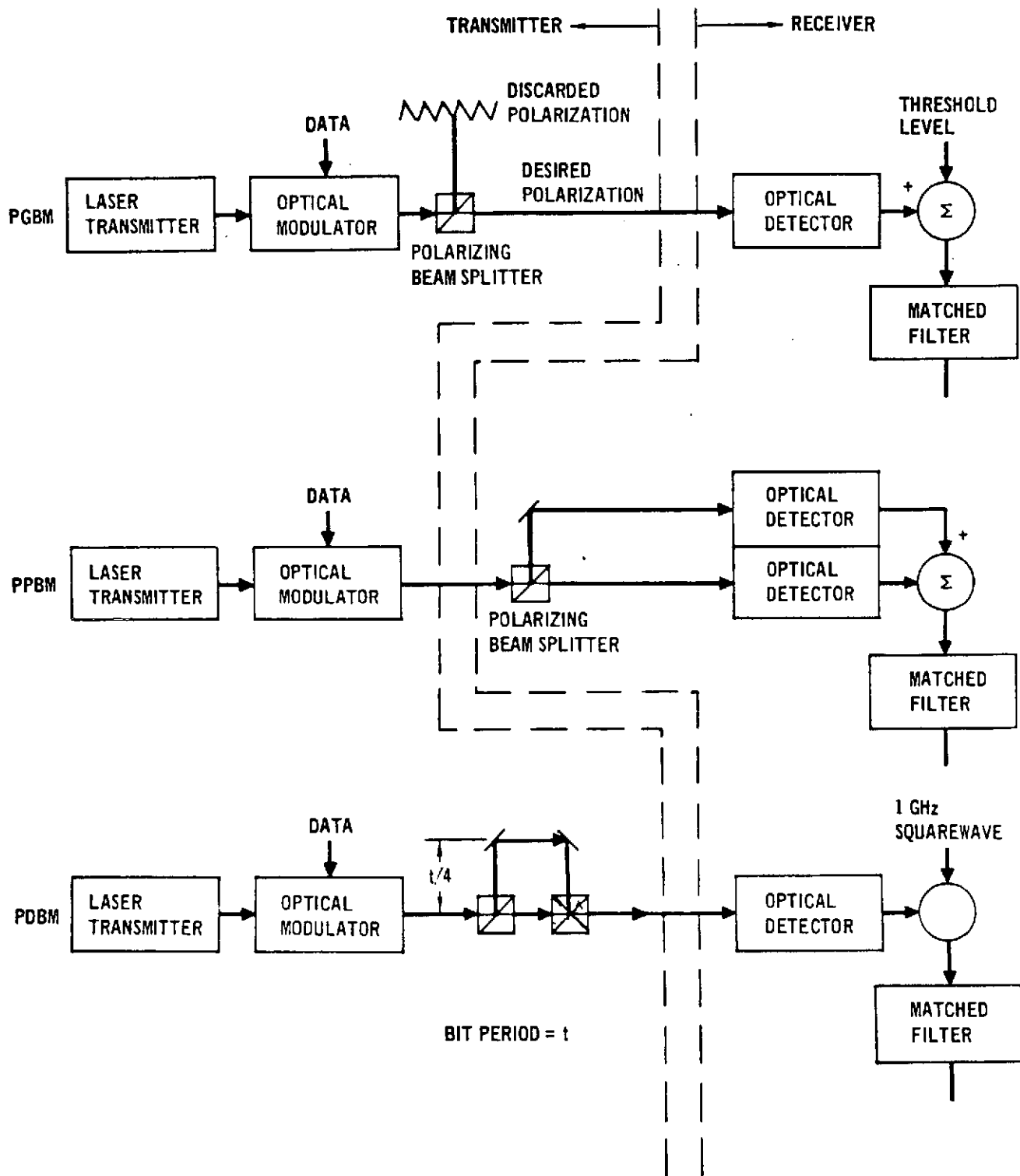


FIGURE A-4 DIGITAL BASEBAND FORMAT



14.0 COMMENTS: COMMUNICATION DETECTOR TYPE

A number of possible communication detectors are available. The best choice is dependent upon the background level encountered for the particular link, the data rate, quantum efficiency, physical size, and ruggedness. Those available that could be used include:

- DCFP - Dynamic cross field photomultiplier
- SCFP - Static Cross Field Photomultiplier
- APD - Avalanche Photo Diode
- FPMT - Fast Photomultiplier Tube

It should be a simple task for a man to change communication detectors and associated electronics.

15.0 COMMENTS: ACQUISITION DETECTOR TYPE

A number of possible acquisition detectors are available. The best choice is dependent upon the link margin analysis (includes such items as quantum efficiency, gain, dark current, and internal noise), acquisition technique, dead zone, physical size, and ruggedness.

Those available that could be used include:

- QPMT - Quadrant Photo Multiplier Tube
- QSPD - Quadrant Silicon Photo Diode
- SSDA - Solid State Detector Array

Man would have to exchange detectors and associated processing electronics and realign the acquisition detector to the optical axis of the system.

16.0 COMMENTS: TRACKING DETECTOR

We have the same choice for a detector in the tracking subsystem as available in the acquisition subsystem plus the DPMT and PMTSR:

- DPMT - Deflectable photomultiplier tube
- QPMT - Quadrant Photomultiplier tube
- QSPD - Quadrant silicon photodiode
- SSDA - Solid state detector array
- PMTSR - Photomultiplier tube with scanning reticle.

TABLE A-12

SYSTEM CONFIGURATION OR PARAMETER VARIABLE: Laser Type

IMPLEMENTATION TECHNIQUES		SUPPORT EQUIPMENT	SUBSYSTEM PERFORMANCE IMPLICATIONS		
			COMMUNICATIONS	ACQUISITION	TRACKING
1. Lamp pumped 2. LED pumped 3. Phase mode locked 4. Loss mode-locked	Communication Laser	alignment instrumentation and laser diagnostic instrumentation.	highly dependent upon stable operation	-	-
5. CW Laser 6. Q-switched	Beacon Laser	alignment and diagnostic instrument	-	laser type dependent (pulse width & pulse rate)	Laser type dependent (pulse width & pulse rate)

304

257

TABLE A-13

SYSTEM CONFIGURATION OR PARAMETER VARIABLE: Communication Detector Type

IMPLEMENTATION TECHNIQUES	SUPPORT EQUIPMENT	SUBSYSTEM PERFORMANCE IMPLICATIONS		
		COMMUNICATIONS	ACQUISITION	TRACKING
1. DCFP 2. SCFP 3. APD 4. FPMT	Appropriate size detector area and associated electronics	Described by theoretical model.	-	-

TABLE A-14

SYSTEM CONFIGURATION OR PARAMETER VARIABLE: Acquisition Detector Type

IMPLEMENTATION TECHNIQUES	SUPPORT EQUIPMENT	SUBSYSTEM PERFORMANCE IMPLICATIONS		
		COMMUNICATIONS	ACQUISITION	TRACKING
DPMT QSPD SSSA QPMT	Alignment Instrumentation	-		-

218

TABLE A-15

SYSTEM CONFIGURATION OR PARAMETER VARIABLE: Tracking Detector Type

IMPLEMENTATION TECHNIQUES	SUPPORT EQUIPMENT	SUBSYSTEM PERFORMANCE IMPLICATIONS		
		COMMUNICATIONS	ACQUISITION	TRACKING
DPMT QSPD SSDA PMT with scanning reticle QPMT	Detector and Associated electronic modules Alignment calibration required when new or different tracking detector is installed			Defined by Computer Model

Table A-16 summarizes the important characteristics of these choices. Man would have to exchange the detector and its associated processing electronics and realign the tracking detector to the optical axis of the system.

**TABLE A-16
TRACKING DETECTOR CHARACTERISTICS**

CHARACTERISTIC	DPMT	QPMT	QSPD	SSDA	PMTSR
Weight	Medium	Highest	Low	Low	Medium
Size	Medium	Largest	Smallest	Smallest	Medium
.53 Q.E	20%	20%	50%	50%	20%
1.06 Q.E.	0.1%	.1%	80%	80%	.1%
Gain	Yes	Yes	None	None	Yes
Instantaneous f.o.v.	Very small	Largest	Largest	Small	Small
Sensitive to Gain	No	Yes	-	-	No
CW Signal Required	Yes	No	No	No	Yes
Mechanical Scanning	No	No	No	No	Yes
Electronic Scanning	Yes	No	No	No	No

17.0 COMMENTS: ACQUISITION TECHNIQUES

Acquisition begins after the two terminals have been activated and open loop pointed to each other. Once initiated, the acquisition process should proceed automatically, as should reacquisition (if one or both terminals lose track). Normally the receiver terminal searches a wide field, such that the transmitter terminal receives a low (B pps) data rate for coarse alignment. This can be accomplished either by scanning a narrow beam, high pulse rate laser, or by using a broad-beam, Bpps laser. The transmitting terminal uses the 10 pps information to point either a spoiled laser beam or scanned laser beam at the receiving terminal. The receiver terminal senses and continuously tracks the incoming signal. The tracking sequence then begins with the beacon

TABLE A-17

SYSTEM CONFIGURATION OR PARAMETER VARIABLE: Acquisition Technique

IMPLEMENTATION TECHNIQUES	SUPPORT EQUIPMENT	SUBSYSTEM PERFORMANCE IMPLICATIONS		
		COMMUNICATIONS	ACQUISITION	TRACKING
1. Broad beam Pulse width Pulse repetition rate 2. Scanning a) Pattern b) cycle time c) dwell time	Required modules & electronic controls Alignment instrumentation		Modeled via computer which describes performance estimate.	

beam being narrowed or the scan field substantially reduced gratly increasing B. The transmitter terminal senses the higher beacon rate and proceeds to fine tracking.

Both broadbeam and scanned beam techniques could be investigated. Different laser configurations are required. A man in the loop could reconfigure the laser to its required design specification to accomplish the alternate mode of operation.

The benefit of decreasing open loop pointing uncertainties could be investigated. The man in the loop could precisely orient the two terminals to a specified open loop condition and measure the acquisition performance as per the acquisition technique.

Various beacon scanning patterns could be investigated.

APPENDIX B
SUPPORTING ANALYSIS FOR REFERENCE SATELLITE SYSTEM DEFINITION

1.0 INTRODUCTION

This appendix contains supporting analyses to justify our selections for the components for the reference satellite system.

1.1 ACQUISITION AND TRACKING DETECTOR SELECTION. The three primary candidate devices for measurement of tracking error are shown in Table B-1. Of the three, the DPMT has the greatest sensitivity. It achieves this sensitivity by electronically steering the photoelectrons from its cathode through a small aperture to the multiplying dynode chain. The effect of this arrangement is that only a small region of the photocathode is processed by the tube at any one time. As a result, only the background induced photoelectrons from the small region of interest contribute to the background noise. Because the signal photoelectrons are scanned across the aperture, the resulting output signal consists of pulses, permitting ac coupling to the signal-conditioning electronics. The input light signal must be either continuous or pulsed at a rate that is fast compared to the tube's scan rate. No. 1.06 μ m tube of this type has been developed. The tube is also known as the image dissector.

The next-most-sensitive device is the QPMT. As yet, no quadrant array of PMT's within the same vacuum envelope has been developed. Consequently, the incoming beam must be optically divided into four separate beams such that the powers of the beams bear the same relationship to each other as do irradiances of four quadrants meeting on axis at the focus of the incoming beam. These four beams then irradiate four separate photomultiplier tubes. The difference between the sum of the outputs of the two tubes on the left and the sum of the outputs of the two tubes on the right is proportional to the azimuth error. In like manner, the difference between the sum of the outputs of the two upper

TABLE B-1
ANGLE - MEASUREMENT DETECTORS

<u>Detector</u>	<u>Characteristics</u>
Quadrant Photomultiplier Tube (QPMT)	High Internal Gain Medium QE at 0.53 μm ; Low QE at 1.06 μm Requires Image-Dividing Optic Requires Chopper for CW light Large Instantaneous F.O.V.
Silicon Quadrant Detector (SQD)	No internal gain High QE at both .53 μm and 1.06 μm No image dividing optics required Solid state device Requires chopper for CW light Large instantaneous FOV
Deflectable Photomultiplier Tube (DPMT)	High Internal Gain Medium QE for 0.53 μm None developed for 1.06 μm Small instantaneous FOV Requires CW light No image dividing optics required

tubes and the sum of the outputs of the two lower tubes is proportional to the elevation error. Normalization by dividing by the sum of the outputs of the four tubes provides amplitude-insensitive angle measurement.

The third candidate detector is the silicon quadrant detector (SQD). This device is a silicon photodiode which has a very narrow, highly resistive region along two perpendicular diameters. Thus, the diode is divided into four electrically isolated quadrants. The currents in the four electrodes are processed in the same way that the PMT outputs are processed for the QPMT above. Because this device has no internal gain, thermal noise in the preamplifiers in the signal conditioning circuits determines the minimum detectable signal for the SQD.

For the reference satellite Package A, we selected the QPMT for both the acquisition and the tracking detectors. This choice hinges upon the assumption that $1.06 \mu\text{m}$ is the wavelength to be used for a high-data-rate one-way optical link in the future. This assumption makes frequency-doubled Nd:YAG light at $0.53 \mu\text{m}$ attractive as a beacon wavelength due to the similarity of the laser at both ends of the link. The use of $0.53 \mu\text{m}$ light makes the SQD unattractive because its primary advantage over the PMT occurs at $1.06 \mu\text{m}$ where the quantum efficiency of silicon is high (50%) and that of typical photocathode is low (0.1%). At $0.53 \mu\text{m}$, the quantum efficiencies are comparable, but the QPMT has the advantage of high internal gain. Use of a low duty cycle Q-switched laser in the beacon transmitter makes the DPMT unattractive because of the high data rate required for its operation. Table B-2 shows quantitatively how the three detectors compare with respect to beacon laser required average power. For this comparison, the DPMT was assumed to dwell on one quadrant of the total field of view for one pulse repetition period, and to process its signals as does the QPMT and SQD. Any other implementation using a pulsed signal and a DPMT is less favorable to the DPMT. Therefore, even though this

TABLE B-2
HIGH DATA-RATE TRANSMITTER ACQUISITION AND TRACKING
Detector Selection Trade

	SYNC-GND Link			LAS-SYNC Link		
	SQD	QPMT	DPMT	SQD	QPMT	DPMT
<u>ACQUISITION PERFORMANCE</u>						
Peak Received Power Required-dBW	-63.8	-77.7	-77.7	-63.8	-89.6	-89.6
Required Transmitter Duty Cycle	3.2×10^{-4}	3.2×10^{-4}	1.28×10^{-3}	3.2×10^{-4}	3.2×10^{-4}	1.28×10^{-3}
Average Received Power Required-dBW	-98.8	-112.7	-106.7	-98.8	-124.6	-118.6
Relative Average Power Required-dB	+13.9	0	+6	+25.8	0	+6
<u>TRACKING PERFORMANCE</u>						
Peak Received Power Required-dBW	-64.3	-83.9	-83.9	-64.3	-84.3	-84.2
Required Transmitter Duty Cycle	3.2×10^{-4}	3.2×10^{-4}	1.28×10^{-3}	3.2×10^{-4}	1.28×10^{-3}	1.28×10^{-3}
Average Received Power Required-dBW	-99.3	-118.9	-118.9	-99.3	-119.2	-113.2
Relative Average Power Required-dB	+19.6	0	+6	+19.9	0	+6

Acquisition Criteria: False alarm rate - 0.5 false alarms per second, probability of detection -95%

Tracking Criterion: 0.25 μ rad rms angle noise in 100 Hz control bandwidth

SQD - Silicon Quadrant detector

QPMT - 4 Photomultiplier Tubes with Quadrant Dividing Optics

DPMT - Deflectable Photomultiplier Tube (Image Dissector)

implementation is impractical due to the precise registration required in scanning the DPMT photocathode to enable it to perform as accurately as the SQD or QPMT, nevertheless, the concept is useful in that it presents a losing candidate detector, the DPMT, in the most favorable light. Referring to Table B-3, the differences in the SYNC-GND link and the LAS-SYNC link consist primarily of background and range. The beacon receiver for a high-data-rate link from SYNC to GND sees a sunlit earth background, which is higher than the moon background seen by the beacon receiver for a LAS-to-SYNC link. The range for LAS-SYNC is longer than that for SYNC-GND at the point when the LAS first comes into view of the synchronous satellite. Note in Table that the QPMT requires the least transmitted average power of the three candidates.

- 1.2 SELECTION OF ACQUISITION FIELD OF VIEW - In order to establish a laser communication link, a beacon transmitter and receiver at opposite ends of the link must be pointed such that (1) the beacon scan pattern illuminates the beacon receiver and (2) the transmitter is within the receiver's field of view. Therefore, the initial pointing uncertainties influence the selection of beam widths and fields of view, which, in turn, affect acquisition time and power requirements. The error sources which comprise the beacon transmitter and receiver pointing errors are:
- o beacon satellite ephemeris error
 - o receiver satellite ephemeris error
 - o beacon or receiver satellite Attitude Reference System error
 - o beacon or receiver package/Attitude Reference System misalignment
 - o beacon or receiver control system accuracy (16 bit encoders).

The 16 bit optical encoder is representative of a high accuracy feedback device which would be required for the beacon or receiver acquisition control system. Higher accuracy (more bits) encoders are significantly larger, heavier, and more costly.

Pointing uncertainties have been computed for the synchronous-satellite to ground communication link and the low-altitude-satellite (LAS) to-synchronous-satellite communication link for values of the error sources. Table B-3 summarizes the standard deviations for the error sources and the resultant standard deviation of the pointing error for the two links for a horizon sensor-star sensor Attitude Reference System and a two star sensor Attitude Reference System. The worst case (3σ) pointing uncertainty areas (azimuth x elevation) are summarized below:

	Horizon Sensor-Star Sensor Attitude Reference System	Star Sensor-Star Sensor Attitude Reference System
Sync to Ground link	1.19 mrad x 3.38 mrad	1.19 mrad x 1.19 mrad
LAS to Sync link	1.34 mrad x 3.64 mrad	1.20 mrad x 1.20 mrad

It should be noted that the two-star-sensor Attitude Reference System is significantly more complex than the horizon sensor-star sensor system because of requirements for star sensor gimbaling, additional star map storage, and additional measurement processing. It would therefore be undesirable to impose a constraint for a two-star sensor Attitude Reference System on a communication satellite.

TABLE B-3
INITIAL POINTING UNCERTAINTIES

Synchronous satellite to ground link

Error source (1σ)	Horizon Sensor-Star Sensor Attitude Reference System ^A		Star Sensor-Star Sensor Attitude Reference System	
	azimuth (μ rad)	elevation (μ rad)	azimuth (μ rad)	elevation (μ rad)
Sync satellite ephemeris error (667 m)	18.7	2.9	18.7	18.7
Ground ephemeris error (20 m)	.6	.6	.6	.6
Star sensor error (122 μ rad)	122.0		122.0	122.0
Horizon sensor error (577 μ rad)		577.0		
Structural misalignment (122 μ rad)	122.0	122.0	122.0	122.0
Control system error (96 μ rad)	96.0	96.0	96.0	96.0
RMS error (1σ)				

Low altitude satellite (LAS) to synchronous satellite link

Error source (1σ)				
Sync satellite ephemeris error (667 m)	18.7	18.7	18.7	18.7
LAS ephemeris error (667 m)	102.9	102.9	18.7	18.7
Star sensor error (122 μ rad)	122.0		122.0	122.0
Horizon sensor error (577 μ rad)		577.0		
Structural misalignment (122 μ rad)	122.0	122.0	122.0	122.0
Control system error (96 μ rad)	96.0	96.0	96.0	96.0
RMS error (1σ)	223.4	606.6	199.2	199.2

A. Assumes local-vertical-orbit-plane reference frame alignment

B. Assumes 16 bit optical encoder

THIS PAGE INTENTIONALLY LEFT BLANK

APPENDIX C
ACQUISITION AND TRACKING SIGNAL REQUIREMENTS

1.0 INTRODUCTION. Signal level requirements for acquisition and tracking depend upon detection probabilities in the former case and upon detector noise characteristics in the latter case.

2.0 PULSED TRACKER ANALYSIS

2.1 ACQUISITION. The detection process is accomplished in the receiver by a threshold comparison, with the threshold automatically set above the noise level in the receiver. This type of thresholding mechanism maintains a constant probability of false alarm.

The peak received signal strength during a pulse at the detector is given by the laser range equation,

$$P_r = \left(\frac{P_{avg}}{f_p \tau} \right) \left(\frac{32}{\theta_t^2} \right) L_t L_p \tau_s \left(\frac{\lambda}{4 \pi R} \right)^2 \left(\frac{\pi D_r}{\lambda} \right)^2 L_r L_f, \quad (1)$$

where

- P_{avg} = the average transmitted power,
- f_p = the transmitted pulse rate,
- τ = pulse width,
- L_t = transmit optics efficiency,
- L_p = antenna pointing error,
- τ_s = atmospheric loss,
- λ = the wavelength,
- R = range,
- D_r = receiver primary diameter,
- L_r = receiver optics efficiency, and
- L_f = optical filter efficiency.
- θ_t = $1/e^2$ beam diameter

The number of signal photoelectrons emitted by the photodetector during a pulse is,

$$n_s = \frac{\eta_\epsilon}{hf} P_r \tau \quad (2)$$

where η_ϵ is the quantum efficiency, and hf (Planck's constant \times frequency) is the energy per photon. The peak signal power at the output of the photodetector is then given as,

$$i_s^2 = \left(\frac{n_s q}{\tau} \right)^2 = \left[\left(\frac{\eta_\epsilon q}{hf} \right) P_r \right]^2 \quad (3)$$

According to Reference 59, the mean square fluctuation in the number of photoelectrons received is equal to the mean rate, n_r , times the integration time of the receiver, τ_I . Thus

$$\left(\Delta n_s \right)^2 = n_r \tau_I = \frac{n_s}{\tau} \tau_I \quad (4)$$

The signal-to-noise ratio is then

$$\frac{n_s^2}{\left(\Delta n_s \right)^2} = n_s \frac{\tau}{\tau_I} = \frac{i_s^2}{i_n^2} \quad (5)$$

where i_n^2 is the mean square shot noise current at the detector output. combining (5) and (3)

$$i_n^2 = \frac{\frac{n_s^2 q^2}{\tau^2}}{n_s \frac{\tau}{\tau_I}} = n_s \frac{q^2}{\tau \tau_I} = i_s \frac{q}{\tau_I}$$

For a receiver post-detection filter that is matched to the received pulse width, $\tau_I = \tau$, and

$$i_n^2 = n_s \frac{q^2}{\tau} = i_s \frac{q}{\tau} \quad (6)$$

Note that the familiar shot-noise current formula can be readily derived from (6) by recalling that the equivalent-noise-bandwidth, B_n , of an integrator which integrates only over the duration of the pulse, τ , is

$$B_n = \frac{1}{2\tau} \quad (7)$$

Substituting 7 into 6,

$$i_n^2 = 2q i_{s_n} B_n. \quad (8)$$

Similarly, the background power incident on the detector is determined from

$$P_B = H_B^2 \pi \left[1 - \cos(\theta/2) \right] B_{opt} \left(\frac{\pi D^2}{4} \right) \tau_s L_r L_f, \quad (9)$$

where H_B = the background radiance,

θ = the receiver field-of-view, and

B_{opt} = optical filter bandwidth

This results in a background current received of

$$I_B = \frac{\eta_e q P_B}{hf} \quad (10)$$

and a shot-noise power component at the photodetector output of

$$i_B^2 = q I_B / \tau_I \quad (11)$$

also, the number of background photoelectrons observed in one integration time is

$$n_B = I_B \frac{\tau_I}{q} = \frac{\eta_e P_B \tau_I}{hf} \quad (12)$$

The preamp thermal noise is added to the signal and background components when the Poisson-distributed photon noise is sufficiently large to appear Gaussian like the thermal noise. In order to reflect the preamp thermal noise back to the detector input, an equivalent number of photoelectrons, n_p , is computed as follows

$$i_{np}^2 = i_p^2 B_n \quad (13)$$

where i_{np}^2 is the mean square preamp thermal noise current, i_p^2 is the mean square current per unit bandwidth of the receiver, and B_n is the equivalent noise bandwidth of the receiver.

Then

$$i_p^2 B_n = \frac{q^2}{2} n_p^2 \tau_I \quad (14)$$

and

$$n_p = \frac{\sqrt{\tau_I}}{q} i_p \sqrt{B_n \tau_I} \quad (15)$$

For a multi-pole low-pass filter matched to a square pulse of width, τ_I ,

$$B_n \tau_I = .424$$

For a PMT detector, the detection statistics were computed using Equations (2) and (12) with Poisson probability distributions for the signal and noise. The probability of false alarm is given by,

$$P_{fa} = 1 - \sum_{i=0}^{Y_B} \frac{E_n^i e^{-E_n}}{i!}, \quad (16)$$

where $E_n = n_B$, assuming negligible strength during the "off" time of the laser. For the case of a silicon quadrant detector, Gaussian statistics were used, with the variance of the distributions increased by n_p^2 to account for the preamp noise.

Using the Gaussian form,

$$P'_{fa} = \frac{1}{\left[2\pi(n_p^2 + n_B)\right]^{1/2}} \int_{Y_B}^{\infty} \exp\left[-\frac{(X-n_B)^2}{2(n_p^2 + n_B)}\right] dx = \frac{1}{2} - \frac{1}{2} \operatorname{Erf}\left[\frac{Y_B - n_B}{\sqrt{2(n_p^2 + n_B)}}\right] \quad (17)$$

where $\operatorname{Erf}(\)$ is the error function. Equations (16) and (17) describe the probability of false alarm per pulse interval in the receiver. For a correlation time of τ_I in the receiver, there are $1/\tau_I$ independent opportunities for a false alarm per second, since no gating is mechanized during acquisition. A Markov-shaped power spectral density for the preamp gives $\tau_c = 1/B_w$ (B_w is the 3 dB bandwidth in Hz) at the $1/e^{2\pi}$ points of the autocorrelation function. Thus, for a desired false alarm rate (FAR), the probability of false alarm per pulse interval is,

$$P'_{fa} = \frac{\text{FAR}}{B_w} .$$

Substituting Equation (12) into Equation (10) or (11), the threshold setting, Y_B , referenced to the photodetector output, may be determined. The probability of detection, using the Poisson statistics is simply expressed as,

$$P_d = 1 - \sum_{i=0}^{Y_B} \frac{E_s^i e^{-E_s}}{i!} , \quad (19)$$

2.2 TRACKING. The QPMT and signal processing electronics produce horizontal and vertical angle outputs which are independent of the signal intensity at the input. This is accomplished by normalizing an angle-sensitive voltage by the total power received. Using the vertical channel for illustration, the output of the sum and difference processor are

$$\Delta = (A + B + n_1 + n_2) - (C + D + n_3 + n_4) \text{ and} \quad (21)$$

$$\Sigma = A + B + C + D + n_1 + n_2 + n_3 + n_4$$

where A and B represent the outputs of the two upper quadrants, C and D the two lower and n_1 , n_2 , n_3 , and n_4 are independent noise voltages associated with channels A, B, C, and D, respectively (See Figure C-1). The output voltage is

$$\begin{aligned} \frac{\Delta}{\Sigma} &= \frac{A + B - C - D + n_1 + n_2 - n_3 - n_4}{A + B + C + D + n_1 + n_2 + n_3 + n_4} \\ &= \frac{A + B - C - D}{A + B + C + D} + \frac{n_1 + n_2 - n_3 - n_4}{A + B + C + D} \\ &= 1 + \frac{n_1 + n_2 + n_3 + n_4}{A + B + C + D} \end{aligned} \quad (22)$$

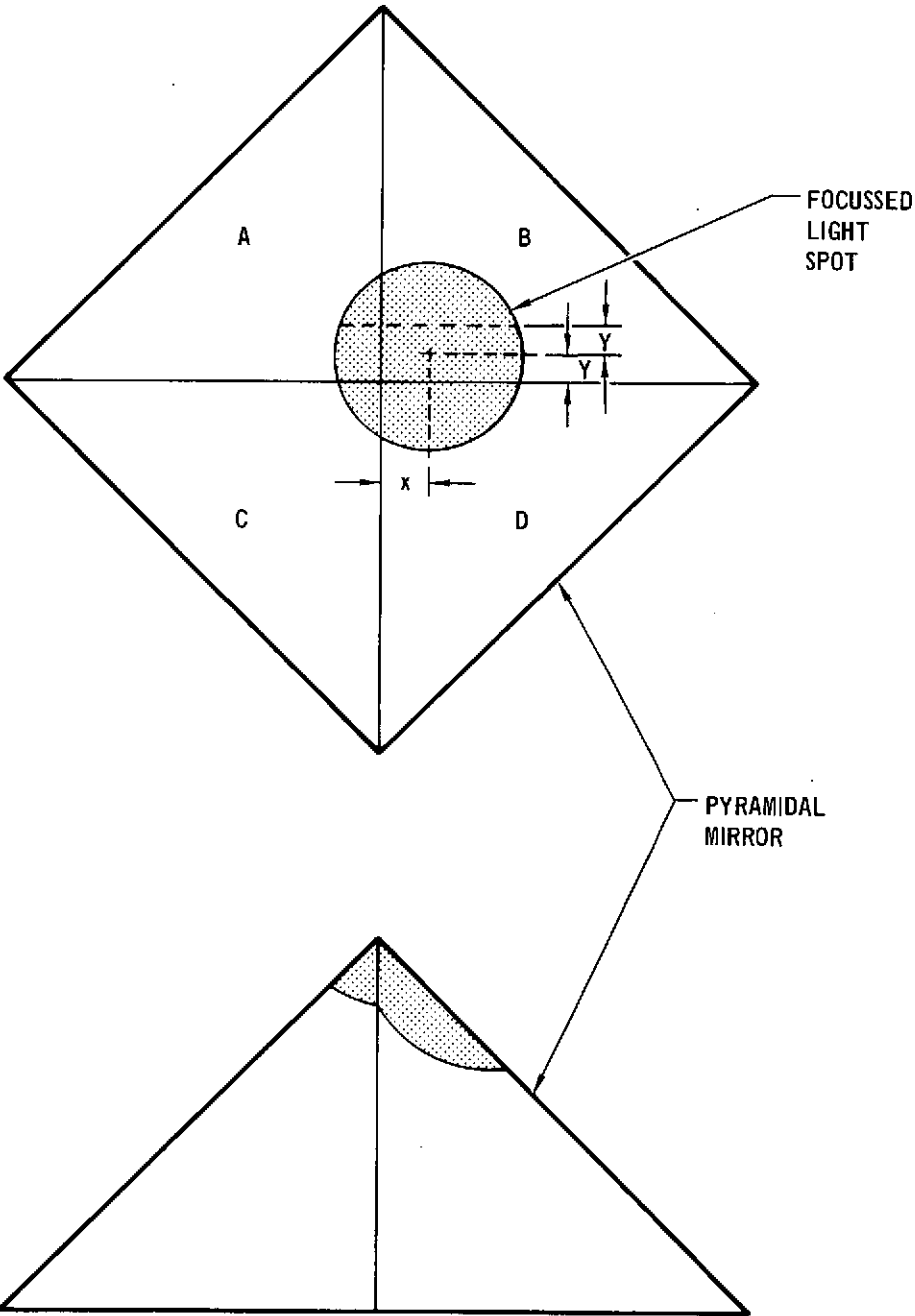
For large signal levels relative to noise,

$$\frac{\Delta}{\Sigma} \approx \left(\frac{A + B - C - D}{A + B + C + D} + \frac{n_1 + n_2 - n_3 - n_4}{A + B + C + D} \right) \left(1 - \frac{n_1 + n_2 + n_3 + n_4}{A + B + C + D} \right) \quad (23)$$

Now, define

$$f(Y) = \frac{A + B - C - D}{A + B + C + D} \quad (24)$$

FIGURE C-1 IMAGE DIVIDER FOR QUADRANT PHOTO MULTIPLIER TUBE (QPMT) DETECTOR



Consider the upper drawing in Figure C-1. Note that for a spot whose illumination is uniformly distributed $f(Y)$ is proportional to the fraction of the total spot area lying between the horizontal solid line and the upper dashed line. To illustrate how this area is computed, consider Figure C-2 where the area in question has been redrawn rotated 90° with the circle centered at the origin of an x-y coordinate system. Note that the shaded area is one fourth the total area. The shaded area, A_s , is computed by

$$\begin{aligned}
 A_s &= \int_0^Y y(x) \, dx \\
 &= \int_0^Y \sqrt{r^2 - x^2} \, dx
 \end{aligned}
 \tag{25}$$

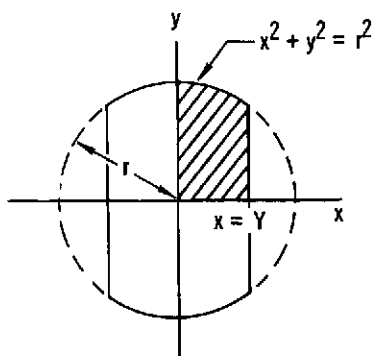
which, from any integral table

$$\begin{aligned}
 A_s &= \frac{x}{2} \sqrt{r^2 - x^2} + \frac{r^2}{2} \arcsin \frac{x}{r} \Big|_0^Y \\
 &= \frac{r^2}{2} \left(\frac{Y}{r} \sqrt{1 - \left(\frac{Y}{r}\right)^2} + \arcsin \frac{Y}{r} \right)
 \end{aligned}
 \tag{26}$$

Then

$$f(Y) = k \frac{4 A_s}{\pi r^2} = \frac{2k}{\pi} \left(\frac{Y}{r} \sqrt{1 - \left(\frac{Y}{r}\right)^2} + \arcsin \frac{Y}{r} \right)$$

FIGURE C-2 COMPUTING $f(Y)$ FOR UNIFORM SPOT



where k is a proportionality constant. Going back to (23)

$$\frac{\Delta}{\Sigma} = f(Y) \left(1 - \frac{n_1 + n_2 + n_3 + n_4}{A + B + C + D} \right) + \frac{n_1 + n_2 - n_3 - n_4}{A + B + C + D} \quad (28)$$

$$- \frac{(n_1 + n_2)^2 - (n_3 - n_4)^2}{(A + B + C + D)^2}$$

Assuming uncorrelated, Gaussian, zero mean value noise sources, the expected value of Δ/Σ is then

$$E \left\{ \frac{\Delta}{\Sigma} \right\} = f(Y) - \frac{\Delta N}{S} \quad (29)$$

where S equals the total signal power,

$$S = (A + B + C + D)^2$$

and ΔN represents a difference in noise power among the 4 channels,

$$\Delta N = \sigma_1^2 + \sigma_2^2 - \sigma_3^2 - \sigma_4^2$$

$$\sigma_i^2 = \text{variance of } n_i.$$

The angle noise is computed from the variance of Δ/Σ

$$\begin{aligned}
 \left(\frac{\Delta}{\Sigma}\right)^2 &= f(Y)^2 \left(1 - \frac{2(n_1 + n_2 + n_3 + n_4)}{\sqrt{S}} + \frac{(n_1 + n_2 + n_3 + n_4)^2}{S}\right) \\
 &+ \frac{(n_1 + n_2 - n_3 - n_4)^2}{S} + \left(\frac{(n_1 + n_2)^2}{S} - \frac{(n_3 + n_4)^2}{S}\right)^2 \\
 &+ 2 f(Y) \left(1 - \frac{n_1 + n_2 + n_3 + n_4}{\sqrt{S}}\right) \frac{n_1 + n_2 - n_3 - n_4}{S} \\
 &- 2 \frac{n_1 + n_2 - n_3 - n_4}{\sqrt{S}} \frac{(n_1 + n_2)^2 - (n_3 + n_4)^2}{S} \\
 &- 2 f(Y) \left(1 - \frac{n_1 + n_2 + n_3 + n_4}{\sqrt{S}}\right) \left(\frac{(n_1 + n_2)^2 - (n_3 + n_4)^2}{S}\right)
 \end{aligned} \tag{30}$$

and

$$E\left\{\left(\frac{\Delta}{\Sigma}\right)^2\right\} = f(Y)^2 \left(1 + \frac{4}{S/N}\right) + \frac{4}{S/N} + \frac{16}{(S/N)^2} - 4 f(Y) \frac{\Delta N}{S} + \frac{2(\Delta N)^2}{S^2}$$

where

$$\frac{S}{N} = \frac{(A + B + C + D)^2}{\frac{1}{4}(\sigma_1^2 + \sigma_2^2 + \sigma_3^2 + \sigma_4^2)}$$

Then the variance of Δ/Σ

$$\begin{aligned}
 \sigma_{\Delta/\Sigma}^2 &= E\left\{\left(\frac{\Delta}{\Sigma}\right)^2\right\} - \left(E\left\{\frac{\Delta}{\Sigma}\right\}\right)^2 \\
 &= \frac{4 f(Y)^2}{S/N} + \frac{4}{S/N} + \frac{16}{(S/N)^2} - 2 f(Y) \frac{\Delta N}{S} + \left(\frac{\Delta N}{S}\right)^2
 \end{aligned}$$

Referring back to (27), the gain in volts per unit angle for the linear region around boresight is the slope of $f(\theta_i)$ at $\theta_i = 0$, where θ_i is the input error angle. If we define $\frac{\phi_L}{2}$ as the input angular error which locates the spot so that its edge, rather than its center, over the peak of the pyramid, then

$$\frac{Y}{r} = \frac{2\theta_i}{\phi_L}$$

and

$$f(Y) = k f(\theta_i) = \frac{2k}{\pi} \left(\frac{2\theta_i}{\phi_L} \sqrt{1 - \left(\frac{2\theta_i}{\phi_L} \right)^2} + \arcsin \frac{2\theta_i}{\phi_L} \right)$$

$$\left. \frac{d f(Y)}{d \theta_i} \right|_{\theta_i = 0} = \frac{8k}{\pi \phi_L}$$

Therefore

$$\sigma_{\theta_i}^2 = \sigma_{\Delta/\Sigma}^2 \left(\frac{\pi \phi_L}{8k} \right)^2 = \frac{\pi^2 \phi_L^2}{16 S/N} \left(1 + f^2(\theta_i) + \frac{4}{S/N} -1/2f(\theta_i) \frac{\Delta N}{N} + \frac{1}{4S/N} \left(\frac{\Delta N}{N} \right)^2 \right)$$

3.0 HIGH-DATA-RATE (HDR) TRACKER ANALYSIS. There are three types of HDR tracker considered here: (1) one which measures directly to d.c value of the detector output current, (2) one which chops the light into the detector, and (3) one which measures the power in the fundamental component of the data stream. The fundamental difference between the HDR tracker and the pulsed tracker are (1) the bandwidth of the signal processed and (2) the fact that (in types 2 and 3 above) rectification

of the signal and noise takes place. The bandwidth difference can be accommodated within the equations developed for the pulsed tracker by simply defining an equivalent integration time based on the noise bandwidth B_n of the filter on the PMT output by

$$\tau_I = \frac{.424}{B_n}$$

With regard to the effects of rectification and video filtering a band-pass process, Wolf has shown (reference 60), that the signal-to-noise ratios at the input and output of a half-wave rectifier/filter combination are related by

$$\frac{(S/N)_{out}}{(S/N)_{in}} = \frac{B}{b}$$

for $(S/N)_{in}$ greater than 5 dB, where B is the bandpass filter bandwidth and b the video filter bandwidth. Where the electronic signal power in the pulsed case is the square of the peak detector current, for the HDR case (types 2 and 3) it is half the square of the amplitude of the harmonic of interest. Gaussian statistics are assumed because of the long integration times with respect to the pulse repetition frequency. Taking these changes into account, the results of the pulsed tracker analysis are valid for the HDR tracker for detection probability and angle noise.

APPENDIX D
LINK MARGINS

A link analysis program, developed under an earlier contract, was utilized to determine a feasible set of parameters for the satellite system. The details of this program are discussed later in this report. The results of the analysis for the reference system are contained in the tables presented in this section.

The program accepts as inputs the parameters listed in Table D-1. Values used for the terminal parameters for the terminals considered in this study are presented in Tables D-2 through D-7. The link parameters for the links considered in this study are presented in Tables D-8 through D-10.

From these parameters we compute the various losses in the link, the received number of photoelectrons, the background and other noise sources present in the system, the required number of photoelectrons, and the link margin. The margin is simply the ratio of received-to-required photoelectrons, expressed in dB. The results of these computations are printed out as shown in Figures D-1 through D-19. The link, channel, and wavelength associated with each table are identified at the top of the link analysis printout. The name of the link (e.g., SYNC TO GROUND in Figure D-1) identifies the direction of the high data rate transmission. There is a beacon link in the opposite direction which provides a reference beam for pointing the high data rate transmitter. The "Channel" designation identifies the beam (data or beacon) and the mode (modulation format, acquisition, or tracking) under consideration. The output list is divided into two parts: S (for signal) parameters and B (for background) parameters. The parameters are expressed in dB relative to optical power so the effect of each on the link margin can be seen readily. The S parameters (S1-S8, S10, S12, and S14) combine to produce S15 - received signal photoelectrons per data

TABLE D-1
LINK ANALYSIS PROGRAM
INPUT PARAMETERS

TRANSMITTER:

S1 - Power, watts
S2A - Modulator, eff
S2B - Optics, eff
ALPHT - Beamwidth, μ rad
A - Pointing Accuracy, μ rad
LAMDA - Wavelength, meters
XNE - Extinction Ratio

LINK:

R - Range, meters
S6A - ATM. transmissibility
S6B - Beam Spread Effect
B1A - Background Radiance
B3B - Background Irradiance
S6C - Beam Wander Effect

RECEIVER:

D - Antenna Diameter, meters
S8A - Antenna Eff.
S8B - Optics Eff.
S8C - Filter transmissibility
S8D - Power Split for Tracking
DATAR - Data Rate, bps
S14 - Quantum, Eff.
B2A - Field-of-view, μ rad
B4 - Filter Bandwidth, A
B6 - Gatewidth, sec.

Other:

ANXEP - Synchronous Polarizer Extinction Ratio
Link = 1 LAS to Sync
 2 Ground to Sync
 3 Sync to Sync
 4 Sync to Ground
 5 Air to Sync
 6 Sync to Air
 7 Ground to Balloon
 8 Balloon to Ground
ICHAN =1 Data
 2 Beacon

TABLE D-2
TERMINAL - SYNCHRONOUS SATELLITE
HIGH DATA RATE TRANSMITTER

Parameter	Configuration		
	Data	Acquisition	Tracking
Transmitter			
Format	PQM		
Power, watts	.200	.200	.200
Transmitter efficiency	.810	.810	.810
Beamwidth, radians	8.126×10^{-6}	1.0×10^{-4}	8.126×10^{-6}
Pointing accuracy, radians	0.1×10^{-5}	0.2×10^{-4}	0.1×10^{-5}
Wavelength, meters	0.106×10^{-5}	0.106×10^{-5}	0.106×10^{-5}
Extinction ratio	0.3×10^2	0.3×10^2	0.3×10^2
Receiver			
Format	PIM, 64		
Detector	QPMT	QPMT	QPMT
Aperture diameter, meters	.191	.191	.191
Receiver efficiency	.507	.507	.507
Power split for tracking	1	1	1
Date rate, bps	$.4 \times 10^2$	$.4 \times 10^2$	$.4 \times 10^2$
Quantum efficiency	.25	.25	.25
Field of view, radians	4.0×10^{-4}	4.0×10^{-3}	4.0×10^{-4}
Filter bandwidth, A	25.0	25.0	25.0
Receiver Gatewidth	2.0×10^{-7}	2.0×10^{-7}	2.0×10^{-7}

TABLE D-3
 TERMINAL - GROUND STATION - (SATELLITE LINK)
 HIGH DATA RATE RECEIVER

Parameter	Configuration		
	Data	Acquisition	Tracking
Transmitter			
Format	PIM, 64		
Power, watts	.200	.200	.200
Transmitter efficiency	.834	.834	.834
Beamwidth, radians	3.8×10^{-4}	3.80×10^{-4}	3.8×10^{-4}
Pointing accuracy, radians	0.1×10^{-4}	0.21×10^{-3}	0.1×10^{-4}
wavelength, meters	0.53×10^{-6}	0.53×10^{-6}	0.53×10^{-6}
Extinction ratio	30	30	30
Receiver			
Format	PQM		
Detector	DCFP	QPMT	QPMT
Aperture diameter, meters	1.524	1.524	1.524
Receiver efficiency	.302	.484	.005
Power split for tracking	0.99	1	.01
Date rate, bps	6.4×10^9	0.1×10^5	0.1×10^5
Quantum efficiency	.010	.010	.010
Field of view, radians	3.0×10^{-4}	4.0×10^{-3}	5.0×10^{-5}
Filter bandwidth, Å	10.0	25.0	25.0
Receiver Gatewidth	3.0×10^{-10}	8.480×10^{-5}	8.480×10^{-5}

TABLE D-4
TERMINAL - LOW ALTITUDE SATELLITE
HIGH DATA RATE TRANSMITTER

Parameter	Configuration		
	Data	Acquisition	Tracking
Transmitter			
Format	PQM		
Power, watts	.200	.200	.200
Transmitter efficiency	.810	.810	.810
Beamwidth, radians	5.079×10^{-6}	6.0×10^{-5}	5.079×10^{-6}
Pointing accuracy, radians	0.1×10^{-5}	0.12×10^{-4}	0.1×10^{-5}
wavelength, meters	0.106×10^{-5}	0.106×10^{-5}	0.106×10^{-5}
Extinction ratio	0.3×10^2	0.3×10^2	0.3×10^2
Receiver			
Format	PIM, 64		
Detector	QPMT	QPMT	QPMT
Aperture diameter, meters	.305	.305	.305
Receiver efficiency	.507	.507	.507
Power split for tracking	1	1	1
Date rate, bps	0.4×10^2	0.4×10^2	0.4×10^2
Quantum efficiency	.250	.250	.250
Field of view, radians	4.0×10^{-4}	4.0×10^{-3}	4.0×10^{-4}
Filter bandwidth, Å	25.0	25.0	25.0
Receiver Gatewidth	2.0×10^{-7}	2.0×10^{-7}	2.0×10^{-7}

TABLE D-5
 TERMINAL - SYNCHRONOUS SATELLITE
 HIGH DATA RATE RECEIVER

Parameter	Configuration		
	Data	Acquisition	Tracking
Transmitter			
Format	PIM, 64		
Power, watts	.025	.025	.025
Transmitter efficiency	.834	.834	.834
Beamwidth, radians	2.7×10^{-4}	6.0×10^{-4}	2.7×10^{-4}
Pointing accuracy, radians	0.1×10^{-5}	0.105×10^{-3}	0.1×10^{-5}
Wavelength, meters	0.53×10^{-6}	0.53×10^{-6}	0.53×10^{-6}
Extinction ratio	0.3×10^2	0.3×10^2	0.3×10^2
Receiver			
Format	PQM		
Detector	DCFP	QPMT	QPMT
Aperture diameter, meters	.610	.610	.610
Receiver efficiency	.302	.484	.005
Power split for tracking	0.99	1	.01
Date rate, bps	0.4×10^9	0.1×10^5	0.1×10^5
Quantum efficiency	.010	.010	.010
Field of view, radians	3.0×10^{-4}	4.0×10^{-3}	2.0×10^{-4}
Filter bandwidth, Å	10.0	10.0	10.0
Receiver Gatewidth	5.0×10^{-10}	8.480×10^{-5}	8.480×10^{-5}

TABLE D-6
TERMINAL - BALLOON
BORNE TRANSCEIVER

Parameter	Configuration			
	Data	Acquisition	Tracking	
Transmitter				
Format	PQM			
Power, watts	.050	.050	.050	
Transmitter efficiency	.640	.652	.652	
Beamwidth, radians	5.0×10^{-4}	5.0×10^{-4}	5.0×10^{-4}	
Pointing accuracy, radians	0.25×10^{-5}	0.1×10^{-4}	0.1×10^{-4}	
Wavelength, meters	0.106×10^{-5}	0.106×10^{-5}	0.106×10^{-5}	
Extinction ratio	0.3×10^2	0.3×10^2	0.3×10^2	
Receiver			Data	Beacon
Format	PGBM			
Detector	DCFP	QPMT	QPMT	QPMT
Aperture diameter, meters	.100	.100	.100	.100
Receiver efficiency	.409	.072	.000	.072
Power split for tracking	.9	1	1	1
Date rate, bps	0.4×10^9	0.4×10^4	0.4×10^4	0.16×10^4
Quantum efficiency	.100	.100	.100	.100
Field of view, radians	3.0×10^{-4}	3.5×10^{-2}	4.0×10^{-3}	4.0×10^{-3}
Filter bandwidth, Å	100.0	100.0	100.0	100.0
Receiver Gatewidth	1.250×10^{-9}	2.120×10^{-4}	2.120×10^{-4}	2.0×10^{-7}
Optical Attenuation	1	1	.005	1

TABLE D-7
 TERMINAL - GROUND STATION
 (BALLOON LINK)

Parameter	Configuration			
	Data	Acquisition	Tracking	
Transmitter				
Format	PGBM			
Power, watts	.100	.100	.100	.100
Transmitter efficiency	.834	.417	.417	.000
Beamwidth, radians	1.0×10^{-4}	1.5×10^{-3}	1.0×10^{-4}	1.0×10^{-4}
Pointing accuracy, radians	0.25×10^{-4}	0.28×10^{-3}	0.5×10^{-5}	0.5×10^{-5}
Wavelength, meters	0.53×10^{-6}	0.53×10^{-6}	0.53×10^{-6}	0.53×10^{-6}
Extinction ratio	0.3×10^2	0.3×10^2	0.3×10^2	0.3×10^2
Receiver				
Format	PQM			
Detector	DCFP	QPMT	QPMT	
Aperture diameter, meters	.760	.760	.760	
Receiver efficiency	.403	.007	.005	
Power split for Tracking	.99	1	.01	
Date rate, bps	0.4×10^9	0.4×10^4	0.4×10^4	
Quantum efficiency	.001	.001	.001	
Field of view, radians	3.0×10^{-4}	1.750×10^{-2}	1.750×10^{-2}	
Filter bandwidth, Å	100.0	100.0	100.0	
Receiver Gatewidth	2.50×10^{-9}	2.120×10^{-4}	2.120×10^{-4}	
Optical Attenuation	1	1	1	

TABLE D-8
LINK: SYNC--GROUND

	Configuration	
	Data	Beacon
Wavelength, meters	0.106×10^{-5}	0.53×10^{-6}
Range, meters	4.110×10^7	4.110×10^7
Atmosphere transmissibility	0.891×10	0.722×10
Beam wander and spread	0.1×10^1	0.1×10^1
Background radiance ($\omega/m^2-A-\Omega$)	0.16×10^{-2}	0.17×10^{-1}
Background source		

TABLE D-9
LINK: LAS-SYNC

	Configuration	
	Data	Beacon
Wavelength, meters	0.106×10^{-5}	0.53×10^{-6}
Range, meters	4.500×10^7	4.500×10^7
Atmosphere transmissibility	0.1×10^1	0.1×10^1
Beam wander and spread	0.1×10^1	0.1×10^1
Background radiance ($\omega/m^2-A-\Omega$)	0.875×10^{-2}	0.0
Background source		

TABLE D-10
LINK: BALLOON-GROUND

	Configuration	
	Data	Beacon
Wavelength, meters	0.106×10^{-5}	0.53×10^{-6}
Range, meters	7.212×10^4	7.212×10^4
Atmosphere transmissibility	0.891×10	0.722×10
Beam wander and spread	0.86	0.675×10
Background radiance ($\omega/m^2-A-\Omega$)	0.0	0.17×10^{-1}
Background source		

FIGURE D-1

LINK CHANNEL	WAVELENGTH	SYNC TO GROUND DATA-PQM	1.06 MICRON	73/61/12		
S1	LASER POWER	DB	-6.99	.210	WATTS	
S2	TRANSMITTER LOSSES	DB	-.92	.810	EFF	
S3	TRANSMIT ANTENNA GAIN	DB	113.40	8.126E-06	RADIANS	
S4	POINTING LOSSES	DB	-.46			
S5	SPACE LOSS	DB	-293.75	4.11E+7	M	
S6	ATMOSPHERIC LOSS	DB	-.50	.891	TRANS	
S7	RECEIVE ANTENNA GAIN	DB	133.10	1.524	M DIA	
S8	RECEIVER LOSSES	DB	-5.20	302		
S9	RECEIVED POWER	DB	-61.31	7.390E-07	WATTS	
S10	BIT PERIOD	DB	-86.02	2.500E-09	SEC	
S11	RECEIVED ENERGY/BIT	DBJ	-147.33	1.846E-15	JOULES	
S12	ENERGY/PHOTON	DBJ	-167.27	1.874E-19	JOULES/PHOTON	
S13	RECEIVED PHOTONS/BIT	DB	39.94	9859.431		
S14	QUANTUM EFFICIENCY	DB	-20.00	.010		
S15	RECEIVED PHOTOELECTRONS/BIT	DB	19.94	98.594		
S16	REQUIRED PHOTOELECTRONS/BIT	DB	10.70	11.737		
S17	MARGIN	DB	9.24	8.610		
B1	BACKGROUND RADIANCE	DBM	-28.46	.001	W/M2-STERRADIANS-A	
B2	RECEIVER FOV	DB	-71.51	3.000E-04	RAD	
B3	BACKGROUND IRRADIANCE	DBA	-0.00	0.	W/M2-A	
B4	OPTICAL FILTER BANDWIDTH	DBA	-10.00	10.000	A	
B5	RECEIVER ANTENNA AREA	DBM	2.61			
B6	RECEIVER GATE WIDTH	DB-SEC	-95.23	3.000E-10	SEC	
B7	RECEIVER LOSSES	DB	-3.20			
B8	RECEIVED ENERGY/BIT	DBJ	-165.78			
B9	ENERGY/PHOTON	DBJ	-167.27			
B10	RECEIVED PHOTONS/BIT	DB	1.49	1.418		
B11	QUANTUM EFFICIENCY	DB	-20.00			
B12	RECEIVED PHOTOELECTRONS/BIT	DB	-18.51	014		

342

FIGURE D-2

LINK CHANNEL		SYNC TO GROUND DATA ACQUISITION		QPHT	
WAVELENGTH		1.06 MICRON		73/11/12. F	
AS1	LASER POWER	DB	-6.99	.200	WATTS
AS2	TRANSMITTER LOSSES	DB	- .92	.810	FFF
AS3	TRANSMIT ANTENNA GAIN	DB	95.05	1.000E-04	RADIANS
AS4	POINTING LOSSES	DB	-2.17		
AS5	SPACE LOSS	DB	-293.75	4.110E+17	M
AS6	ATMOSPHERIC LOSS	DB	- .50	.891	TRANS
AS7	RECEIVE ANTENNA GAIN	DB	133.13	1.524	M DIA
AS8	RECEIVER LOSSES	DB	-3.15	.484	
AS9	RECEIVED POWER	DB	-79.34	1.155E-08	WATTS
AS10	PULSE PERIOD	DB	-40.72	8.475E-09	SEC
AS11	RECEIVED ENERGY/PULSE	DBJ	-120.05	9.875E-13	JOULFS
AS12	ENERGY/PHOTON	DBJ	-187.27	1.874E-19	JOULFS/PHOTON
AS13	RECEIVED PHOTONS/PULSE	DB	67.22	5269689.254	
AS14	QUANTUM EFFICIENCY	DB	-20.03	.010	
AS15	RECEIVED PHOTOELECTRONS/PULSE	DB	47.22	52696.893	
AS15	REQUIRED PHOTOELECTRONS/PULSE	DB	38.44	5981.023	
AS17	MARGIN	DB	8.78	7.549	
AB1	BACKGROUND RADIANCE	DBM	-29.45	.001	W/M2-STERADIANS-A
AB2	RECEIVER FOV	DB	-49.81	4.860E-03	RAD
AB3	BACKGROUND IRRADIANCE	DBA	-100.00	0.	W/M2-A
AB4	OPTICAL FILTER BANDWIDTH	DBA	11.98	25.000	A
AB5	RECEIVER ANTENNA AREA	DBM	2.61		
AB5	RECEIVER GATE WIDTH	DB-SEC	-40.72	8.480E-09	SEC
AB7	RECEIVER LOSSES	DB	-3.15		
AB8	RECEIVED ENERGY/PULSE	DBJ	-104.75		
AB9	ENERGY/PHOTON	DBJ	-187.27		
AB11	RECEIVED PHOTONS/PULSE	DB	62.53	17894040.083	
AB11	QUANTUM EFFICIENCY	DB	-20.90		
AB12	RECEIVED PHOTOELECTRONS/PULSE	DB	62.53	1789404.361	

343

CONTINUED NEXT PAGE

FIGURE D-3

LINK CHANNEL	SYNCHRONIZATION DATA	GROUND TRACKING	WAVELENGTH	1.06 MICRON	QPMT	73/01/12	7
TS1	LASER POWER	DB	-5.99	.210	WATTS		
TS2	TRANSMITTER LOSSES	DB	- .92	.810	FFF		
TS3	TRANSMIT ANTENNA GAIN	DB	116.85	8.126E-16	RADIANS		
TS4	POINTING LOSSES	DB	- .82				
TS5	SPACE LOSS	DB	-293.75	4.110E+17	M		
TS6	ATMOSPHERIC LOSS	DB	- .50	.891	TRANS		
TS7	RECEIVE ANTENNA GAIN	DB	133.19	1.524	M DIA		
TS8	RECEIVER LOSSES	DB	-23.15	.015			
TS9	RECEIVED POWER	DB	-75.18	2.408E-18	WATTS		
TS10	PULSE PERIOD	DB	-43.72	8.475E-15	SEC		
TS11	RECEIVED ENERGY/PULSE	DBJ	-115.90	2.040E-12	JOULFS		
TS12	ENERGY/PHOTON	DBJ	-187.27	1.874E-19	JOULFS/PHOTON		
TS13	RECEIVED PHOTONS/PULSE	DB	70.37	10888437.805			
TS14	QUANTUM EFFICIENCY	DB	-20.09	.010			
TS15	RECEIVED PHOTOELECTRONS/PULSE	DB	60.37	109884.378			
TS16	REQUIRED PHOTOELECTRONS/PULSE	DB	33.84	2422.579			
TS17	MARGIN	DB	15.53	44.946			
TB1	BACKGROUND RADIANCE	DBM	-25.45	.001	W/M2-STERRADIANS-A		
TB2	RECEIVER FOV	DB	-87.07	5.000E-15	RAO		
TB3	BACKGROUND IRRADIANCE	DBA	-100.01	0.	W/M2-A		
TB4	OPTICAL FILTER BANDWIDTH	DBA	13.99	25.000	A		
TB5	RECEIVER ANTENNA AREA	DBM	2.61				
TB6	RECEIVER GATE WIDTH	DB-SEC	-43.72	8.470E-15	SEC		
TB7	RECEIVER LOSSES	DB	-23.15				
TB8	RECEIVED ENERGY/PULSE	DBJ	-162.81				
TB9	ENERGY/PHOTON	DBJ	-187.27				
TB10	RECEIVED PHOTONS/PULSE	DB	24.47	279.594			
TB11	QUANTUM EFFICIENCY	DB	-23.09				
TB12	RECEIVED PHOTOELECTRONS/PULSE	DB	4.47	2.796			

344

CALCULATED FROM DATA IN FIGURE D-1 AND D-2

FIGURE D-4

LINK CHANNEL	SYNC TO GROUND BEACON... ACQUISITION WAVELENGTH					QPNT
	.53 MICROM					73/01/12. 1
AS1	LASER POWER	DB	-5.99	.200	WATTS	
AS2	TRANSMITTER LOSSES	DB	-79	.834	EFF	
AS3	TRANSMIT ANTENNA GAIN	DB	83.46	3.800E-14	RADIANS	
AS4	POINTING LOSSES	DB	-4.25			
AS5	SPACE LOSS	DB	-299.78	4.110E+07	M	
AS6	ATMOSPHERIC LOSS	DB	-2.41	.574	TRANS	
AS7	RECEIVE ANTENNA GAIN	DB	121.05	.191	M DIA	
AS8	RECEIVER LOSSES	DB	-2.95	.507		
AS9	RECEIVED POWER	DB	-112.65	5.421E-12	WATTS	
AS10	PULSE PERIOD	DB	-32.04	6.250E-16	SEC	
AS11	RECEIVED ENERGY/PULSE	DBJ	-144.79	3.388E-15	JOULES	
AS12	ENERGY/PHOTON	DBJ	-184.25	3.748E-19	JOULES/PHOTON	
AS13	RECEIVED PHOTONS/PULSE	DB	39.56	9040.215		
AS14	QUANTUM EFFICIENCY	DB	-6.02	.250		
AS15	RECEIVED PHOTOELECTRONS/PULSE	DB	33.54	2260.854		
AS16	REQUIRED PHOTOELECTRONS/PULSE	DB	27.41	550.748		
AS17	MARGIN	DB	6.13	4.104		
AB1	BACKGROUND RADIANCE	DBM	-19.11	.012	W/M2-STERRADIANS-A	
AB2	RECEIVER FOV	DB	-49.01	4.000E-13	RAD	
AB3	BACKGROUND IRRADIANCE	DBA	-109.09	9.	W/M2-A	
AB4	OPTICAL FILTER BANDWIDTH	DBA	13.95	25.000	A	
AB5	RECEIVER ANTENNA AREA	DBM	-15.45			
AB6	RECEIVER GATE WIDTH	DB-SEC	-66.99	2.000E-07	SEC	
AB7	RECEIVER LOSSES	DB	-2.95			
AB8	RECEIVED ENERGY/PULSE	DBJ	-139.53			
AB9	ENERGY/PHOTON	DBJ	-184.25			
AB10	RECEIVED PHOTONS/PULSE	DB	44.73	29736.078		
AB11	QUANTUM EFFICIENCY	DB	-5.02			
AB12	RECEIVED PHOTOELECTRONS/PULSE	DB	38.71	7434.019		

345

11/11/12 10:00 AM 11/11/12 10:00 AM 11/11/12 10:00 AM 11/11/12 10:00 AM 11/11/12 10:00 AM

FIGURE D-5

LINK CHANNEL	WAVELENGTH	SYNC TO GROUND BFACON... TRACKING 53 MICRON			QPHT	23/01/12	2
TS1	LASER POWER	DB	-5.99	200	WATTS		
TS2	TRANSMITTER LOSSES	DB	-0.79	0.074	FFF		
TS3	TRANSMIT ANTENNA GAIN	DB	83.01	4.010E-04	RADIANS		
TS4	POINTING LOSSES	DB	-0.03				
TS5	SPACE LOSS	DB	-299.70	4.110E+07	M		
TS6	ATMOSPHERIC LOSS	DB	-2.41	0.574	TRANS		
TS7	RECEIVE ANTENNA GAIN	DB	121.06	0.191	M DIA		
TS8	RECEIVER LOSSES	DB	-2.95	0.07			
TS9	RECEIVED POWER	DB	-100.00	1.293E-11	WATTS		
TS10	PULSE PERIOD	DB	-32.04	6.250E-04	SEC		
TS11	RECEIVED ENERGY/PULSE	DBJ	-140.92	8.085E-15	JOULFS		
TS12	ENERGY/PHOTON	DBJ	-184.25	3.748E-19	JOULFS/PHOTON		
TS13	RECEIVED PHOTONS/PULSE	DB	43.36	21569.578			
TS14	QUANTUM EFFICIENCY	DB	-6.02	0.250			
TS15	RECEIVED PHOTOELECTRONS/PULSE	DB	37.32	5392.394			
TS16	REQUIRED PHOTOELECTRONS/PULSE	DB	26.31	427.699			
TS17	MARGIN	DB	11.01	12.689			
TB1	BACKGROUND RADIANCE	DBM	-19.11	0.012	W/M2-STERRADIANS-A		
TB2	RECEIVER FOV	DB	-69.01	4.000E-04	RAD		
TB3	BACKGROUND IRRADIANCE	DBA	-103.00	0.	W/M2-A		
TB4	OPTICAL FILTER BANDWIDTH	DBA	13.98	25.000	A		
TB5	RECEIVER ANTENNA AREA	DBM	-15.45				
TB6	RECEIVER GATE WIDTH	DB-SEC	-65.99	2.000E-07	SEC		
TB7	RECEIVER LOSSES	DB	-2.95				
TB8	RECEIVED ENERGY/PULSE	DBJ	-159.53				
TB9	ENERGY/PHOTON	DBJ	-184.25				
TB10	RECEIVED PHOTONS/PULSE	DB	24.73	297.361			
TB11	QUANTUM EFFICIENCY	DB	-5.02				
TB12	RECEIVED PHOTOELECTRONS/PULSE	DB	10.71	74.340			

346

FIGURE D-6

LINK CHANNEL WAVELENGTH	LAS TO SYNC DATA-PQM	1.56 MICRON			73/01/12
S1	LASER POWER	DB	-6.99	200	WATTS
S2	TRANSMITTER LOSSES	DB	-0.92	810	EFF
S3	TRANSMIT ANTENNA GAIN	DB	117.48	5.079E+06	RADIANS
S4	POINTING LOSSES	DB	-1.18		
S5	SPACE LOSS	DB	-294.54	4.500E+07	M
S6	ATMOSPHERIC LOSS	DB	0.06	1.000	TRANS
S7	RECEIVE ANTENNA GAIN	DB	125.14	.610	M DIA
S8	RECEIVER LOSSES	DB	-5.26	.3.2	
S9	RECEIVED POWER	DB	-66.20	2.399E-07	WATTS
S10	BIT PERIOD	DB	-86.02	2.500E-09	SEC
S11	RECEIVED ENERGY/BIT	DBJ	-152.22	5.998E-16	JOULES
S12	ENERGY/PHOTON	DBJ	-187.27	1.874E-19	JOULES/PHOTON
S13	RECEIVED PHOTONS/BIT	DB	35.05	3200.718	
S14	QUANTUM EFFICIENCY	DB	-20.00	.010	
S15	RECEIVED PHOTOELECTRONS/BIT	DB	15.05	32.037	
S16	REQUIRED PHOTOELECTRONS/BIT	DB	13.70	11.761	
S17	MARGIN	DB	4.35	2.721	
B1	BACKGROUND RADIANCE	DBM	-20.58	.039	W/M2-STERRADIANS-A
B2	RECEIVER FOV	DB	-71.51	3.030E-4	RAD
B3	BACKGROUND IRRADIANCE	DBA	0.00	0.	W/M2-A
B4	OPTICAL FILTER BANDWIDTH	DBA	10.00	10.000	A
B5	RECEIVER ANTENNA AREA	DBM	-6.35		
B6	RECEIVER GATE WIDTH	DB-SEC	-93.81	5.800E-10	SEC
B7	RECEIVER LOSSES	DB	-3.20		
B8	RECEIVED ENERGY/BIT	DBJ	-183.64		
B9	ENERGY/PHOTON	DBJ	-187.27		
B10	RECEIVED PHOTONS/BIT	DB	3.63	2.308	
B11	QUANTUM EFFICIENCY	DB	-20.00		
B12	RECEIVED PHOTOELECTRONS/BIT	DB	-16.37	.023	

347

CONTINUOUS IMPROVEMENTS
MOORE BUSINESS FORMS INC. 77

FIGURE D-7

LINK CHANNEL	LAS TO SYNC DATA ACQUISITION	WAVELENGTH	1.06 MICRON	QPHT	73/01/12. 9
AS1	LASER POWER	DB	-6.99	.200	WATTS
AS2	TRANSMITTER LOSSES	DB	- .92	.810	EFF
AS3	TRANSMIT ANTENNA GAIN	DB	99.49	6.000E-05	RADIANS
AS4	POINTING LOSSES	DB	-2.17		
AS5	SPACE LOSS	DB	-294.54	4.500E+17	M
AS6	ATMOSPHERIC LOSS	DB	0.00	1.000	TRANS
AS7	RECEIVE ANTENNA GAIN	DB	125.14	.610	M DIA
AS8	RECEIVER LOSSES	DB	-3.15	.484	
AS9	RECEIVED POWER	DB	-83.14	4.848E-19	WATTS
AS10	PULSE PERIOD	DB	-41.72	8.475E-15	SEC
AS11	RECEIVED ENERGY/PULSE	DBJ	-123.86	4.109E-13	JOULES
AS12	ENERGY/PHOTON	DBJ	-187.27	1.874E-19	JOULES/PHOTON
AS13	RECEIVED PHOTONS/PULSE	DB	63.41	2192721.123	
AS14	QUANTUM EFFICIENCY	DB	-20.00	.810	
AS15	RECEIVED PHOTOELECTRONS/PULSE	DB	43.41	21927.211	
AS15	REQUIRED PHOTOELECTRONS/PULSE	DB	35.41	4376.879	
AS17	MARGIN	DB	7.00	5.010	
AB1	BACKGROUND RADIANCE	DBW	-20.58	.009	W/M2-STERRADIANS-A
AB2	RECEIVER FOV	DB	-49.01	4.000E-13	RAD
AB3	BACKGROUND IRRADIANCE	DBA	-100.00	0.	W/M2-A
AB4	OPTICAL FILTER BANDWIDTH	DBA	10.00	10.000	A
AB5	RECEIVER ANTENNA AREA	DBM	-5.35		
AB6	RECEIVER GATE WIDTH	DB-SEC	-41.72	8.480E-15	SEC
AB7	RECEIVER LOSSES	DB	-3.15		
AB8	RECEIVED ENERGY/PULSE	DBJ	-108.89		
AB9	ENERGY/PHOTON	DBJ	-187.27		
AB10	RECEIVED PHOTONS/PULSE	DB	74.47	70291853.569	
AB11	QUANTUM EFFICIENCY	DB	-20.00		
AB12	RECEIVED PHOTOELECTRONS/PULSE	DB	58.47	702908.535	

348

FIGURE D-10

LINK CHANNEL	WAVELENGTH	LAS TO SYNC BEACON... TRACKING	.53 MICRON		QPMT	73/01/12	4
TS1	LASER POWER	DB	-16.02	.025	WATTS		
TS2	TRANSMITTER LOSSES	DB	-1.79	.074	EFF		
TS3	TRANSMIT ANTENNA GAIN	DB	85.42	2.700E-04	RADIANS		
TS4	POINTING LOSSES	DB	-1.01				
TS5	SPACE LOSS	DB	-303.56	4.500E+07	M		
TS6	ATMOSPHERIC LOSS	DB	0.00	1.000	TRANS		
TS7	RECEIVE ANTENNA GAIN	DB	125.14	.305	M DIA		
TS8	RECEIVER LOSSES	DB	-2.95	.507			
TS9	RECEIVED POWER	DB	-108.75	1.330E-11	WATTS		
TS10	PULSE PERIOD	DB	-32.04	6.250E-04	SEC		
TS11	RECEIVED ENERGY/PULSE	DBJ	-143.80	8.314E-15	JOULFS		
TS12	ENERGY/PHOTON	DBJ	-184.25	3.748E-19	JOULES/PHOTON		
TS13	RECEIVED PHOTONS/PULSE	DB	43.46	22184.867			
TS14	QUANTUM EFFICIENCY	DB	-5.02	.250			
TS15	RECEIVED PHOTOELECTRONS/PULSE	DB	37.44	5546.217			
TS16	REQUIRED PHOTOELECTRONS/PULSE	DB	29.81	956.824			
TS17	MARGIN	DB	7.63	5.796			
TB1	BACKGROUND RADIANCE	DBM	-100.00	0.000	M/M2-STERRADIANS-A		
TB2	RECEIVER FOV	DB	-69.01	4.000E-04	RAD		
TB3	BACKGROUND IRRADIANCE	DBA	-95.99	2.000E-10	M/M2-A		
TB4	OPTICAL FILTER BANDWIDTH	DBA	13.98	25.000	A		
TB5	RECEIVER ANTENNA AREA	DBM	-11.37				
TB6	RECEIVER GATE WIDTH	DB-SEC	-66.99	2.000E-07	SEC		
TB7	RECEIVER LOSSES	DB	-2.95				
TB8	RECEIVED ENERGY/PULSE	DBJ	-164.32				
TB9	ENERGY/PHOTON	DBJ	-184.26				
TB10	RECEIVED PHOTONS/PULSE	DB	19.94	98.789			
TB11	QUANTUM EFFICIENCY	DB	-6.02				
TB12	RECEIVED PHOTOELECTRONS/PULSE	DB	13.92	24.677			

351

FIGURE D-11

LINK CHANNEL WAVELENGTH	BALLOON TO GROUND DATA-PQM 1.05 MICRON				
S1	LASER POWER	DB	-17.01	0.20	WATTS
S2	TRANSMITTER LOSSES	DB	-1.94	.640	EFF
S3	TRANSMIT ANTENNA GAIN	DB	81.07	5.00E-04	RADIANS
S4	POINTING LOSSES	DB	-0.00		
S5	SPACE LOSS	DB	-238.64	7.212E+24	M
S6	ATMOSPHERIC LOSS	DB	-1.16	.765	TRANS
S7	RECEIVE ANTENNA GAIN	DB	127.05	.760	M DIA
S8	RECEIVER LOSSES	DB	-3.95	.403	
S9	RECEIVED POWER	DB	-60.58	8.748E-16	WATTS
S10	BIT PERIOD	DB	-86.02	2.500E-09	SEC
S11	RECEIVED ENERGY/BIT	DBJ	-136.60	2.187E-14	JOULES
S12	ENERGY/PHOTON	DBJ	-187.27	1.874E-19	JOULES/PHOTON
S13	RECEIVED PHOTONS/BIT	DB	60.67	116714.381	
S14	QUANTUM EFFICIENCY	DB	-30.00	.001	
S15	RECEIVED PHOTOELECTRONS/BIT	DB	20.67	116.714	
S16	REQUIRED PHOTOELECTRONS/BIT	DB	10.69	11.719	
S17	MARGIN	DB	9.98	9.960	
B1	BACKGROUND RADIANCE	DBM	-35.73	.000	W/M2-STERRADIANS-A
B2	RECEIVER FOV	DB	-71.51	3.000E-04	RAD
B3	BACKGROUND IRRADIANCE	DBA	0.00	0.	W/M2-A
B4	OPTICAL FILTER BANDWIDTH	DBA	20.00	-100.000	A
B5	RECEIVER ANTENNA AREA	DBM	-3.43		
B6	RECEIVER GATE WIDTH	DB-SEC	-86.02	2.500E-09	SEC
B7	RECEIVER LOSSES	DB	-1.95		
B8	RECEIVED ENERGY/BIT	DBJ	-176.64		
B9	ENERGY/PHOTON	DBJ	-187.27		
B10	RECEIVED PHOTONS/BIT	DB	0.63	7.235	
B11	QUANTUM EFFICIENCY	DB	-36.00		
B12	RECEIVED PHOTOELECTRONS/BIT	DB	-21.37	.007	

73/01/12.

352

FIGURE D-12

LINK CHANNEL	BALLOON TO GROUND DATA-PGDM	WAVELENGTH	1.06 MICRON			73/01/12.
S1	LASER POWER	DB	-13.01	050	WATTS	
S2	TRANSMITTER LOSSES	DB	-1.16	.765	EFF.	
S3	TRANSMIT ANTENNA GAIN	DB	81.07	5.000E-06	RADIANS	
S4	POINTING LOSSES	DB	-0.00			
S5	SPACE LOSS	DB	-238.66	7.212E+14	M	
S6	ATMOSPHERIC LOSS	DB	-1.16	.765	TRANS	
S7	RECEIVE ANTENNA GAIN	DB	127.05	.760	M DIA	
S8	RECEIVER LOSSES	DB	-3.95	.403		
S9	RECEIVED POWER	DB	-49.81	1.046E-5	WATTS	
S10	BIT PERIOD	DB	-86.02	2.500E-09	SEC	
S11	RECEIVED ENERGY/BIT	DBJ	-135.83	2.615E-14	JOULES	
S12	ENERGY/PHOTON	DBJ	-187.27	1.874E-19	JOULES/PHOTON	
S13	RECEIVED PHOTONS/BIT	DB	51.45	139531.960		
S14	QUANTUM EFFICIENCY	DB	-30.00	.001		
S15	RECEIVED PHOTOELECTRONS/BIT	DB	21.45	139.532		
S16	REQUIRED PHOTOELECTRONS/BIT	DB	15.89	38.794		
S17	MARGIN	DB	5.56	3.597		
B1	BACKGROUND RADIANCE	DBM	-35.73	.000	M/M2-STERRADIANS-A	
B2	RECEIVER FOV	DB	-71.51	3.000E-14	RAD	
B3	BACKGROUND IRRADIANCE	DBA	0.00	0.	M/M2-A	
B4	OPTICAL FILTER BANDWIDTH	DBA	20.00	100.000	A	
B5	RECEIVER ANTENNA AREA	DBM	-3.43			
B6	RECEIVER GATE WIDTH	DB-SEC	-49.83	1.250E-09	SEC	
B7	RECEIVER LOSSES	DB	-1.95			
B8	RECEIVED ENERGY/BIT	DBJ	-181.65			
B9	ENERGY/PHOTON	DBJ	-187.27			
B10	RECEIVED PHOTONS/BIT	DB	5.62	3.648		
B11	QUANTUM EFFICIENCY	DB	-33.00			
B12	RECEIVED PHOTOELECTRONS/BIT	DB	-24.38	.004		

FIGURE D-13

LINK CHANNEL	BALLOON TO GROUND DATA ACQUISITION WAVELENGTH	1.06 MICRON			QPMT	73/11/12	1°
AS1	LASER POWER	DB	-13.01	.050	WATTS		
AS2	TRANSMITTER LOSSES	DB	-1.85	.652	EFF		
AS3	TRANSMIT ANTENNA GAIN	DB	81.97	5.000E-04	RADIANS		
AS4	POINTING LOSSES	DB	-1.02				
AS5	SPACE LOSS	DB	-238.54	7.212E+04	M		
AS6	ATMOSPHERIC LOSS	DB	-1.16	.766	TRANS		
AS7	RECEIVE ANTENNA GAIN	DB	127.05	.760	M DIA		
AS8	RECEIVER LOSSES	DB	-21.86	.807			
AS9	RECEIVED POWER	DB	-68.42	1.538E-07	WATTS		
AS10	PULSE PERIOD	DB	-35.74	2.119E-04	SEC		
AS11	RECEIVED ENERGY/PULSE	DBJ	-105.16	3.046E-11	JOULES		
AS12	ENERGY/PHOTON	DBJ	-187.27	1.874E-19	JOULES/PHOTON		
AS13	RECEIVED PHOTONS/PULSE	DB	82.11	162573000.039			
AS14	QUANTUM EFFICIENCY	DB	-39.09	.001			
AS15	RECEIVED PHOTOELECTRONS/PULSE	DB	52.11	162573.000			
AS16	REQUIRED PHOTOELECTRONS/PULSE	DB	27.56	579.244			
AS17	MARGIN	DB	24.55	285.094			
AB1	BACKGROUND RADIANCE	DBM	-100.00	0.000	W/M2-STERADIAN-A		
AB2	RECEIVER FOV	DB	-35.19	1.759E-02	RAD		
AB3	BACKGROUND IRRADIANCE	DBA	-100.46	9.000E-11	W/M2-A		
AB4	OPTICAL FILTER BANDWIDTH	DBA	20.00	100.000	A		
AB5	RECEIVER ANTENNA AREA	DBM	-3.43				
AB6	RECEIVER GATE WIDTH	DB-SEC	-35.74	2.120E-04	SEC		
AB7	RECEIVER LOSSES	DB	-21.86				
AB8	RECEIVED ENERGY/PULSE	DBJ	-142.49				
AB9	ENERGY/PHOTON	DBJ	-187.27				
AB10	RECEIVED PHOTONS/PULSE	DB	46.79	33097.914			
AB11	QUANTUM EFFICIENCY	DB	-39.09				
AB12	RECEIVED PHOTOELECTRONS/PULSE	DB	14.79	30.098			

354

FIGURE D-14

LINK CHANNEL		BALLOON TO GROUND DATA TRACKING		QPMT	
WAVELENGTH		1.06 MICRON		73/11/12 16	
TS1	LASER POWER	DB	-13.31	.059	WATTS
TS2	TRANSMITTER LOSSES	DB	-1.85	.652	FFF
TS3	TRANSMIT ANTENNA GAIN	DB	81.07	5.000E-04	RADIANS
TS4	POINTING LOSSES	DB	- .02		
TS5	SPACE LOSS	DB	-238.64	7.212E+04	M
TS6	ATMOSPHERIC LOSS	DB	-1.15	.765	TRANS
TS7	RECEIVE ANTENNA GAIN	DB	127.05	.760	M DIA
TS8	RECEIVER LOSSES	DB	-22.83	.005	
TS9	RECEIVED POWER	DB	-69.39	1.150E-07	WATTS
TS10	PULSE PERIOD	DB	-35.74	2.419E-04	SEC
TS11	RECEIVED ENERGY/PULSE	DBJ	-106.13	2.437E-11	JOULES
TS12	ENERGY/PHOTON	DBJ	-187.27	1.874E-19	JOULES/PHOTON
TS13	RECEIVED PHOTONS/PULSE	DB	81.14	130058400.031	
TS14	QUANTUM EFFICIENCY	DB	-30.00	.001	
TS15	RECEIVED PHOTOELECTRONS/PULSE	DB	51.14	130058.400	
TS16	REQUIRED PHOTOELECTRONS/PULSE	DB	33.26	2117.657	
TS17	MARGIN	DB	17.88	61.422	
TB1	BACKGROUND RADIANCE	DBW	-109.00	0.000	W/M2-STERADIANS-A
TB2	RECEIVER FOV	DB	-35.19	1.750E-02	RAD
TB3	BACKGROUND IRRADIANCE	DBA	-109.46	9.000E-11	W/M2-A
TB4	OPTICAL FILTER BANDWIDTH	DBA	20.00	100.000	A
TB5	RECEIVER ANTENNA AREA	DBM	-3.43		
TB6	RECEIVER GATE WIDTH	DB-SEC	-35.74	2.420E-04	SEC
TB7	RECEIVER LOSSES	DB	-22.83		
TB8	RECEIVED ENERGY/PULSE	DBJ	-143.46		
TB9	ENERGY/PHOTON	DBJ	-187.27		
TB10	RECEIVED PHOTONS/PULSE	DB	53.82	24070.331	
TB11	QUANTUM EFFICIENCY	DB	-30.00		
TB12	RECEIVED PHOTOELECTRONS/PULSE	DB	13.82	24.070	

355

CONTINUOUS INTERDISCIPLINARY MODEL-BASED DESIGN INC. 32

FIGURE D-15

LINK CHANNEL	BALLOON TO GROUND BEACON...ACQUISITION	WAVELENGTH	.93 MICRON	QPHY	73/01/16. 13
AS1	LASER POWER	DB	-10.00	.100	WATTS
AS2	TRANSMITTER LOSSES	DB	-35.74	.000	FFF
AS3	TRANSMIT ANTENNA GAIN	DB	83.01	4.000E-14	RADIANS
AS4	POINTING LOSSES	DB	-4.26		
AS5	SPACE LOSS	DB	-244.66	7.212E+14	M
AS6	ATMOSPHERIC LOSS	DB	-3.12	.487	TRANS
AS7	RECEIVE ANTENNA GAIN	DB	115.46	.100	M DIA
AS8	RECEIVER LOSSES	DB	-2.68	.540	
AS9	RECEIVED POWER	DB	-101.99	6.335E-11	WATTS
AS10	PULSE PERIOD	DB	-32.04	5.257E-14	SEC
AS11	RECEIVED ENERGY/PULSE	DBJ	-134.02	3.959E-14	JOULES
AS12	ENERGY/PHOTON	DBJ	-184.26	3.748E-19	JOULES/PHOTON
AS13	RECEIVED PHOTONS/PULSE	DB	54.24	105642.485	
AS14	QUANTUM EFFICIENCY	DB	-10.00	.100	
AS15	RECEIVED PHOTOELECTRONS/PULSE	DB	44.24	10564.249	
AS16	REQUIRED PHOTOELECTRONS/PULSE	DB	30.19	1041.191	
AS17	MARGIN	DB	10.05	10.146	
AB1	BACKGROUND RADIANCE	DBW	-19.11	.012	W/M2-STERRADIANS-A
AB2	RECEIVER FOV	DB	-39.17	3.500E-12	RAD
AB3	BACKGROUND IRRADIANCE	DBA	-100.00	0.	W/M2-A
AB4	OPTICAL FILTER BANDWIDTH	DBA	10.00	10.000	A
AB5	RECEIVER ANTENNA AREA	DBM	-21.05		
AB6	RECEIVER GATE WIDTH	DB-SEC	-65.99	2.000E-17	SEC
AB7	RECEIVER LOSSES	DB	-2.68		
AB8	RECEIVED ENERGY/PULSE	DBJ	-129.99		
AB9	ENERGY/PHOTON	DBJ	-184.26		
AB10	RECEIVED PHOTONS/PULSE	DB	54.27	267273.326	
AB11	QUANTUM EFFICIENCY	DB	-10.00		
AB12	RECEIVED PHOTOELECTRONS/PULSE	DB	44.27	26727.333	

356

FIGURE D-16

LINK	BALLOON TO GROUND					QPMT
CHANNEL	RFACON. TRACKING					73/01/12 14
WAVELENGTH	53 MICRON					
TS1	LASER POWER	DB	-11.00	.100	WATTS	
TS2	TRANSMITTER LOSSES	DB	-35.74	0.00	EFF	
TS3	TRANSMIT ANTENNA GAIN	DB	95.05	1.000E-14	RADIANS	
TS4	POINTING LOSSES	DB	-1.14			
TS5	SPACE LOSS	DB	-244.66	7.212E+04	M	
TS6	ATMOSPHERIC LOSS	DB	-3.12	.467	TRANS	
TS7	RECEIVE ANTENNA GAIN	DB	115.46	.100	M DIA	
TS8	RECEIVER LOSSES	DB	-11.43	0.72		
TS9	RECEIVED POWER	DB	-94.57	3.490E-10	WATTS	
TS10	PULSE PERIOD	DB	-32.04	6.250E-04	SEC	
TS11	RECEIVED ENERGY/PULSE	DBJ	-125.61	2.181E-13	JOULES	
TS12	ENERGY/PHOTON	DBJ	-184.26	3.748E-19	JOULES/PHOTON	
TS13	RECEIVED PHOTONS/PULSE	DB	57.65	582115.056		
TS14	QUANTUM EFFICIENCY	DB	-10.00	.100		
TS15	RECEIVED PHOTOELECTRONS/PULSE	DB	47.65	58201.506		
TS16	REQUIRED PHOTOELECTRONS/PULSE	DB	39.29	8467.584		
TS17	MARGIN	DB	8.37	6.873		
TB1	BACKGROUND RADIANCE	DBM	-19.11	.012	W/M2-STERADIANS-A	
TB2	RECEIVER FOV	DB	-49.01	4.000E-13	RAD	
TB3	BACKGROUND IRRADIANCE	DBA	-109.00	0.0	W/M2-A	
TB4	OPTICAL FILTER BANDWIDTH	DBA	20.00	100.000	A	
TB5	RECEIVER ANTENNA AREA	DBM	-21.05			
TB6	RECEIVER GATE WIDTH	DB-SEC	-65.99	2.000E-07	SEC	
TB7	RECEIVER LOSSES	DB	-11.43			
TB8	RECEIVED ENERGY/PULSE	DBJ	-147.58			
TB9	ENERGY/PHOTON	DBJ	-184.26			
TB10	RECEIVED PHOTONS/PULSE	DB	25.68	4654.556		
TB11	QUANTUM EFFICIENCY	DB	-10.00			
TB12	RECEIVED PHOTOELECTRONS/PULSE	DB	25.68	465.456		

357

CONTINUED FROM PREVIOUS PAGE

FIGURE D-17

LINK CHANNEL	GND TO BALLOON DATA-PGBM	WAVELENGTH	53 MICRON	73/01/12
S1	LASER POWER	DB	-10.00	100 WATTS
S2	TRANSMITTER LOSSES	DB	-7.79	.834 EFF
S3	TRANSMIT ANTENNA GAIN	DB	95.05	1.000E-06 RADIANS
S4	POINTING LOSSES	DB	-1.56	
S5	SPACE LOSS	DB	-244.66	7.212E+04 M
S6	ATMOSPHERIC LOSS	DB	-10.22	.095 TRANS
S7	RECEIVE ANTENNA GAIN	DB	115.46	1.0 M DIA
S8	RECEIVER LOSSES	DB	-3.88	.409
S9	RECEIVED POWER	DB	-60.74	8.509E-7 WATTS
S10	BIT PERIOD	DB	-86.02	2.500E-08 SEC
S11	RECEIVED ENERGY/BIT	DBJ	-146.72	2.127E-15 JOULES
S12	ENERGY/PHOTON	DBJ	-184.26	3.748E-19 JOULES/PHOTON
S13	RECEIVED PHOTONS/BIT	DB	37.54	5676.202
S14	QUANTUM EFFICIENCY	DB	-10.00	1.0
S15	RECEIVED PHOTOELECTRONS/BIT	DB	27.54	567.620
S16	REQUIRED PHOTOELECTRONS/BIT	DB	16.00	39.844
S17	MARGIN	DB	11.54	14.246
B1	BACKGROUND RADIANCE	DBM	-19.11	.612 W/M2-STERRADIANS-A
B2	RECEIVER FOV	DB	-71.51	3.000E-04 RAD
B3	BACKGROUND IRRADIANCE	DBA	0.00	6. W/M2-A
B4	OPTICAL FILTER BANDWIDTH	DBA	20.00	100.000 A
B5	RECEIVER ANTENNA AREA	DBM	-21.06	
B6	RECEIVER GATE WIDTH	DB-SEC	-89.03	1.250E-09 SEC
B7	RECEIVER LOSSES	DB	-1.88	
B8	RECEIVED ENERGY/BIT	DBJ	-102.58	
B9	ENERGY/PHOTON	DBJ	-184.26	
B10	RECEIVED PHOTONS/BIT	DB	1.68	1.473
B11	QUANTUM EFFICIENCY	DB	-10.00	
B12	RECEIVED PHOTOELECTRONS/BIT	DB	-8.32	.147

FIGURE D-18

LINK CHANNEL	GROUND TO BALLOON DATA ACQUISITION	WAVELENGTH	53 MICRON	QPNT	73/11/12. 1A
AS1	LASER POWER	DB	-19.00	.100	WATTS
AS2	TRANSMITTER LOSSES	DB	-3.80	.417	EFF
AS3	TRANSMIT ANTENNA GAIN	DB	71.53	1.500E-03	RADIANS
AS4	POINTING LOSSES	DB	-1.89		
AS5	SPACE LOSS	DB	-244.66	7.212E+04	M
AS6	ATMOSPHERIC LOSS	DB	-1.57	.696	TRANS
AS7	RECEIVE ANTENNA GAIN	DB	115.46	1.00	M DIA
AS8	RECEIVER LOSSES	DB	-11.43	.072	
AS9	RECEIVED POWER	DB	-86.36	2.310E-09	WATTS
AS10	PULSE PERIOD	DB	-36.74	2.119E-04	SEC
AS11	RECEIVED ENERGY/PULSE	DBJ	-123.10	4.894E-13	JOULFS
AS12	ENERGY/PHOTON	DBJ	-184.26	3.748E-19	JOULFS/PHOTON
AS13	RECEIVED PHOTONS/PULSE	DB	61.16	1305976.314	
AS14	QUANTUM EFFICIENCY	DB	-19.00	.100	
AS15	RECEIVED PHOTOELECTRONS/PULSE	DB	51.16	130597.631	
AS16	REQUIRED PHOTOELECTRONS/PULSE	DB	44.81	31252.842	
AS17	MARGIN	DB	6.35	4.317	
AB1	BACKGROUND RADIANCE	DBM	-19.11	.012	W/M2-STERRADIANS-A
AB2	RECEIVER FOV	DB	-30.17	3.500E-02	RAD
AB3	BACKGROUND IRRADIANCE	DBA	-100.00	0.	W/M2-A
AB4	OPTICAL FILTER BANDWIDTH	DBA	20.00	100.000	A
AB5	RECEIVER ANTENNA AREA	DBM	-21.05		
AB6	RECEIVER GATE WIDTH	DB-SEC	-36.74	2.120E-04	SEC
AB7	RECEIVER LOSSES	DB	-11.43		
AB8	RECEIVED ENERGY/PULSE	DBJ	-98.49		
AB9	ENERGY/PHOTON	DBJ	-184.26		
AB10	RECEIVED PHOTONS/PULSE	DB	85.77	377746300.959	
AB11	QUANTUM EFFICIENCY	DB	-10.00		
AB12	RECEIVED PHOTOELECTRONS/PULSE	DB	75.77	37774630.096	

359

© 1995 AMERICAN AIR FORCE AND SPACE SOCIETY, INC. 21

FIGURE D-19

LINK CHANNEL WAVELENGTH	GROUND TO BALLOON DATA ... TRACKING 53 MICRON			QPNT	73/11/12 19
TS1	LASER POWER	DB	-10.60	.100	WATTS
TS2	TRANSMITTER LOSSES	DB	-3.60	.417	FFF
TS3	TRANSMIT ANTENNA GAIN	DB	95.05	1.000E+04	RADIANS
TS4	POINTING LOSSES	DB	-14		
TS5	SPACE LOSS	DB	-244.65	7.212E+04	M
TS6	ATMOSPHERIC LOSS	DB	-3.12	.487	TRANS
TS7	RECEIVE ANTENNA GAIN	DB	115.46	.100	M DIA
TS8	RECEIVER LOSSES	DB	-34.44	.000	
TS9	RECEIVED POWER	DB	-85.64	2.727E-09	WATTS
TS11	PULSE PERIOD	DB	-35.74	2.119E-04	SEC
TS11	RECEIVED ENERGY/PULSE	DBJ	-122.38	5.777E-13	JOULFS
TS12	ENERGY/PHOTON	DBJ	-184.26	3.748E-19	JOULFS/PHOTON
TS13	RECEIVED PHOTONS/PULSE	DB	61.88	1541353.431	
TS14	QUANTUM EFFICIENCY	DB	-10.00	.100	
TS15	RECEIVED PHOTOELECTRONS/PULSE	DB	51.88	154135.343	
TS15	REQUIRED PHOTOELECTRONS/PULSE	DB	36.89	4881.520	
TS17	MARGIN	DB	14.99	31.575	
TB1	BACKGROUND RADIANCE	DBM	-19.11	.012	W/M2-STERADIANS-A
TB2	RECEIVER FOV	DB	-49.01	4.000E-03	RAD
TB3	BACKGROUND IR RADIANCE	DBA	-100.07	0.	W/M2-A
TB4	OPTICAL FILTER BANDWIDTH	DBA	20.09	100.000	A
TB5	RECEIVER ANTENNA AREA	DBM	-21.05		
TB6	RECEIVER GATE WIDTH	DB-SEC	-36.74	2.120E-04	SEC
TB7	RECEIVER LOSSES	DB	-34.44		
TB8	RECEIVED ENERGY/PULSE	DBJ	-140.34		
TB9	ENERGY/PHOTON	DBJ	-184.26		
TB11	RECEIVED PHOTONS/PULSE	DB	43.92	24669.146	
TB11	QUANTUM EFFICIENCY	DB	-10.00		
TB12	RECEIVED PHOTOELECTRONS/PULSE	DB	33.92	2466.915	

360

bit or per beacon pulse - as well as intermediate results S9, S11, and S13. The B parameters (B1-B7, B9, and B11) combine to produce B12 - received background photoelectrons per bit or per pulse - as well as intermediate results B8 and B10. S16, the required photoelectrons, is computed on the basis of the performance required (detection probability, rms tracking error, or bit error probability), the background level, and the magnitude of the other sources of system noise. The margin, S17, is then the ratio of S15 to S16.

THIS PAGE INTENTIONALLY LEFT BLANK

APPENDIX E

ATMOSPHERIC PROPAGATION EFFECTS ANALYSIS

1. INTRODUCTION

In this section we consider the theoretical estimates of the parameters used to characterize communication link performance degradation and those required to predict the expected results of the atmospheric propagation experiments outlined in Section 2.4.5.

For the high data rate transceiver experiment, the behavior of an optical beam propagating through the atmosphere will be primarily affected by random refractive index fluctuations and by scattering and absorption by molecules and aerosols.

The effect of scattering and absorption on the received beam can be simply characterized as an attenuation of the transmitted power. Refractive index fluctuations or turbulence, however, cause the received beam properties to vary in a random manner, thus inducing a random variation in the received optical power. Hence, statistical quantities are required to characterize the effect of turbulence on the received beam properties and in turn on the communication link performance.

Thus, in this analysis, link performance degradation caused by atmospheric propagation is attributed to two causes:

- (1) The fluctuations in received optical power due to the combined effect of scintillation and beam wander.
- (2) The reduction in mean received optical power due to atmospheric attenuation and the combined effect of beam spread and beam wander.

Therefore, we have investigated with the best current theory which predicts the magnitude and effects of the following phenomena:

- (1) Vertical profiles of turbulence
- (2) Scintillation
- (3) Aperture Averaging

- (4) Beam Wander
- (5) Reduction in Mean Received Power
- (6) Angle of Arrival Fluctuations
- (7) Attenuation

2. THE STRENGTH OF TURBULENCE AND THE TURBULENCE PROFILE

The atmosphere is statistically nonstationary and inhomogeneous. In this situation, only a nonstationary stochastic process exactly models the total effect. However, the only situation for which a well developed statistical model exists is the case of homogeneous, locally isotropic stationary turbulence. Here, turbulence is defined as the fluctuations in atmospheric refractive index which are caused primarily by microthermal fluctuations. The present random models of turbulence only apply in the case of well-mixed random fluctuations where the refractive inhomogeneities possess a range (the inertia subrange) of spatial sizes, r , such that $l_0 \ll r \ll L_0$ where l_0 and L_0 are, respectively, the inner and outer scale sizes.²⁸

Tatarski has shown that within the inertial subrange (which dominates most optical effects of interest here), the refractive index structure constant versus altitude is approximately given by²⁹

$$C_n^2(h) = \left[\frac{\rho(h)}{\rho_0} \left(288 + \frac{1.34}{\lambda^2} \right) \frac{10^{-6}}{T(h)} \right]^2 C_T^2(h) \quad (E-1)$$

where $\rho(h)$ = atmospheric density at an altitude h .

ρ_0 = the sea level atmospheric density

λ = wavelength (μm) of light of interest

$T(h)$ = the absolute temperature ($^{\circ}\text{K}$) at altitude h .

and

$C_T^2(h)$ is the temperature structure constant at altitude h .

$C_n^2(h)$ is a measure of the turbulence strength versus altitude, h ,

and

$C_T^2(h)$ is a measure of the mean square temperature difference between

two spatially separated points at an altitude h . They are related by the structure functions of refractive index and temperature

$$D_n(r) = \langle [n(\vec{r}_1) - n(\vec{r}_2)]^2 \rangle = C_n^2 r^{2/3} \quad (\text{E-2})$$

$$D_T(r) = \langle [T(r_1) - T(r_2)]^2 \rangle = C_T^2 r^{2/3} \quad (\text{E-3})$$

where $\langle \rangle$ denotes an ensemble average, $n(\vec{r})$ and $T(\vec{r})$ are, respectively, the refractive index and absolute temperature at the point \vec{r} , $r = |\vec{r}_1 - \vec{r}_2|$, and $l_0 \ll r \ll L_0$. The distance between points at which $D_T(r)$ is measured is r .

The exact turbulence profile, $C_n^2(h)$, cannot be analytically predicted and thus $D_T(r)$ must be experimentally measured simultaneously with the rest of the experiment (because of the nonstationary behavior of turbulence). A number of experiments have been performed with balloon-borne thermosondes by Bufton, et al^{10,12} and several researchers including Hufnagel⁴, Brookner³⁰, Minott³¹, and Titterton³². They have relied on indirect evidence and extrapolations to estimate the shape and strength of a mean turbulence profile. On the basis of these studies, we have selected the following theoretical turbulence profiles to estimate certain parameters of interest in this report.

$$C_n^2(h) = K_0 f(h) \quad (\text{E-4})$$

$$K_0 = 10^{-14} = \text{normalized turbulence strength at } h = 1 \text{ meter}$$

$$f(h) = f_{\text{la}}(h) + f_{\text{trop}}(h) \quad (\text{E-5})$$

where the low altitude contribution is represented by

$$f_{\text{la}}(h) = \begin{cases} h^{-1/3} \exp(-h/h_0), \\ h^{-4/3} \exp(-h/h_0), \text{ or} \\ h^{-4/3} \end{cases} \quad (\text{E-6})$$

for $h_o = 150, 1 \cdot 10^3, 3.2 \cdot 10^3$ meters

$$\text{and } f_{\text{trop}}(h) = D_o \exp \frac{-(h-h_p)^2}{(\sigma \cdot 10^3)^2} \quad (\text{E-7})$$

for $h_p = 1 \cdot 10^4, 1.5 \cdot 10^4, 1.9 \cdot 10^4$ meters

$$D_o = 0.01, 0.001$$

$$\sigma = 1.0, 0.1$$

represents the contribution at tropopause.

It is preferable to have a theoretical model for the refractive index structure constant versus altitude (see Figure E-1 for example) to compare experimental atmospheric data with theory and predict results of turbulence on random beam properties. However, these models can only describe the mean typical behavior of the atmosphere since no model of $C_n^2(h)$ can adequately describe the turbulent layers and fine structure that exist. Figure E-2 shows some typical data measured by Bufton¹³ with a balloon-borne thermosonde on descent and illustrates the extent of the typical fine structure of turbulence.

3. SCINTILLATION EFFECTS

The atmospheric refractive index is, in general, a random function of both space and time. For the current theory of optical beam propagation through the atmosphere, to a first order approximation, only spatial variations are important and the time variations are suppressed. The spatial variations have been observed to cause multiplicative variations in the received beam intensity (scintillation), and hence it is argued with use of the central limit theorem that the logarithm of received power is normally distributed. In this case, the variance and covariance functions of the log of the amplitude (square root of intensity) are all that is required to specify the log normal distribution of received signal provided that no other effects such as beam wander are present. Here, the variance of the log amplitude is defined as

FIGURE E-1 THEORETICAL TURBULENCE PROFILES VERSUS ALTITUDE

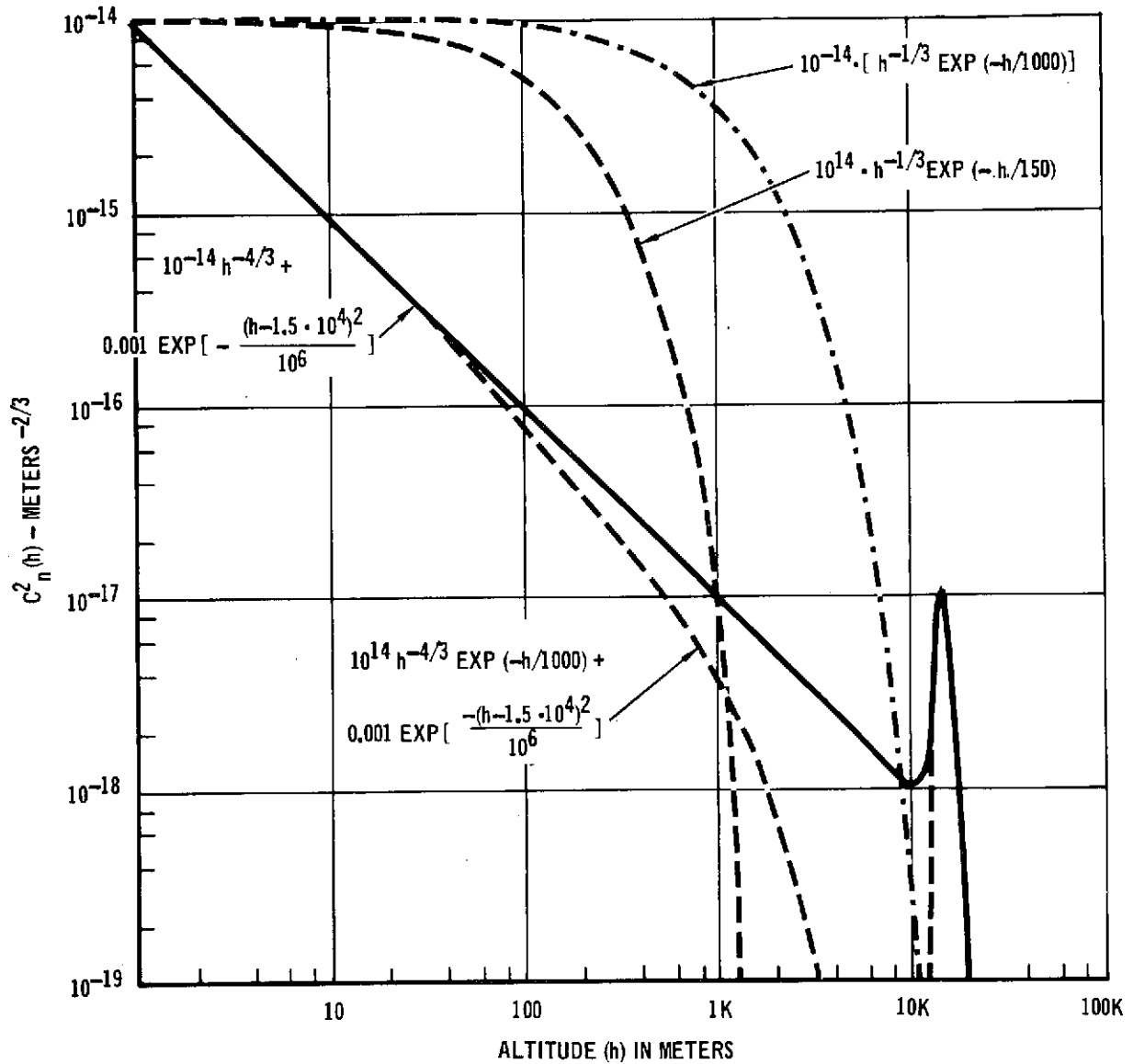
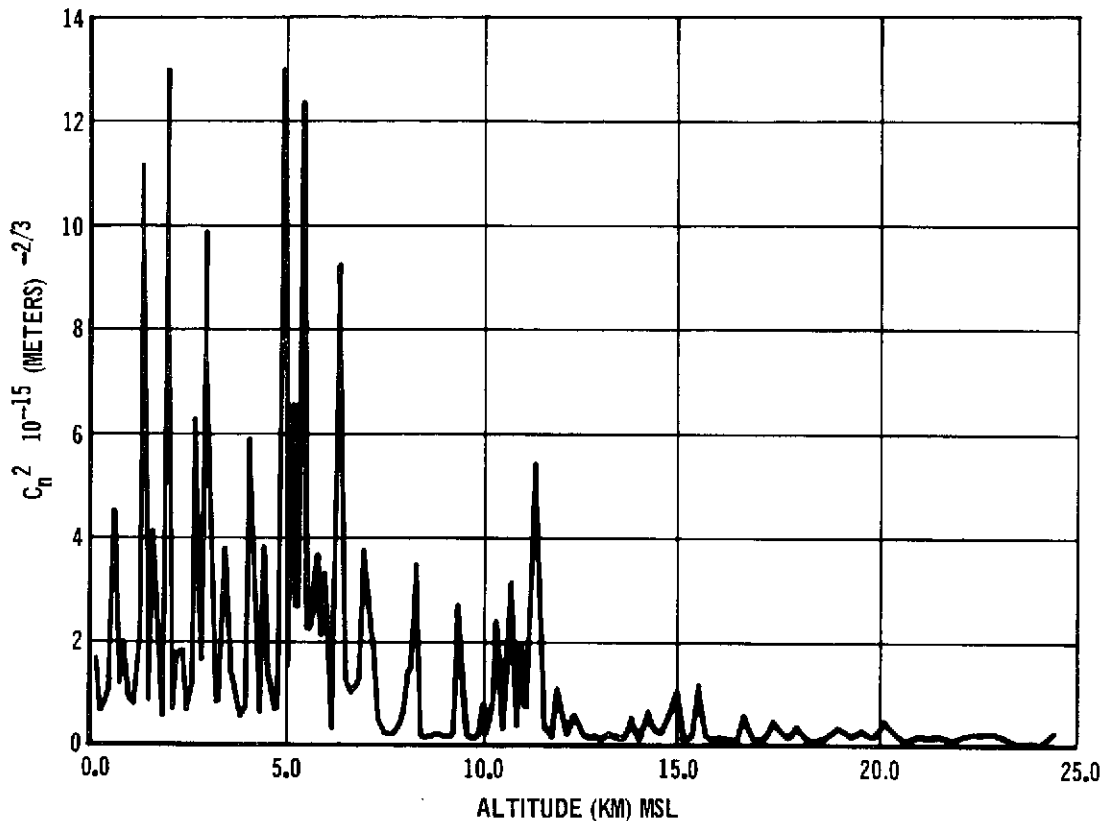


FIGURE E-2 TYPICAL TURBULENCE PROFILE MEASURED WITH
BALLOON BORNE THERMOSONDE AFTER BUFTON (13)



$$C_{\ell}(\sigma) = \langle (\ell - \langle \ell \rangle)^2 \rangle \quad (\text{E-8})$$

where the log amplitude is

$$\ell = \frac{1}{2} \ln \left(\frac{S}{S_0} \right) \quad (\text{E-9})$$

and $S_0 = \langle S \rangle =$ the mean received optical power.

Scintillation refers to the beam breakup and so-called hot spots in the receiver plane. More precisely scintillations are the dynamical fluctuations (that do not result from beam wander) in the instantaneous spatial intensity distribution at a point in the receiver plane. It can be thought of as a result of small scale destructive interference within the beam cross section due to refractive index variations along the propaga-

tion path. The effect of scintillation is observed at the photodetector output as fluctuations in the output signal. These signal fluctuations are proportional to the incident intensity and are well approximated by log normal statistics. The log normality of signal fluctuations caused by atmospheric propagation has been verified by many investigators for both vertical or horizontal paths and the proper atmospheric conditions.

Under the assumption of a normally distributed log amplitude, ℓ , and conservation of energy, Freid³³ has shown

$$\langle \ell \rangle = -C_\ell(o) \quad (E-10)$$

Hence, the probability density, $p(S)$, of the instantaneous received optical power (S) is closely described by¹

$$p(S) = \frac{1}{2S\sqrt{2} C_\ell(o)} \exp \left\{ - \frac{\left(\frac{1}{2} \ln\left(\frac{S}{S_o}\right) + C_\ell(o) \right)^2}{2C_\ell(o)} \right\} \quad (E-11)$$

and can be used to compute the link performance degradation in terms of bit error rate and link outage. See Section 2.3.3.

In this case, the log amplitude variance, $C_\ell(o)$, is the parameter required to specify the $p(S)$ and assess link degradation due to scintillation effects.

3.1 THE LOG AMPLITUDE VARIANCE, $C_\ell(o)$, FOR THE POINT RECEIVER. We have used Schmeltzer's³⁴ formulation along with current experimental measures of $C_\ell(o)$ for vertical propagation paths to arrive at an estimate of $C_\ell(o)$ typical of the balloon launch site at Hollman AFB, New Mexico.

For the general beam wave, the variance of the log amplitude fluctuations was shown by Schmeltzer to be

$$C_\ell(o) = \frac{8.16}{8\pi} k^2 \operatorname{Re} \left\{ \int_0^Z dS C_n^2(S) \int_0^\infty d\sigma \sigma^{-11/6} \right\}$$

$$\cdot \left\{ \exp \left[\frac{\sigma}{2} \operatorname{Re} \left(\gamma(Z, S) \right) \right] - \exp \left[\frac{\sigma}{2} \gamma(Z, S) \right] \right\} \quad (\text{E-12})$$

where $k = \frac{2\pi}{\lambda}$, the wave #, $\lambda =$ wavelength

$Z =$ range from transmitter to receiver,

$\sigma =$ spectral variable of the 2 dimensional spatial Fourier transform of the amplitude correlation function (the Komogorov spectrum is assumed to hold over the entire range of integration),

$C_n^2(S) =$ turbulence profile or the refractive index structure constant at the point S ,

and the integration over S is along the propagation path from transmitter to receiver.

Also,

$$\gamma(Z, S) = \frac{2i(S-Z)}{k} \frac{S-ik \alpha^2}{Z-ik \frac{\alpha^2}{2}} \quad (\text{E-13})$$

$$\text{for } \frac{1}{\alpha^2} = \frac{1}{\alpha_o^2} - \frac{ik}{R}$$

where α is a parameter that specifies the complex radius of curvature of a Gaussian spherical wave³⁵ such that the field at the transmitter aperture is given by:

$$U = A \exp \left[- \frac{r^2}{2 \alpha^2} \right] = A \exp \left[- \left\{ \frac{r^2}{2 \alpha_o^2} - \frac{ik r^2}{2 R} \right\} \right] \quad (\text{E-14})$$

for $w = 2 \alpha_o =$ the beam radius at the e^{-2} irradiance point,

$$\text{i.e. } |u|^2/A^2 = e^{-2}$$

$R =$ the radius of phase front curvature for a Gaussian spherical wave.

Note that for the

defocused beam $R > 0$,

focused beam $R < 0$, and

collimated beam $R = \infty$

For the case of the spherical wave log amplitude variance $C_{\ell}^S(o)$, due to a point source ($w = 0$), we find

$$C_{\ell}^S(o) = 4.79 \cdot K_o \cdot \lambda^{-7/6} \sec^{11/6} \theta_z \cdot \int_0^H f(h) \left[1 - \frac{h}{H}\right]^{5/6} h^{5/6} dh \quad (E-15)$$

where H = altitude of the receiver

θ_z = zenith angle so that $S = h \sec \theta_z$, $H = H \sec \theta_z$

h = the vertical altitude above the transmitter.

We have evaluated the beam wave log amplitude variance, $C_{\ell}(o)$, and the spherical wave log amplitude variance, $C_{\ell}^S(o)$, by numerical integration via a digital computer for the turbulence profiles listed above and for various transmit beam design parameters such as feed beam radius, radius of curvature, and beam width. The major portion of these results are presented in Appendix H.

These computations were performed so that the effect of transmit beam properties on scintillation could be estimated for both the high data transceiver balloon link and reference satellite link. For example, Figures E-3 and E-4 show the variation in the ratio of the beam wave to spherical wave log amplitude variance versus transmit beam radius of curvature for the balloon uplink and downlink and defocused transmit beams.

From the final optics design for the uplink and downlink transmitters, we observe the beam wave log amplitude variance is equivalent to $C_{\ell}^S(o)$, i.e.:

Balloon Uplink

$$\lambda = 0.53 \text{ } \mu\text{m}$$

$$\theta_{BW} = 100 \text{ } \mu\text{rad full angle beam width}$$

$$R = 520 \text{ m}$$

$$w = 0.85 \text{ cm}$$

FIGURE E-3 $C_{\ell}^2(0)/C_{\ell}^S(0)$ VERSUS R WITH FEED BEAM RADIUS, W, AS A PARAMETER FOR THE BALLOON DEFOCUSSED UPLINK

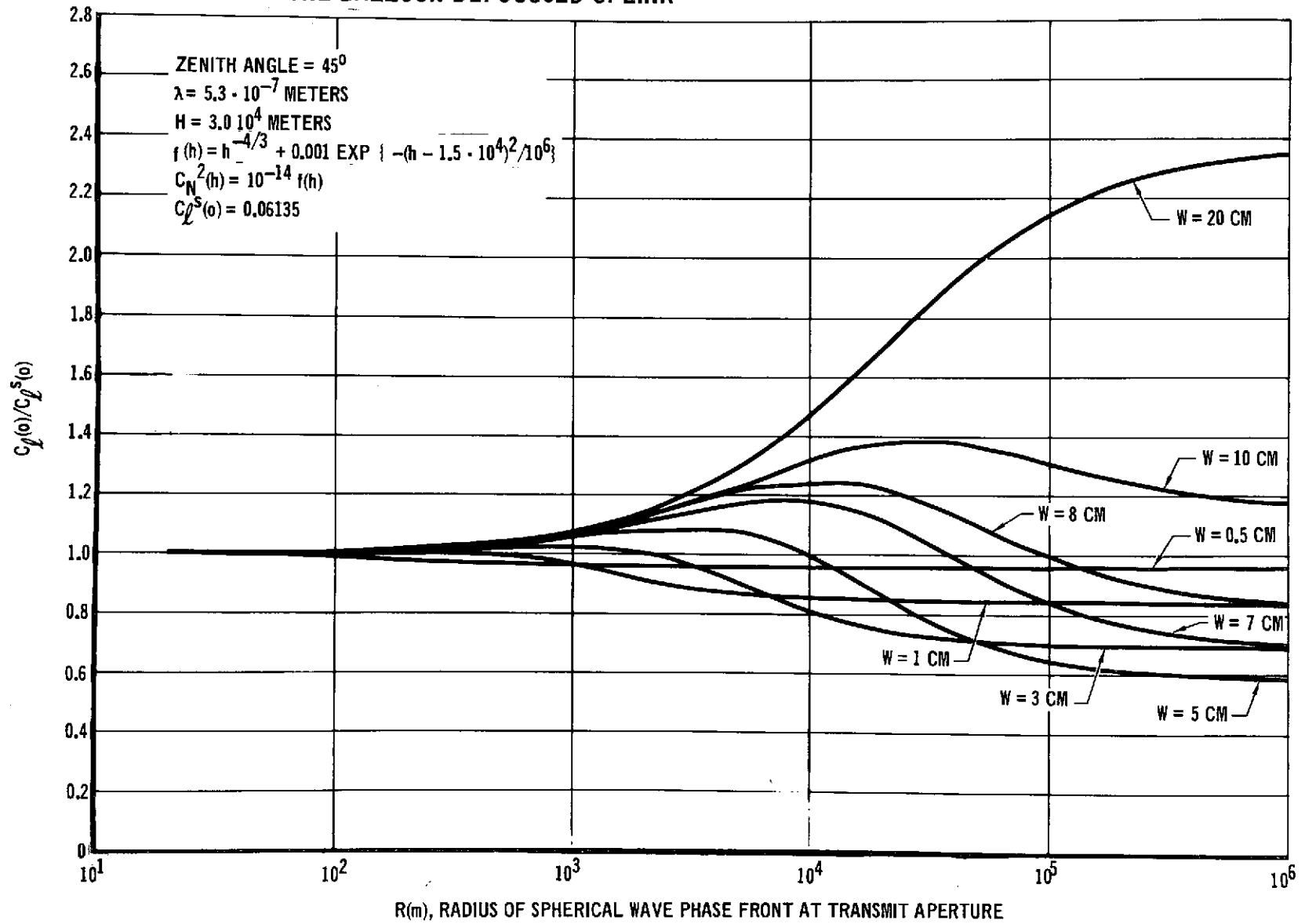
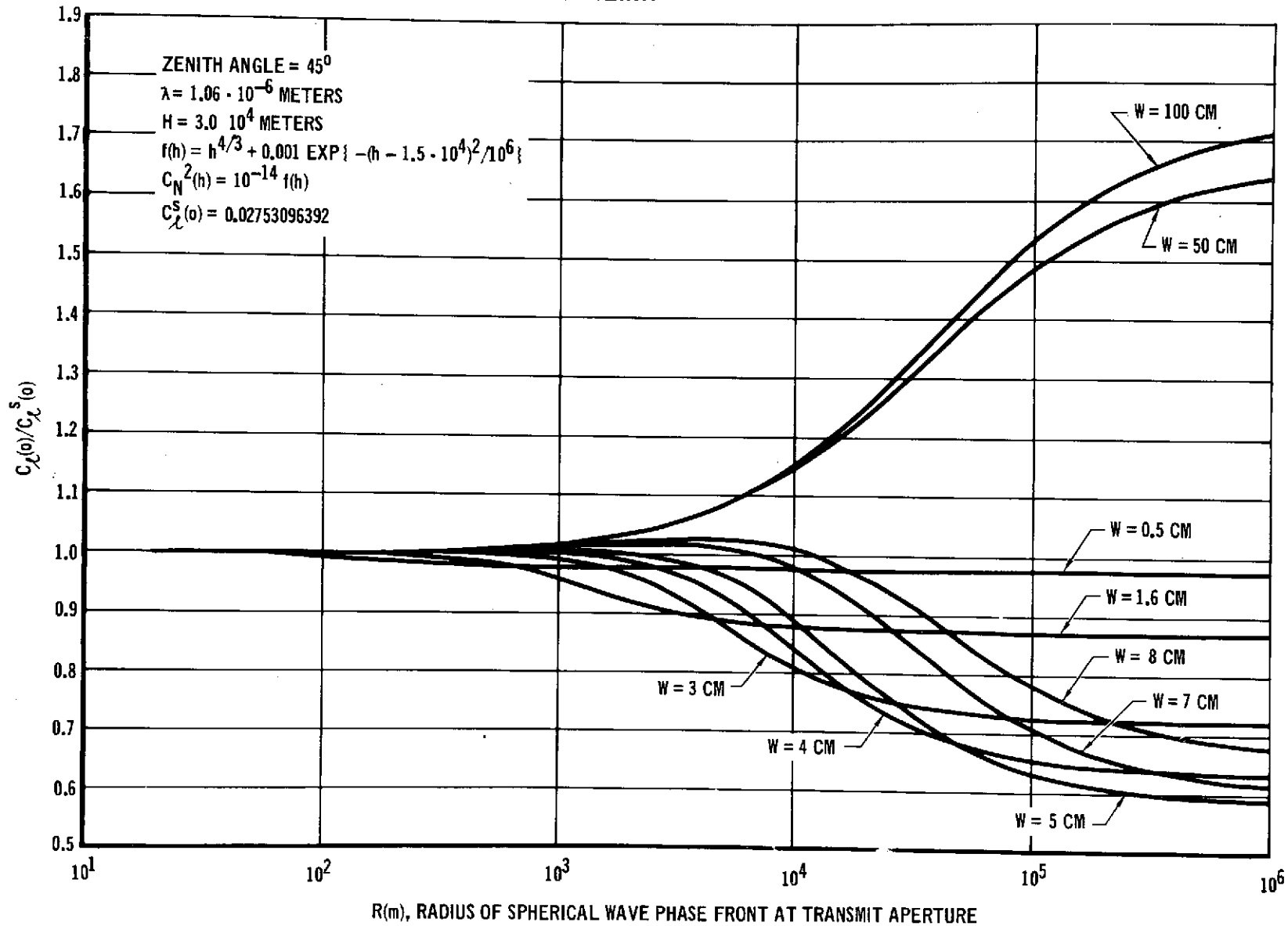


FIGURE E-4 $C_{\ell}^{\ell}(o)/C_{\ell}^S(o)$ VERSUS R WITH FEED BEAM RADIUS, W, AS A PARAMETER FOR BALLOON DEFOCUSSED DOWNLINK



$$H = 30 \text{ km}$$

$$\theta_z = 45^\circ$$

$$\text{implies } C_\ell(o) \approx C_\ell^S(o) = 0.0613$$

HDRT Balloon Downlink

$$\lambda = 1.06 \text{ } \mu\text{m}$$

$$\theta_{\text{BW}} = 500 \text{ } \mu\text{rad full angle beam width}$$

$$R = 406.4 \text{ m}$$

$$w = 5.08 \text{ cm}$$

$$H = 30 \text{ km}$$

$$\theta_z = 45^\circ$$

$$\text{implies } C_\ell(o) \approx C_\ell^S(o) = 0.0275$$

for the assumed turbulence profile and a point receiver. The turbulence profile assumed in this case:

$$C_n^2(h) = 10^{-13} \left[h^{-4/3} + 0.001 \exp \left\{ -(h - 1.5 \cdot 10^4)^2 / 10^6 \right\} \right]$$

was used to obtain these results. However, in order to predict the amount of scintillation expected for these links the available experimental evidence must be weighted.

To date the only experimental measures of $C_\ell(o)$ over vertical propagation paths for laser sources are those from the BAPE I balloon flights and data taken from the GEOS-II satellite by Minott³¹. Minott found

$$\begin{aligned} C_\ell(o) &\approx 0.02 \text{ sec}^{11/6} \theta_z & (E-16) \\ &\approx 0.04 @ \theta_z = 45^\circ \end{aligned}$$

for a 0.4880 μm laser beam propagating from earth to the GEOS-II satellite. This data shows a good agreement with stellar scintillation data measured by Bufton¹² and Protheroe. The mean log amplitude variance measured during the Balloon Atmospheric Propagation Experiment Flights of 1970 (BAPE I) at Holloman AFB, N.M. for a 0.5145 μm laser beam propagating from the ground was:³

$$C_{\ell}(o) = 0.17 = C_{\ell}^S(o) \quad (E-17)$$

Furthermore, the sampled values of $C_{\ell}(o)$ were shown to be approximately log normally distributed with mean

$$\overline{\ln C_{\ell}(o)} = -1.8 \quad (E-18)$$

and standard deviation

$$\sigma_{\ln} [C_{\ell}(o)] = 0.6$$

as illustrated by Figure E-5.

On the basis of this data we have concluded that the following are worst case estimates of the log amplitude variance expected on the uplinks:

Balloon Uplink

$$C_{\ell}(o) \approx 0.1$$

Synchronous Satellite Uplink

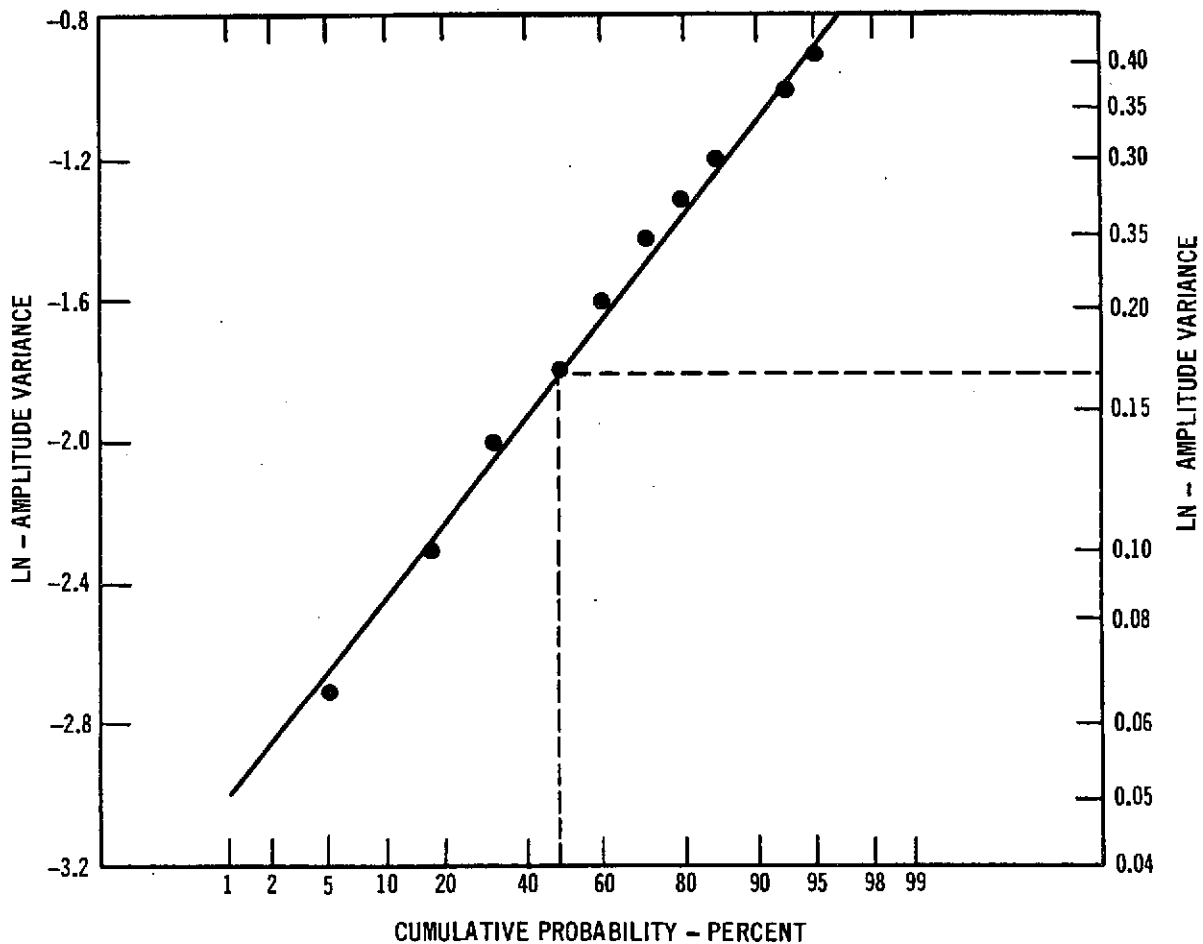
$$C_{\ell}(o) \approx 0.1$$

Note Figure 17 shows 6.8 dB of extra power is required to maintain an error rate of 10^{-6} for these values of $C_{\ell}(o)$ (i.e. for constant $C_{\ell}(o)$).

4. APERTURE AVERAGING EFFECTS

Because the ground receivers for both the HDRT balloon link and synchronous satellite link are respectively 0.75 meters and 1.52 meters, significant reduction of downlink scintillation will occur. The reduction in received intensity fluctuations with the use of a large collection aperture is commonly called aperture averaging. Although there is no generally accepted theory of this effect, there are some experimental results from the work of Mevers et al,⁸ Kerr,⁹ Bufton,¹¹ and Priebe³⁶ that can be used to estimate aperture averaging reduction of scintillation. For example, Bufton used his stellar image monitor and varied the aperture size from 5 cm to 15 cm. He found a significant decrease in the square of the detector output ripple with increasing aperture diameter, with dif-

FIGURE E-5 CUMULATIVE PROBABILITY OF LOG-AMPLITUDE VARIANCE FOR ARGON WAVELENGTH (0.5145 μ)



CUMULATIVE PROBABILITY* OF LOG-AMPLITUDE VARIANCE FOR ARGON WAVELENGTH (5145, A) FOR A 1½ HOUR PERIOD. 4:30 - 7:00 AM MST 21 OCTOBER 1970 AT HOLLOMAN AFB, NEW MEXICO. BAPE I EXPERIMENT.
 *DATA PLOTTED ON NORMAL PROBABILITY SCALE. STRAIGHT LINE INDICATES NORMAL DISTRIBUTION.

ferent formulas applying on different evenings. (If the tropopause has a key effect, these results should apply in daytime as well.)

Priebe used a 5 mile test range from valley floor to "mountain-top," with the path inclined at 6° to the horizontal. In varying the receiver aperture from 12.7 cm to 56 cm they also found a significant decrease in the signal fluctuations.

On the basis of this experimental data, we have computed ¹ the scintillation aperture averaging reduction factor shown in Figure E-6. There the ratio of the log amplitude variance for a receiver aperture diameter, D, to one for D = 0 (a point receiver) is plotted versus aperture diameter. Because of the expected aperture averaging shown in Figure E-6, the amount of scintillation for both downlinks should be negligible. We estimate the log amplitude variance for the balloon downlink will be at least reduced to

$$C_{\ell}(o) \approx 0.005$$

and for the reference synchronous satellite downlink to

$$C_{\ell}(o) \approx 0.001.$$

On the uplink, we have assumed the point source log-amplitude variance is applicable since the receiver diameter is comparable to the estimated spatial correlation length, $\rho \approx 11$ cm, and hence no aperture averaging is expected to occur.

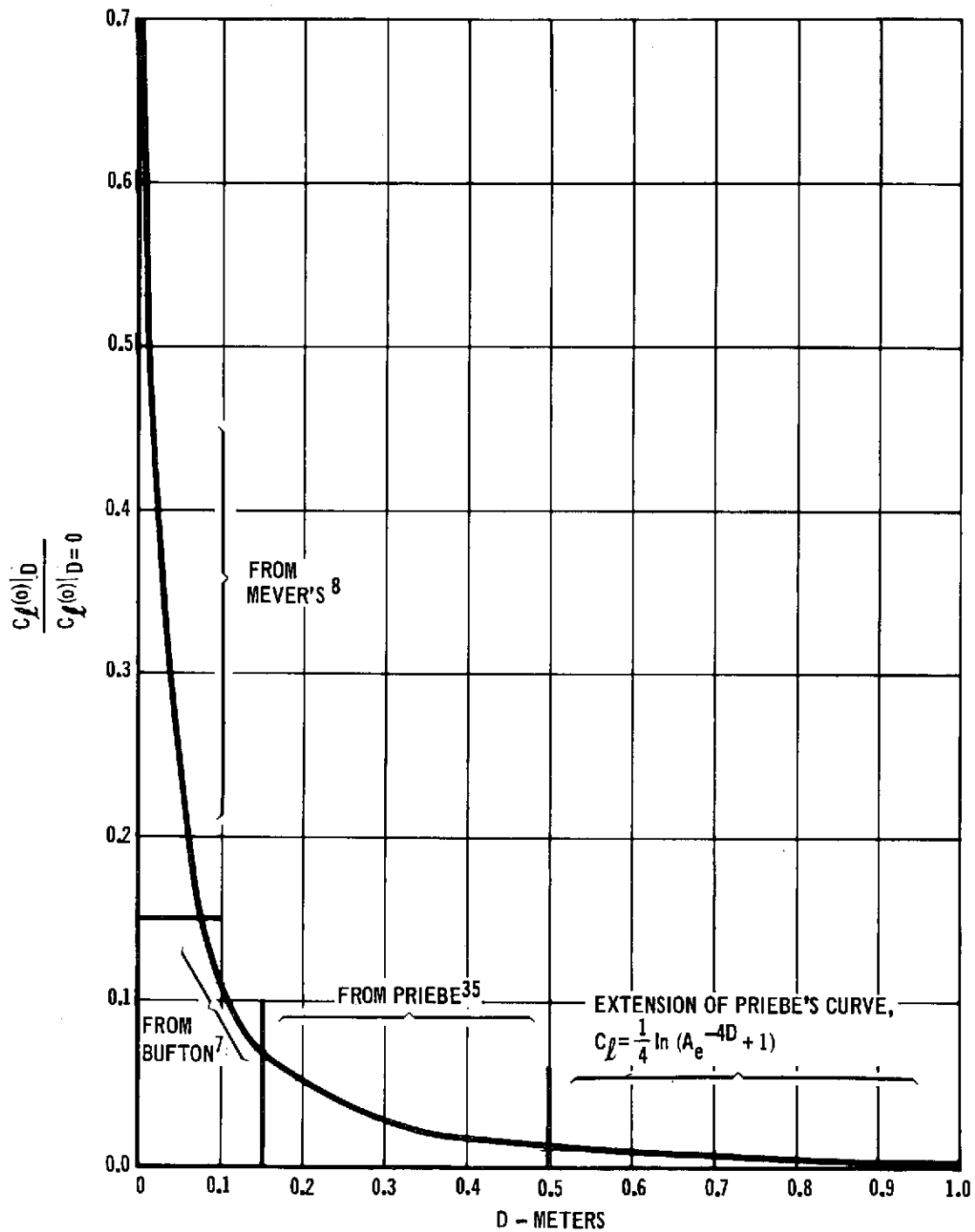
5. BEAM WANDER EFFECTS

Beam Wander or steering is the change in position of the two dimensional intensity distribution peak from its position in the absence of turbulence. This effect is attributed to refractive variations predominately in the larger scale (greater than or equal to the beam cross section) turbulence volumes. The effect of beam wander on the received optical power appears as both a reduction in average power and fluctuations in power as recorded by a fixed detector. For the moment, all power fluctuations caused by scintillation are ignored, and the intensity distribution across the wave front is assumed to be described by a Gaussian profile.¹

If the receiving aperture radius, r, is much less than the beam radius, R, at the e^{-2} point in power density at the receiver plane, Esposito's³⁷ results (also see Appendix F) can be modified to show the probability of received power, S, is:

$$p(S) = \begin{cases} \frac{1}{2 \alpha S_o} \left(\frac{S}{S_o} \right)^{1/2} \alpha^{-1} & , S_o > S > 0 \\ 0 & \text{otherwise} \end{cases} \quad (E-19)$$

FIGURE E-6 LOG AMPLITUDE VARIANCE APERTURE AVERAGING REDUCTION FACTOR VERSUS RECEIVER DIAMETER



where S_o = the mean received power recorded for an observer on the mean center (peak) of the beam in the absence of turbulence, and

$$\alpha = \overline{\rho_c^2} / R^2 \quad (\text{E-20})$$

for $\overline{\rho_c^2}$ the mean square beam displacement from the on-axis position. This particular model follows from the assumption

$$\rho_c = \sqrt{x^2 + y^2} \quad (\text{E-21})$$

where x and y are jointly independent, zero mean Gaussian random variables. The above expression also assumes no static pointing error or beam displacement from the on-axis position in the absence of turbulence. In addition, the mean received power observed on the mean center of the beam profile (assuming no pointing error) is

$$\langle S \rangle = E \{ S \} = \frac{S_o}{1 + 2\alpha} \quad (\text{E-22})$$

and the variance of the power fluctuations is

$$\sigma_s^2 = \frac{4\alpha^2}{4\alpha + 1} \quad (\text{E-23})$$

Hence, we observe α is the critical parameter required to characterize the effect of wander for this particular theoretical model.

There are several alternative expressions that can be used to estimate α . For example, it is easily shown that

$$\begin{aligned} \alpha &= 4 \left(\frac{\theta_{\text{rms}}}{\theta_{\text{BW}}} \right)^2 \\ &= 4 \overline{\rho_c^2} / R^2 \end{aligned} \quad (\text{E-24})$$

where θ_{BW} = the full angle beamwidth

θ_{rms} = the root mean square angular motion of the beam center.

Furthermore, in the Optical Propagation Test Study ³⁸, if beam spread is neglected, it was shown

$$\alpha = w^2 / \rho_o^2 \quad (E-25)$$

for $w^2 = e^{-2}$ optical power density radius at the transmit aperture for a collimated beam

ρ_o = lateral coherence length, i.e., e^{-1} point of the modulation transfer function (MTF) measured at the transmitter for a spherical wave propagating in the opposite direction (see Appendix G).

For a transmit beam with arbitrary beam properties (focused or defocused beam) Titterton ³⁸ has found that

$$\alpha = \frac{w^2}{\rho_o^2} \frac{4R^2 Z^2 + R^2 k^2 w^2}{4R^2 Z^2 + k^2 w^2 (R-Z)^2} \quad (E-26)$$

for Gaussian spherical wave beams

where Z = the distance to the receiver measured from the beam waist

$w = e^{-2}$ optical power density radius beam at the transmitter
(feed beam radius)

k = wave number, $2\pi/\lambda$

Random pointing errors can also be treated by modifying the definition of α .

$$\alpha = 4 \left(\frac{\beta_{rms}^2 + \theta_{rms}^2}{\theta_{BW}^2} \right) \quad (E-27)$$

where β_{rms} = the root mean square angular motion of the beam center caused by a dynamic pointing error

In Appendix G, ρ_o , is evaluated for a variety of turbulence profiles, $C_n^2(h)$, with the relationship

$$\rho_o = 5.04 \times 10^7 \left\{ K_o k^2 \sec \theta_z \int_0^H dh \left[1 - \frac{h}{H} \right]^{5/3} f(h) \right\}^{-3/5}, \quad (E-28)$$

$\lambda_o < 2\pi\rho_o < L_o$

for downlink propagation while for uplink propagation

$$\left[1 - \frac{h}{H} \right]^{5/3} \rightarrow \left(\frac{h}{H} \right)^{5/3}$$

For the transmit beam properties listed in Table E-1 the results of computations have led to the following estimates of the "wander parameter" α and lateral coherence length, ρ_o .

Balloon Uplink

$$\alpha = 0.02 \text{ for } \rho_o = 2.5 \text{ cm}$$

Balloon Downlink

$$\alpha \approx 0.001 \text{ for } \rho_o \approx 5 \text{ cm}$$

Synchronous Satellite Uplink

$$\alpha \approx 0.09 \text{ for } \rho_o \approx 5 \text{ cm}$$

Synchronous Satellite Downlink

$$\alpha \approx 0.001 \text{ for } \rho_o \approx 100 \text{ cm}$$

6. STATISTICS OF THE COMBINED EFFECT OF SCINTILLATION AND BEAM WANDER

Although the effect of scintillation and beam wander on received optical power are treated herein as independent effects, they actually occur simultaneously and are interrelated in a complex manner. For the simplified statistical models of scintillation and wander (see Appendix F), we have shown the probability, $p(S)$, of the instantaneous received optical power is given by

$$p(S) = f_S(S) = \frac{1}{4\alpha} \left(\frac{S}{S'}\right)^{\frac{1}{2\alpha} - 1} \exp(C_\ell(o)/\alpha)$$

$$\cdot \left\{ 1 - G \left(\frac{\ln(S/S')}{4C_\ell(o)} + \sqrt{\frac{2C_\ell(o)}{\alpha}} \right) \right\} \quad (E-29)$$

and the cumulative distribution by

$$F_S(S) = G \left(\frac{\ln(S/S')}{4C_\ell(o)} \right) + \left(\frac{S}{S'}\right)^{1/2\alpha} \exp \left(\frac{2C_\ell(o)}{\alpha} \right)$$

$$\cdot \left\{ 1 - G \left(\frac{\ln(S/S')}{2C_\ell(o)} + \frac{2\sqrt{C_\ell(o)}}{\alpha} \right) \right\} \quad (E-30)$$

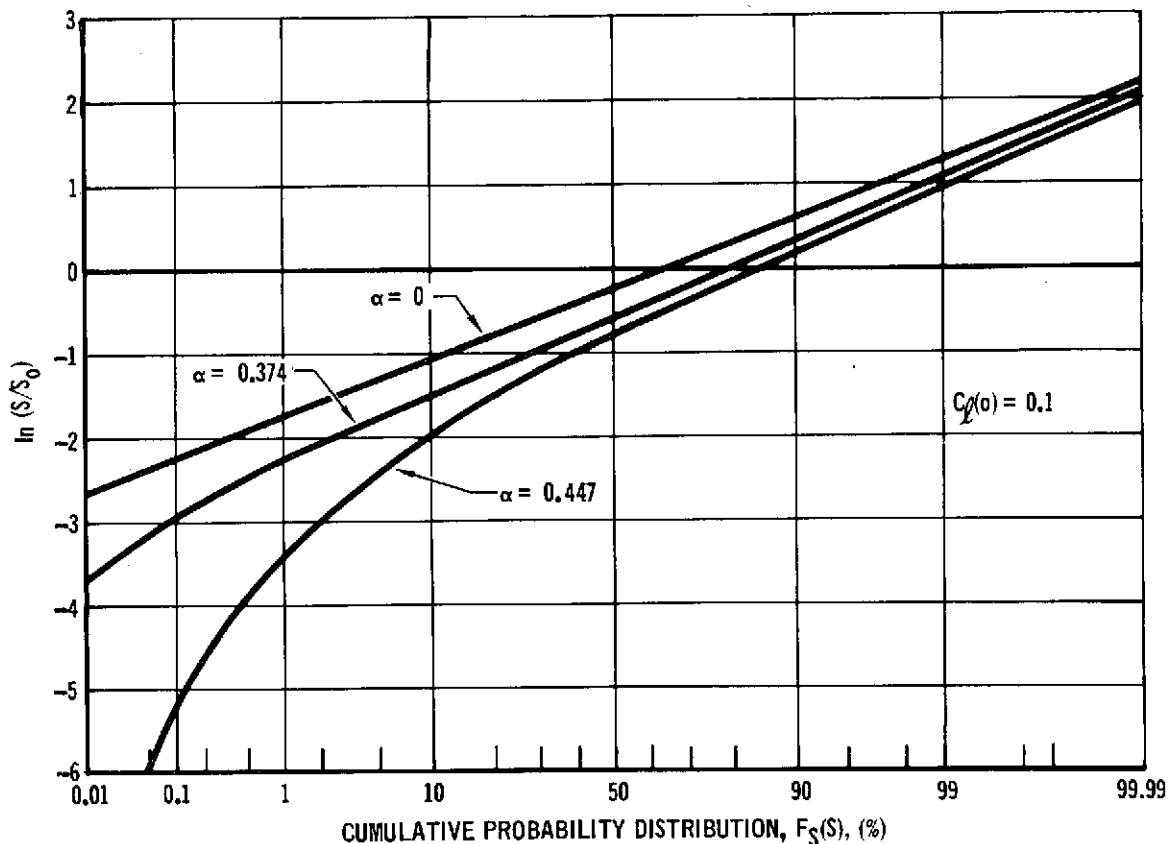
where $S' = S_o \exp(-2C_\ell(o))$ and

$G(x)$ = Normal cumulative distribution for zero mean and unit variance.

The cumulative distribution is plotted against the $\ln(S/S_o)$ in Figure E-7. There we observe, in the absence of wander, the plot is a straight line characteristic of the log normal distribution. As the beam wander increases ($\alpha > 0$) the plots curve toward the lower probabilities. This effect has been experimentally observed by several investigators and attributed to the lack of well developed turbulence along the propagation path. However, we observe here that beam wander caused by turbulence and beam pointing instabilities may also explain the observed data.

Link performance degradation due to atmospheric propagation and manifested by fluctuations in received optical power caused by scintillation and wander can be determined with this statistical distribution. The theoretical effect of scintillation and wander on bit error rate and link outage is presented in Section

FIGURE E-7 CUMULATIVE PROBABILITY DISTRIBUTION OF RECEIVED OPTICAL POWER CONSIDERING SCINTILLATION AND BEAM WANDER



7. REDUCTION IN MEAN RECEIVED POWER

The effect of beam spread and beam wander on the received optical power is to reduce the mean received power. Lutomirski and Yura³⁹ have⁴⁰ extended Huygens-Fresnel principle to a refractive medium so that conceptually one can calculate all moments of the received optical power or irradiance for arbitrary ranges, turbulence conditions, and initial beam shapes.

From this theoretical development Yura⁴¹ has recognized that the total angular beam width caused by the combined effects of beam wander and beam spread in the presence of turbulence is approximately

TABLE E-1
PARAMETERS FOR HIGH DATA RATE OPTICAL TRANSCEIVER BALLOON EXPERIMENT

I. Parameters Common to Both Up and Down Balloon Links

Balloon altitude = $H = 30$ km
 Maximum Zenith angle = $65^\circ - 70^\circ$
 Slant range @ $\theta_z = 65^\circ = 72$ km

II. Parameters of Ground to Balloon Link

Wavelength, $\lambda = 0.53 \mu$
 Full angle beam width = $\theta_{BW} = 500 \mu\text{rad}$
 Effective feed beam diameter = 10 cm
 Receiver diameter @ ground = 75 cm
 Radius of spherical wave phase front curvature at transmit aperture = $R = 521$ meters

III. Parameters of Balloon to Ground Link

Wavelength, $\lambda = 1.06 \mu$
 Full angle beam width = $\theta_{BW} = 500 \mu\text{rad}$
 Effective feed beam diameter = 10 cm
 Receiver diameter @ ground = 75 cm
 Radius of spherical wave phase front curvature at transmit aperture = $R = 406.4\text{m}$

Parameters for Reference System Satellite

Satellite altitude = $4.11 \cdot 10^7$ kilometers
 Range of zenith angles = $0^\circ - 90^\circ$

I. Parameters of Satellite to Ground Link Communications

Wavelength, $\lambda = 1.06 \mu$
 Full angle beam width = $\theta_{BW} = 8.3 \mu\text{rad}$
 Effective feed beam diameter = 0.179 meter
 Receiver diameter at ground = 1.52 meters
 Radius of spherical wave phase front curvature at transmit aperture = $R = 4.8 \cdot 10^4$ meters

TABLE E-1 (Cont'd)
PARAMETERS FOR HIGH DATA RATE OPTICAL TRANSCEIVER BALLOON EXPERIMENT

II. Parameters of Ground to Satellite Link (Beacon)

Wavelength, $\lambda = 0.53$

Full angle beam width = $\theta_{BW} = 400 \mu\text{rad}$

Effective feed beam diameter = 1.5 cm

Receiver diameter at satellite = 19.05 cm

Radius of spherical wave phase front curvature at transmit aperture = $R =$

$$\theta_{\text{turb}} \approx \frac{4 \lambda}{\pi \rho_o} \text{ for } \rho_o \lesssim D \quad (\text{E-31})$$

where θ_{turb} is the full angle beam width at the e^{-2} point of the optical power density in the receiver plane and $\rho_o =$ the lateral coherence length, (i.e., the lateral separation at which the spherical wave modulation transfer function, $\text{MTF}_{\text{sph}}(\rho_o) = e^{-1}$).

With the full angle beam width in the absence of turbulence, θ_{BW} , the reduction in mean received optical power in turbulence is easily shown to be

$$L_{\text{turb}} = \left(\frac{\theta_{BW}}{\theta_{BW} + \theta_{\text{turb}}} \right)^2 \approx \frac{1}{1 + (D/\rho_o)^2} \quad (\text{E-32})$$

for $D = e^{-2}$ point feed beam diameter for the Gaussian intensity profile at the transmit aperture.

From this relationship, we have estimated the typical on axis reduction in mean received optical power expected in turbulence for the transmit beam properties listed in Table E-1.

For these links:

Balloon Uplink

$$L_{\text{turb}} \approx -1.7 \text{ dB for } \rho_o \approx 2.5 \text{ cm}$$

Balloon Downlink

$$L_{\text{turb}} \approx -0.65 \text{ dB for } \rho_o \approx 25 \text{ cm}$$

Synchronous Satellite Uplink

$$L_{\text{turb}} \approx -1.0 \text{ dB for } \rho_o \approx 5 \text{ cm}$$

Synchronous Satellite Downlink

$$L_{\text{turb}} \approx 0.0 \text{ dB for } \rho_o \approx 100 \text{ cm}$$

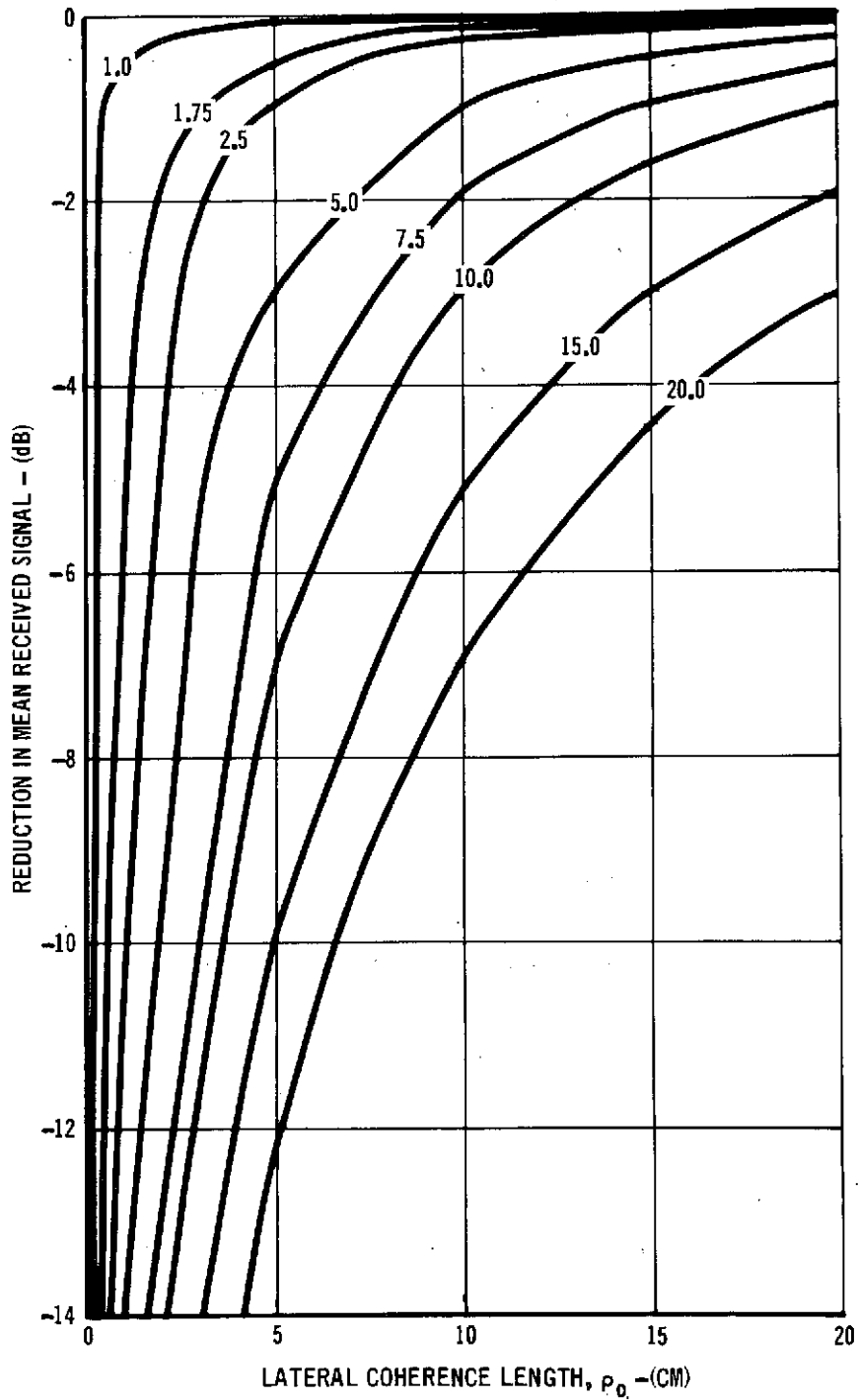
Note, as illustrated in Figure E-8, the reduction in mean power received, which can also be thought of as a reduction in optical antenna gain, can be severe (> -3 dB) for feed beam diameters $D \gtrsim \rho_o$. Hence, the estimate of ρ_o is critical to the determination of expected loss and will also serve to limit the design feed beam diameter. Unfortunately there is a lack of experimental measurements of ρ_o in the literature with which to compare with theory and appraise the above estimates.

8. ANGLE OF ARRIVAL FLUCTUATIONS

Turbulence induced changes in the incident wavefront shape or phase result in fluctuations in the received image centroid as observed with a stationary optical system. Two primary effects result: they include a blurring of the image due to focusing errors, etc., and wavefront tilt and phase shift which appear as image motion. The predominate effect here has been shown to be the effective wavefront tilt across the receiver aperture.⁴²

These phase front variations are caused by the random small phase delays introduced by volumes of air, along the propagation path of the light beam, whose size and refractive index vary. Furthermore, they are assumed to be normally distributed based on arguments using the central limit theorem.

FIGURE E-8: REDUCTION IN MEAN RECEIVED SIGNAL VERSUS LATERAL COHERENCE LENGTH, ρ_0 , WITH FEED BEAM DIAMETER (CM) AS A PARAMETER



Angle of arrival fluctuations refer to the random change in incident light beam, spatial averaged phase front with respect to the plane of the receiver aperture. Here the spatial averaging is over the collection aperture area. The angle of arrival fluctuations may be "tracked out," to a large degree, by automatically adjusting the axis of the receiver optics so that it is collinear with and normal to the spatial mean phase front across the receiving aperture. This may be accomplished with a reciprocity tracker as described in Section 2.4.2.

Theoretical estimates of the angle of arrival fluctuations were evaluated by Tatarski.⁴³ The variance of angle of arrival for a plane wave was shown to be

$$\sigma_{\phi}^2 = K_1 \lambda^{-2} d^{-1/3} \sec^2 \theta_z \int_0^H C_N^2(h) dh, \quad (E-33)$$

$$K_1 = \begin{cases} 18.3 & d > \sqrt{\lambda h} \\ 9.2 & d < \sqrt{\lambda h} \end{cases}$$

H = the distance between the transmitter and receiver

d = the effective receiver aperture diameter

θ_z = zenith angle, and

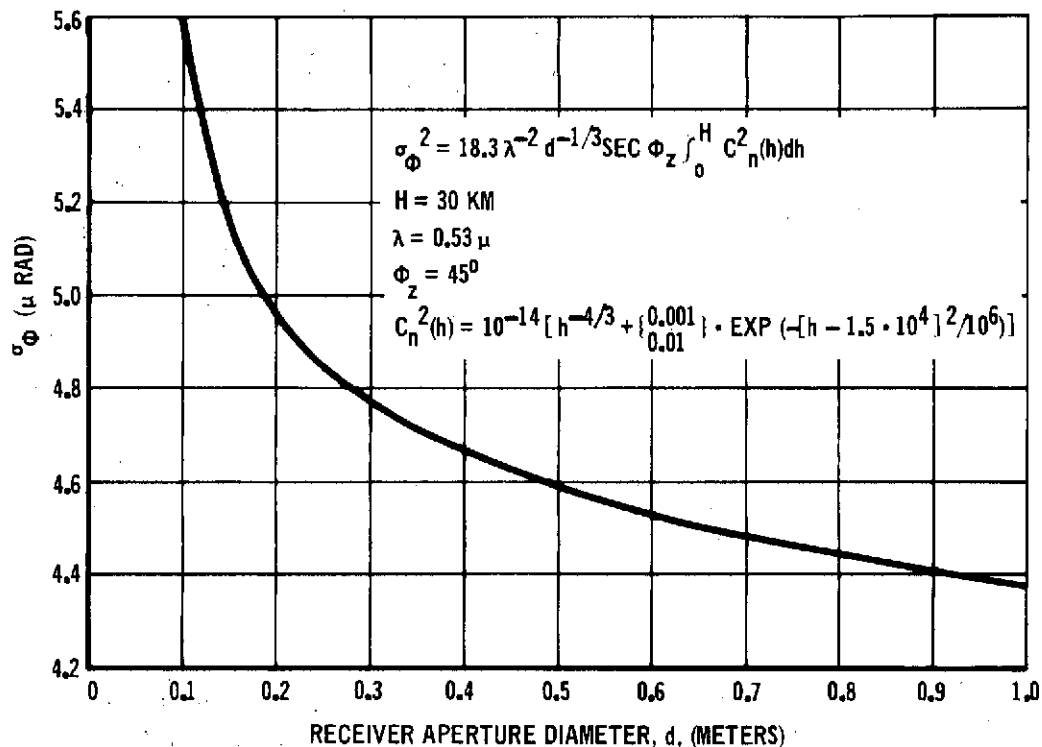
λ = wavelength.

This expression has been generally confirmed by numerous experiments on stellar sources and shows a decrease in fluctuations for larger apertures. The wavefront tilt in different areas of the aperture will be uncorrelated, thus resulting in a decreased angle of arrival variance for larger apertures. For example, Figure E-9 illustrates the theoretical reduction in σ_{ϕ} versus receiver diameter, d.

Daytime experiments have determined $\sigma_{\phi}^2 \leq (7 \mu\text{rad})^2$ measured angle of arrival variance for a d = 5 cm at the zenith.⁴⁴ If we assume daytime turbulence represents a worst case situation, we then expect angle of arrival fluctuations in the range of

$$\sigma_{\phi} = 5-10 \mu\text{rad}.$$

FIGURE E-9 ANGLE OF ARRIVAL STANDARD DEVIATION σ_{ϕ} ,
VERSUS OPTICAL RECEIVER DIAMETER



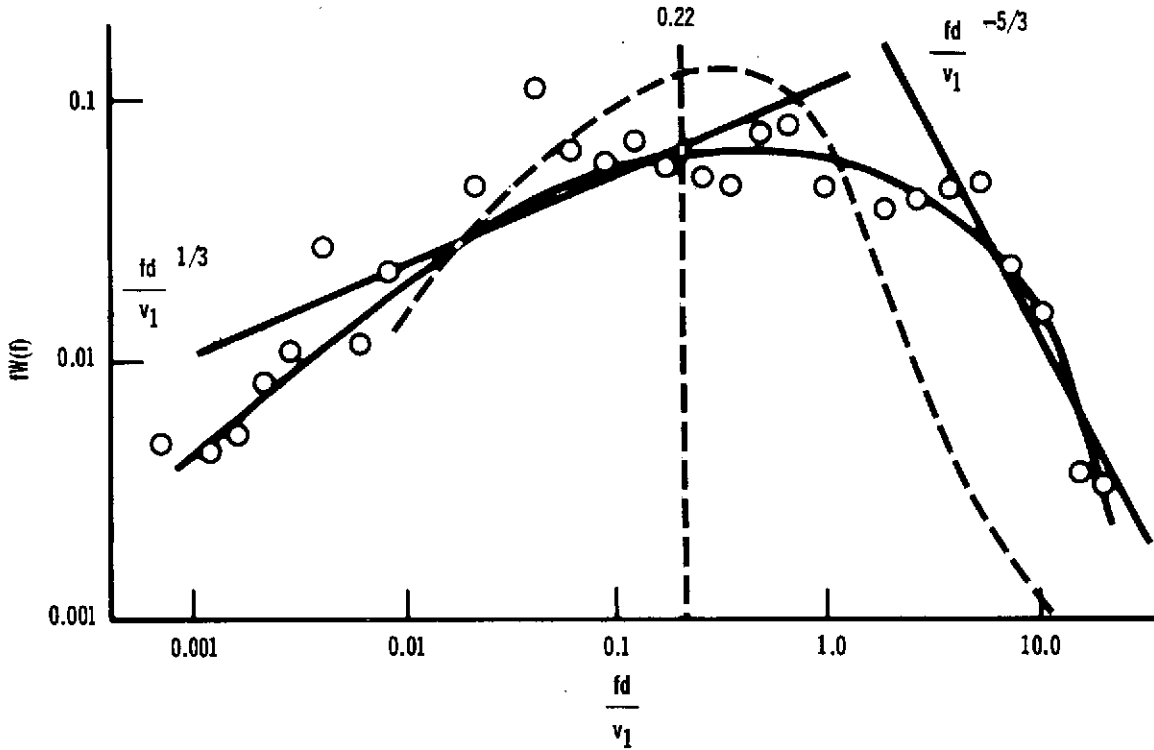
The frequency spectrum of the angle of arrival fluctuations has been well studied. Figure E-10 shows its behavior as a function of transverse wind speed, V_1 , and receiver diameter, d .⁴⁵

More recent experiments have checked this point in detail. As a reference point, for a 60 mph crosswind (in the high turbulence regime only) and a 1 foot diameter receiver, $f d/v_1 = 1$ at a frequency, $f = 88 \text{ Hz}$.^{46,47}

9. ATMOSPHERIC ATTENUATION

The received power in the atmosphere will be decreased by attenuation due to absorption and scattering by molecules and aerosols. Because it was necessary to establish adequate received power margins for these links, the estimates of attenuation based on empirical formula and atmospheric models were investigated.¹

FIGURE E-10 FREQUENCY SPECTRUM FOR THE FLUCTUATIONS OF THE LIGHT ARRIVAL ANGLE



NOTE:
 THE STRAIGHT LINES CORRESPOND TO THEORETICAL ASYMPTOTIC CURVES IN THE REGION OF LOW AND HIGH FREQUENCIES. THE VALUE $fd/v_1 = 0.22$ IS SHOWN VERTICALLY BY BROKEN LINE AND CORRESPONDS TO THE POSITION OF THE MAXIMUM VALUE OF THE THEORETICALLY COMPUTED FUNCTION $fW(f)$. THE BROKEN CURVE SHOWS THE EXPERIMENTAL SPECTRUM OF FLUCTUATIONS OF THE SOUND WAVE ARRIVAL ANGLE. (FROM TATARSKII, REFERENCE 43)

For the links of interest in this report, Rayleigh and Mie scattering are the predominant cause of attenuation. At $0.53\mu\text{m}$ and $1.06\mu\text{m}$ wavelengths molecular absorption can be neglected for these wavelengths. Hence, the total transmissibility will be

$$\tau = \tau_{RS} \cdot \tau_{MS} \quad (\text{E-34})$$

for

τ_{RS} = transmissibility due to Rayleigh scattering

τ_{MS} = transmissibility due to Mie scattering.

Rayleigh scattering is due to molecular sized particles and is inversely proportional to the λ^4 , i.e., shorter wavelengths are scattered more than longer ones. Mie scattering, however, is caused by particles comparable to wavelength such as smoke, fog, and haze.

The total transmissibility is also dependent on the total atmospheric propagation path length and the variation of mean air density along the atmospheric path. Propagation path length is specified by the altitude above sea level of the ground transceiver, the propagation path zenith angle, and transceiver altitude above the ground. For the postulated balloon and reference synchronous satellite link, both high altitude transceivers are above essentially all the scattering particles and only the transceiver altitude above sea level and zenith angle affect the transmissibility.

The typical transmissibility expected to be encountered is illustrated in Figures E-11 and E-12.

The curves for 60° zenith angle represent a worst case estimate since the transmissibility decreases with increasing zenith angle. The curves for clear atmosphere transmissibility represent a 23.5 km sea level visibility and those for light haze a 10 km visibility.⁴⁹

The mean ground elevation at the balloon launch site at Holloman AFB, New Mexico, is ~ 4000 feet. Hence, the estimated atmospheric transmissibility, τ , and optical power loss, L_{at} , will be

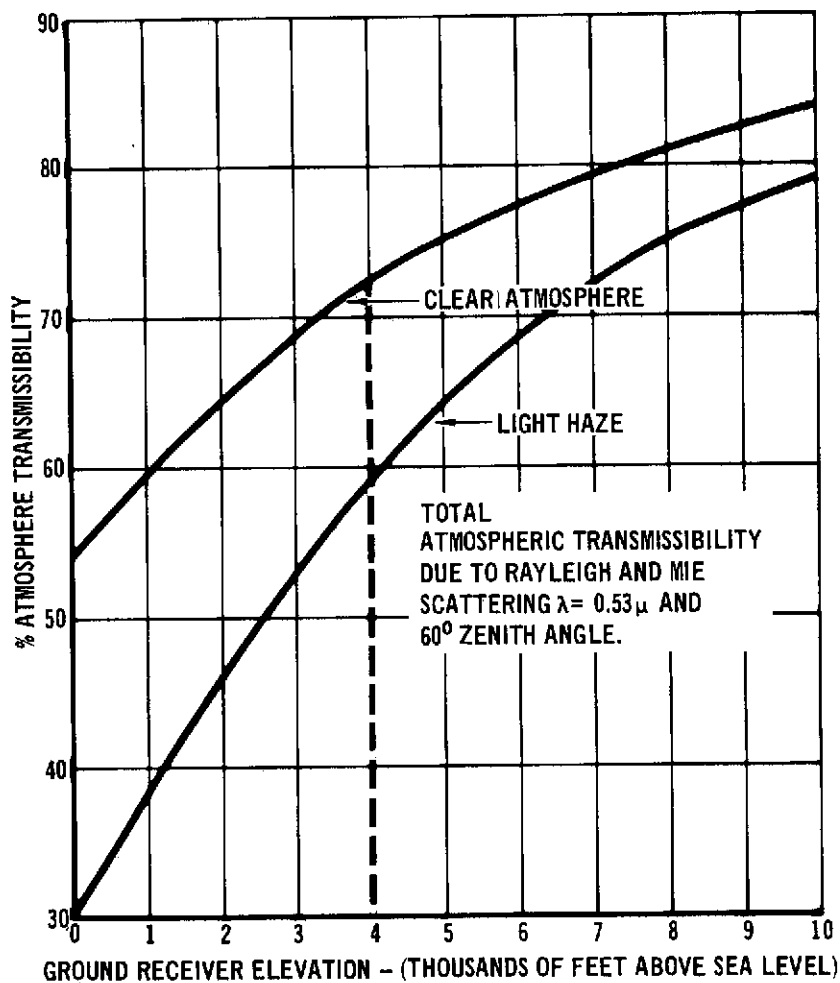
$$\tau = 0.722 \pm 5\%, \quad L_{at} = -1.42 \text{ dB @ } \lambda = 0.53\mu\text{m.}$$

and

$$\tau = 0.891 \pm 5\%, \quad L_{at} = -0.5 \text{ dB @ } \lambda = 1.06\mu\text{m}$$

for a clear atmosphere. These estimates are applicable to both the balloon link and reference synchronous satellite link. The estimates assume the balloon experiment will be performed under clear atmospheric conditions.

FIGURE E-11 TOTAL ATMOSPHERIC TRANSMISSIBILITY DUE TO RAYLEIGH AND MIE SCATTERING $\lambda = 0.53 \mu$ AND 60° ZENITH ANGLE

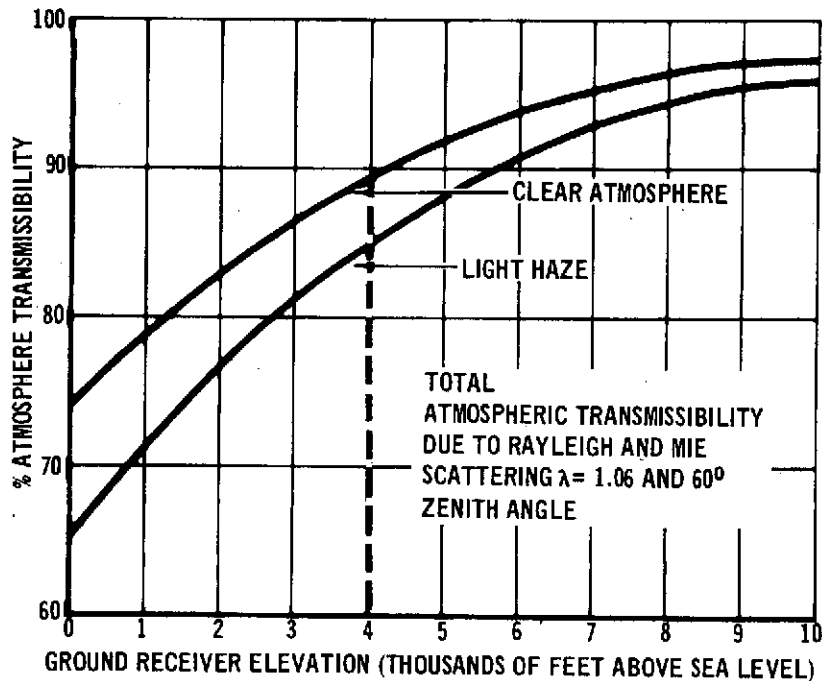


10.0 SUMMARY OF LINK ATMOSPHERIC PROPAGATION LOSSES

In this analysis, the atmospheric losses that cause communication link performance degradation are attributed to three causes:

- (1) The fluctuations in received optical power due to the combined effect of scintillation and beam wander.
- (2) The reduction in mean received power due to the combined effect of beam spread and beam wander.
- (3) The loss in mean received power due to atmospheric attenuation.

FIGURE E-12 TOTAL ATMOSPHERIC TRANSMISSIBILITY DUE TO RAYLEIGH AND MIE SCATTERING $\lambda = 1.06 \mu$ AND 60° ZENITH ANGLE



The last two effects listed are taken into account as a power loss in the link margin.

The received power fluctuations, however, decrease the average bit error rate. Hence, an increase in the average received power is required to maintain a selected bit error rate. The received power may be increased by increasing the laser transmitter power or reducing the beam width of the transmit beam.

Here, the extra power required to maintain an average bit error rate of $P_e = 10^{-6}$ is also treated as a power loss.

The atmospheric losses for the balloon link and reference synchronous satellite link are summarized in Table E-2. For example, losses associated with atmospheric attenuation and reduction in received power due to the combined effects of beam spread and wander are respectively

determined with Equations [E-34] and [E-35]. The power loss associated with the extra power required to maintain $P_e = 10^{-6}$ can be found from Figure . The theoretical explanation of how that graph was generated is given in Section .

**TABLE E-2
SUMMARY OF ATMOSPHERIC LOSSES ON
COMMUNICATION LINK PERFORMANCE**

Balloon Link				
	Scintillation and Beam Wander Losses	Beam Spread Losses	Atmospheric Attenuation Losses	Total Estimated Power Losses
Uplink	-7.1 dB	-1.7 dB	-1.41 dB	-10.2 dB
Downlink	-0.01 dB	-0.65 dB	-0.5 dB	-1.16 dB
Reference Satellite Link				
	Scintillation and Beam Wander Losses	Beam Spread Losses	Atmospheric Attenuation Losses	Total Estimated Power Losses
Uplink	-8.8 dB	-1.0 dB	-1.41 dB	-11.21 dB
Downlink	-0.0 dB	-0.0 dB	-0.5 dB	-0.5 dB

It is important to recognize that the losses presented in Table E-2 represent typical worst case estimates of link degradation caused by propagation through the clear atmosphere. There may be times when the losses will be greater than those stated.

APPENDIX F

PROBABILITY DISTRIBUTION OF RECEIVED POWER IN THE PRESENCE OF ATMOSPHERICALLY INDUCED SCINTILLATION AND BEAM WANDER

This appendix characterizes the joint effects of scintillation and beam wander by finding the probability density of received power in the presence of these effects. In a free space environment the received instantaneous power is determined by the beam characteristics and the receiver aperture. First we assume that the beam has a Gaussian intensity pattern and that the $1/e^2$ intensity radius in the beam normal plane containing the receiver is R . Let r be the radius of the receiver aperture, and let η be the distance from the center of the beam to the center of the receiver aperture.

It then follows that

$$S = S_T \left(1 - Q \left(2\eta/R, 2r/R \right) \right)$$

Where:

S is the received power

S_T is the total power in the beam at the receiving plane.

$Q(\alpha, \beta)$ is the Marcum Q - function:

$$\begin{aligned} Q(\alpha, \beta) &\triangleq \int_{\beta}^{\infty} t e^{-\left[\frac{t^2 + \alpha^2}{2} \right]} I_0(\alpha t) dt \\ &= \sum_{k=0}^{\infty} \left(\frac{\alpha}{\beta} \right)^k I_k(\alpha\beta) e^{-\left[\frac{\alpha^2 + \beta^2}{2} \right]} \end{aligned}$$

$I_k(\cdot)$ is the modified Bessel function of order k .

It can be shown that the following approximation holds asymptotically as β becomes small

$$1 - Q(\alpha, \beta) \approx \left[\beta^2 / 2 \right]^{\frac{1}{2}} e^{-\left[\frac{\alpha^2 + \beta^2}{2} \right]}$$

Hence, as the detector becomes small compared to the beam radius, (i.e. r/R becomes small) we can express the received power as

$$S \approx S_T \left(\frac{2r^2}{R^2} \right) e^{-2\eta^2/R^2} \triangleq S_o e^{-2\eta^2/R^2}$$

Now let

$$p \triangleq \ln(S) = \ln(S_o) - 2\eta^2/R^2 \triangleq p_o - 2\eta^2/R^2.$$

In the presence of atmospheric disturbances p and η are random variables. Scintillation causes fluctuations in the received power which are assumed to be log-normal. Therefore, we write

$$p = p_o - 2\eta^2/R^2 + \alpha',$$

where α' is a normal random variable with mean α_o and variance σ_a^2 . We can consider η to be the resultant of the beam displacement due to wander and tracking error on two orthogonal axes (x, y). We assume that x and y are independent, zero-mean, normal random variables with equal variances, σ_x^2 . Now let

$$v = 2\eta^2/R^2 = \frac{2}{R^2} (x^2 + y^2).$$

The probability density of p can be determined using the convolution integral to be

$$H(p) = G \left(\frac{p - p_o - \alpha_o}{\alpha_a} \right) + e^{\left\{ \frac{p - p_o - \alpha_o}{4\sigma_x^2/R^2} + \frac{2\sigma_a}{\left[4\sigma_x^2/R^2 \right]^2} \right\}} \cdot \left\{ 1 - G \left(\frac{p - p_o - \alpha_o}{\sigma_a} + \frac{2\sigma_a}{4\sigma_x^2/R^2} \right) \right\}$$

where:

$$G(x) = \frac{1}{\sqrt{2\pi}} \int_{-\infty}^x e^{-t^2/2} dt$$

Let us digress a moment to consider $E\{S\}$, where $S = e^P$, for the case where $\sigma_x \rightarrow 0$. For this case, it can be shown that

$$E\{S\} = \exp\{S_0 + \alpha_0 + \sigma_a^2/2\}.$$

Conservation of energy requires that $E\{S\}$ be invariant under scintillation, hence

$$\alpha_0 = -\sigma_a^2/2$$

The distribution function of e^P for $\sigma_x = 0$ is easily written

$$F(S) = H(e^P) = G\left(\frac{\ln(S/S')}{\sigma_a}\right) + \left(\frac{S}{S'}\right)^{\frac{R^2}{4\sigma_x^2}} e^{-\frac{\sigma_a^2 R^2}{2\sigma_x^2}} \left\{ 1 - G\left(\frac{\ln(S/S')}{\sigma_a} + \frac{R^2 \sigma_a}{2\sigma_x^2}\right) \right\}$$

where

$$S' = S_0 e^{\alpha_0} = S_0 e^{-\sigma_a^2/2}$$

The density of S can be found by differentiation to be:

$$f(S) = \frac{R^2}{8\sigma_x^2 P} \left(\frac{S}{S'}\right)^{\frac{R^2}{4\sigma_x^2} - 1} e^{-\sigma_a^2 R^2 / 8\sigma_x^2} \left\{ 1 - G\left(\frac{\ln(S/S')}{\sigma_a} + \frac{\sigma_a R}{2\sigma_x}\right) \right\}$$

The first moments are

$$E\{S\} = \frac{S_0}{1 + 4\sigma_x^2/R^2}$$

$$E\{S^2\} = \frac{S_0^2 e^{\sigma_a^2}}{1 + 8\sigma_x^2/R^2}$$

To relate the parameters used here to those used previously we consider several special cases. For scintillation only, i.e. $\sigma_x \rightarrow 0$, we have.

$$F(S) = G\left(\frac{\ln(S/S_0)}{\sigma_a}\right) = G\left[\frac{\frac{1}{2} \ln(S/S_0) + \sigma_a^2/4}{\sigma_a/2}\right]$$

If we let $\sigma_a^2 = 4 C_\ell(0)$, where $C_\ell(0)$ is the log amplitude variance as defined in¹, i.e.,

$$C_\ell(0) = \text{Var} \left[\frac{1}{2} \ln S/S_0 \right],$$

then

$$f(S) = G \left[\frac{\frac{1}{2} \ln (S/S_0) + C_\ell(0)}{\sqrt{C_\ell(0)}} \right],$$

which corresponds to a log-normal density.

For wander alone, i.e. $\sigma_a \rightarrow 0$, we have

$$F(S) = \left(\frac{S}{S_0} \right)^{R^2/4\sigma_x^2}$$

$$f(S) = \frac{R^2}{4\sigma_x^2 S_0} \left(\frac{S}{S_0} \right)^{(R^2/4\sigma_x^2) - 1}, \text{ for } 0 < S < S_0$$

$$\text{Let } \alpha = \frac{2\sigma_x^2}{R^2}$$

hence

$$f(S) = \begin{cases} \frac{1}{2\alpha S_0^{1/2\alpha}}, & 0 < S < S_0 \\ 0 & \text{elsewhere.} \end{cases}$$

Note that α is the beam wander parameter used in the body of this report. Writing $f(S)$ in terms of α and $C_\ell(0)$ yields:

$$f(S) = \frac{S^{\frac{1}{2\alpha} - 1}}{4\alpha \left(S_0 e^{-2C_\ell(0)} \right)^{1/2\alpha}} e^{(C_\ell(0)/\alpha)} \left(1 - G \left(\frac{\ln \left(\frac{S}{S_0} e^{-2C_\ell(0)} \right)}{\sqrt{C_\ell(0)}} + \sqrt{\frac{2C_\ell(0)}{\alpha}} \right) \right)$$

APPENDIX G

ATMOSPHERIC PROPAGATION EFFECTS: BEAM SPREAD, BEAM WANDER, THE MODULATION TRANSFER FUNCTION, AND LATERAL COHERENCE LENGTH

1. INTRODUCTION

We have reviewed and evaluated the effects of atmospheric propagation on the balloon and reference satellite link performance degradation in Appendix E. Here the relationships between assumed theoretical turbulence profiles and the parameters that characterize beam spread, beam wander, and lateral coherence length are established.

The best available theory for all atmospheric turbulence effects is that developed by Lutomirski and Yura.^{40,41} They modified the Huygens-Fresnel principle to yield the instantaneous irradiance at a point p:

$$I(p) = U(p) U^*(p) = \left(\frac{1 + \cos X_0}{2 \lambda S_0} \right)^2 \iint d^2 r_1 d^2 r_2 \exp \left[ik (S_1 - S_2) \right] \\ \times \exp \left[\psi(r_1) + \psi^*(r_2) \right] U(r_1) U^*(r_2) \quad (G-1)$$

where the integration is over the transmitter aperture;

$S_{1,2}$ is the distance from p to $r_{1,2}$

λ = wavelength = $2\pi/k$

S_0 = average distance from p to the transmitter

$\psi(r_1)$ = complex phase for a beam originating at p.

$U(r_1)$ = field at r_1 as transmitted

The turbulence effects/information are all contained in the complex phase term. Because the instantaneous distribution of turbulence is unknown, we can only predict average values of the irradiance, etc.

In principle one can calculate all the moments of the irradiance for arbitrary ranges, turbulence conditions and initial beam shapes. In practice, the calculations become quite difficult for the higher moments.

1.1 FIRST MOMENT: AVERAGE IRRADIANCE. Lutomirski and Yura showed that for a receiver in the far field of the transmitter, the mean irradiance is given by

$$\overline{I}(\rho) = \left(\frac{k}{2\pi Z}\right)^2 \int d^2\rho \ e^{-\frac{1}{2}D(\rho)} \ e^{-\frac{ik}{Z}(\vec{\rho}\cdot\vec{\rho})} \times \int d^2r \ U(r+\rho/2) \ U^*(r-\rho/2) \ e^{\frac{ik}{Z}(\rho\cdot r)} \quad (G-2)$$

for $Z =$ range, receiver to transmitter

$D(\rho) =$ wave structure function⁴³ for a spherical wave propagating from the receiver to the transformation equations

$$\vec{\rho} = \vec{r}_1 - \vec{r}_2$$

$$\vec{r} = \frac{1}{2}(\vec{r}_1 + \vec{r}_2).$$

If we assume³⁸

- (1) No transmitter truncation, so that the upper limit of the integration $\rightarrow \infty$
- (2) No center blockage, so that the lower limit of the integration $\rightarrow 0$
- (3) A collimated gaussian beam, so that

$$U(r_1) = A_0 e^{-r_1^2/a^2} \quad (G-3)$$

for $a = e^{-2}$ irradiance diameter at the transmitter

We find

$$\overline{I}(p) = \left(\frac{k}{2\pi Z}\right)^2 \frac{\pi a^2}{2} |A_0|^2 2\pi \int_0^\infty d\rho \rho e^{-\frac{1}{2} D(\rho)} e^{-\rho^2/2b^2} J_0\left(\frac{k\rho p}{Z}\right) \quad (G-4)$$

for

$$\frac{1}{2b^2} = \frac{1}{2a^2} + \frac{k^2 a^2}{2(4Z^2)} \quad (G-5)$$

Further assuming⁵⁰

$$(4) \quad e^{-\frac{1}{2} D(\rho)} \equiv \text{MTF} = e^{-(\rho/\rho_0)^{5/3}} \approx e^{-(\rho/\rho_0)^2} \quad (G-6)$$

and using the formula⁵¹

$$\int_0^\infty e^{-\gamma y} J_0(n\sqrt{y}) dy = \frac{1}{\gamma} e^{-n^2/4\gamma} \quad (G-7)$$

we find:

$$\overline{I}(p) = \frac{\pi^2 a^2 d^2}{2} \left(\frac{k}{2\pi Z}\right)^2 |A_0|^2 e^{-\frac{k^2 d^2 p^2}{4Z^2}} \quad (G-8)$$

for

$$\frac{1}{d^2} = \frac{1}{2b^2} + \frac{1}{\rho_0^2} \quad (G-9)$$

Therefore, with these approximations the average beam is broadened as determined by the factor ρ_0 . Note, however, that because this is an average, both beam spread and beam wander are included in this expression.

If instead of a collimated beam we consider the general case with a finite radius of wavefront curvature at the transmitter, then

$$U(r_1) = A_0 \exp - \left\{ \frac{r_1^2}{a^2} + \frac{ik r_1^2}{2R} \right\} \quad (G-10)$$

for R = radius of wavefront curvature (for this formulation $R > 0 \rightarrow$ focusing and $R < 0 \rightarrow$ defocusing).

We find

$$\overline{I}(p) = \frac{\pi^2 a^2 g^2}{2} \left(\frac{k}{2\pi Z} \right)^2 |A_0|^2 e^{-\frac{k^2 g^2 p^2}{4Z^2}} \quad (G-11)$$

for
$$\frac{1}{g^2} = \frac{1}{2f^2} + \frac{1}{\rho_0^2} \quad (G-12)$$

and
$$\frac{1}{2f^2} = \frac{1}{2a^2} + \frac{k^2 a^2}{2 \cdot 4} \left(\frac{1}{Z} - \frac{1}{R} \right)^2 \quad (G-13)$$

1.1.2 Estimate of Wander and Spread from the 1st Moment. Using (G-8) we can write the ratio of irradiance in the presence of turbulence to irradiance in the absence of turbulence as

$$\overline{I}(p) = \frac{1}{(1+2b^2/\rho_0^2)} \exp - \left[\left\{ \frac{\pi^2 p^2}{\lambda^2 Z^2} \right\} \left\{ \frac{1}{1+2b^2/\rho_0^2} \right\} \right] \quad (G-14)$$

and in the far field,
$$\frac{1}{b^2} \approx \frac{1}{a^2} \quad (G-15)$$

Defining
$$\alpha_1 = \frac{a^2}{\rho_0^2}, \text{ we find}$$

$$\overline{I}(0) = \frac{1}{1+2\alpha_1} \quad (G-16)$$

and Δe^{-2} radius $= [1 + 2\alpha_1]^{1/2} \equiv \Delta \overline{w} \quad (G-17)$

Using (G-11), (G-12) and (G-13) for the defocused case, we can write

$$\bar{I}(0) = \frac{1}{1+2\eta_1} \quad (G-18)$$

$$\Delta e^{-2} \text{ radius} = [1 + 2\eta_1]^{1/2} \equiv \Delta \bar{w} \quad (G-19)$$

for³⁸

$$\frac{\eta_1}{\alpha_1} = \frac{4 R^2 Z^2 + R^2 k^2 a^4}{4 R^2 Z^2 + k^2 a^4 (R-Z)^2} \quad (G-20)$$

Using⁵²

$$w^2 = w_0^2 \left[1 + \left(\frac{\lambda Z}{\pi w_0^2} \right)^2 \right] \quad (G-21)$$

$$R = Z \left[1 + \left(\frac{\pi w_0^2}{\lambda Z} \right)^2 \right] \quad (G-22)$$

for $w = e^{-2}$ irradiance radius (= a for defocused case)

R = radius of curvature of the wavefront

$w_0 = e^{-2}$ irradiance radius at the beam waist (= a for collimated case)

Z = distance measured from the waist.

we can find for the case

$$\lambda = 0.53 \mu$$

$$\theta = \text{full angle beam width} = 100 \mu\text{rad}$$

$$a = 1.75 \text{ cm}$$

that

$$\eta_1 = \frac{A^2}{\rho^2} \quad \text{where } A = 0.3475 \text{ cm.}$$

For

$$\lambda = 1.06 \text{ cm}$$

$$\theta = 500 \text{ } \mu\text{radians}$$

and $a = 10 \text{ cm}$,

$$\eta_1 = \frac{A^2}{\rho_o} \quad \text{where } A = 0.1446$$

For reasonable values of ρ_o ($\sim 5 \text{ cm}$) we use 18 and 19 to find for the first case,

$$\overline{I}(\circ) = 0.9628$$

while for the second case

$$\overline{I}(\circ) = 0.9983$$

Therefore, for these two cases, the reduction in average irradiance and/or the increase in e^{-2} radius is negligible.

The analysis can be extended to other parameters in a straightforward manner. Clearly the key in making real estimates is a realistic value of the lateral coherence length, ρ_o . We calculate some values of ρ_o in the next section.

- 1.2 THE LATERAL COHERENCE LENGTH, ρ_o , AND THE MODULATION TRANSFER FUNCTION (MTF). The lateral coherence length, ρ_o , is important for two reasons:
- (1) It characterizes some of the transfer properties of the atmosphere
 - (2) As shown above, it seems to be the key parameter in estimating average irradiance and beam size.

Many different analytic techniques^{39,50,53} have found that the MTF of the atmosphere is given by

$$\text{MTF} = e^{-1/2 D(a,Z)} \quad (\text{G-23})$$

for $D(a,Z)$ the wave structure function,

$a =$ transverse dimension in the beam.

The general expression for the wave structure function from a point source is³⁹:

$$D(a, Z) = \frac{k^2}{2\pi} \int_0^Z dS \int_0^\infty d\sigma \Phi(\sigma^{1/2}; S) \left\{ 1 - J_0 \left(\sigma^{1/2} \frac{aS}{Z} \right) \right\} \quad (G-24)$$

for the propagation path from $S = 0$ to $S = Z$.

k = wave # ($2\pi/\lambda$)

J_0 = Bessel Function of zero-order.

The Kolmogorov spectrum of turbulence fluctuations implies⁴³

$$\Phi(\sigma^{1/2}, S) = 8.16 C_N^2(S) \sigma^{-11/3} \quad (G-25)$$

and the expression for a point source or spherical wave becomes

$$D^{SW}(a) = 2.91 k^2 a^{5/3} \int_0^Z dS C_N^2(S) (S/Z)^{5/3} \quad (G-26)$$

while for a plane wave source

$$D^{PW}(a) = 2.91 k^2 a^{5/3} \int_0^Z dS C_N^2(S) \quad (G-27)$$

for $C_N^2(S)$ = index of refraction structure parameter at S .

Taking the e^{-1} point of the MTF as the definition of ρ_0 , we find for downlink transmission

$$\rho_0^{SW} = 5.04 (10^7) \left[\frac{K_0 k^2}{\cos\theta} \int_0^H dh \left(1 - \frac{h}{H} \right)^{5/3} f(h) \right]^{-3/5} \quad (G-28)$$

$$\rho_0^{PW} = 5.04 (10^7) \left[\frac{K_0 k^2}{\cos\theta} \int_0^H dh f(h) \right]^{-3/5} \quad (G-29)$$

where we have used

$$C_N^2(h) = 10^{-13} K_o f(h) \quad (G-30)$$

θ = zenith angle so that $Z = H/\cos$ and $S = h/\cos$, and we are treating the case(s) of a point source (plane-wave source) at the altitude H .

For the transmitter at satellite altitudes, $H \gg$ all altitudes at which $f(h)$ is > 0 , and

$$\rho_o^{SW} = \rho_o^{PW} \quad (G-31)$$

For balloon altitudes, this is not the case.

For uplink transmission,

$$\rho_o^{SW} = 5.04 \times 10^7 \left[\frac{K_o k^2}{\cos\theta} \int_0^H dh \left(\frac{h}{H}\right)^{5/3} f(h) \right]^{-3/5} \quad (G-32)$$

$$\text{since } D(a,H) = \frac{2.91k^2 a^{5/3}}{\cos\theta} \int_0^H dh C_N^2(h) \left(\frac{h}{H}\right)^{5/3} \quad (G-33)$$

We will now use these equations to calculate ρ_o for various turbulence profiles.

1.2.1 Evaluation for Representative Turbulence Profiles. We have evaluated 28, 29, and 32 for the following turbulence profiles:

$$C_N^2(h) = k_o 10^{-13} f(h) (\text{meters})^{-2/3}$$

where $k_o = 0.4$ and

$$(a) \quad f(h) = h^{-1/3} \exp(-h/h_o) + D_o \exp\left\{-\left[h - h_p\right]^2 / (\sigma_o \cdot 10^3)^2\right\}$$

$$(b) \quad f(h) = h^{-4/3} + D_o \exp\left\{-\left[h - h_p\right]^2 / (\sigma_o \cdot 10^3)^2\right\}$$

where the above constants are given by

$$h_o = \begin{Bmatrix} 3200 \\ 1000 \\ 150 \end{Bmatrix} \text{ meters; } D_o = \begin{Bmatrix} 0.0 \\ 0.001 \\ 0.0024 \\ 0.005 \end{Bmatrix} ;$$

$$h_p = \begin{Bmatrix} 19 \cdot 10^3 \\ 15 \cdot 10^3 \\ 12 \cdot 10^3 \\ 10 \cdot 10^3 \end{Bmatrix} \text{ meters}$$

$$\text{and } \sigma_o = \begin{Bmatrix} 1.0 \\ 10.0 \\ 0.10 \end{Bmatrix}$$

1.2.1.1 Plane wave downlink (applicable to satellite and star sources). Equation (G-29) lends itself to analytic integration for the turbulence profiles above, and we give the results in Table G-1. Extension to other wavelengths and zenith angles is straightforward.

These results indicate how an uplink beam to a satellite receiver will be affected on the average, since ρ_o indicates the behavior of the beam in the opposite direction.

We see from the table just how crucial the near earth behavior of $f(h)$ is, and that $\rho_o \approx 5$ cm implies that $h^{-4/3}$ is the more reasonable choice. There are other more fundamental reasons to choose this form, too.³⁸

1.2.1.2 Point source uplink. Some of the profiles lend themselves to analytic integration, and some have necessitated the use of the GTE Sylvania computer program, which samples $f(h)$ every 50 meters. Representative results are shown in Table G-2.

TABLE G-1
COMPUTED LATERAL COHERENCE LENGTH, ρ_0 , FOR A PLANE WAVE
PROPAGATION DOWN LINK

$$C_n^2(h) = 4.2 \cdot 10^{-14} f(h) \quad \text{for}$$

$$\lambda = 0.53\mu, \quad \theta_z = 45^\circ$$

$$f(h) = h^{-\frac{4}{3}} + D_0 \exp \left[-(h-h_p)^2 / (\sigma \cdot 10^3) \right]^2$$

D_0	h_p	σ	ρ_0 (cm.)
0	-	-	11.56
0.001	19	.1	11.16
		1	8.75
		10	3.66
		.1	11.16
		1	8.75
		10	3.66
	12	.1	11.16
		1	8.75
		10	3.71
		10	11.16
		1	8.75
		10	3.78
.0024	19	.1	10.7
		1	6.81
		10	2.28
		.1	10.7
		1	6.81
		10	2.28
	12	.1	10.7
		1	6.81
		10	2.32

TABLE G-1 (Cont'd)
COMPUTED LATERAL COHERENCE LENGTH, ρ_o , FOR A PLANE WAVE
PROPAGATION DOWN LINK

$$C_n^2(h) = 4.2 \cdot 10^{-14} f(h) \quad \text{for}$$

$$\lambda = 0.53\mu, \theta_z = 45^\circ$$

$$f(h) = h^{-\frac{4}{3}} + D_o \exp \left[-(h-h_p)^2 / (\sigma \cdot 10^3) \right]^2$$

D_o	h_p	σ	ρ_o (cm.)
.0024	10	.1	10.7
		1	6.81
		10	2.37
.005	19	.1	9.9
		1	5.07
		10	1.50
	15	.1	9.9
		1	5.07
		10	1.50
	12	.1	9.9
		1	5.07
		10	1.53
10	10	.1	9.9
		1	5.07
		10	1.56

TABLE G-1 (Cont'd)
COMPUTED LATERAL COHERENCE LENGTH, ρ_o , FOR A PLANE WAVE
PROPAGATING DOWN LINK

$$C_n^2(h) = 4.2 \cdot 10^{-14} f(h) \quad \text{for}$$

$$\lambda = 0.53\mu, \theta_z = 45^\circ$$

$$f(h) = h^{-\frac{1}{3}} \exp(-h/h_o) + D_o \exp(-(h-h_p)^2 / (\sigma \cdot 10^3)^2)$$

h_o	D_o	h_p	σ	ρ_o (cm.)
3.2 km	0	-	-	0.74
1 km	0	-	-	1.17
150 m	0	-	-	2.51
3.2	0.001	19 km	.1	0.74
		"	1	0.735
		"	10	0.712
		15 km	.1	0.74
		"	1	0.735
		"	10	0.713
		12 km	.1	0.74
		"	1	0.735
		"	10	0.714
		10 km	.1	0.74
		"	1	0.735
		"	10	0.714
	.0024	19 km	.1	0.74
		"	1	0.73
		"	10	0.681
		15 km	.1	0.74
		"	1	0.73
		"	10	0.681
		12 km	.1	0.74
		"	1	0.73
		"	10	0.683

TABLE G-1 (Cont'd)
 COMPUTED LATERAL COHERENCE LENGTH, ρ_o , FOR A PLANE WAVE
 PROPAGATING DOWN LINK

$$C_n^2(h) = 4.2 \cdot 10^{-14} f(h) \quad \text{for}$$

$$\lambda = 0.53 \mu, \quad \theta_z = 45^\circ$$

$$f(h) = h^{-\frac{1}{3}} \exp(-h/h_o) + D_o \exp(-(h-h_p)^2 / (\sigma \cdot 10^3))^2$$

h_o	D_o	h_p	σ	ρ_o (cm.)
150 m	.0024	12	.1	2.49
		"	1	2.36
		"	10	1.63
150 m	.0024	10	.1	2.49
		"	1	2.36
		"	10	1.64
	.005	19	.1	2.48
			1	2.21
			10	1.22
		15	.1	2.48
			1	2.21
			10	1.23
		12	.1	2.48
			1	2.21
			10	1.25
	"	.1	1	2.48
			1	2.21
			10	1.26

TABLE G-1 (Cont'd)
 COMPUTED LATERAL COHERENCE LENGTH, ρ_o , FOR A PLANE WAVE
 PROPAGATION DOWN LINK

$$C_n^2(h) = 4.2 \cdot 10^{-14} f(h) \quad \text{for}$$

$$\lambda = 0.53\mu, \theta_z = 45^\circ$$

$$f(h) = h^{-\frac{1}{3}} \exp(-h/h_o) + D_o \exp(-(h-h_p)^2 / (\sigma \cdot 10^3))^2$$

h_o	D_o	h_p	σ	ρ_o (cm.)
1 km	.001	10	.1	1.17
		"	1	1.17
		"	10	1.1
1 km	0.0024	19 km	.1	1.17
		"	1	1.17
		"	10	1.0
		15	.1	1.17
		"	1	1.17
		"	10	1.0
		12	.1	1.17
		"	1	1.17
		"	10	1.0
		"	10	.1
"	1	1.17		
"	10	1.01		
1 km	.005	19 km	.1	1.17
1 km	.005	19 km	1	1.12
		"	10	0.87
		15 km	.1	1.17
		"	1	1.12
"	10	0.873		

TABLE G-1 (Cont'd)
 COMPUTED LATERAL COHERENCE LENGTH, ρ_o , FOR A PLANE WAVE
 PROPAGATION DOWN LINK

$$C_n^2(h) = 4.2 \cdot 10^{-14} f(h) \quad \text{for}$$

$$\lambda = 0.53\mu, \theta_z = 45^\circ$$

$$f(h) = h^{-\frac{1}{3}} \exp(-h/h_o) + D_o \exp(-(h-h_p)^2 / (\sigma \cdot 10^3)^2)$$

h_o	D_o	h_p	σ	ρ_o (cm.)
1 km	.005	12	.1	1.17
		"	1	1.12
		"	10	0.878
		10	.1	1.17
		"	1	1.12
		"	10	0.885
150 m	.001	19 km	.1	2.5
		"	1	2.44
		"	10	1.999
		15	.1	2.5
		"	1	2.44
		"	10	2.0
		12	.1	2.5
		"	1	2.44
		"	10	2.01
	.0024	19	.1	2.49
		"	1	2.36
		"	10	1.60
		15	.1	2.49
		"	1	2.36
		"	10	1.61

TABLE G-1 (Cont'd)
 COMPUTED LATERAL COHERENCE LENGTH, ρ_0 , FOR A PLANE WAVE
 PROPAGATION DOWN LINK

$$C_n^2(h) = 4.2 \cdot 10^{-14} f(h) \quad \text{for}$$

$$\lambda = 0.53 \mu, \quad \theta_z = 45^\circ$$

$$f(h) = h^{-\frac{1}{3}} \exp(-h/h_0) + D_0 \exp(-(h-h_p)^2 / (\sigma \cdot 10^3))^2$$

h_0	D_0	h_p	σ	ρ_0 (cm.)
3.2	.0024	10 km	.1	0.74
		"	1	0.73
		"	10	0.685
3.2	.005	19 km	.1	0.74
		"	1	0.725
		"	10	0.63
		15 km	.1	0.74
		"	1	0.725
3.2	.005	15 km	10	0.632
		12 km	.1	0.74
		"	1	0.725
		"	10	0.634
		10 km	.1	0.74
		"	1	0.725
		"	10	0.637
1 km	0.001	19 km	.1	1.17
		"	1	1.17
		"	10	1.09
		15	.1	1.17
		15	1	1.17
		"	10	1.09
		12	.1	1.17
		"	1	1.17
		"	10	1.09

**TABLE G-2
POINT SOURCE UPLINK**

$\lambda = 1.06, \theta = 45^\circ$

$f(h)$	ρ_o (cm)	
$h^{-1/3} e^{-h/h_o}$	17	} H = 30 km
$h_o = 3200m$	87.5	
1000m	1,246	
150m		
$h^{-4/3}$	478.6	} H = 30 km
$h^{-4/3} + 0.001 \exp - \left\{ \left(\frac{h - 1.5 \times 10^4}{10^3} \right)^2 \right\}$	71.37	} H = 30 km
" + 0.0024 "	42.83	
" + 0.005 "	27.73	
$h^{-1/3} e^{-h/1000} + 0.001$ "	52.6	
+ 0.0024 "	36.9	
+ 0.005 "	25.7	

All these results apply to balloon altitudes. For satellite altitudes the values of ρ_o are far larger. For example, for $f(h) = h^{-4/3}$,

$$\rho_o = 60.9 H^{1/5} \text{ cm}$$

G-34

These results are easily extended to other wavelengths and zenith angles, and indicate how the downlink beam from a balloon (or satellite) will be affected on the average. Since $\rho_o \gg 5$ cm, even the values estimated in Section 1.1.2 are conservative, i.e., the downlink beam spread and wander will be quite negligible.

1.2.1.3 Point source downlink. A large number of calculations for this case were done in reference ³⁸. We can use the results of Table G-1, based on these earlier calculations, by noting for

$$f(h) = h^{-4/3} + 0.001 e^{-\left(\frac{h - 1.5 \times 10^4}{10^3}\right)^2}, \quad \frac{\rho_o^{SW}}{\rho_o^{PW}} = 1.4$$

$$f(h) = h^{-1/3} e^{-h/1000}, \quad \frac{\rho_o^{SW}}{\rho_o^{PW}} = 1.023$$

and $f(h) = h^{-4/3}, \quad \frac{\rho_o^{SW}}{\rho_o^{PW}} = 1.035$

Clearly, the tropopause causes all the significant difference between the ρ_o^{PW} and ρ_o^{SW} results.

From Table , we selected the following "worst case" profiles for numerical integration, and obtained the following results:

Table G-3

H = 30 km

Point Source Downlink

$\lambda = 0.53\mu, \quad \theta = 45^\circ$

f(h)	ρ_o (cm)
$h^{-1/3} e^{-h/1000} + 0.005 \exp\left\{-\left(\frac{h - 10^4}{10^3}\right)^2\right\}$	1.22 cm
$h^{-4/3} e^{-h/1000} + 0.005 \exp\left\{-\left(\frac{h - 10^4}{10^3}\right)^2\right\}$	8.15 cm

This last profile is a new one, chosen to demonstrate the sensitivity of the results to the exponent of h in the near ground region.

These results are useful in calculating the average properties of the beam to be measured at the balloon receiver, and can easily be extended to other wavelengths and zenith angles.

1.3 INTERPRETATION OF THE THEORY. With our earlier assumptions, the normalized average irradiance on axis is given by:

$$\overline{I}(0) = \frac{1}{1+2\alpha_1} \quad \text{for} \quad \alpha_1 = \frac{a^2}{\rho_0^2} \quad (\text{G-34})$$

We extended this analysis in reference ³⁸ and found

$$\overline{\sigma_I^2} \approx \frac{4\alpha_1^2}{4\alpha_1+1} \quad \text{for large transmitters.} \quad (\text{G-35})$$

Finally, we used the Feizulin-Kravtsov work to show that the mean square displacement of the center of energy is given by:

$$\overline{\rho^2} = \left(\frac{\lambda Z}{\pi \rho_0} \right)^2 \quad (\text{G-36})$$

while the beam spread = 0, for the assumptions and approximations used.

These results are consistent with an earlier pure beam wander analysis³⁸ which found:

The mean power is given by

$$\overline{P} = \frac{P_0}{1+2\alpha} \quad (\text{G-37})$$

and the normalized variance of the detected power is given by

$$\frac{\overline{\sigma_p^2}}{\overline{P}^2} = \frac{\overline{P^2} - \overline{P}^2}{\overline{P}^2} = \frac{4\alpha^2}{4\alpha + 1} \quad (\text{C} - 38)$$

so long as $\alpha = \alpha_1$.

Therefore, it is clear that the analysis included herein really only includes beam wander effects. As such, it is a valid estimate of worst case results, as shown earlier by Paddon.¹

APPENDIX H

ATMOSPHERIC PROPAGATION EFFECTS: SCINTILLATION AND LOG AMPLITUDE VARIANCE FOR THE POINT RECEIVER

1. INTRODUCTION

In Appendix E we have observed the fluctuations in received optical power due to scintillation alone are well approximated by log normal statistics. Furthermore, the probability distribution of the instantaneous received optical power, Equation E-11, is completely specified by the mean received optical power, S_o , and the log amplitude variance, $C_\ell(0)$. If the log normal approximation is valid, the normalized variance in received optical power observed will be

$$\sigma_s^2 / S_o^2 = \exp(4C_\ell(0)) - 1 \quad (\text{H-11})$$

For the log normal statistical model, the degradation of link performance caused by turbulence induced scintillation is, therefore, dependent on the estimate of $C_\ell(0)$.

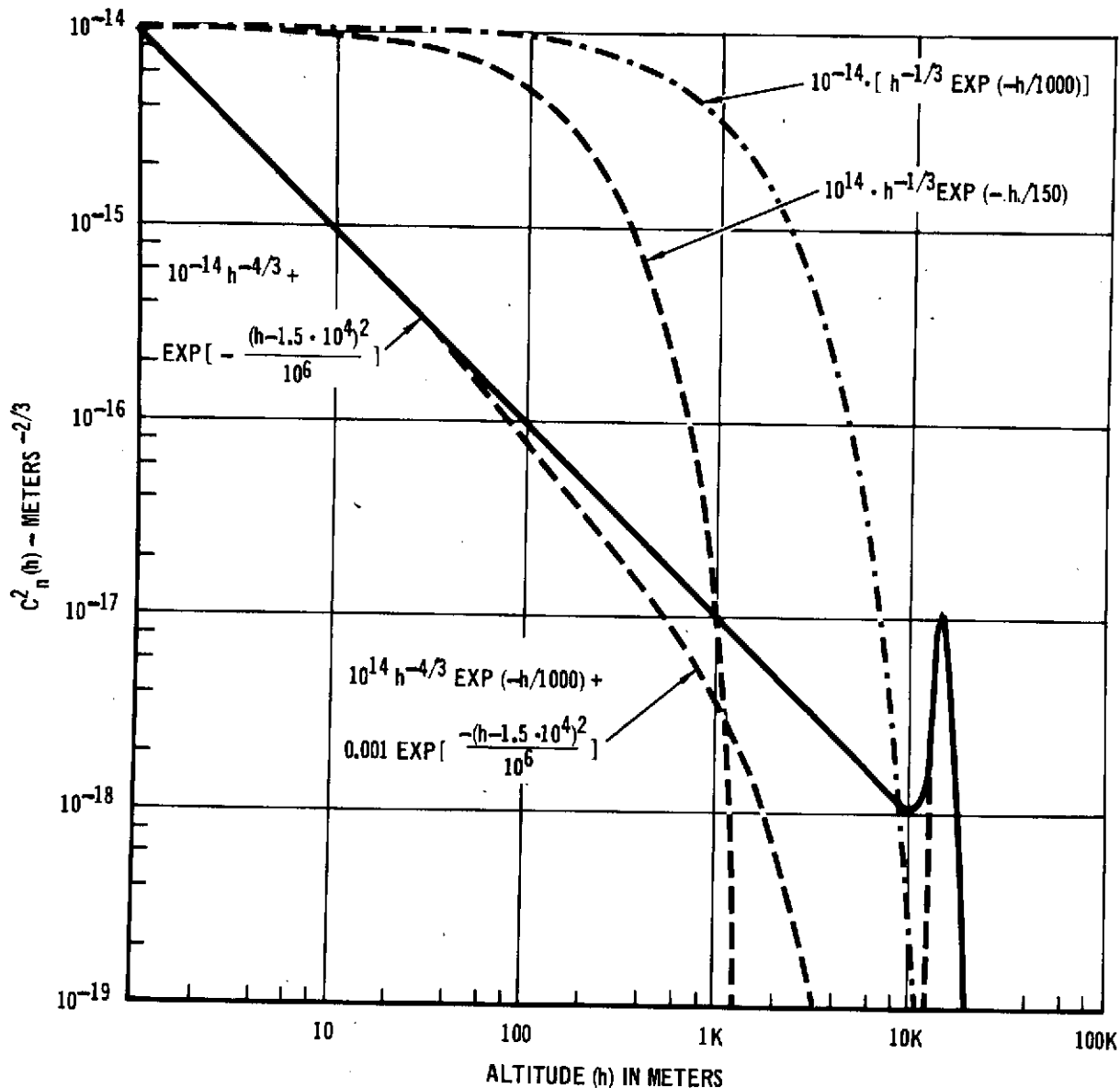
We consider next estimates of the log amplitude variance, $C_\ell(0)$, for the theoretical turbulence profiles as shown in Figure H-1 outlined in Appendix E.

2. LOG AMPLITUDE VARIANCE FOR A POINT RECEIVER

We have used the theoretical relationship derived by Schmelzter³⁴ to evaluate estimates of the log amplitude variance, $C_\ell(0)$, for the balloon and reference synchronous satellite link. Lee and Harp⁵⁵ have shown their theoretical results and those of Schmelzter³⁴ and Ishimaru^{56,57} are equivalent. These treatments all consider the propagation of an arbitrary Gaussian spherical wave beam which is characteristic of output radiation from an ideal single mode laser. Plane and spherical wave propagation are limiting cases of their analyses. All three treatments assume:

- (1) The beam propagation axis remains stationary along a fixed axis in space as long as turbulence remains unchanged.

FIGURE H-1 THEORETICAL TURBULENCE PROFILES VERSUS ALTITUDE



- (2) The fluctuations in the received optical power are measured by a point receiver located near or on the beam axis.

In addition, we assume these theories will hold along the instantaneous position of the beam even in the presence of beam wander. The beam is not expected to wander far from its average position.

2.1 THE SPHERICAL WAVE LOG AMPLITUDE VARIANCE. For the case of spherical wave propagation such that the transmit beam radius, $w = 0$, the Equation

E-12 of Appendix E reduces to

$$C_{\ell}^S(0) = 4.79 K_o \lambda^{-7/6} \sec^{11/6}(\theta_Z) \int_0^H f(h) \left[1 - \frac{h}{H}\right]^{5/6} h^{5/6} dh \quad (H-2)$$

for H = receiver altitude

λ = wavelength

θ_Z = zenith angle

h = vertical altitude above the transmitter

and $C_n^2(h) \equiv K_o f(h)$ is the turbulence profile. We have evaluated the spherical wave log amplitude variance, $C_{\ell}^S(0)$, by numerical integration via a digital computer. The results of those computations are presented in Table H-1. The value of $C_{\ell}^S(0)$ for different wavelengths can be found with conversion factors listed in Table H-2.

2.2 THE BEAM WAVE LOG AMPLITUDE VARIANCE. The log amplitude variance for beam wave propagation, denoted by $C_{\ell}(0)$, was also computed from Equation E-12. These computations were performed to evaluate the effect of transmit beam design parameters such as feed beam radius, radius of phase front curvature, and beam width. For the beam wave, it has been shown³⁸

$$\frac{C_{\ell}(0)}{C_{\ell}^S(0)} = 3.8637 \left[\int_c^H f(h) \left[1 - \frac{h}{H}\right]^{5/6} h^{5/6} dh \right]^{-1} \times \left[\int_0^H f(h) (H-h)^{5/6} \left\{ \left(\frac{M^2 + N^2}{P^2} \right)^{5/12} \cos \frac{5}{6} \left(\tan^{-1} \left(\frac{N}{M} \right) - \left(\frac{M}{P} \right)^{5/6} \right) \right\} dh \right]$$

where $C_{\ell}(0)/C_{\ell}^S(0)$ is the ratio of the beam to spherical wave log amplitude variance,

TABLE H-1
COMPUTED SPHERICAL WAVE LOG

Amplitude Variance, $C_{\ell}^S(0)$, For Assumed Turbulence Profile

$$C_n^2(h) = 10^{-15} \cdot f(h) \text{ for}$$

$H = 30 \text{ km}, \phi_Z = 45^\circ, \text{ and } \lambda = 0.5 \mu\text{m}$

$$f(h) = h^{-1/3} \exp(-h/h_o)$$

h_o	$C_{\ell}^S(0)$
3.2 km	2.811
1 km	0.5926
150 m	0.03283

$$f(h) = h^{-4/3} \exp(-h/h_o)$$

h_o	$C_{\ell}^S(0)$
3.2 km	0.001905
1 km	0.001083
150	0.004010

$$f(h) = h^{-4/3}$$

$C_{\ell}^S(0)$
0.01120

$$f(h) = h^{-1/3} \exp(-h/h_o) + D_o \exp[-(h-h_p)^2 / (\sigma \cdot 10^3)^2]$$

$h_o = 3.2 \text{ km}$

σ	D_o	h_p	$C_{\ell}^S(0)$
-	0	-	2.811
0.1	0.01	10^4	2.8166
0.1	"	"	2.866
1.0	"	"	3.362
0.01	0.001	"	2.8117
0.1	"	"	2.816
1.0	"	"	2.8663

TABLE H-1 (Cont'd)
COMPUTED SPHERICAL WAVE LOG

Amplitude Variance, $C_l^S(0)$, For Assumed Turbulence Profile

$$C_n^2(h) = 10^{-15} \cdot f(h) \text{ for}$$

$$H = 30 \text{ km, and } \phi_z = 45^\circ$$

$$f(h) = h^{-4/3} + D_o \exp[-(h - h_p)^2 / (\sigma \cdot 10^3)^2]$$

$$\lambda = 0.53 \mu\text{m}$$

σ	D_o	h_p	$C_l^S(0)$
-	0	-	0.0045643
0.01	0.01	10^4	0.0097307
0.1	"	"	0.056227
1.0	"	"	0.52008
0.01	0.001	"	0.0050809
0.1	"	"	0.0097306
1.0	"	"	0.056116
0.01	0.01	$1.5 \cdot 10^4$	0.01026
0.1	"	"	0.061556
1.0	"	"	0.57344
0.01	0.001	"	0.00513423
0.1	"	"	0.01026
1.0	"	"	0.0614515
0.01	0.01	$1.9 \cdot 10^4$	0.0099237
0.1	"	"	0.058158
1.0	"	"	0.53941
0.01	0.001	"	0.0051002
0.1	"	"	0.0092368
1.0	"	"	0.05804

$$f(h) = D_o \exp[-(h - h_p)^2 / (\sigma \cdot 10^3)^2]$$

$$\lambda = 0.5 \mu\text{m}$$

D_o	σ	h_p	$C_l^S(0)$
0.001	1	$1.5 \cdot 10^4$	0.060594
1.0	0.1	"	0.69941
1.0	0.001	"	0.6496

TABLE H-1 (Cont'd)
COMPUTED SPHERICAL WAVE LOG

Amplitude Variance, $C_n^2(0)$, For Assumed Turbulence Profile

$$C_n^2(h) = 10^{-15} \cdot f(h) \text{ for}$$

$$H = 30 \text{ km, } \phi_z = 45^\circ, \text{ and } \lambda = 0.5 \mu\text{m}$$

$$f(h) = h^{-4/3} + D_o \exp[-(h-h_p)^2 / (\sigma \cdot 10^3)^2]$$

σ	D_o	h_p	$C_n^2(0)$
1.0	1.0	$1.5 \cdot 10^4$	243.58
"	"	10^4	220.73
"	"	$1.9 \cdot 10^4$	229.00
0.1	"	$1.5 \cdot 10^4$	203.03
"	"	10^4	221.38
"	"	$1.9 \cdot 10^4$	229.65
10.0	"	$1.5 \cdot 10^4$	1982.65
"	"	10^4	1785.03
"	"	$1.9 \cdot 10^4$	1854.34
1.0	0.01	$1.5 \cdot 10^4$	2.4551
0.1	"	"	0.26360
10.	"	"	19.8459
"	"	10^4	17.86
"	"	$1.9 \cdot 10^4$	18.56
1.0	0.001	$1.5 \cdot 10^4$	0.26315
0.1	"	"	0.044003
10.0	"	"	2.00223
1.0	"	10^4	0.2403
"	0.001	$1.9 \cdot 10^4$	0.2485

TABLE H-1 (Cont'd)
COMPUTED SPHERICAL WAVE LOG

Amplitude Variance, $C_{\lambda}^S(0)$, For Assumed Turbulence Profile

$$C_n^2(h) = 10^{-15} \cdot f(h) \text{ for}$$

$$H = 30 \text{ km, } \phi_Z = 45^\circ, \text{ and } \lambda = 0.5 \mu\text{m}$$

$$f(h) = h^{-4/3} \exp(-h/h_o) + D_o \exp[-(h-h_p)^2 / (\sigma \cdot 10^3)^2]$$

$$h_o = 150\text{m}$$

σ	D_o	h_p	$C_{\lambda}^S(0)$
-	0	-	0.0004010
0.01	0.01	10^4	0.00593
0.1	"	10^4	0.05569
1.0	"	"	0.55218
0.01	0.001	"	0.00095405
0.1	"	"	0.005930
1.0	"	"	0.055579
0.01	0.01	$1.5 \cdot 10^4$	0.006501
0.1	"	"	0.061401
1.0	"	"	0.6092900
0.01	0.001	"	0.0010110
0.1	"	"	0.006501
1.0	"	"	0.061289
0.01	0.01	$1.9 \cdot 10^4$	0.006137
0.1	"	"	0.0577648
1.0	"	"	0.57287
0.01	0.001	"	0.0009747
0.1	"	"	0.006137
1.0	"	"	0.057648

TABLE H-1 (Cont'd)
COMPUTED SPHERICAL WAVE LOG

Amplitude Variance, $C_l^S(0)$, For Assumed Turbulence Profile

$$C_n^2(h) = 10^{-15} \cdot f(h) \text{ for}$$

$H = 30 \text{ km}$, $\phi_Z = 45^\circ$, and $\lambda = 0.5 \mu\text{m}$

$$f(h) = h^{-4/3} \exp(-h/h_o) + D_o \exp[-(h - h_p)^2 / (\sigma \cdot 10^3)^2]$$

$$h_o = 1 \text{ km}$$

σ	D_o	h_p	$C_l^S(0)$
-	0	-	0.001083
0.01	0.01	10^4	0.006613
0.1	"	"	0.05638
1.0	"	"	0.05529
0.01	0.001	"	0.001636
0.1	"	"	0.006613
1.0	"	"	0.05626
0.01	0.01	$1.5 \cdot 10^4$	0.007183
0.1	"	"	0.06208
1.0	"	"	0.6099
0.01	0.001	"	0.001693
0.1	"	"	0.007183
1.0	"	"	0.06197
0.01	0.01	$1.9 \cdot 10^4$	0.006820
0.1	"	"	0.05845
1.0	"	"	0.5736
0.01	0.001	"	0.001657
0.1	"	"	0.006820
1.0	"	"	0.05833

TABLE H-1 (Cont'd)
COMPUTED SPHERICAL WAVE LOG

Amplitude Variance, $C_{\ell}^S(0)$, For Assumed Turbulence Profile

$$C_n^2(h) = 10^{-15} \cdot f(h) \text{ for}$$

$$H = 30 \text{ km}, \phi_Z = 45^\circ, \text{ and } \lambda = 0.5 \mu\text{m}$$

$$f(h) = h^{-4/3} \exp(-h/h_o) + D_o \exp[-(h - h_p)^2 / (\sigma \cdot 10^3)^2]$$

$$h_o = 3.2 \text{ km}$$

σ	D_o	h_p	$C_{\ell}^S(0)$
-	0	-	0.001905
0.01	0.01	10^4	0.007438
0.1	"	"	0.05720
1.0	"	"	0.05537
0.01	0.001	"	0.002457
0.1	"	"	0.007437
1.0	"	"	0.05708
0.01	0.01	$1.5 \cdot 10^4$	0.008005
0.1	"	"	0.06290
1.0	"	"	0.06107
0.01	0.001	"	0.0025149
0.1	"	"	0.008005
1.0	"	"	0.06279
0.01	0.01	$1.9 \cdot 10^4$	0.007641
0.1	"	"	0.05927
1.0	"	"	0.05744
0.01	0.001	"	0.0024786
0.1	"	"	0.0076413
1.0	"	"	0.0591525

TABLE H-1 (Cont'd)
COMPUTED SPHERICAL WAVE LOG

Amplitude Variance, $C_{\lambda}^S(0)$, For Assumed Turbulence Profile

$$C_n^2(h) = 10^{-15} \cdot f(h) \text{ for}$$

$$H = 30 \text{ km, } \phi_Z = 45^\circ, \text{ and } \lambda = 0.5\mu\text{m}$$

$$f(h) = h^{-1/3} \exp(-h/h_o) + D_o \exp[-(h - h_p)^2 / (\sigma \cdot 10^3)^2]$$

$$h_o = 150,$$

σ	D_o	h_p	$C_{\lambda}^S(0)$
-	0	-	0.03283
0.01	0.01	10^4	0.03836
0.1	"	"	0.08131
1.0	"	"	0.5846
0.01	0.001	"	0.03386
0.1	"	"	0.03836
1.0	"	"	0.08801
0.01	0.01	$1.5 \cdot 10^4$	0.03893
0.1	"	"	0.09383
1.0	0.01	"	0.06417
0.01	0.001	"	0.03344
0.1	"	"	0.03893
1.0	"	"	0.09372
0.01	0.01	$1.9 \cdot 10^4$	0.03857
0.1	"	"	0.09019
1.0	"	"	0.6053
0.01	0.001	"	0.03340
0.1	"	"	0.03857
1.0	"	"	0.09008

TABLE H-1 (Cont'd)
COMPUTED SPHERICAL WAVE LOG

Amplitude Variance, $C_l^S(0)$, For Assumed Turbulence Profile

$$C_n^2(h) = 10^{-15} \cdot f(h) \text{ for}$$

$$H = 30 \text{ km, } \phi_Z = 45^\circ, \text{ and } \lambda = 0.5 \mu\text{m}$$

$$f(h) = h^{-1/3} \exp(-h/h_o) + D_o \exp[-(h-h_p)^2 / (\sigma \cdot 10^3)^2]$$

$$h_o = 1 \text{ km}$$

σ	D_o	h_p	$C_l^S(0)$
-	0	-	0.50926
0.01	0.01	10^4	0.51442
0.1	"	"	0.560923
1.0	"	"	1.02478
0.01	0.001	"	0.50977
0.1	"	"	0.514426
1.0	"	"	0.560812
0.001	0.01	$1.5 \cdot 10^4$	0.5149597
0.1	"	"	0.566252
1.0	"	"	1.0781325
0.01	0.001	"	0.50983
0.1	"	"	0.51495
1.0	"	"	0.566147
0.01	0.01	$1.9 \cdot 10^4$	0.51461
0.1	"	"	0.56285
1.0	"	"	1.044124
0.01	0.001	"	0.50978
0.1	"	"	0.514619
1.0	"	"	0.56274

TABLE H-2
SPHERICAL WAVE LOG AMPLITUDE
Wavelength Dependence Conversion Factors

$$[c_{\lambda}^S(\lambda^-)] = c_{\lambda}^S(\lambda) (\lambda/\lambda^-)^{7/6}$$

(λ/λ^-)	$(\lambda/\lambda^-)^{7/6}$
1.0	1.0
0.5/1.06	0.4161738
0.5/0.53	0.93427879
0.5/0.63	0.7636617
0.63/0.53	1.2234197
0.63/1.06	0.5449715
1.06/0.63	1.834958
1.06/0.53	2.244924
0.5/0.48	1.04877

$$P = \left(H \cdot B \sec(\theta_z) + A^2/R \right)^2 + A^2$$

$$N = \left(h \cdot B \sec(\theta_z) + A^2/R \right) \left(H \cdot B \sec(\theta_z) + A^2/R \right) + A^2$$

$$M = A \cdot B \sec(\theta_z) (H-h)$$

$$B = 1 + (A/R)^2$$

and

$$A = \pi w^2 / \lambda$$

In the above relationships,

w = the transmit beam radius at the e^{-2} power point

R = the radius of phase front curvature for a Gaussian spherical wave at the transmit aperture.

θ_z = zenith angle

H = the receiver altitude and

λ = wavelength

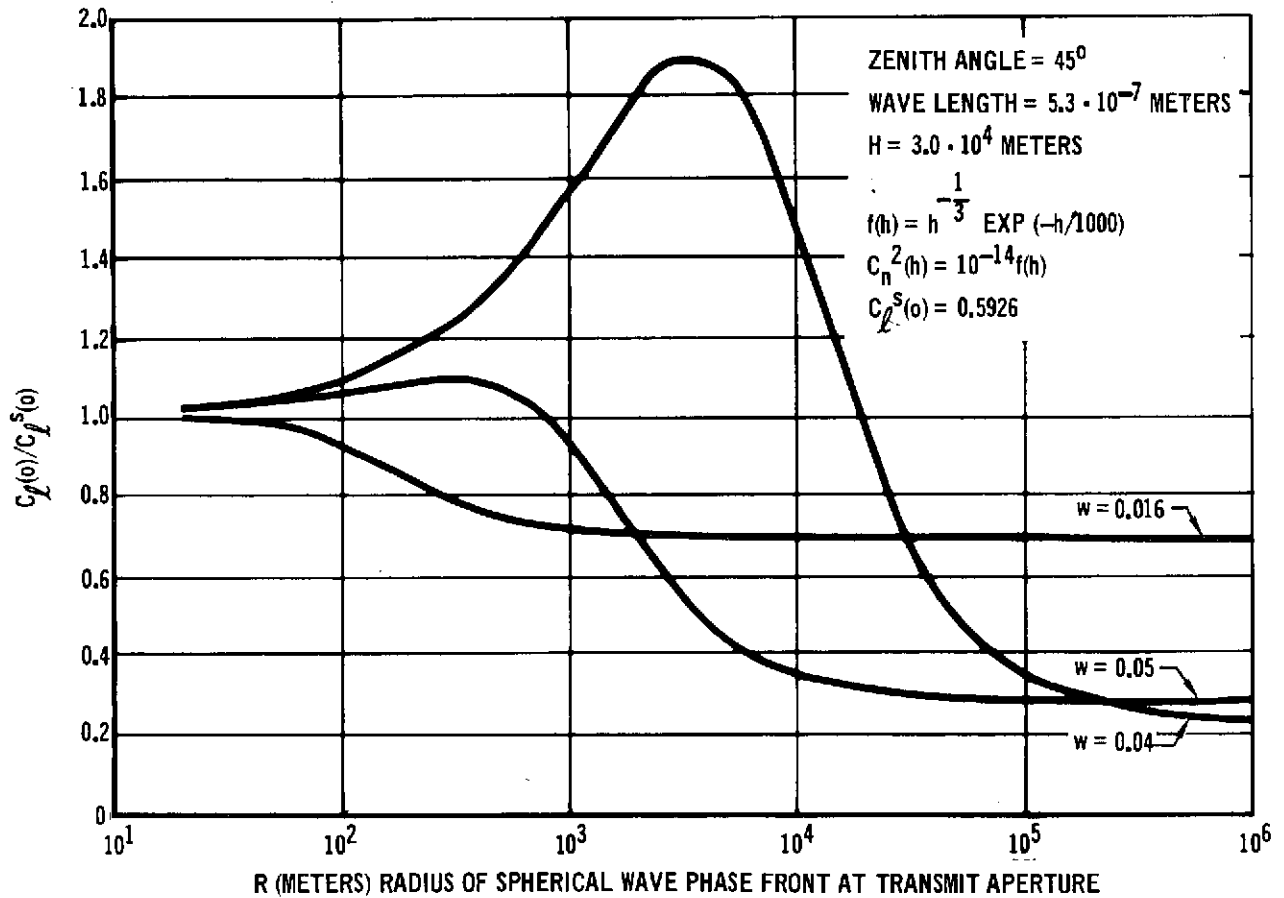
Also in the limit as $w \rightarrow 0$, it is easily shown $C_\ell^o(o)/C_\ell^s(o) \rightarrow 1$. The ratio of $C_\ell^o(0)/C_\ell^s(0)$ was evaluated with a digital computer for both the balloon and reference satellite link.

The results of these computations for the balloon link are illustrated in Figures H2 through H-8. In those figures the ratio $C_\ell^o(o)/C_\ell^s(o)$ is plotted versus the radius of phase front curvature at the transmit aperture with the transmit feedbeam radius, w , as a parameter. The feed beam radius has dimensions in meters unless otherwise stated.

In general these curves indicated the following:

- (1) For a defocused beam ($R \rightarrow 0$ at the transmit aperture) the scintillation increases.
- (2) For a collimated beam ($R = \infty$), the scintillation is decreased.
- (3) For a collimated beam ($R = \infty$), the scintillation decreases as feed beam radius increases as shown by Freid .
- (4) For a focused beam ($R < 0$ at the transmit aperture), the scintilla-

FIGURE H-2 $C_{\ell}^S(o)/C_{\ell}^S(o)$ VERSUS R WITH FEED BEAM RADIUS, W, AS A PARAMETER FOR THE BALLOON DEFOCUSSED UPLINK

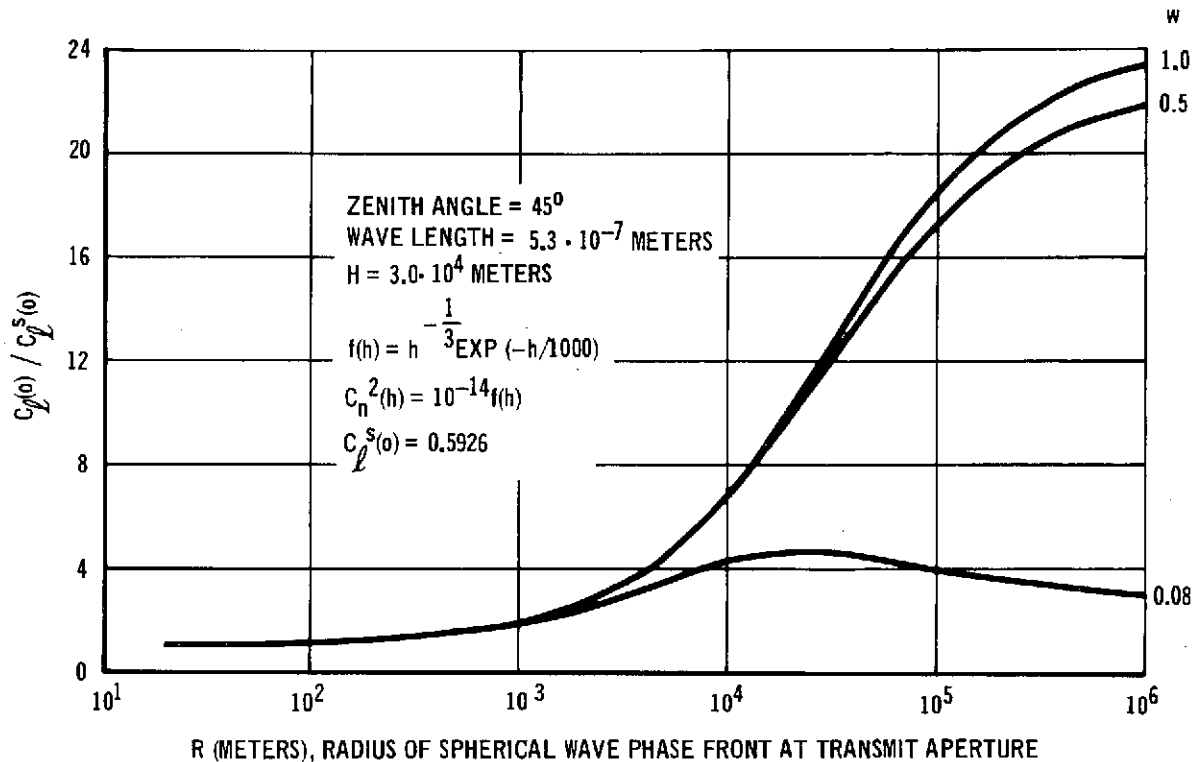


tion may be decreased significantly as shown in Figures H-7 and H-8. In this case the minimum beam spot should be positioned at or above tropopause.

The physical validity of these results is questionable for they apply to a stationary beam and to scintillation near the beam axis. In addition, as Lawrence and Strohbehn⁵⁸ point out, the concept of a focused beam would seem to be meaningless because of the wavefront breakup after propagation through short distance in turbulence.

However, the idea of focusing the beam to the transmitter has been tested qualitatively by Kerr⁹ over horizontal paths and he found a reduction in scintillation. His findings suggest that at least a qualitative test of

FIGURE H-3: $C_{\ell}^2(o) / C_{\ell}^s(o)$ VERSUS R WITH FEED BEAM RADIUS, W, AS A PARAMETER FOR BALLOON DEFOCUSSED UPLINK



the scintillation variation with transmit beam characteristics should be investigated for vertical paths.

Figures H-9 and H-10 illustrate the variation in scintillation versus transmit beam characteristics for the reference synchronous satellite uplink. For both a focused and defocused beam, we observe the scintillation ($C_{\ell}^2(o)$) decreases with increasing feed beam radius. However, increasing the feed beam diameter may increase the beam spread and the loss in mean received optical power. Increasing the feed beam diameter to reduce link performance degradation, contradicts the hypothesis of Yura and Lutomirski.^{39,41} See also Appendix E.

For a further discussion of reducing the effects of scintillation on the uplink by focusing the beam to above tropopause, see the Optical Propagation Test Study³⁸.

FIGURE H-4 $C_{\ell}(o)/C_{\ell}^S(o)$ VERSUS R WITH FEED BEAM RADIUS, W, AS A PARAMETER FOR THE BALLOON DEFOCUSSED UPLINK

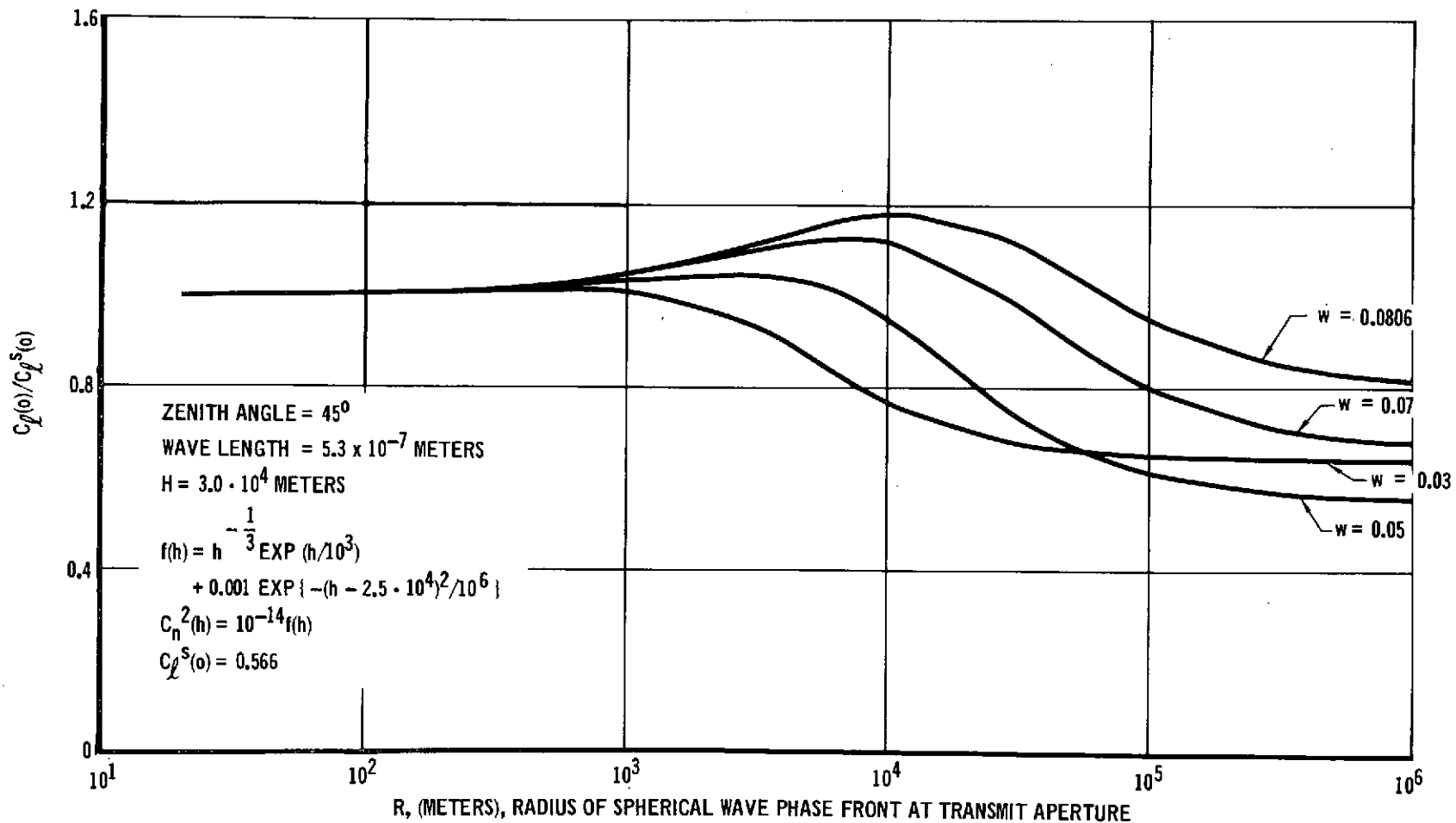


FIGURE H-5 $C_{\rho}(o)/C_{\rho}^S(o)$ VERSUS R WITH FEED BEAM RADIUS, W, AS A PARAMETER FOR THE BALLOON DEFOCUSSED UPLINK

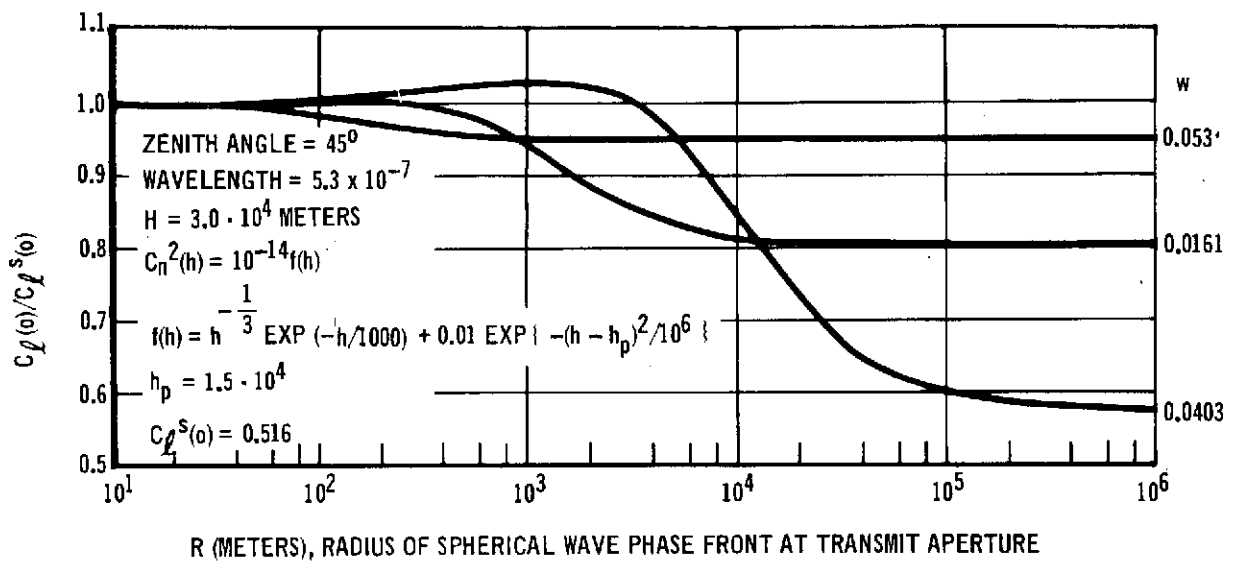


FIGURE H-6 $C_{\ell}^2(o)/C_{\ell}^S(o)$ VERSUS $|R|$ WITH FEED BEAM RADIUS, W , AS A PARAMETER FOR THE BALLOON FOCUSED UPLINK

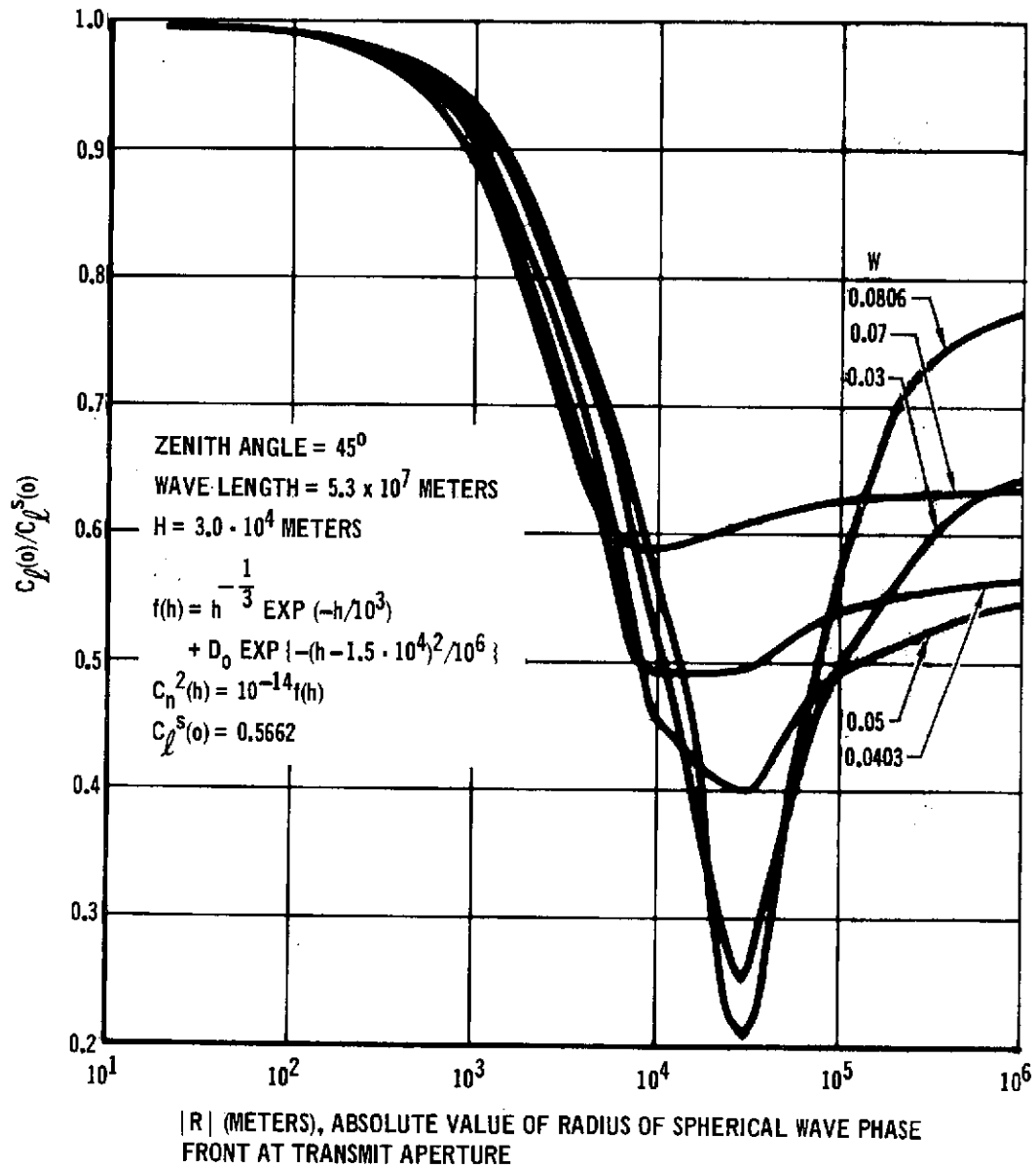


FIGURE H-7 $C_L^S(o)/C_L^S(o)$ VERSUS $|R|$ WITH FEED BEAM RADIUS, W , AS A PARAMETER FOR THE BALLOON FOCUSED UPLINK

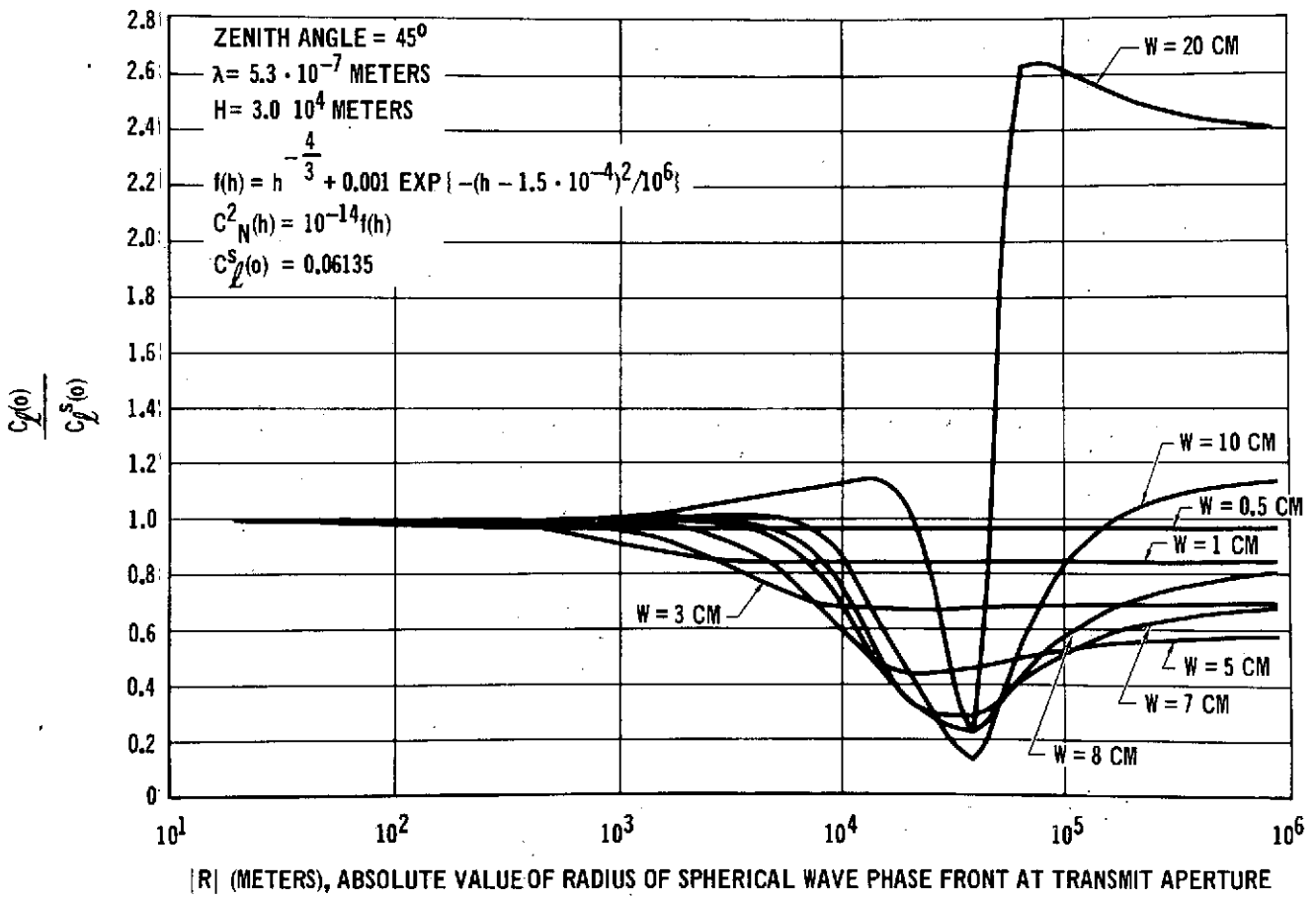


FIGURE H-8 $C_{\ell}(o)/C_{\ell}^S(o)$ VERSUS R WITH FEED BEAM RADIUS, W, (m) AS A PARAMETER FOR THE BALLOON FOCUSED DOWNLINK

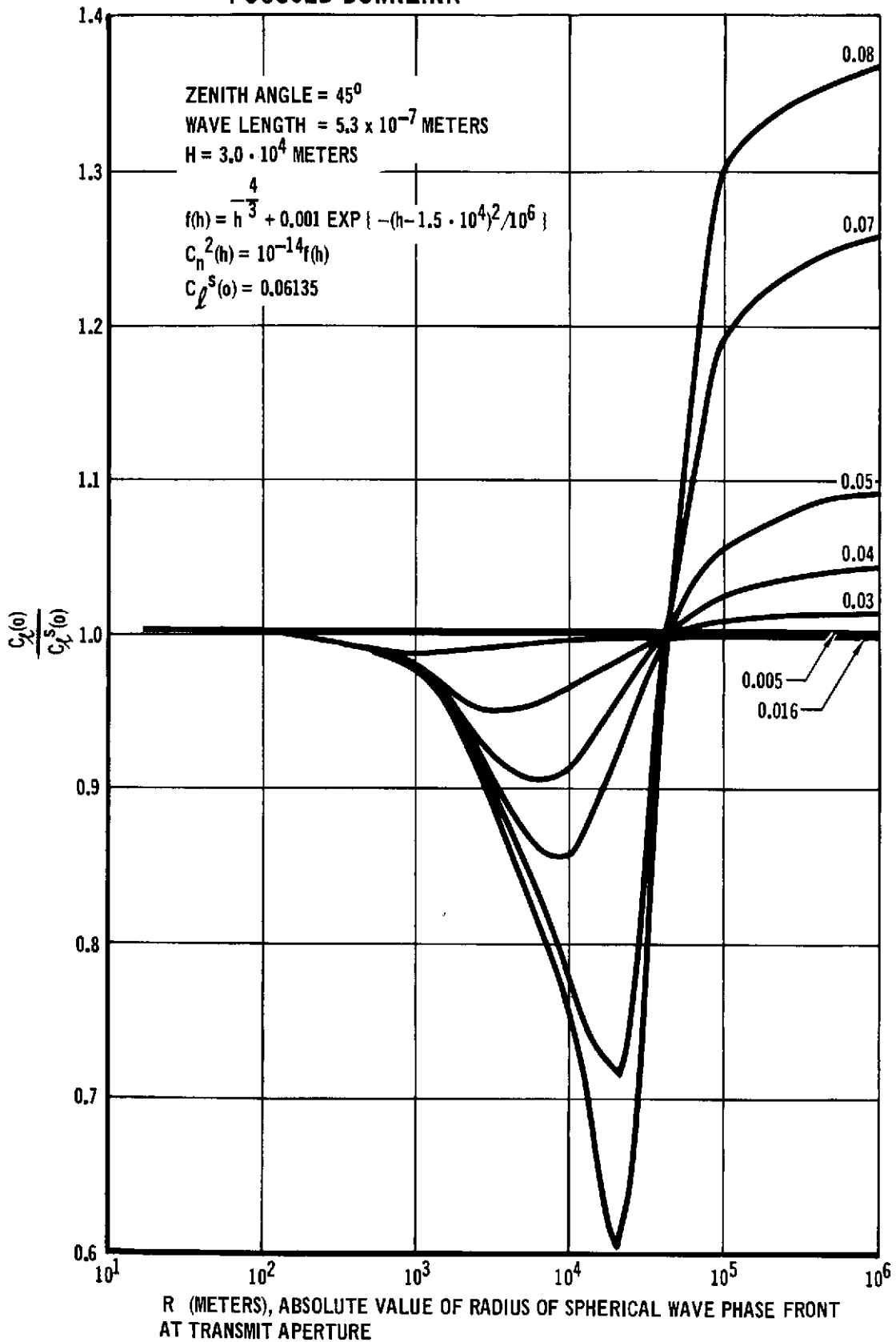


FIGURE H-9 $C_{\ell}(o)/C_{\ell}^S(o)$ VERSUS R WITH FEED BEAM RADIUS, W,
AS A PARAMETER FOR THE SYNCHRONOUS SATELLITE
TO GROUND DEFOCUSSED UPLINK

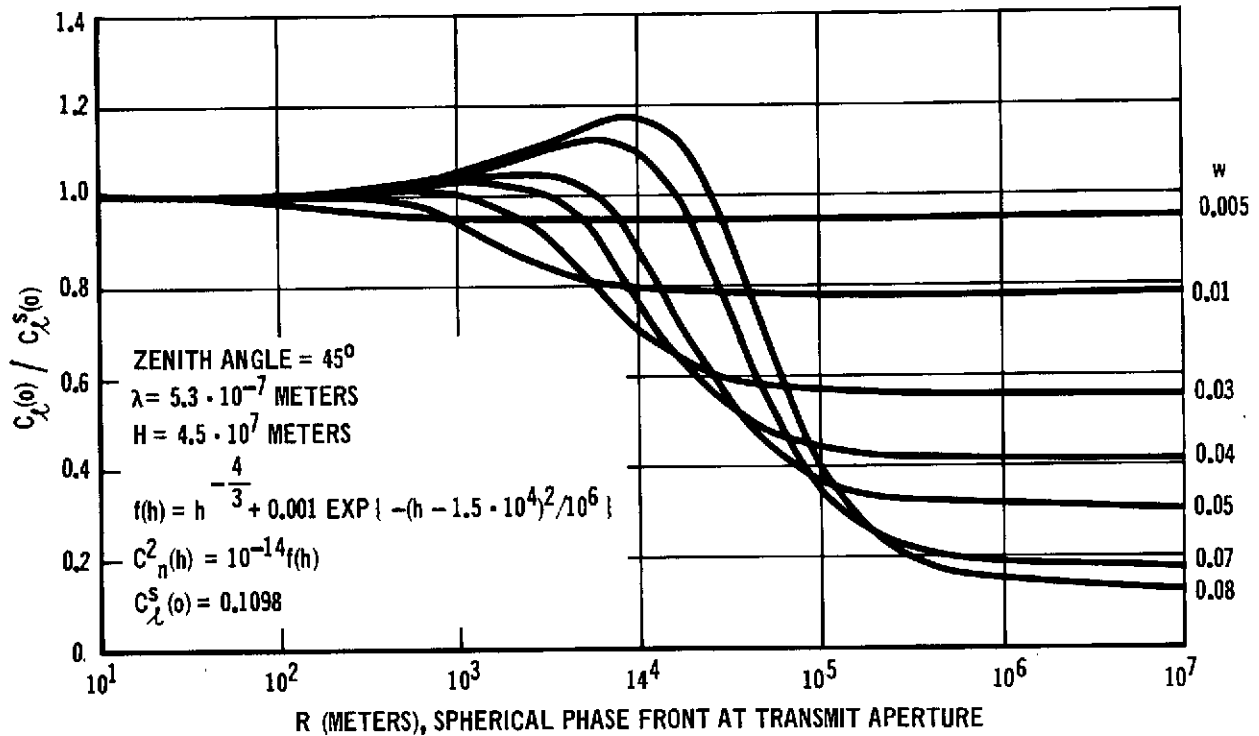
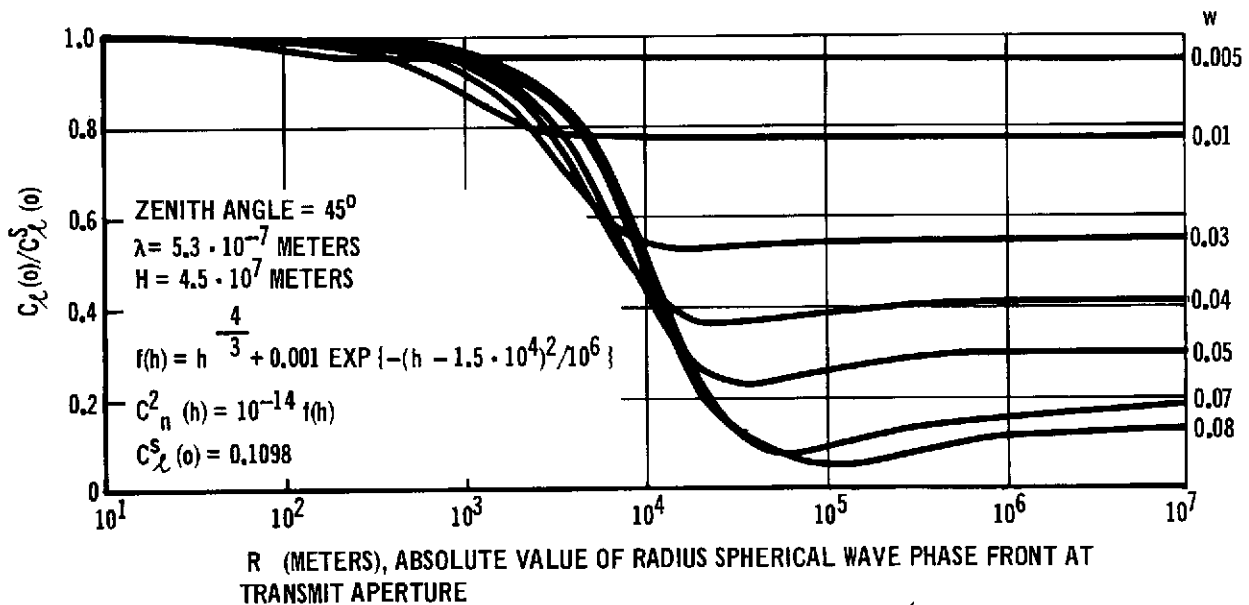


FIGURE H-10 $C_{\ell}(o)/C_{\ell}^S(o)$ VERSUS R WITH FEED BEAM RADIUS, W,
AS A PARAMETER FOR THE SYNCHRONOUS SATELLITE
TO GROUND FOCUSED UPLINK



THIS PAGE INTENTIONALLY LEFT BLANK

APPENDIX I

COMPUTER PRINTOUT FOR OPTICAL TOLERANCE ANALYSIS

Figures I-1 and I-2 contain the computer output for Cases A and B, respectively, as described in Section 2.4.4.2. The program name is OTOL, and it was written by D. S. Grey Associates. It is currently available as part of Control Data Corporation's Computer Optics Package.

The printout lists the input perturbation for the optical surfaces associated with each page at the top of each page. The surfaces are numbered consecutively from the front of the telescope back through the optical system. DX is the shift of the element of interest along the optical axis, DY is the azimuth (meridional) shift, and DZ is the elevation (sagittal) shift all in millimeters. TILTY and TILTZ are the rotations about axes perpendicular to the optical axis in radians. The columns below the input statement present the computed cumulative azimuth and elevation components of image position shift as a function of field angle: NF = 1 represents $-2 \mu\text{rad}$, NF = 2 represents $-1 \mu\text{rad}$, NF = 3 is on axis, NF = 4 is $+L \mu\text{rad}$, and NF = 5 is $+2 \mu\text{rad}$. The focal plane shift in millimeters is shown. A positive number indicates the focal plane has been shifted away from the front of the telescope. The focal plane tilt in radians is also given.

At the bottom of each page is the cumulative path length error (in wavelengths) and intercept error analyses. These results are based on 41 rays traced for each field angle. RMS and worst case results are presented.

FIGURE I-1 COMPUTER ANALYSIS RESULTS FOR CASE A

```

PERTURBATION
BEGIN END DX DY DZ TILTY TILTZ DC DN DT DRMS MORE
2 9 -0 -1.880E-07 -1.044E+00 -4.470E-02 2.000E-04 3.000E-05 -0. -0. 0. 0.
WEIGHTED SUM**2 PL# 4.01581354E-03 RMS# 6.93737286E-03 5.34180293E-03 4.19547174E-03 6.34162596E-07 6.93642732E-03
    
```

```

IMAGE POSITION SHIFT NF# 1 1.83137326E-01
IMAGE POSITION SHIFT NF# 1 -1.33065801E-02
    
```

```

IMAGE POSITION SHIFT NF# 2 1.83003621E-01
IMAGE POSITION SHIFT NF# 2 -1.33105447E-02
    
```

```

IMAGE POSITION SHIFT NF# 3 2.61392502E-01
IMAGE POSITION SHIFT NF# 3 -1.90163195E-02
    
```

```

IMAGE POSITION SHIFT NF# 4 1.83003513E-01
IMAGE POSITION SHIFT NF# 4 -1.33105447E-02
    
```

```

IMAGE POSITION SHIFT NF# 5 1.83136986E-01
IMAGE POSITION SHIFT NF# 5 -1.33065801E-02
    
```

```

FOCAL PLANE SHIFT -5.19297021E-08
    
```

```

FOCAL PLANE TILT Y-DIRECTION -9.43465769E-05
    
```

```

COMPENSATORS
BEGIN END DX DY DZ TILTY TILTZ DC DN DT DRMS MORE
22 22 -0 -0. -0. -0. 1.000E-03 -0. -0. -0. 2.294E-01 2.951E-10 -0
31 31 -0 -0. -0. -0. -0. 1.000E-03 -0. -0. 1.616E-01 3.417E-09 -0
    
```

WEIGHTED SUM**2 PL# 7.19196959E-11 RMS#

SINE ANGLE	PL ERROR IN WAVES	INTERCEPT ERROR IN MICRONS
0.002000	RMS .0017 WORS# .0084 (2.7)	.19 .63 (1)
0.001000	RMS .0018 WORS# .0132 (3.1)	.34 1.73 (1)
0.000000	RMS .0007 WORS# .0028 (3.39)	.11 .30 (1)
0.001000	RMS .0018 WORS# .0131 (41.39)	.34 1.73 (41)
0.002000	RMS .0017 WORS# .0084 (35.40)	.19 .62 (41)

FIGURE I-1 COMPUTER ANALYSIS RESULTS FOR CASE A (Continued)

PERTURBATION
 BEGIN END DX DY DZ TILTY TILTZ DC ON OT DRMS MORE
 10 20 -0. 1.053E+00 2.997E-01 4.370E-02 -2.900E-05 1.600E-05 -0. -0. 0. 0. 2
 PERTURBATION IS CONTINUED FROM LAST PERTURBATION CARD*****
 WEIGHTED SUM**2 PL= 0.86813871E-04 RMS= 6.9478543E-03 3.48011878E-03 2.5223869E-03 4.65831884E-03 0.05814251E-03

IMAGE POSITION SHIFT NF# 1 1.28635318E+00
 IMAGE POSITION SHIFT NF# 1 3.12983171E-03

IMAGE POSITION SHIFT NF# 2 1.27873185E+00
 IMAGE POSITION SHIFT NF# 2 3.13097934E-03

IMAGE POSITION SHIFT NF# 3 1.81645638E+00
 IMAGE POSITION SHIFT NF# 3 4.47456443E-03

IMAGE POSITION SHIFT NF# 4 1.26447777E+00
 IMAGE POSITION SHIFT NF# 4 3.13097934E-03

IMAGE POSITION SHIFT NF# 5 1.25774929E+00
 IMAGE POSITION SHIFT NF# 5 3.12983171E-03

FOCAL PLANE SHIFT 1.09712057E+00

FOCAL PLANE TILT Y-DIRECTION 1.36760059E-02

COMPENSATORS
 BEGIN END DX DY DZ TILTY TILTZ DC ON OT DRMS MORE
 22 22 -0 -0. -0. -0. 1.000E-03 -0. -0. -0. 6.402E+00 2.299E-07 -0
 31 31 -0 -0. -0. -0. -0. 1.000E-03 -0. -0. -0. 6.831E-02 6.109E-10 -0

WEIGHTED SUM**2 PL= 1.10540372E-08 RMS=

SINE ANGLE		PL ERROR IN WAVES	INTERCEPT ERROR IN MICRONS
-0.002000	RMS	.0277	1.76
	WORS	.1098 (1+14)	3.58 (1)
-0.001000	RMS	.0170	2.49
	WORS	.0842 (3+ 1)	11.03 (1)
0.000000	RMS	.0082	1.11
	WORS	.0318 (3+29)	2.14 (1)
.001000	RMS	.0132	1.44
	WORS	.0595 (24+ 1)	7.05 (41)
.002000	RMS	.0240	1.31
	WORS	.1009 (24+41)	3.08 (39)

FIGURE I-1 COMPUTER ANALYSIS RESULTS FOR CASE A (Continued)

```

PERTURBATION
BEGIN END DX DY DZ TILTY TILTZ DC DN DT DRMS MORE
22 22 -0 1.430F-01 0. 0. -1.700E-05 1.800E-05 -0. -0. 0. 0. 2
PERTURBATION IS CONTINUED FROM LAST PERTURBATION CARD*****
WEIGHTED SUM**2 PL= 1.24026692E-04 RMS= 2.7936957E-01 2.83216198E-01 2.89502796E-01 2.49783843E-01 2.93813653E-01
    
```

```

IMAGE POSITION SHIFT NF= 1 1.28247094F+00
IMAGE POSITION SHIFT NF= 1 5.89258108E-03

IMAGE POSITION SHIFT NF= 2 1.27679654F+00
IMAGE POSITION SHIFT NF= 2 5.89317846F-03

IMAGE POSITION SHIFT NF= 3 1.81645633F+00
IMAGE POSITION SHIFT NF= 3 8.42028874F+03

IMAGE POSITION SHIFT NF= 4 1.26641301F+00
IMAGE POSITION SHIFT NF= 4 5.89317846E-03

IMAGE POSITION SHIFT NF= 5 1.26163184F+00
IMAGE POSITION SHIFT NF= 5 5.89258108F+03

FOCAL PLANE SHIFT 7.99079797E-01

FOCAL PLANE TILT Y-DIRECTION 1.36760055F-02
    
```

```

COMPENSATORS
BEGIN END DX DY DZ TILTY TILTZ DC DN DT DRMS MORE
22 22 -0 -0. -0. -0. 1.000E-03 -0. -0. -0. 6.419E+00 2.311E-07 -0
31 31 -0 -0. -0. -0. -0. 1.000E-03 -0. -0. -6.332E-02 5.250E-10 -0
WEIGHTED SUM**2 PL= 1.01683914E-08 RMS=
    
```

SINE ANGLE	PL ERROR IN WAVES	INTERCEPT ERROR IN MICRONS
-0.002000	RMS: .0268 WORS: .1068(1+16)	1.48 3.45(3)
-0.001000	RMS: .0157 WORS: .0789(3+ 1)	2.25 10.51(1)
0.000000	RMS: .0065 WORS: .0261(3+28)	.82 1.69(1)
.001000	RMS: .0127 WORS: .0882(94+ 1)	1.43 7.98(41)
.002000	RMS: .0240 WORS: .0991(24+41)	1.21 3.15(39)

FIGURE I-1 COMPUTER ANALYSIS RESULTS FOR CASE A (Continued)

PERTURBATION		DX	DY	DZ	TILTY	TILTZ	DC	DN	DT	DRMS	MORE
23	30	-0.320E-02	7.049E-01	1.260E-01	2.800E-04	1.800E-05	-0.	-0.	0.	0.	2
PERTURBATION IS CONTINUED FROM LAST PERTURBATION CARD*****											
WEIGHTED SUM**2 PL#		4.30594323E-02	RMS# 2.63007896E-01 2.72882344E-01 2.87984972E-01 3.03101515E-01 3.12398232E-01								

IMAGE POSITION SHIFT NF# 1 7.47788006E-02
 IMAGE POSITION SHIFT NF# 1 7.22991636E-02

IMAGE POSITION SHIFT NF# 2 6.91805497E-02
 IMAGE POSITION SHIFT NF# 2 7.22839599E-02

IMAGE POSITION SHIFT NF# 3 9.09234038E-02
 IMAGE POSITION SHIFT NF# 3 1.03257076E-01

IMAGE POSITION SHIFT NF# 4 5.80796075E-02
 IMAGE POSITION SHIFT NF# 4 7.22839599E-02

IMAGE POSITION SHIFT NF# 5 9.23194037E-02
 IMAGE POSITION SHIFT NF# 5 7.22991636E-02

FOCAL PLANE SHIFT 9.47223495E-01

FOCAL PLANE TILT Y-DIRECTION -5.98435856E-03

COMPENSATORS		DX	DY	DZ	TILTY	TILTZ	DC	DN	DT	DRMS	MORE
22	22	-0.	-0.	-0.	1.000E-03	-0.	-0.	-0.	-3.991E+00	8.935E-08	-0
31	31	-0.	-0.	-0.	-0.	1.000E-03	-0.	-0.	4.720E-01	2.916E-08	-0
WEIGHTED SUM**2 PL#		1.16450755E-08 RMS#									

SINE ANGLE	PL ERROR IN WAVES	INTERCEPT ERROR IN MICRONS
-0.002000 RMS#	.0216	2.12
WORS#	.0984 (24, 1)	4.41 (9)
-0.001000 RMS#	.0175	2.01
WORS#	.0685 (15, 1)	4.31 (9)
0.000000 RMS#	.0145	1.97
WORS#	.0547 (24, 21)	3.59 (16)
.001000 RMS#	.0200	2.59
WORS#	.0817 (39, 13)	7.70 (41)
.002000 RMS#	.0211	2.37
WORS#	.0854 (39, 32)	5.05 (37)

FIGURE I-1 COMPUTER ANALYSIS RESULTS FOR CASE A (Continued)

PERTURBATION
 BEGIN END DX DY DZ TILTY TILTZ DC DN DT DRMS MORE
 31 31 -0 0.900E-01 0. 0. -2.000E-04 -2.000E-05 -0. -0. 0. 0. 2
 PERTURBATION IS CONTINUED FROM LAST PERTURBATION CARD*****
 WEIGHTED SUM**2 PL= 1.01668169E-01 RMS= 1.51750255E+00 1.50798134E+00 1.49261674E+00 1.47693996E+00 1.46703188E+00

IMAGE POSITION SHIFT NF= 1 -3.04346081E-02
 IMAGE POSITION SHIFT NF= 1 7.22991631E-02

IMAGE POSITION SHIFT NF= 2 -3.59446713E-02
 IMAGE POSITION SHIFT NF= 2 7.22439592E-02

IMAGE POSITION SHIFT NF= 3 -5.92968182E-02
 IMAGE POSITION SHIFT NF= 3 1.03257075E-01

IMAGE POSITION SHIFT NF= 4 -4.70856134E-02
 IMAGE POSITION SHIFT NF= 4 7.22839592E-02

IMAGE POSITION SHIFT NF= 5 -5.28940050E-02
 IMAGE POSITION SHIFT NF= 5 7.22991631E-02

FOCAL PLANE SHIFT 2.72722350E+00

FOCAL PLANE TILT Y-DIRECTION -7.12103509E-03

COMPENSATORS
 BEGIN END DX DY DZ TILTY TILTZ DC DN DT DRMS MORE
 22 22 -0 -0. -0. -0. 1.000E-03 -0. -0. -0. -4.886E+00 1.232E-07 -0
 31 31 -0 -0. -0. -0. -0. 1.000E-03 -0. -0. 4.920E-01 3.168E-08 -0

WEIGHTED SUM**2 PL= 1.26136767E-08 RMS=

SINE ANGLE		PL ERROR IN WAVES	INTERCEPT ERROR IN MICRONS
-0.002000	RMS	.0233	2.11
	WORS	.1058(24, 1)	4.29(9)
-0.001000	RMS	.0175	1.93
	WORS	.0679(24, 1)	4.13(9)
0.000000	RMS	.0145	1.97
	WORS	.0547(24, 2)	3.59(16)
0.001000	RMS	.0208	2.70
	WORS	.0863(39, 13)	8.44(41)
0.002000	RMS	.0226	2.44
	WORS	.0934(19, 32)	5.21(41)

FIGURE I-2 COMPUTER ANALYSIS RESULTS FOR CASE B

PERTURBATION
 BEGIN END DX DY DZ TILTY TILTZ DC DN DT DRMS MORE
 2 9 -0 -1.140E-02 -9.131E-01 -1.069E-01 1.900E-04 3.000E-05 -0. -0. 0. 0.
 WEIGHTED SUM**2 PL= 1.82537467E-03 RMS= 6.2035814E-03 4.93648830E-03 3.99211750E-03 4.93638618E-03 6.20295122E-03

IMAGE POSITION SHIFT NF= 1 P.51051356E-02
 IMAGE POSITION SHIFT NF= 1 4.52469438E-03

IMAGE POSITION SHIFT NF= 2 8.50053782E-02
 IMAGE POSITION SHIFT NF= 2 6.52131322E-03

IMAGE POSITION SHIFT NF= 3 1.21404030E-01
 IMAGE POSITION SHIFT NF= 3 9.31532691E-03

IMAGE POSITION SHIFT NF= 4 8.50053129E-02
 IMAGE POSITION SHIFT NF= 4 6.52131322E-03

IMAGE POSITION SHIFT NF= 5 8.51049292E-02
 IMAGE POSITION SHIFT NF= 5 4.52469438E-03

FOCAL PLANE SHIPT -3.14958971E-08

FOCAL PLANE TILT Y-DIRECTION -1.19437825E-03

COMPENSATORS
 BEGIN END DX DY DZ TILTY TILTZ DC DN DT DRMS MORE
 22 22 -0 -0. -0. -0. 1.000E-03 -0. -0. -0. -2.034E-01 2.320E-10 -0
 31 31 -0 -0. -0. -0. -0. 1.000E-03 -0. -0. 6.592E-02 5.688E-10 -0

WEIGHTED SUM**2 PL= 5.64105467E-11 RMS=

SINE ANGLE		PL ERROR IN WAVES	INTERCEPT ERROR IN MICRONS
-.002000	RMS	.0015	.13
	WORS	.0060(29*41)	.42(1)
-.001000	RMS	.0015	.22
	WORS	.0083(3* 1)	1.04(1)
0.000000	RMS	.0006	.11
	WORS	.0026(29*13)	.27(1)
.001000	RMS	.0015	.22
	WORS	.0083(41*13)	1.04(41)
.002000	RMS	.0015	.13
	WORS	.0060(1*13)	.42(41)

FIGURE I-2 COMPUTER ANALYSIS RESULTS FOR CASE B (Continued)

PERTURBATION
 BEGIN END DX DY DZ TILTY TILTZ DC DN DT DRMS MORE
 10 20 -0 9.212E-01 2.327E-01 -2.590E-01 -1.800E-04 7.400E-05 -0. -0. 0. 0. 2
 PERTURBATION IS CONTINUED FROM LAST PERTURBATION CARD*****
 WEIGHTED SUM**2 PL= 8.23462516E-03 RMS= 9.93814542E-03 8.57878759E-03 8.29354421E-03 8.95284655E-03 1.05931327E-02

IMAGE POSITION SHIFT NF= 1 9.38471503E-01
 IMAGE POSITION SHIFT NF= 1 -1.42853058E-01

IMAGE POSITION SHIFT NF= 2 9.31849699E-01
 IMAGE POSITION SHIFT NF= 2 -1.42895584E-01

IMAGE POSITION SHIFT NF= 3 1.32220956E+00
 IMAGE POSITION SHIFT NF= 3 -2.04153138E-01

IMAGE POSITION SHIFT NF= 4 9.19377408E-01
 IMAGE POSITION SHIFT NF= 4 -1.42895584E-01

IMAGE POSITION SHIFT NF= 5 9.13443195E-01
 IMAGE POSITION SHIFT NF= 5 -1.42853058E-01

FOCAL PLANE SHIFT 9.59980517E-01

FOCAL PLANE TILT Y-DIRECTION 9.34507741E-03

COMPENSATORS
 BEGIN END DX DY DZ TILTY TILTZ DC DN DT DRMS MORE
 22 22 -0 -0. -0. -0. 1.000E-03 -0. -0. -0. 4.587E+00 1.170E-07 -0
 31 31 -0 -0. -0. -0. -0. 1.000E-03 -0. -0. 1.673E+00 3.664E-07 -0

WEIGHTED SUM**2 PL= 8.24379056E-09 RMS=

SINE ANGLE		PL ERROR IN WAVES	INTERCEPT ERROR IN MICRONS
-0.002000	RMS	.0204	1.40
	WORS	.0832(1:16)	2.92(9)
-0.001000	RMS	.0132	1.98
	WORS	.0654(3: 1)	8.43(1)
0.000000	RMS	.0071	1.00
	WORS	.0260(3:29)	2.27(16)
.001000	RMS	.0101	1.12
	WORS	.0453(24: 1)	4.95(41)
.002000	RMS	.0174	1.05
	WORS	.0742(24:41)	2.20(39)

FIGURE I-2 COMPUTER ANALYSIS RESULTS FOR CASE B (Continued)

```

PERTURBATION
BEGIN END DX DY DZ TILTY TILTZ DC DN DT DRMS MORE
22 22 -0 1.730E-01 0. 0. -2.180E-04 6.900E-05 -0. -0. 0. 0. 2
PERTURBATION IS CONTINUED FROM LAST PERTURBATION CARD*****
WEIGHTED SUM**> PL= 1.00077017E-02 RMS= 3.41454831E-01 3.44252577E-01 3.42488448E-01 3.48718073E-01 3.51417171E-01
    
```

```

IMAGE POSITION SHIFT NF= 1 9.33774364E-01
IMAGE POSITION SHIFT NF= 1 -1.32262519E-01
    
```

```

IMAGE POSITION SHIFT NF= 2 9.29508394E-01
IMAGE POSITION SHIFT NF= 2 -1.32307158E-01
    
```

```

IMAGE POSITION SHIFT NF= 3 1.32220951E+00
IMAGE POSITION SHIFT NF= 3 -1.89027861E-01
    
```

```

IMAGE POSITION SHIFT NF= 4 9.21718650E-01
IMAGE POSITION SHIFT NF= 4 -1.32307158E-01
    
```

```

IMAGE POSITION SHIFT NF= 5 9.18140271E-01
IMAGE POSITION SHIFT NF= 5 -1.32262519E-01
    
```

```

FOCAL PLANE SHIFT 5.99413702E-01
    
```

```

FOCAL PLANE TILT Y-DIRECTION 9.34507704E-03
    
```

```

COMPENSATORS
BEGIN END DX DY DZ TILTY TILTZ DC DN DT DRMS MORE
22 22 -0 -0. -0. -0. 1.000E-03 -0. -0. -0. 4.785E+00 1.285E-07 -0
31 31 -0 -0. -0. -0. -0. 1.000E-03 -0. -0. 1.692E+00 3.748E-07 -0
    
```

WEIGHTED SUM**2 PL= 5.34216533E-09 RMS=

SINE ANGLE		PL ERROR IN WAVES	INTERCEPT ERROR IN MICRONS
-0.002000	RMS	.0193	1.18
	WORS	.0795(1.16)	2.53(1)
-0.001000	RMS	.0115	1.69
	WORS	.0589(3.1)	7.80(1)
0.000000	RMS	.0049	.67
	WORS	.0192(3.29)	1.66(16)
.001000	RMS	.0093	1.08
	WORS	.0414(24.1)	5.58(41)
.002000	RMS	.0173	.91
	WORS	.0721(24.41)	2.28(39)

FIGURE I-2 COMPUTER ANALYSIS RESULTS FOR CASE B (Continued)

PERTURBATION
 BEGIN END DX DY DZ TILTY TILTZ DC DN DT DRMS MORE
 23 30 -0 2.310E-02 6.304E-01 1.667E-01 2.800E-04 4.900E-05 -0. -0. 0. 0. 2
 PERTURBATION IS CONTINUED FROM LAST PERTURBATION CARD*****
 WEIGHTED SUM**2 PL= 1.07694471E-01 RMS= 3.26706654E-01 3.34836561E-01 3.47655513E-01 3.60463544E-01 3.68197353E-01

IMAGE POSITION SHIFT NF= 1 -1.47639690E-01
 IMAGE POSITION SHIFT NF= 1 -4.53497038E-02

IMAGE POSITION SHIFT NF= 2 -1.51190840E-01
 IMAGE POSITION SHIFT NF= 2 -4.54147959E-02

IMAGE POSITION SHIFT NF= 3 -2.21241883E-01
 IMAGE POSITION SHIFT NF= 3 -6.49053045E-02

IMAGE POSITION SHIFT NF= 4 -1.58596970E-01
 IMAGE POSITION SHIFT NF= 4 -4.54147959E-02

IMAGE POSITION SHIFT NF= 5 -1.62407175E-01
 IMAGE POSITION SHIFT NF= 5 -4.53497038E-02

FOCAL PLANE SHIFT 9.20197974E-01

FOCAL PLANE TILT Y-DIRECTION -8.17406998E-03

COMPENSATORS
 BEGIN END DX DY DZ TILTY TILTZ DC DN DT DRMS MORE
 22 22 -0 -0. -0. -0. 1.000E-03 -0. -0. -0. -0. 4.521E+00 1.147E-07 -0
 31 31 -0 -0. -0. -0. -0. 1.000E-03 -0. -0. -0. 2.399E+00 7.533E-07 -0

WEIGHTED SUM**2 PL= 0.60063101E-09 RMS=

SINE ANGLE	PL ERROR IN WAVES	INTERCEPT ERROR IN MICRONS
0.002000 RMS	.0150	.90
WORSI	.0695(10:41)	2.32(1)
0.001000 RMS	.0096	.97
WORSI	.0408(10:41)	4.44(1)
0.000000 RMS	.0035	.42
WORSI	.0147(29:41)	.77(33)
0.001000 RMS	.0091	.65
WORSI	.0371(1:10)	2.44(41)
0.002000 RMS	.0196	.87
WORSI	.0834(41:10)	2.09(39)

FIGURE I-2 COMPUTER ANALYSIS RESULTS FOR CASE B (Continued)

```

PERTURBATION
BEGIN END DX DY DZ TILTY TILTZ DC DN DT DRMS MORE
31 31 -0 7.370E-01 0. 0. -2.000E-04 -2.000E-05 -0. -0. 0. 0. 2
PERTURBATION IS CONTINUED FROM LAST PERTURBATION CARD*****
WEIGHTED SUM**2 PL= 1.15747179E-01 RMS= 1.14814669E+00 1.14028252E+00 1.12719616E+00 1.11387181E+00 1.10564747E+00
    
```

```

IMAGE POSITION SHIFT NF# 1 -2.52853139E-01
IMAGE POSITION SHIFT NF# 1 -4.53497042E-02
    
```

```

IMAGE POSITION SHIFT NF# 2 -2.56356101E-01
IMAGE POSITION SHIFT NF# 2 -4.54147964E-02
    
```

```

IMAGE POSITION SHIFT NF# 3 -3.71462103E-01
IMAGE POSITION SHIFT NF# 3 -6.49053051E-02
    
```

```

IMAGE POSITION SHIFT NF# 4 -2.63762231E-01
IMAGE POSITION SHIFT NF# 4 -4.54147964E-02
    
```

```

IMAGE POSITION SHIFT NF# 5 -2.67620624E-01
IMAGE POSITION SHIFT NF# 5 -4.53497042E-02
    
```

```

FOCAL PLANE SHIFT 1.99419797E+00
    
```

```

FOCAL PLANE TILT Y-DIRECTION -9.31074698E-03
    
```

```

COMPENSATORS
BEGIN END DX DY DZ TILTY TILTZ DC DN DT DRMS MORE
22 22 -0 -0. -0. -0. 1.000E-03 -0. -0. -0. -5.217E+00 1.527E-07 -0
31 31 -0 -0. -0. -0. -0. 1.000E-03 -0. -0. 2.419E+00 7.659E-07 -0
    
```

WEIGHTED SUM**2 PL= 5.43326098E-09 RMS=

SINE ANGLE	PL ERROR IN WAVES	INTERCEPT ERROR IN MICRONS
-0.002000	RMS WORSI	1.00 2.51(1)
-0.001000	RMS WORSI	1.10 5.18(1)
0.000000	RMS WORSI	.42 .74(33)
.001000	RMS WORSI	.75 3.19(41)
.002000	RMS WORSI	.45 2.38(39)

THIS PAGE INTENTIONALLY LEFT BLANK

REFERENCES

1. Space Data Relay Subsystem: Laser Communications; Preliminary Subsystem Design, Nov. 1971, SAMSO TR-71-251.
2. Lab Subsystem Performance Evaluation, Jan. 1973, AFAL-TR-385
3. P. O. Minott, J. L. Bufton, and M. W. Fitzmaurice, Results of the Balloon Atmospheric Propagation Experiment Flights of 1970 (BAPE I), March 1972, NASA X-524-72-125.
4. R. E. Hufnagel, Restoration of Atmospherically Degraded Images, Woods Hole Summer Study, (1966), Vol. 2, Appendix 3, p. 15-18.
5. M. E. Gracheva, A. S. Gurvich, and M. A. Kallistratova, Measurements of the Variance of 'Strong' Intensity Fluctuations of Laser Radiation in the Atmosphere, Izv. Vyssh. Ucheb. Zaved. Radiofiz., vol. 13, pp. 55-60, 1970.
6. G. R. Ochs and R. S. Lawrence, Measurements of Laser Beam Spread and Curvature Over Near-horizontal Atmospheric Paths, U. S. Govt. Printing Office, Washington, D. C., ESSA Tech. Rept. ERL 106-WPL 6, 1969.
7. G. R. Ochs, Measurements of 0.63 μ m Laser-beam Scintillation in Strong Atmospheric Turbulence, U. S. Govt. Printing Office. Washington, D.C., ESSA Tech. Rept. ERL 154-WPL 10, 1970.
8. G. E. Meyers, M. P. Keister, Jr., and D. L. Fried, Optical Propagation Measurements at Emerson Lake-1968, Dec. 1968, C8-3042/401.
9. J. R. Kerr, Experiments on Turbulence Characteristics and Multiwavelength Scintillation Phenomina, J. Opt. Soc. Am. Vol. 62, (9) Sept. 1972 pp. 1040-1048.
10. J. L. Bufton, P. O. Minott, M. W. Fitzmaurice and P. J. Titterton, Measurements of Turbulence Profiles in the Troposphere, J. Opt. Soc. Am. Vol. 62, (9) Sept. 1972, pp. 1068-1070.
11. Space Data Relay Subsystem: Laser Communications; Preliminary Subsystem Design, Nov. 1971, SAMSO TR-71-251. Appendix K.
12. J. L. Bufton, An Investigation of Atmospheric Turbulence by Stellar Observations, Aug. 1971, NASA TR-R-369

13. J. L. Bufton, Correlation of Microthermal Turbulence Data With Meteorological Soundings in the Troposphere, (to be published).
14. R. S. Lawrence, G. R. Ochs, and S. F. Clifford, Measurements of Atmospheric Turbulence Relevant to Optical Propagation, June 1970, J. Opt. Soc. Am., Vol. 60 (6), pp. 826-830.
15. Hardy, K. R. and Katz, I., Probing the Clear Atmosphere with High Power, High Resolution Radars, 1969, Proc. IEEE, 57, 468-480.
16. B. M. Koprov and L. R. Tsvang, Direct Measurements of Turbulent Heat Flux from an Airplane, Izv. Atmos. and Ocean Phys., 1965, Vol. 1 (6), pp. 643-648.
17. M. Subramanian, Atmospheric Turbulence Profile in Troposphere, April 1971, Opt. Soc. Am. Meeting, Tucson, paper WB21.
18. L. R. Zwang, Measurements of Temperature Pulse Frequency Spectra in the Surface Layer of the Atmosphere, 1960, Izv. Geophys. Ser., pp. 1252-1262.
19. L. R. Zwang, Measurements of the Spectrum of Temperature Fluctuations in the Free Atmosphere, 1960, Izv. Geophys. Ser., pp. 1674-1678.
20. P. J. Titterton, L. E. Mallery and T. A. Arken, Lightweight Thermosonde System, Dec. 1971, Contract NAS5-11493.
21. R. B. Fluchel, D. A. Fogle, G. M. Lee, Non-Ideal Photoelectron Counting, Submitted to IEEE Transactions on Information Theory.
22. Military Standardization Handbook, Metallic Materials and Elements for Aerospace Vehicle Structures, 1 Sept. 1971, MIL-HDBK-5B.
23. Non Metallic Materials, Society of Aerospace Material and Process Engineers, 1972.
24. Laser Communication Preliminary Subsystem Design for the Space Data Relay Subsystem, Final Report SAMSO TR-71-252, Nov. 1971.
25. J. Jackson, Relationships of Optics Weight to Pulse Gating Capability of the Detector in a High Data Rate Pulsed Laser Communication System, Nov. 1968, MDAC Memo 413-AT-81194.
26. Short Pulse Laser Modulation Techniques, June 1970, Final Report AFAL-TR-70-130.
27. J. Jackson, et. al., Parabolic Array of Spherical Segments for a Direct Detection Optical Receiver, Dec. 1970, Appl. Optics. Vol. 9, pp. 2798-99.

28. V. I. Tatarski, Wave Propagation in a Turbulent Medium, (Dover, New York) 1967, Chapter 10.
29. Derivable from $n - 1 = \left\{ 77.6 \frac{P}{T} + \frac{0.584}{T\lambda^2} P \right\} 10^{-6}$, found in the Handbook of Geophysics, (New York, 1960), the perfect gas law and the experimentally verified assumption that pressure variations are negligible, pp. 13-1, 13-2.
30. E. Brookner, Improved Model for the Structure Constant Variations with Altitude, Aug. 1971, App. Opt., Vol. 10 (8), pp. 1960-1962.
31. P. O. Minott, Scintillation in an Earth-to-Space Environment, July 1972, J. Opt. Soc. Am., Vol 62 (7), pp. 885-888.
32. P. J. Titterton, Estimate of Scale Height of Atmospheric Refractive-Index Structure Constant, March 1970, J. Opt. Soc. Am., Vo. 60 (3), pp. 417-418.
33. D. L. Freid, Diffusion Analysis for the Propagation of Mutual Coherence, July 1968, J. Opt. Soc. Am., Vol. 58 (7), pp. 961-969.
34. R. A. Schmeltzer, Means, Variances and Covariances for Laser Beam Propagation Through a Random Medium, 1967, Quart. Appl. Math., vol., 24, pp. 339-354.
35. H. Kogelnik and T. Li, Laser Beams and Resonators, 1966, Proc. IEEE, Vol. 54 (10), pp. 1312-1329.
36. J. R. Priebe, A Narrow Beam, Broad Bandwidth Optical Communication System, Sept. 15, 1969, N71-17347.
37. R. Exposito, Power Scintillations Due to the Wandering of the Laser Beam, Aug. 1967, Proc. IEEE (Letters), Vol. 55 (8), pp. 1533-1534.
38. P. J. Titterton, D. P. Woodman et. al., Sept. 1972, Optical Propagation Tests Study, AFAL-TR-72-307.
39. R. F. Lutomirski and H. T. Yura, July 1971, Propagation of Finite Optical Beam in an Inhomogeneous Medium, July 1971, App. Opt., Vol. 10 (7), pp. 1652-1658.
40. R. F. Lutomirski and H. T. Yura, Wave Structure Function and Mutual Coherence Function on an Optical Wave in a Turbulent Atmosphere, April 1971, J. Opt. Soc. Am., Vol. 61 (4), pp. 482-487.
41. H. T. Yura, Atmospheric Turbulence Induced Beam Spread, Dec. 1971, Applied Optics, Vol. 10 (12), pp. 2771-2773.

42. D. L. Fried, Statistics of a Geometric Representation of Wavefront Distortion, Nov. 1965, J. Opt. Soc. Am., Vol. 55 (11), pp. 1427-1435.
43. V. I. Tatarski, Wave Propagation in a Turbulent Medium, 1967, (Dover, New York).
44. M. A. Kallistratova, Fluctuations in the Direction of Propagation of Light Waves in an Inhomogeneous Turbulent Medium, 1966, Izv. Vuz Radiofizika, Vol. 9 (1), pp. 50-56.
45. Reference 43, pp. 154, 155.
46. R. S. Lawrence and J. W. Strohbehn, A Survey of Clear-Air Propagation Effects Relevant to Optical Communications, Oct. 1970, Proc. IEEE, Vol. 58 (10), pp. 1543, Figure 10.
47. S. F. Clifford, Temporal-Frequency Spectra for a Spherical Wave Propagating Through Atmospheric Turbulence, 1971, J. Opt. Soc. Am., Vol. 61 (10), pp. 1285-1292.
48. Reference 24, Appendix B.
49. Space Data Relay Subsystem: Laser Communications, Preliminary Subsystem Design, Nov. 1971, SAMSO TR-71-251, pp. (1-15)-(1-18).
50. D. L. Fried, Limiting Resolution Looking Down Through the Atmosphere, 1966, J. Opt. Soc. Am., Vol. 56 (10), pp. 1380-1389.
51. F. Bowman, Introduction to Bessel Functions, 1958, (Dover, New York).
52. H. Kogelnik and T. Li, Laser Beams and Resonators, 1966, Proc. IEEE, Vol. 54 (10), pp. 1312-1329.
53. R. E. Hufnagel and N. R. Stanley, Modulation Transfer Function Associated with Image Transmission through Turbulent Media, Jan. 1964, J. Opt. Soc. Am., Vol. 54, pp. 52-61.
54. Z. I. Feizulin and Yu A. Kravtsov, Broadening of a Laser Beam in a Turbulent Medium, Radiophysics and Quantum Electronics, 1967, Vol. 10 (1) pp. 33-35
55. R. W. Lee and J. C. Harp, Weak Scattering in Random Media, with Applications to Remote Probing, April 1969, Proc. IEEE, Vol. 57, pp. 375-406.

56. A. Ishimaru, Fluctuations of a Beam Wave Propagating through a Locally Homogeneous Medium, 1969, Radio Sci., Vol. 4, pp. 295-305.
57. Fluctuations of a Focused Beam Wave for Atmospheric Turbulence Probing, April 1969, Proc. IEEE, Vol. 57, pp. 407-414.
58. R. S. Lawrence and J. W. Strohbehn, A Survey of Clear-Air Propagation Effects Relevant to Optical Communications, Oct. 1970, Proc. IEEE, Vol. 58 (10), pp. 1523-1545.
59. Ross, M, Laser Receivers, John Wiley and Sons, Inc.
New York, 1966
60. Wolf, J. D., McDonnell Douglas Astronautics Company, Private
Communication, 19 May 1969.